ABSTRACT

Title of Dissertation: THE DIVERSITY OF MASSIVE STELLAR DEATH AND RELATIVISTIC JETS: UNRAVELING A COSMIC TANDEM

Gokul Prem Srinivasaragavan
Doctor of Philosophy, 2026

Dissertation Directed by: Professor M. Coleman Miller
Department of Astronomy

Stellar engine-driven transients are spectacular cosmic explosions that occur when a massive star undergoes a core-collapse supernova (SN) and collapses into a black hole or neutron star (compact object), launching relativistic jets. These jets are beams of plasma that are the fastest moving objects in the Universe, moving at 99.999% of the speed of light. Studies of stellar engine-driven transients probe extreme physics, allowing tests of gravity, dense matter, accretion, and particle acceleration in environments impossible to recreate on Earth. This dissertation delves into different observational studies on various classes of stellar engine-driven transients, aiming to shed light on a fundamental question in astrophysics: how do some compact objects generate the fastest and most powerful outflows in the Universe?

This dissertation begins with a brief overview of the landscape of stellar engine-driven transients, and is broken into four parts, corresponding to four distinct classes of stellar engine-driven

phenomena. Part 1 features two chapters on single-object studies studying SNe accompanying long gamma-ray bursts (LGRBs). Historically, the most studied class of stellar engine-driven transients is LGRBs, which are discovered via their high-energy gamma-ray prompt emission. They are followed by afterglows that light up the entire EM spectrum for months. LGRBs are usually found at distances too far to detect their associated SNe – only ~ 50 LGRBs have robust SN associations (LGRB-SNe) compared to thousands of LGRB discoveries, making every new LGRB-SN discovery significant. Chapter 2 focuses on GRB 221009A, the brightest and most energetic GRB ever detected. Chapter 3 focuses on GRB 230812B, another nearby and highly energetic LGRB. In addition to characterizing their associated SNe, I performed a statistical analysis of the most updated sample of LGRB–SNe ever presented in the literature, revealing no correlation between LGRB energetics and their associated SN brightness. This demonstrated that the physics powering stellar collapse is decoupled from the mechanisms that launch relativistic jets in LGRB-SNe.

Nearly all LGRB-SNe are broad-lined Type Ic SNe (SNe Ic-BL). These SNe originate from massive stars stripped of their outer hydrogen and helium envelopes and have high ejecta velocities. The local LGRB rate is 10^{-3} – 10^{-6} times the local SNe Ic-BL rate, and even after accounting for viewing angle effects, it is clear most SNe Ic-BL do not produce relativistic outflows. To probe why, Part 2 and Chapter 4 of this dissertation feature the largest systematic study of SNe Ic-BL to date, analyzing 36 events detected by the Zwicky Transient Facility (ZTF). A subset of these events was observed at radio wavelengths. Radio observations probe non-thermal emission associated with the fastest moving ejecta, which could be due to relativistic jets in SNe Ic-BL. Through a joint optical–radio analysis of the subsample, I surprisingly found no correlations between optical and radio properties.

Wide-field optical surveys such as ZTF are discovering afterglows without corresponding gamma-ray triggers. Some of these events have no associated gamma-ray counterparts, and are thus known as orphan afterglows. It is not well understood why – viewing angle effects, complex jet structures, and baryon-loaded GRBs or "dirty fireballs" have all been proposed scenarios. Part 3 and Chapter 5 of this dissertation features a multi-wavelength study of AT 2023sva, the sixth orphan afterglow with a redshift measurement. Through detailed light-curve modeling, I showed its missing gamma-ray emission is best explained by observing a structured jet slightly off-axis, with its energy concentrated in a narrow core, dropping off at wider angles. This placed AT 2023sva among a small set of engine-driven events with direct evidence for angular jet structure.

X-ray flashes (XRFs) are engine-driven explosions with unknown progenitors whose spectra peak at lower energies than those of LGRBs (hundreds of keV), but higher energies than those of SNe (tens of eV). Their past discoveries were limited by the lack of sensitive all-sky soft X-ray instruments. However, the recently launched Einstein Probe (EP) is well-equipped to discover XRFs, with over 100 times the field of view and vastly greater sensitivity than previous missions. Part 4 of this dissertation features two chapters presenting multi-wavelength studies on two SNe accompanying XRFs (XRF-SNe). Chapter 6 features EP250108a/SN 2025kg, one of the earliest EP XRF–SN discoveries. I found the progenitor system was likely a black hole formed after stellar collapse that launched a relativistic jet, which interacted strongly with an extended circumstellar medium (CSM). Chapter 7 features EP250827b/SN 2025wkm. I determined the event showed direct evidence for prolonged central engine activity and was likely powered by a magnetar remnant and CSM interaction.

THE DIVERSITY OF MASSIVE STELLAR DEATH AND RELATIVISTIC JETS: UNRAVELING A COSMIC TANDEM

by

Gokul Prem Srinivasaragavan

Dissertation submitted to the Faculty of the Graduate School of the
University of Maryland, College Park in partial fulfillment
of the requirements for the degree of
Doctor of Philosophy
2026

Advisory Committee:
Professor M. Coleman Miller, Chair/Advisor
Dr. S. Bradley Cenko, Co-Advisor
Professor Sylvain Veilleux
Professor Anna Y.Q. Ho (External Examiner)
Professor Jordan Goodman (Dean's Representative)

© Copyright by
Gokul Prem Srinivasaragavan
2026

Preface

The works presented in chapters 2, 3, and 6 (Srinivasaragavan et al., 2023, 2024a, 2025a) are published in the Astrophysical Journal Letters, the work presented in chapter 4 (Srinivasaragavan et al., 2024b) is published in the Astrophysical Journal, and the work presented in chapter 5 (Srinivasaragavan et al., 2025b) is published in the Monthly Notices of the Royal Astronomical Society. The work presented in chapter 7 (Srinivasaragavan et al., 2025c) is in the review process for the Astrophysical Journal Letters. These chapters are presented either as-is, or with minor modifications from the published or submitted versions of the manuscripts.

Acknowledgments

This dissertation would not have been possible without the support of many who provided me guidance, love, and friendship throughout the past five years, and many for much longer prior to me beginning graduate school.

To my advisor, Brad Cenko: thank you for being the GOAT (greatest of all time) advisor. Your unwavering support in my academic endeavors and your calm, kind demeanor no matter what situation presented itself gave me the perfect environment to succeed as a graduate student. It has been an honor to learn from you the past five years, and you will always be one of my main academic role models. To my campus advisor Cole Miller: thank you for being such a strong advocate for me over the past five years. You saw potential in me that I did not see in myself during the beginning of my graduate school career, and your guidance over the years has helped mold me into the scientist I am today. To Anna Ho: thank you for taking me under your wing as an external graduate student three years ago. Being a member of the Cornell Transients group allowed me to blossom and expand my horizons during the final chapter of my graduate school career, and your guidance and trust in me to lead multiple publications associated with your group changed the trajectory of my graduate school career. To Mansi Kasliwal: thank you for continuing to support and be such a strong advocate for me, continuing from my years working with you as an undergraduate student. The opportunity to be a visiting student researcher at Caltech during the final year of my PhD also changed the trajectory of my graduate school career,

and allowed me to begin building my life together with Simi, and I am endlessly grateful to you.

To Tony Piro and Nikhil Sarin: thank you for sharing your seemingly endless theoretical knowledge on transient astrophysics with me over the past few years. Creating strong collaborations with theorists was a major goal of mine going into my final years of graduate school, and I am extremely lucky to have such strong and kind theorists in my corner as I progress in my career. To Jesper Sollerman and Daniel Perley: thank you for your support over my graduate school career - sharing your knowledge on time-domain astronomy, especially through your very detailed comments on my papers before submission, have made me a much stronger scientist. To Ronald Gamble: thank you for being such a strong advocate and mentor for me over the past few years. Your support and the opportunity to be a leader in the NASA Cosmic Pathfinders program expanded my professional horizons and was one of the highlights of my graduate school career. To all of the coauthors for the works presented in this dissertation: thank you so much for your help and support over the past five years. I have thoroughly enjoyed doing science and collaborating with everyone who is a part of the papers I have written, and I am grateful. To Maryam Modjaz: thank you for being a strong supporter of my work, and helping me advise my first student researcher. To Muhammad Mousa: thank you for being a joy to work with as a undergraduate researcher. I look forward to all of your future success in this field, your future is extremely bright.

To my time-domain astronomy friends, Tomás Ahumada, Shreya Anand, Kaustav Das, Erica Hammerstein, K-Ryan Hinds, Wynn Jacobson-Galán, Brendan O'Connor, Jillian Rastinejad, Genevieve Schroeder, and many more: thank you for your friendship over my graduate school career. I am blessed to have made so many kind, supportive friends through my research network, and look forward to continuing our friendships as the years move forward. To my graduate

school friends: Amethyst Barnes, Giannina Guzmán Caloca, Serena Cronin, Jordan Ealy, Jordan Forman, Emma Mirizio, and more: thank you for all of the memories over the past five years. The community that surrounded me during graduate school was a major reason that I had the success I did in my career. To the Caltech Men's Basketball Team and Coaching Staff: thank you for all of the memories we made during my year as an assistant coach during the final year of my PhD. I am grateful for the trust you placed in me as a first-year assistant, and look forward to seeing the program's success in the future.

To my friends who have become family, Isiah Holt and Kavic Kumar: thank you for all of your support over the past five years. I will forever cherish the memories we made during graduate school, and I am proud to call you my brothers. To Noah Barnes and Renee Su: thank you for making Baltimore a second home for me during my PhD. All those weekends we spent together and the memories we made were some of the best times of the past five years. To Johnny Seebeck and Rae Moar: thank you for your friendship since my undergraduate years. I am so grateful that we ended up in the same place for graduate school. To Laith Anqud and Emily Yee: thank you for being some of my strongest supporters over the years. Simi and I are so excited to spend the upcoming years together in Chicago. To Ashal Shahzad and Rokaya Shenasa: thank you for always putting smiles on our faces over the years. Simi and I are so grateful for all the weekends you drove down to LA to see us, and we look forward to all the memories we will make in the future. To Brendon Macias: thank you for your support since our high school years, you have always been like a big brother to me. To Ishan Shah and Jason Zhou: thank you for your friendship since our high school years, and continuing to make time to hang out even during the busiest years of your life in medical school. I can't wait to see where your hard work takes you in the future. To Jon Babu: thank you for all the memories and laughs since our high school years,

we've been through too much together to describe in words and it's always love. To Eric Hsueh, Nick Ngyuen, and Aman Johal: thank you for your friendship since our high school years, and continuing to be some of my strongest supporters and advocates for a decade since. I appreciate you all.

To my family whom without none of this would be possible, Simi Bhullar: thank you for your unwavering love, support, and care over the past five years. I am so excited to begin our lives together as husband and wife, and so much of this dissertation is a product of our relationship and love. Rahul Srinivasaragavan: thank you for all of your support for the past 21 years. I am so proud to have seen all your growth over the past five years and to see you grow into a young man. Srini Venkatesan and Prema Thirunavukkarasu, Appa and Amma: this dissertation is the culmination of the past 26 years of unwavering and unconditional love and support you poured into me. I am forever grateful for everything you have done for me and for being my biggest role models in life.

Table of Contents

Preface ii

Acknowledgements iii

Table of Contents vii

List of Tables xiii

List of Figures xv

List of Abbreviations xx

Chapter 1: Introduction 1
- 1.1 LGRB-SNe . . . 8
- 1.2 SNe Ic-BL . . . 11
- 1.3 Orphan Afterglows . . . 12
- 1.4 X-ray Flashes . . . 15
- 1.5 Organization of Dissertation . . . 18

Chapter 2: A Sensitive Search for Supernova Emission Associated with the Extremely Energetic and Nearby GRB 221009A 21
- 2.1 Introduction . . . 21
- 2.2 Observations . . . 23
  - 2.2.1 GIT . . . 24
  - 2.2.2 LDT . . . 26
  - 2.2.3 Gemini-South . . . 26
- 2.3 Analysis and Model Selection . . . 27
  - 2.3.1 Previous Broadband Modeling Results . . . 27
  - 2.3.2 Optical Afterglow Modeling . . . 28
  - 2.3.3 Model Selection . . . 29
- 2.4 Supernova Parameter Estimation . . . 37
  - 2.4.1 Nickel Mass Estimates . . . 37
  - 2.4.2 Additional Explosion Properties . . . 41
- 2.5 Comparison to other GRB-SN . . . 43
- 2.6 Conclusion . . . 47

Chapter 3: Characterizing the Ordinary Broad-lined Type Ic SN 2023pel from the Energetic GRB 230812B 50
3.1 Introduction . . . 50
3.2 Observations . . . 53
3.2.1 *Swift* . . . 53
3.2.2 ZTF . . . 54
3.2.3 SEDM . . . 56
3.2.4 LT . . . 56
3.2.5 LDT . . . 57
3.2.6 GIT . . . 59
3.2.7 HCT . . . 60
3.2.8 Keck . . . 60
3.3 Afterglow Analysis . . . 61
3.3.1 Characterization of X-ray and Optical Afterglow . . . 61
3.3.2 SN Bump . . . 64
3.3.3 Spectrum Analysis . . . 67
3.4 SN Analysis . . . 69
3.4.1 Magnetar Model . . . 71
3.4.2 Arnett Model and SN parameters . . . 76
3.4.3 Comparison to GRB-SN population . . . 81
3.5 Conclusion . . . 84

Chapter 4: Optical and Radio Analysis of Systematically Classified Broad-lined Type Ic Supernovae from the Zwicky Transient Facility 89
4.1 Introduction . . . 89
4.2 SN Sample Description . . . 92
4.3 Observations . . . 96
4.3.1 ZTF . . . 97
4.3.2 SEDM . . . 97
4.3.3 SPRAT . . . 98
4.3.4 LRIS . . . 98
4.3.5 DBSP . . . 98
4.3.6 ALFOSC . . . 99
4.3.7 *Swift XRT and UVOT* . . . 99
4.3.8 VLA . . . 100
4.4 Supernova Lightcurves . . . 102
4.4.1 Light curve interpolation . . . 102
4.4.2 Light Curve Empirical Parameters . . . 106
4.4.3 Explosion epochs . . . 111
4.5 Supernova Spectra . . . 114
4.5.1 Photospheric Velocities . . . 116
4.5.2 Na I Equivalent Width . . . 117
4.6 Bolometric LCs and Properties . . . 121
4.6.1 Bolometric light curves and peak luminosites . . . 121
4.6.2 Blackbody Temperature and Radii Evolution . . . 122

4.7 Explosion Properties . . . 125
4.7.1 SN 2020wgz – a SLSN-I? . . . 133
4.8 Discussion in Context of Multi-Wavelength Observations . . . 135
4.8.1 Search for Gamma-rays . . . 136
4.8.2 Comparison of Explosion Properties with Radio Observations . . . 137
4.9 Summary and Conclusions . . . 139

Chapter 5: Multi-Wavelength Analysis of AT 2023sva: a Luminous Orphan Afterglow With Evidence for a Structured Jet 146
5.1 Introduction . . . 146
5.2 Observations . . . 150
5.2.1 ZTF Discovery . . . 150
5.2.2 Follow-up Observations . . . 152
5.2.3 Search for Associated GRB . . . 156
5.3 Optical and Radio Analysis . . . 159
5.3.1 Optical LC . . . 159
5.3.2 Optical SED and Spectroscopy . . . 161
5.3.3 Closure Relations . . . 163
5.3.4 Constraints from Radio Scintillation . . . 169
5.4 Physical Interpretation of the Outflow . . . 174
5.4.1 Multiwavelength Modeling . . . 174
5.4.2 Why the lack of γ-rays? . . . 182
5.4.3 Comparison to GRB Afterglows . . . 187
5.5 Summary and Conclusion . . . 191

Chapter 6: EP250108a/SN 2025kg: A Jet-Driven Stellar Explosion Interacting With Circumstellar Material 198
6.1 Introduction . . . 198
6.2 Observations . . . 201
6.2.1 X-ray and Gamma-Ray Observations . . . 202
6.2.2 LT . . . 203
6.2.3 NOT . . . 204
6.2.4 IMACS . . . 205
6.2.5 GHTS . . . 205
6.2.6 LRIS . . . 206
6.2.7 Binospec . . . 207
6.2.8 GMOS . . . 207
6.2.9 VLA . . . 208
6.3 Analysis . . . 208
6.3.1 Light Curve Analysis . . . 208
6.3.2 Bolometric Luminosity Light Curve . . . 211
6.3.3 Spectral Analysis . . . 213
6.3.4 Radio Analysis . . . 221
6.3.5 X-ray Analysis . . . 225
6.4 Light curve Modeling . . . 225

6.4.1 Radioactive Decay Model . . . 230
6.4.2 Model (a): SN Ejecta – CSM . . . 232
6.4.3 Model (b): Collapsar Jet-Driven Shocked Cocoon . . . 235
6.4.4 Model (c): Collapsar Jet-Driven Shocked Cocoon – CSM . . . 237
6.5 Expected X-ray Emission . . . 238
6.5.1 Model (a): SN Ejecta – CSM . . . 239
6.5.2 Model (b): Collapsar Jet-Driven Shocked Cocoon . . . 241
6.5.3 Model (c): Collapsar Jet-Driven Shocked Cocoon – CSM . . . 243
6.6 Discussion . . . 246
6.6.1 The Extended CSM Properties . . . 246
6.6.2 Understanding the X-ray and Radio Emission . . . 248
6.7 Conclusions . . . 252

Chapter 7: EP250827b/SN 2025wkm: An X-ray Flash-Supernova Powered by a Central Engine and Circumstellar Interaction 256
7.1 Introduction . . . 256
7.2 Observations . . . 261
7.2.1 X-ray Prompt Emission . . . 261
7.2.2 X-ray Follow-up Observations . . . 263
7.2.3 Gamma-Ray Constraints . . . 264
7.2.4 Radio Observations . . . 264
7.2.5 Photometric Observations . . . 265
7.2.6 Spectroscopic Observations . . . 271
7.3 Analysis . . . 273
7.3.1 X-ray Analysis . . . 273
7.3.2 Ultraviolet, Optical, and Near-Infrared Light Curve Analysis . . . 275
7.3.3 Bolometric Luminosity Light Curve . . . 280
7.3.4 Spectral Analysis . . . 283
7.3.5 Radio Analysis . . . 290
7.4 Estimating the X-ray Prompt Emission . . . 294
7.4.1 Cocoon Shock Breakout . . . 294
7.4.2 SN Ejecta Shock Breakout With an Extended CSM . . . 296
7.5 Modeling the Optical Emission . . . 299
7.5.1 Modeling the Late-time SN Emission . . . 300
7.5.2 Modeling the First Peak . . . 308
7.6 Discussion . . . 313
7.6.1 Invocation of Circumstellar Interaction . . . 313
7.6.2 The Progenitor System Landscape for XRF-SNe . . . 319
7.7 Conclusion . . . 323

Chapter 8: A Look to the Future 331

Appendix A: Supplementary Materials for Chapter 2 334

Appendix B: Supplementary Materials for Chapter 3 343

Appendix C: Supplementary Materials for Chapter 4 347
C.1 Discovery Paragraphs . . . 347
C.1.1 SN 2018bvw . . . 347
C.1.2 SN 2018ell . . . 347
C.1.3 SN 2018gep . . . 348
C.1.4 SN 2018hsf . . . 348
C.1.5 SN 2018keq . . . 348
C.1.6 SN 2019hsx . . . 349
C.1.7 SN 2019gwc . . . 349
C.1.8 SN 2019lci . . . 349
C.1.9 SN 2019moc . . . 349
C.1.10 SN 2019oqp . . . 350
C.1.11 SN 2019pgo . . . 350
C.1.12 SN 2019qfi . . . 350
C.1.13 SN 2020zg . . . 351
C.1.14 SN 2020ayz . . . 351
C.1.15 SN 2020bvc . . . 352
C.1.16 SN 2020dgd . . . 352
C.1.17 SN 2020hes . . . 352
C.1.18 SN 2020hyj . . . 352
C.1.19 SN 2020jqm . . . 353
C.1.20 SN 2020lao . . . 353
C.1.21 SN 2020rfr . . . 353
C.1.22 SN 2020rph . . . 354
C.1.23 SN 2020tkx . . . 354
C.1.24 SN 2020wgz . . . 354
C.1.25 SN 2020abxl . . . 354
C.1.26 SN 2020abxc . . . 355
C.1.27 SN 2020adow . . . 355
C.1.28 SN 2021bmf . . . 356
C.1.29 SN 2021epp . . . 356
C.1.30 SN 2021fop . . . 356
C.1.31 SN 2021hyz . . . 356
C.1.32 SN 2021ktv . . . 357
C.1.33 SN 2021ncn . . . 357
C.1.34 SN 2021qjv . . . 358
C.1.35 SN 2021too . . . 358
C.1.36 SN 2021ywf . . . 358
C.2 Spectral Sequences . . . 358
C.3 Multiwavelength Modeling . . . 365

Appendix D: Supplementary Materials for Chapter 5 384
D.1 Photometry and Radio observations of AT 2023sva . . . 384
D.2 Corner Plots . . . 389

Appendix E: Supplementary Materials for Chapter 6 392
E.1 Photometric, Spectroscopic, and Radio Observations 392
E.2 Corner Plots 394

Appendix F: Supplementary Materials for Chapter 7 399
F.1 Photometric, Spectroscopic and X-ray Observations 399
F.2 Corner Plots 415

Appendix G: Facilities and Software Used in this Thesis 417
G.1 Facilities 417
G.2 Software 418

Bibliography 420

List of Tables

2.1 Bayesian model selection fitting parameters for the afterglow+host and the afterglow+host+SN model. . . . 35
2.2 Best-fit physical parameters and their statistical 1σ errors corresponding to the three different host extinction scenarios presented in §2.4.1. . . . 41

4.1 Discovery properties of the SNe Ic-BL sample . . . 96
4.2 Priors used for the Bazin fits. . . . 106
4.3 Empirical parameters, explosion epochs, and peak r-band times for the SNe Ic-BL sample derived through the methods outlined in §4.4. We draw from results in previous works where applicable (described in §4.4.2.) . . . 110
4.4 Na I EW and resulting host galaxy extinction upper limits derived for events that show evidence of Na I absorption. . . . 121
4.5 Explosion properties and photospheric velocities for the SNe Ic-BL sample. Values reported include those newly derived and those presented in previous works. . . 128

5.1 Table of priors for `redback` fits. $\theta_{\rm w}$ is ignored by the tophat model and β is only used by the power law model. . . . 177
5.2 Final best-fit and median $\pm 1\sigma$ parameters for the power-law structured jet model, which is the most favored model for AT 2023sva. The best-fit parameters correspond to the model that possesses the maximum log likelihood and the corner plot corresponding to median parameters and their 1σ confidence intervals are presented in the Appendix. . . . 179

6.1 Photospheric velocity measurements of SN 2025kg. *The first measurement must be treated with caution, due to the uncertainty of a Fe II feature in the first spectra (see §6.3.3 for details). . . . 216
6.2 Explosion properties of SN 2025kg's radioactive decay (second) peak from LC modeling. . . . 232
6.3 Properties of model (a) for SN 2025kg (first peak) from LC modeling . . . 235
6.4 Properties of model (b) for SN 2025kg from LC modeling . . . 237
6.5 Properties of model (c) for SN 2025kg from LC modeling . . . 238
6.6 CSM Parameters for SNe Ic-BL in the literature. . . . 247

7.1 Spectral results of X-ray observations of EP250827b/SN 2025wkm. Errors represent the 1σ uncertainties. The upper limits are at the 90% confidence level. . . . 275
7.2 Photospheric velocity measurements of SN 2025wkm. . . . 287
7.3 Explosion properties of SN 2025wkm from the Arnett (1982) model . . . 302

7.4 Explosion properties of SN 2025wkm from the magnetar model (Omand & Sarin, 2024a). . . . 306
7.5 Peak Energy and CSM Parameters for EP XRF-SNe. . . . 319

A.1 Optical photometry and associated 1σ errors of GRB 221009A, which includes contributions from its afterglow, host galaxy, and associated SN 2022xiw. All times are in the observer frame. The magnitudes are not corrected for Galactic extinction. The photometry here was obtained by members of our collaboration. . . 337
A.2 Optical photometry and 1σ errors of GRB 221009A, including contributions from its afterglow, host galaxy, and associated SN 2022xiw, from publicly available GCNs. All times are in the observer frame. The magnitudes are not corrected for Galactic extinction. . . . 342

B.1 Optical photometry and 1σ errors of GRB 230812B/SN 2023pel. The photometry includes contributions from the afterglow and associated SN, and are all image-subtracted to correct for the host galaxy contribution. All times are in the observer frame, and the magnitudes are not corrected for Galactic extinction. . . . 346

C.1 Spectral log of observations. Spectrum phase is in rest-frame with respect to r-band maximum . . . 365
C.2 Model parameters, description, and priors used for the `arnett + tophat` model in the `redback` fitting. . . . 367
C.3 Model parameters, description, and priors used for the Radio SSA model (Chevalier, 1998) in the `redback` fitting. . . . 368

D.1 Optical photometry of AT 2023sva. The photometry in this table is not corrected for MW or host-galaxy extinction. . . . 388
D.3 AMI radio observations of AT 2023sva, obtained at 15.5 GHz. . . . 388

E.1 Optical photometry and 1σ errors of EP250108a/SN 2025kg. All times are in the observer frame, and the magnitudes are not corrected for Galactic extinction. Photometry obtained by GCNs is indicated with citations. . . . 393
E.2 Spectroscopic observations of EP250108a/SN 2025kg. Epochs are given in observer times since T_0. . . . 394
E.3 Very Large Array observations of EP 250108A. Upper limits correspond to 3σ. . . . 394

F.2 Photometry Log (magnitudes have not been corrected for Galactic Extinction $E(B-V) = 0.05$ mag. . . . 413
F.1 Log of X-ray observations . . . 414
F.3 Spectroscopic observations of EP250827b/SN 2025kg. Epochs are given in observer times since t_0. . . . 414

List of Figures

1.1 "Onion-skin" model of a CCSN progenitor, with the different layers resulting from nuclear burning of elements, starting from Hydrogen and ending with Iron. The layer thicknesses are not to scale. Figure from Jerkstrand et al. (2026). 2
1.2 Example spectra of different classes of CCSNe, with characteristic emission and absorption features labeled. Figure from Modjaz et al. (2019). 4
1.3 An artistic depiction of emission from a LGRB, including the prompt emission and afterglow phase. I note here that a neutron star engine can also create a LGRB. Figure credit NASA GSFC and ICRAR. 5
1.4 Kinetic energy profile of normal stripped envelope SNe (red), relativistic SNe (orange) found without an associated LGRB, sub-energetic LGRBs (light blue), and LGRBs (blue), compared to the velocity of their ejecta (computed at one rest-frame day after explosion). Circles represent inferences made from radio observations, while squares are from optical observations. All events with open circles are SNe Ic-BL. The magnetar-excluded region is at the top of the Figure, representing the maximum energy allowed from an explosion resulting from the spin-down of a magnetar progenitor. The black solid lines represent analytical models corresponding to purely hydrodynamical explosions ($(\Gamma\beta)^{-5.2}$; Tan et al. 2001), long-lived engine-driven explosions ($(\Gamma\beta)^{-0.4}$; Lazzati et al. 2012), and short-lived partially engine-driven explosions ($(\Gamma\beta)^{-2.4}$; Lazzati et al. 2012). Figure from Margutti et al. (2014) 7
1.5 Updated sample of LGRB-SNe from literature 10
1.6 Artistic depiction of possible progenitor scenarios for orphan afterglows. Figure credit Prof. Anna Ho. 14
1.7 Spectra and LCs of XRF-SNe from literature 17
1.8 Artistic depiction of different classes of stellar engine-driven transients, divided into successful and unsuccessful LGRBs. 19

2.1 LDT images of the optical afterglow of GRB 221009A. 25
2.2 Observed r′- and i′-band photometry of GRB 221009A 30
2.3 Model comparisons with and without SN contribution to GRB 221009A 34
2.4 SN model fits to GRB 221009A 40
2.5 Comparison of SN brightness to GRB isotropic equivalent luminosity for GRB-SN population 45

3.1 LDT images of the optical afterglow of GRB 230812B/SN 2023pel 58
3.2 Broadband modeling of the GRB afterglow from optical to X-ray wavelengths . . 63
3.3 Observed r and i band photometry of GRB 230812B 66

3.4 Spectrum of GRB 230812B/SN 2023pel . . . 70
3.5 Magnetar SN model fit to GRB 230812B/SN 2023pel . . . 75
3.6 LC of SN 2023pel . . . 76
3.7 Comparison of SN brightness to GRB isotropic equivalent energy for GRB-SN population . . . 83

4.1 Redshift distribution for the SNe Ic-BL sample . . . 94
4.2 SNe Ic-BL LCs and colors . . . 104
4.3 Example of LC fits for Sn 2020tkx . . . 105
4.4 M_r^{max} distribution of the SNe Ic-BL sample . . . 107
4.5 Investigation of the Malmquist bias on the SNe Ic-BL sample . . . 109
4.6 $\Delta m_{-10}(r)$ plotted against $\Delta m_{15}(r)$ for 32 SNe Ic-BL . . . 112
4.7 M_r^{max} plotted against $\Delta m_{15}(r)$ for 34 SNe Ic-BL . . . 113
4.8 Photospheric phase spectra and the SNID best match templates for the Ic-BL sample 115
4.9 Example of Fe II feature fit for the photospheric phase spectrum of SN 2018hsf . 118
4.10 Peak v_{ph} distribution for SNe Ic-BL sample . . . 119
4.11 v_{ph} as a function of time for the SNe Ic-BL sample . . . 120
4.12 M_{bol}^{max} distribution for SNe Ic-BL sample . . . 123
4.13 Bolometric luminosity LCs for the SNe Ic-BL sample . . . 124
4.14 Blackbody temperatwure and radii evolution for the SNe Ic-BL sample . . . 126
4.15 Histograms of the explosion properties derived for the SNe Ic-BL sample . . . 130
4.16 Explosion properties (M_{Ni}, M_{ej}, and E_K) plotted against each other. . . . 131
4.17 The best-fit magnetar powered model fit to SN 2020wgz . . . 135
4.18 Histograms showing the distribution of explosion properties and v_{ph} for the SNe Ic-BL with radio observations . . . 138
4.19 Best-fit Linmix linear regression model fitting between the peak radio luminosities and the explosion properties and v_{ph} . . . 140

5.1 Optical LC of AT 2023sva in the g, r, and i bands . . . 152
5.2 The IPN 3σ localization region for GRB 230917A compared to the point-source location of AT 2023sva . . . 160
5.3 Optical spectrum of AT 2023sva, obtained by the OSIRIS instrument . . . 162
5.4 The AMI and VLA radio LCs of AT 2023sva . . . 165
5.5 VLA Radio SEDs of AT 2023sva . . . 167
5.6 uGMRT observations of AT 2023sva . . . 168
5.7 Upper limit on the initial Lorentz factor Γ_0 plotted against the assumed rest-frame deceleration time t_{dec} . . . 171
5.8 Comparison of source size upper limits derived from ISS analyses for LGRBs and orphan afterglows . . . 172

5.9 *Left panel*: The optical observations of AT 2023sva, along with the best-fit power-law structured jet, tophat jet, and Gaussian structured jet fit to the observed LC. Optical fluxes have been multiplied by a constant factor for viewing purposes and have been corrected for MW and host galaxy extinction. *Right panel*: The 15.5 GHz radio observations of AT 2023sva and the X-ray upper limit, along with the best-fit power-law structured jet, tophat jet, and Gaussian structured jet fit to the observed LC. The X-ray limit has been multiplied by a constant factor for viewing purposes. . . . 178
5.10 Best-fit power-law structured jet model of AT 2023sva fit to multiwavelength data set . . . 179
5.11 Simulated optical SEDs from the best fit power-law structured jet model . . . 181
5.12 Comparison of the Lorentz factor evolution of $\Gamma \gg 300$ and $\Gamma \ll 300$ jet models with respect to different observed deceleration times. . . . 186
5.13 $E_{\gamma,\,\mathrm{iso}}$ plotted against the absolute r-band magnitude at 11 hours for GRBs in the literature and AT 2023sva . . . 188
5.14 Comparison of AT 2023sva's radio LC to other GRB afterglow LCs from literature 189

6.1 LT images of EP 250108a/SN 2025kg The left, large panel shows the wider field of view of EP 250108a, in r band 9.3 days after T_0. The right panels show the observations taken in the g, r, and i bands, as well as the Pan-STARRS1 templates used for photometry. The host galaxy is faint ($r \sim 23.2$; Dey et al. 2019), so image subtraction is not necessary until the final epoch. Images have been smoothed for display purposes. . . . 204
6.2 LC of SN 2025kg in g, r, and i bands . . . 209
6.3 Bolometric luminosity LC of SN 2025kg . . . 214
6.4 Optical spectra of SN 2025kg . . . 215
6.5 Spectra of SN 2025kg compared to spectra of SN 2006aj and SN 2020bvc . . . 217
6.6 Photospheric velocity evolution for SN 2025kg . . . 219
6.7 The 10 GHz radio light curve of our VLA non-detections of EP 250108A . . . 223
6.8 Comparison of 0.3 – 10 keV X-ray upper limits of EP 250108a/SN 2025kg to X-ray LCs of other GRBs . . . 226
6.9 Fitting of SN ejecta – CSM and the radioactive decay model in combination to the photometry of SN 2025kg . . . 234
6.10 Fitting of mCollapsar Jet-Driven Shocked Cocoon and radioactive decay model in combination to the photometry of SN 2025kg . . . 236
6.11 Fitting of Collapsar Jet-Driven Shocked Cocoon in Extended CSM and radioactive decay model in combination to the photometry of SN 2025kg . . . 239

7.1 WXT image and LC of EP250827b . . . 263
7.2 WXT observed spectrum of EP250827b . . . 274
7.3 Comparison of 0.3 – 10 keV X-ray upper limits of EP250827b/SN 2025kg to the X-ray LCs of other events . . . 276
7.4 LC of EP250827b/SN 2025wkm in UVM2, UVW1, and $grizJ$ bands . . . 277
7.5 g-band LC of SN 2025wkm in comparison to other double-peaked SN Ic-BL . . . 279
7.6 Bolometric luminosity LC of SN 2025wkm . . . 281

7.7 Blackbody temperature and radius evolution as a function of time for EP250827b 282
7.8 Spectra series of EP250827b/SN 2025wkm . . . 284
7.9 Close-up spectra of EP250827b/SN 2025wkm at 3.8 days and 18.8 days $+t_0$ (rest-frame) . . . 285
7.10 Photospheric velocity evolution for SN 2025wkm . . . 288
7.11 Late-time Keck LRIS spectrum of EP250827b . . . 290
7.12 0 GHz radio light curve of EP250827b compared to other events and models . . . 291
7.13 Radioactive decay model fit to photometry of SN 2025wkm . . . 302
7.14 Magnetar model fit to photometry of SN 2025wkm . . . 306
7.15 Semi-analytic fit of a subrelativistic energy distribution to the early time data of EP250827b . . . 312
7.16 Artistic depiction of the magnetar-driven disk cooling model . . . 314
7.17 r-band rest-frame LCs of EP XRF-SNe . . . 321
7.18 Amati relation of GRBs and XRFs in the literature . . . 323

C.1 Spectral sequences of SN 2018ell, SN 2018hsf, and SN 2018keq. The phases next to each spectrum are the rest-frame days since the maximum r-band flux from the GP processing. The spectra for the rest of the events except for those presented in single-object works (SN 2018bvw, SN 2018gep, and SN 2020bvc) are presented in a similar format below. . . . 369
C.2 Spectral sequences of SN 2019hsx, SN 2019gwc, SN 2019lci. . . . 370
C.3 Spectral sequences of SN 2019moc, SN 2019oqp, SN 2019pgo. . . . 371
C.4 Spectral sequences of SN 2019qfi, SN 2020zg, SN 2020ayz. . . . 372
C.5 Spectral sequences of SN 2020dgd, SN 2020hes, SN 2020hyj. . . . 373
C.6 Spectral sequences of SN 2020jqm, SN 2020lao, SN 2021qjv. . . . 374
C.7 Spectral sequences of SN 2020rfr, SN 2020rph, SN 2020tkx. . . . 375
C.8 Spectral sequences of SN 2020wgz, SN 2020abxl, SN 2020abxc. . . . 376
C.9 Spectral sequences of SN 2020adow, SN 2021bmf, SN 2021epp. . . . 377
C.10 Spectral sequences of SN 2021fop, SN 2021hyz, SN2021ktv. . . . 378
C.11 Spectral sequences of SN 2021ncn, SN 2021too, SN 2021ywf. . . . 379
C.12 `Redback` modeling results for SN 2020tkx, with the `arnett + tophat` model above and the Radio SSA model below. . . . 380
C.13 `Redback` modeling results for SN 2021ywf, with the `arnett + tophat` model above and the Radio SSA model below. . . . 381
C.14 `Redback` modeling results for SN 2020adow, with the `arnett + tophat` model above and the Radio SSA model below. . . . 382
C.15 `Redback` modeling results for SN 2020wgz, for the magnetar and nickel powered model. . . . 383

D.1 Corner plot for the power-law structured jet model, generated through `redback`. 389
D.2 Corner plot for the tophat model, generated through `redback`. . . . 390
D.3 Corner plot for the gaussian structured jet model, generated through `redback`. . . 391

E.1 Corner plots associated with fitting the Arnett (1982) radioactive decay model to the bolometric luminosity LC's second peak. . . . 395

E.2 Corner plots associated with fitting the combined SCE model from Piro et al. (2021) and radioactive decay model from Arnett (1982) to the photometry. 396
E.3 Corner plots associated with fitting the combined shocked cocoon model from Nakar & Piran (2017) and radioactive decay model from Arnett (1982) to the photometry. 397
E.4 Corner plots associated with fitting the combined shocked cocoon model in an extended CSM from Nakar (2015) and radioactive decay model from Arnett (1982) to the photometry. 398

F.1 Corner plot of fitting a Arnett (1982) radioactive decay model to the late-time SN LC at $t_0 + 7$ days. 415
F.2 Corner plot of fitting a combination of a Arnett (1982) radioactive decay model and spindown of a millisecond magnetar (Omand & Sarin, 2024a; Sarin et al., 2022) the late-time SN LC at $t_0 + 7$ days. 416

List of Abbreviations

ALFOSC	Alhambra Faint Object Spectrograph and Camera
AMI-LA	Arcminute Microkelvin Imager
ASM	All sky monitor
ATLAS	Asteroid Terrestrial-impact Last Alert System
BAT	Burst alert telescope
BC	Bolometric Correction
BIC	Bayesian Information Criterion
BTS	Bright Transient Survey
CSM	Circumstellar Medium
DBSP	Double Beam Spectrograph
DEIMOS	Deep Imaging Multi-Object Spectrograph
EP	Einstein Probe
EW	Equivalent width
EFXT	Extragalactic fast X-ray transient
FTW	Fraunhofer Telescope at Wendelstein Observatory
FXT	Follow-up X-ray Telescope
GALEX	Galaxy Evolution Explorer
GCN	General Coordinates Network
GBM	Gamma-Ray Burst Monitor
GIT	GROWTH India Telescope
GMOS	Gemini Multi-Object Spectrograph
GTC	Gran Telescopio Canarias
HAFFET	Hybrid Analytic Flux FittEr for Transients
HCT	Himalayan Chandra Telescope
HST	Hubble Space Telescope
iPTF	Intermediate Palomar Transient Factory
IPN	Interplanetary Network
ISM	Interstellar medium
ISS	Interstellar scintillation
JWST	James Webb Space Telescope
KCWI	Keck Cosmic Web Image
LC	Light Curve
LCO	Las Cumbres Observatory

LFBOT	Luminous fast blue optical transient
LGRB	Long Gamma-ray Burst
LDT	Lowell Discovery Telescope
LMI	Large Monolithic Imager
LRIS	Low Resolution Imaging Spectrometer
LT	Liverpool Telescope
MCMC	Markov chain Monte Carlo
MW	Milky Way
NGPS	Next Generation Palomar Spectrograph
NOT	Nordic Optical Telescope
NS	Neutron star
PS1	Panoramic Survey Telescope and Rapid Response System
PC	Photon Counting
PSF	Point spread function
SBO	Shock breakout
SCE	Shock cooling emission
SDSS	Sloan Digital Sky Survey
SED	Spectral energy distribution
SEDM	Spectral Energy Distribution Machine
SGRB	Short Gamma-ray Burst
SLSN	Superluminous supernova
SPRAT	Spectrograph for the Rapid Acquisition of Transients
SNe	Supernovae
SSA	Self-Synchrotron Absorption
TDE	Tidal disruption event
TNOT	Tsinghua-Nanshan Optical Telescope
TNS	Transient Name Server
TRT	Thai Robotic Telescope
VLA	Very Large Array
VLASS	Very Large Array Sky Survey
WISE	Wide-field Infrared Survey Explorer
WXT	Wide-field X-ray Telescope
XRF	X-ray Flash
XRT	X-ray Telescope
ZTF	Zwicky Transient Facility

Chapter 1: Introduction

The traditional picture for the end of massive stars' lives with zero-age main sequence (ZAMS) masses $\gtrsim 8\,\mathrm{M}_\odot$ involves different types of core-collapse supernovae (CCSNe) corresponding to the progenitor's properties, eventually resulting in the formation of a compact object remnant. Understanding massive stellar deaths is interesting for a variety of reasons to the broader astrophysical community – these spectacular explosions are important probes of stellar evolution, are the sites of heavy element formation through nucleosynthesis, and play important mediating roles in galactic evolution, producing feedback and quenching star formation.

From a stellar evolution perspective, massive stars undergo every stage of nuclear burning, successively fusing elements from Hydrogen to Iron in their cores (e.g., Janka et al. 2007; Woosley et al. 2002, 1995). Convective mixing processes feed the star's core with nuclear fusion fuel throughout this process (e.g., Burbidge et al. 1956; Heger et al. 2005; Woosley et al. 2002, 1995), leading to newly fused elements being transported back into the core, continuing the nuclear burning cycle. Once the star's core is composed of Iron, nuclear fusion stops, as it is the last energetically favorable element created through nuclear fusion (e.g., Bowers & Wilson 1982; Heger et al. 2003; Ohyama 1963). This results in an "onion skin"-like structure for massive stars, illustrated in Figure 1.1 from Jerkstrand et al. (2026). Though the Iron core does not undergo any further exothermic reactions to create heat and stabilize itself, it is instead supported by elec-

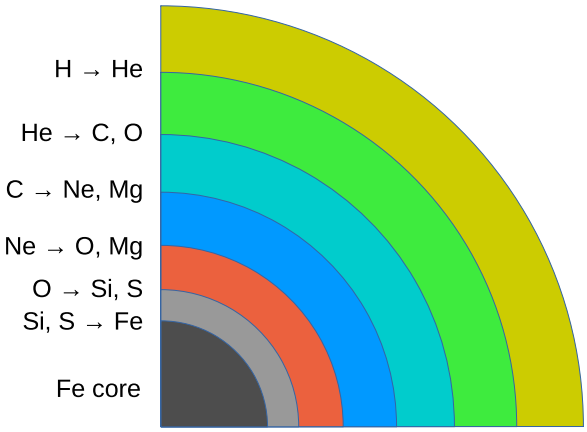

Figure 1.1: "Onion-skin" model of a CCSN progenitor, with the different layers resulting from nuclear burning of elements, starting from Hydrogen and ending with Iron. The layer thicknesses are not to scale. Figure from Jerkstrand et al. (2026).

tron degeneracy pressure, which balances against the star's gravitational collapse. Therefore, the Iron core acts as a white dwarf, which grows in mass until it reaches the Chandrasekhar limit of $\gtrsim 1.4\,\mathrm{M}_\odot$ (Chandrasekhar, 1931). At this point, electron degeneracy pressure cannot withstand the gravitational forces, and the star collapses, undergoing a CCSN (e.g., Janka et al. 2007; Woosley et al. 2002; Woosley & Weaver 1986).

The majority of stars retain their outer Hydrogen and Helium envelopes prior to stellar collapse, and are observed as Type II SNe. These SNe are classified by characteristic Hydrogen features in their spectra (Gal-Yam, 2017a). There are various subtypes of Type II SNe, including Type IIn SNe which possess narrow Hydrogen emission lines as a result of strong interaction with the surrounding circumstellar environment, and Type IIb SNe whose Hydrogen features are weaker and eventually transition to a spectrum dominated by Helium (Gal-Yam, 2017a).

However, some stars go through extremely intense mass-loss episodes, stripping their outer envelope layers, resulting in the formation of a Wolf-Rayet star. This mass-loss may be a product of stellar winds and radiatively driven mass-loss (Conti & Walborn, 1976) for very massive stars ($M_{\mathrm{ZAMS}} > 30\,\mathrm{M}_\odot$) or common envelope binary interactions (Lyman et al., 2016a; Taddia et al.,

2019a; Yoon et al., 2010a) for less massive stars ($M_{\rm ZAMS} < 30\,{\rm M}_{\odot}$). When they collapse, these Wolf-Rayet stars undergo what are known as stripped-envelope SNe. The spectra of these SNe are devoid of Hydrogen features, and are classified as Type Ib SNe if Helium absorption features are present, Type Ibn SNe if narrow Helium emission features are present, and Type Ic SNe if no Helium features are present. A subset of Type Ic SNe display broad absorption features in their optical spectra, corresponding to photospheric expansion velocities $\sim$ 15,000 to 30,000 km s^{-1} (Srinivasaragavan et al., 2024b; Taddia et al., 2019a), and are known as broad-lined Type Ic SNe (SNe Ic-BL). Figure 1.2 from Modjaz et al. (2019) shows the main classes of CCSNe and their corresponding spectra.

A small subset of SNe Ic-BL are accompanied by Long Gamma-ray Bursts (LGRBs; duration $T_{90} > 2\,{\rm s}$), which are short-lived flashes of gamma-ray photons released from highly collimated, ultra-relativistic jets driven by compact object central engines. They are the most electromagnetically luminous phenomena ever detected (Piran, 2004) and are often discovered at cosmological distances, providing a window into the early universe during their existence. LGRBs are prime sites for studying particle acceleration processes, accretion physics, relativistic jet formation mechanisms, and many other extreme physics impossible to probe on Earth.

Traditionally speaking, emission from LGRBs is twofold- the prompt emission (which lasts on the order of seconds) in the gamma-rays comes from accretion onto the black hole remnant or the rotational spin-down of the neutron star remnant, generating extremely collimnated ($\theta_0 \approx 10^{\circ}$) ultra-relativistic jets with initial Lorentz factors $\Gamma > 100$; and the afterglow emission (which lasts for months after the prompt emission) across the electromagnetic spectrum comes from the interaction of these jets with the surrounding circumstellar (CSM) and interstellar medium (ISM) (Woosley, 1993). Figure 1.3 shows an artistic depiction of the emission from LGRBs. LGRBs

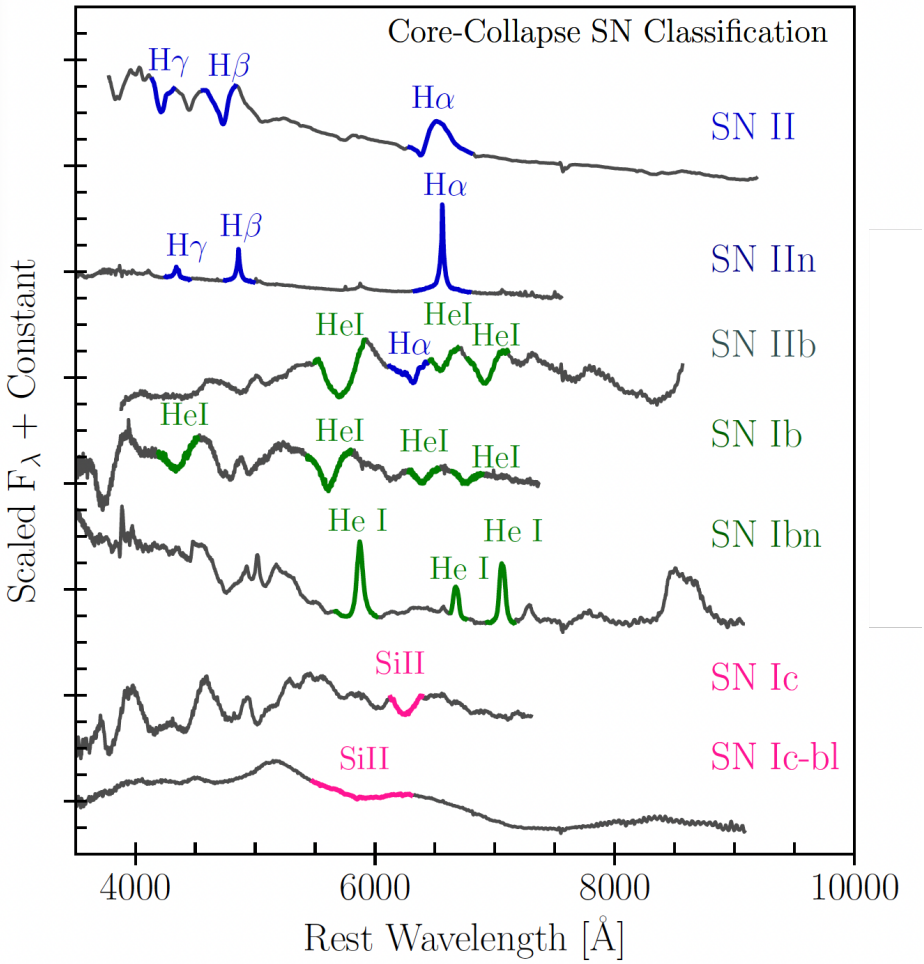

Figure 1.2: Example spectra of different classes of CCSNe, with characteristic emission and absorption features labeled. Figure from Modjaz et al. (2019).

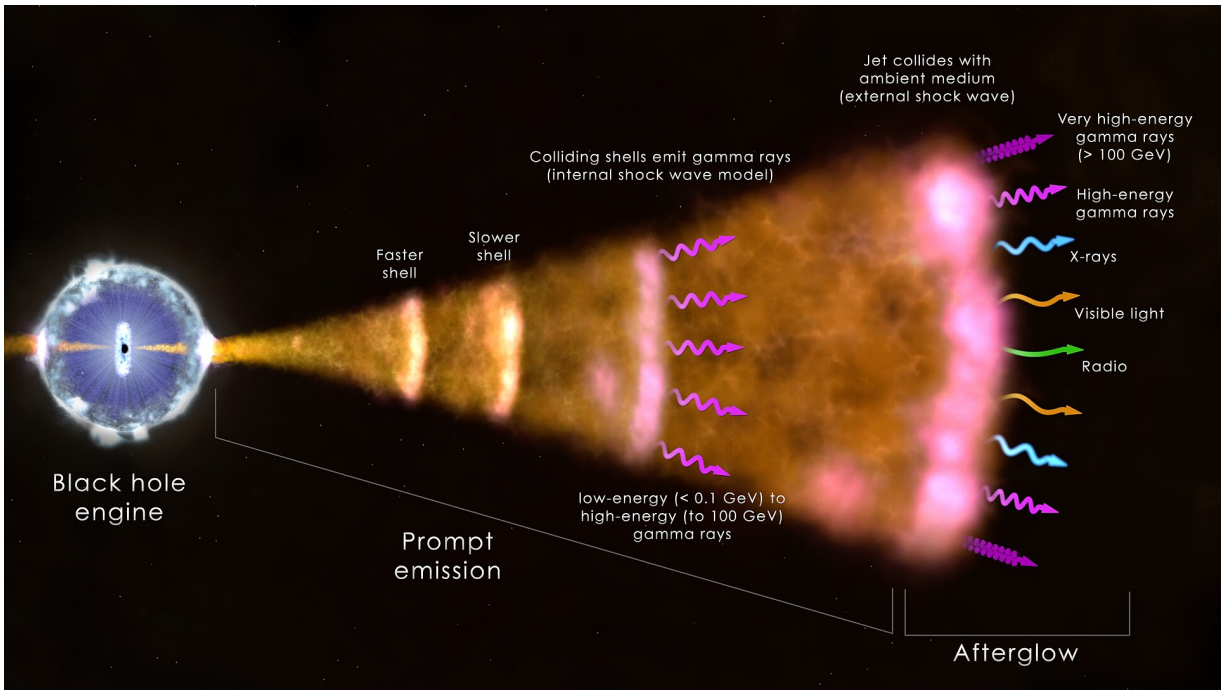

Figure 1.3: An artistic depiction of emission from a LGRB, including the prompt emission and afterglow phase. I note here that a neutron star engine can also create a LGRB. Figure credit NASA GSFC and ICRAR.

only arise from Wolf-Rayet progenitors, as jets cannot successfuly escape from stars that retain their dense outer Hydrogen and Helium envelopes (MacFadyen & Woosley, 1999).

LGRBs have been extensively studied over the past two decades, as many time-domain instruments focused on studying gamma-ray sky. Gamma-ray instruments such as *Fermi*'s Gamma-ray Burst Monitor (Meegan et al., 2009) and *Swift*'s Burst Alert Telescope (Barthelmy et al., 2005) significantly advanced the field, leading to the discoveries of thousands of LGRBs. However, many initial conditions need to be satisfied for LGRBs to be successfully observed. The jets need to be largely baryon-free, as matter-dominated jets will stifle gamma-ray emission through pair-production processes (Dermer et al., 1999). They also need to be pointed directly in the line of sight of Earth, as they are only visible within narrow angles due to relativistic beaming (Rhoads, 1997). In fact, most jets never escape their progenitor stars, getting choked or stifled

by various physical processes (Nakar & Piran, 2017), while jets that do escape are often pointed away from Earth. These scenarios do not produce visible gamma-ray emission, but can produce radiation at other wavelengths across the electromagnetic spectrum.

Therefore, relying on gamma-ray satellites to discover LGRBs exposes us to only a fraction of extreme stellar deaths, that are ultimately just a small slice of a broader landscape of "stellar engine-driven transients". I define these transients as the explosions associated with a massive star undergoing a CCSN and collapsing into a compact object, launching a relativistic jet in the process. There are no restrictions on the initial conditions here - it does not matter whether the jet was pointed towards Earth or not, whether or not the jet successfully escaped from its progenitor star, or even if it was a lower Lorentz factor moving jet. Stellar engine-driven transients can therefore be discovered across the electromagnetic spectrum, from radio to gamma-ray wavelengths, making them extremely important and versatile probes of a broad range of astrophysics.

Figure 1.4 from Margutti et al. (2014) shows a visualization of the landscape of stellar engine-driven transients, from the perspective of their kinetic energies and ejecta velocities, probed by either optical or radio observations. Optical observations (squares) probe thermal emission associated with the photosphere of the associated SNe, while radio observations (circles) probe non-thermal emission associated with the fastest-moving ejecta, either due to the emission from a relativistic jet in engine-driven systems, or self-synchrotron absorption from SN ejecta interacting with its surrounding CSM. All events that have open circles have associated SNe Ic-BL. The Figure shows that SNe Ic-BL exist in all regions of this parameter space, from non-relativistic, low-energy events to ultra-relativistic, high-energy events. In addition, there are several events whose radio observations show that they are in the border regime between non-relativistic and relativistic, with kinetic energies in between those of LGRBs and ordinary Type

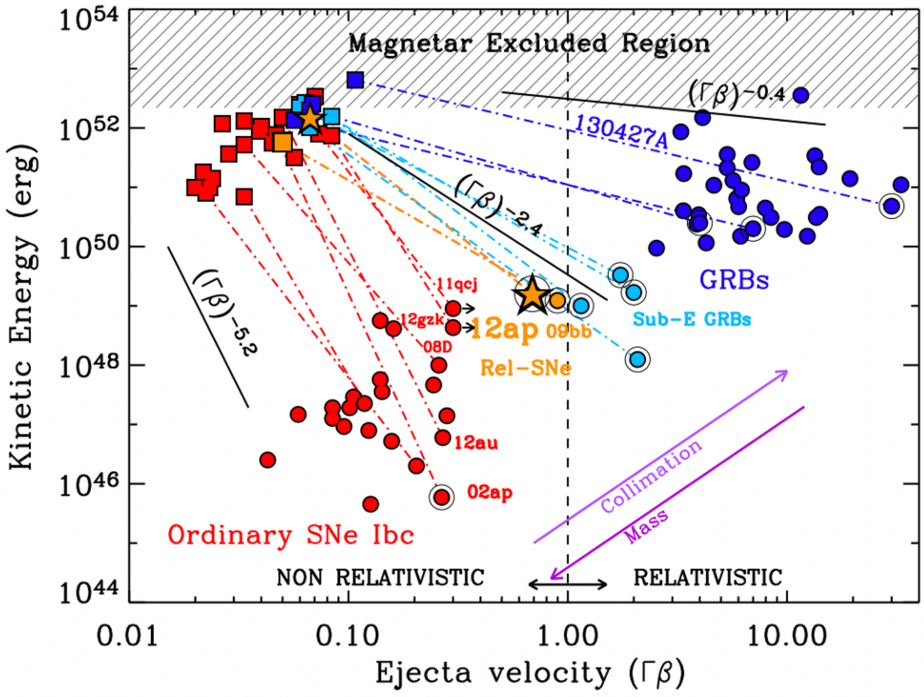

Figure 1.4: Kinetic energy profile of normal stripped envelope SNe (red), relativistic SNe (orange) found without an associated LGRB, sub-energetic LGRBs (light blue), and LGRBs (blue), compared to the velocity of their ejecta (computed at one rest-frame day after explosion). Circles represent inferences made from radio observations, while squares are from optical observations. All events with open circles are SNe Ic-BL. The magnetar-excluded region is at the top of the Figure, representing the maximum energy allowed from an explosion resulting from the spin-down of a magnetar progenitor. The black solid lines represent analytical models corresponding to purely hydrodynamical explosions ($(\Gamma\beta)^{-5.2}$; Tan et al. 2001), long-lived engine-driven explosions ($(\Gamma\beta)^{-0.4}$; Lazzati et al. 2012), and short-lived partially engine-driven explosions ($(\Gamma\beta)^{-2.4}$; Lazzati et al. 2012). Figure from Margutti et al. (2014)

.

Ic SNe.

This emphasizes that LGRBs represent just the tip of the iceberg in stellar engine-driven transient science. Events in the border regime represent progenitors whose initial conditions do not satisfy the requirements to observe normal LGRBs. This region of the parameter space is still vastly underexplored to this day, and the properties of these progenitor systems are a mystery. SNe Ic-BL seem to be the unifying factor between events in different regions of this parameter space, but it is still not clear how SNe Ic-BL can arise from systems with vastly different kinetic energies and ejecta velocities.

These are just few of the many unanswered questions in this parameter space that can only be resolved by detailed, multi-wavelength studies of stellar engine-driven transients. My dissertation does exactly that, delving into six observational studies of various classes of stellar engine-driven transients discovered at gamma-ray, X-ray, and optical wavelengths. Through this dissertation, I investigate the diversity of massive stellar death and relativistic jets to shed light on a fundamental question in astrophysics: *how do some compact objects generate the fastest and most powerful outflows in the Universe?* For the rest of this introduction, I introduce the classes of stellar engine-driven transients that I study in this dissertation, along with some major open questions regarding each of these classes.

1.1 LGRB-SNe

From an observational point of view, the LGRB-SN connection was established for the first time in 1998. GRB 980425's proximity ($z = 0.0085$) allowed for the test of the theory that LGRBs originate from CCSNe, and SN 1998bw (Clocchiatti et al., 2011; Iwamoto et al., 1998a;

Patat et al., 2001) was found temporally and spatially coincident to GRB 980425, giving evidence for the LGRB-SN connection. Over the past few decades, over 50 SNe with associated LGRBs have been discovered (see, e.g., Blanchard et al. 2024; Cano et al. 2017a; Hjorth 2013; Hu et al. 2021; Kumar et al. 2022a; Melandri et al. 2019a; Rossi et al. 2022b; Srinivasaragavan et al. 2023, 2024a), and are known as LGRB-SNe. For events with observed spectroscopy measurements, studies have shown that all (except for SN 2011kl associated with ultra-long GRB 111209A, which was a superluminous SN; Kann et al. 2019) are SNe Ic-BL.

There are a number of open questions regarding the LGRB-SN connection, with recent discoveries highlighting the need for further probing of the parameter space. A SN is not always detected for nearby LGRBs (Della Valle et al., 2006; Fynbo et al., 2006; Gal-Yam et al., 2006; Tanga et al., 2018). Two LGRBs have actually shown evidence for an associated kilonova (Gillanders et al., 2023; Levan et al., 2023a; Rastinejad et al., 2022; Troja et al., 2022; Yang et al., 2022, 2023), which is an outflow associated with the merger of two compact objects. The observed population of LGRBs is primarily detected at $z \gtrsim 1$, with isotropic equivalent energy releases ($E_{\gamma,\mathrm{iso}}$) between 10^{50} to 10^{54} erg (e.g., Jakobsson et al. 2006). However, most LGRB-SNe have $z \lesssim 1$ with $E_{\gamma,\mathrm{iso}} \sim 10^{48} - 10^{50}$ erg (Cano et al., 2017a). This is primarily an observational effect, as LGRB-SNe are much fainter than their associated LGRBs and are only detectable within a much smaller volume. Figure 1.5 shows the sample of spectroscopically confirmed LGRB-SNe, illustrating this effect. The relationship between LGRB energetics and their associated SN properties is also a scattered picture (shown in Figure 1.5), and there is not a clear understanding of how the central engine impacts the SN explosion.

Therefore, it is important to characterize every newly discovered LGRB-SNe. In my dissertation, I performed studies on two nearby ($z < 1$) and energetic ($E_{\gamma,\mathrm{iso}} > 10^{53}$ erg) LGRB-SNe

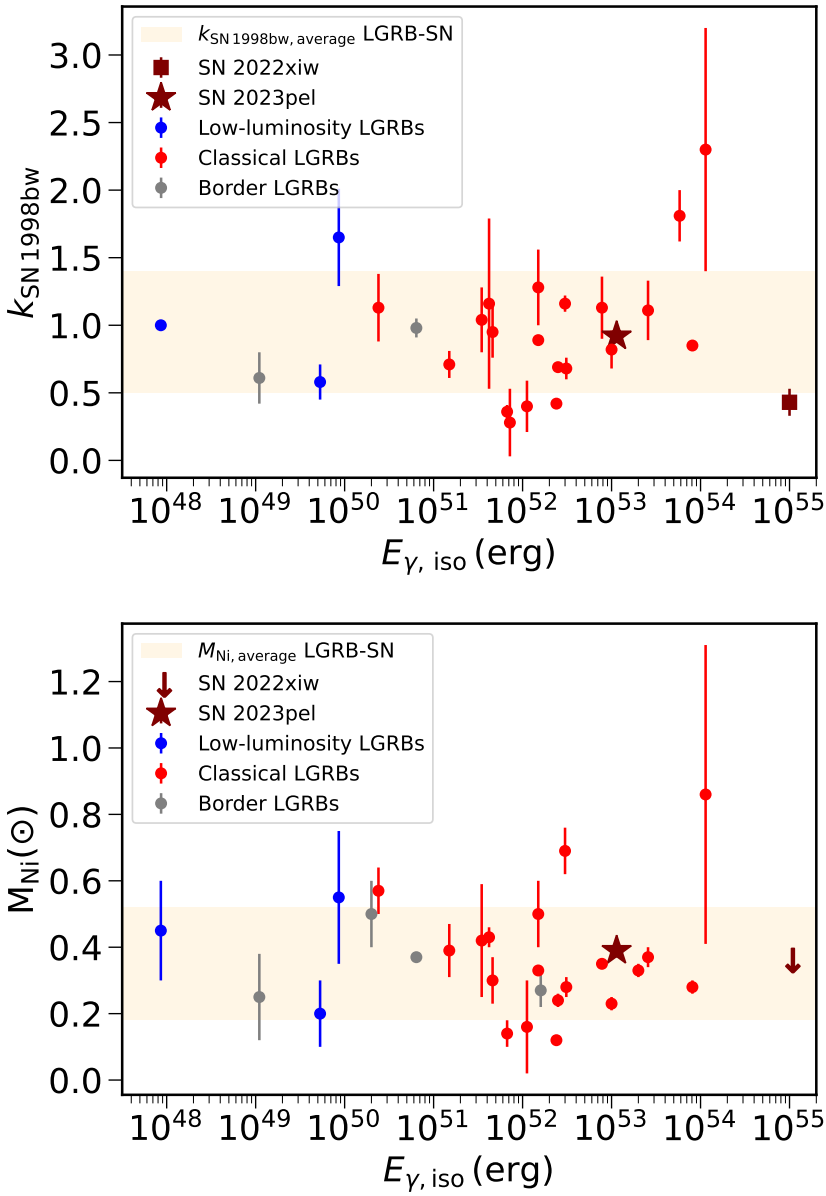

Figure 1.5: The most comprehensive analysis of LGRB-SNe presented in the literature, modified from Srinivasaragavan et al. (2024a). The y-axes are the peak luminosity of LGRB-SNe relative to the prototypical LGRB-SN 1998bw (left; k_{SN1998bw}), and the inferred Nickel masses of the explosion (right; $\mathrm{M_{Ni}}$). The average LGRB-SN values ($\pm\,1\sigma$) for these parameters are shaded in orange. The x-axes are the isotropic equivalent energy release ($E_{\gamma,\mathrm{iso}}$) of the LGRBs' prompt emission. LGRBs are divided into low-luminosity, border, and classical LGRBs.

(Srinivasaragavan et al., 2023, 2024a) presented in Chapters 2 and 3, which includes one study on the brightest GRB of all time, GRB 221009A (Burns et al., 2023). These studies focused on analyzing optical data, including photometry and spectroscopy of both the LGRBs' afterglows along with their associated SNe.

1.2 SNe Ic-BL

As mentioned earlier, nearly all LGRB-SNe are SNe Ic-BL. These SNe are usually found in lower metallicity environments than normal Type Ib/c SNe, suggesting that their progenitors are younger and more massive (Cano, 2013; Sanders et al., 2012). Their light curves (LCs) also rise faster than normal Type Ib/c SNe and are brighter at peak magnitude (Lyman et al., 2016a; Prentice et al., 2016; Taddia et al., 2018). LC modeling of these events has shown that they can possess explosion energies (10^{52} erg) an order of magnitude higher than normal Type Ib/c events (10^{51} erg); though peculiarly, their ejecta masses are similar (Lyman et al., 2016a; Prentice et al., 2016; Srinivasaragavan et al., 2024b; Taddia et al., 2018).

SNe Ic-BL challenge the picture associated with the standard explosion mechanism of CC-SNe, as the extra order of magnitude of energy possessed by some of these explosions necessitates a deviation from the traditional picture of neutrino irradiation from a proto-neutron star (NS) reviving the bounce-back shock in the progenitor's core. A compelling hypothesis is that a relativistic jet driven from the core of the progenitor's proto-NS transfers the extra order of magnitude energy needed to the surrounding stellar medium such that its explosion can reach the order of 10^{52} erg (Burrows et al., 2007; Woosley & Bloom, 2006). Since nearly every LGRB-SNe is a SN Ic-BL, there is significant evidence for this hypothesis.

However, the local LGRB rate is 10^{-3} – 10^{-6} times the local Type Ic-BL SNe rate (Ho et al., 2020a), and even after accounting for the beaming fraction of GRBs (due to relativistic beaming, we miss a fraction of GRBs because we are not in their line of sight), it is clear that most SNe Ic-BL do not produce GRBs. Furthermore, radio studies of SNe Ic-BL tracing the fastest-moving ejecta at late times ruled out off-axis afterglows for the majority of the nearby SNe Ic-BL population (Corsi et al., 2016, 2023). Therefore, relativistic ejecta are not ubiquitous to SNe Ic-BL. Ultimately, this alludes to intrinsic differences in the explosion mechanisms within the SNe Ic-BL population, between engine-driven and normal SNe Ic-BL. Dedicated sample studies of SNe Ic-BL are necessary to probe this question further.

There have been a very limited number of historical SNe Ic-BL sample studies, with most coming from literature collections (e.g., Cano 2013; Lyman et al. 2016a; Prentice et al. 2016), or suffering from small sample sizes (Taddia et al., 2015). The most recent dedicated sample study on SNe Ic-BL in the literature was published in 2019 (Taddia et al., 2019a), which utilized 34 events discovered and observed by the Zwicky Transient Facility's (ZTF's) predecessor, the Palomar Transient Factory. In my dissertation, I performed the largest study of SNe Ic-BL ever presented in the literature, analyzing 36 events detected by ZTF, presented in Chapter 4. This study features analysis of optical, ultraviolet, and radio data, providing a full characterization of the sample from a population-level perspective.

1.3 Orphan Afterglows

Recently, ground-based wide-field optical surveys such as ZTF have begun detecting LGRB afterglows serendipitously, without the use of a gamma-ray trigger (Ho et al., 2022). In a handful

of cases, no gamma-ray emission has been found after post-facto searches, even with sensitive high-energy limits at the time and location inferred for the explosion. These events are known as orphan afterglows. There are many open questions in LGRB science that can only be answered by studying these events, including understanding the true rate and angular structure of relativistic jets, how important mass-loading is for successful jet production, and understanding the role that ultra-relativistic ejecta plays in powering engine-driven systems.

These events also represent a mysterious endpoint for stellar evolution, as the conditions necessary for a progenitor to produce them are still not well understood. The simplest explanation is that no GRB satellite with prompt notification capability was pointed at the LGRB location at the explosion time, or that the afterglow was not robustly localized, allowing for an accurate search of high-energy catalogs. But for other events this explanation does not appear viable. Viewing angle effects are one possibility, as LGRBs are ultra-relativistic. This leads to their emission only being observable within a viewing angle of $\theta \sim \frac{1}{\Gamma}$ (Rhoads, 1997). LGRBs have high initial Lorentz factors on the order of $\Gamma \sim 100$ during their prompt emission; therefore, gamma-rays are only detectable within a very small viewing angle. However, optical facilities could still detect emerging afterglows as the jet slows down and the Lorentz factor decreases, even if Earth was not in the line of sight of the initial collimated gamma-ray emission.

A "structured" LGRB jet is also a possible explanation, where a LGRB's energy profile varies with respect to viewing angle. In the past, LGRB jets have usually been modeled as simple top hats, with constant energy per viewing angle. However, detailed studies of LGRBs and orphan afterglows have shown that structured jets may be more common than previously thought (e.g., Salafia et al. 2015; Srinivasaragavan et al. 2025b). This means that even slightly off-axis observers that observe an event within the jet's viewing angle but outside of its narrow high-Γ

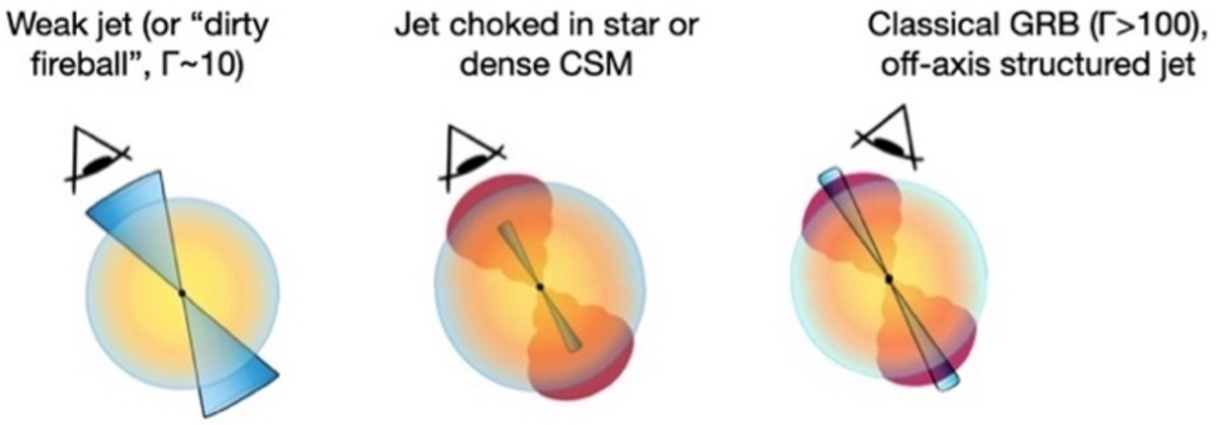

Figure 1.6: Artistic depiction of possible progenitor scenarios for orphan afterglows. Figure credit Prof. Anna Ho.

core could see an orphan afterglow.

In addition, there are theorized baryon-loaded LGRBs known as dirty fireballs, which may only have initial Lorentz factors of $\Gamma \sim 5 - 10$, failing to produce observable gamma-rays altogether due to pair production processes (Dermer et al., 1999). Optical facilities could also catch the afterglows from these dirty fireballs. There have been no confirmed dirty fireballs discovered thus far, and the discovery of even one would dramatically change our view of LGRB phenomena. Yet another possible scenario is that a LGRB's jet might be ultra-relativistic and successfully escape its progenitor star, but ends up getting "choked" by a dense surrounding CSM (Duffell & Ho, 2020), leading to gamma-rays being trapped and reprocessed to longer wavelengths. Figure 1.6 shows an artistic depiction of several of these possible scenarios.

Despite their importance, orphan afterglows are extremely rare, with only six confirmed events with redshift measurements (Li et al., 2024). Therefore, every new orphan afterglow discovery presents us with a rare opportunity to probe their progenitor systems and make headway towards answering many major open questions in LGRB science. In my dissertation, I performed a multi-wavelength study on the sixth orphan afterglow with a redshift measurement, AT 2023sva

(Srinivasaragavan et al., 2025b), presented in Chapter 5. This study features analysis of gamma-ray, X-ray, optical, and radio data, and is one of the most robustly observed and modeled orphan afterglows presented in the literature.

1.4 X-ray Flashes

Past soft X-ray missions such as BeppoSAX and HETE-2 detected bursts with peak energies between those of classical LGRBs (hundreds of keV) and supernovae (tens of eV)– known as "X-ray flashes" (XRFs), defined by possessing peak energies $\lesssim$ 30 keV. These XRFs were detected at rates comparable to classical LGRBs (Heise et al., 2001; Sakamoto et al., 2005), and the simplest idea was that the XRFs are LGRBs viewed off-axis, where the prompt γ-ray emission is missed due to viewing angle effects. However, XRF analyses revealed a variety different possible progenitors, including the shock break-out of supernovae (Alp & Larsson, 2020), the jetted emission of a tidal disruption event (Yao et al., 2024), the emission from the newly formed accretion disk in a compact binary merger (Lu & Quataert, 2023), or flares from highly magnetized stars (Lin et al., 2022), among others. Understanding the progenitor systems for XRFs is a major open question, as it is not clear whether they represent an entirely new class of phenomena than LGRBs altogether, or whether all, or just a subset originate from massive stellar deaths.

Despite their importance, XRF past discoveries were limited by the lack of sensitive all-sky soft X-ray instruments. However, the recently launched Einstein Probe (EP) is well-equipped to discover XRFs. EP carries the "Wide X-ray Telescope" (WXT; 0.5–4 keV), a lobster-eye X-ray imager with a 3600 deg^2 field-of-view (FoV) (Yuan et al., 2018). With over 100 times the FOV and vastly greater sensitivity than any previous soft X-ray mission, EP has also enabled

rapid multi-wavelength follow-up of X-ray transients for the first time with WXT's ~ 5 arcmin angular resolution. In addition, the recently launched Space Variables Objects Monitor (SVOM) is a GRB mission with sensitivity down to 4 keV, also capable of making XRF discoveries (Wei et al., 2016a).

A major missing piece in understanding historical XRFs was securing associations with their optical counterparts to obtain redshift measurements. New wide-field transient surveys such as ZTF have begun finding these counterparts in near real-time, through fine-tuning survey experiments to respond rapidly to EP and SVOM discoveries. In addition, contemporaneous high-energy observations from gamma-ray satellites like *Fermi*-GBM and *Swift*-BAT can rule out gamma-ray counterparts for events, while SVOM's broad 4–120 keV energy range allows it to independently constrain the spectral peak for detected bursts on its own to find XRF candidates. Therefore, there has never been a more opportune time to advance our understanding of XRFs and probe their progenitor systems.

Obtaining multi-wavelength follow-up observations of XRF candidates and modeling their emission panchromatically is essential for this. Only a handful of these events have multi-wavelength counterparts, and there are even fewer XRFs with SN counterparts, known as XRF-SNe. Prior to the launch of EP and SVOM, there were only six confirmed XRF-SNe (e.g., Bersier et al. 2006; Bufano et al. 2012; Campana et al. 2006; Cano et al. 2011; Fynbo et al. 2004; Maund et al. 2009; Mazzali et al. 2008; Soderberg et al. 2005; Thomsen et al. 2004; Tominaga et al. 2004). In the first two years of EP and SVOM operations, four new XRF-SNe have been discovered (e.g., Li et al. 2025c; Rastinejad et al. 2025; Srinivasaragavan et al. 2025a,c; Srivastav et al. 2025; Sun et al. 2024; van Dalen et al. 2025), greatly increasing the discovery rate. Figure 1.7 shows the landscape of XRF-SNe, with spectra around maximum light and LCs displayed for

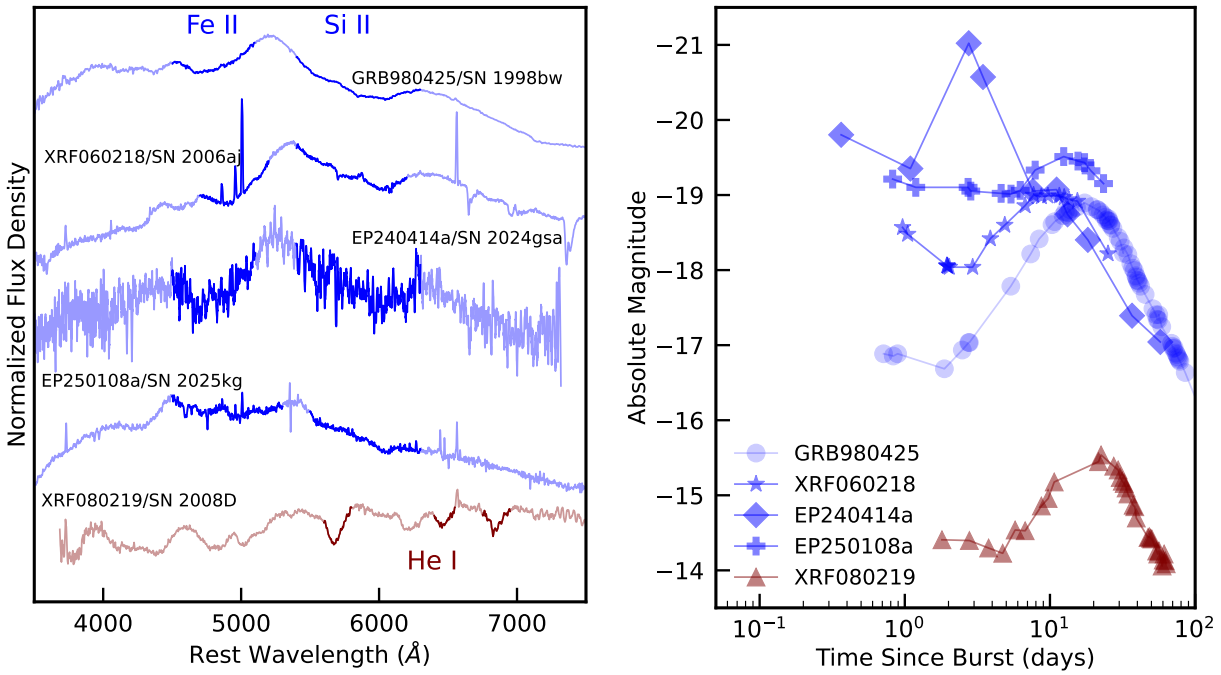

Figure 1.7: *Left*: Spectra of XRF-SNe[1] around maximum light (Modjaz et al., 2006, 2009; Patat et al., 2001), including two recent EP XRF-SNe (Rastinejad et al., 2025; Sun et al., 2024). XRF080219/SN 2008D displays strong He features (labeled in bold), leading to a Type Ib SN classification. The other four events all display broad Fe II and Si II features (labeled in bold) leading to SNe Ic-BL classifications. *Right*: LCs of XRF-SNe, shown in the rest frame (Clocchiatti et al., 2011; Modjaz et al., 2006, 2009; Srinivasaragavan et al., 2025a; van Dalen et al., 2025). The LCs show clear diversity, ranging seven orders of magnitude in brightness.

five events.

All spectroscopically classifed XRF-SNe are SNe Ic-BL except for one, XRF080219/SN 2008D, which showed strong Helium absorption features leading to a Type Ib SN classification (Modjaz et al., 2009). This gives evidence that the majority of XRF-SNe are likely at least distantly related to the same class of progenitors that produce LGRB-SNe, though clearly not all, as a progenitor star that has retained its Helium envelope cannot produce a successful LGRB. The X-ray luminosity of XRF080109 was also few orders of magnitude less than those of XRF-SNe that are SNe Ic-BL, pointing to different sources of non-thermal emission as well. The LCs of

[1]GRB980425 has a peak energy $\sim$ 50 keV (Daigne & Mochkovitch, 2007) making it a borderline XRF.

XRF-SNe are also diverse, both in shape and in brightness (see Figure 1.7). The diversity of XRF-SNe, especially when compared to the relative homogeneity of LGRB-SNe (Srinivasaragavan et al., 2024a), gives evidence that their progenitors differ from those of LGRB-SNe to at least some degree, making every new XRF-SNe important to characterize.

In my dissertation, I performed multi-wavelength studies of two XRF-SNe discovered by EP, EP250108a/SN 2025kg (Srinivasaragavan et al., 2025a) and EP250827b/SN 2025wkm (Srinivasaragavan et al., 2025c), presented in Chapters 6 and 7. These studies feature analysis of gamma-ray, X-ray, ultraviolet, optical, and radio data, and are some of the most extensively observed and modeled XRF-SNe in the literature.

1.5 Organization of Dissertation

This dissertation is organized into four different parts, and eight total chapters. The four parts correspond to the four different classes of stellar engine-driven transients I described above - LGRB-SNe, SNe Ic-BL, Orphan Afterglows, and XRF-SNe. Chapters 2 through 7 feature publications I first-authored over the course of my thesis, with Chapters 2 through 6 already published in journals, and Chapter 7 currently in the review process. In Chapter 8, I take a look towards the future of stellar engine-driven transient science. In Figure 1.8, I show an artistic depiction of the different classes of stellar engine-driven transients I study in this dissertation.

My life has always been innately connected to basketball, so it is fitting that this dissertation has four parts, similar to the four quarters of a game. Now that we have finished warm-ups and layup lines, I invite readers to the tip-off – the first quarter is about to begin! It is shaping up to be a great game.

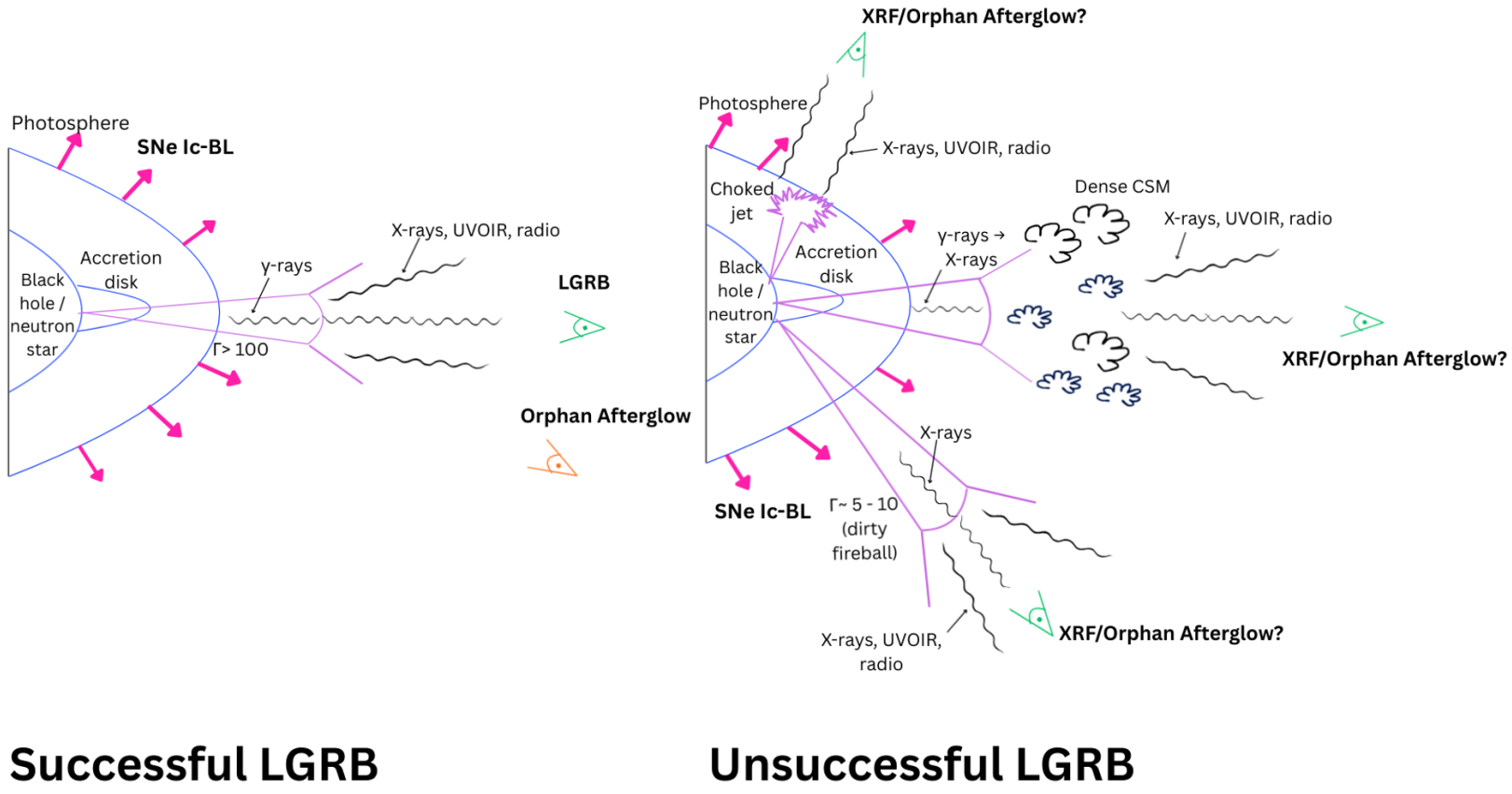

Figure 1.8: Artistic depiction of different classes of stellar engine-driven transients, divided into successful and unsuccessful LGRBs.

Quarter 1. Long Gamma-ray Burst – Supernovae

"I hoop was never good enough to ever be a Laker

But these words I record got me ballin', Jordan."

- J. Cole

Chapter 2: A Sensitive Search for Supernova Emission Associated with the Extremely Energetic and Nearby GRB 221009A

2.1 Introduction

Over the past two and a half decades, a link has been established between long-duration gamma-ray bursts (LGRBs) and core-collapse supernovae (CCSNe; Woosley & Bloom 2006). Over two dozen LGRBs have been associated with CCSNe, either indirectly (e.g., through late-time "bumps" in their optical afterglow light curves), or directly through tell-tale spectroscopic signatures (Cano et al., 2017a). All of these SNe are of the Ic-BL type (Filippenko, 1997): they lack H and He lines in their optical spectra, and possess broad lines indicative of higher ejecta velocities than seen in normal Type Ic SNe.

Despite this progress, a number of key open questions regarding the nature of the GRB-SN connection remain. One of the foremost of these is understanding why a much smaller fraction of Type Ic-BL SNe have associated LGRBs than the converse. A number of studies (Corsi et al., 2016, 2022; Soderberg et al., 2006a) have shown that this dichotomy cannot be explained solely by viewing angle effects, and that relativistic ejecta are not ubiquitous to SNe Ic-BL ($< 19\%$ of Ic-BL events are SN 1998bw-like, the prototypical SN associated with a GRB; Corsi et al. 2022). Therefore, there are intrinsic differences in the explosion mechanisms and/or environments be-

tween jet-powered Type Ic-BL SNe and normal Ic-BL events, and understanding this dichotomy can provide important insights into stellar evolution and the landscape of stellar explosions.

The observed population of LGRBs is comprised predominantly of cosmological ($z \gtrsim 1$) events, with $E_{\gamma,\rm iso}$ between 10^{50} to 10^{54} erg (e.g., Jakobsson et al. 2006). On the other hand, the majority of GRBs that have associated spectroscopically confirmed SNe (GRB-SN) are low-luminosity events, with isotropic equivalent energies ($E_{\gamma,\rm iso}$) between 10^{48} to 10^{50} erg (Cano et al., 2017a). This is the natural consequence of low-luminosity GRBs dominating the population of events nearby enough for spectroscopic investigations ($z \lesssim 0.3$), even with large-aperture optical facilities. Here we attempt to characterize the supernova associated with a rare energetic LGRB discovered in the nearby universe.

GRB 221009A [α (J2000)= $19^{\rm h}13^{\rm m}03.50^{\rm s}$, δ (J2000) = $+19^\circ4624''.23$; Laskar et al. 2022] was discovered by the Burst Alert Telescope (BAT; Barthelmy et al. 2005) on the Neil Gehrels Swift Observatory (Swift; Gehrels et al. 2004), though initially classified as a potential Galactic transient (Dichiara et al., 2022). Subsequently, the Fermi Gamma-Ray Burst Monitor (GBM; Meegan et al. 2009) reported an extremely bright LGRB detected ≈ 55 min earlier[1] consistent with this localization (Lesage et al., 2022). Further observations revealed that the BAT triggered on the bright X-ray afterglow of GRB 221009A, a first in the nearly 18 years of Swift operations (Williams et al., 2023).

The unprecedented brightness led to extensive follow-up across the electromagnetic spectrum (e.g., Fulton et al. 2023; Kann et al. 2023; Laskar et al. 2023; O'Connor et al. 2023; Williams et al. 2023). Spectroscopy of the optical afterglow led to a redshift measurement of $z = 0.151$ (Castro-Tirado et al., 2022; de Ugarte Postigo et al., 2022b; Malesani et al., 2023a). Its associ-

[1] At 13:16:59.00 UTC on 9 Oct 2022, which we establish hereafter as $\rm T_0$.

ated gamma-ray isotropic energy release is well in excess of 10^{54} erg, making GRB 221009A an extremely rare example of a highly energetic LGRB nearby enough to search for an associated SN Ic-BL.

In this *Letter*, we present optical observations that display a late-time flattening in the afterglow decay of GRB 221009A, and we investigate how these measurements can constrain the possible associated SN (SN 2022xiw; Postigo et al. 2022). In §2.2 we report the observations of the optical afterglow of GRB 221009A; in §2.3 we analyze the observations, and statistically compare models with and without a supernova component; in §2.4 we constrain physical parameters of SN 2022xiw; in §2.5 we place GRB 221009A/SN 2022xiw in the context of the GRB-SN sample in literature; and in §2.6 we summarize our conclusions. In the final stages of manuscript preparation, studies reporting conflicting results on the existence of SN emission were posted on the arXiv (Fulton et al., 2023; Kann et al., 2023; Levan et al., 2023b; Shrestha et al., 2023) – where relevant we highlight differences in our approach and contrasts in our results.

2.2 Observations

The main telescopes used for this work are the GROWTH-India Telescope (GIT), Lowell Discovery Telescope (LDT), and the Gemini-South Telescope. The results of the GIT, LDT, and Gemini-South observations are presented in Table B.1. To provide additional coverage at early times and help constrain the afterglow behavior, we have also considered optical afterglow measurements from the Liverpool Telescope (LT) reported in Laskar et al. (2023), and supplemented these with preliminary results reported in the GCN circulars (Belkin et al., 2022a,b,c; Bikmaev et al., 2022a,b; Brivio et al., 2022; D'Avanzo et al., 2022; de Wet et al., 2022; Ferro et al., 2022;

Groot et al., 2022; Gupta et al., 2022a; Huber et al., 2022; Im et al., 2022; Izzo et al., 2022; Kim et al., 2022a; Kumar et al., 2022b; Pellegrin et al., 2022; Rajabov et al., 2022; Rossi et al., 2022a; Schneider et al., 2022; Shrestha et al., 2022; Vinko et al., 2022). The GCN photometry is provided in tabular form in the Appendix. All times used in this work are in the observer frame. Below we describe the data reduction processes for each of the telescopes we use.

2.2.1 GIT

We used the GIT located at the Indian Astronomical Observatory (IAO), Hanle-Ladakh, to acquire observations of the GRB 221009A optical afterglow (Kumar et al., 2022c). The source was observed in Sloan g', r', i' and z' bands. Data were downloaded and processed in real-time by the GIT data reduction pipeline. We used individual exposures for photometry in the early stages when the afterglow was bright. Later, we stacked images with `SWarp` (Bertin, 2010a) to increase the S/N ratio of detections.

The data were reduced in a standard manner using the GIT pipeline (Kumar et al., 2022d). All images were pre-processed by subtracting bias, flat-fielding, and cosmic-ray removal via the `Astro-SCRAPPY` (McCully & Tewes, 2019) package. Astrometry was performed on the resulting images using the offline `solve-field` astrometry engine. Sources were detected using `SExtractor` (Bertin & Arnouts, 1996a) and were crossed-matched against the Pan-STARRS1 DR1 catalog (PS1; Flewelling et al. 2020a) through `VizieR` to obtain the zero-point. Finally, the pipeline performed point spread function (PSF) fit photometry to obtain the magnitudes of the GRB 221009A afterglow (Table B.1).

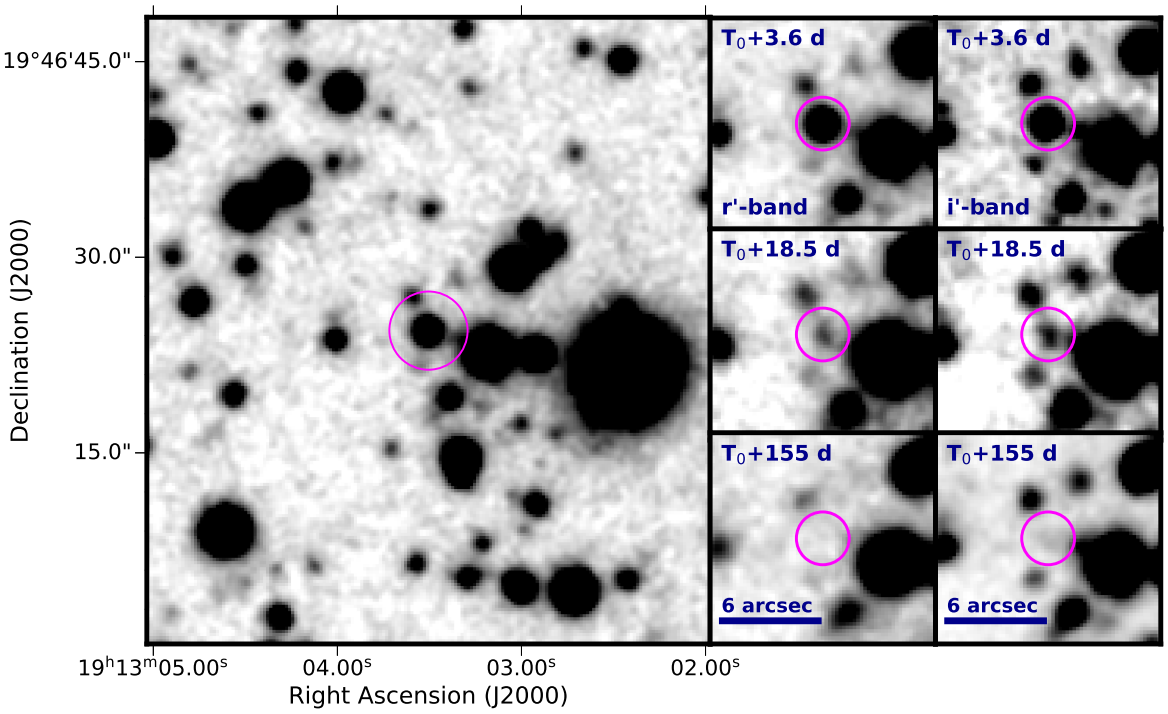

Figure 2.1: LDT images of the optical afterglow of GRB 221009A. All of the panels show the position of GRB 221009A circled in pink. The left, large panel shows the wider field of view of GRB 221009A, in r′ band 3.6 days after T_0. The right panels show the evolution over time of the optical afterglow, in both r′ and i′ bands. The image at 155 days is devoid of afterglow and SN contribution, and the host galaxy is faintly seen in i′ band. The images have been smoothed for display purposes.

2.2.2 LDT

We also observed GRB 221009A in r′, i′, and z′ with the 4.3m Large Monolithic Imager (LMI) on the LDT through an approved target-of-opportunity (ToO) program. We reduced the images using a custom `Python`-based image analysis pipeline (Toy et al., 2016), that can perform data reduction, astrometry, registration, source extraction and PSF photometry using `SExtractor`, which was calibrated using point-sources from the PS1 catalog (Table B.1). These observations were also reported in O'Connor et al. (2022a,b, 2023). Figure 2.1 shows both the wider field of view of GRB 221009A's position on the sky, as well as the individual evolution of its flux over time in both filters.

2.2.3 Gemini-South

Two additional publicly available i′-band observations obtained with GMOS-S mounted on the 8.1m Gemini-South Telescope (PI: Rastinejad, O'Connor; Rastinejad & Fong 2022) were also analyzed. The data were reduced using `DRAGONS`[2] (Labrie et al., 2019) to align and stack individual frames. PSF photometry was calibrated using nearby point-sources in the PS1 catalog (Table B.1).

[2] `https://dragons.readthedocs.io/`

2.3 Analysis and Model Selection

2.3.1 Previous Broadband Modeling Results

We draw upon three results from previous studies of the broadband afterglow of GRB 221009A in order to inform our approach to characterizing the associated SN emission. First, fits to the broadband spectral energy distribution (SED) revealed that the frequency range from optical to hard X-rays is not well fit by a single power-law (i.e., $f_\nu \propto \nu^{-\beta}$). Instead, a change in spectral slope, physically attributed to the synchrotron cooling frequency (ν_c), is inferred around the X-ray bandpass (O'Connor et al., 2023; Williams et al., 2023). As a result, in standard synchrotron afterglow theory, we do not expect the optical afterglow to decay with the same power-law index as the X-rays (e.g., Sari et al. 1998). Thus, to remove the afterglow contribution we must model the optical decay separately from the X-rays (c.f., Fulton et al. 2023 and the first approach in Shrestha et al. 2023).

Second, in addition to significant extinction due to dust in the Milky Way galaxy, broadband SED fits indicate the possible existence of absorption beyond the nominal value of $E(B-V) = 1.30$ mag reported in Schlafly & Finkbeiner (2011a). Given the low redshift, it is difficult to disentangle a larger than expected Galactic extinction (e.g., due to small-scale variations in Galactic dust), or extinction in the GRB host galaxy. Existing works differ on the significance of this extinction component, with inferred values ranging from $E(B-V) = 1.30$ mag (i.e., no additional extinction; O'Connor et al. 2023) to $E(B-V) = 1.80$ mag (Fulton et al., 2023; Williams et al., 2023). Given these uncertainties, we consider the implications of differing host extinction levels throughout this work.

Finally we correct for underlying host galaxy light in our analysis, derived by Levan et al. (2023b) through GALFITM modeling of late-time HST observations. We use their measurements of F625W $= 24.88 \pm 0.08$ mag, and F775W $= 23.80 \pm 0.14$ mag, which approximately correspond to the r′ and i′ bands. Previous analyses (Fulton et al., 2023; Kann et al., 2023; Shrestha et al., 2023) did not incorporate the host contribution explicitly in their analysis (though Pan-STARRS and DECam photometry in Fulton et al. 2023, and DECam photometry in Shrestha et al. 2023 is subjected to template subtraction, which negates the host contribution to a degree).

2.3.2 Optical Afterglow Modeling

Assuming the optical afterglow is powered by synchroton emission from the forward shock (Mészáros & Rees, 1997), we fit the early-time light curve with power-law models ($f_\nu \propto t^{-\alpha}$) to attempt to isolate the contribution from the supernova. Prior to $T_0 + 1$ d, the optical data display a shallow initial slope with $\alpha = 0.88 \pm 0.05$ (Kann et al., 2023; O'Connor et al., 2023). Beyond this time there is a clear steepening in the decay, and a single power-law does not provide a good fit to all optical data (D'Avanzo et al., 2022).

Since a SN will contribute negligibly (compared to the bright afterglow here) in the first days post explosion, we perform a power-law fit of all g′, r′, i′, and z′ data between 1 and 6 days post-explosion. We find a best fit decay index of $\alpha = 1.434 \pm 0.004$. As found by other authors, this index is appreciably shallower than the X-ray decay found at this time (Laskar et al., 2023; O'Connor et al., 2023; Williams et al., 2023). Figure 2.2 shows the best-fit power-law derived, along with the addition of the host galaxy emission to that power law.

The late-time behavior shows possible deviations from this power-law, even after the host

galaxy emission is accounted for. Though it is possible that central-engine activity can cause re-brightening of the optical afterglow in excess of what is expected from a power-law decay, this usually occurs directly after the prompt emission in the early-time evolution of the GRB (Kann et al., 2007; Oates et al., 2009). Because the brightening occurs weeks after the initial prompt emission (see Figure 2.1), we determine that there is a possibility that an associated SN is contributing excess flux to the optical emission, and further investigate this in §2.3.3.

2.3.3 Model Selection

In order to evaluate the statistical significance of the excess late-time emission, we perform a Bayesian model selection using the PyMultiNest package (Buchner et al., 2014; Feroz et al., 2009). We consider two empirical models – one where the optical emission is explained as the sum of the afterglow (i.e., synchrotron radiation) and a (constant) host galaxy emission, and one where an additional SN component is added as well. For each model, we calculate the Bayesian evidence, and use those the calculate the Bayes factor to see which is statistically preferred (Trotta, 2008). We limit the analysis to the r′ and i′ bands, as the large Galactic extinction makes g′ band uninformative, and z′ band SN templates are less available due to a lack of spectral coverage in that wavelength range.

For the afterglow+host model, we assume a single power-law decay in both bands at times after $T_0 + 1$ d. While the index is fixed to be identical in both the r′ and i′ bands, we do not require its value be equal to that derived from 1–6 d post-explosion (§2.3.2); rather, we allow the index to vary to provide the best fit to the entire data set. The host galaxy emission is incorporated as a free parameter in the fit, using a Gaussian prior with the mean and standard deviation measured

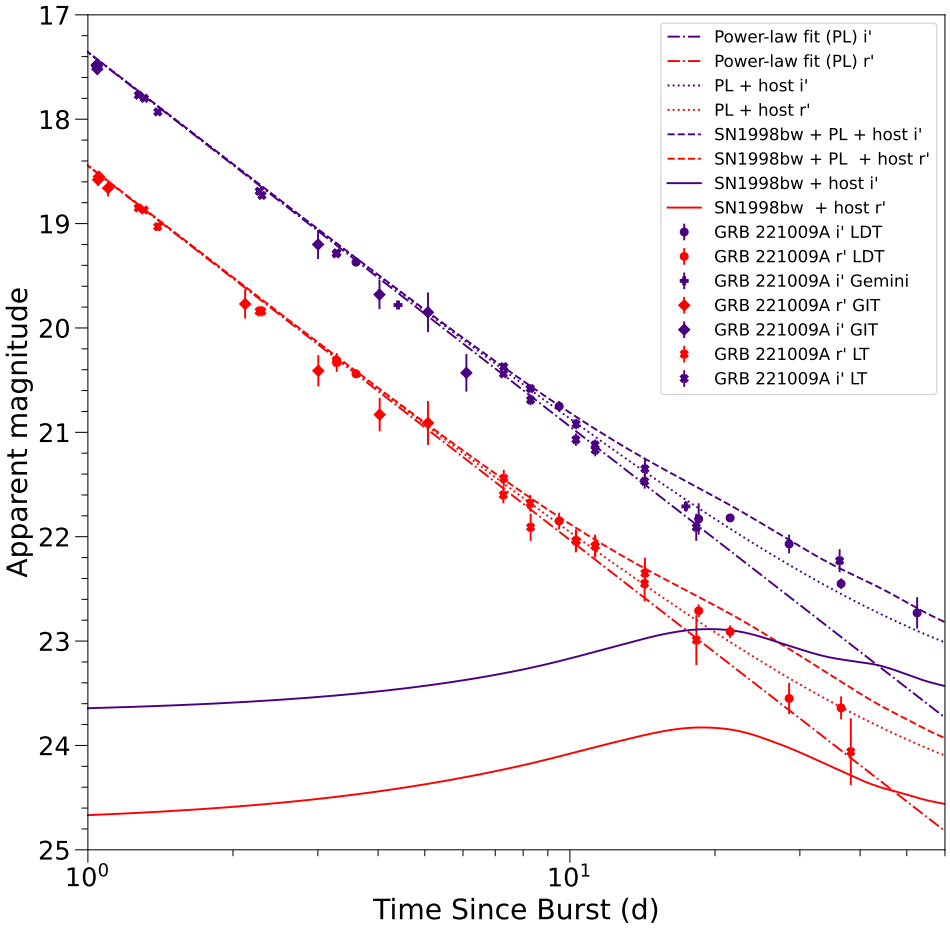

Figure 2.2: Observed r′- and i′-band photometry of GRB 221009A after $T_0 + 1\,\mathrm{d}$, along with the best-fit optical afterglow model corresponding to a power-law decay index of $\alpha = 1.434$, with the addition of the host galaxy emission. The LCs for a SN 1998bw-like source in r′ and i′ band, redshifted to $z = 0.151$ and reddened according to the Galactic and host galaxy extinction of GRB 221009A, are also shown.

by HST (Levan et al., 2023b).

For the SN model, an additional component is added to the afterglow+host model to mimic SN behavior. We take the LC of SN 1998bw (Clocchiatti et al., 2011), and (de)redden and K-correct it to match the relevant properties of GRB 221009A, using SNCosmo (Barbary et al., 2016). Specifically we adopt $E(B-V)_{MW} = 1.30$ mag (Schlafly & Finkbeiner, 2011a), $E(B-V)_{host} = 0.3$ mag, which is the most conservative value found in (Williams et al., 2023), and apply the Milky Way extinction law from Cardelli et al. (1989a) with $R_V = 3.1$. The resulting r′ and i′-band LCs for a SN 1998bw-like source at $z = 0.151$ [and behind an extinction of $E(B-V)_{\rm MW} = 1.30$ mag and $E(B-V)_{\rm host} = 0.3$ mag] are shown in Figure 2.2.

The final SN model used in the model selection has two free parameters: a flux-stretching factor $k_{\rm SN\,1998bw}$ and a time-stretching factor $s_{\rm SN\,1998bw}$ (e.g., Klose et al. 2019). Both of these parameters have priors drawn from a bivariate normal distribution fit to values derived for previous GRB-SN (Cano et al., 2017a). We also allow the afterglow power-law decay index (α) to be free with uniform priors, the flux constants of proportionality ($a_{\rm AG}$) to be free with uniform priors in log space, and add the host galaxy emission in both bands utilizing the same Gaussian priors. Therefore, the full SN model is:

$$f_\nu(t_{\rm obs}) = k_{\rm SN}(f_\nu^{\rm SN1998bw}(t_{\rm obs}/s_{\rm SN\,1998bw})) + a_{\rm AG}(t_{\rm obs})^{-\alpha} + f_\nu^{\rm host}, \tag{2.1}$$

where $f_\nu^{\rm SN\,1998bw}(t_{\rm obs})$ is the flux seen of the SN at a time in the observer frame, $t_{\rm obs}$ is the time in the observer frame, and $f_\nu^{\rm host}$ is the flux contribution from the host galaxy.

Initially, we fit the two models concurrently to the r′ and i′-bands, while assuming the errors are the nominal values reported in Table B.1 and Laskar et al. (2023) for the LT photometry. We

calculate the Bayes factor ($K_{\rm Bayes}$) between the two models to determine the likelihood that a SN is contributing excess flux to the optical afterglow in addition to the host galaxy emission, and find $K_{\rm Bayes} = 10^{4.0}$, which indicates that the SN model is strongly favored. However, when we calculate the χ^2 statistic for each of the models, we find that $\chi^2_{\rm PL+host} = 120.83$ for 62 degrees of freedom and $\chi^2_{\rm PL+host+SN} = 112.62$ for 60 degrees of freedom. Though the $\Delta\chi^2 = 8.21$ for 2 additional degrees of freedom is also indicative of a preference for the SN model, the χ^2 statistics themselves indicate that neither model adequately fits the data. This is likely because in the initial fitting, we did not account for systematic uncertainties that arise from combining data from multiple telescopes in the full photometric data set, or S-corrections (Stritzinger et al., 2002).

Therefore, we modify the fitting procedure to numerically optimize the likelihood function, where we assume that the reported errors under-estimate the true uncertainty. To account for this, we include an error-stretching factor (β) in the fitting procedure to represent the S-correction effect, and recalculate $K_{\rm Bayes}$. The log-likelihood function we minimize, with the addition of the error-stretching factor, is:

$$\ln p(y \,|\, m, s_n) = -\frac{1}{2}\sum_n \frac{(y_n - m_n)^2}{s_n^2} + \ln(2\pi s_n^2), \tag{2.2}$$

where y_n is the observed data, m_n is the modeled data, and s_n^2 is:

$$s_n^2 = \sigma_n^2 + \beta^2(m_n^2), \tag{2.3}$$

where σ_n are the nominal errors to the observed data.

The new Bayes factor we find is $K_{\rm Bayes} = 10^{1.2}$, which indicates the SN model is moderately, but not conclusively, preferred. We report the median parameters with their 1σ errors, along with the best-fit parameters which minimize the log-likelihood function in Table 2.1. The best-fit models are shown in Figure 2.3, along with their associated χ values. According to the model selection analysis, the optimal error-stretching factor increases the error bars by $\sim 3\%$ with respect to the model value at the observed time, for both the afterglow+host and SN model. We also calculated the Bayesian evidences for the two models, while incorporating independent error stretching factors (β_i) for each telescope rather than a single factor across all data sets. We did so to investigate if the way we account for systematic uncertainties plays a role in biasing the model preferences. We still find similar results, as the SN model is favored by a Bayes factor of $K_{\rm Bayes} = 10^{0.7}$.

Next, we analyze the LDT and LT photometry separately using their nominal error bars, to identify if the combination of photometry from different telescopes plays a role in biasing the model preferences. We do not fit the Gemini-South and GIT photometry separately, as there are only two Gemini-South photometry points, and the GIT photometry are all at early times where any SN excess contributing to the afterglow would be negligible. We find that the afterglow+host model is favored with a Bayes factor of $K_{\rm Bayes} = 10^{0.9}$ for the LDT photometry, while the two models are indistinguishable for the LT photometry. Figure 2.2 shows that the majority of the LDT photometry is at late times, where excess flux from a SN would be identifiable. This, in addition to only five and six photometry points being available respectively in the r′ and i′ bands leads to the model selection converging towards a shallow power-law decay slope in its fitting procedure, in order to fit for the excess flux. The best-fit power-law decay index is $\alpha = 1.36$ (median $\pm 1\sigma = 1.36 \pm 0.02$) , which is shallower than what is derived from the early-time

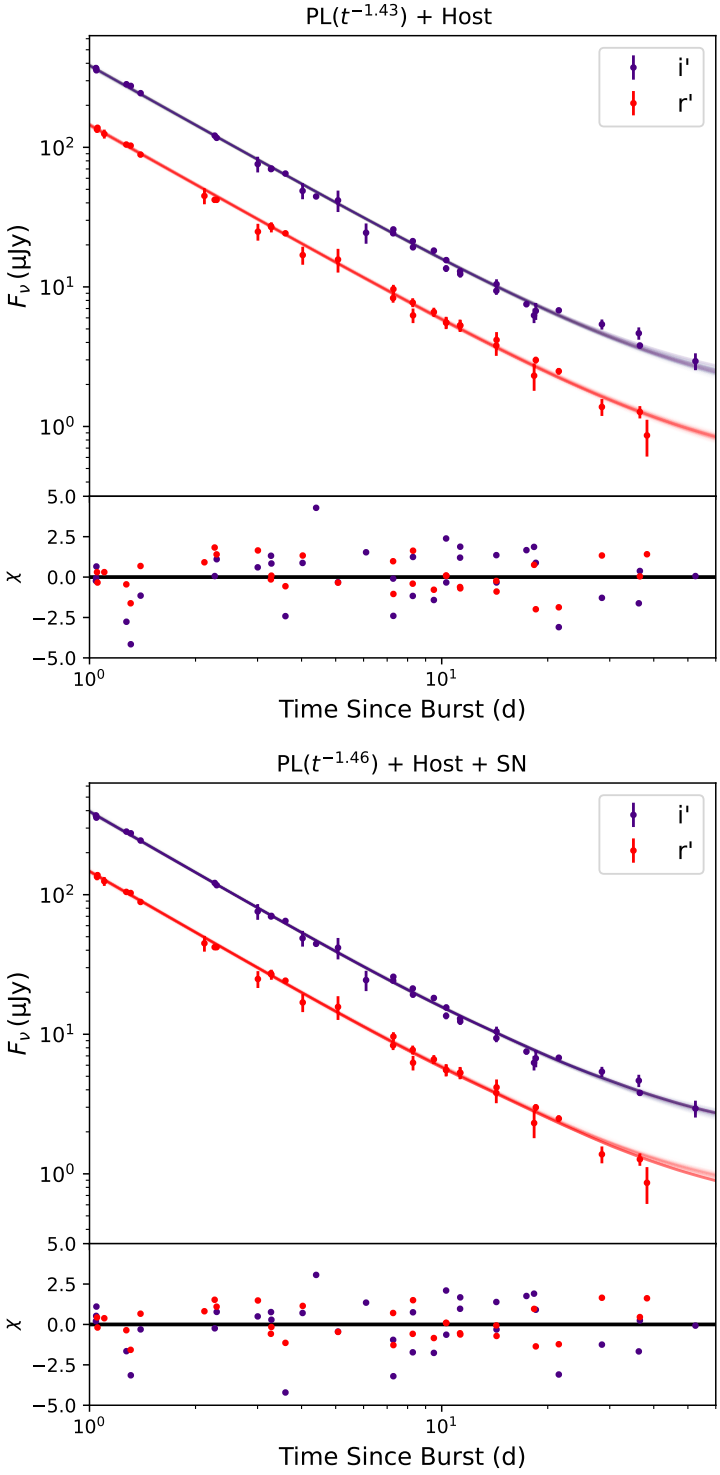

Figure 2.3: *Left panel*: The best-fit afterglow+host model, along with its a posteriori possible models and χ values. *Right panel*: The best-fit SN model, along with its a posteriori models and χ values. The SN model is moderately but not conclusively favored, with a Bayes factor $K_{\rm Bayes} = 10^{1.2}$, and the best-fit parameters for each model are shown in Table 2.1.

	$a_{\rm r'}$ (μJy)	$a_{\rm i'}$ $a_{\rm i',\,AG}$	α	$f^{\rm host}_{\nu,\rm r'}$ (μJy)	$f^{\rm host}_{\nu,\rm i'}$ (μJy)	$k_{\rm SN\ 1998bw}$	$s_{\rm SN\ 1998bw}$	$\ln(\beta)$
Afterglow+Host (Best-fit)	146	388	1.43	0.44	1.64	-	-	-3.37
Afterglow+Host (Median $\pm1\sigma$)	144 ± 2	384^{+5}_{-6}	1.42 ± 0.01	0.41 ± 0.03	1.33 ± 0.11	-	-	-3.30 ± 0.21
Afterglow+Host+SN (Best-fit)	147	394	1.46	0.35	1.17	0.39	0.69	-3.51
Afterglow+Host+SN (Median $\pm1\sigma$)	146 ± 2	395^{+5}_{-6}	1.47 ± 0.01	0.39 ± 0.03	$1.12^{+0.11}_{-0.12}$	0.43 ± 0.10	0.63 ± 0.09	$-3.50^{+0.23}_{-0.24}$

Table 2.1: Bayesian model selection fitting parameters for the afterglow+host and the afterglow+host+SN model.

optical photometry fitting in §2.3.2. Therefore, although the afterglow+host model is preferred for the LDT data, the lack of early-time data biases the fit towards a power-law decay index that is shallower than expected in order to fit for the excess flux.

On the other hand, the majority of LT data is at early times and at a significantly higher cadence than the LDT photometry. The best-fit power-law decay index for the afterglow+host model is $\alpha = 1.46$ (median $\pm\, 1\sigma = 1.45 \pm 0.01$), which is consistent with the power-law decay index derived in §2.3.2. The two models are indistinguishable due to a few photometry points that do show excess emission at later times, which the afterglow model cannot account for. Therefore, it is necessary to incorporate a combination of data sets in the modeling, in order to have optimal temporal coverage such that a sufficient amount of photometry points at both early and late times are accounted for in the fitting. After accounting for S-corrections modeled through our error-stretching factor, it is clear that the most accurate physical description of the LC comes from incorporating the entire data set, which we find favors the SN model moderately.

As a final sanity check, we perform a similar analysis using the observed light curve of SN 2013dx associated with GRB 130702A (D'Elia et al., 2015a; Toy et al., 2016) with the extinction values described above, again optimizing the likelihood function and allowing for an error-stretching factor. Due to the similar redshift ($z = 0.145$) to GRB 221009A, this avoids the requirement of calculating K-corrections (Fulton et al., 2023; Shrestha et al., 2023). In this case

we find a comparable Bayes factor to the analysis using SN 1998bw: $K_{\rm Bayes} = 10^{0.7}$, preferring the SN model. Thus we infer that the SN model preference is relatively insensitive to the details of the template SN used. We also emphasize that the detailed value of the host extinction adopted has little impact on the model selection. Since the SN flux is scaled by the free parameter $k_{\rm SN}$, increasing or decreasing the host extinction is largely offset in the modeling by a corresponding change in $k_{\rm SN}$.

Our preference for the SN model agrees with Fulton et al. (2023), as they find significant evidence of excess emission in the optical afterglow that is well-modeled by an additional SN component. However, they did not account for any host galaxy emission in their analysis, and Figure 2.2 shows that the host galaxy makes non-negligible contributions to the optical afterglow at late times. This is likely why they were able to find significant evidence of excess emission, while our preference for the SN model is moderate. Shrestha et al. (2023) and Levan et al. (2023b) report no evidence for *bright* SN emission, while Kann et al. (2023) does not find any strong evidence for or against SN emission. None of them rule out the possibility of a faint associated SN, and one of the conclusions of Levan et al. (2023b) is that an associated SN to GRB 221009A must be either substantially ($\sim 10 - 40\%$) fainter or bluer than SN 1998bw. Our findings point towards the former being true, as the best-fit flux-scaling factor for SN 2022xiw with respect to SN 1998bw is $k_{\rm SN\,1998bw} = 0.39$, with an upper limit at the 99% confidence interval of $k_{\rm SN\,1998bw} < 0.67$.

2.4 Supernova Parameter Estimation

2.4.1 Nickel Mass Estimates

The decay of ^{56}Ni to ^{56}Co and to ^{56}Fe releases the energy that powers the optical LC of Type I SNe, so the ^{56}Ni mass is a key physical parameter that can provide insight into properties of the explosion and progenitor (Arnett 1982; hereafter A82). Therefore, we fit semi-analytic LC models from A82 to the observed r′ and i′-band photometry after day 7 to constrain the ^{56}Ni mass. Equation 36 in A82 provides an analytic expression for the bolometric luminosity of Type I SNe, assumming full γ-ray trapping of the ejecta along with further radioactive inputs (Valenti et al., 2008). We use the infrastructure from the Hybrid Analytic Flux FittEr for Transients (HAFFET; Yang & Sollerman 2023) to perform the fits, where the two free parameters are the Nickel mass ($M_{\rm Ni}$) and the photon diffusion timescale ($\tau_{\rm m}$).

Given a bolometric LC from the model, it is necessary to extract associated r′ and i′-band LCs to compare to the observed photometry. It is possible to derive light curves in individual bands from a bolometric magnitude LC using bolometric correction (BC) coefficients:

$$\mathrm{BC}_x = M_{bol} - M_x, \tag{2.4}$$

where x is the relevant filter.

For stripped-envelope SNe, Lyman et al. (2014a) derive a g-band BC coefficient of:

$$\mathrm{BC}_g = 0.054 - 0.195 \times (g - r) - 0.719 \times (g - r)^2. \tag{2.5}$$

Here we assume that the color evolution of SN 2022xiw is identical to that of SN 1998bw. We use the BC coefficient, along with the color evolution of SN 1998bw, to generate r′ and i′-band LCs to fit to the SN photometry. First, we convert the BVRI photometry of SN 1998bw from Clocchiatti et al. (2011) to SDSS filters using conversions from Jester et al. (2005). At the time of each observation, we compute BC_g, along with g-r and g-i colors. Given a bolometric absolute magnitude LC from A82, we derive a g-band absolute magnitude LC from BC_g. We then compute the associated r and i-band LCs from the g-r and g-i colors derived above. Finally we apply the distance modulus, host galaxy emission, and extinction corrections described below, along with conversions from r and i band to r′ and i′ band[3], to produce observed r′ and i′-band LCs for comparison with the data. Best fit models with associated uncertainties are generated using MCMC techniques.

Given the large uncertainty in the host extinction (§2.3.1), we perform the fitting under three different assumptions: 1) $E(B-V)_{\rm host}$ allowed to freely vary between 0.3 and 0.5 mag; 2) $E(B-V)_{\rm host}$ fixed to a value of 0.3 mag; and, 3) $E(B-V)_{\rm host}$ fixed to a value of 0. For all three scenarios we allow $M_{\rm Ni}$, $\tau_{\rm m}$, and $\rm E(B-V)_{MW}$ to vary as additional free parameters. We allow $\rm E(B-V)_{MW}$ to vary due to the high uncertainty in the Galactic extinction at the location of GRB 221009A, and adopt uniform priors corresponding to the minimum and maximum values from Schlafly & Finkbeiner (2011a). Additionally, we allow the host galaxy emission in the r′ and i′ bands to vary as free parameters, with Gaussian priors corresponding to the values presented in Levan et al. (2023b). We adopt uniform priors for $M_{\rm Ni}$ and $\tau_{\rm m}$ based on values from previous Type Ic-BL SNe studies (Corsi et al., 2016, 2022; Taddia et al., 2019a).

[3] https://classic.sdss.org/dr5/algorithms/jeg_photometric_eq_dr1.html#usno2SDSS

We note that there are varying interpretations of the intrinsic extinction and hydrogen column density of the host that are model-dependent on the spectral shape of the afterglow (e.g. $E(B-V)_{\rm host} < 0.1\,{\rm mag}$; O'Connor et al. 2023, $N_{\rm H} \approx 4\times10^{21}\,{\rm cm}^{-2}$; Tiengo et al. 2023). However, we believe that the most likely physically plausible situation is the first where $E(B-V)_{\rm host}$ is allowed to vary freely between 0.3 and 0.5 mag, due to the possibility of a significant amount of intrinsic hydrogen column density in the host that may be up to $N_{\rm H} \approx 1.29\times10^{22}\,{\rm cm}^{-2}$ (Williams et al., 2023). We present the best-fit model from this scenario and 100 random samples from the posterior distribution in Figure 2.4, along with the associated corner plots for each parameter.

The best-fit values derived in all three scenarios are displayed in Table 2.2, and we find $M_{\rm Ni} = 0.05$ – $0.25\,{\rm M}_\odot$, depending on the scenario. Because the SN flux is only marginally detectable with respect to the afterglow and host galaxy emission, these best-fit values should be taken with a grain of salt. However, we can more robustly determine an upper limit, and find that at the 99% confidence level, that $M_{\rm Ni} < 0.36\,{\rm M}_\odot$. The $M_{\rm Ni}$ we find is systematically lower than that of SN 1998bw ($M_{\rm Ni} = 0.3$–$0.9\,{\rm M}_\odot$; Sollerman et al. 2000), which agrees with the results from §2.3.3, that SN 2022xiw must be substantially fainter than SN 1998bw.

Finally, we note that if we repeat the analysis under the same assumptions as Fulton et al. (2023), who do not explicitly account for host galaxy emission, and assume an additional 0.8 mags of extinction in the optical when compared to the nominal galactic extinction from Schlafly & Finkbeiner (2011a), we find $M_{\rm Ni} = 0.59 \pm 0.04\,{\rm M}_\odot$. This $M_{\rm Ni}$ is lower, but marginally consistent with their value of $M_{\rm Ni} = 1.0^{+0.6}_{-0.4}\,{\rm M}_\odot$. The lower $M_{\rm Ni}$ in comparison to their work is expected, due to their use of a steeper optical afterglow power-law decay slope ($f_\nu \propto t^{-1.556\pm0.002}$, see §2.3.1), which in turn leads to more luminous SN emission, and a higher $M_{\rm Ni}$.

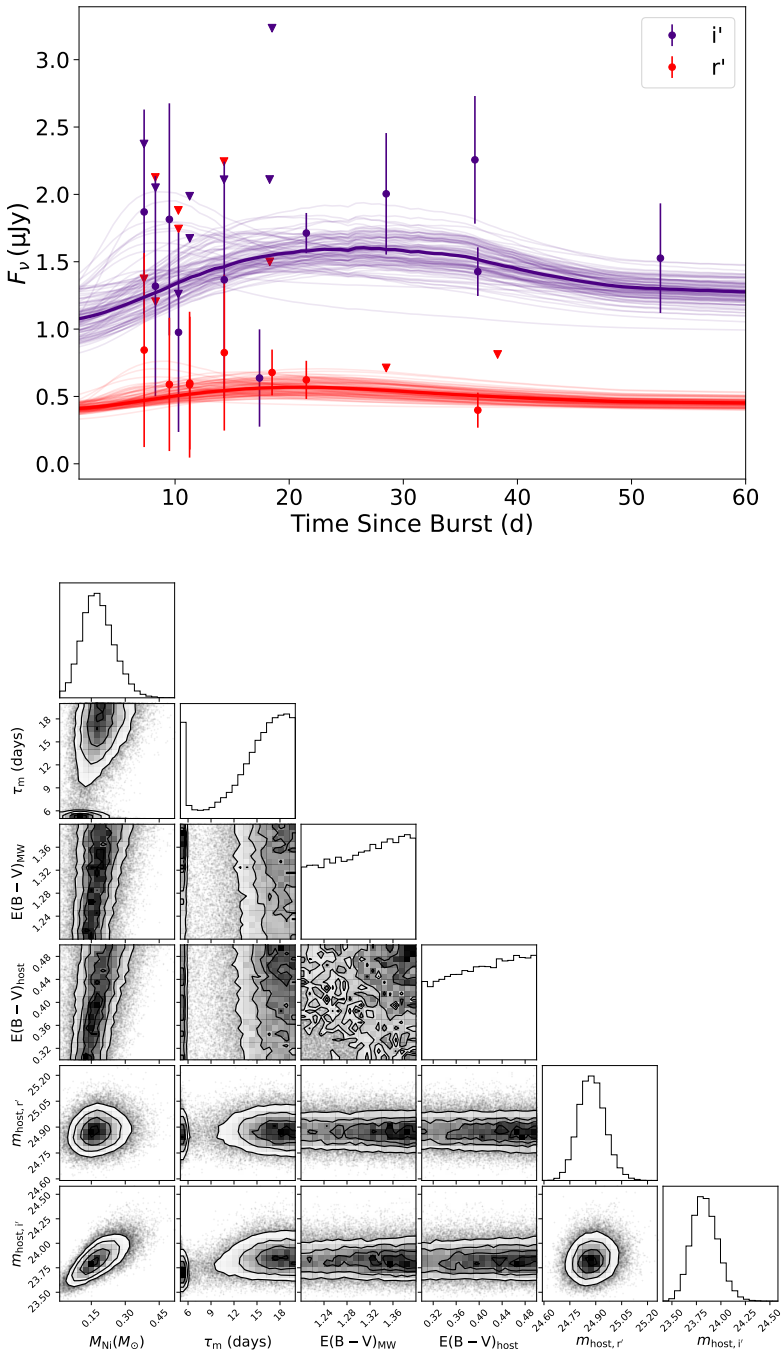

Figure 2.4: *Top panel*: Best-fit r′ and i′-band LCs in flux space extrapolated from the best-fit bolometric LC constructed from the A82 model (details in §2.4), assuming the host galaxy extinction is a free parameter between $E(B-V)_{host} = 0.3 - 0.5$ mag. The best-fit values are $M_{\rm Ni} = 0.18^{+0.07}_{-0.06}\,{\rm M}_\odot$, $\tau_{\rm m} = 15.98^{+2.77}_{-5.36}$ days, $\rm E(B-V)_{MW} = 1.31^{+0.06}_{-0.07}$ mag, $\rm E(B-V)_{host} = 0.41^{+0.06}_{-0.07}$ mag, $m_{\rm host,r'} = 24.88^{+0.08}_{-0.07}$ mag, and $m_{\rm host,i'} = 23.83^{+0.14}_{-0.12}$ mag. 100 random a posteriori possible models from the MCMC fitting samples are plotted,, along with the best fits in bold. *Bottom panel*: Corner plots associated with the MCMC fits of the A82 model, corresponding to the top panel. A total of 33,250 samples were generated in the posteriors.

	$M_{\rm Ni}$ ($M_\odot$)	$\tau_{\rm m}$ (days)	$E(B-V)_{\rm MW}$ (mag)	$E(B-V)_{\rm host}$ (mag)	$M_{\rm ej}$ ($M_\odot$)	$E_{\rm KE}$ (erg)	$m_{\rm host,r'}$ (mag)	$m_{\rm host,i'}$ (mag)
$E(B-V)_{\rm host} = 0.3-0.5$ mag	$0.18^{+0.07}_{-0.06}$	$15.98^{+2.77}_{-5.36}$	$1.31^{+0.06}_{-0.07}$	$0.41^{+0.06}_{-0.07}$	$7.93^{+2.99}_{-4.43}$	$3.71^{+1.40}_{-2.07} \times 10^{52}$	$24.88^{+0.08}_{-0.07}$	$23.83^{+0.14}_{-0.12}$
$E(B-V)_{\rm host} = 0.3$ mag	$0.14^{+0.05}_{-0.04}$	$16.56^{+2.35}_{-3.24}$	$1.31^{+0.06}_{-0.07}$	0.3	$8.53^{+2.59}_{-3.01}$	$3.99^{+1.21}_{-1.41} \times 10^{52}$	$24.88^{+0.08}_{-0.07}$	$23.84^{+0.13}_{-0.12}$
$E(B-V)_{\rm host} = 0$ mag	0.07 ± 0.02	$16.26^{+2.52}_{-3.34}$	$1.31^{+0.06}_{-0.07}$	0	$8.22^{+2.74}_{-3.03}$	$3.84^{+1.28}_{-1.42} \times 10^{52}$	$24.89^{+0.08}_{-0.07}$	$23.82^{+0.13}_{-0.11}$

Table 2.2: Best-fit physical parameters and their statistical 1σ errors corresponding to the three different host extinction scenarios presented in §2.4.1.

2.4.2 Additional Explosion Properties

Given the photon diffusion timescale $\tau_{\rm m}$, it is possible to derive the total ejecta mass ($M_{\rm ej}$) of a SN, through equation A1 of Valenti et al. (2008):

$$\tau_{\rm m}^2 = \frac{2\kappa_{\rm opt} M_{\rm ej}}{\beta c v_{\rm sc}}, \tag{2.6}$$

where $\kappa_{\rm opt} = 0.07\,{\rm cm^{-2}\,g^{-1}}$ is a constant, average opacity that is able to produce consistent results with hydrodynamical LC modeling of stripped-envelope SNe (Taddia et al., 2018), $\beta = 13.8$ is a constant, c is the speed of light, and $v_{\rm sc}$ is a scale velocity, which is set observationally to the photospheric velocity $v_{\rm ph}$, which is roughly related to the line velocity at the peak epoch.

Given that we assumed the color and spectral evolution of SN 2022xiw were identical to that of SN 1998bw, we also assume it has a comparable photospheric velocity: $v_{\rm ph} = 28,000\,{\rm km\,s^{-1}}$ (Iwamoto et al., 1998a). We note that SN 1998bw's photospheric velocity is high with respect to the population of GRB-SN in literature, which possesses an average of $v_{\rm ph} = 20,200\,{\rm km\,s^{-1}}$, with a dispersion $\sigma = 8,500\,{\rm km\,s^{-1}}$ (Cano et al., 2017a). However, a spectrum taken of the optical afterglow at $T_0 + 8\,{\rm d}$ reported the possible existence of broad features with velocities slightly larger than SN 1998bw (de Ugarte Postigo et al., 2022a). Therefore, our assumption of SN 2022xiw's peak photospheric velocity is valid, and may possibly under-represent the true photospheric velocity. We report the derived values in Table 2.2, and find $M_{\rm ej} = 3.5-11.1\,{\rm M_\odot}$.

Given $M_{\rm ej}$ and $v_{\rm sc}$, it is possible to derive the kinetic energy $E_{\rm KE}$ of the explosion, assuming that it is a constant density sphere undergoing homologous expansion (Lyman et al., 2016a):

$$v_{\rm sc}^2 \equiv v_{\rm ph}^2 = \frac{5}{3}\frac{2E_{\rm K}}{M_{\rm ej}}. \tag{2.7}$$

The derived values are again reported in Table 2.2, and we find $E_{\rm KE} = (1.6 - 5.2) \times 10^{52}\,{\rm erg}$. These values are consistent with the values Fulton et al. (2023) derive, who find $M_{\rm ej} = 7.1^{+2.4}_{-1.7}\,{\rm M}_\odot$ and $E_{\rm KE} = (2.7 - 6.3) \times 10^{52}\,{\rm erg}$. We note that both $M_{\rm ej}$ and $E_{\rm K}$ largely depend on the photon diffusion timescale, and the corner plots in Figure 2.4 show that $\tau_{\rm m}$ is close to hitting the bounds of the priors. This is unsurprising given the nature of the data set, and the faintness of the SN with respect to the afterglow and host galaxy emission. Therefore, both the $M_{\rm ej}$ and $E_{\rm KE}$ we derive should also be considered as estimates, and we are unable to derive robust upper limits in this case due to the nature of the posterior of $\tau_{\rm m}$.

We note that throughout this analysis, systematic uncertainties likely arise from the assumptions made with the color and spectral evolution of SN 2022xiw being identical to that of SN 1998bw, as well as assuming that explosion is undergoing homologous expansion, as the presence of a relativistic jet likely impacts the spherical symmetry of the explosion. An asymmetric explosion would likely impact $\kappa_{\rm opt}$ and the assumptions made in Eq. 2.6 from Taddia et al. (2019a). However, despite these caveats, the statistical uncertainties we find are large and likely dominate over any of these systematic uncertainties.

2.5 Comparison to other GRB-SN

Based on our previous modeling, we attempt to contextualize SN 2022xiw with respect to the overall GRB-SN population. The range of $M_{\rm Ni}$ found for previous GRB-SN, derived under the same assumption that the luminosity is powered by the radioactive decay of ^{56}Ni, has an average value of $M_{\rm Ni} = 0.37\,{\rm M}_{\odot}$ with a dispersion $\sigma = 0.20\,{\rm M}_{\odot}$ (Cano et al., 2017a). The $M_{\rm Ni}$ we derive for the scenarios where we take into account host galaxy extinction ($M_{\rm Ni} = 0.10$–$0.25\,M_{\odot}$) are within this range, while the $M_{\rm Ni}$ we derive for the scenario with zero host galaxy extinction is outside of this range. The upper limit for the $M_{\rm Ni}$ we derive ($< 0.36\,M_{\odot}$) shows that despite GRB 221009A's highly energetic nature, its associated SN does not possess an exceptional $M_{\rm Ni}$ in comparison with the overall GRB-SN population- in fact, its $M_{\rm Ni}$ is likely lower with respect to the average. For the ejecta mass and kinetic energy, the average values inferred for previous GRB-SN are $M_{\rm ej} = 6\,{\rm M}_{\odot}$ with a dispersion $\sigma = 4\,{\rm M}_{\odot}$ and $E_{\rm KE} = 2.5 \times 10^{52}\,{\rm erg}$, with a dispersion $\sigma = 1.8 \times 10^{52}\,{\rm erg}$ (Cano et al., 2017a). Despite the caveat mentioned in §2.4.2 with the values we derive, both the ejecta masses and kinetic energies for all scenarios are well within these values.

Through these comparisons, we see that SN 2022xiw possesses explosion properties that are overall broadly consistent with the GRB-SN population. This is despite its highly energetic relativistic ejecta, as it possesses an isotropic-equivalent peak γ-ray luminosity of $L_{\gamma,\rm iso} = 2.1 \times 10^{54}\,{\rm erg\,s^{-1}}$ (Frederiks et al., 2023a), making it the most luminous GRB-SN ever detected (Burns et al., 2023; Cano et al., 2017a). Figure 3 in Hjorth & Bloom (2012) suggests that a relationship may exist between the energy release of GRBs and their associated SN brightness. In their Figure, they plot the $L_{\gamma,\rm iso}$ of GRBs against the peak absolute magnitude in V

band ($M_{\rm V}$) of their associated SNe, and make the distinction between low luminosity GRBs ($L_{\gamma,\rm iso} < 10^{48.5} \rm erg\,s^{-1}$), and high-energy jet GRBs ($L_{\gamma,\rm iso} > 10^{49.5} \rm erg\,s^{-1}$). They report a possible direct relationship between $L_{\gamma,\rm iso}$ and $M_{\rm V}$ in low-luminosity GRBs, that turns over into a possible inverse relationship in the high-energy jet GRB region of the parameter space.

In Figure 2.5, we recreate the results from Hjorth & Bloom (2012) to test for these correlations, with a larger data set and a few modifications. We update the GRB-SN sample to include all GRB-SN with an A, B, or C classification from Cano et al. (2017a) and distinguish between low-luminosity GRBs in blue, high-energy jet GRBs in red, and events in the middle in gray. We plot $L_{\gamma,\rm iso}$ against the flux-stretching factor with respect to SN 1998bw ($k_{\rm SN\,1998bw}$), along with $M_{\rm Ni}$. These two parameters are both proxies for the brightness of the associated SN LC ($M_{\rm V}$) that Hjorth & Bloom (2012) used. We use them both in tandem as they have the additional advantage that one is a directly observable feature from the LC ($k_{\rm SN\,1998bw}$), while the other is a physical parameter derived from modeling the explosion ($M_{\rm Ni}$). We also add a few additional events to the sample of Cano et al. (2017a), namely GRB 200826A/AT 2020scz (Ahumada et al., 2021) to the $k_{\rm SN\,1998bw}$ plot, and GRB 161219B/SN 2016jca (Ashall et al., 2019) and GRB 171010A/SN 2017htp (Melandri et al., 2019a) to the $M_{\rm Ni}$ plot. Finally, we add the results from this work to both plots, with the best-fit flux-stretching factor from Table 2.1, $k_{\rm SN\,1998bw} = 0.39$ denoted as a star, and the limit of $M_{\rm Ni} < 0.36\,M_{\odot}$ denoted as an upper limit.

In addition, we also plot the average $k_{\rm SN\,1998bw}$ ($k_{\rm SN\,1998bw,\,average} = 0.97$) and dispersion ($\sigma = 0.44$) for the GRB-SN plotted with the exception of SN 2022xiw shaded in orange, and the average $M_{\rm Ni}$ ($M_{\rm Ni,\,average} = 0.35\,\rm M_{\odot}$) and dispersion ($\sigma = 0.17\,\rm M_{\odot}$) for the GRB-SN plotted with the exception of SN 2022xiw shaded again in orange, along with for the Type Ic-BL population not associated with GRBs ($M_{\rm Ni,\,average} = 0.31\,\rm M_{\odot}$, $\sigma = 0.16\,\rm M_{\odot}$; Taddia et al. 2019a)

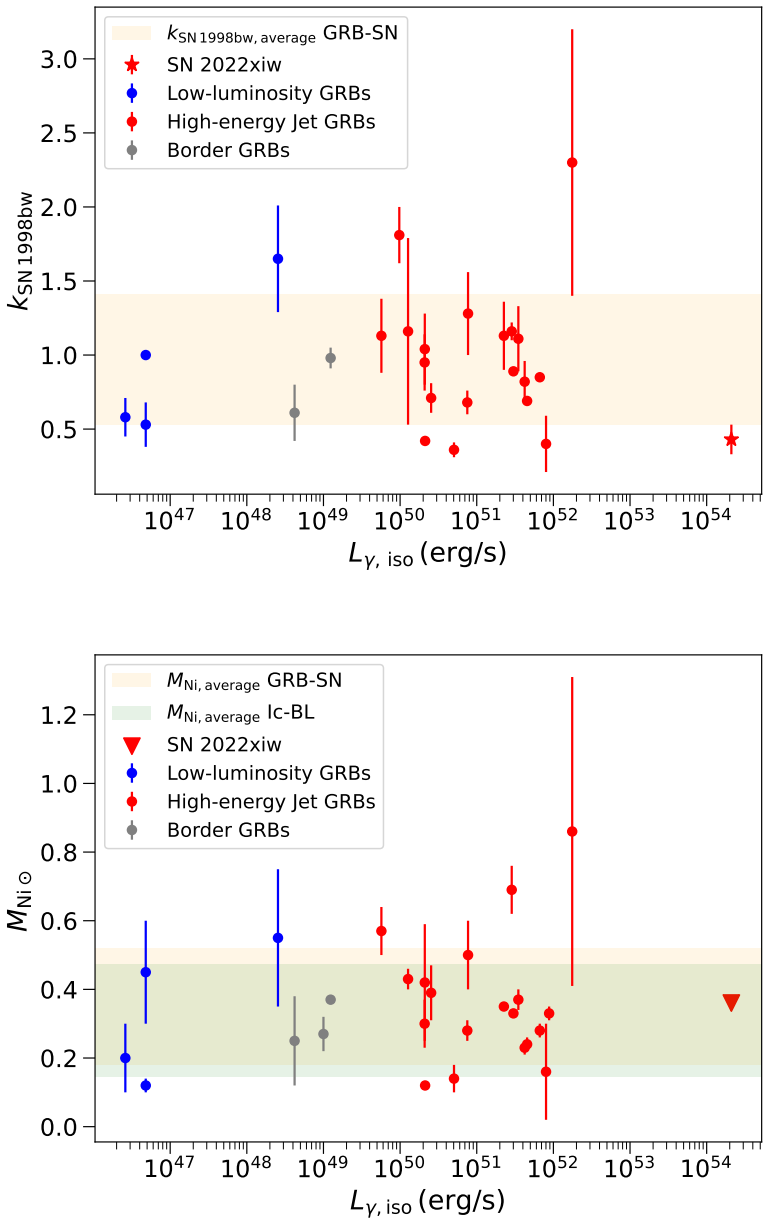

Figure 2.5: *Left panel*: Modification of Fig. 3 from Hjorth & Bloom (2012), where the flux-stretching factor of SNe with respect to SN 1998bw ($k_{\rm SN\,1998bw}$) is plotted against the isotropic equivalent γ-ray luminosity ($L_{\gamma,\rm iso}$) for their associated GRBs. We distinguish between low-luminosity GRBs, high-energy jet GRBs, and GRBs in the border regime. We indicate the results from this work, GRB 221009A/SN 2022xiw with a star. We also show the average $k_{\rm SN\,1998bw}$ for GRB-SN in the plot with the exception of GRB 2201009A/SN 2022xiw, along with its dispersion. *Right panel*: A similar modification of Fig. 3 from Hjorth & Bloom (2012), where the $M_{\rm Ni}$ in $M_\odot$ of SNe is plotted against the isotropic equivalent γ-ray luminosity ($L_{\gamma,\rm iso}$) for their associated GRBs. We make the same distinctions between GRBs as in the above panel, and label the results from GRB 221009A/SN 2022xiw with an upper limit. We also show the average $M_{\rm Ni}$ and dispersion for the GRB-SN plotted with the exception of GRB 221009A/SN 2022xiw, along with that of the Type Ic-BL sample not associated with GRBs from Taddia et al. (2019a).

shaded in green. From the Figure, we notice that SN 2022xiw's $k_{\mathrm{SN\,1998bw}}$ is slightly lower than the average range for the rest of the sample, despite the burst being orders of magnitude more energetic. Furthermore, SN 2022xiw's M_{Ni} is also likely on the lower end with respect to the overall population. The overlap between the average M_{Ni} in normal Type Ic-BL SNe and GRB-SNe suggest that there are no intrinsic differences between the brightness of SN associated with GRBs with those that are not.

We use the Pearson Correlation Coefficient Test to determine if there are correlations between $L_{\gamma,\mathrm{iso}}$ and $k_{\mathrm{SN\,1998bw}}$ and $L_{\gamma,\mathrm{iso}}$ and M_{Ni}, between the low-luminosity GRBs, high-energy jet GRBs, and the entire data set. In the low-luminosity regime, we do find a correlation for both $k_{\mathrm{SN\,1998bw}}$ and M_{Ni}, with coefficients of 0.90 and 0.68 respectively. However, this correlation must be taken with caution, as there are only 4 low-luminosity GRBs in the sample. When testing the high-energy jet GRBs, we find no significant evidence for any correlations in the data, with coefficients of -0.27 and 0.00 for $k_{\mathrm{SN\,1998bw}}$ and M_{Ni} respectively. When testing the overall data set including the border GRBs, we also find no significant evidence for any correlations, with coefficients of -0.22 and 0.01 for $k_{\mathrm{SN\,1998bw}}$ and M_{Ni} respectively. These tests done on the high-energy jet GRBs and entire data set all had p-values greater than 0.25. The lack of correlations are quite interesting, especially because $L_{\gamma,\mathrm{iso}}$ ranges over 7 orders of magnitude. This suggests that SN emission appears to be largely decoupled from any central engine activity in GRB-SN systems.

2.6 Conclusion

By modeling the optical emission from GRB 221009A, we find moderate, but not conclusive statistical evidence ($K_{\rm Bayes} = 10^{1.2}$) for the presence of associated supernova emission, and find that GRB 221009A's associated SN 2022xiw must be substantially fainter than SN 1998bw. We also extract physical parameters associated with the SN, assuming three different host galaxy extinction scenarios: 1) $E(B-V)_{host}$ is allowed to vary as a free parameter between 0.3 and 0.5 mag; 2) $E(B-V)_{host}$ = 0.3 mag; and 3) there is no host galaxy extinction. The most physically plausible scenario is the first, as there is evidence for extinction larger than the nominal Schlafly & Finkbeiner (2011a) value, though with a large degree of associated uncertainty (Kann et al., 2023; Levan et al., 2023b; Williams et al., 2023).

We derive $M_{\rm Ni} = 0.05 - 0.25\,{\rm M}_\odot$, $M_{\rm ej} = 7.2 - 11.8\,{\rm M}_\odot$, and $E_{\rm KE} = (3.3 - 5.5) \times 10^{52}\,{\rm erg}$. These values are weakly constrained due to the faintness of the SN emission with respect to the afterglow and host emission, but we robustly constrain an upper-limit on the $M_{\rm Ni}$ of $M_{\rm Ni} < 0.36\,{\rm M}_\odot$. All of the explosion parameters lie within the range of those found in previous GRB-SN in literature (Cano et al., 2017a), suggesting that even the most extreme GRBs can produce SNe with explosion properties typical of the overall GRB-SN population. We investigate the explosion parameters with respect to the overall GRB-SN population, and find that there is no significant correlation between the luminosity of GRBs and their associated SN's brightness. This suggests that central engine activity in GRB-SN systems and SN emission are largely decoupled, and further studies in the future pinpointing why will be of utmost importance to unraveling the GRB-SN connection in totality. This event is an important addition to the GRB-SN population, and is a prime example for why it is extremely important to continue analyzing high-energy

GRBs to further understand the GRB-SN connection.

Acknowledgements

G. P. S. acknowledges Geoffrey Ryan for useful discussions about Bayesian modeling techniques, as well as Mansi Kasliwal, Kishalay De, Ryan Lau, Viraj Karambelkar, Michael Ashley, Jacob Jencson, and the Palomar Gattini Infrared Survey team for discussions about the paper during the drafting process. G. P. S. thanks James Bauer and Quanzhi Ye for their assistance obtaining LDT observations, and Simi Bhullar for her moral support throughout the paper writing process. M. W. C. acknowledges support from the National Science Foundation with grant numbers PHY-2010970 and OAC-2117997. R. S. acknowledges support from grant number 12073029 from the National Natural Science Foundation of China (NSFC). J. H. G. and E. T. acknowledge support from the European Research Council (ERC) under the European Union's Horizon 2020 research and innovation programme, grant 101002761. A. J. D. was supported, and M. C. M. was supported in part, by NASA ADAP grant 80NSSC21K0649 The material is based upon work supported by NASA under award number 80GSFC21M0002.

These results made use of Lowell Observatory's Lowell Discovery Telescope (LDT), formerly the Discovery Channel Telescope. Lowell operates the LDT in partnership with Boston University, Northern Arizona University, the University of Maryland, and the University of Toledo. Partial support of the LDT was provided by Discovery Communications. LMI was built by Lowell Observatory using funds from the National Science Foundation (AST-1005313). These results were also based on observations obtained at the international Gemini Observatory, a program of NSF's NOIRLab, which is managed by the Association of Universities for Research

in Astronomy (AURA) under a cooperative agreement with the National Science Foundation on behalf of the Gemini Observatory partnership: the National Science Foundation (United States), National Research Council (Canada), Agencia Nacional de Investigación y Desarrollo (Chile), Ministerio de Ciencia, Tecnología e Innovación (Argentina), Ministério da Ciência, Tecnologia, Inovações e Comunicações (Brazil), and Korea Astronomy and Space Science Institute (Republic of Korea). The GROWTH India Telescope (GIT) is a 70-cm telescope with a 0.7-degree field of view, set up by the Indian Institute of Astrophysics (IIA) and the Indian Institute of Technology Bombay (IITB) with funding from Indo-US Science and Technology Forum and the Science and Engineering Research Board, Department of Science and Technology (DST), Government of India. It is located at the Indian Astronomical Observatory (Hanle), operated by IIA an autonomous institute under DST. We acknowledge funding by the IITB alumni batch of 1994, which partially supports operations of the telescope.

Chapter 3: Characterizing the Ordinary Broad-lined Type Ic SN 2023pel from the Energetic GRB 230812B

3.1 Introduction

A clear link has been established over the past two decades between long-duration gamma-ray bursts (LGRBs; $T_{90} > 2$ s) and core-collapse supernovae (CCSNe) from an observational basis (Woosley & Bloom, 2006). Photometrically, a characteristic SN "bump" arises in the afterglow light curve (LC) within 10 to 20 days, as the afterglow fades. Over 40 LGRBs with this characteristic bump have been discovered (see, e.g., Blanchard et al. 2024; Cano et al. 2017a; Hjorth & Bloom 2012; Hu et al. 2021; Kumar et al. 2022a; Melandri et al. 2019a; Rossi et al. 2022b; Srinivasaragavan et al. 2023), and are known as GRB-SNe. Spectroscopic observations of these SNe have revealed that almost all (SN 2011kl associated with GRB 111209A was a super-luminous SN; Greiner et al. 2015a; Kann et al. 2019) are broad-lined Type Ic SNe (Type Ic-BL; Woosley & Bloom 2006); they lack hydrogen and helium lines in their optical spectra, and have broad lines corresponding to ejecta velocities higher than those seen in normal Type Ic explosions. Before this work, 28 GRB-SNe have been spectroscopically confirmed (see, e.g., Blanchard et al. 2024; Cano et al. 2017a,b; Hu et al. 2021; Kumar et al. 2022a; Melandri et al. 2019a; Rossi et al. 2022b; Wang et al. 2018).

However, there remain a number of open questions surrounding the GRB-SN connection, and recent discoveries have shown that our understanding of the connection may not be as complete as once thought. A SN is not always detected for nearby LGRBs (Della Valle et al., 2006; Fynbo et al., 2006; Gal-Yam et al., 2006; Tanga et al., 2018), and the physical link between LGRBs and their associated SN is also not clear. Studies of the brightest GRB of all time, GRB 221009A (Burns et al., 2023; Frederiks et al., 2023b; Kann et al., 2023; Laskar et al., 2023; Lesage et al., 2023b; LHAASO Collaboration et al., 2023; Malesani et al., 2023b; O'Connor et al., 2023; Williams et al., 2023), have shown that its associated SN has a peak luminosity consistent with those of the rest of the GRB-SN population (Blanchard et al., 2024; Fulton et al., 2023; Kann et al., 2023; Levan et al., 2023b; Shrestha et al., 2023; Srinivasaragavan et al., 2023), despite the GRB being more luminous by orders of magnitude. On the other hand, SN 1998bw associated with GRB 0980425 was a very nearby ($z = 0.0085$; Clocchiatti et al. 2011; Iwamoto et al. 1998a; Patat et al. 2001) and relatively luminous SN, with a derived nickel mass ($M_{\rm Ni}$) powering the SN as high as 0.9 $\rm M_\odot$ (Sollerman et al., 2000). Its associated GRB 980425 was a low-luminosity GRB, with an isotropic equivalent energy of $E_{\gamma,\rm iso} \sim 10^{48}\,\rm erg$ (Galama et al., 1998), which is three to four orders of magnitude fainter than what is seen for cosmological GRBs. Numerous observational studies have also been done on GRB-SNe whose associated GRBs have energies in between GRB 221009A and GRB 0908425 (see, e.g., Malesani et al. 2004; Matheson et al. 2003; Mazzali et al. 2006a; Schulze et al. 2014; Starling et al. 2011), and they paint a scattered picture regarding the relationship between GRB energetics and SN properties.

The origin and classification of LGRBs based solely on their T_{90} has also come into question, as GRB 211211A ($T_{90} \sim 34.3\,\rm s$; Mangan et al. 2021) and GRB 230307A ($T_{90} \sim 35\,\rm s$;

Dalessi et al. 2023) may have had associated kilonova emission, pointing towards a compact object origin (Gillanders et al., 2023; Levan et al., 2023a; Rastinejad et al., 2022; Troja et al., 2022; Yang et al., 2022, 2023). Studies of LGRBs' surrounding interstellar medium also show evidence for LGRBs that do not arise from the collapse of massive stars, but rather compact object mergers as well (Leśniewska et al., 2022). Therefore, it is important to follow up nearby, bright LGRBs and their associated SNe across the electromagnetic spectrum in order to shed light on some of these questions surrounding the GRB-SN connection. Here we report on the characterization of one such GRB-SN.

GRB 230812B was discovered by the *Fermi* Gamma-Ray Burst Monitor (GBM; Meegan et al. 2009) at 18:58:12 UTC on 12 August 2023, which we establish hereafter as T_0 (Lesage et al., 2023a). The burst has a $T_{90} = 2.95 \pm 1.02$ s, and a fluence of $2.69 \pm 0.01 \times 10^{-4}\,\mathrm{erg\,cm^{-2}}$ in the 10–1000 keV band. The afterglow was subsequently detected as an X-ray point source by the *Swift* X-Ray Telescope (XRT; Burrows et al. 2005) at $\mathrm{T}_0 + 0.297$ days (Beardmore et al., 2023). Its brightness prompted follow-up across the electromagnetic spectrum (Lipunov et al., 2023a,b; Salgundi et al., 2023; Zheng et al., 2023a), and the optical counterpart was discovered by Zheng et al. (2023b) and Salgundi et al. (2023). Spectroscopic observations of the optical afterglow led to a redshift measurement of $z = 0.36$ (de Ugarte Postigo et al., 2023a). At this redshift using a flat ΛCDM cosmology with $\Omega_\mathrm{m} = 0.286$ and $\mathrm{H}_0 = 69.6$ km s^{-1} Mpc^{-1} to convert redshifts to distances, the burst has an isotropic equivalent energy release of $E_{\gamma,\mathrm{iso}} \sim 1.1 \times 10^{53}\,\mathrm{erg}$. Using the T_{90} reported, the burst has an isotropic equivalent average gamma-ray luminosity of $L_{\gamma,\mathrm{iso}} \sim 8.8 \times 10^{52}\,\mathrm{erg\,s^{-1}}$. Comparing these values to the LGRB population with observationally confirmed SN, GRB 230812B possesses the fifth highest $E_{\gamma,\mathrm{iso}}$ and second highest $L_{\gamma,\mathrm{iso}}$. This makes GRB 230812B a rare example of an energetic LGRB nearby enough to search for an

associated Type Ic-BL SN.

In this *Letter*, we present optical observations of the afterglow of GRB 230812B that display a clear late-time flattening consistent with an associated SN (SN 2023pel; Agui Fernandez et al. 2023a), and spectroscopic observations confirming SN 2023pel as a Type Ic-BL SN. In §3.2 we report our observations of the optical counterpart; in §3.3 we analyze the optical counterpart and find its associated SN 2023pel; in §3.4 we analyze SN 2023pel and characterize its key properties; and in §3.5 we summarize our conclusions. Hussenot-Desenonges et al. (2023) also report an analysis of this event, and where relevant we compare our results with theirs.

3.2 Observations

3.2.1 *Swift*

Observations of the afterglow with the *Neil Gehrels Swift Observatory* (Gehrels et al., 2004) XRT began at $\mathrm{T}_0 + 25$ ks (Beardmore et al., 2023), localizing the afterglow of the GRB. The data were obtained in Photon Counting (PC) mode. We retrieved the time-averaged XRT PC mode spectrum from the *Swift*-XRT GRB Lightcurve Repository[1] (Evans et al., 2009). The spectrum contains 5.0 ks of data obtained between $\mathrm{T}_0 + 25$ ks to $\mathrm{T}_0 + 38$ ks, with a midtime of $\mathrm{T}_0 + 8.8$ hr. The data are grouped to a minimum of 1 count per bin. We also retrieve the X-ray LC, which contains data obtained between $\mathrm{T}_0 + 25$ ks to $\mathrm{T}_0 + 1421$ ks.

We likewise retrieved the data obtained by the Ultra-Violet/Optical Telescope (UVOT; Roming et al., 2005a) from the *Swift* Data Archive[2]. All observations were obtained using the broadband *white* filter (hereafter, *wh*). We focused on the initial *wh*-filter data (ObsID:

[1] https://www.swift.ac.uk/xrt_curves/
[2] https://heasarc.gsfc.nasa.gov/cgi-bin/W3Browse/swift.pl

00021619001) with a total exposure of 4,881 s. The data were combined using the `uvotimsum` task within `HEASoft v6.29c` (Nasa High Energy Astrophysics Science Archive Research Center (Heasarc), 2014). Due to an issue with the *Swift* gyroscope affecting attitude control (Cenko, 2023) the image point spread function (PSF) is elongated. We therefore utilized a lenticular source region with position angle (PA) of 302° to match the shape of the PSF and selected two nearby, source-free circular regions of $15''$radius as background. We used the `uvotsource` and `uvot2pha` task to measure the photometry and retrieve the spectral files. At this epoch, we measure a source brightness of $wh = 19.29 \pm 0.06$ AB mag. We obtain similar results (consistent within 1σ errors) using `uvotdetect`, which automatically selects the source region. Therefore, we conclude that our treatment of the elongated PSF is reasonable.

3.2.2 ZTF

The Zwicky Transient Facility (ZTF; Bellm et al. 2019; Dekany et al. 2020a; Graham et al. 2019; Masci et al. 2019) is a public-private survey that images the entire northern sky every two days in the g and r bands. The transient detection with ZTF relies on image subtraction, using templates of predefined fields. Any high significance difference ($> 5\sigma$) generates an *alert* containing information about the transient (Patterson et al., 2019a). We query the alert stream via Kowalski (Duev et al., 2019) through an alert filtering scheme on Fritz previously described in SGRB and gravitational-wave searches (Ahumada et al., 2021, 2022; Kasliwal et al., 2020). In a nutshell, we select sources that are spatially and temporally consistent with the GBM localization, are far from PS1 stars (based on Tachibana & Miller 2018a) or bright sources, are real based on the real-bogus score (Duev et al., 2019), have a positive residual, and that have at least two

detections separated by a minimum of 15 minutes.

We ingested the GBM localization map (Goldstein et al., 2022) into Fritz (van der Walt et al., 2019a), the ZTF instance of SkyPortal (Coughlin et al., 2023; van der Walt et al., 2019b), an interactive tool design to plan and schedule ToO observations for ZTF. The observing plan was generated using `gwemopt` (Coughlin et al., 2019), by taking the healpix *Fermi*-GBM localization map, slicing the skymap into predefined tiles of the size and shape of the ZTF field of view, determining which fields have the highest enclosed probability, and optimizing observations based on airmass and visibility windows. For this purpose, we used a modified version of the 'greedy' algorithm (Almualla et al., 2020; Coughlin et al., 2018), only allowing for the use of the ZTF primary grid. The final schedule consisted of 300 s exposures in the r and g bands, starting 8.6 hours after the GBM detection. The observing plan for the first night covered 420 square degrees beginning at 2023-08-13 03:34:57, using 3 epochs of 9 fields, totaling 2.25 hours. This corresponds to 78% of the probability enclosed in the Earth-occultation corrected GRB localization map. The exposures reached median depths of 21.9 mag in both g and r band (Salgundi et al., 2023). The first ZTF detection of the afterglow ZTF23aaxeacr happened 8.61 hours after the burst, during the first ZTF exposure of the field, as the transient was sitting in the ZTF field that covered the highest probability.

For GRB 230812B, ZTF detected 22154 sources in the GBM error region in difference imaging, though only 55 sources passed our filtering criteria. These sources were cross-matched against the *Wide-field Infrared Survey Explorer* (*WISE*; Cutri et al. 2013), milliquas (Flesch, 2019), and the Minor Planet Center, to ensure these were not active galactic nuclei (Stern et al., 2012) or solar system objects. Finally, we queried the IPAC-ZTF forced photometry service using a month-long baseline to reject young SNe. The majority of the candidates were ruled

out by one (or multiple) of the criteria previously described. The afterglow of GRB 230812B, ZTF23aaxeacr/SN 2023pel [α (J2000)= $16^{\rm h}36^{\rm m}31.48^{\rm s}$, δ (J2000) = +47°5132.″26; Salgundi et al. 2023], was found during the first night of observations due to the fast evolution of 2 mag day^{-1} showed in the r-band ZTF data. No other candidate showed a photometric evolution consistent with an afterglow, and the source was reported to TNS (AT 2023pel; Salgundi et al. 2023) once its fast evolution was confirmed. Our TNS report came only 4 minutes after the refined *Swift* XRT localization, and our source was consistent (within 6 arcsec) with the center of the XRT region (Page & Swift-XRT Team, 2023).

3.2.3 SEDM

Once the afterglow was identified, we used the Rainbow Camera on the Spectral Energy Distribution Machine (SEDM; Blagorodnova et al. 2018a; Rigault et al. 2019a) mounted on the Palomar 60-inch telescope to acquire $u-$, $g-$, $r-$, and $i-$ band imaging in 300 s exposures. The SEDM images started 11.02 hours after the burst. The SEDM images were processed with a `Python`-based pipeline version of the `Fpipe` (Fremling et al., 2016), which includes photometric calibrations and image subtraction using reference images from The Sloan Digital Sky Survey (SDSS; Abazajian et al. 2009).

3.2.4 LT

The location of the GRB was observed with IO:O, the optical imager on the 2m robotic Liverpool Telescope (Steele et al., 2004) at the Observatorio del Roque de los Muchachos. Observations were taken on three separate nights: 2023-08-14 ($griz$ filters), 2023-08-16 (gri), and

2023-09-04 (r).

Reduced images were downloaded from the LT archive and processed with custom image-subtraction and analysis software (K. Hinds and K. Taggart et al., in prep.) Image stacking and alignment is performed using SWARP (Bertin, 2010b) where required. Image subtraction is performed using a pre-explosion reference image in the appropriate filter from the Panoramic Survey Telescope and Rapid Response System 1 (PS1; Flewelling et al. 2020b). The photometry is measured using PSF fitting methodology relative to PS1 standards and is based on techniques in Fremling et al. (2016).

3.2.5 LDT

We also observed GRB 230812B's optical counterpart in r and i with the 4.3m Large Monolithic Imager (LMI) on the Lowell Discovery Telescope (LDT) for 5 epochs between UT 2023-08-26 and 2023-09-09. We reduced the images using a custom `Python`-based image analysis pipeline (Toy et al., 2016), that performs data reduction, astrometry, registration, source extraction and PSF photometry using SourceExtractor (Bertin & Arnouts, 1996b). SourceExtractor was calibrated using point-sources from PS1 DR1 catalog. We then performed image subtraction using the PS1 templates and the ZOGY algorithm-based `Python` pipeline (Kumar et al., 2022a; Zackay et al., 2016) to remove the host contribution. Figure 3.1 shows both the wider field of view of GRB 230812B's position on the sky, as well as its flux in both filters at $T_0 + 14$ days.

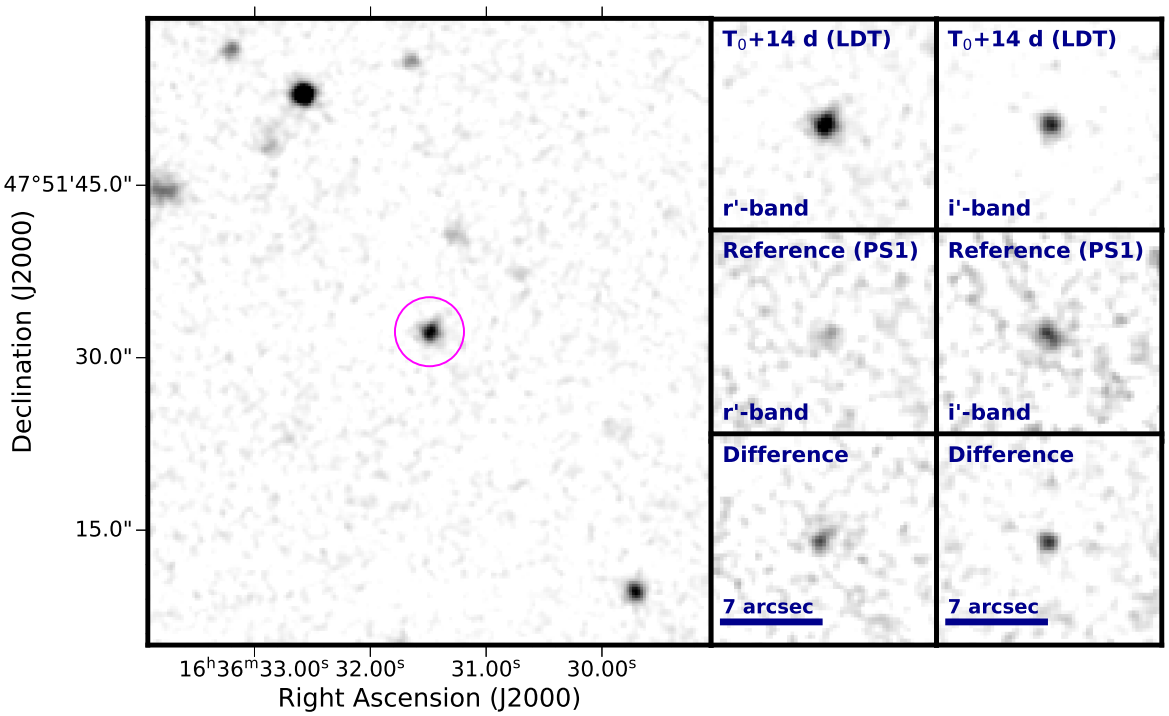

Figure 3.1: LDT images of the optical afterglow of GRB 230812B/SN 2023pel. The left, large panel shows the wider field of view of GRB 230812B, in r band 14 days after T_0. The right panels show the observations taken of the GRB that include the host galaxy contribution, the reference images from PS1 used for image subtraction, and the resulting subtracted images used for photometry, in both r and i bands. The images have been smoothed for display purposes.

3.2.6 GIT

We used the 0.7m GROWTH-India Telescope (GIT) (Kumar et al., 2022c) located at the Indian Astronomical Observatory (IAO), Hanle-Ladakh, to acquire data of GRB 230812B's optical counterpart. The counterpart was observed in Sloan g', r' and i' bands starting 20 h after T_0. We continued observations for up to seven days by acquiring multiple 300 s exposures. Data were downloaded and processed in real time by the GIT data reduction pipeline (Kumar et al., 2022d). We used individual exposures of 300 s for photometry in the early stages when the afterglow was bright. Later, we stacked images with SWarp (Bertin, 2010a) to increase the S/N ratio of detections.

All images were pre-processed by subtracting bias images, flat-fielding, and removing cosmic-rays via Astro-SCRAPPY (McCully & Tewes, 2019) package. Astrometry was performed on the resulting images using the offline solve-field (Lang et al., 2010a) astrometry engine. Subsequently, refined astrometry was conducted using the SCAMP (Bertin, 2006) package to facilitate image stacking with SWarp (Bertin, 2010a). Sources were detected using SourceExtractor (Bertin & Arnouts, 1996a) and were crossed-matched against the PS1 DR1 catalog (Chambers et al., 2016a) through Vizier to obtain the zero-point in images. Using the ZOGY algorithm-based `Python` pipeline, we performed image subtraction on all the images using the PS1 templates. Finally, the pipeline performed point spread function (PSF) fit photometry on subtracted images to obtain magnitudes.

3.2.7 HCT

The 2-meter Himalayan Chandra Telescope (HCT) situated at the Indian Astronomical Observatory (IAO) in Hanle-Ladakh was used to observe the optical counterpart of GRB 230812B. This counterpart was observed in Sloan r' and i' bands, beginning 3 days after T_0. During the period of UT 2023-08-15 to 2023-08-24, we conducted four observations, capturing multiple exposures lasting between 20 to 40 minutes each. Standard image reduction techniques were applied, including bias subtraction and flat-fielding, as well as cosmic-ray removal using the Astro-SCRAPPY package. Astrometry was conducted on the resulting images using the offline solve-field astrometry engine. We then use the same methods as §3.2.6 to extract sources, perform image subtraction, and perform PSF photometry to get magnitudes of the GRB counterpart.

3.2.8 Keck

We obtained a spectrum of GRB 230812B/SN 2023pel on UT 2023-09-09 05:31:47 using the Deep Imaging Multi-Object Spectrograph (DEIMOS; Faber et al. 2003) mounted on the 10-m Keck II telescope. Our configuration used a 600ZD grating, a central wavelength of 7500 $\AA$ and the OG 550 filter to maximize redder wavelength coverage. The observation consisted of 3 $\times$ 1800s exposures and one 900s exposure totalling 1.75 hr. The data were calibrated and reduced using Pypeit (Prochaska et al., 2020a).

3.3 Afterglow Analysis

3.3.1 Characterization of X-ray and Optical Afterglow

We start with determining some of the basic afterglow properties, and note that an in-depth, multi-wavelength study of the afterglow is forthcoming in Pathak et al. (in preparation). We find that the power-law temporal decay indices of the X-ray (*Swift* XRT) and optical data (using g, r and i-bands prior to when the SN emission affects the LC, $< T_0 + 4$ days), are consistent, with $\alpha_X = 1.31^{+0.07}_{-0.06}$ ($\chi^2_{\rm reduced} = 0.96$), and $\alpha_O = 1.31 \pm 0.02$ ($\chi^2_{\rm reduced} = 2.14$). We then calculate the spectral index in the optical, using SEDM observations in the u, g, r, and i bands from SEDM at $\rm T_0 + 10.8$ hours. We derive $\beta_O = 0.74 \pm 0.02$ ($\chi^2_{\rm reduced} = 0.76$) after correcting for line-of-sight extinction through the Galactic plane ($A_V = 0.06$ mag; Schlafly & Finkbeiner 2011a). These values are consistent with the results of Hussenot-Desenonges et al. (2023), who find $\alpha_O = 1.35 \pm 0.02$ and $\beta_O = 0.74 \pm 0.01$.

We then perform an X-ray analysis through `XSPEC v12.12.0` using the initial PC mode XRT spectrum. We modelled the spectrum assuming an absorbed power-law model `tbabs*ztbabs *pow`, which is a Tuebingen-Boulder interstellar medium (ISM) absorption model that calculates the cross-section for X-ray absorption by the ISM (Wilms et al., 2000a). We fix the Galactic hydrogen column density to $N_{H,\rm MW} = 2.0 \times 10^{20}$ cm^{-2} (Willingale et al., 2013) and a redshift of $z = 0.36$. We fit the data by minimizing Cash statistics (Cash, 1979). We obtain a best-fit (C-stat = 259 for 332 dof) X-ray photon index of $\Gamma_X = 1.765 \pm 0.085$ and intrinsic hydrogen column density $N_{H,z} = (1.2 \pm 0.4) \times 10^{21}$ cm^{-2}. This corresponds to an X-ray spectral index of $\beta_X = \Gamma_X - 1 = 0.765 \pm 0.085$. The consistency between the optical and X-ray spectral indices

suggests that the optical and X-ray data lie on the same spectral segment (see Figure 3.2).

Therefore, we include the early optical data (u, g, r, and i filters) obtained by SEDM, each shifted to a midtime of 8.8 hr using the best-fit temporal power-law, to constrain the possibility of dust intrinsic to the GRB environment, through modeling the broadband spectral energy distribution (SED) again in `XSPEC v12.12.0`. We fix the Milky Way dust reddening to $E(B-V)_{\rm MW} = 0.02$ mag (Schlafly & Finkbeiner, 2011a). The broadband SED was fit using the model `tbabs*ztbabs*redden*zdust*pow`, which again uses the Tuebingen-Boulder ISM absorption model to account for absorption and extinction both in the Milky Way and the host galaxy. We applied a Milky Way extinction law with $R_V = 3.1$ (Cardelli et al., 1989a), and derive a photon index of $\Gamma_{XO} = 1.73 \pm 0.02$, $N_{H,z} = (1.1 \pm 0.2) \times 10^{21}$ cm^{-2}, and $E(B-V)_z < 0.07$ mag (3σ) for a $\chi^2 = 363$ for 336 dof. This is consistent with the results of Hussenot-Desenonges et al. (2023), who find $E(B-V)_z < 0.03$ mag. We show the broadband modeling described, along with the X-ray and optical data at a midtime of $\rm T_0 + 8.8$ hours in Figure 3.2. Given the low upper limit derived, we ignore the host galaxy extinction for rest of our analysis.

The spectral index we derive ($\beta_{\rm OX} = 0.73 \pm 0.02$) does not match with a locally fast cooling environment ($\nu_m < \nu_c < \nu$, where ν_m is the injection frequency of the electrons and ν_c is the cooling frequency), as the slope of the electron energy distribution p would be abnormally low (1.46 ± 0.04), according to the standard closure relations (Granot & Sari, 2002; Sari et al., 1998). Instead, a more reasonable value of $p = 2.46 \pm 0.04$ is obtained for $\nu_m < \nu < \nu_c$, assuming an adiabatic jet and constant density ISM. This points towards a slow-cooling regime for the synchrotron afterglow in the optical to X-ray bands (see Pathak et al., in preparation, for more details).

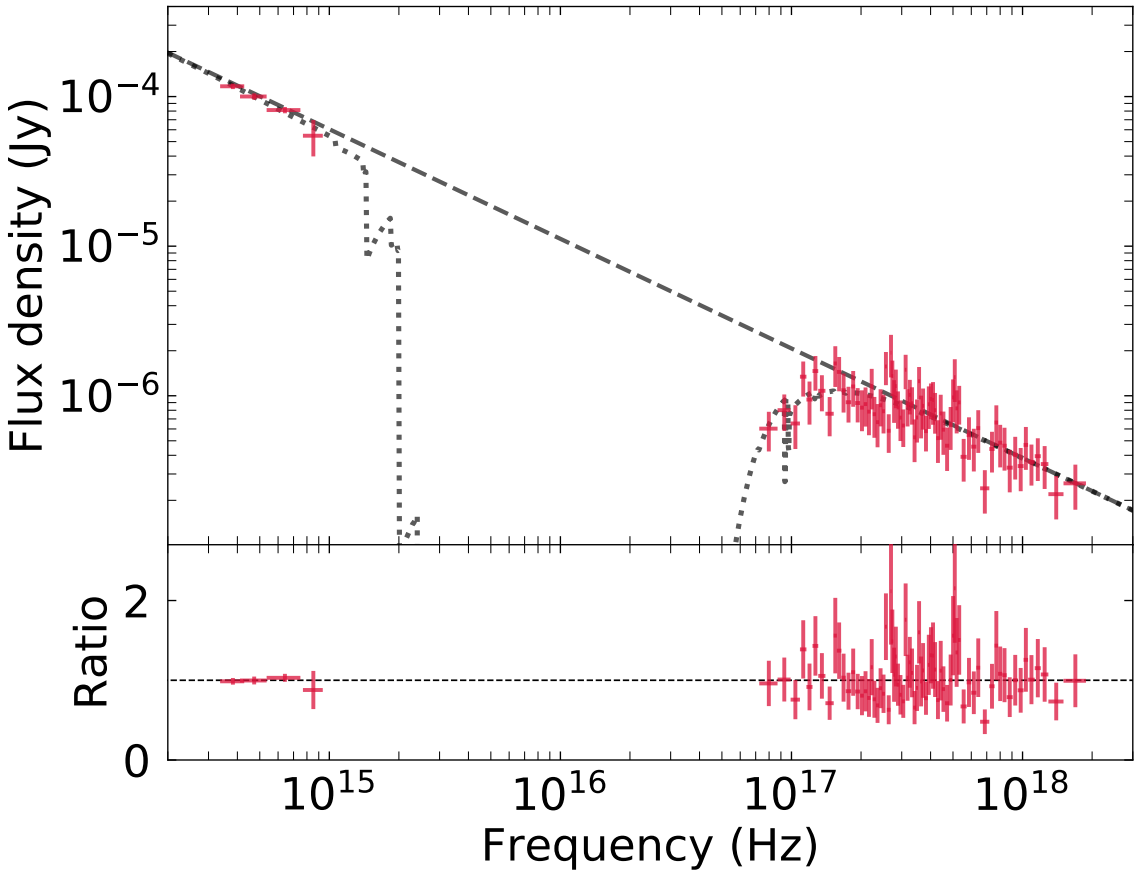

Figure 3.2: Broadband modeling of the GRB afterglow from optical (ZTF and SEDM; $ugri$) to X-ray (*Swift*) wavelengths at a midtime of $\mathrm{T}_0 + 8.8$ hours. The model is a simple absorbed power-law shown by the gray dotted line and the unabsorbed model is shown as the gray dashed line, both corrected for Galactic extinction. The bottom panel shows the ratio between the data and the absorbed power-law model with the black dashed line showing a ratio of unity.

3.3.2 SN Bump

A clear late-time flattening is seen as soon as $T_0 + 7$ days in Figure 3.3, in both the r and i bands, which we interpret as due to rising SN emission. Kann et al. (2007) and Oates et al. (2009) have shown that if the central engine is still active, a re-brightening of the optical afterglow may occur shortly after the prompt emission. Greiner et al. (2009) has also shown that optical flaring due to refreshed or reversed shocks can cause brightening episodes in the early-time optical afterglow LC. However, the X-ray LC of GRB 230812B (see Figure 3.5) shows no evidence of flaring at early times, and does not re-brighten when the optical afterglow begins to, which occurs a week after the prompt emission. Therefore, we determine that the late-time flattening cannot be explained by central engine activity.

It has been shown that the LGRBs 211211A and 230307A have evidence of associated kilonova emission (Levan et al., 2023a; Rastinejad et al., 2022; Troja et al., 2022; Yang et al., 2022). In order to determine if the late-time flattening could be due to a kilonova, we transform the kilonova LC associated with GRB 130603B (Berger et al., 2013) to the redshift of GRB 230812B ($z = 0.36$), and apply the line-of-sight Galactic extinction. We find that the kilonova peaks around 26 mag in H band, and therefore, would be even fainter in the optical bands. This is too faint to cause any significant late-time flattening in the optical afterglow LC, which leads us to determine that the late-time flattening cannot be explained by an associated kilonova.

Therefore, the most likely explanation for the late-time flattening is an associated SN. In order to compare the associated SN to SN 1998bw (the prototypical SN associated with a GRB used in modeling studies, due to the proximity of the SN at $z = 0.0085$), we use the PyMultiNest Bayesian modeling package (Buchner et al., 2014; Feroz et al., 2009) to find the best-fit flux-

stretching factor ($k_{\rm SN1998bw}$) and time-stretching factor ($s_{\rm SN1998bw}$) of the SN with respect to SN 1998bw. The full model that we use is:

$$f_\nu(t_{\rm obs}) = k_{\rm SN1998bw}(f_\nu^{\rm SN1998bw}(t_{\rm obs}/s_{\rm SN\,1998bw})) + a_{\rm AG}(t_{\rm obs})^{-\alpha}, \tag{3.1}$$

where $f_\nu^{\rm SN1998bw}(t_{\rm obs})$ is the flux seen of SN 1998bw at $z = 0.36$ at a time in the observer frame, $t_{\rm obs}$ is the time in the observer frame, α is the power-law decay index, and $a_{\rm AG}$ is the flux constant of proportionality. We derive $f_\nu^{\rm SN1998bw}$ by (de)reddening and K-correcting the nugent-hyper model (Levan et al., 2005) in SNCosmo (Barbary et al., 2016) to match the relevant properties of GRB 230812B. We perform the fitting concurrently in the r and i bands, fixing $\alpha = 1.31$ and $a_{\rm AG}$ (derived in §3.3.1). Therefore, the free parameters in our fitting procedure corresponding are $k_{\rm SN1998bw}$ and $s_{\rm SN1998bw}$. Because a possible correlation may exist between these two parameters (Cano, 2014), we create priors for both of the parameters drawn from a bivariate normal distribution fit to the $k_{\rm SN1998bw}$ and $s_{\rm SN1998bw}$ values derived for GRB-SN in literature (Cano et al., 2017a). Furthermore, in order to account for systematic uncertainties due to combining data from multiple telescopes (S-corrections; Stritzinger et al. 2002), we numerically optimize the likelihood function assuming that the reported errors actually underestimate the true uncertainty. We do this through using the same method as Srinivasaragavan et al. (2023), by introducing an error-stretching factor β in the fitting procedure to represent the S-correction.

We find that the best-fit values for the flux-stretching and time-stretching factors are $k_{\rm SN1998bw} = 0.92$ and $s_{\rm SN1998bw} = 0.76$, with median $\pm 1\sigma$ values of $k_{\rm SN1998bw} = 0.93^{+0.04}_{-0.03}$ and $s_{\rm SN1998bw} = 0.76 \pm 0.02$. The reduced chi-squared statistic is $\chi^2_{\rm reduced} = 1.2$, indicative that the model is an adequate fit to the observed data. Our $k_{\rm SN1998bw}$ is consistent with the value found by Hussenot-

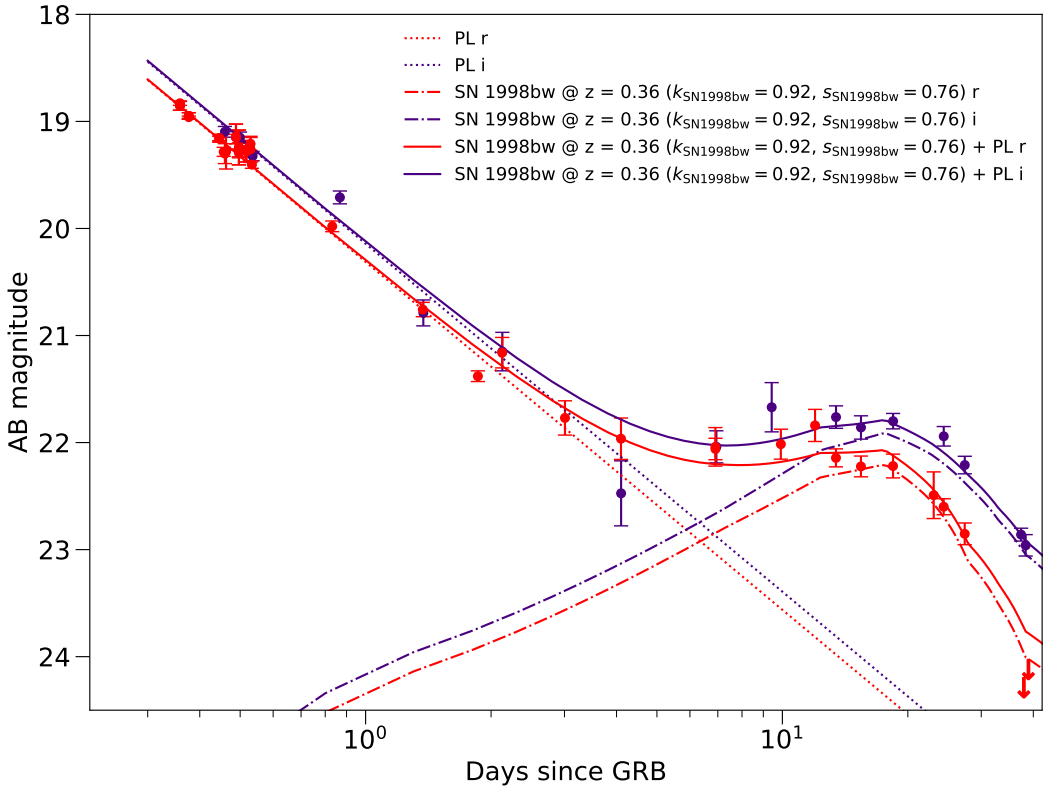

Figure 3.3: Observed r and i band photometry of GRB 230812B from the optical instruments listed in §7.2, with all magnitudes already host-galaxy subtracted. The photometry values are reported in Table B.1, and all times are in the observer frame. We also show the best-fit power law decay to the optical data derived in §3.3.1, corresponding to a power-law decay index of $\alpha = 1.31$. The LCs for a SN 1998bw-like source in r and i bands, redshifted to $z = 0.36$, reddened according to the line-of-sight Galactic extinction of GRB 230812B, with a flux-stretching factor of $k = 0.92$ and time-stretching factor of $s = 0.76$ (derived in §3.3.2) applied, are also shown.

Desenonges et al. (2023) of $k_{\rm SN1998bw} = 1.04 \pm 0.09$, and our $s_{\rm SN1998bw}$ is consistent at the 2σ level with theirs of $s_{\rm SN1998bw} = 0.68 \pm 0.05$. Therefore, we find that the SN associated with GRB 230812B, SN 2023pel, is about as bright as SN 1998bw, but evolves on a quicker timescale. We will revisit this when we model the SN parameters in §3.4.2. We note that the presence of a jet break in the optical LC is a possible source of systematic error for this analysis; however, the lack of a jet break in the X-ray LC and our well-sampled optical data set make this an unlikely possibility.

After subtracting the best-fit power law value from the brightest r-band photometry point seen in the late-time flattening and correcting for the Galactic extinction, we find that the observed peak absolute magnitude of SN 2023pel is $M_r = -19.46 \pm 0.18$ mag, which is consistent with the peak magnitude found in Hussenot-Desenonges et al. (2023), $M_r = -19.41 \pm 0.10$. As expected from the flux-stretching factor we derived, this is consistent with the peak absolute magnitude of SN 1998bw, $M_R = -19.36 \pm 0.05$ mag (Galama et al., 1998), and brighter than what is seen for the the overall Type Ic-BL SN population ($M_r = -18.6 \pm 0.5$ mag; Taddia et al. 2019a). We confirm that SN 2023pel is indeed a Type Ic-BL SN in §3.3.3.

3.3.3 Spectrum Analysis

As described in §3.2.8, we obtained a DEIMOS spectrum on UT 2023-09-09 05:31:47 of GRB 230812B/SN 2023pel, and we show the observed, reduced spectrum after correcting for telluric features in gray in the top panel of Figure 3.4. Hβ, Hα, and [O III] galaxy emission lines are clearly seen in the spectrum, and we use PySpecKit's SPLOT interactive fitting routine (Ginsburg & Mirocha, 2011; Ginsburg et al., 2022) to fit these lines to a redshift. We find $z =$

0.36112 ± 0.00004 (where the error is the root mean square error), providing an independent confirmation of the redshift of GRB 230812B/SN 2023pel.

We then use the Next Generation Super Fitter (NGSF; Goldwasser et al. 2022) to model the SN and host together. For this, we allow NGSF to explore all the available SN and galaxy templates, while fixing the value for the redshift and limiting the SN phase to a window between 5 and 25 days after peak. The results show that the NGSF best fit is to an Elliptical galaxy with a SN-Ic BL ($\chi^2/\mathrm{dof} \sim 7.45$). However, elliptical hosts for LGRBs are extremely rare, as they usually originate from active star-forming galaxies. So far, GRB 050219A is the only example of a LGRB found in an elliptical (Rossi et al., 2014) galaxy, and the presence of narrow emission lines at the redshift of the host leads us to conclude that the host is most likely not an elliptical galaxy. Therefore, we use the next-best fit with a SN-Ic BL, a S0 spiral galaxy ($\chi^2/\mathrm{dof} \sim 9.80$), to represent the host contribution. We note that NGSF does not include nebular emission in their galaxy templates, though we mask the galaxy lines before performing the fits. When re-doing the analysis using the Elliptical galaxy template, all of our derived results were consistent within error bars. The particular template used does not seem to significantly impact our analysis.

We scale the host contribution to the spectrum to the same percentage (44%) of the host contribution to the r-band photometry of GRB 230812B's optical counterpart at the time closest to the spectrum ($T_0 + 27.394$ days), derived from comparing the LDT magnitudes before and after image subtraction. We show the template in brown in the top panel Figure 3.4, and subtract this template from the observed spectrum. We also subtract the afterglow's spectral model, corresponding to $F_\nu \propto \nu^{-\beta_O}$, where $\beta_O = 0.74$ is the optical spectral index derived in §3.3.1, from the observed spectrum. We scale the spectral model of the afterglow to the same percentage (14%) of the afterglow's contribution to the observed r-band photometry at the time of the spectrum,

through using the best-fit temporal power-law derived in §3.3.1. We show the spectral model in pink in the top panel of Figure 3.4.

The final host and afterglow-subtracted, smoothed, and normalized spectrum of SN 2023pel is shown in black in the top panel of Figure 3.4. The phase of the spectrum corresponds to 15.5 days after the observed peak in r band. We then use the IDL routine WOMBAT to remove the galaxy emission lines, and show that spectrum in the bottom panel of Figure 3.4. The spectrum shows clear broad absorption features characteristic of Type Ic-BL SNe, confirming the classification from Agui Fernandez et al. (2023b). We indicate the Fe II and Si II features in the Figure. We then run the SN Identification code (SNID; Blondin & Tonry 2007a) to determine the best match Ic-BL templates. We find that the template for SN 2002ap, 13 days after its peak, and SN 1998bw, 28 days after its peak, are good matches to the spectrum. As mentioned in §3.3.2, we determined that SN 2023pel evolves on a quicker timescale than SN 1998bw. This agrees with the best-fit SN 1998bw template SNID found, as the matching template has a phase 13 days later than the observed phase of the spectrum of SN 2023pel. We show the observed spectra of SN 2002ap (Mazzali et al., 2002) and SN 1998bw (Patat et al., 2001) at the time of these best-fit templates, in pink and green in the bottom panel of Figure 3.4.

3.4 SN Analysis

After showing evidence that a SN is the source of the late-time flattening of the afterglow LC, we shift our focus to the analysis of the SN itself. In this section, we investigate whether the SN can be powered by a millisecond magnetar (§3.4.1), or if the observed data are better described by the conventional Arnett (1982) radioactive decay model (§3.4.2), and report progenitor

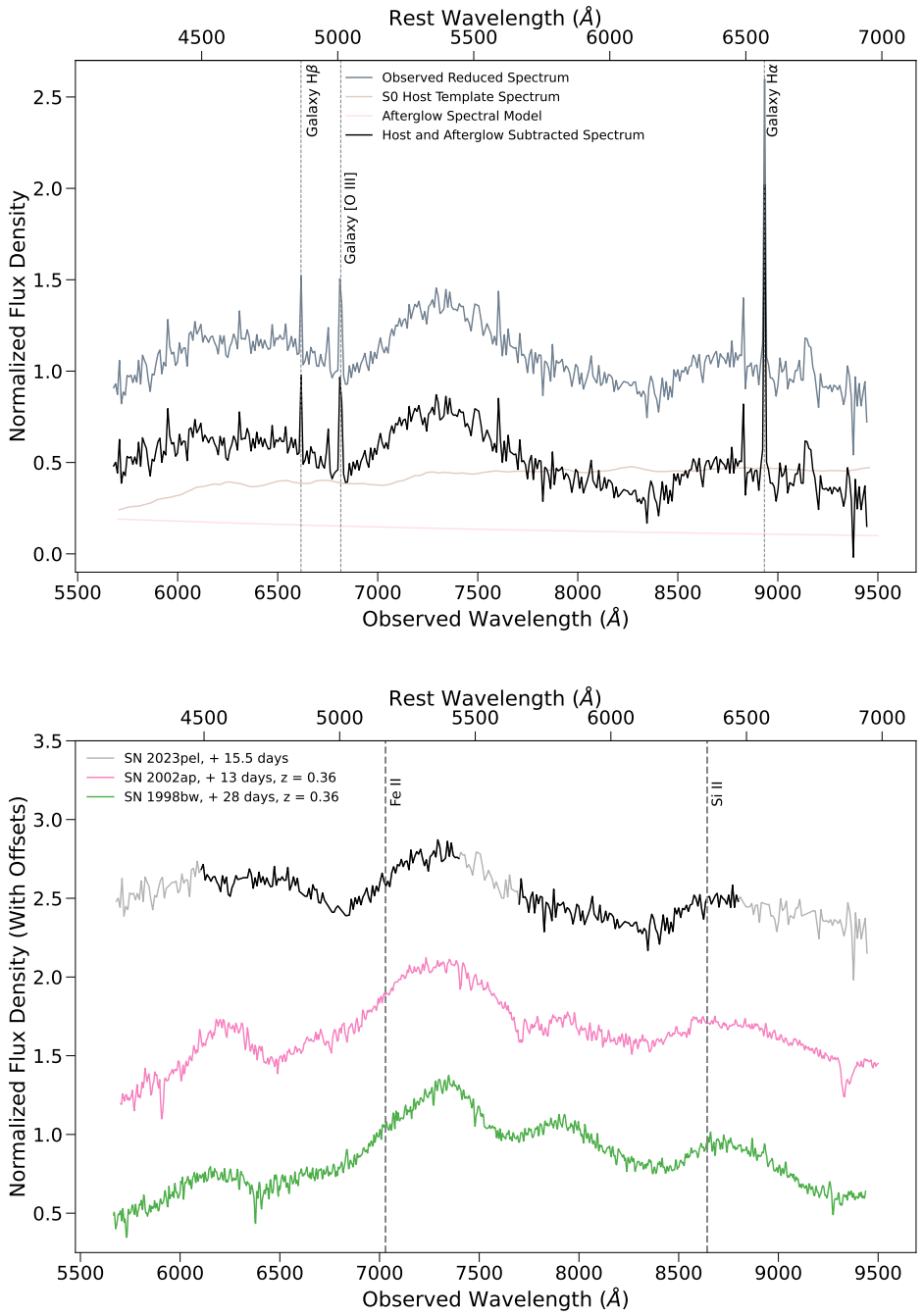

Figure 3.4: *Top panel*: DEIMOS spectrum obtained of GRB 230812B/SN 2023pel, 15.5 days after the observed peak in r band. We show the original reduced spectrum, the best-fit S0 host galaxy template spectrum from NGSF and the afterglow spectral model with their fluxes scaled to the time of the spectrum, and the final, host and afterglow-subtracted spectrum of SN 2023pel, smoothed and normalized for display purposes. The spectrum shows the strong Hβ, Hα, and [O III] galaxy emission lines at $z = 0.36$. *Bottom panel*: We show the spectrum of SN 2023pel, after manually removing narrow galaxy emission lines. We also show the observed spectrum of SN 2002ap, 13 days after peak, and redshifted to $z = 0.36$, and of SN 1998bw, 28 days after peak, also redshifted to $z = 0.36$. All three spectra show broad Fe II and Si II features, characteristic of Type Ic-BL SNe, and we label the lines as well as show the broadened features in bold for SN 2023pel.

and SN properties corresponding to the respective models. We then analyze a spectrum taken of GRB 230812B/SN 2023pel (§3.3.3), and end by comparing the properties of GRB 230812B/SN 2023pel to those of the rest of the GRB-SN population (§3.4.3).

3.4.1 Magnetar Model

Although the Arnett (1982) radioactive heating model (see §3.4.2) is the frequently adopted model used to describe Type Ic-BL LCs, theories have shown that a millisecond magnetar central engine can power LGRBs (Usov, 1992), and observational studies of multiple GRB-SNe have suggested evidence for a magnetar origin (Cano et al., 2016; Greiner et al., 2015b; Lü et al., 2018; Toma et al., 2007; Zhang et al., 2022). We investigate whether our observed X-ray and optical LCs can be explained within the context of this model, using the formulation from Cano et al. (2016), before using the Arnett (1982) model. The millisecond magnetar model consists of three phases: an afterglow component whose emission is due to the GRB ejecta colliding with the surrounding medium; a component whose emission is due to the powering of the central engine; and the SN component whose emission is also due to the powering of the central engine. The X-ray LC is described just by the first two phases, as the SN emission is not significant in the X-ray bandpasses, while the optical LC is described by the addition of all three phases. In order for this model to be viable, the initial magnetic field strength (B_0) and spin period (P_0) derived from the X-ray and optical LC analysis must be consistent with each other. We note that this model assumes that the magnetic field is dipolar in nature, and unevolving over time. Therefore, there are no considerations for multipolar and rapidly evolving magnetic fields within the context of this model.

The full derivation of the model can be found in Cano et al. (2016), and here we provide a brief description of the components. The afterglow is modeled by two components – an impulsive energy input term, and a continuous energy input term. The impulsive energy input term (Zhang & Mészáros, 2001) is represented by a simple power law (SPL; Rowlinson et al. 2013):

$$L_{\rm SPL}(t) = \Lambda t^{-\alpha} \tag{3.2}$$

where Λ is a normalisation constant and α is the power-law decay index. We assume that $\alpha = \Gamma_\gamma + 1$, where Γ_γ is the photon index of the prompt emission. This definition of α comes from the assumption that the decay slope is governed by the curvature effect (Panaitescu & Kumar, 2000; Piran, 2004).

The continuous energy input term is due to the magnetar central engine depositing Poynting flux into the ejecta, where the neutron star is assumed to have a mass of $1.4\,{\rm M}_\odot$ and a radius of 10^6 cm. This emission creates a characteristic plateau in the LC, and is represented as:

$$L_{\rm AG}(t) = L_0 \left(1 + \frac{t}{t_0}\right)^{-2} \tag{3.3}$$

where L_0 is the luminosity of the plateau emission, and t_0 is the duration of the plateau.

Finally, the SN component is modeled by the central engine depositing its energy directly into the SN after the initial jet spreads. The analytical prescription has been derived by many works (Barkov & Komissarov, 2011; Chatzopoulos et al., 2011; Kasen & Bildsten, 2010; Ostriker & Gunn, 1971), and the equation (Arnett, 1980, 1982; Chatzopoulos et al., 2009, 2011; Valenti et al., 2008) is represented as:

$$L_{\rm SN}(t) = \frac{E_{\rm p}}{t_{\rm p}} \exp\left(\frac{-x^2}{2}\right) \int_0^x \frac{z \exp\left(\frac{z^2}{2}\right)}{(1+yz)^2} \, {\rm d}z \tag{3.4}$$

where $E_{\rm p}$ is the initial energy of the magnetar in units of erg, $t_{\rm p}$ is the characteristic spin-down time of the magnetar in units of days, $x = t/t_{\rm diff}$, $y = t_{\rm diff}/t_{\rm p}$, and $t_{\rm diff}$ is the diffusion timescale of the SN in units of days. As mentioned earlier, all of this is considering an $l = 2$ dipole. We can rewrite $E_{\rm p}$ and $t_{\rm p}$ in terms of L_0 and t_0 through

$$E_{\rm p} = \frac{2.00}{2.05} \, L_0 t_0 \tag{3.5}$$

and

$$t_{\rm p} = 2 \, t_0 \tag{3.6}$$

The final model we fit for the X-ray LC is

$$L_{\rm total}^{\rm X-ray}(t) = L_{\rm AG} + L_{\rm SPL} \tag{3.7}$$

and the optical LC, which we fit to the r band, is

$$L_{\rm total}^{r}(t) = L_{\rm AG} + \Phi L_{\rm SN} + L_{\rm SPL} \tag{3.8}$$

where Φ is an additional free-parameter used to normalize the model to the optical data. Even if the properties of the magnetar derived from the X-ray and optical LCs match, if $\Phi > 1$, an additional source of energy is necessary to power the SN in addition to the magnetar central

engine.

Finally, after fitting the observed LCs with the models presented, the L_0 and t_0 derived can be used to find B_0 and P_0 through

$$\frac{B_0}{10^{15}\ \mathrm{G}} = \sqrt{\frac{4.2}{L_{0,49}t_{0,3}^2}} \tag{3.9}$$

and

$$\frac{P_0}{1\ \mathrm{ms}} = \sqrt{\frac{2.05}{L_{0,49}t_{0,3}}} \tag{3.10}$$

where $L_{0,49} = L_0/10^{49}$ erg s^{-1} and $t_{0,3} = t_0/10^3$ s.

Given this formulation, we begin by fitting Eq. 3.7 to the *Swift* XRT LC, where we convert the 0.3–10 keV flux LC to a rest-frame 0.3–10 keV X-ray luminosity LC through the same method described in Section 3 of Cano et al. (2016), fitting the power-law decay index to $\alpha = \Gamma_\gamma + 1 = 3.16$ (Scotton et al., 2023). The best-fit LC is shown in black in Figure 3.5, and we derive $L_0 = 2.62^{+0.45}_{-0.28} \times 10^{45}\,\mathrm{erg\,s^{-1}}$ and $t_0 = 3.75^{+0.51}_{-0.61} \times 10^4\,\mathrm{s}$. This in turn corresponds to $B_0 = 3.37^{+0.91}_{-0.63} \times 10^{15}\,\mathrm{G}$ and $P_0 = 14.44^{+2.29}_{-1.93}$ ms. We then convert our r band LC into luminosity space, and fit Eq. 3.8 to the LC, where the best-fit LC is shown in red in Figure 3.5. We derive $L_0 = 1.03 \pm 0.09 \times 10^{45}\,\mathrm{erg\,s^{-1}}$, $t_0 = 1.89^{+0.15}_{-0.13} \times 10^4\,\mathrm{s}$, and $\Phi = 8.84^{+0.62}_{-0.63}$, which shows clearly that an additional source of energy is needed to power the SN. These parameters correspond to $B_0 = 1.07^{+0.13}_{-0.12} \times 10^{16}\,\mathrm{G}$ and $P_0 = 32.41^{+2.67}_{-2.48}$ ms.

There is therefore a clear discrepancy found in the values derived for the magnetar through independently fitting the X-ray and optical LCs. This shows that the magnetar model under the assumption of a dipolar, unevolving magnetic field, is not viable to satisfactorily describe the

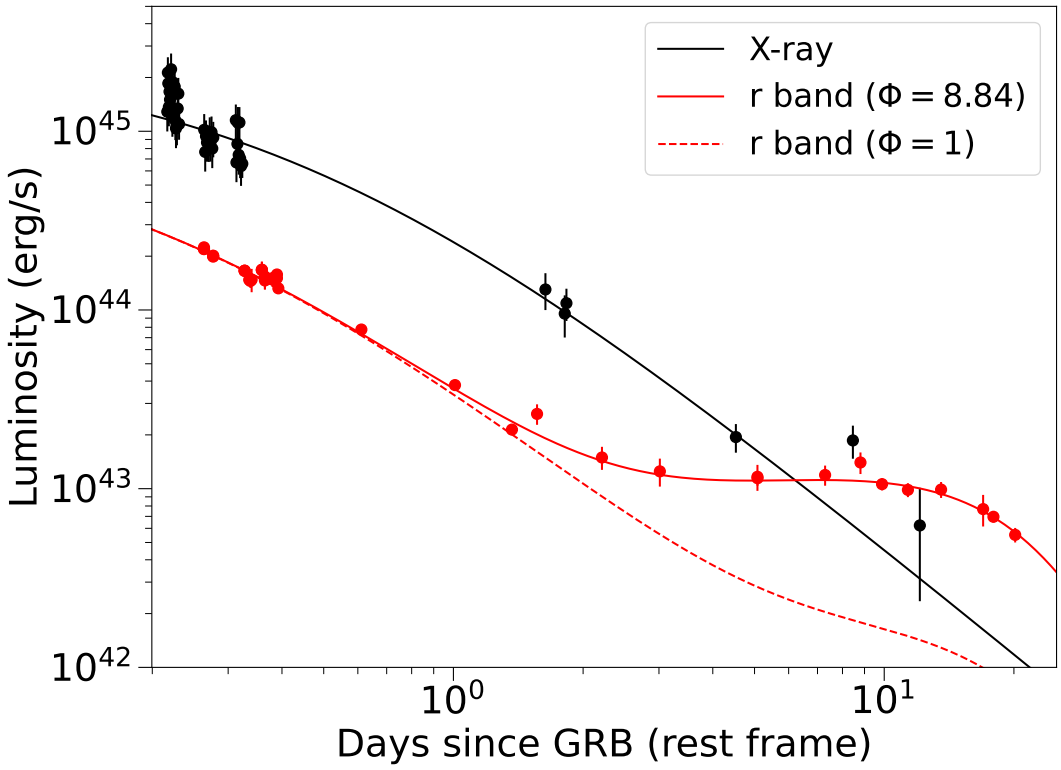

Figure 3.5: The magnetar model from Cano et al. (2016) fit to both the *Swift* XRT X-ray LC and r-band LC of GRB 230812B/SN 2023pel independently. The properties of the magnetar derived are not consistent when comparing the X-ray and optical analysis, where we find that $B_0 = 3.37^{+0.91}_{-0.63} \times 10^{15}$ G and $P_0 = 14.44^{+2.29}_{-1.93}$ ms from the X-ray fitting, and $B_0 = 1.07^{+0.13}_{-0.12} \times 10^{16}$ G and $P_0 = 32.41^{+2.67}_{-2.48}$ ms from the optical fitting. We find that an additional flux-stretching factor of $\Phi = 8.84^{+0.62}_{-0.63}$ is necessary to fit for the SN bump in the r-band LC, and we show the r-band LC with and without the inclusion of this stretching factor in the plot. These findings all show that the magnetar model is not viable to describe the LC of GRB 230812B/SN 2023pel, and that an additional source of power is necessary to describe the observed flux.

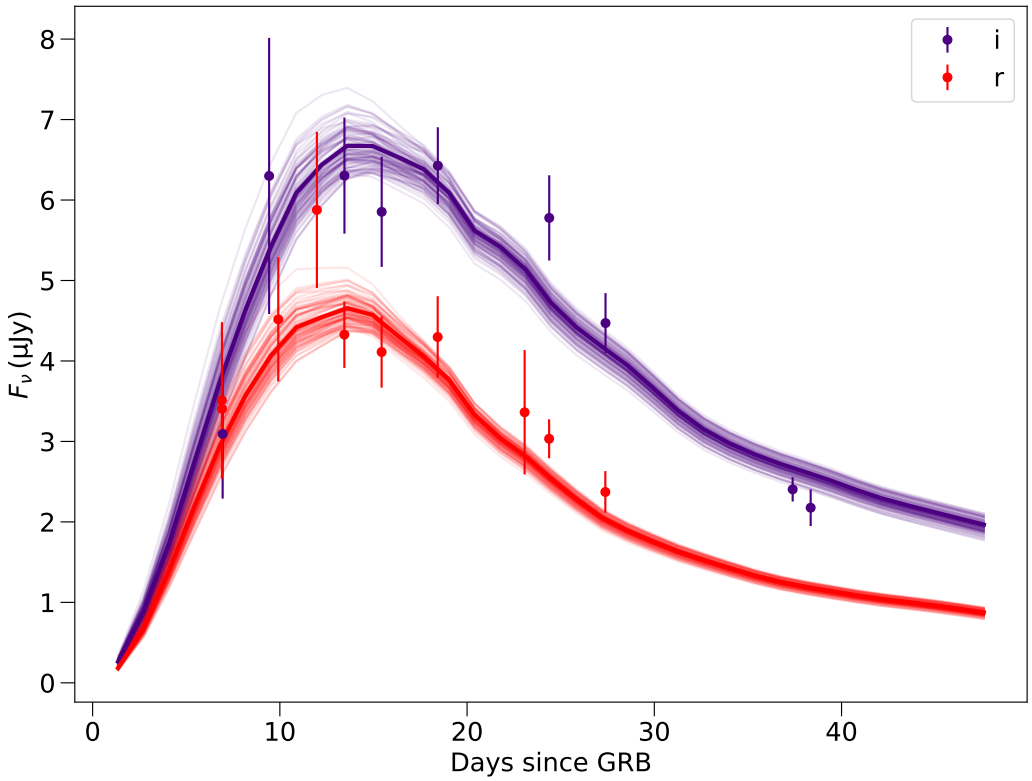

Figure 3.6: The afterglow and host-subtracted SN flux LC of SN 2023pel, corrected for Galactic extinction. In addition, we plot the best-fit r and i-band flux LCs in the observer frame obtained from the best-fit bolometric LC constructed from the A82 radioactive heating SN model, assuming the color and spectral evolution of SN 2023pel is identical to that of SN 2002ap. We derive the best-fit values $M_{\rm Ni} = 0.38 \pm 0.01\,{\rm M}_\odot$, $\tau_{\rm m} = 7.64^{+0.34}_{-0.33}$ days. 100 random a posteriori possible models from the MCMC fitting samples are also plotted with the best fits shown in bold.

observed phases of GRB 230812B/SN 2023pel.

3.4.2 Arnett Model and SN parameters

We then consider the conventional Arnett (1982) model. This model, also known as the radioactive heating model, assumes that the optical emission is due to the decay of ^{56}Ni to ^{56}Co and to ^{56}Fe. We use Equation 36 from Arnett (1982) to model the bolometric optical luminosity,

assuming full gamma-ray trapping of the ejecta, in addition to further radioactive inputs (Valenti et al., 2008). The ^{56}Ni mass is a key parameter that can be used to provide insights into both the explosion and the progenitor, and is one of the major SN parameters we fit for in our modeling.

In order to fit the Arnett (1982) model, we begin by isolating the SN flux, by subtracting the best-fit power-law from §3.3.1 from the observed photometry after $\mathrm{T}_0 + 5$ days, when the afterglow has faded enough for the SN flux to make relevant contributions to the LC. SN 2023pel's flux LC, corrected for Galactic extinction, is shown in Figure 3.6. We then generate semi-analytic bolometric luminosity LC models from Arnett (1982) using the Hybrid Analytic Flux FittEr for Transients (HAFFET; Yang & Sollerman 2023), where the two free parameters are the Nickel mass ($M_{\rm Ni}$) and the photon diffusion timescale ($\tau_{\rm m}$). $\tau_{\rm m}$ is an important parameter that relates to the mass of the total ejecta and the kinetic energy of the explosion, which we show in §3.3.3.

Given a bolometric luminosity LC from the models, we need to extract associated r and i-band LCs corresponding to the models to compare to our observed photometry. We do so through a similar method as in Srinivasaragavan et al. (2023), where we use bolometric correction (BC) coefficients at every epoch to convert from a bolometric luminosity LC to individual filter LCs, assuming that the color and spectral evolution of the SN is identical to that of the Type Ic-BL SN 2002ap (see §7.3.4; Mazzali et al. 2002). The BC corrections are defined as:

$$\mathrm{BC}_x = M_{\rm bol} - M_x, \tag{3.11}$$

where x is the relevant filter, $M_{\rm bol}$ is the optical absolute bolometric magnitude, and M_x is the absolute magnitude in the relevant filter. For stripped-envelope SNe in the photospheric phase, the g-band coefficient (Lyman et al., 2014a) is:

$$\mathrm{BC}_g = 0.054 - 0.195 \times (g-r) - 0.719 \times (g-r)^2. \tag{3.12}$$

We derive the g-band coefficients at every epoch from a SN 2002ap-like LC at $z = 0.36$ generated through SNCOSMO, as well as the $g-r$ and $g-i$ colors. Then, at every epoch, we convert the bolometric luminosity computed from the Arnett (1982) model to a bolometric absolute magnitude, and use Eq. 3.11 to compute a g-band LC. Finally, we use the associated $g-r$ and $g-i$ colors at every epoch to generate r and i-band LCs. After applying the correct distance modulus and K-corrections to these LCs, we compare them to our observed SN flux using Markov Chain Monte Carlo (MCMC) techniques with the `Python` package EMCEE (Foreman-Mackey et al., 2013a) to fit for the nickel mass and the photon diffusion timescale, which have uniform priors corresponding to values derived in literature (Corsi et al., 2016, 2022; Taddia et al., 2019a). We note that this method (though instead using a SN 1998bw-like LC) was also used to estimate the nickel mass of SN 2022xiw, the SN associated with GRB 221009A, in Srinivasaragavan et al. (2023). They derived results consistent with those of Blanchard et al. (2024), who analyzed a *JWST* NIRSpec spectrum to constrain the nickel mass of SN 2022xiw.

The best-fit LCs from our fitting are shown in Figure 3.6. We derive $M_{\mathrm{Ni}} = 0.38 \pm 0.01\,\mathrm{M}_\odot$ and $\tau_{\mathrm{m}} = 7.64^{+0.34}_{-0.33}$. We note that this error is the statistical uncertainty, and there are likely systematic uncertainties that arise from the Arnett (1982) model. Specifically, the assumptions of spherical symmetry along with full gamma-ray trapping of the ejecta play the biggest role in these uncertainties. The M_{Ni} we find is consistent with studies of SN 1998bw ($M_{\mathrm{Ni}} = 0.3$–$0.9\,\mathrm{M}_\odot$; Sollerman et al. 2000). This is expected as the brightness of the SN is about the same as SN 1998bw (see §3.3.2), and the nickel mass is a proxy for the brightness of the SN. These values

correspond to a peak bolometric luminosity of $L_{\rm bol} \sim 1.3 \times 10^{43}\,{\rm erg\,s^{-1}}$, which is consistent with the average found for the overall GRB-SN sample of $L_{\rm bol} = 1 \times 10^{43}\,{\rm erg\,s^{-1}}$ with dispersion $\sigma = 0.4 \times 10^{43}\,{\rm erg\,s^{-1}}$ (Cano et al., 2017a).

We then estimate the photospheric expansion velocity ($v_{\rm ph}$), through measuring the absorption velocity of the Fe II feature at 5169 $\AA$ from the SN spectrum (shown in Figure 3.4), which has been shown to be a good proxy for $v_{\rm ph}$ (Modjaz et al., 2016). We use the same method as Anand et al. (2023), using SESNSpectraPCA (Williamson et al., 2019) to smooth the spectrum. We then use SESNSpectraLib (Liu et al., 2016; Modjaz et al., 2016) to fit for the Fe II absorption velocity, by convolving the spectrum with Type Ic SN templates. From our fitting procedure, we estimate that $v_{\rm ph} = 11,300 \pm 1,600\,{\rm km\,s^{-1}}$. This is lower than the velocities expected at peak for Type Ic-BL SNe, but consistent with values derived for spectra taken around the same phase after peak for other Type Ic-BL events (Modjaz et al., 2016; Taddia et al., 2019a). For a sanity check, we estimate the photospheric velocity for SN 2002ap (Mazzali et al., 2002) and SN 1998bw (Patat et al., 2001) at the phases of the best-fit SNID templates. We find that $v_{\rm ph} = 11,900 \pm 1,150\,{\rm km\,s^{-1}}$ for SN 2002ap, and $v_{\rm ph} = 14,100 \pm 800\,{\rm km\,s^{-1}}$ for SN 1998bw. Therefore, the photospheric velocities we estimate for SN 2023pel are consistent with SN 2002ap at the 1σ level at a similar phase, and consistent with SN 1998bw at the 2σ level at a later phase corresponding to a best-fit template from SNID.

Given τ_m and $v_{\rm ph}$, we can derive the total mass ejected in SN 2023pel ($M_{\rm ej}$), and the total kinetic energy of the explosion ($E_{\rm KE}$), using the equations from Lyman et al. (2016a). Assuming that the explosion is a constant density sphere undergoing homologous expansion, $M_{\rm ej}$ is described as

$$M_{\rm ej} = \frac{\tau_{\rm m}^2 \beta c v_{\rm sc}}{2\kappa_{\rm opt}}, \tag{3.13}$$

and $E_{\rm KE}$ is described as

$$E_{\rm KE} = \frac{3 v_{\rm sc}^2 M_{\rm ej}}{10}, \tag{3.14}$$

where $\beta = 13.8$ is a constant, c is the speed of light, $\kappa_{\rm opt}$ is a constant, average optical opacity, and $v_{\rm sc}$ is observationally set to the photospheric velocity $v_{\rm ph}$ at maximum light. We note that $\kappa_{\rm opt}$ for stripped-envelope SNe varies in literature (Nagy 2018 quotes $\kappa_{\rm opt} = 0.18\,{\rm cm^{-2}\,g^{-1}}$ for Type Ib SNe, and $\kappa_{\rm opt} = 0.10\,{\rm cm^{-2}\,g^{-1}}$ for Type Ic SNe), but we adopt the value used by Chugai (2000), Tartaglia et al. (2021), and Barbarino et al. (2020) for stripped-envelope SNe, $\kappa_{\rm opt} = 0.7\,{\rm cm^{-2}\,g^{-1}}$, shown to accurately model observed stripped-envelope SNe in hydrodynamical LCs (Taddia et al., 2018). Because our observed spectrum is taken 15.5 days after the peak, we cannot use the photospheric velocity we derived earlier to estimate these parameters, and can only derive lower limits. We find $M_{\rm ej} > 0.58\,{\rm M_\odot}$ and $E_{\rm KE} > 3.2 \times 10^{50}\,{\rm erg}$.

In order to derive $v_{\rm sc}$ and these parameters, we use the photospheric velocity evolution of the Type Ic-BL SNe sample from Modjaz et al. (2016) to estimate SN 2023pel's photospheric velocity at maximum light. Using the values from Table 3 in Modjaz et al. (2016), we find the median photospheric velocities and standard deviations at every time epoch between -15 and 20 days from maximum light, and shift the median and 1σ time evolution curves to our derived velocity, $v_{\rm ph} = 11,300 \pm 1,600\,{\rm km\,s^{-1}}$, at 11.3 rest-frame days after SN 2023pel's observed peak. We then extrapolate to the time of maximum light (0 days), and derive $v_{\rm sc} = 14,800 \pm 7,500\,{\rm km\,s^{-1}}$, which is broadly consistent with the results from Hussenot-Desenonges et al. (2023) who derive a photospheric velocity at peak of $v_{\rm sc} = 17114 \pm 2993\,{\rm km\,s^{-1}}$. Then,

using the derived photospheric velocity at peak, we find $M_{\rm ej} = 1.0 \pm 0.6\,{\rm M}_\odot$ and $E_{\rm KE} = 1.3^{+3.3}_{-1.2} \times 10^{51}\,{\rm erg}$.

3.4.3 Comparison to GRB-SN population

Here, we contextualize GRB 230812B/SN 2023pel with respect to the overall GRB-SN population. The average values and dispersion of $k_{\rm SN1998bw}$ and $M_{\rm Ni}$ for the GRB-SN population are $k_{\rm SN1998bw} = 0.95$ with $\sigma = 0.45$, and $M_{\rm Ni} = 0.37\,{\rm M}_\odot$ with $\sigma = 0.20\,{\rm M}_\odot$ (Cano et al., 2017a). Therefore, the $k_{\rm SN1998bw}$ and $M_{\rm Ni}$ we derive for SN 2023pel are consistent with the overall GRB-SN population. The average values and dispersion of $M_{\rm ej}$ and $E_{\rm KE}$ for previous GRB-SN are $M_{\rm ej} = 6\,{\rm M}_\odot$ with a dispersion $\sigma = 4\,{\rm M}_\odot$ and $E_{\rm KE} = 2.5 \times 10^{52}\,{\rm erg}$, with a dispersion $\sigma = 1.8 \times 10^{52}\,{\rm erg}$ (Cano et al., 2017a). We find that our derived ejecta masses and kinetic energies are slightly lower than those of the overall population. This is due to the quick time evolution of the SN, leading to a relatively low photon diffusion timescale.

Because most luminous LGRBs are cosmological in origin, their associated SNe are too faint for current optical facilities to detect. However, GRB 221009A provided a rare example of an extremely energetic ($E_{\gamma,{\rm iso}} = 1 \times 10^{55}\,{\rm erg}$; Burns et al. 2023) and luminous ($L_{\gamma,{\rm iso}} = 2.1 \times 10^{54}\,{\rm erg\,s^{-1}}$; Frederiks et al. 2023a) LGRB that was close enough ($z = 0.151$) to study its associated SN. Despite GRB 221009A's large gamma-ray energy, its associated SN's properties were consistent with the overall GRB-SN population (Blanchard et al., 2024; Fulton et al., 2023; Kann et al., 2023; Levan et al., 2023b; Shrestha et al., 2023; Srinivasaragavan et al., 2023), and its brightness may have in fact been a little lower than the average seen in the population. The prompt emission from GRB 230812B is not nearly as energetic or luminous as GRB 221009A,

but its properties are still on the high end with respect to the GRB-SN population. Therefore, it provides us with another opportunity to understand where SN parameters lie in the higher-energy regime of the GRB-SN population.

In Figure 3.7, we add GRB 230812B/SN 2023pel to a modification of Figure 5 from Srinivasaragavan et al. (2023), and compare GRBs' $E_{\gamma,\mathrm{iso}}$ to their associated SNe's $k_{\mathrm{SN\,1998bw}}$ and M_{Ni}, classifying the GRBs into low-luminosity ($L_{\gamma,\mathrm{iso}} < 10^{48.5}\,\mathrm{erg\,s^{-1}}$) and high-energy jet GRBs ($L_{\gamma,\mathrm{iso}} > 10^{49.5}\,\mathrm{erg\,s^{-1}}$), with events in between labeled as intermediate GRBs. We shift our focus from the average isotropic gamma-ray luminosities for GRBs analyzed in Srinivasaragavan et al. (2023) to their isotropic equivalent gamma-ray energies instead, as it is a more relevant property for comparisons between the associated SN's parameters connected to its luminosity ($k_{\mathrm{SN\,1998bw}}$ and M_{Ni}). We also plot the average k_{SN1998bw} for the GRB-SN population, and M_{Ni} for the GRB-SN and overall Type Ic-BL SNe population (Taddia et al., 2019a) in the Figure. We find that SN 2023pel's properties are very ordinary with respect to the rest of the GRB-SN population.

Srinivasaragavan et al. (2023) also tested for statistical correlations between $L_{\gamma,\mathrm{iso}}$ and $k_{\mathrm{SN\,1998bw}}$, and $L_{\gamma,\mathrm{iso}}$ and M_{Ni}, and they found no significant correlations present. We do the same with $E_{\gamma,\mathrm{iso}}$, for the high-energy jet GRB population and the entire population, using the Pearson Correlation Coefficient Test. For the nickel mass, we find a coefficient of 0.40 and a p-value of 0.18 for the high-energy jet GRBs, and a coefficient of 0.35 with a p-value of 0.19 for the entire population. For $k_{\mathrm{SN\,1998bw}}$, we find a coefficient of -0.16 and a p-value of 0.48 for the high-energy jet GRBs, and a coefficient of -0.15 with a p-value of 0.46 for the entire population. Therefore, there are no significant correlations present again. This, along with other events in literature (see, e.g., MichałowskI et al. 2018; Tanvir et al. 2010) suggests a decoupling between

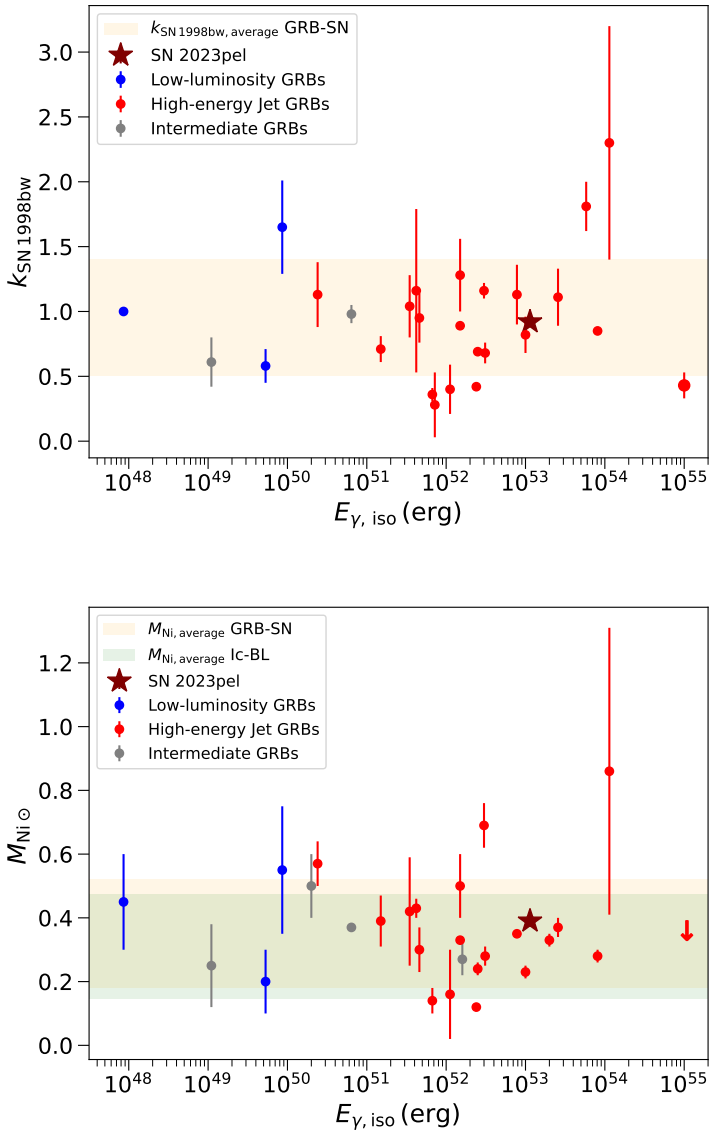

Figure 3.7: *Left panel*: Modification of Figure 5 from Srinivasaragavan et al. (2023), where $k_{\rm SN1998bw}$ is plotted against the isotropic equivalent gamma-ray energy ($E_{\gamma,\rm iso}$) for observationally confirmed GRB-SNe. The plot distinguishes between low-luminosity GRBs, high-energy jet GRBs, and GRBs in the intermediate regime, and also shows the average $k_{\rm SN1998bw}$ for GRB-SNe in the plot and its dispersion, without accounting for GRB 230812B/SN 2023pel. We indicate the results from this work, GRB 230812B/SN 2023pel, with a maroon star. *Right panel*: A similar update of Figure 5 from Srinivasaragavan et al. (2023), where the $M_{\rm Ni}$ in $\rm M_{\odot}$ of GRB-SNe is plotted against the isotropic equivalent gamma-ray energy ($E_{\gamma,\rm iso}$) from the prompt emission for the GRBs. The same distinctions for GRBs are made as for the left panel, and we show the results from this work with a maroon star. We also show the average $M_{\rm Ni}$, along with their dispersion, for GRB-SN in the plot, with the exception of GRB 230812B/SN 2023pel as well as GRB 221009A/SN 2022xiw, because only a robust upper limit was derived for the event from Srinivasaragavan et al. (2023) We also show the average $M_{\rm Ni}$, along with their dispersion for the Type Ic-BL SNe sample not associated with GRBs from Taddia et al. (2019a).

the central engine activity that powers relativistic ejecta in GRBs, and SN emission in GRB-SN systems.

3.5 Conclusion

We analyze the optical counterpart of GRB 230812B, and determine it possesses a late-time flattening consistent with an associated SN, SN 2023pel. SN 2023pel has a peak r-band magnitude of $M_r = -19.46 \pm 0.18$ mag, and has a similar brightness to SN 1998bw, while evolving on quicker timescales. We confirm SN 2023pel is a Type Ic-BL SN through analyzing a spectrum taken by DEIMOS 15.5 days after the SN peak in r band, and confirming broad Fe II and Si II features. We then rule out a millisecond magnetar central engine powering the GRB-SN (Cano et al., 2016) in the context of a dipolar, unevolving magnetic field, through an independent fitting of the X-ray and optical LCs. Using the Arnett (1982) radioactive decay model, we find that SN 2023pel has a nickel mass $M_{\rm Ni} = 0.38 \pm 0.01\,{\rm M}_\odot$, which is consistent with both the GRB-SN population and the overall Type Ic-BL SNe population. We derive a photospheric expansion velocity of $v_{\rm ph} = 11,300 \pm 1,600\,{\rm km\,s^{-1}}$ at that phase, and extrapolate a velocity at maximum light of $v_{\rm ph} = 14,800 \pm 7500\,{\rm km\,s^{-1}}$. Using this velocitiy, we derive estimates of the ejecta mass and kinetic energy: $M_{\rm ej} = 1.0 \pm 0.6\,{\rm M}_\odot$ and $E_{\rm KE} = 1.3^{+3.3}_{-1.2} \times 10^{51}\,{\rm erg}$.

Our analysis of GRB 230812B/SN 2023pel shows that SN 2023pel is a rather ordinary SN with respect to the overall GRB-SN population. GRB 230812B/SN 2023pel adds more evidence that the central engine and SN powering mechanisms are decoupled in GRB-SN systems. As optical surveys become more sensitive in the future, we will uncover more GRB-SN events that possess a $E_{\gamma,{\rm iso}}$ between GRB 230812B and GRB 221009A, a region of the parameter space that

has been sparsely explored, as seen in Figure 3.7. These events have the potential to help understand why this decoupling between the GRB central engine and SN emission occurs. Therefore, we encourage future studies of nearby, energetic GRB-SNe, in order to continue shedding light on the outstanding open questions of the GRB-SN connection.

Acknowledgements

G.P.S. dedicates this paper to Keagan Jaravata, and to the Alvir and Jaravata families. SN 2023pel will always be connected to the memory of Keagan's life.

G.P.S. thanks Isiah Holt for useful discussions on MCMC techniques, and Simi Bhullar for her moral support throughout the paper-writing porcess. The material is based upon work supported by NASA under award number 80GSFC21M0002. B. O. acknowledges useful discussions with Noel Klingler regarding UVOT data analysis and the impact of the ongoing attitude control issues. B. O. gratefully acknowledges support from the McWilliams Postdoctoral Fellowship at Carnegie Mellon University. M.C.M. was supported in part by NASA ADAP grants 80NSSC21K0649 and 80NSSC20K0288. G.C. Anupama thanks the Indian National Science Academy for support under the INSA Senior Scientist programme. M.W.C. acknowledges support from the National Science Foundation with grant numbers PHY-2010970 and OAC-2117997. SY is supported by the National Natural Science Foundation of China under Grant No. 12303046.

These results made use of Lowell Observatory's Lowell Discovery Telescope (LDT), formerly the Discovery Channel Telescope. Lowell operates the LDT in partnership with Boston University, Northern Arizona University, the University of Maryland, and the University of Toledo. Partial support of the LDT was provided by Discovery Communications. LMI was

built by Lowell Observatory using funds from the National Science Foundation (AST-1005313). The GROWTH India Telescope (GIT) is a 70-cm telescope with a 0.7-degree field of view, set up by the Indian Institute of Astrophysics (IIA) and the Indian Institute of Technology Bombay (IITB) with funding from Indo-US Science and Technology Forum and the Science and Engineering Research Board, Department of Science and Technology (DST), Government of India. It is located at the Indian Astronomical Observatory (Hanle), operated by IIA an autonomous institute under DST. We acknowledge funding by the IITB alumni batch of 1994, which partially supports operations of the telescope. Telescope technical details are available at `https://sites.google.com/view/growthindia/`. The 2m Himalayan Chandra telescope (HCT) located at the Indian Optical Observatory (IAO) at Hanle. We thank the staff of IAO, Hanle and CREST, Hosakote, that made these observations possible. HCT observations were carried out under the ToO program of proposal number HCT-2023-C2-P15. The facilities at IAO and CREST are operated by the Indian Institute of Astrophysics, Bangalore. The Liverpool Telescope is operated on the island of La Palma by Liverpool John Moores University in the Spanish Observatorio del Roque de los Muchachos of the Instituto de Astrofisica de Canarias with financial support from the UK Science and Technology Facilities Council.

Some of the data presented herein were obtained at the W.M. Keck Observatory, which is operated as a scientific partnership among the California Institute of Technology, the University of California and the National Aeronau- tics and Space Administration. The Observatory was made possible by the generous financial support of the W.M. Keck Foundation. The authors wish to recognize and acknowledge the very significant cultural role and reverence that the summit of Mauna Kea has always had within the indigenous Hawaiian community. We are most fortunate to have the opportunity to conduct observations from this mountain. SED Machine is based

upon work supported by the National Science Foundation under Grant No. 1106171. Based on observations obtained with the Samuel Oschin Telescope 48-inch and the 60-inch Telescope at the Palomar Observatory as part of the Zwicky Transient Facility project. ZTF is supported by the National Science Foundation under Grant No. AST-2034437 and a collaboration including Caltech, IPAC, the Weizmann Institute of Science, the Oskar Klein Center at Stockholm University, the University of Maryland, Deutsches Elektronen-Synchrotron and Humboldt University, the TANGO Consortium of Taiwan, the University of Wisconsin at Milwaukee, Trinity College Dublin, Lawrence Livermore National Laboratories, IN2P3, University of Warwick, Ruhr University Bochum and Northwestern University. Operations are conducted by COO, IPAC, and UW. The ZTF forced-photometry service was funded under the Heising-Simons Foundation grant #12540303 (PI: Graham). The Gordon and Betty Moore Foundation, through both the Data-Driven Investigator Program and a dedicated grant, provided critical funding for SkyPortal.

Quarter 2. Broad-lined Type Ic Supernovae

"Look at the newer me, fate pursuing me

I can feel the energy in the air

It feel like I'm supposed to be here."

- Kendrick Lamar

Chapter 4: Optical and Radio Analysis of Systematically Classified Broad-lined Type Ic Supernovae from the Zwicky Transient Facility

4.1 Introduction

Type Ic supernovae (SNe) represent the final fate of massive stars ($M_{\rm ZAMS} \gtrsim 8\,{\rm M}_{\odot}$) whose hydrogen and helium envelopes have been stripped prior to explosion (Gal-Yam, 2017b). These SNe are part of a larger sample of stripped-envelope SNe whose progenitors are either very massive stars ($M_{\rm ZAMS} \lesssim 30\,M_{\odot}$) whose outer layers have been stripped due to stellar winds or eruptions (Conti & Walborn, 1976), or less massive stars ($M_{\rm ZAMS} \gtrsim 30\,M_{\odot}$) whose outer hydrogen and/or helium layers have been stripped by binary interactions (Lyman et al., 2016a; Taddia et al., 2018; Yoon et al., 2010b).

Optical spectra of Type Ic SNe usually display photospheric expansion velocities of up to 10,000 km $\rm s^{-1}$ at peak from their Fe II lines (Modjaz et al., 2016). A subset of these events display broader Fe II and O I lines in their spectra, corresponding to velocities between 10,000 and 30,000 $\rm km\,s^{-1}$. These events are referred to as broad-lined Type Ic (Ic-BL) SNe, and are usually found in lower metallicity environments (Arcavi et al., 2011; Schulze et al., 2021) than normal stripped-envelope SNe. Their progenitors are also younger and more massive (Cano, 2013; Sanders et al., 2012). The lightcurves (LCs) of Type Ic-BL events also rise faster than normal stripped-envelope

SNe and are brighter at peak magnitude (Cano, 2013; Drout et al., 2011; Lyman et al., 2016a; Prentice et al., 2016; Taddia et al., 2015). LC modeling of these events has shown that they often have a larger amount of ^{56}Ni synthesized in the explosion, and they sometimes possess explosion energies (10^{52} erg) an order of magnitude higher than normal stripped-envelope events (10^{51} erg); though peculiarly, their ejecta masses are similar (e.g., Barbarino et al. 2021; Cano 2013; Lyman et al. 2016a; Prentice et al. 2016; Taddia et al. 2015, 2018).

SNe Ic-BL challenge the standard picture associated with the standard explosion mechanism of CCSNe, as the extra energy possessed by some of these explosions necessitate a deviation from the traditional picture of neutrino irradiation from a proto-neutron star (NS) reviving the bounce-back shock in the progenitor's core. A major open question is understanding how the same amount of ejecta can lead to higher amounts of ^{56}Ni and higher kinetic energies. A hypothesized scenario is that a relativistic jet driven from the core of the progenitor's proto-NS transfers the extra energy needed to the surrounding stellar medium such that an explosion can reach the order of 10^{52} erg observed in some events (Woosley et al., 2003). In fact, Rodríguez et al. (2024a) found evidence of a non-radioactive power source for the majority of stripped-envelope SNe in their sample of 54 events, including 9 SNe Ic-BL.

This scenario is supported observationally by the detection of long gamma-ray bursts (LGRBs) unambiguously associated with a handful of SNe Ic-BL. Nearly all nearby LGRBs have observationally associated SNe Ic-BL (see, e.g., Blanchard et al. 2024; Cano et al. 2017a; D'Elia et al. 2015b; Galama et al. 1998; Hjorth et al. 2003; Hu et al. 2021; Kumar et al. 2022a; Melandri et al. 2012, 2019a; Pian et al. 2006; Rossi et al. 2022b; Srinivasaragavan et al. 2023, 2024a). For more distant events, non-detections are not particularly constraining (with the exception of a few events, see Della Valle et al. 2006; Fynbo et al. 2006; Gal-Yam et al. 2006; Tanga et al. 2018).

This is due to a few reasons – at high redshifts, detected GRBs usually have very luminous afterglows that wash out their associated SN signature in their LCs, the SN spectral peak shifts to the near-infrared at high redshifts making it difficult to detect with optical telescopes, and Type Ic-BL SNe rarely get brighter than -20 mag, giving a constraint on how far they can be detected regardless of their associated GRB.

However, it is clear that the majority of SNe Ic-BL do not have GRB counterparts. It has been suggested that some SNe Ic-BL may produce off-axis GRBs, whose jets are initially out of our line-of-sight, and emerge within our viewing angle through their radio emission at later times. Studies have shown that relativistic ejecta are not fully ubiquitous to SNe Ic-BL, and viewing angle effects soley cannot account for the lack of GRBs associated with most Type Ic-BL events (Corsi et al., 2016, 2023; Soderberg et al., 2006a). Therefore, there are possible intrinsic differences in the explosion mechanisms between jet-powered SNe Ic-BL and normal SNe Ic-BL, and understanding this dichotomy can provide important insights into the current understanding of the landscape of massive stellar explosions.

In this work, we present a sample of 36 SNe Ic-BL observed with the Zwicky Transient Facility (ZTF; Bellm et al., 2019; Dekany et al., 2020a; Graham et al., 2019; Masci et al., 2019), and analyze their optical properties. This sample builds on the sample of ZTF's predecessor, the intermediate Palomar Transient Facility (iPTF), whose 34 SNe Ic-BL were analyzed in Taddia et al. (2019b). This work is the largest systematic study done on SNe Ic-BL in literature thus far. In addition to presenting the sample and analyzing its optical characteristics, we perform systematic comparisons of key optical properties between events that have radio detections and non-detections, to see if the optical properties of SNe Ic-BL can provide a link to their radio observations, and therefore any insight into their jet formation mechanisms.

The structure of the paper is: in §4.2 we describe how the sample was created; in §4.3 we describe the facilities used to obtain observations of our sample; in §4.4 we describe the analysis done on the photometric observations; in §4.5 we describe the analysis done on the spectroscopic observations; in §4.6 we describe the creation of bolometric LCs and their analysis; in §4.7 we describe the derivation of explosion properties; in §4.8 we describe analysis done on a subset of events with radio observations; and in §4.9 we present a summary and conclusions of the work. We also present an Appendix, where we include discovery paragraphs on every event, their full spectral sequences, as well as efforts to model the LCs that have multiwavelength data.

4.2 SN Sample Description

The sample was created by compiling all of the events that passed the internal quality cuts in ZTF's Bright Transient Survey (BTS) that were spectroscopically classifed as SNe Ic-BL. BTS is a magnitude-limited survey that spectroscopically classifies all SNe $\lesssim 18.5$ mag at peak brightness (Fremling et al., 2020; Perley et al., 2020). The quality cuts ensure that the objects have adequate LC coverage before and after peak. In addition, they ensure that the reference images used for image subtraction are uncontaminated by transient light, are in fields that are still visible one month after peak, and have low Galactic extinction ($A_V < 1$ mag). The final sample has a total of 36 events, selected from the BTS explorer website. Three events in the sample are subjects of single-object studies already published (SN 2018bvw, SN 2018gep, and SN 2020bvc; Ho et al. 2019a, 2020b,c; Izzo et al. 2020; Leung et al. 2021a; Li et al. 2023; Pritchard et al. 2021; Rho et al. 2021), and we refer to those works when necessary. Six events in the sample are also presented in Anand et al. (2024), in the context of near-infrared follow-up to

search for r-process nucleosynthesis, as well as eight events in Corsi et al. (2023), in the context of radio follow-up observations searching for relativistic ejecta.

In Figure 4.1, we show the redshift distribution of events in our sample, which ranges from $z = 0.017$ to $z = 0.1785$. All of the events except for SN 2020wgz and SN 2018hsf have $z < 0.082$, and K-corrections are close to negligible for these events. To quantify this, we generate a SN 1998bw-like LC using SNCosmo (Barbary et al., 2016), setting the peak absolute magnitude of the SN equivalent to the average value of the sample found in §4.4.2 of -18.51 mag. We find that at peak light, the K-correction at $z = 0.082$ is just ~ 0.1 mag. SN 2020wgz is a unique event that may be a superluminous SN (SLSN; see §4.7.1). The event has poor spectral coverage, with only three spectra obtained. Because of its unique evolution, utilizing existing templates to compute its K-corrections will not be sufficient, and more complex methods are necessary. SN 2018hsf is another event at high redshift ($z = 0.119$), that also has poor spectral coverage with only three spectra, and though it passed the quality cut, there are only a few photometry points pre-peak. This event also is likely not powered by radioactive decay (more in §4.7), and therefore also likely exhibits unique spectral evolution that cannot be modeled with existing templates. Therefore, we do not apply K-corrections to our sample, following Anand et al. (2024) and Corsi et al. (2023).

In the Appendix, we include descriptions of all the events in this paper that have not been presented in previous works. We provide the first ZTF magnitudes along with the discovery and classification details in each of the descriptions. All magnitudes are reported in the AB system, and UT dates are used throughout this paper. We estimate and use the explosion dates throughout the paper, and measure the phases in rest-frame days with respect to the explosion epochs. We also use a flat ΛCDM cosmology $H_0 = 69.6\,\mathrm{km\,s^{-1}\,Mpc^{-1}}$, $\Omega_\mathrm{M} = 0.286$, $\Omega_\mathrm{vac} =$

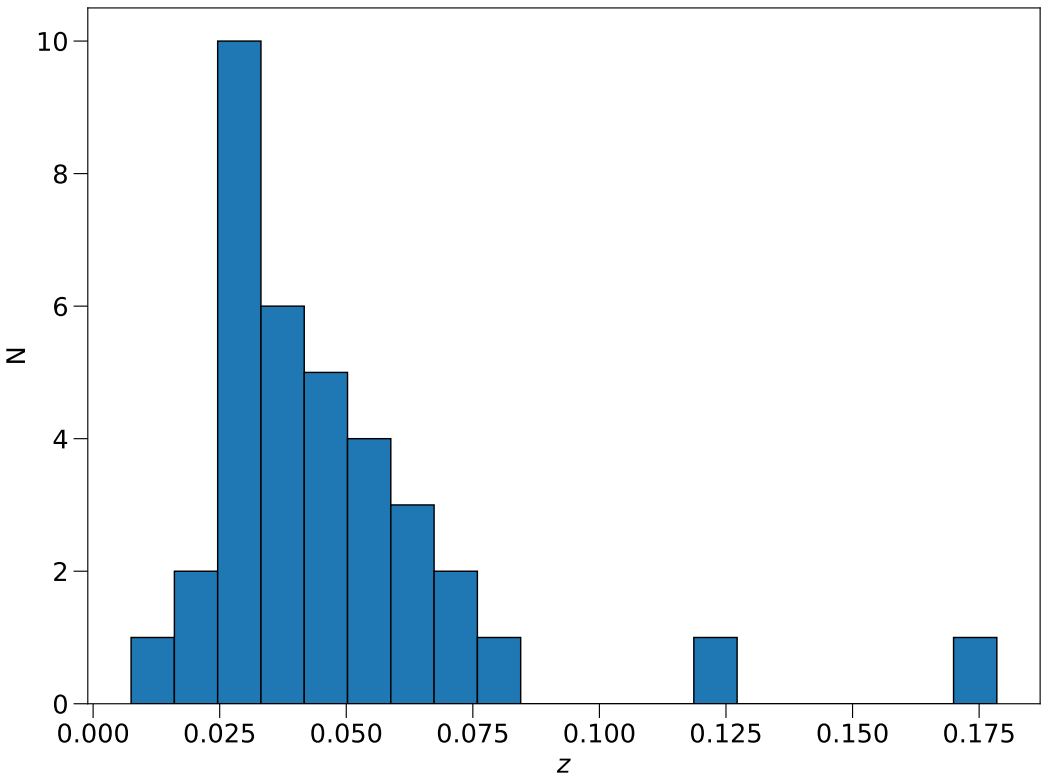

Figure 4.1: Redshift distribution for the SNe Ic-BL sample.

0.714 (Bennett et al., 2014), to convert redshifts to distances. In Table 4.1 we provide the SN IAU name, the ZTF name, RA and Dec coordinates to the transient, redshift, distance, and Milky way extinction (Schlafly & Finkbeiner, 2011b). All average values and errors are calculated through bootstrapping the sample with replacement 10,000 times, and drawing from the 16th, 50th, and 84th percentile means derived in the process. We use the Hybrid Analytic Flux FittEr for Transients (HAFFET; Yang & Sollerman 2023) code for the analyses presented in §4.4, 4.6, 4.7. A detailed description of the methodologies used for these analyses is presented in Yang & Sollerman (2023), which we summarize in the applicable sections.

ZTF name	SN name	RA (hms)	Dec (° ‘ “)	z	$A_{v,MW}$ (mag)	First Presented In
ZTF18aaqjovh	SN 2018bvw	11:52:43.62	+25:40:30.1	0.054	0.062	Ho et al. (2020b)
ZTF18abhhnnv	SN 2018ell	16:49:57.02	+27:38:26.7	0.0638	0.16	–
ZTF18abukavn	SN 2018gep	15:17:02.54	+03:56:38.7	0.0442	0.124	e.g.,[1]
ZTF18acbvpzj	SN 2018hsf	02:40:12.79	-19:58:44.9	0.1184	0.093	–
ZTF18acxgoki	SN 2018keq	23:22:41.97	+21:00:43.2	0.0384	0.341	–
ZTF19aawqcgy	SN 2019hsx	18:12:56.21	+68:21:45.2	0.020652	0.129	Anand et al. (2024)
ZTF19aaxfcpq	SN 2019gwc	16:03:26.88	+38:11:02.6	0.038	0.036	Anand et al. (2024)
ZTF19abfsxpw	SN 2019lci	16:31:01.61	+08:28:23.7	0.0292	0.208	–
ZTF19ablesob	SN 2019moc	23:55:45.94	+21:57:19.7	0.055	0.171	Anand et al. (2024)
ZTF19abqshry	SN 2019oqp	16:38:33.20	+45:37:52.2	0.03082	0.037	–
ZTF19abupned	SN 2019pgo	23:53:00.04	+25:07:16.4	0.0500	0.156	–
ZTF19abzwaen	SN 2019qfi	21:51:07.89	+12:25:38.4	0.028	0.19	Anand et al. (2024)
ZTF20aafmdzj	SN 2020zg	04:02:36.39	-16:11:54.4	0.0557	0.087	–
ZTF20aaiqiti	SN 2020ayz	12:12:04.89	+32:44:01.7	0.025	0.038	–
ZTF20aalxlis	SN 2020bvc	14:33:57.00	+40:14:37.3	0.0252	0.031	e.g.,[2]
ZTF20aapcbmc	SN 2020dgd	15:45:35.54	+29:18:38.4	0.032	0.071	Anand et al. (2024)
ZTF20aaurexl	SN 2020hes	17:47:05.71	+42:46:39.7	0.0700	0.106	–
ZTF20aavcvrm	SN 2020hyj	16:23:47.22	+29:58:58.5	0.055	0.077	–
ZTF20aazkjfv	SN 2020jqm	13:49:18.57	-03:46:10.3	0.03696	0.096	Corsi et al. (2023)
ZTF20abbplei	SN 2020lao	17:06:54.60	+30:16:17.3	0.030814	0.138	Anand et al. (2024)
ZTF20abrmmah	SN 2020rfr	22:39:49.30	-06:26:16.0	0.0725	0.105	–
ZTF20abswdbg	SN 2020rph	03:15:17.81	+37:00:50.6	0.042	0.65	Anand et al. (2024)
ZTF20abzoeiw	SN 2020tkx	18:40:09.00	+34:06:59.5	0.027	0.226	Anand et al. (2024)
ZTF20achvlbs	SN 2020wgz	08:57:33.27	+62:34:00.1	0.1785	0.217	–
ZTF20acvcxkz	SN 2020abxl	05:04:22.76	-14:02:46.4	0.0815	0.344	–
ZTF20acvmzfv	SN 2020abxc	01:00:34.04	-08:07:00.7	0.0600	0.255	–
ZTF20adadrhw	SN 2020adow	08:33:42.26	+27:42:43.7	0.0075	0.124	–
ZTF21aagtpro	SN 2021bmf	16:33:29.41	-06:22:49.4	0.017	0.85	Anand et al. (2024)
ZTF21aaocrlm	SN 2021epp	08:10:55.27	-06:02:49.3	0.0385	0.15	Corsi et al. (2023)
ZTF21aapecxb	SN 2021fop	07:46:42.90	+07:12:38.6	0.077	0.089	–
ZTF21aartgiv	SN 2021hyz	09:27:36.50	+04:27:11.0	0.046	0.125	Corsi et al. (2023)
ZTF21aaxxihx	SN 2021ktv	11:03:03.88	+08:51:39.7	0.0700	0.071	–
ZTF21abchjer	SN 2021ncn	22:36:32.92	+25:45:40.5	0.02461	0.143	–
ZTF20abcjdwu	SN 2021qjv	15:10:47.05	+49:12:18.0	0.03803	0.04	–
ZTF21abmjgwf	SN 2021too	21:40:54.28	+10:19:30.4	0.035	0.171	Anand et al. (2024)
ZTF21acbnfos	SN 2021ywf	05:14:10.99	+01:52:52.2	0.028249	0.292	Anand et al. (2024)

Table 4.1: Discovery properties of the SNe Ic-BL sample

4.3 Observations

We describe here the facilities used to obtain photometric and spectroscopic observations of the SN sample. We note that for two events (SN 2020abxl and SN 2021epp), we did not obtain any spectroscopic observations, and utilize publicly available spectra from the ESO Spectroscopic

Survey of Transient Objects (ePESSTO+; Smartt et al. 2015) on the Transient Name Server for clasissification purposes.

4.3.1 ZTF

The ZTF camera (Dekany et al., 2020b) on the Palomar 48-inch telescope was used for supernova discovery and photometric follow-up. ZTF surveys the entire observable northern sky every two to three days in the r and g bands, in addition to the i band for some selected observations, reaching a median 5σ detection depth of 20.5 $\mathrm{m_{AB}}$ in the g and r bands. The default observing mode is 30 s exposures, and alerts according to 5σ changes in brightness relative to the reference image are sent out through an avro format (Patterson et al., 2019b). Real-time filtering through machine-learning classifiers (Mahabal et al., 2019), star-galaxy classifiers (Tachibana & Miller, 2018b), and light curve properties is also performed for candidate events. ZTF observations of the SN sample last to $\sim$ 60 days after peak, until the SN is fainter than 20.5 mag. For more information about the data processing and image subtraction pipelines, see Masci et al. (2019). We utilized both the GROWTH marshal (Kasliwal et al., 2019a) and the Fritz SkyPortal (Coughlin et al., 2023; van der Walt et al., 2019a) to gather the datasets needed for this work.

4.3.2 SEDM

BTS used the Spectral Energy Distribution Machine's (SEDM, Blagorodnova et al. 2018b; Rigault et al. 2019a) low-dispersion (R$\sim$100) integral field spectrograph (IFU) to obtain classification spectra shortly after discovery for many of the objects in our sample. The spectra obtained with the IFU are reduced through a custom data reduction pipeline (Rigault et al., 2019b) that

utilizes flat-fielding, wavelength calibration, extraction, flux calibration, and telluric corrections.

4.3.3 SPRAT

We used the Spectrograph for the Rapid Acquistion of Transients (SPRAT; Piascik et al. 2014), a low-resolution, (R$\sim$ 350), spectrograph mounted on the 2.0 meter Liverpool Telescope (LT; Steele et al. 2004) on La Palma, Spain to obtain spectra for some of our events. Spectra are reduced and flux calibrated using a custom pipeline for the LT (Smith et al., 2016).

4.3.4 LRIS

We used the Low Resolution Imaging Spectrometer (LRIS; Oke et al. 1995a) on the 10 meter Keck I telescope to obtain spectra for some of the events in our sample. We utilized typical exposure times of 600 s, longslit masks of 1.0$''$ or 1.5$''$ width, and the 400/3400 grism on the blue arm and the 400/8500 grating on the red arm, with a central wavelength of 7830 Å. This enabled wavelength coverage from 3,200-10,000 Å. The reduction was done using LPipe (Perley et al., 2019).

4.3.5 DBSP

We used the Double Beam Spectrograph (DBSP; Oke & Gunn 1982) on the Palomar 200-in telescope to obtain low to medium resolution (R$\sim$1000-10000) spectra of many of the events in our sample. DBSP has a pixel scale of 0.293$''$/pixel (red side) and 0.389 $''$/pixel (blue side). We utilized a red grating of 316/7500, a blue grating of 600/400, a D55 dichroic, and slitmasks of 1$''$, 1.5$''$, and 2$''$. The data reduction was done using a custom PyRAF DBSP reduction pipeline

(Bellm & Sesar, 2016) while the rest were reduced using a custom DBSP Data Reduction pipeline relying on Pypeit (Prochaska et al., 2019; Roberson et al., 2021).

4.3.6 ALFOSC

We used the Alhambra Faint Object Spectrograph and Camera (ALFOSC)[3] on the 2.56 m Nordic Optical Telescope (NOT) at the Observatorio del Roque de los Muchachos on La Palma (Spain) to obtain low-resolution (R $\sim$ 700) spectra for some events in our sample. The spectra were obtained with a 1.0" wide slit and grism #4 with a spectral resolution of 360. We reduced the data with IRAF and Pypeit.

4.3.7 *Swift XRT and UVOT*

The Neils Gehrels *Swift* observatory (Gehrels et al., 2004) observed a handful of events in our sample. Corsi et al. (2023) reports the observations taken with the X-ray telescope (XRT; Burrows et al. 2005), with five non-detections (SN 2020lao, SN 2020tkx, SN 2020jqm, SN 2020rph, SN 2021hyz) and 2 detected events (SN 2019hsx, SN 2019ywf). In addition, Ho et al. (2019a, 2020b,c) report *Swift* non-detections for 2 more events in the sample (SN 2018bvw, SN 2018gep) and 1 more detected event (SN 2020bvc). SN 2020adow was also detected by the XRT, but was not included in Corsi et al. (2023). We utilize the X-ray detections for the subset of events in our sample in §4.8. In this work, we also utilize observations taken with *Swift*'s Ultra-Violet/Optical Telescope (UVOT; Roming et al., 2005a), to better constrain the blackbody temperature and radii of the events in our sample. UVOT observed SN 2018etk, SN 2018hom, SN 2019hsx, SN 2020jqm, SN 2020lao, SN 2020rph, SN 2020tkx, and SN 2021ywf, across the v, b, u, uvw1,

[3]http://www.not.iac.es/instruments/alfosc

uvm2, and uvw2 filters. In addition to these observations, we also obtained ToOs in 2022 in the same filters as the SN initial measurements, to obtain late-time photometry of the host galaxies of these SNe. We did this in order to correct for any host-galaxy contamination in the SN photometry. We used the `uvotsource` task to measure the photometry, and utilize the photometry in §4.6.2 to better constrain the blackbody temperature and radii for part of the sample. We note that SN 2020adow also had measurements from UVOT; however, this event was added to our sample in 2024, and due to *Swift's* pointing constraints, this event will not be visible again until late 2024. Therefore, we omit the *Swift* data.

4.3.8 VLA

4.3.8.1 Individual Observations

Corsi et al. (2023) observed eight events in our sample using the Very Large Array (VLA). Five events in the sample (SN 2020lao, SN 2021hyz, SN 2020rph, SN 2021epp, SN 2019hsx) had radio non-detections or detections that were consistent with emission from the host galaxy. Three events (SN 2020jqm, SN 2020tkx, and SN 2021ywf) have radio detections compatible with point sources along with variability over the timescale of observations. SN 2020adow was also observed by the VLA (Corsi et al., 2021), and has multiple radio point source detections that evolve with time. In addition, Ho et al. (2019a, 2020b,c) and Izzo et al. (2020) report radio point source detections for three more events in our sample (SN 2018gep, SN 2018bvw, SN 2020bvc). SN 2018bvw and SN 2020bvc were clear transient radio sources.

At the time of publication in Ho et al. (2019a), SN 2018gep's radio detections could not be ruled out from being due to its host galaxy. Ho et al. (2019a) reports three detections in the

VLA D configuration (of 34, 24.4, and 26.8 μJy at 9, 9.7, and 14 GHz) and two non-detections in the VLA C configuration two months after the last detection (of < 16 and < 17 μJy at 9 and 14 GHz), which is a comparable level to the declining trend in flux. Because the C configuration has a different resolution than the D configuration, it was unclear whether the detections in the D configuration were from the host galaxy and were simply being resolved out in the C configuration observations. Therefore, in April 2021 more than two years after the initial observations, SN 2018gep's location was observed by VLA program ID 21A-308 (PI Ho) in the D configuration, with the same setup as the initial observations. The source was not detected, to an upper limit of $< 18\,\mu$Jy, confirming the transient SN 2018gep displays fading radio emission with time. We therefore conclude that the radio detections of SN 2018gep reported in Ho et al. (2019a) are from the transient.

4.3.8.2 VLASS

The Karl G. Jansky Very Large Array Sky Survey (VLASS) is conducted across multiple epochs in the S-Band at 2-4 GHZ to monitor and analyze the radio sky. The VLASS is divided into three distinct epochs, each with its own timeline:

- Epoch 1: Commenced on September 13, 2017, and concluded on July 22, 2019.
- Epoch 2: Started on May 27, 2020, and ended on March 7, 2022.
- Epoch 3: Began on February 1, 2023, with observations planned to continue until the end of 2024.

The typical RMS noise for an individual epoch detection in the VLASS is around 0.12

mJy, which provided a baseline for assessing the sensitivity of the survey and the significance of detections.

Using a cross-matching effort between the BTS and the VLASS, we searched for radio emission for the 36 SNe Ic-BL in our sample, and found that SN 2021bmf was the only object that showed transient radio emission across the three epochs. The first VLASS epoch had a non-detection on June 17, 2019, 19 months before the SNe. The second epoch had a detection on September 26, 2021, 8 months after the SN's peak with a peak flux of 5.57 ± 0.526 mJy. This corresponds to a peak luminosity of 4.2×10^{28} erg s^{-1} Hz$^{-}1$.

Therefore, we consider eight events to have radio counterparts (SN 2018gep, SN 2018bvw, SN2020bvc, SN 2020jqm, SN 2020tkx, SN 2020adow, SN2021bmf, and SN 2021ywf), and five events to have radio non-detections (SN 2019hsx, SN 2020lao, SN 2020rph, SN 2021epp, SN 2021hyz).

4.4 Supernova Lightcurves

4.4.1 Light curve interpolation

Before creating LCs for the events, we correct ZTF photometry for Galactic extinction with the Milky Way color excess $E(B-V)_{MW}$ toward the position of every SN from Schlafly & Finkbeiner (2011b). We use the Cardelli et al. (1989b) extinction law to perform reddening corrections, setting $R_V = 3.1$. To be consistent with Anand et al. (2024) and Corsi et al. (2023), we also assume zero host galaxy extinction (more in §4.5.2).

We use ZTF forced photometry to construct optical LCs for each event in the sample, and show the LCs in Figure 4.2, along with the $g-r$ colors. The ZTF forced photometry is unevenly

sampled, making it difficult to derive LC parameters. Therefore, we use a non-parametric data-driven interpolation technique, Gaussian Processing (GP) to interpolate the LCs. We focus on the g and r band fluxes and use the `GEORGE` (Ambikasaran et al., 2015) package with a stationary Matern 3/2 kernel and a flat mean function for the flux form. When the data either has large uncertainties or becomes more sparse, we fit the interpolated data with the analytic function from Bazin et al. (2009), where the flux is represented as

$$F(t) = A\frac{e^{-(t-t_{0,\mathrm{Bazin}})/\tau_{\mathrm{fall,Bazin}}}}{1+e^{-(t-t_{0,\mathrm{Bazin}})/\tau_{\mathrm{rise,Bazin}}}} + B \tag{4.1}$$

where $\tau_{\mathrm{rise,Bazin}}$ and $\tau_{\mathrm{fall,Bazin}}$ represents the rising (which we note differs from τ_{rise} reported in §4.4.3, corresponding to the rise time of the SN from the explosion epoch to peak light), and declining time, A is a normalization parameter, $t_{0,\mathrm{Bazin}}$ is a characteristic timescale (which we note differs from t_0 reported in §4.4.2), while B is the baseline flux. After running a Monte Carlo simulation on the rest-frame LCs with priors and boundaries listed in Table 4.2, we find the best-fitting Bazin function for each of our events, and use it in addition to the ZTF forced photometry and GP interpolated data to help derive LC parameters. An example of this fitting procedure is shown in Figure 4.3. This same LC interpolation process was done for the events also presented in Corsi et al. (2023) and Anand et al. (2024), and for those events we redo the fits and find that they are consistent. For parameters that were already derived in their works, we re-quote their results.

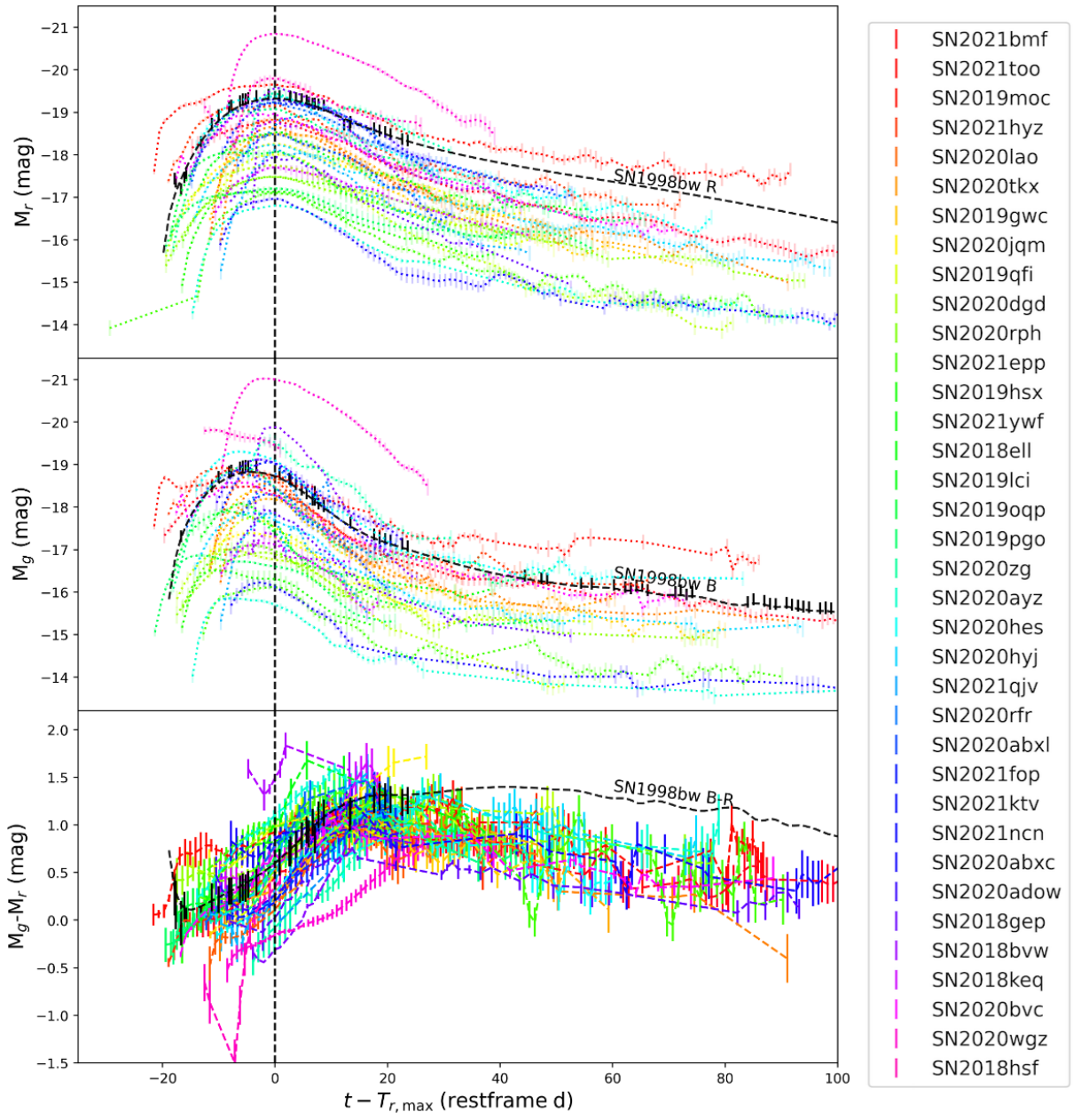

Figure 4.2: LC and color comparison between the SNe Ic-BL sample and SN 1998bw in r/R- and g/B-bands, with all magnitudes corrected for Galactic extinction, and the GP processed LCs shown. The colors are computed with a combination of the data binned within 1 day, as well as the GP processed LCs. The LC of SN 1998bw (Clocchiatti et al., 2011) was interpolated through GP techniques, and is shown as the black dashed lines.

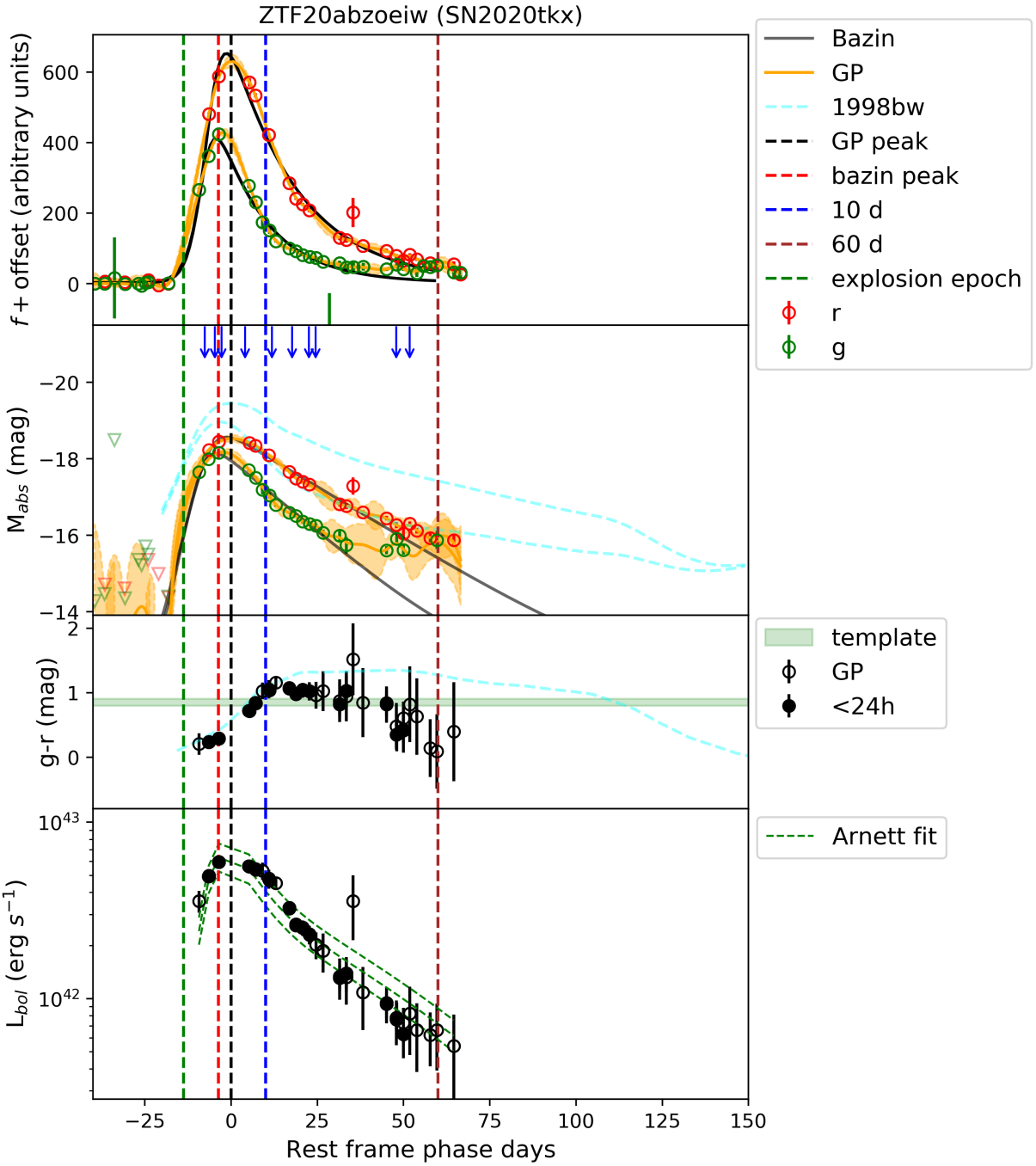

Figure 4.3: Example of LC fits for SN 2020tkx. *Upper panel*: The photometry in flux space together with the GP interpolation and fit to the Bazin formula. This allows for estimates of peak time and other LC parameters, provided in Table 4.3. Peak magnitudes are shown in r band, along wit the derived explosion epoch. *Second panel*: The absolute magnitude LC, along with the GP inteprolation and best-fit Bazin function. SN 1998bw's LCs are plotted as comparison. The blue arrows indicate epochs were spectra were taken. *Third panel*: The color evolution, along with that of SN 1998bw. The template shown is a range of colors for normal stripped envelope SNe from Sollerman et al. (2022). *Lower panel*: The bolometric luminosity LC, along with the best-fit Arnett (1982) model.

Parameter	Prior	Boundary
$\tau_{\rm rise,Bazin}$	10	[0, 60] days
$\tau_{\rm fall,Bazin}$	-15	[0, 120] days
t_0	0	[-10, 10] days
A	$F_{\rm max}$	[$F_{\rm max}$*0.5, $F_{\rm max}$*2]
B	5	[-20, 20]

Table 4.2: Priors used for the Bazin fits.

4.4.2 Light Curve Empirical Parameters

After interpolating the LCs, we derive empirical LC parameters for every event, and show the results in Table 4.4.2. For events shared with Corsi et al. (2023) and Anand et al. (2024), we report the peak absolute magnitudes in r band ($\rm M_r^{max}$), the explosion epochs ($t_{\rm exp,r}$), and the peak time in r band (t_0) derived in their works.

We begin by determining $\rm M_r^{max}$ and t_0 for new events, using the GP-processed LCs. We show a histogram of the peak r-band absolute magnitude distributions of our sample in Figure 4.4. The distribution ranges over 4 magnitudes from -16.86 mag to -20.89 mag. SN 2020wgz is a clear outlier with respect to the rest of the sample, with $\rm M_r^{max} = -20.89 \pm 0.11$ mag, placing it in the luminosity regime of SLSNe. We discuss this event's properties at length in §4.7.1. The average peak magnitude is $\overline{\rm M_r}^{\rm max} = -18.51 \pm 0.15$ mag, with an associated 1σ standard deviation of 0.90 mag (shown in the Figure as dashed lines). The average absolute magnitude derived is consistent with that found in the iPTF sample of Taddia et al. (2019b) for events without an associated GRB ($\overline{\rm M_r}^{\rm max} = -18.6$ mag, with a 1σ standard deviation of 0.5 mag). When excluding SN 2020wgz from the sample, we find a mean peak magnitude of $\overline{\rm M_r}^{\rm max} = -18.44 \pm 0.14$ mag, and a 1σ standard deviation of 0.82 mag. The uncertainty that we report is derived from the uncertainty in photometric observations, and these magnitudes are all

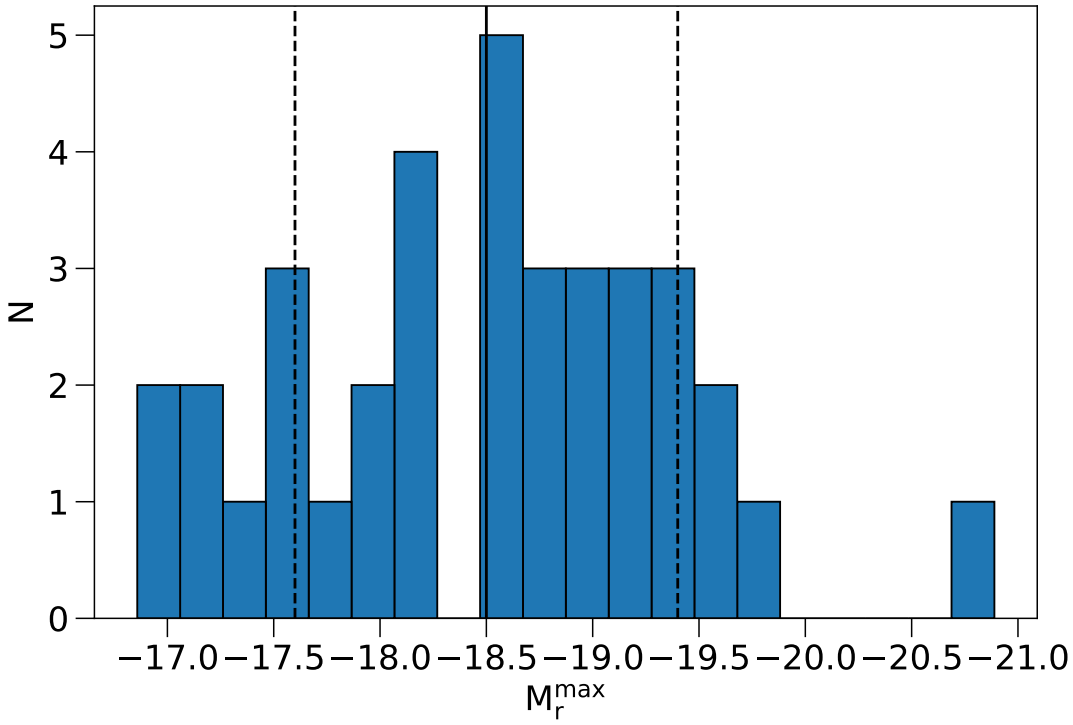

Figure 4.4: $\mathrm{M_r^{max}}$ distribution of the SNe Ic-BL sample, with the mean magnitude (-18.51 mag) shown with a solid line, and standard deviation (0.90 mag) range shown with dashed lines.

corrected for MW extinction.

We then derive the $g-r$ colors for each of the events in the sample 10 days after peak: $(g-r)_{10}$, to compare the color evolution of the sample. We find an average value of $\overline{(g-r)}_{10}$ = 1.00 ± 0.06 mag, with a 1σ standard deviation of 0.43 mag. All of the events in the sample except for SN 2020ayz, SN 2018gep, SN 2020wgz, and SN 2020zg have $(g-r)_{10}$ values consistent within the average and 1σ standard deviation, showing that the sample has broadly consistent color evolution.

We then investigate the effects of the Malmquist bias on the peak r-band absolute magnitudes of the sample. The Malmquist bias arises because more luminous objects can be detected out to greater distances than less luminous objects. Because our sample is magnitude-limited, it

is likely that ZTF failed to detect fainter SNe that occurred at greater distances, and we quantify this effect below.

We plot the peak magnitudes and distance modulus (μ) for each event in the sample in Figure 4.5. The faintest peak absolute r-band magnitude of the sample is -16.86. The BTS survey detects objects with an apparent magnitude as faint as $\sim$ 19 mag, so we use this value as the upper limit for SN detectability for the BTS survey. The minimum peak absolute r-band magnitude and upper limit for SN detectability sets $\mu = 35.86$ as the distance modulus for which we observe the complete peak magnitude distribution. We then utilize the method described in Richardson et al. (2014) to simulate the magnitude of missing SNe randomly in one magnitude bins, cutting off the sample at the furthest event. The results of the simulation are shown in Figure 4.5. We calculate a new average r-band peak absolute magnitude of -18.3 mag, with a 1σ dispersion of 0.91 mag. Therefore, the Malmquist bias produces a difference of $\sim$ 0.2 mag in the average peak magnitude distribution for the sample. This is the same difference found in Taddia et al. (2019b) for their sample. We note that this difference is just an estimate, and more complicated effects (e.g., the distribution of events with respect to their position in the Milky Way plane, the assumption that there are no events fainter than the faintest in our sample for the whole population) were not accounted for.

We also derive the decline parameter $\Delta m_{15}(r)$ and rise parameter $\Delta m_{-10}(r)$, which is the difference in magnitudes in the r-band from the peak to 15 days after the peak, and from 10 days before the peak to the peak, for every event in the sample. In Figure 4.6, we show $\Delta m_{-10}(r)$ plotted against $\Delta m_{15}(r)$ for our sample, with the exception of SN 2018hsf, SN 2019lci, SN 2020zg, and SN 2018gep, (the first three events lacked sufficient photometry at the times necessary to calculate these parameters while SN 2018gep had a rise time from the explosion epoch to peak

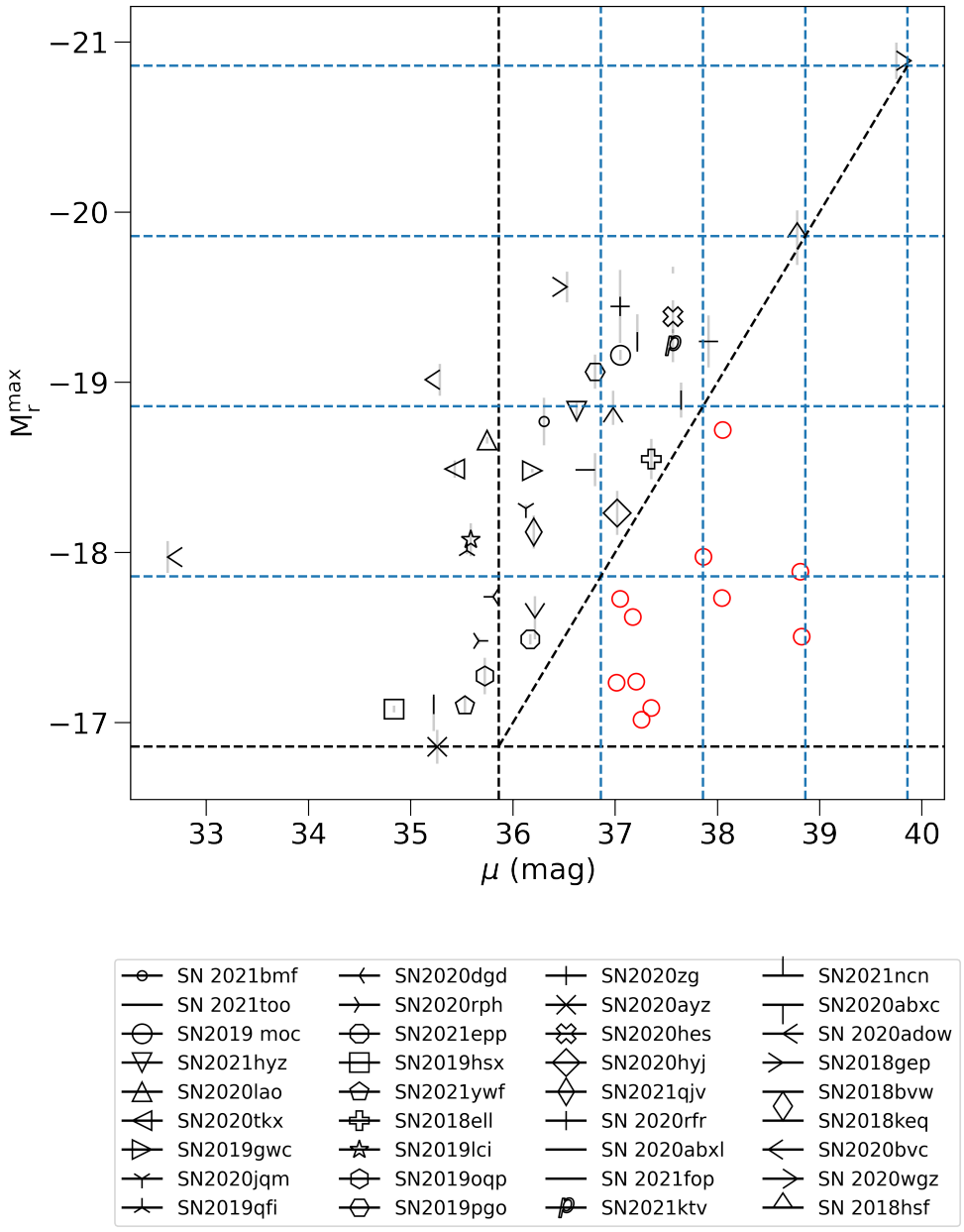

Figure 4.5: Investigation of the Malmquist bias on the sample. M_r^{max} and the distance modulus (μ) for the events are plotted, with the minimum absolute magnitude (-16.86 mag) of the sample shown as a black dashed horizontal line. The distance modulus where the sample is complete ($\mu = 35.86$ mag) is shown as a black dashed vertical line. One magnitude by one magnitude bins are marked by dashed blue lines, where the cutoff distance for the sample is marked by a black dashed vertical line. The random simulated events created through the method described in Richardson et al. (2014) are shown as red circles. The overall effect of the Malmquist bias is a 0.2 mag decrease in the overall average M_r^{max} of the sample.

ZTF name	SN name	$(g-r)_{10}$ (mag)	Δm_{15} (mag)	Δm_{-10} (mag)	$M_{r,peak}$	$t_{exp,r}$ (days)	t_0 (JD)
ZTF18aaqjovh	SN 2018bvw	-	0.63 (0.05)	1.42 (0.04)	-18.85 (0.10)	$-8.09^{+2.04}_{-2.04}$	2458248.80
ZTF18abhhnnv	SN 2018ell	1.13 (0.49)	0.87 (0.09)	0.65 (0.12)	-18.55 (0.12)	$-16.15^{+0.8}_{-0.84}$	2458330.71
ZTF18abukavn	SN 2018gep	0.51 (0.03)	1.15 (0.02)	-	-19.56 (0.09)	$-4.09^{+0.01}_{-0.01}$	2458374.74
ZTF18acbvpzj	SN 2018hsf	-	-	0.59 (0.36)	-19.85 (0.16)	$-12.43^{+2.43}_{2.43}$	2458432.83
ZTF18acxgoki	SN 2018keq	1.26 (0.22)	0.33 (0.11)	0.78 (0.17)	-17.62 (0.13)	$-14.07^{+4.1}_{-4.1}$	2458475.68
ZTF19aawqcgy	SN 2019hsx	1.32 (0.47)	0.88 (0.09)	0.65 (0.11)	-17.08 (0.02)	$-15.63^{+0.38}_{-0.53}$	2458647.57
ZTF19aaxfcpq	SN 2019gwc	0.90 (0.14)	0.88 (0.06)	1.14 (0.06)	-18.48 (0.01)	$-12.78^{+0.46}_{-0.46}$	2458651.08
ZTF19abfsxpw	SN 2019lci	0.87 (0.39)	-	0.07 (0.03)	-18.07 (0.10)	$-18.1^{+0.47}_{-0.2}$	2458693.71
ZTF19ablesob	SN 2019moc	1.00 (0.11)	0.77 (0.13)	0.21 (0.14)	-19.16 (0.03)	$-20.02^{+0.27}_{-3.23}$	2458716.26
ZTF19abqshry	SN 2019oqp	0.89 (0.16)	0.69 (0.19)	0.21 (0.07)	-17.27 (0.11)	$-22.45^{+0.41}_{-0.41}$	2458737.71
ZTF19abupned	SN 2019pgo	1.39 (0.1)	0.85 (0.04)	0.43 (0.04)	-19.06 (0.10)	$-15.85^{+0.38}_{-0.66}$	2458743.91
ZTF19abzwaen	SN 2019qfi	1.03 (0.53)	0.92 (0.16)	0.76 (0.39)	-18.01 (0.02)	$-15.09^{+1.4}_{-1.4}$	2458754.06
ZTF20aafmdzj	SN 2020zg	0.37 (0.08)	0.37 (0.22)	-	-19.45 (0.21)	$-5.06^{+0.95}_{-0.95}$	2458867.74
ZTF20aaiqiti	SN 2020ayz	1.75 (0.13)	0.81 (0.03)	0.52 (0.06)	-16.86 (0.10)	$-14.33^{+0.32}_{-0.51}$	2458887.97
ZTF20aalxlis	SN 2020bvc	1.00 (0.02)	0.84 (0.03)	0.48 (0.02)	-19.02 (0.09)	$-18.11^{+0.89}_{-0.89}$	2458901.06
ZTF20aapcbmc	SN 2020dgd	1.10 (0.8)	0.75 (0.37)	0.28 (0.14)	-17.74 (0.02)	$-18.03^{+2.5}_{-2.5}$	2458914.55
ZTF20aaurexl	SN 2020hes	0.77 (0.13)	1.02 (0.09)	0.41 (0.03)	-19.39 (0.10)	$-16.03^{+4.97}_{-4.97}$	2458964.99
ZTF20aavcvrm	SN 2020hyj	0.92 (0.11)	0.66 (0.02)	0.66 (0.06)	-18.23 (0.13)	$-15.01^{+0.98}_{-0.98}$	2458969.94
ZTF20aazkjfv	SN 2020jqm	1.13 (0.5)	0.56 (0.08)	0.55 (0.08)	-18.26 (0.02)	-17^{+1}_{-1}	2458996.71
ZTF20abbplei	SN 2020lao	0.92 (0.07)	0.83 (0.08)	2.88 (0.1)	-18.66 (0.02)	$-10.6^{+0.99}_{-0.99}$	2459004.42
ZTF20abrmmah	SN 2020rfr	1.40 (0.26)	0.05 (0.11)	2.21 (0.14)	-18.90 (0.10)	$-6.99^{+1.96}_{-1.96}$	2459078.86
ZTF20abswdbg	SN 2020rph	0.96 (0.27)	0.48 (0.08)	0.49 (0.06)	-17.48 (0.02)	$-19.88^{+0.02}_{-0.02}$	2459092.84
ZTF20abzoeiw	SN 2020tkx	1.01 (0.15)	0.72 (0.13)	0.79 (0.22)	-18.49 (0.05)	$-12.77^{+4.54}_{-4.54}$	2459117.00
ZTF20achvlbs	SN 2020wgz	0.06 (0.05)	0.64 (0.04)	2.53 (0.09)	-20.89 (0.11)	$-10.04^{+0.15}_{-0.15}$	2459140.01
ZTF20acvcxkz	SN 2020abxl	1.45 (0.31)	0.8 (0.05)	0.45 (0.03)	-19.24 (0.15)	$-13.25^{+0.01}_{-0.01}$	2459200.97
ZTF20acvmzfv	SN 2020abxc	0.90 (0.14)	0.56 (0.05)	0.69 (0.05)	-19.30 (0.10)	$-12.95^{+0.47}_{-0.88}$	2459203.73
ZTF20adadrhw	SN 2020adow	0.59 (0.01)	0.99 (0.01)	1.9 (0.01)	-17.97 (0.09)	$-10.59^{+2.4}_{-2.4}$	2459218.95
ZTF21aagtpro	SN 2021bmf	0.72 (0.13)	1.14 (0.17)	0.13 (0.06)	-18.77 (0.14)	$-23.76^{+5.68}_{-5.52}$	2459265.62
ZTF21aaocrlm	SN 2021epp	1.30 (0.23)	0.32 (0.04)	0.4 (0.06)	-17.49 (0.03)	$-15.12^{+1.48}_{-1.48}$	2459292.33
ZTF21aapecxb	SN 2021fop	0.74 (0.15)	0.68 (0.08)	2.08 (0.36)	-18.49 (0.10)	$-7.05^{+5.01}_{-5.01}$	2459292.75
ZTF21aartgiv	SN 2021hyz	0.84 (0.19)	1.04 (0.19)	1.52 (0.08)	-18.83 (0.05)	$-12.88^{+0.94}_{-0.94}$	2459319.81
ZTF21aaxxihx	SN 2021ktv	1.15 (0.29)	0.53 (0.09)	0.92 (0.07)	-19.22 (0.10)	$-12.04^{+2.94}_{-2.94}$	2459344.79
ZTF21abchjer	SN 2021ncn	1.01 (0.13)	1.1 (0.10)	1.19 (0.15)	-17.05 (0.10)	$-10.02^{+0.01}_{-0.01}$	2459364.97
ZTF20abcjdwu	SN 2021qjv	1.31 (0.08)	0.87 (0.10)	2.83 (0.20)	-18.12 (0.10)	$-10.01^{+0.02}_{-0.02}$	2459389.83
ZTF21abmjgwf	SN 2021too	1.20 (0.18)	0.59 (0.15)	0.22 (0.08)	-19.66 (0.02)	$-23.23^{+0.41}_{-0.41}$	2459434.59
ZTF21acbnfos	SN 2021ywf	1.1 (0.6)	0.68 (0.42)	0.44 (0.25)	-17.10 (0.05)	$-17.47^{+0.49}_{-0.49}$	2459485.95

Table 4.3: Empirical parameters, explosion epochs, and peak r-band times for the SNe Ic-BL sample derived through the methods outlined in §4.4. We draw from results in previous works where applicable (described in §4.4.2.)

quicker than 10 days). Through a Spearman rank coefficient test, we do not find any correlation between the two parameters, with a p-value of 0.98. This contrasts with the results found in Taddia et al. (2019b), who found that fast-rising objects also are fast-decliners, with a p-value of 0.06. However, they only tested the correlation for 12 of the best-sampled events in their sample, while we test the correlation using 32 events, utilizing the GP interpolations and Bazin fits. Therefore, we show that when removing observational biases with respect to the best-sampled LCs, that fast-rising SNe Ic-BL are not necessarily also fast decliners.

We then test for the presence of a Phillips Relation (Phillips, 1993), between $\mathrm{M_r^{max}}$ and $\Delta m_{15}(r)$. A relation between the decline rate and luminosity was established for SNe Ia through this relation (Burns et al., 2011) and was also found for GRB-SNe (Cano, 2014; Li & Hjorth, 2014). We show these two parameters plotted against each other for 34 events in our sample (with the exception of SN 2018hsf and SN 2019lci), as well as the Phillips Relation for SNe Ia from Burns et al. (2011) in Figure 4.7. We do not find this relation present in our sample, consistent with the findings from Taddia et al. (2019b). Therefore, less luminous SNe do not necessarily decline faster than more luminous events.

4.4.3 Explosion epochs

When sufficient early-time photometry is available, we determine the explosion epoch ($t_{\mathrm{exp,r}}$) and rise time (τ_{rise}) of every newly presented SN through Monte Carlo approaches, after characterizing the early emission of the transients in g and r bands through a power law following the methodology of Miller et al. (2020)[4] The power law is fit from the estimated baseline up to 40 percent of the maximum flux determined by the Bazin fit. For those SNe which do

[4]https://github.com/adamamiller/ztf_early_Ia_2018.

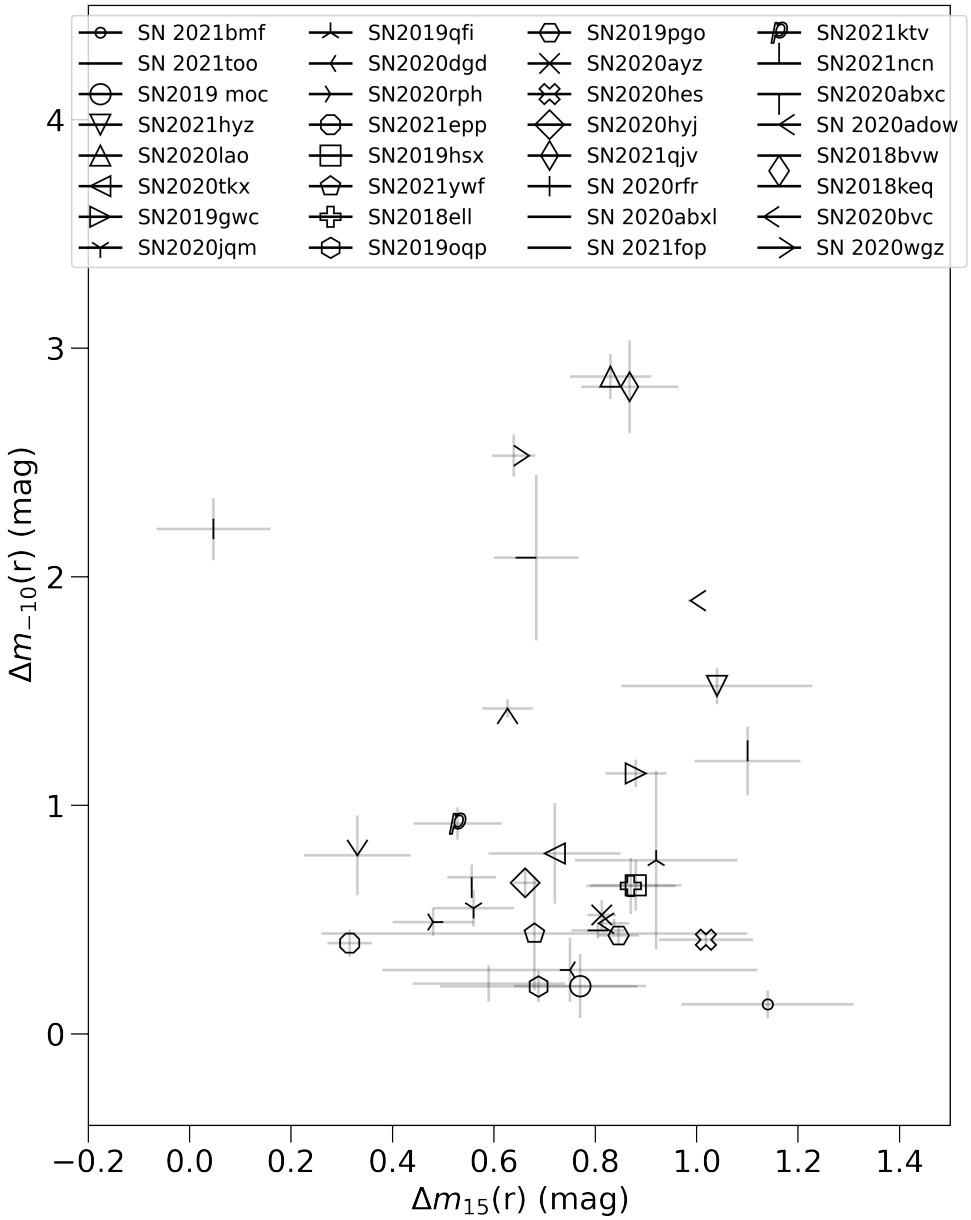

Figure 4.6: $\Delta m_{-10}(r)$ plotted against $\Delta m_{15}(r)$ for 32 events in the sample. We found no correlations between the two parameters, with a p-value of 0.98.

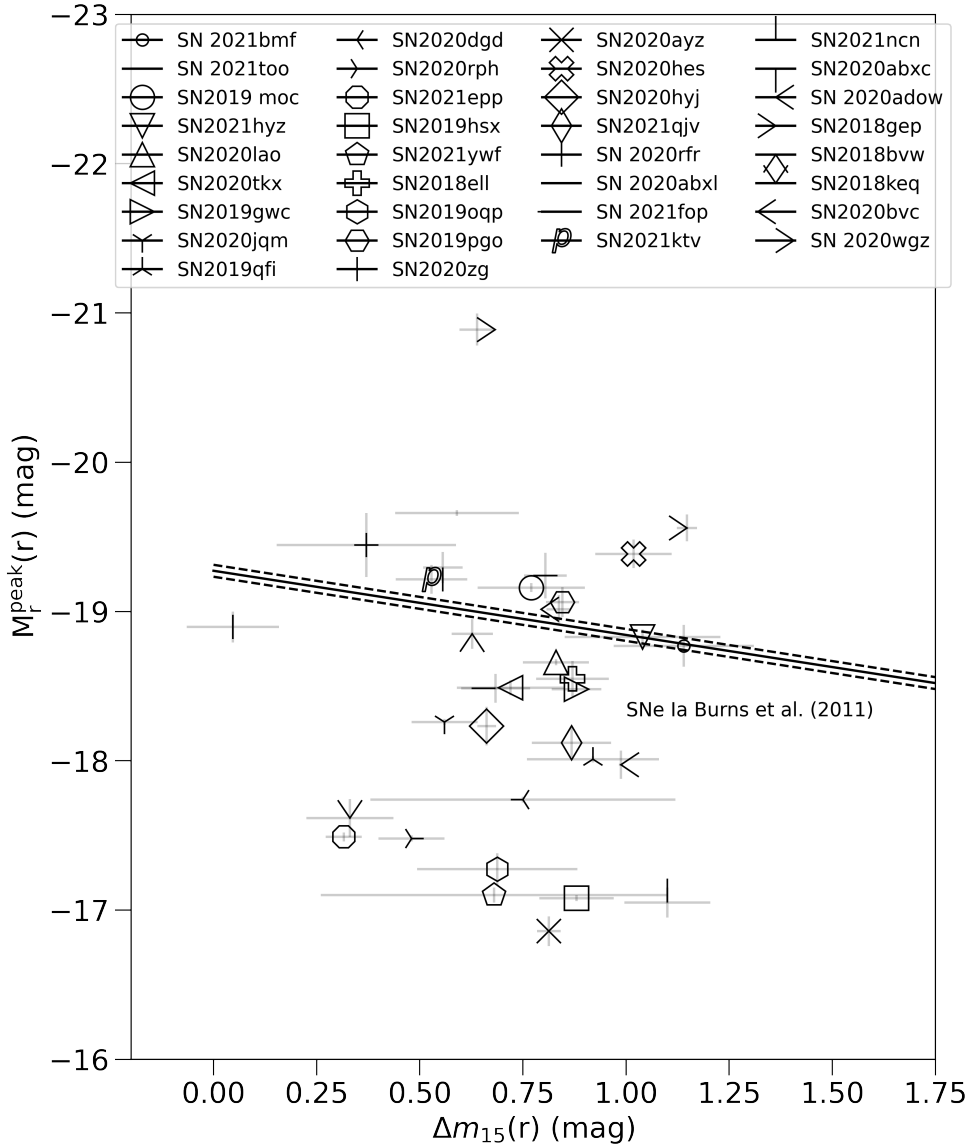

Figure 4.7: $\mathrm{M_r^{max}}$ plotted against $\Delta m_{15}(r)$ for 34 events in the sample. There is no evidence for a Phillips relation, which is shown for SNe Ia as the black line with the dashed lines representing the errors from Burns et al. (2011).

not have sufficient early-time photometry, we take the average of the first detection and the last non-detection in ZTF forced photometry as the explosion epoch, and determine the error through the half-width. SN 2018hsf did not have a ZTF non-detection prior to the first detection, due to the instrument not operating for some time period before. For this case, we use the last ATLAS non-detection in o band to calculate the explosion epoch. We calculate the rise time $\tau_{\rm rise}$ obtained for our sample, measured from the derived explosion epoch to the peak epoch in r-band, along with the average value and 1σ standard deviation. We find $\overline{\tau}_{\rm rise} = 14.0 \pm 0.8$ days, with a 1σ standard deviation of 5.81 days. This is consistent with the value obtained in Taddia et al. (2019b), who found $\overline{\tau}_{\rm rise} = 15$ days with a 1σ standard deviation of 6 days.

4.5 Supernova Spectra

We present the photospheric phase spectra for each of the new events in our sample in Figure 4.8, not presented in previous works. In §4.3, we detail the instruments used to obtain spectra of the events in our sample. All of the spectra were reduced in a standard manner, with wavelength and flux calibrations. All spectra will be made publicly available on WISeREP (Yaron & Gal-Yam, 2012).

As shown in Figure 4.8, none of the spectra display hydrogen and helium features, while they all share characteristic broad absorption features. Their broad features are the result of the blending of multiple absorption lines due to Doppler broadening effects, and the Fe II and Si II absorption lines are indicated in the Figure.

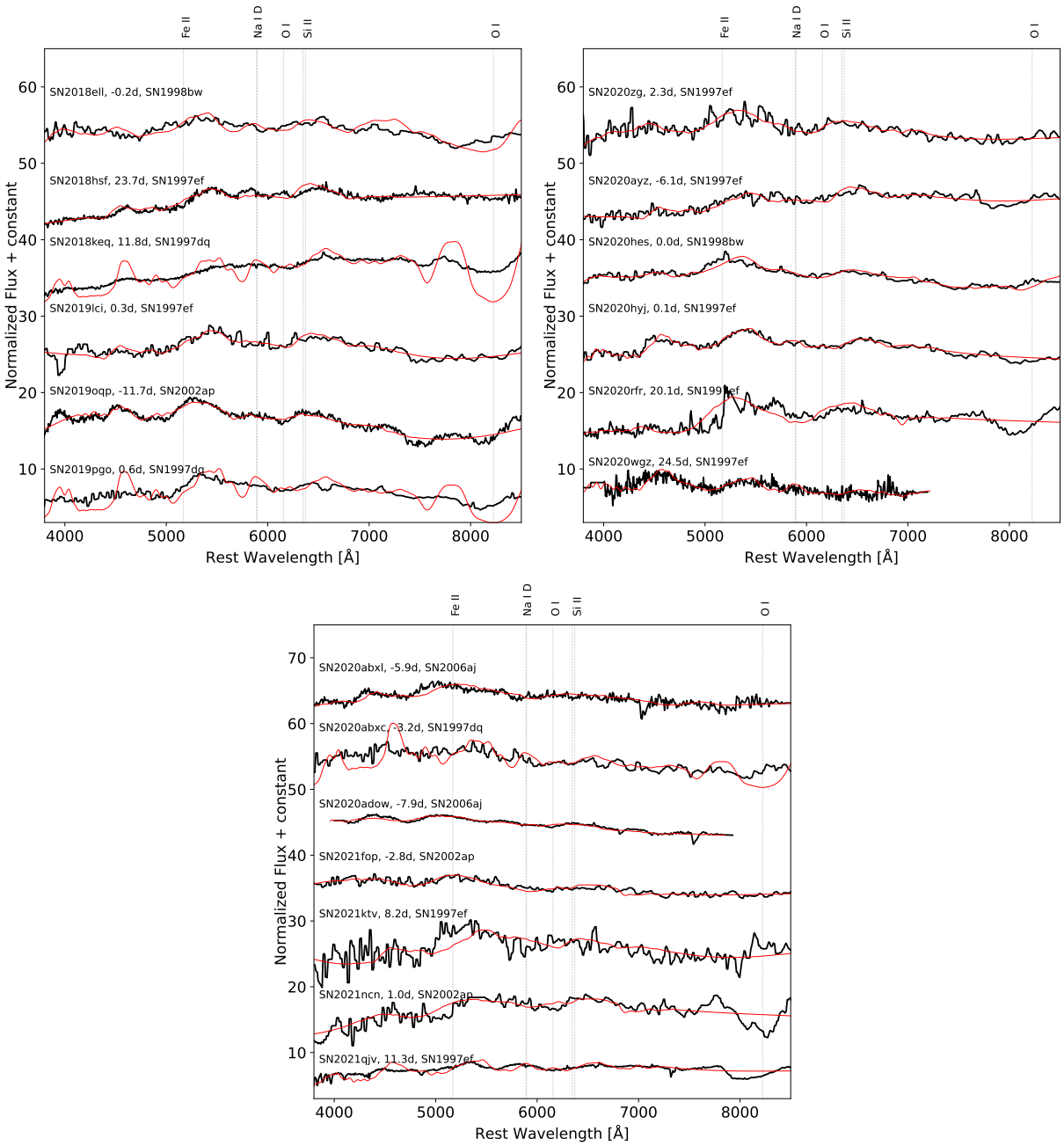

Figure 4.8: Photospheric phase spectra (black) and the SNID best match templates (red) for the Ic-BL sample that has not been presented in previous works. The text shows the name of the transient, the observer-frame spectroscopic phase since r-band maximum, and the name of the transient template used for the fitting.

4.5.1 Photospheric Velocities

In addition to the broadened features, the center of the absorption troughs are blueshifted relative to the rest frame Fe II and Si II absorption line wavelengths, due to the high velocity of the ejecta towards the observer. Modjaz et al. (2016) showed that the blueshifted absorption velocity of the Fe II line at 5169 $\AA$ is a good proxy for the photospheric expansion velocity (v_{ph}), and we calculate these velocities for each of the events in our sample. We use a similar method to Anand et al. (2024), beginning by using `WOMBAT` to remove host galaxy emission lines and telluric features, and use SESNSpectraPCA (Williamson et al., 2019) to smooth the spectra. Finally, we utilize SESNSpectraLib (Liu et al., 2016; Modjaz et al., 2016) to fit for the Fe II absorption velocity, by convolving a blueshifted Gaussian with a Type Ic SN template, and measuring the blueshift of the Fe II feature with respect to these templates.

In order to derive v_{ph} at the peak of the SNe LCs, we use the highest quality spectrum available closest to the peak of the SNe to measure the velocities. For some events, this is different than the spectrum used for classification purposes. The full set of spectra for each SN in our sample is shown in the Appendix. Through this method, we were able to obtain either an estimate or constraint of the peak v_{ph} for 26 out of the 36 events in our sample (10 events had spectra that lacked sufficent SNR to obtain an accurate velocity measurement). For six of the events, we could only obtain velocity measurements more than 15 days post peak light, and therefore their velocities are not representative of the peak velocity. All the velocities are reported in Table 4.5, where we report the velocities derived for new events, along with those already presented in literature. We present an example of the velocity fitting procedure in Figure 4.9. In Figure 4.10, we show a histogram of the distribution of the peak v_{ph}, without the events with spectra taken

greater than 15 days from peak. We find an average value of 16,100 $\pm$ 1,100 km s^{-1}, with a 1σ standard deviation of 5,600 km s^{-1}. In Figure 4.11, we show the evolution of $\mathrm{v_{ph}}$ over time for the sample, compared to other GRB-SNe, X-ray flash (XRF)-SNe, a "normal" Type Ic SN, the iPTF sample of Taddia et al. (2019b), and the samples from Anand et al. (2024) and Corsi et al. (2023). We see that our sample's evolution is broadly consistent with that of the iPTF sample and the other single object events shown, with the exception of the "normal" Type Ic SN 1994I.

4.5.2 Na I Equivalent Width

Out of the 36 events in the sample, 20 had spectra from either DBSP or LRIS, which are the highest resolution spectra in the sample (though still low-resolution in general). We measure the equivalent width (EW) of the Na I absorption feature for every event in the sample, as this feature has been shown to be a proxy for the amount of host-galaxy extinction present (Stritzinger et al., 2018). 14 events, including the majority of events in Corsi et al. (2023) and Anand et al. (2024) had Na I EWs consistent to 0 within error bars. There are five new events not previously analyzed in literature that have EWs greater than 0: SN 2018hsf, SN 2018keq, SN 2019lci, SN 2020ayz, and SN 2020bvc. One event from Anand et al. (2024), SN 2019hsx, showed a significant Na I feature, which is at odds with their conclusion that no events in the sample demonstrated the feature. The EWs are shown in Table 4.4.

It is possible to convert the EWs to host-galaxy extinctions through the relation from Stritzinger et al. (2018): $A_{\mathrm{V}}^{\mathrm{host}}[\mathrm{mag}] = 0.78(\pm 0.15) \times \mathrm{EW}_{\mathrm{Na\,I}}$. However, this relation only holds strongly when using high-resolution spectra for these measurements; when using low-resolution spectra, Poznanski et al. (2011) showed that even though a weak correlation exists, the large scat-

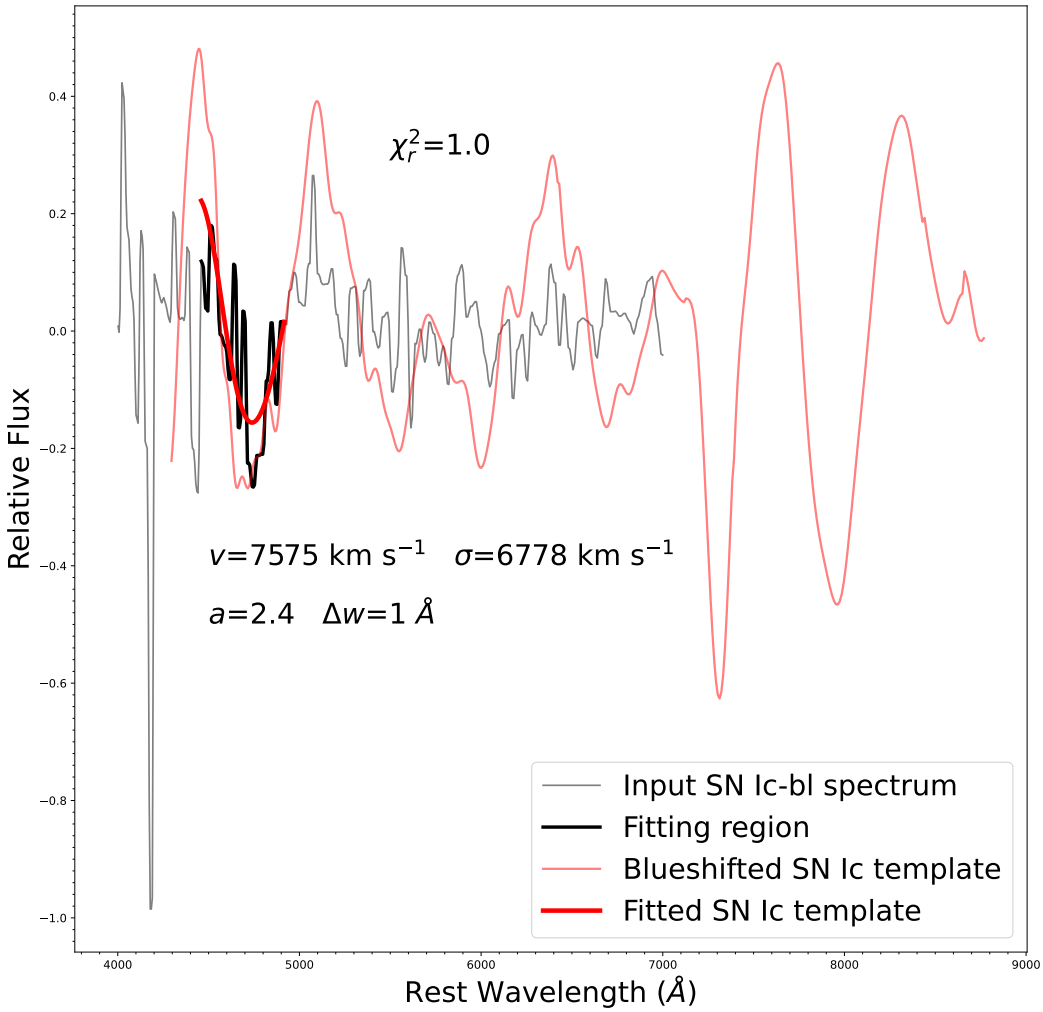

Figure 4.9: Example of the convolution fitting of the Fe II feature for the photospheric phase spectra of SN 2018hsf. The spectrum of the transient is shown in gray, with the fitting region bolded in black. The blueshifted Ic template is shown in red, with the fitting region bolded in red. The reduced chi-square value for the fit is shown (χ_r^2), along with the blueshifted velocity with respect to the Ic template (v), the Doppler broadened line width velocity (σ), the amplitude (a), and the wavelength range (δw).

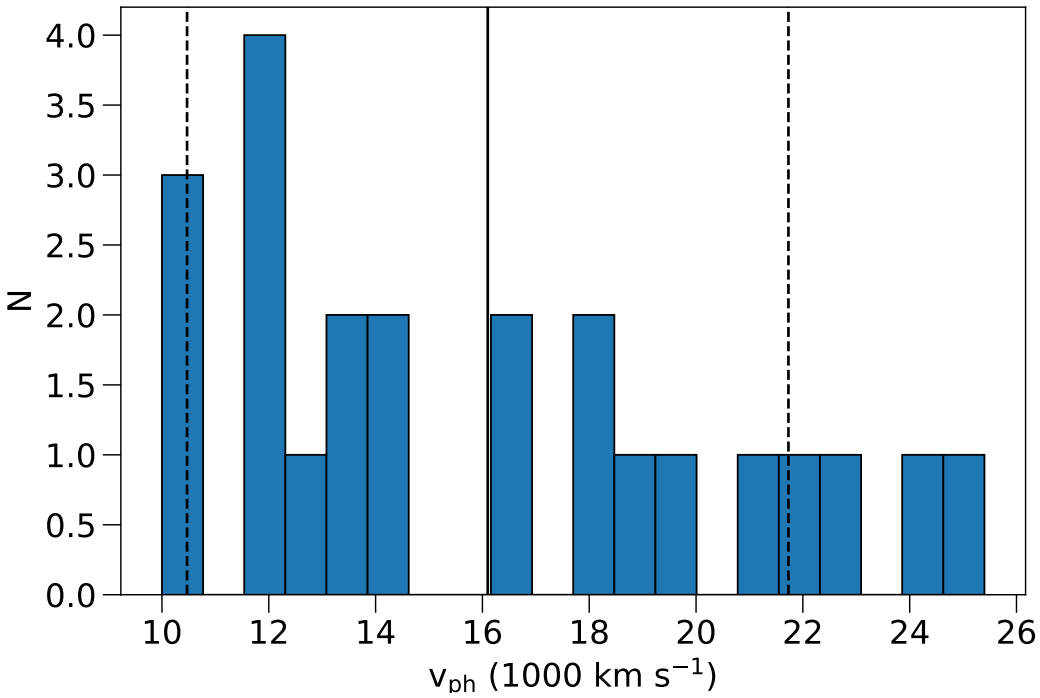

Figure 4.10: The peak v_{ph} for the sample, with the mean velocity (16,100 km s^{-1}) shown with a solid line, and 1σ standard deviation (5,600 km s^{-1}) range shown with dashed lines.

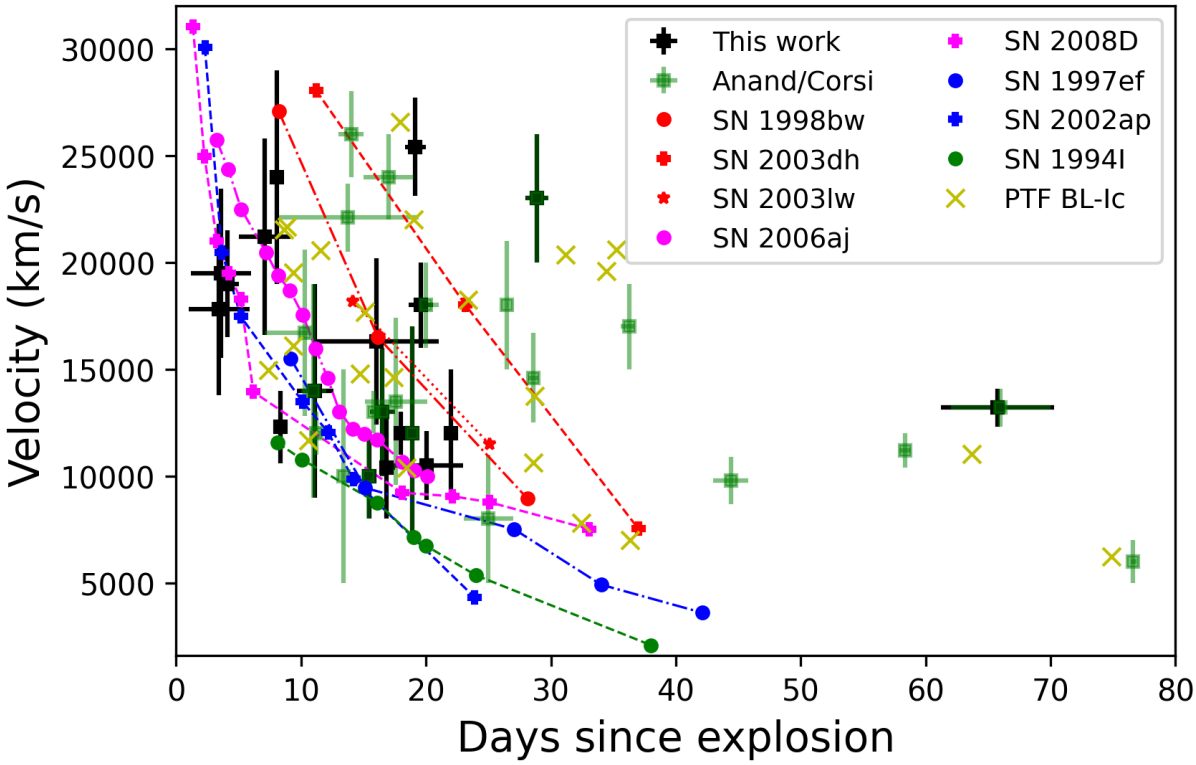

Figure 4.11: SN velocities measured from the Fe II 5169Å line as a function of the spectroscopic phase for every event in the sample that a velocity was able to be obtained (26 events). The black points indicate the velocities at the spectral epoch, plotted with measured velocities of SNe Ic-BL from literature, the iPTF sample (Taddia et al., 2019b), and the samples from Anand et al. (2024) and Corsi et al. (2023). Red symbols represent GRB-SNe (Iwamoto et al., 1998b; Mazzali et al., 2003, 2006b); magenta represents XRF/X-ray transient-SNe (Mazzali et al., 2006c; Modjaz et al., 2009; Pian et al., 2006); blue represents SNe Ic-BL (Mazzali, 2000; Mazzali et al., 2002); and green represents the "normal" Type Ic SN 1994I (Sauer et al., 2006).

Event	$EW_{\rm Na\,I}$	$< A_{\rm V}^{\rm host}$[mag]
SN 2018hsf	1.23 ± 0.14	1.3
SN 2018keq	1.01 ± 0.33	1.2
SN 2019hsx	0.80 ± 0.39	1.1
SN 2019lci	0.47 ± 0.22	0.6
SN 2020ayz	1.52 ± 0.13	1.5
SN 2020bvc	0.55 ± 0.17	0.7

Table 4.4: Na I EW and resulting host galaxy extinction upper limits derived for events that show evidence of Na I absorption.

ter makes any relation between the two quantities useless. Therefore, it is possible that these six events have additional host galaxy extinction; however due to the lack of high-resolution spectra, we cannot quantify the amount or say with certainty that a significant amount of extinction is present. Therefore, we compute a conservative upper limit on the amount of host-galaxy extinction for these events, and show the results in Table 4.4. However, given the lack of constraints, we do not correct for host-galaxy extinction for any of these events during our analysis.

4.6 Bolometric LCs and Properties

4.6.1 Bolometric light curves and peak luminosites

There is a lack of complete multi-band coverage for the majority of events in our sample – in particular the coverage in the i band is sparse. Therefore, due to the sufficient coverage in g and r bands, we use the $g-r$ colors calculated in §4.4.2 along with the bolometric correction (BC) coefficients of Lyman et al. (2014b, 2016b) to compute bolometric LCs for our sample. According to Lyman et al. (2014b), stripped-envelope supernovae possess a BC as follows:

$$\mathrm{BC}_g = 0.054 - 0.195 \times (g-r) - 0.719 \times (g-r)^2. \tag{4.2}$$

This BC is valid after the initial shock-breakout phase. We calculate the $\mathrm{BC_g}$ coefficient for every epoch in our sample using the GP-interpolated data. Then, using the definition of BC coefficients:

$$\mathrm{BC}_x = \mathrm{M_{bol}} - \mathrm{M_x}, \tag{4.3}$$

where x is the relevant filter, $\mathrm{M_{bol}}$ is the absolute bolometric magnitude, and $\mathrm{M_x}$ is the absolute magnitude in the relevant filter, we calculate $\mathrm{M_{bol}}$ at every epoch. In Figure 4.12, we show the distribution of $\mathrm{M_{bol}^{max}}$ for the sample. The distribution ranges from -16.28 to -20.91 mag, and we find an average $\overline{\mathrm{M}}_{bol}^{max}$ of -18.34 ± 0.16 mag, with a 1σ standard deviation of 0.98 mag. This is consistent with the value found in Taddia et al. (2019b), who found $\overline{\mathrm{M}}_{\mathrm{bol}}^{\mathrm{max}} = -18.5$ with a 1σ standard deviation of 0.5 mag. When excluding SLSN SN 2020wgz from the sample, we find an average $\overline{\mathrm{M}_{\mathrm{bol}}^{\mathrm{max}}}$ of -18.27 ± 0.15 mag, with a 1σ standard deviation of 0.89 mag.

We then convert $\mathrm{M_{bol}}$ to a bolometric luminosity. To calculate uncertainties we include the photometric uncertainty on the peak magnitude that we estimate from the GP analysis and a 15% correction to take into account MW extinction, a peculiar velocity correction uncertainty of 150 km s^{-1}, and the uncertainty of the Hubble constant, ± 3 km s^{-1} Mpc^{-1}. In Figure 4.13, we show the bolometric luminosity LCs of our sample.

4.6.2 Blackbody Temperature and Radii Evolution

Because we have multi-band photometry, we are able to investigate the spectral energy distribution (SED) evolution over time for the events in our sample. In particular, we calculate how the blackbody temperature and radius evolve over time, through fitting a diluted blackbody function to the SEDs:

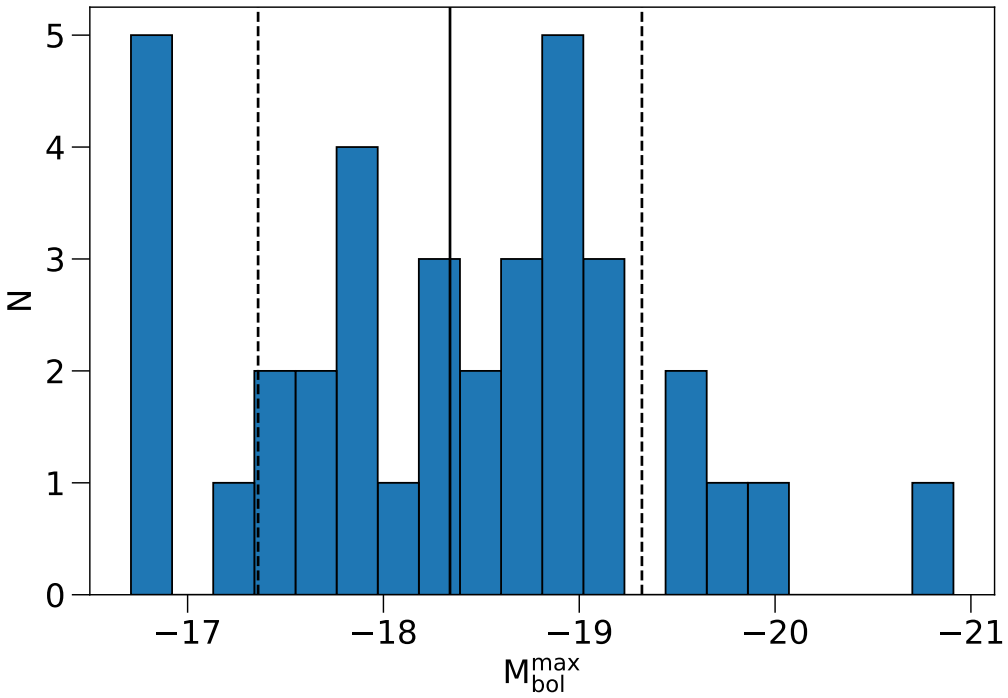

Figure 4.12: $\mathrm{M}_{\mathrm{bol}}^{\mathrm{max}}$ of all SNe in the sample, with the mean magnitude (-18.34 mag) shown with a solid line, and 1σ standard deviation range (0.98 mag) shown with dashed lines.

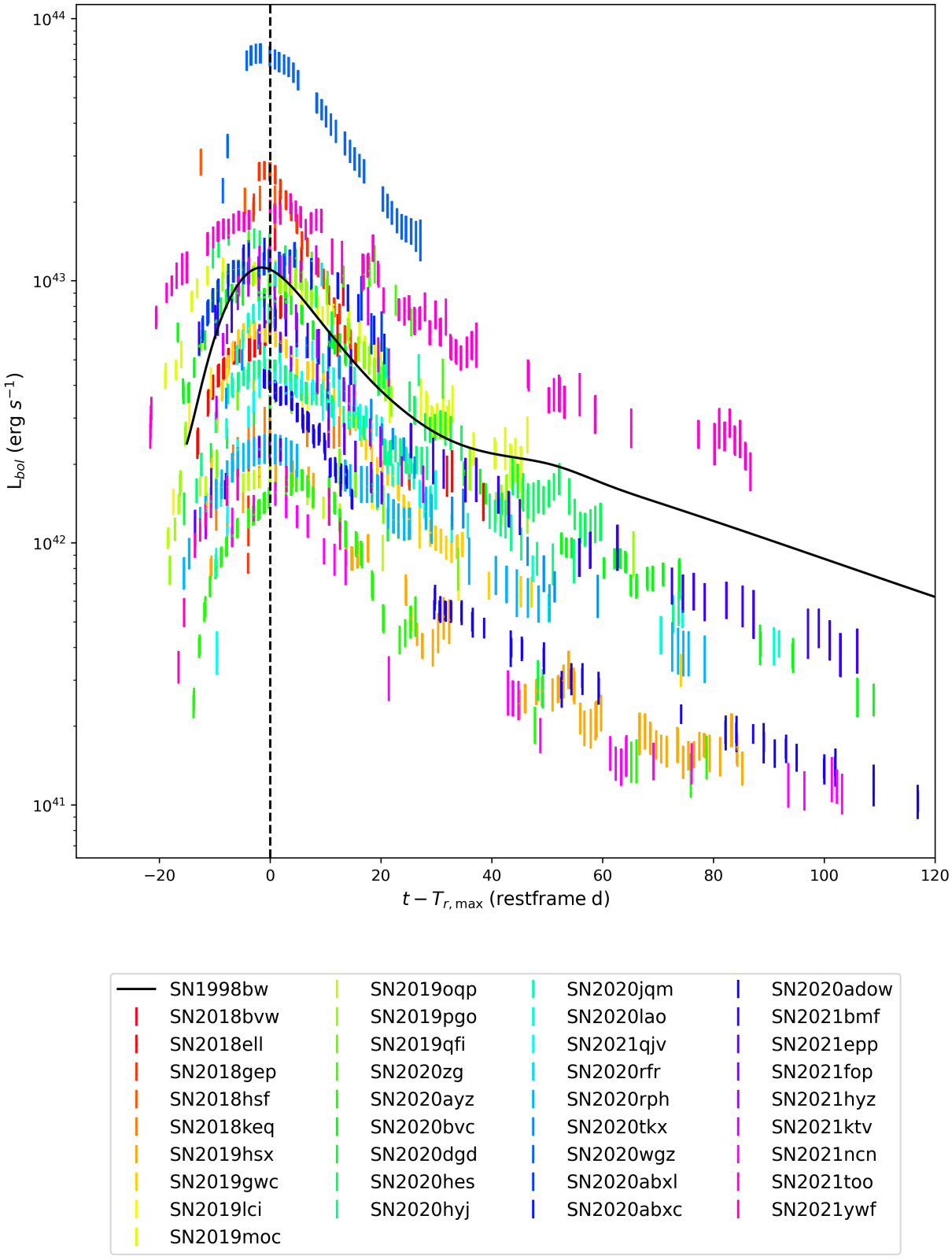

Figure 4.13: Bolometric luminosity LCs for the SNe Ic-BL sample, calculated using Lyman BC coefficients (described in §4.6.1). The bolometric luminosity LC of SN 1998bw (Clocchiatti et al., 2011) is also shown as comparison.

$$F_\lambda = (R/d)^2 \cdot \epsilon^2 \cdot \pi \cdot B(\lambda, T) \times 10^{-0.4 \cdot A_\lambda}. \quad (4.4)$$

In this function, F_λ is the flux at wavelength λ, B is the Planck function, A_λ is the extinction, T is the temperature, R is the radius, d is the distance, and ϵ is the dilution factor (Dessart & Hillier, 2005; Eastman et al., 1996; Hamuy et al., 2001) representing a correction between the BB distribution we fit to the observed fluxes.

The SEDs consist of photometry binned within 0.5 days of each other, using g, r, and i-band data. For some cases, we also have *Swift* host-corrected UVOT photometry (detailed in §4.3.7), and include those points in the SEDs when available. We estimate the luminosity by integrating the blackbody distributions from 2000 $\mathring{A}$ to 20000 $\mathring{A}$. The blackbody temperature and radius evolution over time are shown in Figure 4.14. We find that the temperature shows a progressive decline until ~ 5 days after peak, when the distribution begins to flatten out between 4000 and 7000 K, which is similar to what is found in Taddia et al. (2019b). We find that the radius increases to around 10 days after peak and then decreases for the majority of the sample, again consistent to what is found in Taddia et al. (2019b).

4.7 Explosion Properties

After computing bolometric LCs, we fit the LCs up to the peak luminosity (usually 20 to 60 rest-frame days from first detection) to analytic models from Arnett (1982). In these models, the instantaneous heating rate from the decay of ^{56}Ni and ^{56}Co is equivalent to the peak bolometric luminosity of the SN. The model also assumes spherical symmetry in the explosion, and full gamma-ray trapping of the ejecta. In these models, the nickel mass (M_{Ni}) and characteristic

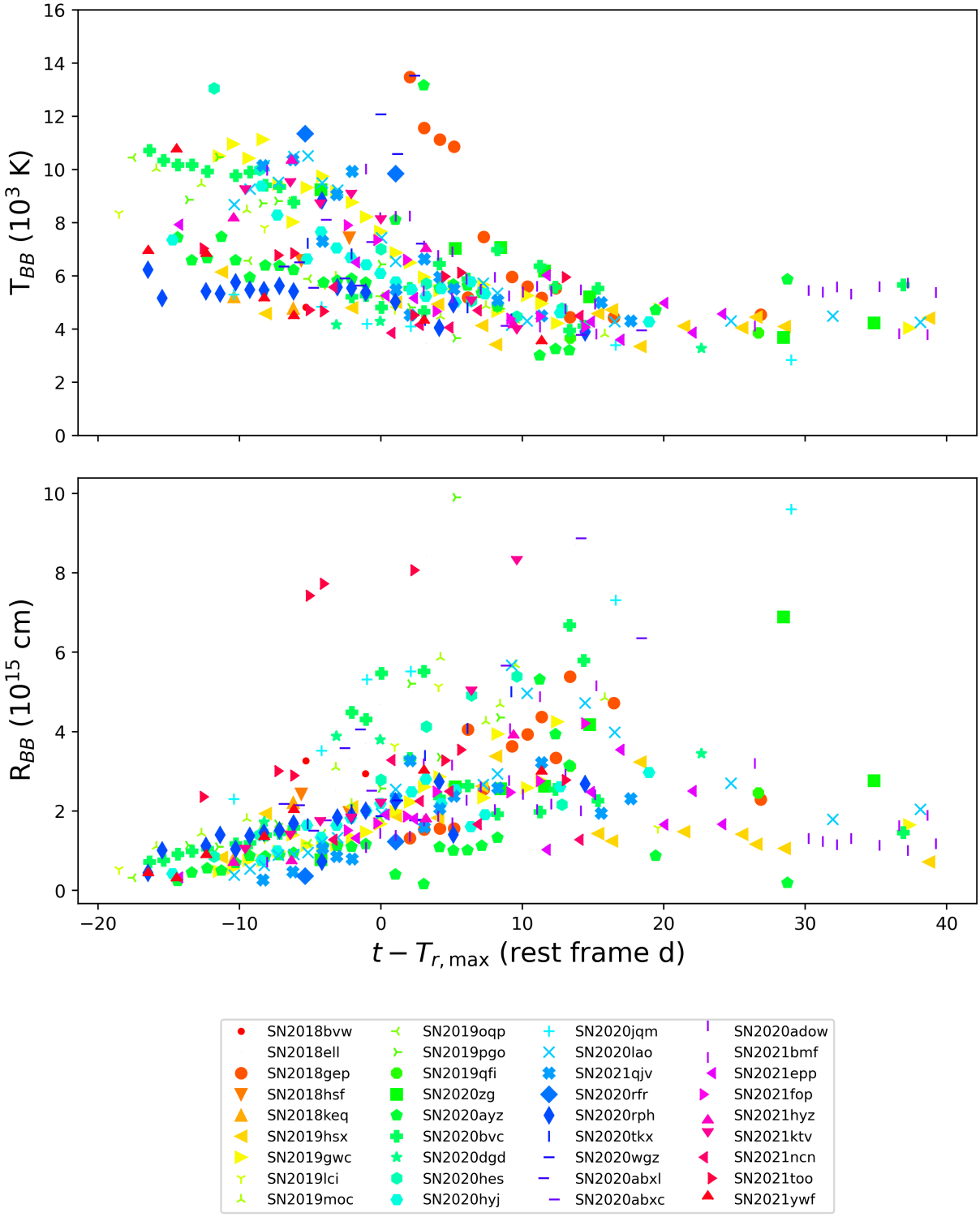

Figure 4.14: Blackbody temperatwure and radii evolution for the SNe Ic-BL sample, calculated through the methods reported in §4.6.2.

photon diffusion time scale (τ_m) are free parameters. These parameters are important probes of the explosion mechanisms, as the amount of $\mathrm{M_{Ni}}$ powers the bolometric LC, while τ_m is a proxy for the rise timescale of the SN, along with relating to the kinetic energy ($\mathrm{E_K}$) and ejecta mass ($\mathrm{M_{ej}}$) of the SN. We note that Corsi et al. (2023) and Anand et al. (2024) used the same methods to derive the explosion parameters for events in their sample, so for overlapping events we report the values derived in their works.

We use HAFFET to generate semi-analytic bolometric luminosity LCs corresponding to different $\mathrm{M_{Ni}}$ and τ_m values, and use MCMC techniques to find the best-fit and 16, 50, and 84% confidence interval values corresponding to each event not presented in Corsi et al. (2023) and Anand et al. (2024). The distribution of $\mathrm{M_{Ni}}$ masses derived is shown in Figure 4.15, and the values along with their statistical uncertainties are reported in Table 4.5. The values range from 0.05 to 2.46 $\mathrm{M_\odot}$, with a mean of $0.37^{+0.08}_{-0.06}\,\mathrm{M_\odot}$ and a 1σ standard deviation of 0.42. This is consistent with the normal SNe Ic-BL SN sample from Taddia et al. (2019b), who found a mean value of 0.31 $\mathrm{M_\odot}$ with a 1σ standard deviation of 0.17 $\mathrm{M_\odot}$. 12 events in our sample were also included in Rodríguez et al. (2023a), who performed a systematic study of the iron yield in different classes of stripped-envelope SNe. They find an average Nickel mass of SNe Ic-BL of 0.14 ± 0.02, which is around a factor of 2 less than the value we derived. This is due to a different fitting procedure, as they calculated the Nickel masses based on the radioactive decay tail, rather than the peak of the LC using the Arnett (1982) model. Due to the Malmquist bias (see §4.4.2, where the peak absolute magnitude distribution is 0.2 mag lower after accounting for this effect), the corrected Nickel mass distribution is 17% lower than what we measure (Taddia et al., 2019b), which is a small effect. When we exclude the SLSN SN 2020wgz from the sample, we find a new mean of $0.32 \pm 0.03\,\mathrm{M_\odot}$, and 1σ standard deviation of 0.21 $\mathrm{M_\odot}$.

ZTF name	SN name	M_{Ni} ($M_\odot$)	E_K (10^{51}erg)	M_{ej} ($M_\odot$)	v_{ph} (10^3 km s^{-1})	Spectrum phase (d)
ZTF18aaqjovh	SN 2018bvw	$0.52^{+0.05}_{-0.05}$	4.45 ± 2.7	1.66 ± 0.5	21.2 ± 4.6	-1
ZTF18abhhnnv	SN 2018ell	$0.31^{+0.01}_{-0.01}$	11.44 ± 3.84	3 ± 0.35	25.4 ± 2.3	3.2
ZTF18abukavn	SN 2018gep	$0.61^{+0.01}_{-0.01}$	0.7 ± 0.6	0.2 ± 0.04	24 ± 5	4
ZTF18acbvpzj	SN 2018hsf	$0.7^{+0.13}_{-0.1}$	> 0.07	> 0.31	8.2 ± 0.94	23.7
ZTF18acxgoki	SN 2018keq	$0.16^{+0.05}_{-0.05}$	-	-	-	-
ZTF19aawqcgy	SN 2019hsx	$0.07^{+0.01}_{-0.01}$	0.99 ± 0.5	1.64 ± 0.43	10 ± 2	-0.2
ZTF19aaxfcpq	SN 2019gwc	$0.22^{+0.01}_{-0.01}$	> 0.44	> 0.6	11.1 ± 0.9	46.0
ZTF19abfsxpw	SN 2019lci	$0.24^{+0.01}_{-0.01}$	-	-	-	-
ZTF19ablesob	SN 2019moc	$0.52^{+0.01}_{-0.02}$	3.48 ± 1.85	2.09 ± 0.5	16.8 ± 3.9	-9.7
ZTF19abqshry	SN 2019oqp	0.08^{+0}_{-0}	-	-	-	-
ZTF19abupned	SN 2019pgo	$0.55^{+0.01}_{-0.01}$	0.89 ± 0.6	1.37 ± 0.4	10.4 ± 2.4	1
ZTF19abzwaen	SN 2019qfi	$0.13^{+0.01}_{-0.01}$	> 0.7	> 1.22	9.59 ± 1.2	29.3
ZTF20aafmdzj	SN 2020zg	$0.5^{+0.01}_{-0.01}$	-	-	-	-
ZTF20aaiqiti	SN 2020ayz	$0.07^{+0}.01_{-0.01}$	1.85 ± 0.92	2 ± 0.3	12.3 ± 1.7	-6.1
ZTF20aalxlis	SN 2020bvc	$0.41^{+0.01}_{-0.01}$	5.15 ± 2.45	2.39 ± 0.45	19 ± 2.5	-14
ZTF20aapcbmc	SN 2020dgd	$0.13^{+0.03}_{-0.03}$	3.07 ± 2.42	2.81 ± 1.5	13.5 ± 3.9	-0.43
ZTF20aaurexl	SN 2020hes	$0.58^{+0.01}_{-0.01}$	2 ± 1.9	1.26 ± 0.36	16.3 ± 3.9	0
ZTF20aavcvrm	SN 2020hyj	$0.22^{+0.01}_{-0.01}$	-	-	-	-
ZTF20aazkjfv	SN 2020jqm	$0.29^{+0.05}_{-0.04}$	5 ± 3	5 ± 1	13 ± 3	-0.5
ZTF20abbplei	SN 2020lao	$0.23^{+0.01}_{-0.01}$	2.48 ± 0.71	1.22 ± 0.16	18 ± 2	9
ZTF20abrmmah	SN 2020rfr	$0.47^{+0.03}_{-0.03}$	-	-	-	-
ZTF20abswdbg	SN 2020rph	$0.07^{+0.01}_{-0.01}$	3.08 ± 2.81	3.83 ± 1.59	12 ± 5	-1
ZTF20abzoeiw	SN 2020tkx	$0.22^{+0.01}_{-0.01}$	> 1.5	> 1.5	13.2 ± 0.9	53
ZTF20achvlbs	SN 2020wgz	$2.46^{+0.02}_{-0.02}$	> 0.12	> 0.48	11.1 ± 0.3	25
ZTF20acvcxkz	SN 2020abxl	$0.4^{+0.01}_{-0.01}$	-	-	-	-
ZTF20acvmzfv	SN 2020abxc	$0.61^{+0.02}_{-0.02}$	-	-	-	-
ZTF20adadrhw	SN 2020adow	$0.14^{+0.02}_{-0.02}$	2.2 ± 1.1	1 ± 0.2	19.5 ± 3.96	-7.9
ZTF21aagtpro	SN 2021bmf	$0.98^{+0.16}_{-0.17}$	23.63 ± 16.14	8.05 ± 5.37	21.9 ± 1.5	-10.0
ZTF21aaocrlm	SN 2021epp	$0.12^{+0.02}_{-0.02}$	6 ± 5	5 ± 2	14 ± 5	-4
ZTF21aapecxb	SN 2021fop	0.19^{+0}_{-0}	-	-	-	-
ZTF21aartgiv	SN 2021hyz	$0.29^{+0.01}_{-0.02}$	> 4	> 1.3	23 ± 3	16
ZTF21aaxxihx	SN 2021ktv	$0.48^{+0.01}_{-0.01}$	0.63 ± 0.4	0.95 ± 0.2	10.5 ± 1.6	8.2
ZTF21abchjer	SN 2021ncn	$0.05^{+0.01}_{-0.01}$	-	-	-	-
ZTF20abcjdwu	SN 2021qjv	$0.17^{+0.01}_{-0.01}$	1 ± 1	1.16 ± 0.35	12 ± 3	11.3
ZTF21abmjgwf	SN 2021too	$0.92^{+0.03}_{-0.03}$	6.42 ± 2.09	5.06 ± 0.78	14.4 ± 2.1	5.4
ZTF21acbnfos	SN 2021ywf	$0.06^{+0.01}_{-0.01}$	0.9 ± 0.3	1.1 ± 0.2	12 ± 1	0.5

Table 4.5: Explosion properties and photospheric velocities for the SNe Ic-BL sample. Values reported include those newly derived and those presented in previous works.

We note that for SN 2020bvc, the M_{Ni} we derive (0.41 ± 0.01 $M_{\odot}$) is inconsistent with what is derived in Ho et al. (2020c) of 0.13 ± 0.01 $M_{\odot}$. The reason for this discrepancy is that Ho et al. (2020c) used the radioactive decay tail to derive M_{Ni}, rather than the peak of the LC. However, the M_{Ni} we derive is consistent with the results from Rho et al. (2021), who found $M_{Ni} \sim 0.4\,M_{\odot}$. This value is likely more accurate as they used hydrodynamical LC modeling to derive this value. The value we derive for SN 2018gep ($M_{Ni} = 0.13 \pm 0.01$ $M_{\odot}$) is consistent with what is found in Ho et al. (2019a), where they find $M_{Ni} < 0.3\,M_{\odot}$. The value we derive for SN 2018bvw ($M_{Ni} = 0.52 \pm 0.05$ $M_{\odot}$) is slightly larger than the value derived in Ho et al. (2020b) of ~ 0.3 $M_{\odot}$, though they did not report any errors in their work.

Armed with τ_m and v_{ph}, we then derive the M_{ej} and E_{KE} for each of the events in our sample using the equations from Lyman et al. (2016a). M_{ej} is described as

$$M_{ej} = \frac{\tau_m^2 \beta c v_{sc}}{2\kappa_{opt}}, \tag{4.5}$$

and E_{KE} is described as

$$E_{KE} = \frac{3 v_{sc}^2 M_{ej}}{10}, \tag{4.6}$$

where $\beta = 13.8$ is a constant, c is the speed of light, κ_{opt} is a constant, average optical opacity, and v_{sc} is the photospheric velocity v_{ph} at maximum light. κ_{opt} varies in the literature for stripped-envelope SNe, and we adopt the value used by Chugai (2000), Tartaglia et al. (2021), and Barbarino et al. (2021), $\kappa_{opt} = 0.07\,cm^2\,g^{-1}$ (which was shown to accurately recreate hydrodynamical LCs of observed stripped-envelope SNe; Taddia et al. 2018).

Because a measurement of v_{ph} is needed to derive M_{ej} and E_{KE}, we were able to derive values for the 20 events that we estimated v_{ph} at peak for (described in §4.5). For the six events

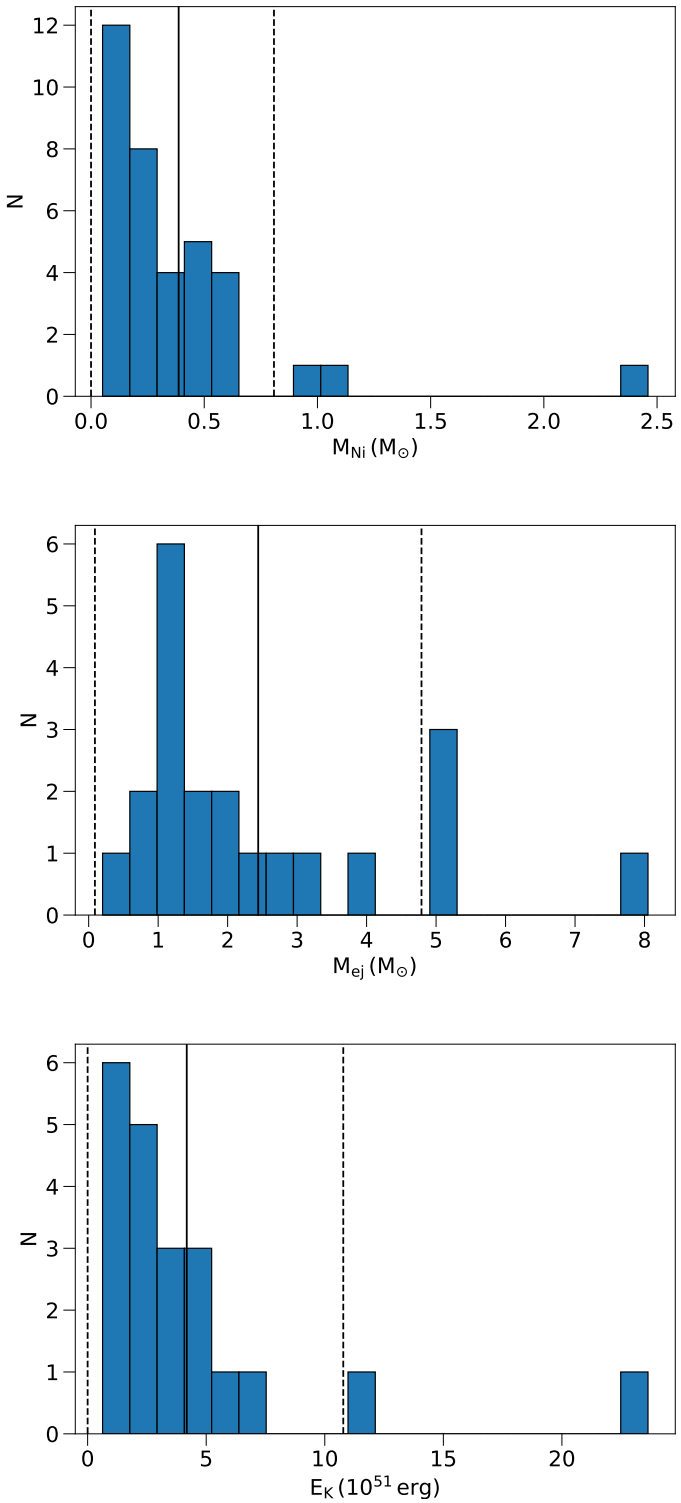

Figure 4.15: Histograms of the explosion properties derived for the Ic-BL sample. The mean values and 1σ dispersions for the properties are shown with solid and dashed lines respectively. *Top panel*: The $\mathrm{M_{Ni}}$ distribution for the SNe Ic-BL sample. *Middle panel*: The $\mathrm{M_{ej}}$ distribution for the SNe Ic-BL sample. *Lower panel*: The $\mathrm{E_K}$ distribution for the SNe Ic-BL sample.

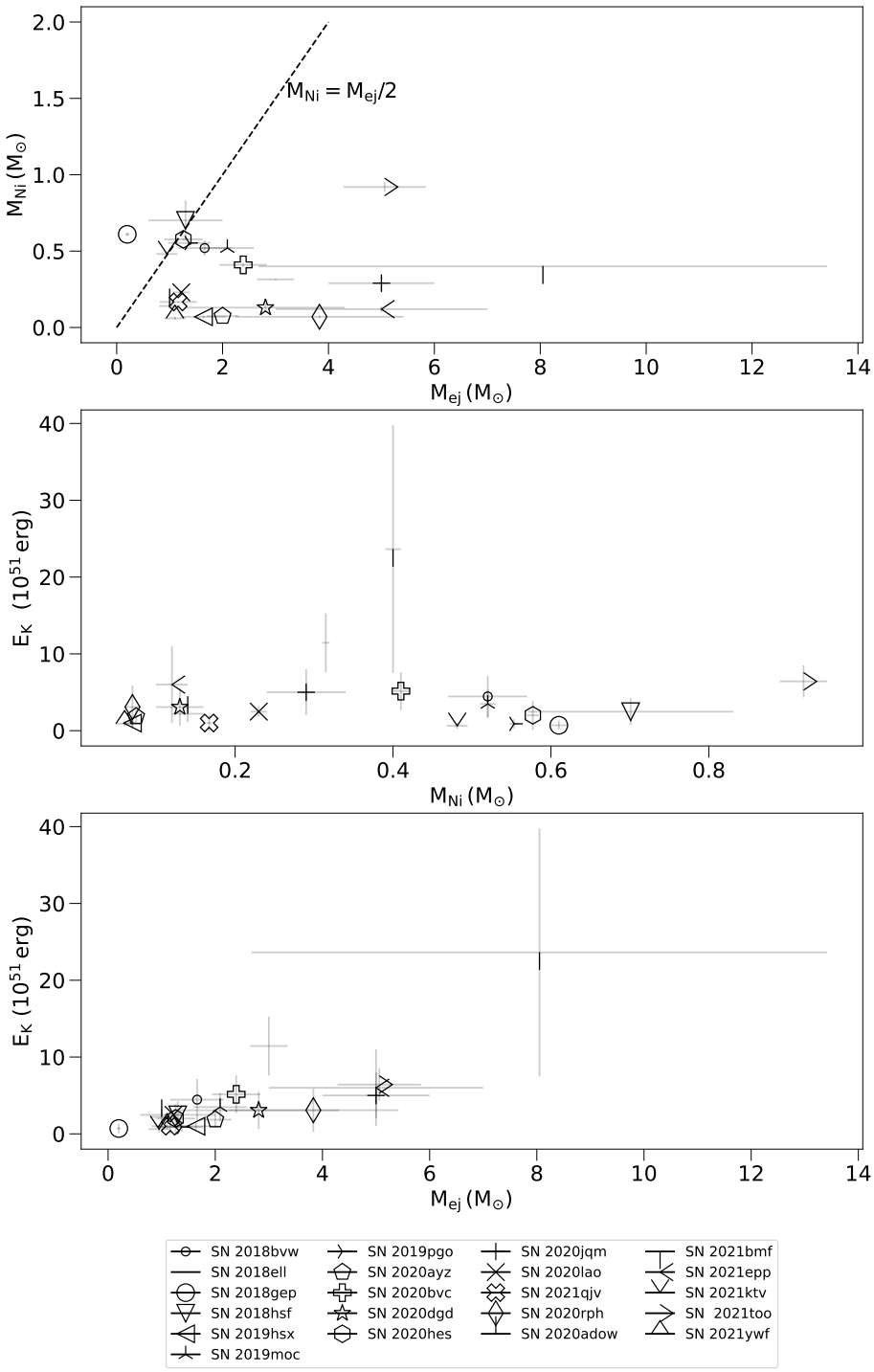

Figure 4.16: Explosion properties (M_{Ni}, M_{ej}, and E_K) plotted against each other. *Top panel*: M_{Ni} plotted against M_{ej}. We do not find any correlations between the two, with a p-value of 0.86. The dashed line indicates the boundary of $M_{Ni} = M_{ej}/2$. Events above that boundary are likely not soley powered by radioactive decay (Kasen & Bildsten, 2010). *Middle panel*: E_K plotted against M_{Ni}. We do not find any correlation between the two, with a p-value of 0.75. *Bottom panel*: E_K plotted against M_{ej}. We find a significant correlation between the two, with a p-value of 0.007.

that did not have spectra within 15 days of the peak epoch, we derive lower limits on their M_{ej} and E_{KE}. We present the values in Table 4.5, and show their distributions in Figure 4.15. The M_{ej} values range from 0.2 to 8.05 $M_{\odot}$, with a mean of $2.45^{+0.47}_{-0.41}$ $M_{\odot}$ and 1σ standard deviation of 2.35 $M_{\odot}$. This is consistent with the normal Ic-BL sample from Taddia et al. (2019b), who found a mean value of 4.0 $M_{\odot}$ with a 1σ standard deviation of 2.9 $M_{\odot}$. E_{KE} ranges from 6.6×10^{50} erg to 2.4×10^{52} erg, with an average of $4.02^{+1.37}_{-1.00} \times 10^{51}$ erg and 1σ standard deviation of 6.60×10^{51} erg. This is consistent with the distribution found in Taddia et al. (2019b), who found an average of 7×10^{51} erg with a 1σ standard deviation of 5.8×10^{51} erg.

In Figure 4.16, we plot the three explosion parameters against each other to test for the presence of any correlations using the Spearman rank test. We find no significant correlations between M_{Ni} and M_{ej} (p-value of 0.86), no correlation between M_{Ni} and E_K (p-value of 0.75), and a significant correlation between M_{ej} and E_K (p-value of 0.007). The correlation between M_{ej} and E_K is expected due to the relationships shown in Eq. 4.5 and 4.6.

We also show the boundary of $M_{Ni} = M_{ej}/2$, which is the boundary used by Taddia et al. (2019b) that indicates a shift from an event powered by radioactive decay up to its peak luminosity, to one that must be powered by additional mechanisms, including the spindown of a magnetar (Kasen & Bildsten, 2010). We note that there is one event (SN 2018gep) that is clearly in this regime, and Ho et al. (2019a) showed that this event is best modeled as a shock breakout event in a dense CSM. There are two events whose error bars extend into this regime (SN 2019pgo and SN 2020hes), and one event that has $M_{Ni} > M_{ej}/2$, SN 2021ktv. However, SN 2021ktv's error bars for M_{ej} make it uncertain that it solely exists in this regime, so we cannot firmly establish the presence of any additional powering mechanisms for these three events through this method. SN 2018hsf possesses a relatively high $M_{Ni} = 0.7\,M_{\odot}$, and the lower limits derived for M_{ej} find

$M_{ej} > 0.31$. Therefore, it is possible that SN 2018hsf possesses additional powering mechanisms. SN 2020wgz also likely exists in this regime, as it possesses an extremely high $M_{Ni} = 2.46\,M_{\odot}$, and also has a luminosity that places it in the regime of SLSN. However, only lower limits on its M_{ej} and E_K were derived due to a lack of a velocity measurement close to peak light. We provide more details on this event in §4.7.1.

4.7.1 SN 2020wgz – a SLSN-I?

SLSNe are a sub-class of SNe that can reach peak magnitudes of ~ -21 mag, a factor of 100 more than normal CCSNe (Gal-Yam, 2012; Quimby et al., 2011). A subset of SLSNe do not show hydrogen features in their spectra, and are classified as SLSN-I. These events have slow rise times and peak much later than normal CCSNe (typically 20 - 100 days after explosion). SLSN-I spectra possess a blue continuum, often along with Fe II, Mg II, and O II absorption lines. Due to their high luminosity and spectral composition, the spin-down of magnetar is the most favored physical model for describing these events (Dessart et al., 2012).

SN 2020wgz possesses a peak absolute bolometric magnitude of $M_{bol}^{max} = -20.91 \pm 0.09$ mag, placing it in the luminosity class of SLSNe. The two spectra obtained near peak light shown in the Appendix show no hydrogen features, along with a blue featureless continuum. The spectra are too low-quality/noisy to make out the presence of any absorption features. Therefore, SN 2020wgz's LC and early-time spectra have similarities to SLSN-I. However, SN 2020wgz has a rapid-rise time of ~ 10 days, differing from normal SLSN-I. Furthermore, a spectrum taken 21 days after peak shows a transition to a redder continuum, along with the development of broad spectral features, which enabled a classification of SN Ic-BL.

SN 2011kl is a SLSN-I that was associated with an ultra-long GRB 111209A (Greiner et al., 2015a). To date, it is the only SN associated with a GRB that is not a SNe Ic-BL. SN 2020wgz possesses a peak absolute magnitude around one order of magnitude higher than SN 2011kl ($M_{\rm bol}^{\rm max} \sim -20.0$ mag), and has a similar rise time to SN 2011kl ($\sim$ 14 days). However, SN 2011kl's spectra do not show the same transition to a redder continuum and the development of broad absorption features that SN 2020wgz does. LC modeling of SN 2011kl showed that it likely was solely powered by a magnetar.

This spectral transition was seen in a few other objects (e.g., Pastorello et al. 2010), and most recently in SLSN-I SN 2017dwh (Blanchard et al., 2019), which was a Nickel-rich SLSN-I possessing a similar but slightly fainter peak absolute magnitude of ~ -20.5 mag, and a slightly longer rise time of $\sim$ 19 days. Blanchard et al. (2019) found that the high amount of Nickel in the explosion may be due to enhanced production, or due to more efficient mixing of Fe group elements in the outer ejecta. They concluded that SN 2017dwh was likely powered by a combination of the spindown of a magnetar and radioactive decay. This event provides evidence that the progenitors for SLSN-I and SNe Ic-BL might be similar for certain cases.

In §4.7, we determined that SN 2020wgz had too high of a Nickel mass to be powered purely by the Arnett (1982) model. Utilizing the spectral similarities to SN 2017dwh, we use the open-source electromagnetic transient Bayesian fitting software package `redback` to fit a `general magnetar driven supernova` model (Omand & Sarin, 2024b) to the observed r and g-band LCs. This model utilizes the combination of both the spindown of a magnetar along with radioactive decay to power the LC. We show the best-fit model in Figure 4.17, along with the corner plot in the Appendix. We see that the model fits the LC well in both the g and r bands, showing that it is likely SN 2020wgz was powered by a magnetar, at least to some

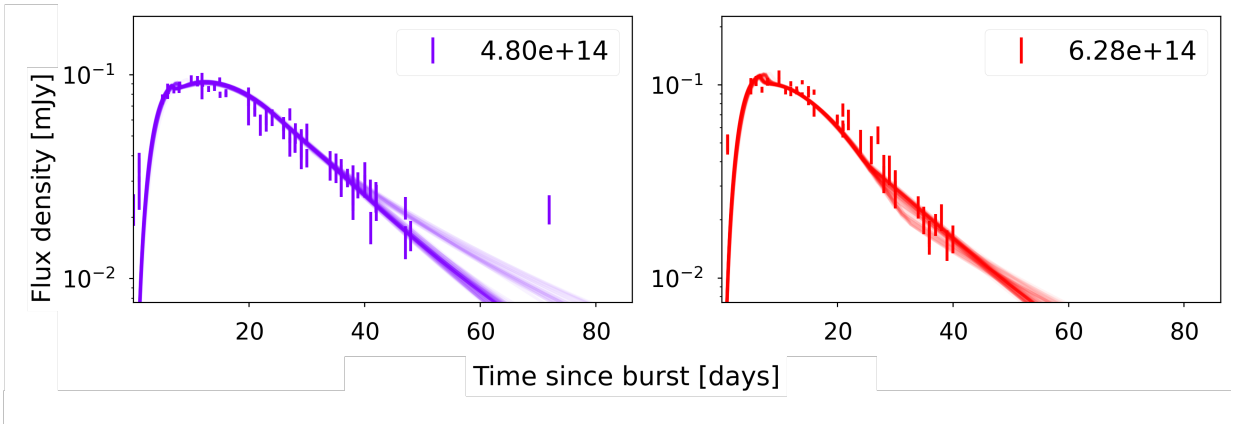

Figure 4.17: The best-fit magnetar powered model fit to SN 2020wgz, in the r band on the left, and g band on the right.

extent.

4.8 Discussion in Context of Multi-Wavelength Observations

There are eight events in the sample that have transient radio counterparts (SN 2018bvw, SN 2018gep, SN 2020tkx, SN 2020jqm, SN 2020bvc, SN 2020adow, SN 2021bmf, and SN 2021ywf). SN 2018bvw, SN 2018gep, and SN 2020tkx are subjects of single-object papers, and the physical mechanisms of their explosions are discussed at length in those works. SN 2018bvw likely is a transition event between engine-driven GRB-SNe (Ho et al., 2020b) and normal SNe Ic-BL, and the event shows possible signs of harboring a mildly relativistic jet. SN 2018gep originates from a shock breakout in a massive shell of dense circumstellar material without an accompanying relativistic jet (Ho et al., 2019a; Leung et al., 2021a; Pritchard et al., 2021), and SN 2020bvc shows a double peak LC due to shock cooling emission followed by radioactive decay, with the event showing similar multiwavelength features to low-luminosity GRB 060218/SN 2006aj. This event also shows signs of mildly relativistic ejecta (Ho et al., 2020c; Izzo et al., 2020). Furthermore, Corsi et al. (2023) showed that SN 2020jqm's erratic radio LC and derived

shock properties place it in the same regime as radio-loud CSM interacting SNe like PTF11qcj (Corsi et al., 2014). The rest of the events only have one to two radio observations, making multi-wavelength modeling efforts for these objects rather non-constraining with respect to both model comparison and parameter estimation. However, we include multi-wavelength modeling efforts for SN 2020tkx, SN 2020adow, and SN 2021ywf in the Appendix. Modeling efforts for SN 2021bmf will be explored in a future work.

4.8.1 Search for Gamma-rays

Using the derived explosion epochs for the sample, we search for potential GRB coincidences in several online archives. Corsi et al. (2023) did this search for their sample of events, which includes 8 of the events in our sample. They found no *Swift* or *Fermi* GRBs spatially and temporally coincident to any of their events. The only coincident GRBs were from the WIND satellite on the Konus instrument, which does not provide localizations. They found that the number of events found within the explosions epochs were consistent with random fluctuations, and also found that no events with an explosion epoch constrained to less than 1 day had a coincident GRB within that time frame. Furthermore, Ho et al. (2019a) and Ho et al. (2020c) determined that SN 2018gep and SN 2020bvc had no GRB counterparts. Ho et al. (2020b) found that SN 2018bvw had one possible GRB counterpart from Konus-WIND, corresponding to a low-luminosity GRB on 2018 May 3 03:41:01; however, they determine that this association is most likely due to chance.

We repeat this search for the 25 events in our sample not covered above. We find no spatially and temporally coincident *Swift* or *Fermi* GRBs for any of the events. There were 11 SNe

that had KONUS-*Wind* GRBs that were detected within their explosion epochs, corresponding to 31 coincident GRB events over a time period of 78.29 days searched. This rate is also consistent with random fluctuations. Therefore, we determine that no events in the sample have certain, coincident gamma-ray emission.

4.8.2 Comparison of Explosion Properties with Radio Observations

We then test whether statistical differences exist between the explosion properties for the subsample of 13 events that have radio observations, between the eight events with detections and five events with non-detections (Corsi et al., 2023). In Figure 4.18, we show the distributions of $\mathrm{M_{Ni}}$, $\mathrm{M_{ej}}$, $\mathrm{E_K}$, and $\mathrm{v_{ph}}$ for the sub-sample with radio observations. Through running a two-sample Kolmogorov-Smirnov (K-S) test, we do not find statistical differences between the populations for any of the properties, though we note that due to the small sample sizes, moderately different populations cannot be ruled out. We note that for the $\mathrm{M_{ej}}$ and $\mathrm{E_K}$ analysis, we do not include events that only have lower limits derived. Specifically, we compute a K-S test statistic of 0.50 with a $p-$value of 0.31 for the $\mathrm{M_{Ni}}$ distribution, a K-S test statistic of 0.42 with a p-value of 0.66 for the $\mathrm{M_{Ej}}$ distribution, a K-S test statistic of 0.32 with a p-value of 0.89 for the $\mathrm{E_K}$ distribution, and a K-S test statistic of 0.71 with a p-value of 0.12 for the $\mathrm{v_{ph}}$ distribution.

We also investigate whether correlations exist between the peak radio luminosity and explosion properties. If correlations do exist, they may point to a connection between the optically described explosion properties and the existence of radio emission, possibly from accompanying off-axis relativistic jets. In order to check this, we extrapolate the peak radio fluxes for every event to 6 GHz through assuming a spectrum $F_\nu \propto \nu^{-1}$, and convert this flux to a luminosity

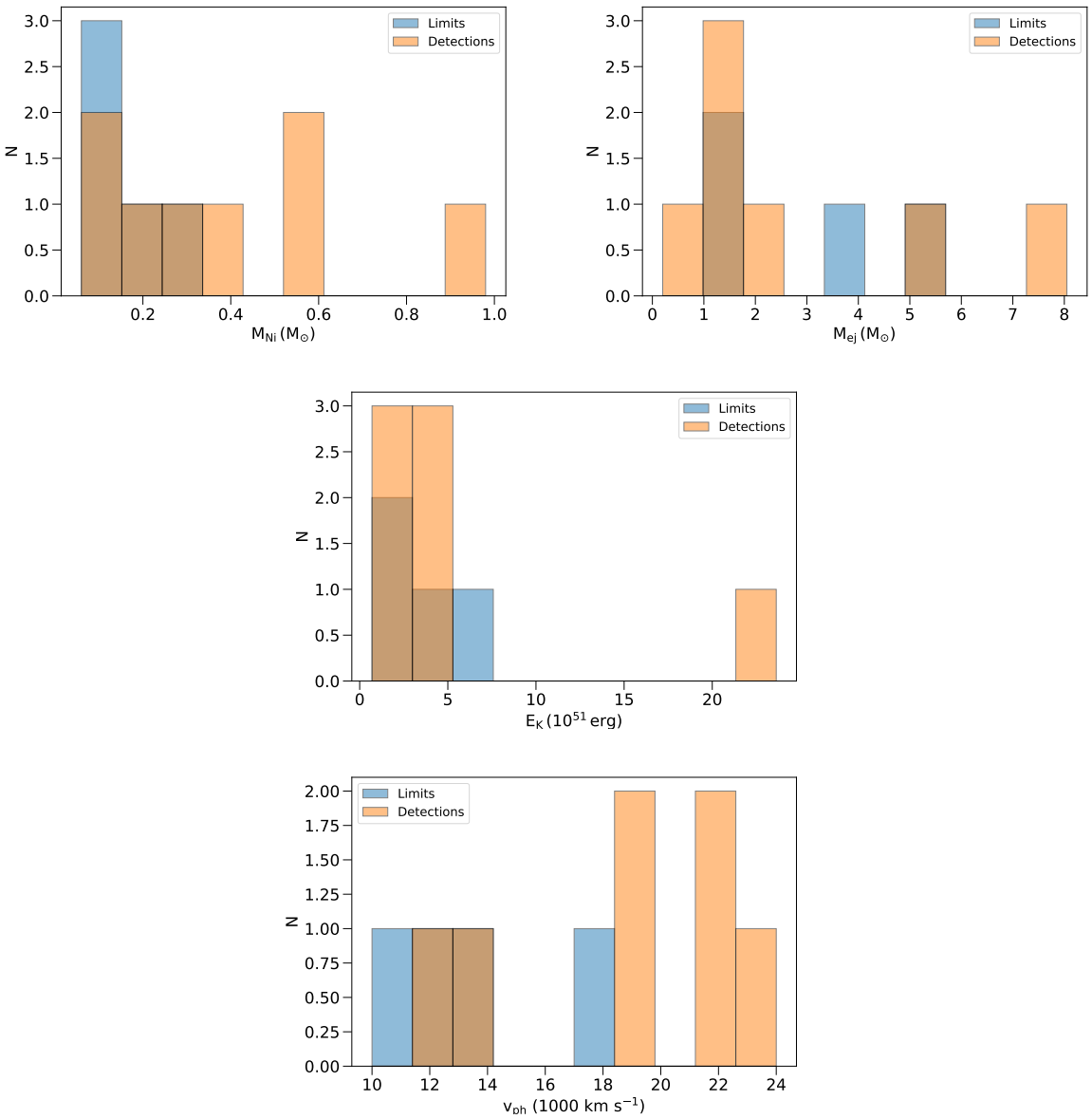

Figure 4.18: Histograms showing the distribution of explosion properties and v_{ph} for the population of events with radio observations. We distinguish events that have radio detections in orange, and events that have radio non-detections in blue. We find no statistical differences between the populations for any of the properties.

using the distance of the SN. Once armed with the radio luminosities, we use a linear regression code, `Linmix`, that takes into account both detections and non-detections when fitting linear models to the data (Kelly, 2007). `Linmix` assumes symmetric error bars, so for M_{Ni} values that have asymmetric error bars, we assume the larger error bar value for both the positive and negative error.

We show the linear regression results in Figure 4.19. For M_{Ni}, we calculate a linear correlation coefficient of 0.32 ± 0.32, with a p-value of 0.33 showing there are no significant correlations present between the radio luminosity and the M_{Ni}. For M_{ej}, we calculate a linear correlation coefficient of 0.46 ± 0.32, with a p-value of 0.18, while for E_K we calculate a linear correlation coefficient of 0.58 ± 0.33 with a p-value of 0.11, again showing a lack of significant correlations. Finally, for v_{ph}, we calculate a linear correlation coefficient of 0.17 ± 0.42, with a p-value of 0.70. We note that we do not include events that have lower limits for this analysis.

Therefore, we find that there are no statistically significant correlations between the radio luminosities and the explosion properties derived from optical data of SNe Ic-BL. We note that there do seem to be slightly positive correlations between the radio luminosities and M_{ej} and E_K; however, these correlations are not statistically significant. Future radio observations of SNe Ic-BL will increase the sample of radio detected-events, and future analyses can use this work as a stepping stone to probe deeper into the relationship between events' optical and radio properties.

4.9 Summary and Conclusions

We analyzed 36 SNe Ic-BL from ZTF between March 2018 and August 2021 as part of the BTS survey, building upon iPTF's sample reported by Taddia et al. (2019b). We present the ZTF

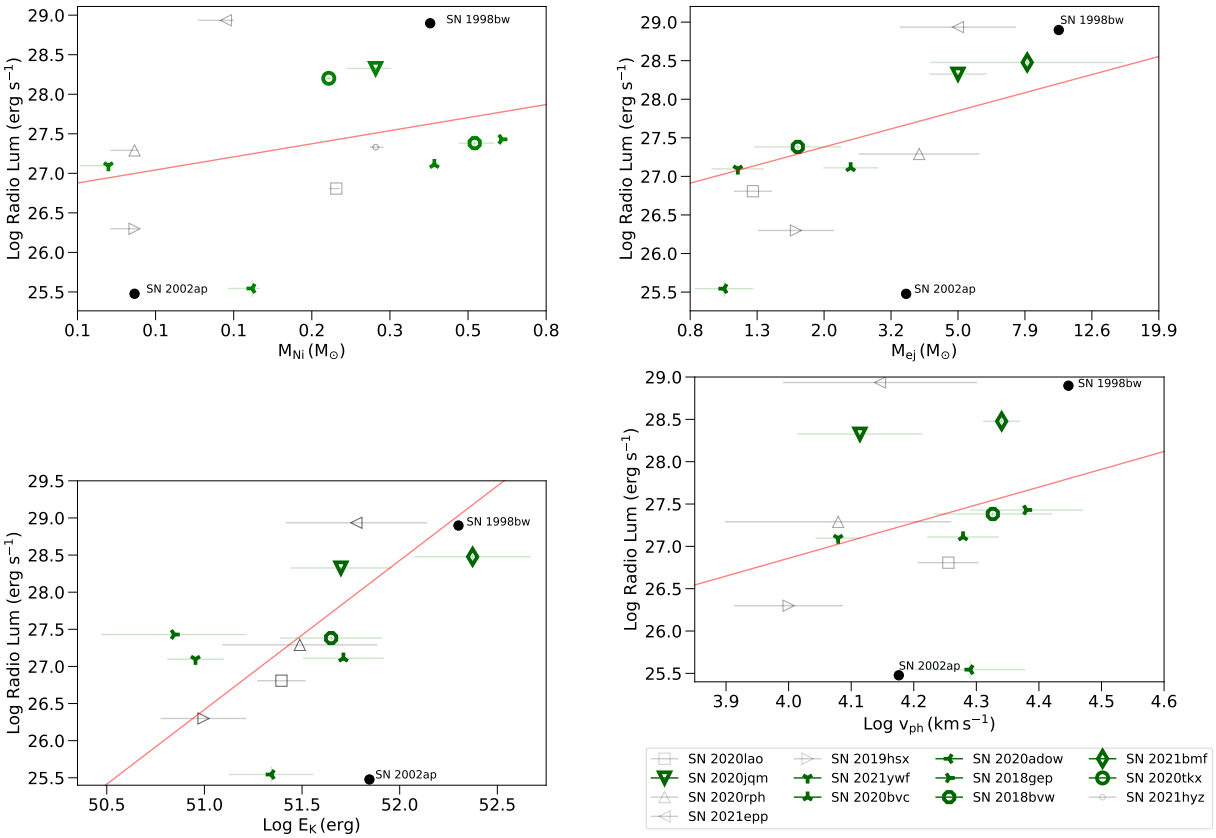

Figure 4.19: Best-fit Linmix linear regression model fitting between the peak radio luminosities and the explosion properties and photospheric velocities shown in red. Black points indicate limits while green points indicate detections. We find no statistically significant correlations between the peak radio luminosities and any of the parameters. The parameters for SN 1998bw (Sollerman et al., 2000; Weiler et al., 2001) and SN 2002ap (Berger et al., 2002; Mazzali et al., 2002) are shown as reference.

LCs, along with spectra obtained for every event. Below we present a summary of some of our findings:

- We find the average peak absolute magnitude in r band of the sample $\overline{\mathrm{M}}_r^{\mathrm{max}} = -18.51 \pm 0.15$ mag, with a 1σ standard deviation of 0.90 mag. This is consistent with the distribution from Taddia et al. (2019b).

- We calculate expansion velocities for each event with sufficient SNR spectra, to estimate the photospheric velocity at peak, and find an average of 16,100 $\pm$ 1,100 km s^{-1}, with a 1σ standard deviation of 5,600 km s^{-1}.

- We also utilize the Arnett (1982) model to determine the explosion properties for each of the events. We determine an average $\mathrm{M_{Ni}}$ of $0.39^{+0.08}_{-0.06}$ $\mathrm{M}_\odot$ and 1σ standard deviation of 0.42 $\mathrm{M}_\odot$, an average $\mathrm{M_{ej}}$ of $2.45^{+0.47}_{-0.41}$ $\mathrm{M}_\odot$ and 1σ standard deviation of 2.35 $\mathrm{M}_\odot$, and an average $\mathrm{E_{KE}}$ of $4.02^{+1.37}_{-1.00} \times 10^{51}$ erg and 1σ standard deviation of 6.5×10^{51} erg. All these values are consistent with the averages found in the previous sample of Taddia et al. (2019b).

- SN 2020wgz has the luminosity and spectral features of a SLSN-I that transitions to a SN Ic-BL. Its LC fits well to a magnetar and nickel-powered combined model.

- We do not find associated gamma-ray emission for any of the events, through searches of archival data from gamma-ray satellites.

- We find that SN 2018gep's radio detections reported in Ho et al. (2019a) are from the transient and not its host galaxy. We also search the VLASS survey for any transient radio

emission for the SNe, and find SN 2021bmf displays transient radio emission over the three epochs of the survey.

- When comparing the optical properties of the radio-loud and radio-quiet population, we find no correlations between the radio luminosity and optical properties of the sample, showing evidence that the optically inferred explosion parameters alone are not sufficient to make inferences about relativistic jet formation mechanisms in SNe Ic-BL.

Disentangling the picture of SNe Ic-BL and their different physical mechanisms continues to be a challenging task, and this work shows that purely studying the global optical properties of SNe Ic-BL will limit our understanding of these explosions. Future radio studies are integral to understanding this landscape. These studies should follow up a large fraction of optically discovered SNe Ic-BL at early times across multiple epochs, enabling the creation of robust radio LCs or deep, constraining upper limits for a large amount of events. Furthermore, the next generation of X-ray space based missions like Einstein Probe (Yuan et al., 2022a) and SVOM (Wei et al., 2016a) can be utilized to discover low-luminosity GRBs and X-ray Flash events that peak at lower peak energies than normal GRBs. This will allow for more opportunities to study these understudied events' associated SNe Ic-BL and characterize a new subset of events within the landscape of relativistic stellar explosions.

Acknowledgements

G.P.S. thanks Alexander Dittman, Cole Miller, Isiah Holt, Muhammad Mousa, and Maryam Modjaz for useful discussions regarding this work. G.P.S. thanks Cristina Barbarino, Tassilo Schweyer, Joonas Viuho, Amanda Djupvik for obtaining spectra from NOT. G.P.S. also thanks

Simi Bhullar for her moral support throughout the paper-writing process. SY acknowledges the funding from the National Natural Science Foundation of China under Grant No. 12303046 and the Henan Province High-Level Talent International Training Program. S. A. acknowledges generous support from the David and Lucile Packard Foundation and the National Science Foundation GROWTH PIRE grant No. 1545949. A.C. acknowledges support from the National Science Foundation via AST-2431072, and from NASA Swift GI program via the award 80NSSC23K0314. S. Schulze is partially supported by LBNL Subcontract NO. 7707915. N.S. acknowledges support from the Knut and Alice Wallenberg foundation through the "Gravity Meets Light" project (PIs: Rosswog & Jerkstrand).

This work was supported by the GROWTH project (Kasliwal et al., 2019b) funded by the National Science Foundation under Grant No 1545949. MMK acknowledges generous support from the David and Lucille Packard Foundation. Some of the data presented herein were obtained at the W.M. Keck Observatory, which is operated as a scientific partnership among the California Institute of Technology, the University of California and the National Aeronau- tics and Space Administration. The Observatory was made possible by the generous financial support of the W.M. Keck Foundation. The authors wish to recognize and acknowledge the very significant cultural role and reverence that the summit of Mauna Kea has always had within the indigenous Hawaiian community. We are most fortunate to have the opportunity to conduct observations from this mountain. SED Machine is based upon work supported by the National Science Foundation under Grant No. 1106171. Based on observations obtained with the Samuel Oschin Telescope 48-inch and the 60-inch Telescope at the Palomar Observatory as part of the Zwicky Transient Facility project.

ZTF is supported by the National Science Foundation under Grant No. AST-2034437 and a

collaboration including Caltech, IPAC, the Weizmann Institute of Science, the Oskar Klein Center at Stockholm University, the University of Maryland, Deutsches Elektronen-Synchrotron and Humboldt University, the TANGO Consortium of Taiwan, the University of Wisconsin at Milwaukee, Trinity College Dublin, Lawrence Livermore National Laboratories, IN2P3, University of Warwick, Ruhr University Bochum and Northwestern University. Operations are conducted by COO, IPAC, and UW. The ZTF forced-photometry service was funded under the Heising-Simons Foundation grant #12540303 (PI: Graham). The Gordon and Betty Moore Foundation, through both the Data-Driven Investigator Program and a dedicated grant, provided critical funding for SkyPortal.The Liverpool Telescope is operated on the island of La Palma by Liverpool John Moores University in the Spanish Observatorio del Roque de los Muchachos of the Instituto de Astrofisica de Canarias with financial support from the UK Science and Technology Facilities Council.

Quarter 3. Orphan Afterglows

"All along was meant to be, I'm the one, the one is me

This who they gon' come to see, I walk it out so comfortably."

- Damian Lillard

Chapter 5: Multi-Wavelength Analysis of AT 2023sva: a Luminous Orphan Afterglow With Evidence for a Structured Jet

5.1 Introduction

A small subset of stripped-envelope core-collapse supernova (CCSN) explosions are accompanied by Long Gamma-ray Bursts (LGRBs; duration $T_{90} > 2\,\mathrm{s}$; Cano et al. 2017a). LGRBs are powered by accretion onto a black hole remnant or the rotational spin-down of a neutron star remnant, generating collimated ($\theta_0 \approx 10^\circ$) ultra-relativistic ($\Gamma > 100$) jets (MacFadyen & Woosley, 1999). Traditionally, emission from GRBs is divided into two phases – the prompt emission in γ-rays originates from within the jets and the afterglow emission across the electromagnetic spectrum originates from the interaction of these jets with the surrounding medium (Panaitescu & Kumar, 2000; van Paradijs et al., 2000).

There have been hundreds of optical afterglows detected through follow-up observations of well-localized LGRB triggers, along with over 50 of their associated supernovae (see, e.g., Blanchard et al. 2024; Cano et al. 2017a; Galama et al. 1998; Hjorth & Bloom 2012; Hjorth et al. 2003; Hu et al. 2021; Kumar et al. 2022a; Melandri et al. 2019a; Rossi et al. 2022b; Srinivasaragavan et al. 2023, 2024a). The advent of state-of-the art time domain surveys including the Zwicky Transient Facility (ZTF; Bellm et al. 2019; Dekany et al. 2020a; Graham et al. 2019;

Masci et al. 2019) have also enabled the serendipitous discovery of optical afterglows without an associated GRB trigger. Searches of GRB archives post-facto to several optical afterglow discoveries have shown a number of events possess associated GRBs not discovered by high-energy satellites (Bhalerao et al., 2017; Cenko et al., 2015; Ho et al., 2022; Melandri et al., 2019b; Stalder et al., 2017). Possible explanations for these optical discoveries include GRBs producing γ-ray emission that do not notify GRB satellites to send out prompt alerts, or the lack of a robust afterglow localization.

If post-facto searches through GRB archives do not find observed associated γ-ray emission, these afterglows are known as "orphan" afterglows[1]. These orphan afterglows may arise from a few different scenarios. The simplest explanation is that GRB satellites may have missed the prompt γ-ray emission due to limited coverage in certain regions of the sky, or being turned off due to operational reasons. Another explanation is due to extremely off-axis classical GRBs. Since GRBs are ultra-relativistic, emission from the jet at early times is only observable within a viewing angle of $\theta \sim 1/\Gamma$. As the jet slows down, the relativistic beaming cone widens (Mészáros et al., 1998; Rhoads, 1997) and by the time the afterglow generates emission at optical wavelengths, the cone could include Earth's line of sight. The invocation of a "structured" jet is also a possible explanation, where a GRB's energy profile varies with respect to viewing angle (Gottlieb et al., 2022, 2021; Granot & Ramirez-Ruiz, 2010). For a structured jet, even slightly off-axis observers viewing an event within the jet's viewing angle but outside the jet's narrow high-Γ core would see an orphan afterglow (Cenko et al., 2013; Freeburn et al., 2024; Huang et al., 2020; Lamb & Kobayashi, 2017a; Lamb et al., 2018a; Nakar & Piran, 2003; O'Connor et al., 2023;

[1]The term "apparently" orphan is a more precise term to describe these events, as this is a purely observational definition. Physically, an associated GRB to some isotropic energy limit usually cannot be ruled out for optically-discovered afterglows, and it is possible that γ-ray emission may be present in these systems, but was just not observed. For brevity, we refer to these events purely as "orphan" for the rest of the text.

Rossi et al., 2008; Salafia et al., 2015; Sarin et al., 2021), sometimes dubbed an "on-axis" orphan (Nakar & Piran, 2003).

Another possibility is that a GRB's jet is extremely baryon-loaded, reducing its Lorentz factor. The higher density of baryons can result in pair production processes absorbing γ-ray prompt emission, reradiating it at longer wavelengths. These baryon-loaded LGRBs have been proposed as "dirty fireballs" (Dermer et al., 1999), though there have been no observationally confirmed dirty fireballs discovered thus far in the literature. The discovery of even one genuine dirty fireball would change our picture of GRB phenomena, confirming long-held theories that baryon-loaded jets can successfully break out of their progenitor stars (Dermer et al., 1999; Paczyński, 1998). Some other proposed scenarios include stalled, choked jets forming a cocoon of shocked material that produces little to no γ-rays (Gottlieb et al., 2018a), with the interaction of the cocoon with the surrounding medium producing an afterglow similar to classical GRB jets at a lower luminosity (Nakar & Piran, 2017), and low radiative efficiency bursts (Sarin et al., 2022).

The study of optically-discovered afterglows started only around 14 years ago. The first ever discovery was in 2011, PTF11agg (Cenko et al., 2013). The event did not have a confirmed redshift, though it was argued to be between $z = 1$ and $z = 2$. Follow-up observations using the Jansky Very Large Array (VLA; Perley et al. 2011) showed that there was a long-lived scintillating radio counterpart to the optical transient. Two other optically-discovered afterglows (iPTF14yb and ATLAS17aeu) were discovered in a similar manner to PTF11agg at extragalactic distances (Bhalerao et al., 2017; Cenko et al., 2015; Melandri et al., 2019b; Stalder et al., 2017). However, searches through GRB archives after their discoveries showed that both events had associated observed γ-ray emission that high-energy satellites did not promptly send out

notifications for regarding their discovery.

The discovery space for these events changed dramatically with ZTF, as its rapid near-nightly cadence and wide field of view made it a prime instrument for discovering optical afterglows serendipitously. Through dedicated afterglow searches, 11 ZTF-discovered afterglows have been published since ZTF's inception in March 2018 (Andreoni et al., 2021, 2022; Ho et al., 2020d, 2022; Li et al., 2024; Perley et al., 2024). Nine of these events have confirmed redshift measurements through optical spectroscopy and five have no associated GRB found post-facto, making them orphan events (AT 2019pim, AT 2020blt, AT 2021any, AT 2021lfa, and AT 2023lcr).

Because there have been so few orphan afterglow discoveries, studies probing the physical origins of newly discovered events are important for understanding their nature. Though optical observations are utilized for their discovery, understanding their full physical picture necessitates follow-up observations in the X-ray and radio wavelengths, where jet physics and ejecta characteristics can be probed. Indeed, modeling of AT 2021any's X-ray through radio emission suggests a possible low-Lorentz factor origin (Xu et al., 2023) or a classical GRB missed by high-energy satellites (Gupta et al., 2022b; Li et al., 2024), AT 2020blt and AT 2023lcr were best modeled as classical GRBs missed by high-energy satellites (Ho et al., 2020d; Li et al., 2024), and AT 2019pim and AT 2021lfa were best modeled as originating from either low-Lorentz factor GRBs or slightly off-axis structured jet GRBs (Li et al., 2024; Lipunov et al., 2022; Perley et al., 2024).

In this work, we present the optical, radio, and X-ray observations of an orphan afterglow, ZTF23abelseb (AT 2023sva) at $z = 2.28$, making it the sixth such event presented in the literature. We utilize AT 2023sva's multi-wavelength observations to physically characterize the source. The paper is organized as follows: in §5.2 we present optical, X-ray, and radio obser-

vations of AT 2023sva, in §5.3 we analyze the multi-wavelength data set, in §5.4 we provide a physical interpretation of the afterglow, and in §5.5 we summarize our results and present conclusions. We note that throughout this paper we utilize a flat ΛCDM cosmology with $\Omega_{\rm m} = 0.315$ and $H_0 = 67.4$ km s^{-1} Mpc^{-1} (Planck Collaboration et al., 2020) to convert the redshift to a luminosity distance and correct for the Milky Way extinction of $E(B-V)_{\rm MW} = 0.24$ (Schlafly & Finkbeiner, 2011a), and host galaxy extinction of $E(B-V)_{\rm host} = 0.09$ mag (see §5.3.2). All magnitudes reported in the text and figures are in the AB system.

5.2 Observations

5.2.1 ZTF Discovery

AT2023sva was discovered by ZTF (Vail et al., 2023) at $r = 17.71 \pm 0.05$ mag, on 2023-09-17 09:38:31.20 (all times are given in UTC), at a location α (J2000)= $00^{\rm h}56^{\rm m}5920^{\rm s}$, δ (J2000) = +80°0844.″13. ZTF is a survey on the 48-inch telescope at Palomar Observatory that covers around 10000 deg^2 every night (Bellm et al., 2019), enabling it to survey the entire northern sky in the g and r bands every two nights, along with i band for certain pre-selected fields. The survey's observing system is described in Dekany et al. (2020a) and transient discovery applies an image subtraction pipeline (Zackay et al., 2016) utilizing deep reference images of fields (Masci et al., 2019). We use the ZTF Fritz marshal to store the photometry (Coughlin et al., 2023; van der Walt et al., 2019a).

The line of sight MW extinction is $E(B-V)_{\rm MW} = 0.24$, corresponding to $A_V = 0.74$ mag. Correcting for MW extinction and for the host-galaxy extinction derived in §5.3.2, at a redshift of $z = 2.28$ (see §5.2.2.2), this first detection corresponds to an absolute magnitude in r band of

$M_r \sim -30.0$ mag, making AT 2023sva an extremely luminous optical transient. The source was flagged by human scanners after passing a filter in the ZTF alert stream (Patterson et al., 2019b) that searches for young and fast transients (described in Ho et al. 2020d). The source was not detected to a limiting magnitude of $r > 20.36$ mag two nights before on 2023-09-15 05:50:11.95, implying a rapid rise rate of > 1.3 mag day^{-1}. There was no host galaxy counterpart detected in the ZTF reference images (the deepest upper limit was $g > 20.7$ mag) nor in PanSTARRS images of the field. The source also decayed rapidly, at a rate of 3 mag day^{-1} in the r band after the initial observations.

Optically-discovered afterglows are classified and differentiated from false positives by their rapid rises and decays, red colors indicative of a synchrotron spectrum, extragalactic redshifts, and extremely high luminosities (a full description of how optical afterglows are discovered in ZTF's alert stream is presented in Ho et al. 2020d). The primary false positives in optically-discovered afterglow searches are stellar flares in the Milky Way. These flares possess blackbody temperatures of around 10,000 K (Kowalski et al., 2013), and in the optical bands, their spectrum lies on the Rayleigh–Jeans tail. This corresponds to a spectrum with $f_\nu \propto \nu^2$, or an extinction-corrected blue color of $g - r = -0.17$ mag. Afterglows, on the other hand, have characteristic red colors due to their synchrotron spectrum, with $f_\nu \propto \nu^{-\beta}$ where f_ν is the flux density and β is the spectral index, the exponential factor that relates the flux density of a source to its frequency. A g-band observation was obtained of AT 2023sva shortly after the initial r-band detection, of $g = 18.52 \pm 0.02$, on 2023-09-17 10:41:57.034. Extrapolating this g-band detection to the time of the first r-band detection assuming a simple power-law evolution (detailed in §5.3.1), the extinction corrected $g - r$ color at the time of discovery is ~ 0.5 mag. The fast-rise, red colors, and lack of a host galaxy counterpart made AT 2023sva an optically-discovered

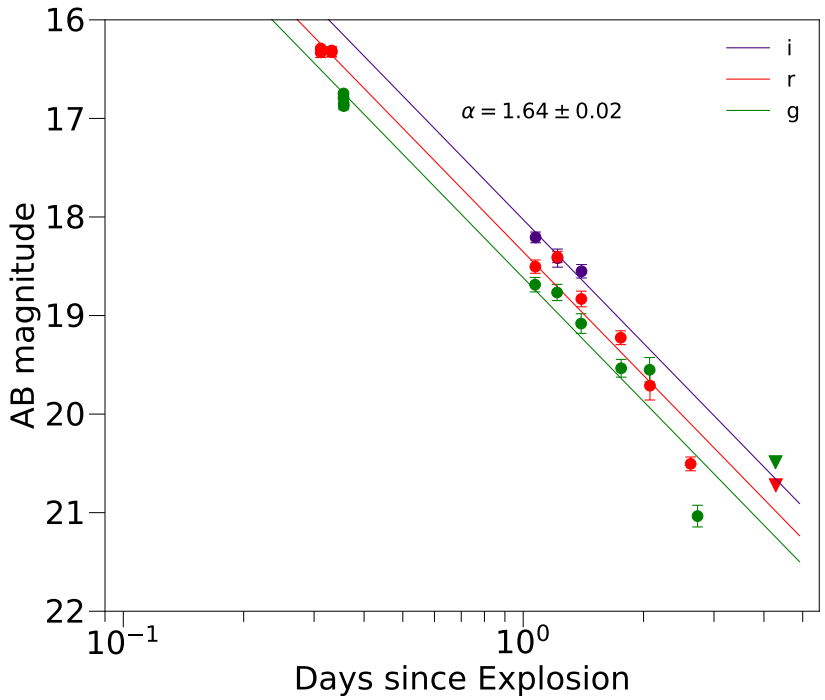

Figure 5.1: Optical LC of AT 2023sva in the g, r, and i bands and the earliest 3σ upper limits, along with a best fit power-law decay model. The photometry is taken from Table D.1, and then corrected for both MW and host-galaxy extinction.

afterglow candidate and motivated follow-up observations.

5.2.2 Follow-up Observations

5.2.2.1 Optical Photometry

We triggered a Target of Opportunity (ToO) program on the Spectral Energy Distribution Machine (SEDM; Blagorodnova et al. 2018b; Rigault et al. 2019a) on the automated 60-inch telescope at Palomar Observatory, to obtain imaging of AT 2023sva in the g, r, and i bands. The images were processed utilizing a `Python`-based version of the `Fpipe` (Fremling et al., 2016) pipeline. The pipeline includes photometric calibrations and image subtraction utilizing

reference images from The Sloan Digital Sky Survey (SDSS; Abazajian et al. 2009). SEDM obtained four epochs of photometry, from 2023-09-18 03:56:16.080 to 2023-09-19 03:57:27.101. These follow-up observations showed AT 2023sva's light curve (LC) rapidly decayed by 2.2 mag in r band, in just 0.74 days (see Figure 5.1).

We also triggered a ToO program on the 0.7-m GROWTH-India Telescope (GIT; Kumar et al., 2022c) located at the Indian Astronomical Observatory (IAO), Hanle-Ladakh, to obtain an additional epoch of g and r band imaging of AT 2023sva. The observations began on 2023-09-19 17:06:25.574. We utilized the `ZOGY` algorithm-based `Python` pipeline to perform image subtraction on the images using PS1 templates and to obtain the final photometry.

A single ToO observation in the g and r bands was also secured with the 2.56-m Nordic Optical Telescope (NOT), located in the Canary Islands (Spain) equipped with the ALFOSC imager, on 2023-09-18 20:15:12.96. Data reduction was carried out following standard techniques and photometric calibration was computed against the Pan-STARRS catalog. The complete photometry obtained of AT 2023sva is presented in Table D.1.

5.2.2.2 Optical Spectroscopy

We secured spectroscopy of AT2023sva using OSIRIS+ (Cepa et al., 2000) on the 10.4-m Gran Telescopio Canarias (GTC) on 2023-09-19 03:55:51.011. The observation was carried out using the R1000B grism, which covers the wavelength range 3600–7800 Å, and consisted of 3 exposures of 900 s each (de Ugarte Postigo et al., 2023b). The slit position angle was set to parallactic to minimize differential slit losses.

The data were reduced using a self-developed pipeline based on IRAF routines. Data re-

duction included bias and response correction and wavelength calibrations using HgAr and Ne lamps, which were also used to do a 2D distortion correction. Cosmic rays were removed using the `lacos_spec` routine (van Dokkum, 2001). The 1D spectrum was obtained through optimal extraction (Horne, 1986).

5.2.2.3 X-ray Observations

Observations of AT 2023sva with the *Neil Gehrels Swift Observatory* (Gehrels et al., 2004) X-ray Telescope (XRT; Burrows et al., 2005) began at 2023-09-21 18:00:00.000, through a ToO trigger submitted by our team after the optical afterglow discovery. Observations lasted for 7.5 ks after the initial trigger. The data were obtained in Photon Counting (PC) mode. The transient was not detected in the observations, up to a 0.3 – 10 keV flux limit of $< 1.2 \times 10^{-13}\,\mathrm{erg\,cm^{-2}\,s^{-1}}$. We convert this integrated flux limit to a maximum estimated flux density limit at 5 keV (to use in §6.4 when we model the multi-wavelength data), through assuming a photon index of $\Gamma = 1.75$. We use this value, which corresponds to the optical spectral index of $\beta = 0.75$, because we determine that the X-ray and optical data likely do not lie on the same spectral segment in §5.3.2. The true X-ray spectral index must be steeper than $\beta = 0.75$, so we use $\beta = 0.75$ conservatively to extrapolate the 0.3 – 10 keV flux limit to the flux density limit at 5 keV, in order for the upper limit derived to be the maximum allowed. We derive a flux density upper limit at 5 keV of $< 8.65 \times 10^{-15}\,\mathrm{erg\,cm^{-2}\,s^{-1}\,keV^{-1}}$.

5.2.2.4 Radio Observations

The Arcminute Microkelvin Imager – Large Array (hereafter AMI—LA) is a 8-dish interferometer based at the Mullard Radio Astronomy Observatory outside Cambridge in the UK. It observes at a central frequency of 15.5 GHz with a bandwidth of 5 GHz (Hickish et al., 2018; Zwart et al., 2008). Observations of AT 2023sva commenced with AMI—LA on 2023-09-19 02:08:35UT (1.2 days after the discovery). Each observation consisted of a series of 600 second scans of the target interleaved with 100 second of the phase calibrator J0017+8135, adding up to a total of 4 hours on target (except on 2023-10-07 which was only 2 hours). Once per day AMI—LA also observes a bandpass/flux calibrator 3C286. AT 2023sva was observed over 12 epochs spanning 1 to 60 days post-discovery. Data from AMI—LA is reduced using custom software REDUCE_DC (Perrott et al., 2013) which performs flux scaling, bandpass and complex gain calibration as well as flagging for radio frequency interference and antenna shadowing. The calibrated data are then output in *fits* format so they can be read into CASA for imaging and any further flagging that is required (McMullin et al., 2007a). Imaging was performed interactively using *tclean* within CASA. The AMI observations are presented in Table D.3.

We also observed AT 2023sva with the Karl G. Jansky Very Large Array (VLA) on six occasions between November 2023 and August 2024 (program ID 24A-130). The first observation used the S, C, X, Ku, and Ka-band receivers (3, 6, 10, 15, and 33 GHz); subsequent observations used only a subset of these receivers. Data were calibrated and imaged using standard procedures in the Astronomical Image Processing System (AIPS). Flux density measurements were performed using `imfit`. The VLA observations are presented in Table D.2.

We also carried out Upgraded Giant Metrewave Radio Telescope (uGMRT) observations of

AT 2023sva at two epochs during 22-31 March and 17-20 May 2024. The data were recorded in standard continuum observing mode with a time integration of 10 seconds in bands-3 (250−500 MHz), 4 (550−850 MHz), and 5 (1000−1460 MHz). We used a bandwidth of 200 MHz in bands 3 and 4 and 400 MHz in band-5 split into 2048 channels. 3C48 was the flux density and bandpass calibrator and 2344+824 (bands-4 and 5) and 0229+777 (band-3) were the phase calibrators. We used Astronomical Image Processing Software (AIPS; Greisen, 2003) to reduce the data following standard procedure (Nayana et al., 2017). The data were initially inspected for non-working antennae and radio frequency interference. The corrupted data were flagged using tasks `UVFLG`, `TVFLG`, and `SPFLG` and then calibrated. The calibrated target data were imaged using task `IMAGR` in an interactive mode followed by a few rounds of phase-only self-calibration.

5.2.3 Search for Associated GRB

The γ-ray sky is monitored by the third Interplanetary Network (IPN), whose most sensitive instruments are the *Swift* Burst Alert Telescope (BAT), *Fermi* Gamma-ray Burst Monitor (GBM; Meegan et al. 2009), and the Konus-Wind (Barthelmy et al., 2005) instrument. We searched the archives of these three instruments, as well as the AstroSat Cadmium Zinc Telluride Imager (CZTI; Bhalerao et al. 2017) instrument, to determine if there is an associated GRB temporally and spatially coincident with AT 2023sva. We searched the time periods between the last ZTF non-detection and the first detection (see §5.2.1). Though there were several GRBs in this time period, we found no *Fermi* or *Swift* GRBs temporally and spatially coincident to AT 2023sva, through searching the *Fermi* GBM Burst Catalog, the *Fermi* GBM Subthreshold Trigger list, and the *Swift* GRB Archive. There were reports of a candidate GRB on the Gamma-Ray Coordinates

Network archives; however this counterpart was later classified as a likely solar flare and deemed unrelated to AT 2023sva (Roberts et al., 2023). Due to the 2 day time period between the last non-detection and first detection, there was a significant amount of time that both *Fermi* and *Swift* were not viewing the field of AT 2023sva due to being occulted by the Earth.

However, because of Konus-Wind's 4π FOV and its interplanetary orbit at the Earth-Sun L1 Lagrange point, AT 2023sva's location was always visible to the instrument. Konus-Wind detected two GRBs not detected by *Fermi* during the time period of interest. The first, which occurred on 2023-09-15 06:54:20, resulted in Konus-Wind's ecliptic latitude response clearly being inconsistent with AT 2023sva's position. Both Konus-Wind and AstroSat-CZTI detected the second GRB, GRB 230917A on 2023-09-17 00:44:38.873 by Konus-Wind and on 2023-09-17 00:44:43.5 by Astrosat-CZTI (Navaneeth et al., 2023). We utilized the propagation time delay between Konus-Wind and AstroSat-CZTI and the Konus-Wind ecliptic latitude response to calculate the 3σ IPN localization region and determine if it is consistent with the position of AT 2023sva.

We show the localization region in Figure 5.2, along with contours showing various Earth-occulted regions for the different satellites, along with the $> 10\%$ coded FOV of *Swift*. We see that GRB 230917A's 3σ localization region is clearly not consistent with AT 2023sva's location. The lack of detections from *Fermi* and *Swift* are also consistent with this localization, as GRB 230917A's location was occulted by the Earth for *Fermi* and was outside *Swift*'s coded FOV. We also localized the burst through the AstroSat-CZTI localization framework (Saraogi et al., 2024). Since the burst was not bright, the localization was quite coarse, placing AT 2023sva within the 57% contour. This also supports the possibility that the burst may not be associated with the optical transient. Therefore, we determine that AT 2023sva does not possess a detected GRB

counterpart.

We calculate the AstroSat-CZTI upper limits in the time window between the last non-detection and first detection (a window size of 21600 s; with a confidence of 97.44%), utilizing the methodology in Sharma et al. (2021). We analyzed AstroSat-CZTI's duty cycle during the 50+ hour window ($\sim$ 19 AstroSat-CZTI orbits) between the first non-detection and detection. With the source's high declination, AstroSat had continuous visibility of the source, but $\sim$ 29% of the time was lost to South Atlantic Anomaly downtime and 3% to slewing. AstroSat-CZTI detects a confident GRB approximately every 120 hours. Our extended time window significantly increases the false alarm rate, leading to the flux upper limits having a relatively low confidence ($\sim$ 87%). Additionally, the method for estimating flux limits requires 10 "witness" neighboring orbits, which is insufficient to reliably estimate the background for our time window. As a result, the upper limits we derived were not meaningful.

We then utilize the Konus-Wind non-detection to derive a peak flux upper limit for AT 2023sva's GRB counterpart. During the interval of interest Konus-Wind was continuously observing the whole sky in the waiting mode with temporal resolution 2.944 s. In this mode count rates are recorded in the three energy bands: 19–80 keV (G1), 80–325 keV (G2), and 325–1290 keV (G3). The instrument background count rate varied slowly at timescale of a day at $< 7\%$. There were a number of minor data gaps of a size of about a few $\times$ 2.944 s, accounting for 4 % of the time between the last non-detection and first detection. After the trigger on GRB 230917A, there was an hour long data gap in the waiting mode record due to instrument data readout. During this interval, only the G2 count rate was available with $\sim$ 4 s resolution.

Using the waiting mode data free from GRBs detected in the time period between the last non-detection and first detection of AT 2023sva and the response for AT 2023sva's po-

sition, we estimate an upper limit (90% confidence) on the 20–1500 keV peak flux to $1.5 \times 10^{-7}\,\mathrm{erg\,cm^{-2}\,s^{-1}}$ for a typical LGRB spectrum (a Band function with $\alpha = -1$, $\beta = -2.5$, E_{peak} =300 keV) and a 2.944 s timescale. The lack of a detected GRB counterpart suggests that AT 2023sva's limiting fluence is comparable to that of the weakest burst from Tsvetkova et al. (2021), who did a study on Konus-Wind bursts simultaneously detected by *Swift*-BAT. This fluence is $4 \times 10^{-7}\mathrm{erg\,cm^{-2}}$ and given the redshift $z = 2.28$, this corresponds to an isotropic equivalent energy upper limit of $E_{\gamma,\mathrm{iso}} < 1.6 \times 10^{52}$ erg for AT 2023sva's GRB counterpart.

5.3 Optical and Radio Analysis

5.3.1 Optical LC

We show the optical LC in Figure 5.1 and the optical transient fades very rapidly. There is a possible break in the LC that occurs between one to two days after explosion; however, this break cannot be constrained because of the transient's rapidly fading nature. This leads to a lack of detections at later times to truly constrain the presence of a break (or lack thereof). Therefore, we fit a simple power-law to the early-time data in g, r, and i bands simultaneously with different normalization factors, $F_\nu \propto (t - t_0)^{-\alpha}$, where α is the power-law decay index, and t_0 is the estimated time of explosion. We set t_0 equal to the best-fit time of explosion derived in §6.4, of $t_0 = 60204.09$ MJD, or 7.5 hours prior to the first detection. We refer to this t_0 as the time of explosion for the rest of this work. We note that we did try to let t_0 be a free parameter in the fit as well. Through this fitting procedure, we found that t_0 was constrained to the midpoint between the last non-detection and the first detection, likely due to the small number of data points. Before fitting a power-law, we first correct the optical magnitudes for both the Milky Way

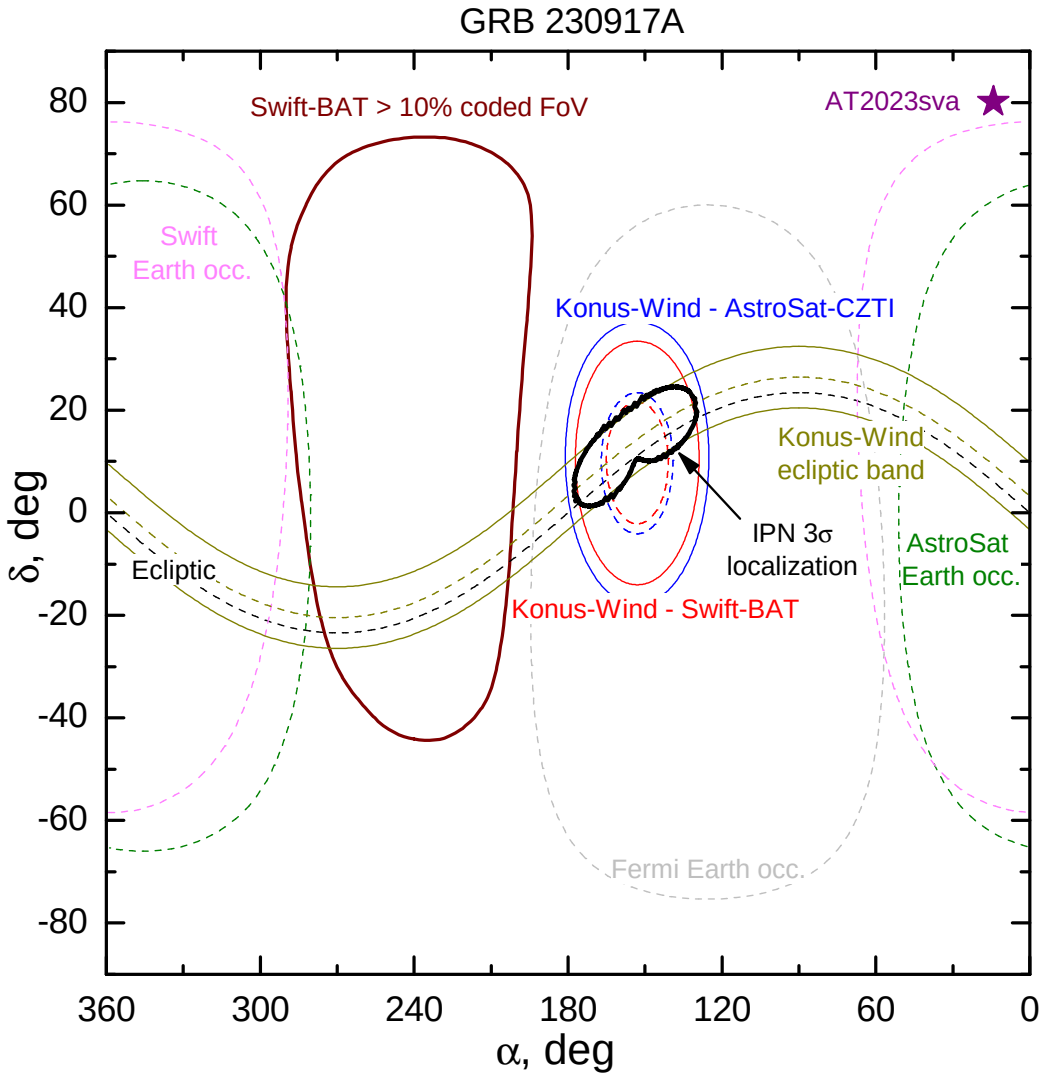

Figure 5.2: The IPN 3σ localization region for GRB 230917A (the thick solid black line), compared to the point-source location of AT 2023sva (star). In addition, we show the Swift-BAT field of view (FOV; the solid white line), the Earth occulted regions for Swift, Fermi, and Astrosat-CZTI (dashed lines), the ecliptic plane (the dashed black line), the Konus-Wind ecliptic latitude constraint (the solid dark green lines indicates the 3σ uncertainty and the dashed dark green line indicates the most probable burst source ecliptic latitude), the Konus-Wind – AstroSat-CZTI and Konus-Wind – Swift-BAT 3σ triangulation annuli (solid blue and red lines), and the most probable burst location utilizing the Konus-Wind – AstroSat-CZTI and Konus-Wind – Swift-BAT triangulation (dashed blue and red lines). We conclude that GRB 230917A is not associated with AT 2023sva.

($E(\mathrm{B}-\mathrm{V})_{\mathrm{MW}} = 0.24$ mag), and host galaxy ($E(B-V)_{\mathrm{host}} = 0.09$; see §5.3.2) extinction. We derive a power-law decay index $\alpha = 1.64 \pm 0.02$.

From our best-fit LC, we see that the single power-law decay model does not fit the last epoch of observations well. This is due to the possible break in the LC mentioned earlier, which is likely from the synchrotron cooling frequency ν_{c} passing through the optical bands, resulting in a change of the temporal power-law decay index of the LC (Granot & Sari, 2002; Ryan et al., 2020a). We provide more evidence for this in §6.4.

5.3.2 Optical SED and Spectroscopy

We fit the gri data from SEDM taken over three separate epochs (detailed in Table D.1) to a spectral power-law model $F_\nu \propto \nu^{-\beta}$, after correcting for the Milky Way extinction. We obtain a spectral index of $\beta = 0.95 \pm 0.15$. When including the X-ray upper-limit in the fitting extrapolated to the midpoint of the SEDM observations, we constrain the optical to X-ray spectral index $\beta_{\mathrm{OX}} > 1.1$. Therefore, we determine that the X-ray and optical data likely do not lie on the same spectral segment.

In Figure 5.3, we show the OSIRIS spectrum of AT 2023sva (details of observations in §5.2.2.2). The spectrum shows a clear Lyman-α feature and various other absorption features, at a redshift $z = 2.280 \pm 0.002$. We measure the equivalent widths (EWs) of the O I, C IV, and Fe II absorption features. We find strengths of 1.9 ± 1.1, 2.63 ± 0.70, and 1.42 ± 0.56 $\AA$. We then compare the line strengths of AT 2023sva with other GRBs in the literature through calculating the line strength parameter (LSP), described in de Ugarte Postigo et al. (2012). We calculate a LSP of -1.70 ± 0.58, which corresponds to the 1.03th percentile of GRBs. Therefore, 99%

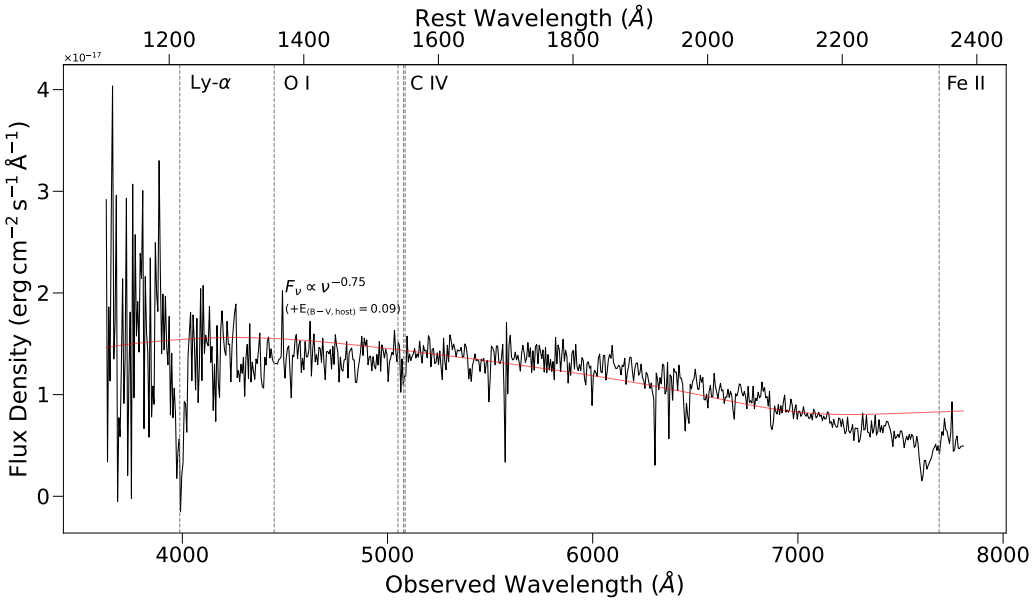

Figure 5.3: Optical spectrum of AT 2023sva, obtained by the OSIRIS instrument (details in §5.3.2). We show the Lyman-α absorption feature along with absorption features characteristic to GRB afterglows at a redshift $z = 2.280 \pm 0.002$, and a best-fit spectral power-law model with additional host-galaxy extinction (details in §5.3.2).

of the GRBs in the literature have line strengths greater than AT 2023sva, pointing towards an extremely low-density sight line to the source.

Because only an X-ray upper limit was obtained, we could not make any inferences about the presence of host-galaxy extinction from the SED fitting. However, in Figure 5.3, we see that the Milky Way extinction-corrected spectrum shows a distinct curvature that is likely due to extra extinction from the host galaxy. Therefore, we fit a power-law to the optical spectrum with the addition of host-galaxy extinction as a free parameter, using the Cardelli et al. (1989c) extinction law, with $R_v = 3.1$. We find a best-fit spectral index of $\beta = 0.75 \pm 0.07$ and $E(B - V)_{\rm host} = 0.09 \pm 0.01$ mag. We note that there is no prominent 2175 Å feature in the spectrum, which is a characteristic feature of the Cardelli et al. (1989c) model. It has also been shown that GRB host galaxies in general rarely show strong evidence for this feature, though in most cases it also cannot be ruled out (Schady et al., 2012). Therefore, the uncertainties reported here

are statistical uncertainties and there are likely larger uncertainties dominated by the use of a particular extinction model.

5.3.3 Closure Relations

There are characteristic closure relations between α, β, and p (the electron spectral index) that correspond to different astrophysical environments (a constant density ISM environment or a stellar wind environment), as well as cooling regimes within the synchrotron spectrum (Granot & Sari, 2002; Sari et al., 1998). We test the values derived for α and β within these regimes, assuming a standard, tophat jet structure. First, we determine whether we are in the fast or slow cooling regime. In the fast cooling regime, the synchrotron frequency corresponding to the minimum Lorentz factor that electrons are accelerated to in the shockwave in the context of a power-law distribution ($\nu_{\rm m}$, also known as the peak frequency) is larger than the synchrotron cooling frequency $\nu_{\rm c}$, so most electrons are expected to quickly cool to $\nu_{\rm c}$. In this regime, the optical bands can either be below $\nu_{\rm m}$ ($\nu_{\rm c} < \nu < \nu_{\rm m}$) or above $\nu_{\rm m}$ ($\nu_{\rm c} < \nu_{\rm m} < \nu$). For the case where $\nu_{\rm c} < \nu < \nu_{\rm m}$, $\beta = 0.5$ (Granot & Sari, 2002; Sari et al., 1998) for both the ISM and wind environment. For the case where $\nu_{\rm c} < \nu_{\rm m} < \nu$, $\beta = p/2$ for both environments (Granot & Sari, 2002; Sari et al., 1998). It is clear that the β we derive is not consistent with the $\nu_{\rm c} < \nu < \nu_{\rm m}$ case. Furthermore, if the optical bands were above the peak frequency, then that would imply $p = 1.5 \pm 0.14$. This is an abnormally small, non-physical value for p, which is generally expected to be between 2 and 3 (Curran et al., 2010). Therefore, this implies that we are not in a fast cooling environment.

For a slow cooling environment, $\nu_{\rm m}$ is less than $\nu_{\rm c}$ and electron cooling is not efficient. In

this regime the optical bands can be either below or above ν_c. If $\nu_m < \nu < \nu_c$, then $\beta = (p-1)/2$, for both an ISM and wind environment. This would imply $p = 2.50 \pm 0.14$, which is a reasonable value. If $\nu_m < \nu_c < \nu$, $\beta = p/2$ for both environments, this implies $p = 1.50 \pm 0.14$, which again is an unreasonable value. So from this analysis, we determine that assuming a tophat jet, we are in a slow cooling environment where the optical bands are below the cooling frequency. For a constant density ISM environment, $\alpha = 3\beta/2$ in this regime (Sari et al., 1999), which would imply $\alpha = 1.13 \pm 0.15$, which clearly does not match the derived value of $\alpha = 1.64 \pm 0.02$. For the wind environment, $\alpha = (3\beta + 1)/2$ in this regime, which would imply $\alpha = 1.63 \pm 0.15$. This is consistent with our observed α. However, the jet's structure may be more complex than just a tophat and we revisit the closure relations within this context in §6.4.

The radio LC at select frequencies is shown in Figure 5.4. We see that the 15.5 GHz LC shows a gradual rise ($t^{0.4}$) at early times, until around ten days after the explosion. The LC then exhibits a shallow decay ($t^{-0.5}$) and thereafter transitions to a steep decay (t^{-2}), seen at lower frequencies as well. Lower frequency (< 11 GHz) observations begin at around day 70 and there is significant short-term variability in the first couple of epochs in the 4 and 5 GHz LCs, likely indicative of strong interstellar scintillation (ISS). The initial rise in the 15.5 GHz LC until around 10 days and then shallow decay until around 70 days, can be attributed to the spectral break ν_m passing through the 15.5 GHz band. The subsequent steepening across all frequencies is most likely attributed to a jet break. We model the radio LC in §6.4.

In Figure 5.5, we show the coeval radio SEDs, at six different epochs presented in the observer frame. We see that the SED at 72 days has multiple sharp spectral breaks. This is due to ISS and the modulations are a factor of ~ 2. We see this behavior continues to persist at lower frequencies until the epoch at 131 days, though the strength of the scintillation diminishes.

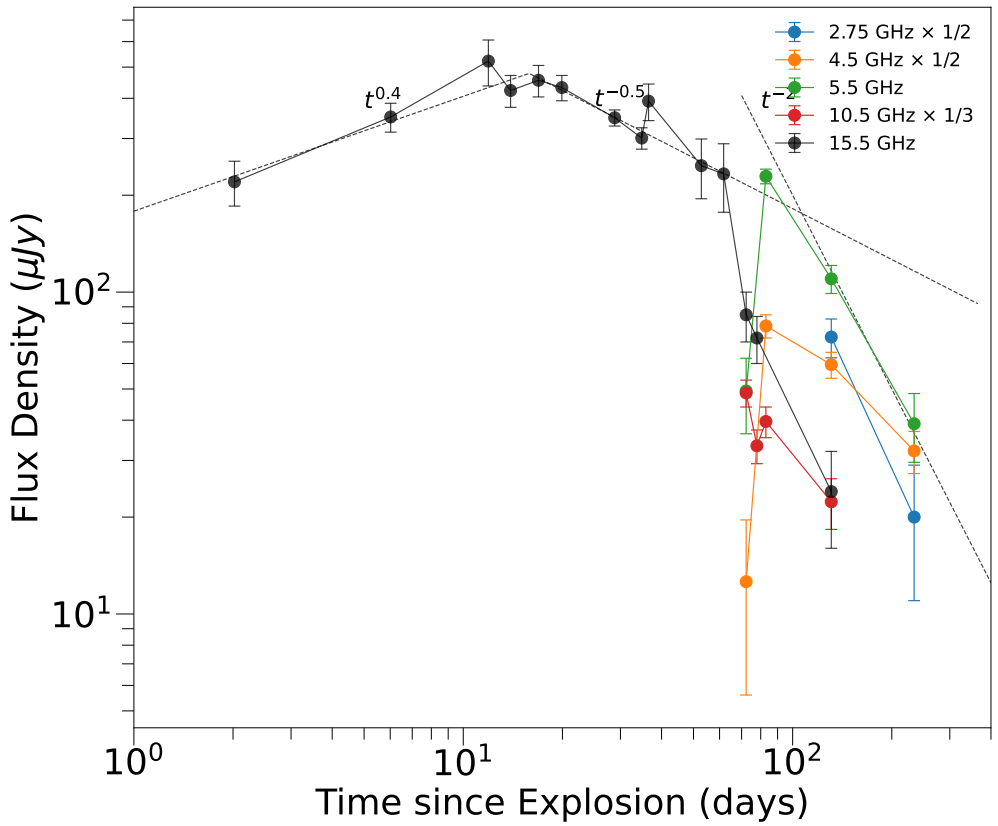

Figure 5.4: The AMI (15.5 GHz) and VLA (15.5 GHz and other frequencies) radio LCs with respect to the observed time since explosion. The 15.5 GHz LC is the most well-sampled over time and we fit a power-law to the initial rise, shallow decay, and then the steep decay. This behavior is most likely attributed to the peak synchrotron frequency passing through the radio bands and then a jet break at late times. The lower frequency radio LCs show high variability, due to the presence of interstellar scintillation.

We expect $\nu_{\rm m}$ to pass through the radio bands over time, leading to spectral breaks in the SEDs. Due to the variability caused by ISS, we were not able to identify any clear breaks in the first two epochs. However, starting from the epoch at 84 days, we see that the spectrum shows a clear rise and peak at low frequencies and the location of the peak moves lower in frequency space, until it is not visible anymore in the 333 day spectrum, starting from $\sim$ 10 GHz in the 72 day epoch to $\sim$ 3 GHz in the 234 day epoch. We likely are still below the cooling frequency $\nu_{\rm c}$ at the times the SEDs were taken, as we do not see a steepening of the power-law at later times. We fit a spectral power-law model ($F_\nu \propto \nu^{-\beta}$) to every spectral epoch except for the 72 day epoch, both to the regions below and above $\nu_{\rm m}$. For frequencies below $\nu_{\rm m}$, we find an average value of $\beta = 2.2$, with a range of 1.4 to 4.1, and for frequencies above $\nu_{\rm m}$, we find an average value of $\beta = -1.2$, with a range of -0.5 to -2.1. We note that the spectral indices derived below $\nu_{\rm m}$ have large error bars and are poorly constrained, as there are only two points below the peak frequency in the 84 day epoch and three points in the 131 day and 234 day epochs.

In Figure 5.6, we also show the low frequency uGMRT observations. Radio emission was not detected at the source position in any of the GMRT maps providing 3-sigma flux density limits of $< 75\,\mu$Jy at 1.4 GHz, $< 180\,\mu$Jy at 0.6 GHz, and $< 300\,\mu$Jy at 0.4 GHz at the source position. The first observation took place between 188 and 197 days after t_0 and the second took place between 243 and 246 days after t_0. The upper limits derived are consistent with the power-laws derived from fitting the 131 day and 235 day epochs.

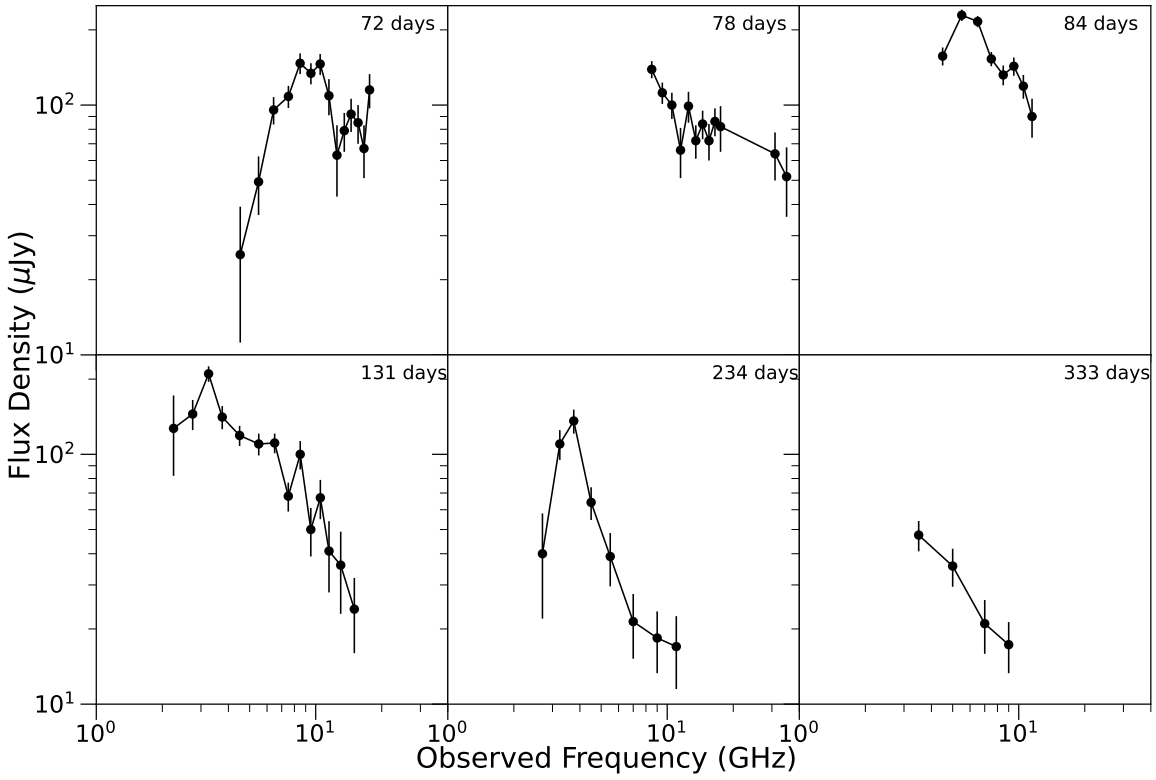

Figure 5.5: VLA Radio SEDs of AT 2023sva, with the observer frame time of the epochs with respect to the best-fit explosion time shown in the plots. The spectrum at 72 days shows multiple sharp spectral breaks due to the presence of interstellar scintillation. The sharp breaks continue at lower frequencies until the epoch at 131 days.

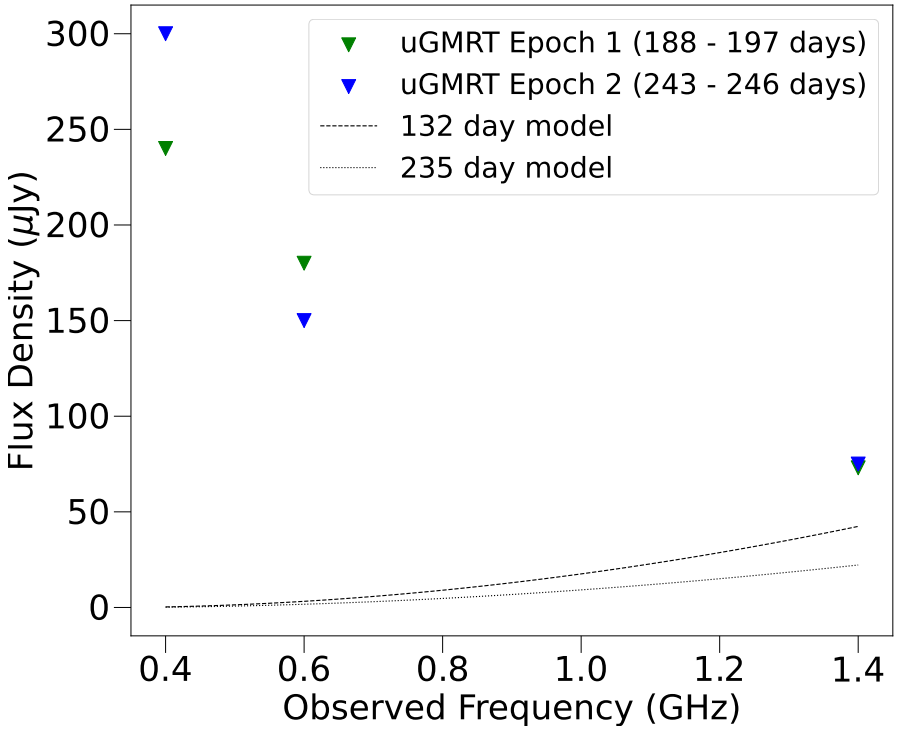

Figure 5.6: uGMRT observations of AT 2023sva, where the upside down markers represent the 3σ derived upper limits. Two power-law models corresponding to the low-frequency VLA observations at 131 and 234 days are also shown and the upper limits are consistent with the VLA observations.

5.3.4 Constraints from Radio Scintillation

The radio SED shows clear variations in frequency space in the earliest epoch at 72 days, across all frequencies. The radio LC also shows clear modulations by a factor of ~ 2 at lower frequencies up to 100 days. We interpret these variations as being due to ISS, which is the result of small-scale inhomogeneities in the ISM, which change the phases of incoming wavefronts of radio sources. Because the line of sight from Earth to the source changes as the Earth moves, this causes a change in flux, due to scattering from electrons along the line of sight through our Galaxy. There is a characteristic transition frequency $\nu_{\rm ss}$ where strong scattering transitions ($\nu < \nu_{\rm ss}$) to weak scattering ($\nu > \nu_{\rm ss}$). GRB radio observations are expected to be affected by ISS (e.g., Granot & van der Horst 2014a) and analyzing their ISS can provide insights towards their angular size and Lorentz factors.

We utilize a similar method that Perley et al. (2024) used for AT 2019pim, to derive AT 2023sva's source size. From Figures 1-2 of Walker (1998) (erratum Walker 2001), we determine that the transition frequency $\nu_{\rm ss}$ along the line of sight of AT 2023sva is ~ 15 GHz and the Fresnel scale at that frequency is $\theta_{F0} \approx 2\,\mu{\rm arcsec}$. At the angular diameter distance of AT 2023sva, this corresponds to a physical size of 5.2×10^{16} cm. From the radio SED in Figure 5.5, we see that there is strong ISS at $\nu_{\rm ss}$ during the earlierst epoch at 72 days and it significantly decreases in later epochs. For strong ISS to exist near $\nu_{\rm ss}$, the source size must be comparable or smaller than the physical size corresponding to the Fresnel scale. Therefore, we estimate AT 2023sva's physical size to be at most 5.2×10^{16} cm at 72 days. Converting this to an average Lorentz factor in the rest-frame, we get $\Gamma_{\rm av,22.0\,d} \leq 2.4$. In the ISM, as the jet is decelerating, the projected size increases over time as $R \propto t^{5/8}$, or $\Gamma \propto t^{-3/8}$ (Galama et al., 2003). Extrapolating the ISS limit

to the time of first detection (7.5 hours after explosion in the observer frame, or 2.3 hours after in the rest-frame), we derive a Lorentz factor upper limit of $\Gamma_{\rm av,2.3\,hr} \leq 19$.

However, Γ at the time of first detection is different than the initial Lorentz factor, Γ_0, as it is dependent on the time of explosion and the initial deceleration timescale, $t_{\rm dec}$. If we assume that $t_{\rm dec} \sim 20$ s (Ghirlanda & Salvaterra, 2022) from the explosion epoch (corresponding to the typical rest-frame timescale for a GRB optical LC to peak) and also assume that the Lorentz factor is constant from the beginning of the explosion up to the beginning of deceleration (coasting phase), we derive an initial Lorentz factor limit at the start of deceleration of $\Gamma_0 < 178$. We note that this assumption has many caveats, as it has been shown that $t_{\rm dec}$ varies greatly for GRBs (Ghirlanda et al., 2018). Therefore, in Figure 5.7 we show the parameter space for allowed Γ_0, given our scintillation limit, for a range of $t_{\rm dec}$ starting from the last non-detection and ending with the first detection. We see that if $t_{\rm dec} \gtrsim 94$ s, that $\Gamma \lesssim 100$, which would indicate a more moderately relativistic outflow than the known population of cosmological GRBs. However, our observations are not constraining enough to make this claim.

There have only been a handful of scintillation measurements for GRBs confirmed in the literature, as they necessitate high-cadence, multi-frequency radio observations of GRBs out to late times. There have been seven classical GRBs whose source sizes were able to be constrained by the presence of strong ISS (GRB 970508, Frail et al. 2000; GRB 030329, Berger et al. 2003b; Pihlström et al. 2007; Taylor et al. 2004, 2005; GRB 070125, Chandra et al. 2008; GRB 130427A, van der Horst et al. 2014; GRB 161219B, Alexander et al. 2019; GRB 210702A, Anderson et al. 2023; and GRB 201216C, Rhodes et al. 2022), and four orphan afterglows (AT 2019pim, Perley et al. 2014; AT 2021any, AT 2021lfa, and AT 2023lcr; Li et al. 2024). We show the source size upper limits of these sources from the literature in Figure 5.8, along with that of AT 2023sva,

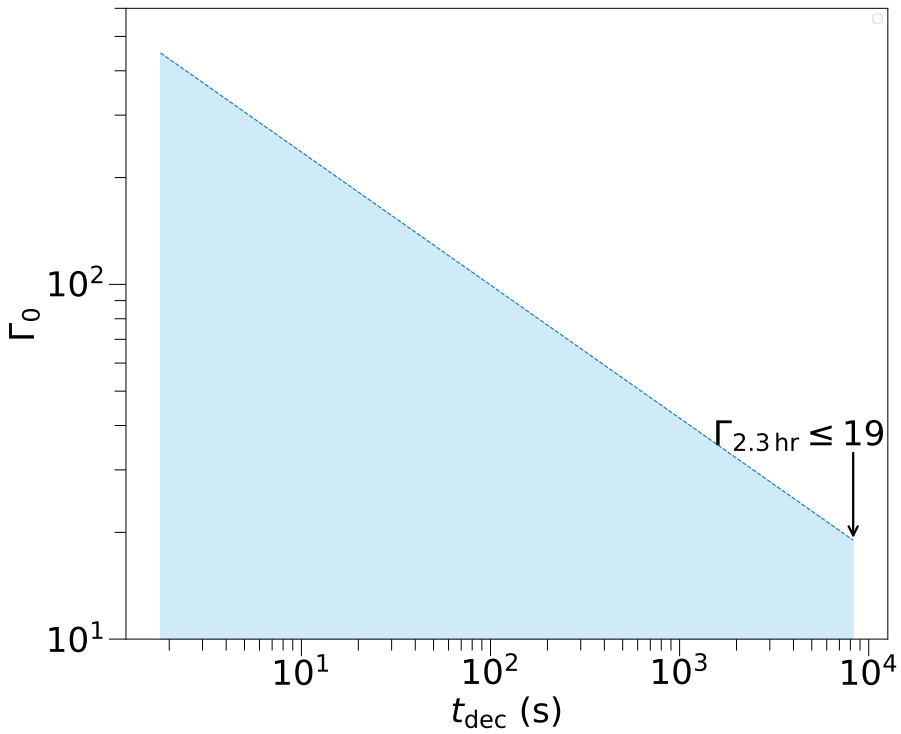

Figure 5.7: Upper limit on the initial Lorentz factor Γ_0 plotted against the assumed rest-frame deceleration time t_{dec}. The limit is derived from the limit obtained from scintillation analysis in §5.3.4 and assuming $\Gamma \propto t^{-3/8}$. The allowed values are shown as the shaded region.

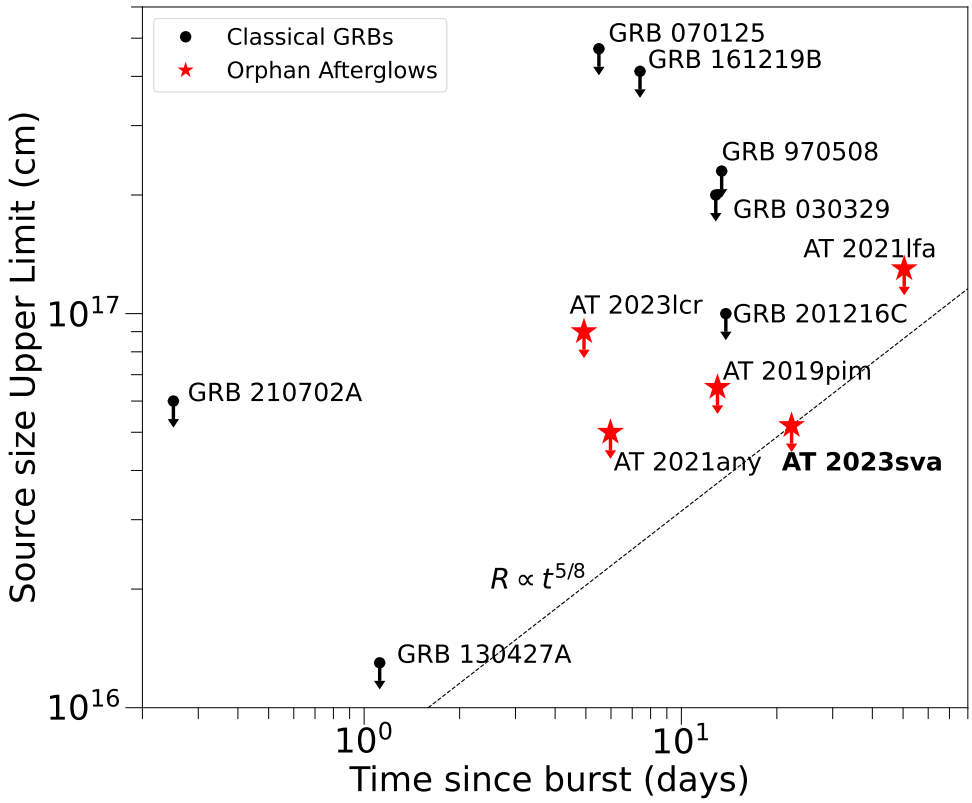

Figure 5.8: Comparison of source size upper limits derived from ISS analyses in seven classical GRBs (GRB 907508, GRB 030329, GRB 070125, GRB 130427A, GRB 161219B, GRB 210702A, and GRB 201216C), and five orphan afterglows (AT 2019pim, AT 2021any, AT 2021lfa, AT 2023lcr, and AT 2023sva), with respect to their rest-frame times since explosion. We also show AT 2023sva's source size upper limit as a function of time, assuming a constant density ISM environment.

along with its source size upper limit as a function of time, assuming a constant density ISM environment. We see that AT 2023sva has the smallest source size upper limit when compared to the entire population.

The source most similar to AT 2023sva in this parameter space is AT 2019pim, which possesses a source size $< 6.5 \times 10^{16}$ cm 30 days after explosion, which corresponds to $\sim$ 13 days in the rest-frame. Figure 5.8 suggests that the orphan afterglow population as a whole seems to have smaller source sizes than those of classical GRB afterglows for measurements taken around the same time, as they seem to mark out a different parameter space in the plot. We

note that though GRB 210702A and GRB 130427A have smaller source sizes than the rest of the population, this is mainly due to their early-time observations. When extrapolating their source sizes to around the epoch the rest of the sample was observed ($\sim$ 20 days), GRB 210702A and GRB 130427A have respective source size upper limits of 10^{18} and 7×10^{16} cm.

We then utilize the Anderson-Darling test to determine if the source limits for the classical GRB and orphan afterglow sample are drawn from different statistical distributions. We derive a test-statistic of 4.78, which is greater than the critical value at the 2.5% significance level of 4.59, with a p-value of 0.004. This indicates that the source size upper limits for the sample of classical GRBs and orphan afterglows with ISS source size constraints are drawn from different statistical distributions. We note that the classical GRB population analyzed here is likely a biased population, as ISS analysis is usually only performed for the brightest GRBs.

One possible explanation for this difference is orphan afterglows have lower Lorentz factor origins when compared to classical GRBs, either intrinsically or due to viewing angle effects. Modeling of AT 2020blt and AT 2023lcr showed that they were best modeled as classical GRBs missed by high-energy satellites (Ho et al., 2020d; Li et al., 2024). However, Li et al. (2024) showed that the inclusion of early-time data in modeling can lead to different conclusions and neither event had early-time data to constrain the afterglow's rise. AT 2021any was also modeled well as a classical GRB (Gupta et al., 2022b; Li et al., 2024), though a low-Lorentz factor solution was also proposed (Xu et al., 2023). Modeling of AT 2019pim and AT 2021lfa showed that both low-Lorentz factor solutions and off-axis structured jet solutions were viable (Li et al., 2024; Perley et al., 2024), and our analysis of AT 2023sva was not able to place any constraints on the actual nature of the initial outflow at early times, as we determined it could range from highly relativistic to moderately relativistic (see Figure 5.7).

Therefore, the small observed source sizes for the orphan afterglow population may not be soley due to low-Lorentz factor jets. Some other possibilities are variations in the circumstellar density within the timescale of the observations, small-scale structure contaminating the afterglow images at later times, or stronger scintillation effects than the simple models used for this analysis (Alexander et al., 2019). Further observations of ISS in both orphan afterglows and classical GRBs are needed in order to understand if the trend holds true for a broader population, and to what extent low-Lorentz factor jets play a role.

5.4 Physical Interpretation of the Outflow

5.4.1 Multiwavelength Modeling

We model AT 2023sva's LC, utilizing the open-source electromagnetic transient Bayesian fitting software `redback` (Sarin et al., 2024), to fit different jet models from `afterglowpy` (Ryan et al., 2020a). For the fitting, we utilize the gri optical data, the X-ray upper limit, as well as the 15.5 GHz radio LC. We do not include the lower frequency radio LCs in our fitting procedure as these frequencies are all below $\nu_{\rm ss}$ and are affected strongly by ISS. In order to derive posteriors and perform the sampling, we utilize `bilby` (Ashton et al., 2019) and `Dynesty` (Speagle, 2020).

We note that `afterglowpy` has limitations and address the relevant ones individually within the context of AT 2023sva. `afterglowpy` disables jet spreading effects when fixing a finite initial Lorentz factor for the explosion and assumes an infinite initial Lorentz factor when accounting for jet spreading. Because we lack early-time data (two days between the last non-detection and first detection) it is unlikely we will be able to place any constraints on the initial

Lorentz factor through modeling. Furthermore, late-time data is largely independent of the initial Lorentz factor, as the jet would have already underwent significant deceleration, so we enable jet spreading effects in our fitting. We note that the corner plots for our modeling presented in the Appendix still show the initial Lorentz factor as a fitting parameter even after enabling jet spreading effects; however, this is just a randomly selected value and has no actual impact on the fitting procedure.

`afterglowpy` does not account for synchrotron self-absorption (SSA), that is a primarily low-frequency radio phenomenon. Though there is a possibility that the early-time 15.5 GHz LC may be affected by SSA, its high frequency and lack of a prominent LC break at early times implies that SSA effects are negligible at that frequency. Finally, `afterglowpy` does not account for the possibility of a stellar wind medium environment surrounding the blast and assumes a constant density ISM environment. Though it is generally expected that a massive star progenitor should have a stellar wind medium, multiple previous works have shown that a constant density ISM environment still fits well to many LGRBs (though there are exceptions, e.g., Panaitescu & Kumar 2001) – Schulze et al. (2011) found that out of 27 *Swift* events, two-thirds are compatible with a constant density ISM and Gompertz et al. (2018) found that out of 56 *Fermi* events, half are compatible with a constant density ISM. Furthermore, most GRBs are modeled utilizing a constant density ISM in the literature, making it useful for future comparisons.

We test three different jet structure models from `afterglowpy` implemented in `redback`: a tophat jet, a structured jet with a Gaussian profile, and a structured jet with a power-law profile. Tophat jets have a constant energy per unit solid angle, where the bulk of relativistic ejecta is

inside the solid angle of the jet. They can be represented by:

$$E(\theta) = \begin{cases} E_{\mathrm{K,\,iso}},\ \theta < \theta_{\mathrm{c}} \\ \\ 0,\ \theta > \theta_{\mathrm{c}} \end{cases} \tag{5.1}$$

where $E(\theta)$ is the energy with respect to viewing angle, $E_{\mathrm{K,\,iso}}$ is the isotropic kinetic energy of the jet, θ is the angle within the jet, and θ_c is the half-opening angle of the jet's core. The tophat jet has no structure and is the canonical model assumed for most GRB afterglow analyses. However, observations of some GRBs show significant evidence that their jets possess structure (more in §5.4.3), with weaker emission farther from the jet axis (e.g., Cunningham et al. 2020; Gill & Granot 2023; O'Connor et al. 2023; Troja et al. 2019). Therefore, we also test the Gaussian structured jet, which is represented by

$$E(\theta) = \begin{cases} E_{\mathrm{K,\,iso}}(e^{-\theta^2/2\theta_c^2}),\ \theta < \theta_{\mathrm{w}} \\ \\ 0,\ \theta > \theta_{\mathrm{w}} \end{cases} \tag{5.2}$$

where θ_w is a "wing truncation angle" that represents the relativistic ejecta spreading past the jet's core into wing-like structures. The third model we test is the power-law structured jet, which is represented by

$$E(\theta) = \begin{cases} E_{\mathrm{K,\,iso}}\left(1 + \left(\frac{\theta^2}{b\theta_c^2}\right)^{-b/2}\right),\ \theta < \theta_{\mathrm{w}} \\ \\ 0,\ \theta > \theta_{\mathrm{w}} \end{cases} \tag{5.3}$$

where b is a power-law index that parameterizes the jet's structure.

Parameter	Unit	Description	Prior (Uniform)
t_0	[MJD]	estimated burst time from first detection	[60202.24, 60204.40]
$\theta_{\rm v}$	[rad]	viewing angle	[0, 1.57]
$\log_{10}(E_{\rm K,iso}/{\rm erg})$		isotropic equivalent kinetic energy of blast wave along jet axis	[44, 54]
$\theta_{\rm c}$	[rad]	half-opening angle of jet core	[0.01, 0.1]
$\theta_{\rm w}$	[rad]	wing truncation angle of a structured jet	$[1, 8] \times \theta_{\rm c}$
$\log_{10}(n_0/{\rm cm}^{-3})$		number density of protons in circumburst medium	$[-5, 2]$
p		power law index of relativistic electron energy distribution	[2, 3]
b		power law index of jet angular energy distribution	[0.5, 10]
$\log_{10}\epsilon_e$		fraction of thermal energy in relativistic electrons	$[-5, 0]$
$\log_{10}\epsilon_B$		fraction of thermal energy in magnetic field	$[-5, 0]$
ξ_N		fraction of accelerated electrons	[0, 1]

Table 5.1: Table of priors for `redback` fits. $\theta_{\rm w}$ is ignored by the tophat model and β is only used by the power law model.

We list the priors used for our fitting procedure in Table 5.1 and note that we allow for the time of explosion to also be a free parameter, due to the lack of constraints mentioned in §5.2.1. We show the best-fit models plotted against the observed data in Figure 5.9. We derive the Bayesian evidences for each of the models and find $\log Z_{\rm tophat} = 15.37$, $\log Z_{\rm Gaussian} = 11.92$, and $\log Z_{\rm Power-law} = 24.41$. We also calculate the Bayesian Information Criterion for every model, which accounts for possible overfitting to the data due to the use of extra parameters in the structured jet models and find ${\rm BIC}_{\rm Power-Law} = -77.63$, ${\rm BIC}_{\rm Gaussian} = -68.12$, and ${\rm BIC}_{\rm Tophat} = -75.23$, where a lower BIC corresponds to a better fit. Therefore, it is clear the power-law structured jet model is favored, within the `afterglowpy` models.

Furthermore, in both the tophat and Gaussian jet corner plots shown in the Appendix, the posterior for p is hitting the limit $p < 3$, implying that the best-fit p is likely $p > 3$. This is not the case for the power-law structured jet – though the median p is a high value, it is constrained strongly within the priors of $p = 2.85 \pm 0.09$. From our closure relations in §5.3.3, we determined $p = 2.50 \pm 0.14$ in the regime $\nu_{\rm m} < \nu < \nu_{\rm c}$ – therefore, the derived p for the tophat and gaussian structured jet models is inconsistent with the p inferred from the modeling. We note that though the relations we used in that section assumed a tophat jet, the relations between β and p are

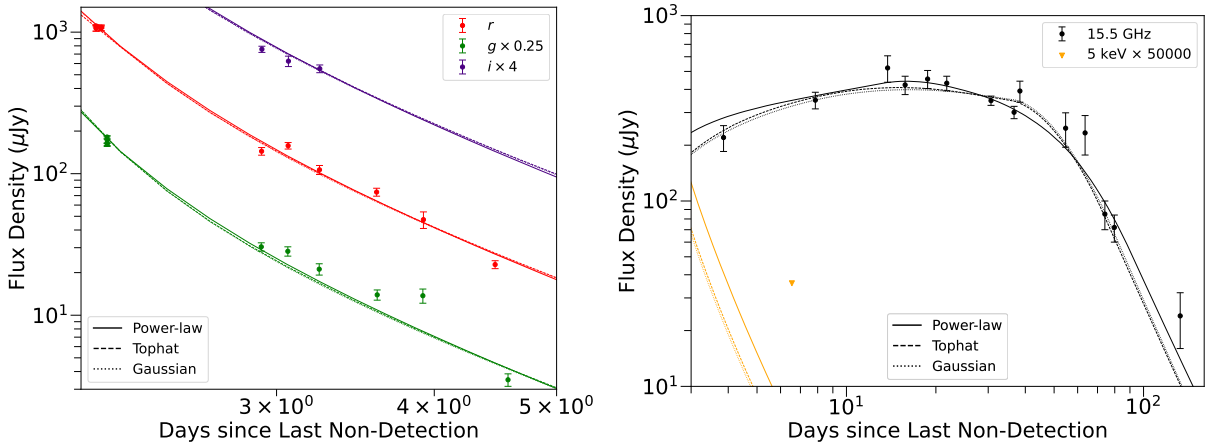

Figure 5.9: *Left panel*: The optical observations of AT 2023sva, along with the best-fit power-law structured jet, tophat jet, and Gaussian structured jet fit to the observed LC. Optical fluxes have been multiplied by a constant factor for viewing purposes and have been corrected for MW and host galaxy extinction. *Right panel*: The 15.5 GHz radio observations of AT 2023sva and the X-ray upper limit, along with the best-fit power-law structured jet, tophat jet, and Gaussian structured jet fit to the observed LC. The X-ray limit has been multiplied by a constant factor for viewing purposes.

identical given a structured jet (Ryan et al., 2020a). This gives further evidence that a power-law structured jet is favored.

We present the 90% credible interval of the predicted LCs from the posterior samples of the power-law structured jet model, along with the full multi-wavelength set of observations, in Figure 5.10. We note that this is the preferred model in the context of the `afterglowpy` model and without considerations for any more complex physics contributing to the LC and spectra. Therefore, we stress that though AT 2023sva shows significant evidence for possessing a power-law structured jet within this context, we cannot definitely claim that this is the only possible scenario.

We then compute the angular size of the best-fit power-law afterglow model's image on the sky, as a function of frequency and time, to compare it to the size derived from the ISS of the observed LC described in §5.3.4. We find that at 73 days at 15.5 GHz, the source has an

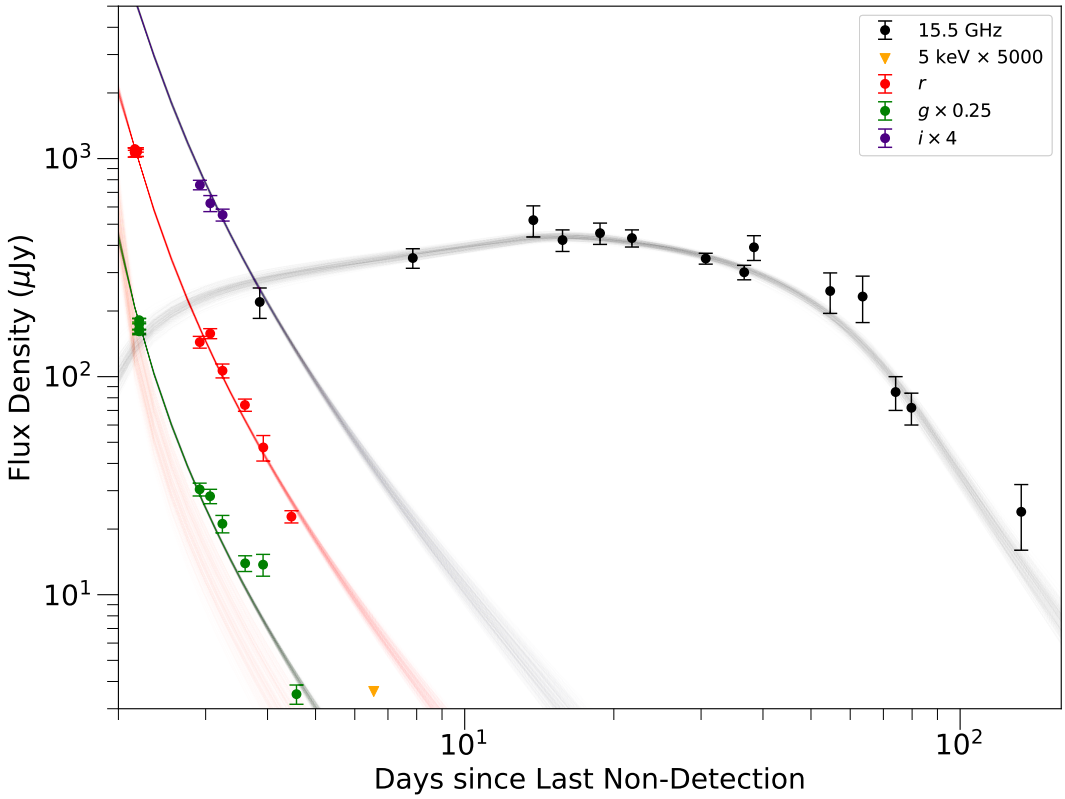

Figure 5.10: Multiwavelength data set of AT 2023sva, along with the 90% credible interval of the predicted LCs from our posterior samples for the power-law structured jet model. Fluxes are multiplied by constant factors for visual purposes.

Table 5.2: Final best-fit and median $\pm 1\sigma$ parameters for the power-law structured jet model, which is the most favored model for AT 2023sva. The best-fit parameters correspond to the model that possesses the maximum log likelihood and the corner plot corresponding to median parameters and their 1σ confidence intervals are presented in the Appendix.

Parameter	Best-fit Result	Median $\pm 1\sigma$
t_0 [MJD]	60204.09	$60204.09^{+0.03}_{-0.03}$
$\theta_{\rm v}$ [rad]	0.08	0.07 ± 0.02
$\log_{10}(E_{\rm K,iso}/{\rm erg})$	53.63	$53.33^{+0.27}_{-0.21}$
$\theta_{\rm c}$ [rad]	0.05	0.06 ± 0.02
$\theta_{\rm w}$ [rad]	$7.71 \times \theta_{\rm c}$	$6.81^{+0.79}_{-1.01} \times \theta_{\rm c}$
$\log_{10}(n_0/{\rm cm}^{-3})$	1.41	$1.40^{+0.40}_{-0.74}$
p	2.84	2.85 ± 0.09
b	1.02	$0.99^{+0.36}_{-0.23}$
$\log_{10}\epsilon_e$	-0.77	$-0.53^{+0.18}_{-0.28}$
$\log_{10}\epsilon_B$	-3.32	$-3.18^{+0.45}_{-0.26}$
ξ_N	0.42	$0.70^{+0.19}_{-0.27}$

angular size of $\theta \approx 1.95\,\mu$arcseconds. This is consistent with the ISS analysis (§5.3.4), where we determined that AT 2023sva's angular size needed to be comparable or smaller than the Fresnel scale (2 μarcsec). This gives us an independent confirmation that our modeling results match well with the radio observations. From the best-fit parameters shown in Table 5.2, we see that we are viewing the power-law structured jet slightly off-axis, where $\theta_{\rm v} \gtrsim \theta_{\rm c}$. Furthermore, the power-law index of the energy distribution as a function of viewing angle is quite shallow, as we derive $b = 1.02$ for the best-fit model and a median $\pm 1\sigma$ is $0.99^{+0.36}_{-0.24}$. We discuss the implications of this in §5.4.3.

In Figure 5.11, we show the simulated optical SEDs generated by `afterglowpy` utilizing the best-fit power-law structured jet model, along with the optical observations of AT 2023sva. We see that generally the simulated SEDs match well with the observations across all epochs. Furthermore, we see there is a clear break in the optical SED in the 0.3 day epoch at around 4×10^{14} Hz and this break moves further down in frequency over time. This is the cooling break $\nu_{\rm c}$. This implies that the optical bands lie just above the cooling break, which is at odds with our analysis in §5.3.3, where we determined that the optical bands should lie below the cooling break to imply a physical p. This discrepancy between the two analyses can be explained by the fact that spectral breaks are smooth over orders of magnitude. Because the optical bands have barely passed $\nu_{\rm c}$ at the time the spectral index was derived (~ 2 days), the slope has not fully steepened yet, leading to a fulfillment of the relation in the $\nu_{\rm m} < \nu < \nu_{\rm c}$ regime. Furthermore, Figure 5.1 shows evidence of a possible temporal break in the early-time LC, which would correspond to $\nu_{\rm c}$ fully passing through the optical bands.

Given that the best-fit model and posteriors indicate that we are viewing the jet slightly off-axis just outside the jet's core, ($\theta_{\rm v} \gtrsim \theta_{\rm c}$), we utilize the closure relations provided by Ryan

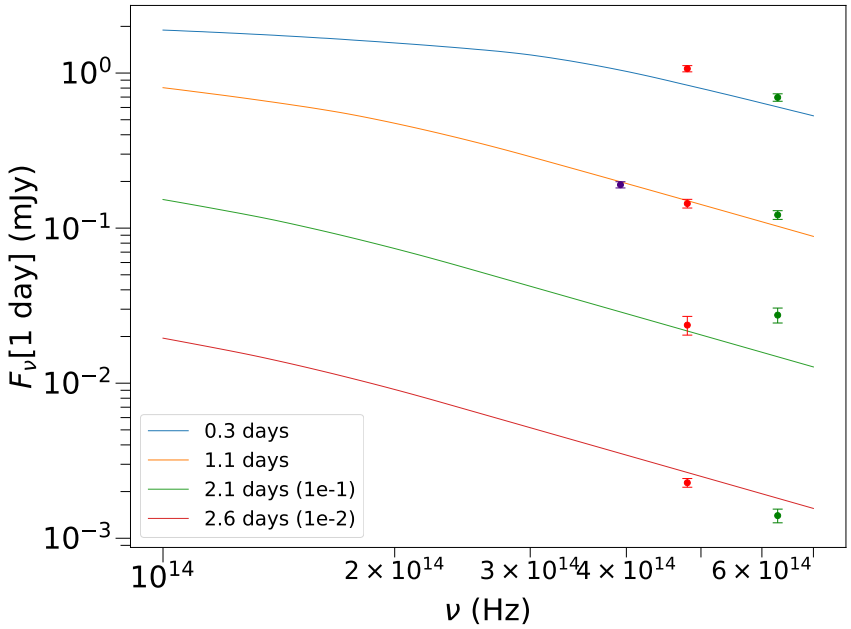

Figure 5.11: Simulated optical SEDs from the best fit power-law structured jet model and the optical observations. The fluxes are scaled for visual purposes.

et al. (2020a) for a structured jet for misaligned viewers, to check if the relationship between α, p, and b hold true. We test the relations in two different regimes: for $\nu_{\rm m} < \nu < \nu_{\rm c}$ the relation is $\alpha = (3 - 6p + 3g)/(8 + g)$ and for $\nu_{\rm m} < \nu_{\rm c} < \nu$, the relation is $\alpha = (1 - 6p + 2g)/(8 + g)$. The g parameter accounts for the angular structure of the jet in the relations and is given by

$$g = \frac{2b(\theta_{\rm obs} - \theta_{\rm eff})\theta_{\rm eff}}{b{\theta_{\rm c}}^2 + {\theta_{\rm eff}}^2}, \tag{5.4}$$

where for a power-law structured jet, $\theta_{\rm eff}$ is

$$\theta_{\rm eff} = \theta_{\rm obs}\Big[1.8 + 2.1b^{-1.25} + (0.49 - 0.86b^{-1.15})\theta_{\rm obs}/\theta_{\rm c}\Big]^{-1/2} \quad . \tag{5.5}$$

Utilizing the best-fit values from the modeling, we find $\theta_{\rm eff} = 0.044$ and $g = 0.72$. Applying the closure relations, we find $\alpha \sim 1.4$ for $\nu_{\rm m} < \nu < \nu_{\rm c}$ and $\alpha \sim 1.7$ for $\nu_{\rm m} < \nu_{\rm c} < \nu$. In §5.3.1, we found $\alpha = 1.64 \pm 0.02$, which matches well with the $\nu_{\rm m} < \nu_{\rm c} < \nu$ case – and from the simulated spectra in Figure 5.11, we know that the optical bands lie in this regime. This gives further evidence favoring the power-law structured jet model.

5.4.2 Why the lack of γ-rays?

The question arises as to why we did not detect any associated γ-ray emission for AT 2023sva, at least to an upper limit of $E_{\gamma,\rm iso} < 1.6 \times 10^{52}\,{\rm erg}$. Studies suggest that for structured jets, prompt γ-ray emission may only be efficiently produced in the core of the jet (e.g., Beniamini et al., 2020; Beniamini & Nakar, 2019; Gill et al., 2020; O'Connor et al., 2023). Since the Lorentz factor of a structured jet will also decrease with angle, this leads to an increase in the opacity due to photon-pair production processes (Gill et al., 2020). A lower Lorentz factor along the line of sight will also decrease the dissipation radius of the prompt emission, so that at large viewing angles, the photospheric radius is larger than the dissipation radius, resulting in high optical depth regions (Beniamini et al., 2020; Lamb & Kobayashi, 2016). These effects are highly dependent on the angular Lorentz factor profile and the initial core Lorentz factor.

Both of these effects suppress the γ-ray emission (Gill et al., 2020) and decrease the observed γ-ray efficiency, which describes how efficiently the jet converts its energy to radiation along the line of sight. Therefore, structured jets need to be viewed extremely close to on-axis to detect their associated γ-ray prompt emission (e.g., O'Connor et al., 2024), even if the viewing angle is within the wing truncation angle. Through our modeling analysis, the posteriors indicate

$\theta_v = 0.07 \pm 0.02$ and $\theta_c = 0.06 \pm 0.02$. Therefore, we are likely viewing AT 2023sva slightly off-axis, making this scenario a strong possibility to explain the lack of γ-rays, depending on the steepness of the angular Lorentz factor profile and initial core Lorentz factor.

We then quantify the γ-ray radiative efficiency of AT 2023sva. The radiative efficency is calculated through

$$\eta_\gamma = \frac{E_{\gamma,\rm iso}}{E_{\rm K,iso} + E_{\gamma,\rm iso}}. \tag{5.6}$$

Using the upper limit for $E_{\gamma,\rm iso}$ and the 1σ range of $E_{\rm K,iso}$ from the best-fit power-law structured jet model, we derive $\eta_\gamma < 4 - 11\%$. These efficiencies are on the lower end of the distribution observed from LGRBs (Wang et al., 2015), but are consistent with the $\sim 1\%$ efficiency derived from the internal shock model used to describe the prompt emission of bursts (Kumar, 1999). Several other orphan afterglows in the literature have demonstrated possible low efficiencies – AT 2020blt ($< 0.3 - 4.5\%$; Sarin et al. 2022, $< 0.2 - 17.9\%$; Li et al. 2024), AT 2020lfa ($< 0.01 - 0.05\%$; Ye et al. 2024) and AT 2023lcr ($< 1.3 - 3.4\%$; Li et al. 2024), which provides evidence that the lack of associated γ-ray emission for at least some orphan afterglows may be attributed to their low radiative efficiencies.

It is important to note that these efficiencies are calculated along the line of sight, so if viewed off-axis, low efficiencies are a natural consequence of structured jets. It is also possible that on-axis jets may have intrinsic low efficiencies, as suggested for AT 2020blt in Sarin et al. (2022). It is more likely that AT 2023sva's low efficiency is due to viewing the event slightly off-axis; however, an intrinsic low efficiency cannot be ruled out, as the posteriors from the modeling do not indicate an extremely off-axis viewing angle.

If the outflow is intrinsically moderately relativistic in its core, a low Lorentz factor in

comparison to classical LGRBs ($\Gamma > 100$) could be a possible reason for the lack of associated γ-rays, as pair production processes can reprocess γ-rays to X-rays if the jet is baryon-loaded, leading to a low Lorentz factor. It has been shown that even jets with moderately high Lorentz factors ($\Gamma \sim 50$) can have their high-energy emission suppressed (Lamb & Kobayashi, 2016; Matsumoto et al., 2019). This cannot be ruled out for AT 2023sva, as its small source size at late times (see §5.3.4) gives possible evidence for this case.

Therefore, we try to measure the initial Lorentz factor Γ_0 through the relationship between Γ_0, $t_{\rm dec}$, $E_{\rm K,\,iso}$, and the circumburst medium density n_0, in the case of a constant density ISM environment. This is given by

$$\Gamma_{2.5} = \left(\frac{10\,{\rm s}(1+z)}{t_{\rm dec}}\right)^{3/8} \left(\frac{E_{53}}{n_0}\right)^{1/8}, \tag{5.7}$$

from Mészáros (2006), where n_0 is the number density of the circumburst medium in cm^{-3}, $E_{53} = E_{\rm K,iso}/10^{53}$ erg, and $\Gamma_{2.5} = \Gamma_0/10^{2.5}$. We first derive a lower limit, assuming that $t_{\rm dec}$ is at the time of first detection, or 7.5 hours after the explosion in the observer frame (see Figure 5.7 for how different assumptions of $t_{\rm dec}$ impact Γ_0). Using the full, weighted posterior distributions of $E_{\rm K,\,iso}$ and n_0 from modeling the power-law structured jet, we derive a lower limit on the initial Lorentz factor of $\Gamma_0 > 16^{+5}_{-3}$. If we assume that $t_{\rm dec}$ is 20 seconds in the rest frame as we did in our radio ISS analysis (see §5.3.4), we find $\Gamma_0 = 182^{+49}_{-27}$. This is consistent with the upper limit derived in §5.3.4 assuming the same $t_{\rm dec}$, where $\Gamma_0 < 178$. Again, we note that the assumed $t_{\rm dec}$ is a major caveat, as past GRBs have derived values between 1 and 1000 seconds (Ghirlanda et al., 2018). If $t_{\rm dec} \gtrsim 94$ seconds, that would imply $\Gamma_0 \lesssim 102^{+27}_{-15}$, meaning that AT 2023sva possesses ejecta more moderately relativistic than the classical GRB population. This is

consistent to the limit derived in §5.3.4, where we found if $t_{\rm dec} \gtrsim 94$ seconds, that would imply $\Gamma_0 \lesssim 100$ as well.

We then test the physical models of Dermer et al. (1999) in Figure 5.12. Dermer et al. (1999) introduce functions that model the synchrotron emission produced by relativistic blast waves driven from GRB jets with $\Gamma_0 \gg 300$ and $\Gamma_0 \ll 300$, that track the Lorentz factor evolution with time. Dermer et al. (1999) make the distinction between clean and dirty fireballs for these two different jets; however, true dirty fireballs are now characterized by $\Gamma \lesssim 10$. Therefore, we perform this analysis not to characterize AT 2023sva as a true dirty fireball or not, but to provide another independent constraint of the Lorentz factor. In order to do this, we utilize Equations 4, 6, 11, 27, and 30 from Dermer et al. (1999), which are sensitive to n_0, ϵ_e, and ϵ_b, which we constrain to our best-fit values from §6.4. These equations are also sensitive to the observed $t_{\rm dec}$ and we show a range of values for $t_{\rm dec}$ in Figure 5.12, along with the Lorentz factor upper limit derived from the source size in §5.3.4.

This analysis indicates that AT 2023sva originates from a jet with $\Gamma \ll 300$, which is consistent with our previous analyses. This modeling is very sensitive to the choice of n_0, ϵ_e, and ϵ_b, which is affected by the caveats associated with our afterglow modeling in §6.4, so it is difficult to make any more robust conclusions. Overall, through all the independent methods used to constrain Γ_0, we cannot rule out that AT 2023sva has a classical, high Γ origin, and we find that the lack of associated γ-rays is most likely due to viewing a structured jet slightly off-axis – though we also cannot rule out an on-axis, low radiative efficiency burst, or a more moderately relativistic outflow than classical GRBs. Further constraints on $t_{\rm dec}$ would allow us to place more robust constraints on Γ_0, highlighting the importance of high-cadence early-time observations in orphan afterglow observations.

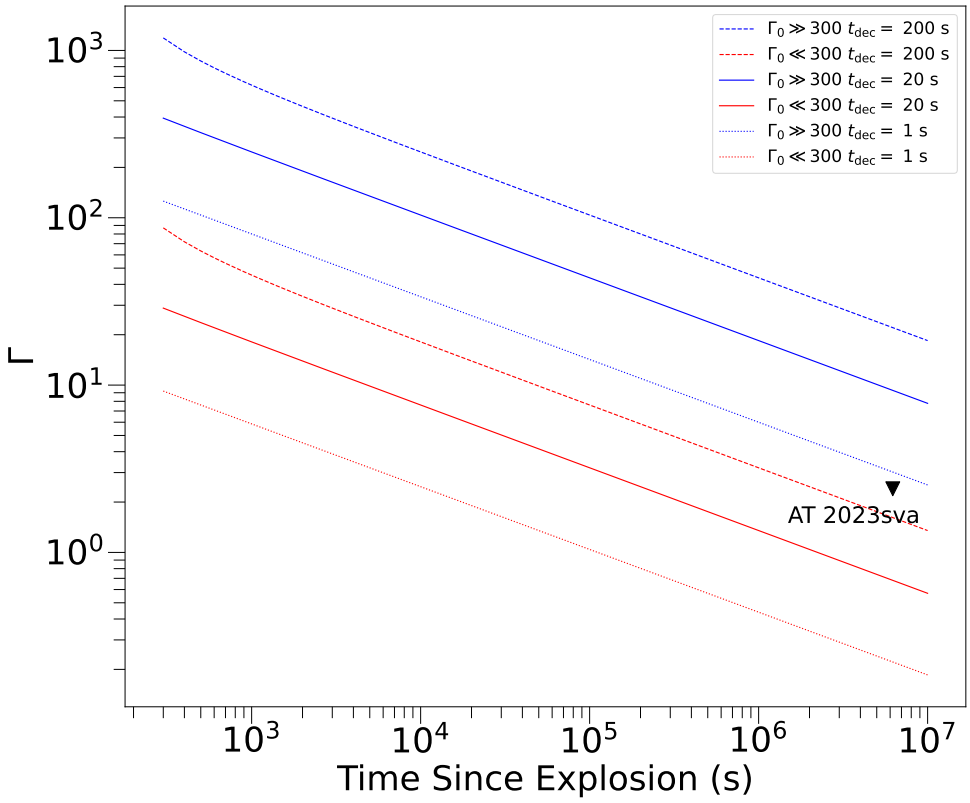

Figure 5.12: Comparison of the Lorentz factor evolution of $\Gamma \gg 300$ and $\Gamma \ll 300$ jet models (from Dermer et al. 1999) with respect to different observed deceleration times. We also show the upper limit for AT 2023sva's Lorentz factor at the observed time of 72 days from the scintillation analysis ($\Gamma_{\mathrm{av,72\,d}} < 2.4$).

5.4.3 Comparison to GRB Afterglows

In Figure 5.13, we show AT 2023sva in the context of other LGRBs in the literature (Nysewander et al., 2009) that have measurements of $E_{\gamma,\,\mathrm{iso}}$ and an optical afterglow detection. We use the upper limit of $E_{\gamma,\,\mathrm{iso}} < 1.6 \times 10^{52}$ erg derived in §5.2.3. The optical magnitudes are all normalized to 11 hours after explosion in every GRB's respective rest frame, in the rest-frame r band. Extrapolating our first observed r band measurement (corrected for galactic and host-galaxy extinction) to 11 hours after explosion and utilizing $\beta = 0.75$ (see §5.3.2) to transform to the rest-frame r band, we find $M_{\mathrm{abs},\,r} \sim -30.4$ mag, making it the most luminous optical afterglow in the sample.

In Figure 5.14, we show AT 2023sva's radio LC compared to other GRB afterglows in the literature (plot modified from Chandra & Frail 2012; Perley et al. 2014). The LCs are plotted with respect to their 16 GHz rest-frame luminosity, which corresponds to a flux density at 5 GHz at $z = 2.28$. The flux densities were converted to luminosities through multiplying by the distance luminosity associated with $z = 2.28$. The plot is also color-coded with respect to the GRBs' associated $E_{\gamma,\,\mathrm{iso}}$. The large rise between the first two epochs is due to ISS, as the redshift of AT 2023sva places it in a regime where the rest-frame 16 GHz LC is affected heavily by ISS. We see that AT 2023sva is quite radio-loud and most GRBs that have a similar radio luminosity have $E_{\gamma,\,\mathrm{iso}} > 10^{52}$ erg. However, in §5.2.3 we ruled out a GRB counterpart to an upper limit of $E_{\gamma,\,\mathrm{iso}} < 1.6 \times 10^{52}$ erg. This makes AT 2023sva a unique event in this parameter space.

Now, we visit AT 2023sva's preference for a structured jet model within the context of GRB afterglow jets from the literature. Structured jets have been proposed as possible models for GRB afterglows for some time, as it is natural that a jet with structure should develop due

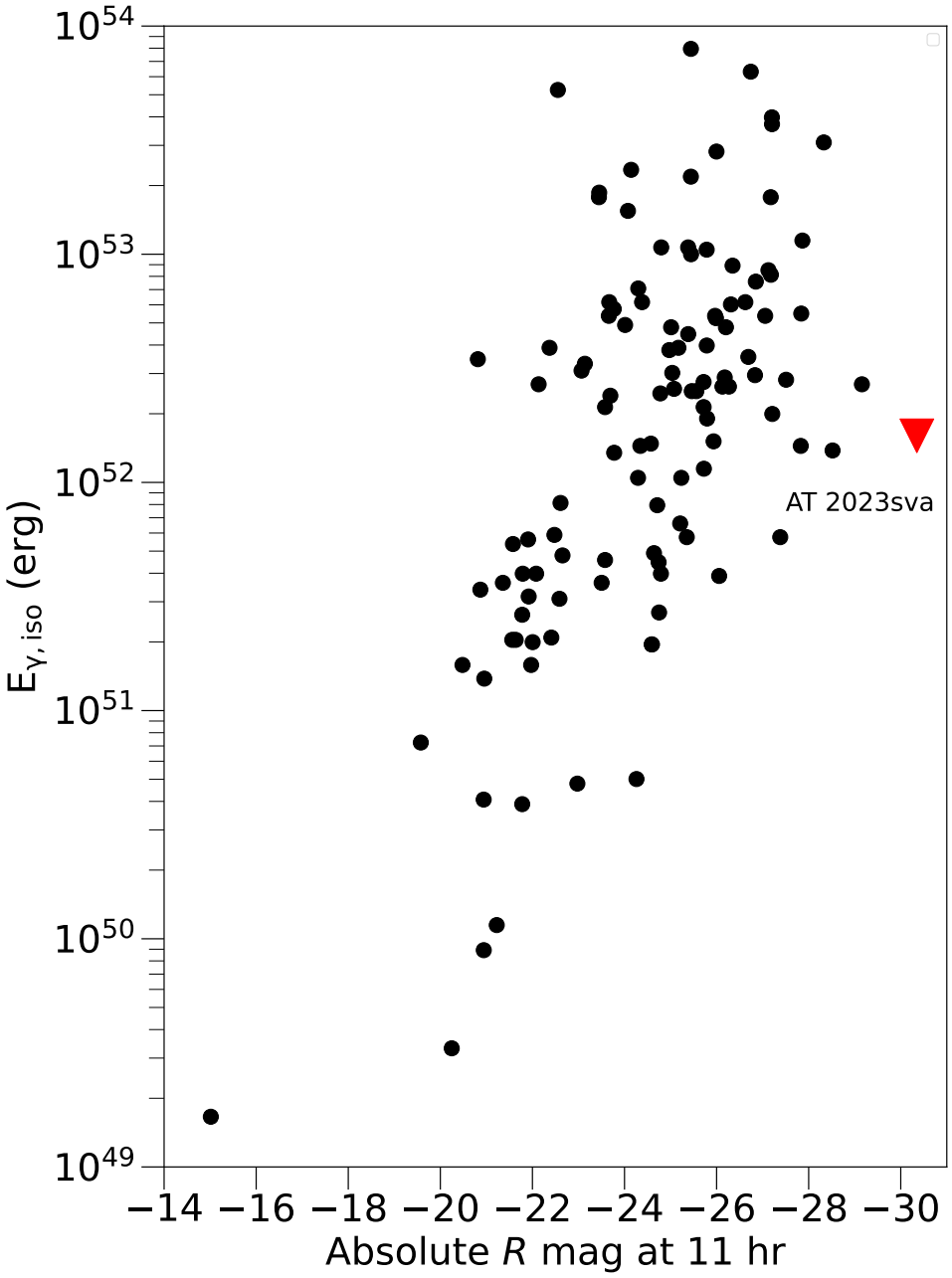

Figure 5.13: $E_{\gamma,\,\mathrm{iso}}$ plotted against the absolute r-band optical magnitude at 11 hours for GRBs in the literature (from Nysewander et al. 2009) along with AT 2023sva, shown in red.

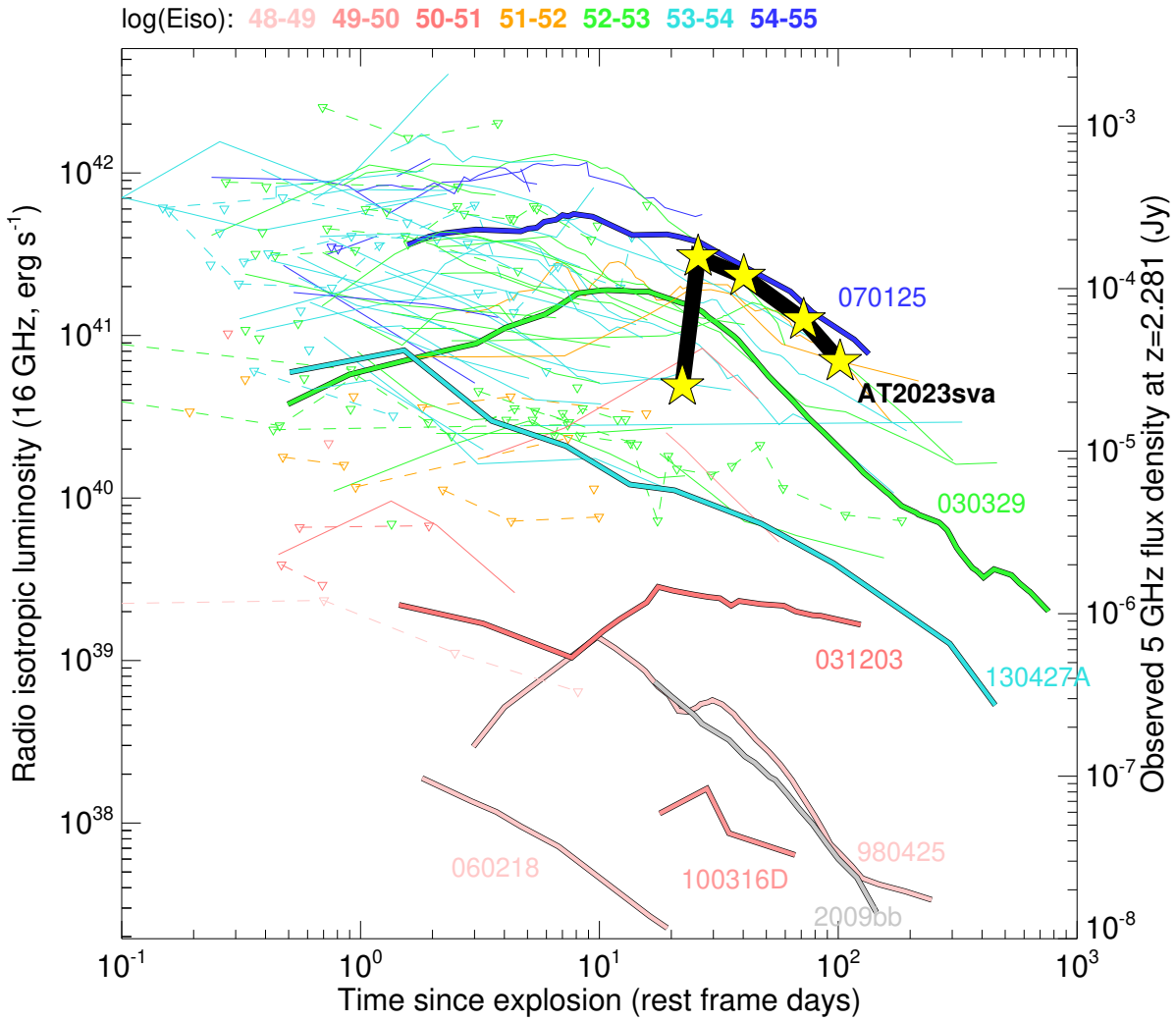

Figure 5.14: Comparison of AT 2023sva's radio LC (stars) to other GRB afterglow LCs from literature (Chandra & Frail, 2012; Perley et al., 2014). We show the rest-frame 16 GHz luminosity LC, which corresponds to an observed flux density LC at 5 GHz at a redshift $z = 2.28$. Events are also color-coded with respect to their $E_{\gamma,\,\mathrm{iso}}$, except fot AT 2023sva.

to breaking out of a dense stellar environment (e.g., Gottlieb et al., 2022, 2021). However, there have only been a few possible structured jet models inferred through afterglow analyses in the literature. GRB 030329 showed two different jet breaks – one in the optical at around 0.55 days and another in the radio at around 9.8 days, leading to an interpretation of its afterglow as a two-component structured jet (Berger et al., 2003b), though alternative models were not excluded. GRB 130427A's X-ray LC was suggested to arise from a power-law structured jet (De Pasquale et al., 2016), though other models were also discussed. GRB 160625B showed strong evidence for possessing a Gaussian-structured jet, when compared to a tophat jet or power-law structured jet (Cunningham et al., 2020). GRB 190828A was also suggested to have a two-component jet model, to discriminate between the early X-ray and optical emission and late-time X-ray and radio emission (Sato et al., 2021).

Finally, the two most famous examples of structured jets are in GRB 170817A and GRB 221009A. GRB 170817A was a short GRB that also had associated gravitational waves (e.g., Abbott et al. 2017), making it one of the most extensively followed-up astrophysical sources in history. Through extensive modeling efforts across the electromagnetic spectrum, it became clear that a structured jet was the only model that could explain the multiwavelength observations (both power-law and Gaussian structured jets are presented as viable models in various works; e.g., Lazzati et al. 2018; Margutti et al. 2018; Ryan et al. 2023; Troja et al. 2018). GRB 221009A was the brightest GRB ever detected with respect to its fluence (e.g., Frederiks et al., 2023b; Lesage et al., 2023b) and it is one of the most energetic GRBs ever detected (Burns et al., 2023). O'Connor et al. (2023), Gill & Granot (2023), LHAASO Collaboration et al. (2023), and Rhodes et al. (2024) suggest that it possesses a shallow structured jet best modeled using a broken-power law energy distribution. As an alternative explanation a two-component jet model was

also proposed by Sato et al. (2023).

In this work, we show evidence that AT 2023sva should be added to the above list and it is the third orphan event to show possible evidence for possessing complex jet structure. The other two are AT 2019pim (Perley et al., 2024) and AT 2021lfa (Li et al., 2024), as both of these events are modeled well by both low-Lorentz factor solutions or off-axis structured jet solutions. AT 2023sva's shallow power-law index for its structured jet's energy distribution with respect to viewing angle ($b = 0.99^{+0.36}_{-0.24}$) is similar to the index derived by O'Connor et al. (2023) for GRB 221009A, as they derived indices of 0.75 and 1.15 for their broken-power law distribution, and Gill & Granot (2023) who found an index of 0.8. However, the energetics of GRB 221009A and AT 2023sva are quite different – GRB 221009A possessed an $E_{\gamma,\rm iso} \approx 10^{55}$ erg (Lesage et al., 2023b) and had strong X-ray emission. This gives evidence that the simplified jet model assumed for GRBs may need to be revised, as one of the most energetic, explosive GRBs ever detected along with an orphan event both show evidence for possessing shallow structured jets.

5.5 Summary and Conclusion

In this work, we present the discovery of an orphan afterglow, AT 2023sva, at a redshift $z = 2.28$. We analyze the optical, X-ray, and radio observations of AT 2023sva and place it in the context of GRBs in the literature. Our main findings are:

- AT 2023sva does not possess an associated GRB counterpart, based on a search of γ-ray satellite archives between the last non-detection and first detection of AT 2023sva (a two day window), to an isotropic equivalent energy upper limit of $E_{\gamma,\,\rm iso} < 1.6 \times 10^{52}$ erg.

- There is additional host-galaxy extinction present ($E_{\rm B-V,\,host} = 0.09 \pm 0.01$), due to a

characteristic curvature in the optical spectrum. Only a few absorption features are present in the spectrum and their line strengths are weaker than 99% of GRBs in the literature.

- The radio LC and SED shows clear presence of interstellar scintillation 72 days after the explosion in the observer frame. We use this to provide an upper limit constraint on the bulk Lorentz factor in the rest frame of $\Gamma_{\rm av,22.0\,days} \leq 2.4$ and extrapolating back to the time of first detection, we derive a constraint of $\Gamma_{\rm av,2.3\,hr} \leq 19$. A more stringent constraint on the initial Lorentz factor was not able to be determined, due to a lack of earlier-time observations.

- AT 2023sva has a small source size upper limit (5.2×10^{16} cm) derived from ISS constraints when compared to most classical GRBs and shares scintillation properties in common with other orphan afterglows. We determine that the orphan afterglow population has statistically lower source-size upper limits than the classical GRB population, for events whose limits were derived from ISS analyses.

- The model that can best reproduce the multi-wavelength observations is a slightly off-axis ($\theta_{\rm v} \gtrsim \theta_{\rm c}$) shallow power-law structured jet, which we determined through Bayesian multi-wavelength modeling of the afterglow. We only model the source in a constant density ISM and cannot rule out the possibility of the source originating from a wind medium. AT 2023sva's shallow jet structure is remarkably similar to that of GRB 221009A (Gill & Granot, 2023; LHAASO Collaboration et al., 2023; O'Connor et al., 2023; Rhodes et al., 2024).

- The lack of a detected associated GRB counterpart is most likely due to viewing the struc-

tured jet slightly off-axis, just outside the opening angle of the jet's core. However, this is not the only possibility and we determine that it may be due to its lower radiative efficiency, or possibly a more moderately relativistic outflow than classical GRBs.

Because the early evolution of afterglow LCs depends strongly on the jet's structure, it is vital that orphan afterglow searches in the future calibrate their observation strategies with more complex structured jet models (e.g., Freeburn et al. 2024; Lamb & Kobayashi 2017b; Lamb et al. 2018b; Xie & MacFadyen 2019). This is incredibly important in the coming years, as new instruments like the Vera Rubin Observatory (Ivezić et al., 2019a) will vastly increase the discovery space of orphan afterglows, due to increased sensitivity. However, this discovery space can only be utilized if observing strategies are broadened to incorporate the diverse range of angular energy profiles of GRB jets.

Furthermore, the recently launched Einstein Probe (EP; Yuan et al. 2022b) and the Space-based multi-band astronomical Variable Objects Monitor (SVOM; Wei et al. 2016b) will increase the number of afterglows detected without associated γ-ray emission, through discovering their X-ray "prompt" emission, providing another avenue for characterizing these events. In fact, EP has already began detecting GRB-related events in the soft X-rays. One such event, EP 240414a, did not have significant associated γ-ray emission (Bright et al., 2024) and was followed by the detection of an associated broad-lined Type Ic supernova (Srivastav et al., 2024; Sun et al., 2024; van Dalen et al., 2024), confirming its collapsar origin. Radio analyses constrained the outflow to have at least a moderate Γ (Bright et al., 2024), similar to AT 2023sva.

EP and SVOM are opening the door to detecting the prompt emission of events that previously would have been orphan afterglows, enabling a full characterization of their prompt and

afterglow emission across the electromagnetic spectrum. Therefore, the coming years hold the tantalizing prospect of breaking historical degeneracies between different GRB models and getting closer to deciphering the landscape of relativistic jets originating from massive stellar deaths.

Data Availability

All of AT 2023sva's optical photometry, radio flux densities, and X-ray upper limits are available in this article. We will make the spectrum available in the supplementary material available online.

Acknowledgments

G.P.S. thanks Isiah Holt for useful discussions on nested sampling techniques, Tony Piro for reading the paper on request, and Simi Bhullar for her moral support through out the paper-writing process. A.Y.Q.H. was supported in part by NASA Grant 80NSSC23K1155. M.W.C acknowledges support from the National Science Foundation with grant numbers PHY-2308862 and PHY-2117997. M.B.S. acknowledges the Finnish Cultural Foundation grant number 00231098 and Finnish Centre for Astronomy with ESO (FINCA) grant. G.C.A. thanks the Indian National Science Academy for support under the INSA Senior Scientist Programme. M.M.K acknowledges generous support from the David and Lucille Packard Foundation. B.O. is supported by the McWilliams Postdoctoral Fellowship at Carnegie Mellon University. A.T. acknowledges the financial support from "ASI-INAF Accordo Attuativo HERMES Pathinder operazioni n. 2022-25-HH.0".

SED Machine is based upon work supported by the National Science Foundation under

Grant No. 1106171. Based on observations obtained with the Samuel Oschin Telescope 48-inch and the 60-inch Telescope at the Palomar Observatory as part of the Zwicky Transient Facility project. ZTF is supported by the National Science Foundation under Grant No. AST-2034437 and a collaboration including Caltech, IPAC, the Weizmann Institute of Science, the Oskar Klein Center at Stockholm University, the University of Maryland, Deutsches Elektronen-Synchrotron and Humboldt University, the TANGO Consortium of Taiwan, the University of Wisconsin at Milwaukee, Trinity College Dublin, Lawrence Livermore National Laboratories, IN2P3, University of Warwick, Ruhr University Bochum and Northwestern University. Operations are conducted by COO, IPAC, and UW. The ZTF forced-photometry service was funded under the Heising-Simons Foundation grant #12540303 (PI: Graham). The Gordon and Betty Moore Foundation, through both the Data-Driven Investigator Program and a dedicated grant, provided critical funding for SkyPortal.

The GROWTH India Telescope (GIT, Kumar et al. 2022) is a 70-cm telescope with a 0.7-degree field of view, set up by the Indian Institute of Astrophysics (IIA) and the Indian Institute of Technology Bombay (IITB) with funding from DST-SERB and IUSSTF. It is located at the Indian Astronomical Observatory (Hanle), operated by IIA. We acknowledge funding by the IITB alumni batch of 1994, which partially supports the operations of the telescope. Telescope technical details are available at https://sites.google.com/view/growthindia/. CZTI is built by a TIFR-led consortium of institutes across India, including VSSC, URSC, IUCAA, SAC, and PRL. The Indian Space Research Organisation funded, managed, and facilitated the project. This work is partially based on observations made with the Gran Telescopio Canarias (GTC), installed at the Spanish Observatorio del Roque de los Muchachos of the Instituto de Astrofísica de Canarias, on the island of La Palma. This work was also based on observations made with the Nordic

Optical Telescope, owned in collaboration by the University of Turku and Aarhus University, and operated jointly by Aarhus University, the University of Turku and the University of Oslo, representing Denmark, Finland and Norway, the University of Iceland and Stockholm University at the Observatorio del Roque de los Muchachos, La Palma, Spain, of the Instituto de Astrofisica de Canarias. The National Radio Astronomy Observatory is a facility of the National Science Foundation operated under cooperative agreement by Associated Universities, Inc. We thank the staff of the GMRT that made these observations possible. GMRT is run by the National Centre for Radio Astrophysics of the Tata Institute of Fundamental Research. We thank the staff of the Mullard Radio Astronomy Observatory for their invaluable assistance in the operation of the Arcminute Microkelvin Imager.

Quarter 4. X-ray Flash – Supernovae

"Then reach the stars, you take the time

To look behind and say,

Look where I came, look how far I done came

They say that dreams come true

And when they do, that there's a beautiful thing"

- J. Cole

Chapter 6: EP250108a/SN 2025kg: A Jet-Driven Stellar Explosion Interacting With Circumstellar Material

6.1 Introduction

Gamma-ray missions have discovered thousands of γ-ray bursts (GRBs), whose populations are relatively well characterized (Piran, 2004). However, satellites sensitive to soft X-rays (HETE-2's Wide-field X-ray Monitor, Beppo-Sax, $\sim$ 2 – 25 keV; MAXI, $\sim$ 0.5 – 30 keV) have found a much smaller number of bursts (Heise et al., 2001; Negoro et al., 2016; Sakamoto et al., 2005) with peak energies below those of classical GRBs (hundreds of keV). The origins of these extragalactic fast extragalactic X-ray transients (EFXTs) and X-ray flashes (XRFs)[1] are an open question. Some possibilities include high-z (Heise et al., 2001) or off-axis (Mészáros et al., 1998; Rhoads, 1997) GRBs, "dirty fireballs", or baryon-loaded GRBs with low Lorentz factors (Dermer et al., 1999), supernova (SN) shock breakout or cooling (Balberg & Loeb, 2011; Colgate, 1974), tidal disruption events (TDEs; Quirola-Vásquez et al. 2022), off-axis GRBs (Sarin et al., 2021), magnetars after binary neutron star mergers (Lin et al., 2022; Quirola-Vásquez et al., 2024), or new, exotic classes of transient phenomena. The archival nature of most EFXTs' discoveries and

[1] In the literature, there are often contradictions between how EFXTs and XRFs are defined. We define EFXTs as short flashes of X-ray emission that last a few minutes to a couple of hours, that are discovered in the soft X-rays (0.3 – 10 keV). We define X-ray Flashes (XRFs) as bursts of X-rays with true peak energies $E_p \lesssim 25\,\mathrm{keV}$. Therefore, an EFXT need not be an XRF, as they are defined by their discovered energy range, not their true peak energy. On the other hand, many XRFs are part of the EFXT population, as long as their peak energy is between 0.3 and 10 keV.

lack of real-time follow up (Quirola-Vásquez et al., 2022) made their characterizations historically difficult.

The Tianguan Telescope, or Einstein Probe (EP; Yuan et al. 2022b, 2015, 2018, 2025) is changing the landscape of X-ray time domain science, with its wide-field, soft X-ray capabilities. EP possesses an all sky monitor (ASM) Wide-field X-ray Telescope (WXT) that has an instantaneous field of view of 3600 $\deg^2$, operating from 0.4 to 5 keV. It has over 100 times the field of view of MAXI (Matsuoka et al., 2009), the only other currently operational X-ray ASM. In addition to WXT, EP also possesses two conventional X-ray focusing telescopes operating from 0.3 – 10 keV that can provide arcsecond localizations.

In its first year of operations, EP has already found a multitude of EFXTs, many of which have possible relations to GRBs and XRFs. EP240219a was interpreted as an X-ray rich (stronger X-ray than γ-ray emission) GRB (Yin et al., 2024). EP240315a had an optical and radio counterpart, and likely originated from a LGRB (Liu et al., 2025; Ricci et al., 2025) or a relativistic TDE (Gillanders et al., 2024). EP 240408A had no accompanying γ-ray emission and its X-ray properties are inconsistent with most known transient classes (Zhang et al., 2025). Possible origins include a white dwarf disrupted by an intermediate mass black hole or an exotic GRB (O'Connor et al., 2025a). EP240801a was a confirmed XRF, and was interpreted as either an off-axis or intrinsically weak jet (Jiang et al., 2025). EP241021a had no accompanying γ-ray emission, and also had a very luminous optical and radio counterpart (Busmann et al., 2025; Gianfagna et al., 2025; Shu et al., 2025; Wu et al., 2025; Yadav et al., 2025). Its interpretation is also not clear, though refreshed GRB shocks accompanying a low-luminosity GRB have been proposed as one scenario (Busmann et al., 2025), along with a compact star merger producing a compact object or binary compact object system (Wu et al., 2025), an intermediate mass black hole tidal disruption

event (Shu et al., 2025), an off-axis jet (Gianfagna et al., 2025), and more.

In addition, EP has discovered a few events that show clear SN associations, with a range of interpretations in the literature. EP240414a (Hamidani et al., 2025b; Srivastav et al., 2025; Sun et al., 2024; van Dalen et al., 2025; Zheng et al., 2025) is one such event. It had no accompanying γ-ray emission, and its peak energy was determined to be < 1.3 keV, making it an XRF. Its optical counterpart was a broad-lined Type Ic SN (SN Ic-BL), the type of SN found observationally associated to long GRBs (see, e.g., Cano et al. 2017a; Galama et al. 1998; Hjorth et al. 2003). It also possessed a mysterious red peak prior to the SN, which was described as interaction of a GRB jet with a dense circumstellar medium (van Dalen et al., 2025), shock cooling emission (SCE) following interaction with a dense circumstellar medium (Sun et al., 2024), an afterglow from a mildly relativistic cocoon (Hamidani et al., 2025b) or off-axis jet (Zheng et al., 2025), or refreshed shocks from a GRB (Srivastav et al., 2025). There have also been suggested resemblances (van Dalen et al., 2025) to luminous fast blue optical transients (LFBOTS; Drout et al. 2014; Ho et al. 2023; Margutti et al. 2019; Perley et al. 2019; Prentice et al. 2018; Pursiainen et al. 2018) due to its rise time, though its red colors indicate otherwise. Recently, EP250304a showed spectroscopic evidence that its optical counterpart was also a SN Ic-BL (Izzo et al., 2025), while possessing no associated γ-ray emission (Ravasio et al., 2025a).

Multi-wavelength studies of EP events with associated SNe Ic-BL are integral to understanding the link between EFXTs, XRFs, GRBs, SNe, and other classes of high-energy phenomena. In this Letter, we present EP250108a/SN 2025kg (Eyles-Ferris, 2025a), an EP transient without associated γ-ray emission and a SN Ic-BL optical counterpart, displaying a double-peaked LC. At the time of writing this Letter, two papers on this source have been published on arXiv, Eyles-Ferris et al. (2025) and Rastinejad et al. (2025). Eyles-Ferris et al. (2025) studies

the initial optical peak up to 6 days after the X-ray burst in addition to the X-ray and radio data, while Rastinejad et al. (2025) studies the accompanying SN Ic-BL from 6 days to 66.5 days after the X-ray burst. We provide comparisons of our analysis to each of these two works throughout the paper. Furthermore, we note that during the referee process, Li et al. (2025c) also published their paper on arXiv. This paper is from the EP science team, and presents the full prompt emission analysis (which was not available publicly at the time we submitted this work), in addition to characterizing the optical counterpart. Because this work was published during the referee process, we do not provide as detailed comparisons to their work as we do to Eyles-Ferris et al. (2025) and Rastinejad et al. (2025), but we still do compare important results when relevant.

The Letter is structured as follows: in §6.2 we present the optical photometry and spectroscopy, as well as radio and X-ray observations of EP 250108a/SN 2025kg, in §6.3 we present the analysis of these observations, in §6.4 we model the optical light curve, in §6.5 we estimate the prompt X-ray signal from the different models we tested, in §6.6 we discuss the implications of our results, and in §6.7 we provide a summary. We note that throughout this paper we utilize a flat ΛCDM cosmology with $\Omega_{\rm m} = 0.315$ and $H_0 = 67.4$ km s^{-1} Mpc^{-1} (Planck Collaboration et al., 2020) to convert the redshift to a luminosity distance and correct for the Milky Way extinction of $E(B-V)_{\rm MW} = 0.02$ (Schlafly & Finkbeiner, 2011a) mag, using the Cardelli et al. (1989c) extinction law with $R_v = 3.1$.

6.2 Observations

In this section, we present the observations used in our analysis of EP250108a/SN 2025kg. Hereafter, we refer to $\rm T_0$ as the beginning time of the X-ray prompt detection, or UT 2025-01-

08 12:30:28.34. The X-ray and γ-ray observations presented in §6.2.1 are taken from GCNs[2], and we also supplement our optical photometry with observations from GCNs at early times (Eyles-Ferris, 2025b; Izzo, 2025; Kumar et al., 2025; Moskvitin et al., 2025; Zhu et al., 2025b; Zou et al., 2025), as our photometry only begins at T_0 + 3.3 days. We will make all of our observations publicly available on WISeREP upon publication (Yaron & Gal-Yam, 2012). A log of spectroscopic observations and photometric observations are provided in the Appendix.

6.2.1 X-ray and Gamma-Ray Observations

The WXT on EP triggered on EP 250108a on UT 2025-01-08 12:30:28.34, at a location α (J2000)= 55.623 degrees and δ (J2000) = -22.509 degrees, with an uncertainty radius of 2.2 arcminutes (Li et al., 2025a). According to (Li et al., 2025a), the event lasted more than 2500 seconds, possessing a peak flux in the 0.5 – 4 keV band of $1.4 \times 10^{-10}\,\mathrm{erg\,cm^{-2}\,s^{-1}}$, and a time-averaged flux of $6.38^{+22.52}_{-3.00} \times 10^{-11}\mathrm{erg\,s^{-1}\,cm^{-2}}$. However, the prompt emission analysis from the EP Science team presented in Li et al. (2025c) report that the event lasted 960^{+3092}_{-208} s, with the large error bars due to an interruption in later observations due to the Earth's occultation.

Given the redshift $z = 0.176$ determined through optical spectroscopy (Zhu et al., 2025c) (corresponding to a distance 881 Mpc), the peak flux corresponds to a peak X-ray isotropic-equivalent luminosity of $\sim 1.3 \times 10^{46}\,\mathrm{erg\,s^{-1}}$, and an average isotropic-equivalent luminosity of $5.92^{+20.88}_{-2.77} \times 10^{45}\,\mathrm{erg\,s^{-1}}$. The source was followed up by EP's on-board follow-up X-ray telescope at UT 2025-01-09 10:42:46, 22.1 hours after the WXT trigger. No source was detected in 0.5 – 10 keV to an upper limit $3 \times 10^{-14}\mathrm{erg\,cm^{-2}\,s^{-1}}$ (Li et al., 2025b). The source was also followed up with the Neil Gehrels *Swift* Observatory's X-ray Telescope (Burrows et al., 2005;

[2]https://gcn.nasa.gov/

Gehrels et al., 2004) on UT 2025-01-10 15:17:00, 2.12 days after the WXT trigger. A source was not detected in 0.3 – 10 keV, to an upper limit 3.8×10^{-3} counts s^{-1} (Levan et al., 2025). For a canonical counts to flux conversion of 4×10^{-11} given the lack of an X-ray spectrum at this time, this count rate upper limit corresponds to a flux upper limit of $1.5 \times 10^{-13}\,\mathrm{erg\,cm^{-2}\,s^{-1}}$.

At the time of the burst, the burst's location was occulted by the Earth (Ravasio et al., 2025b) to *Fermi*'s Gamma-Ray Burst Monitor (Meegan et al., 2009). The location was visible 415 seconds after the burst, and assuming a Band function spectrum with $E_{\rm peak}$ = 70 keV, $\alpha = -1.9$, $\beta = -3.7$, and a duration of 8.192 s, the most conservative sky-averaged upper limit is a flux of $2.6 \times 10^{-8}\,\mathrm{erg\,cm^{-2}\,s^{-1}}$ from 10 – 1,000 keV (Ravasio et al., 2025b). At a redshift $z = 0.176$, this corresponds to an isotropic luminosity upper limit of $2.4 \times 10^{48}\,\mathrm{erg\,s^{-1}}$, or isotropic energy upper limit of $2.0 \times 10^{49}\,\mathrm{erg}$. Because the field was only visible shortly after the burst began, these values cannot be taken as a strict upper limits for the prompt emission. However, these values are very low in comparison to those derived for classical GRBs, and are similar to low-luminosity GRBs (LLGRBs; $L_{\rm iso} < 10^{49}\,\mathrm{erg\,s^{-1}}$ Liang et al. 2007; Virgili et al. 2009a).

6.2.2 LT

We obtained Liverpool Telescope (LT; Steele et al. 2004) observations with the IO:O camera in the SDSS g, r, and i filters at multiple epochs, starting at three days post EP trigger. Basic reductions (bias subtraction, flat fielding, and astronomy) were provided by the automatic IO:O pipeline, and these reduced images were downloaded from the LT archive. The signal-to-noise of the first three epochs is low due to poor observing conditions, and a small number of frames affected by tracking errors or with very poor seeing were discarded. The remaining frames were

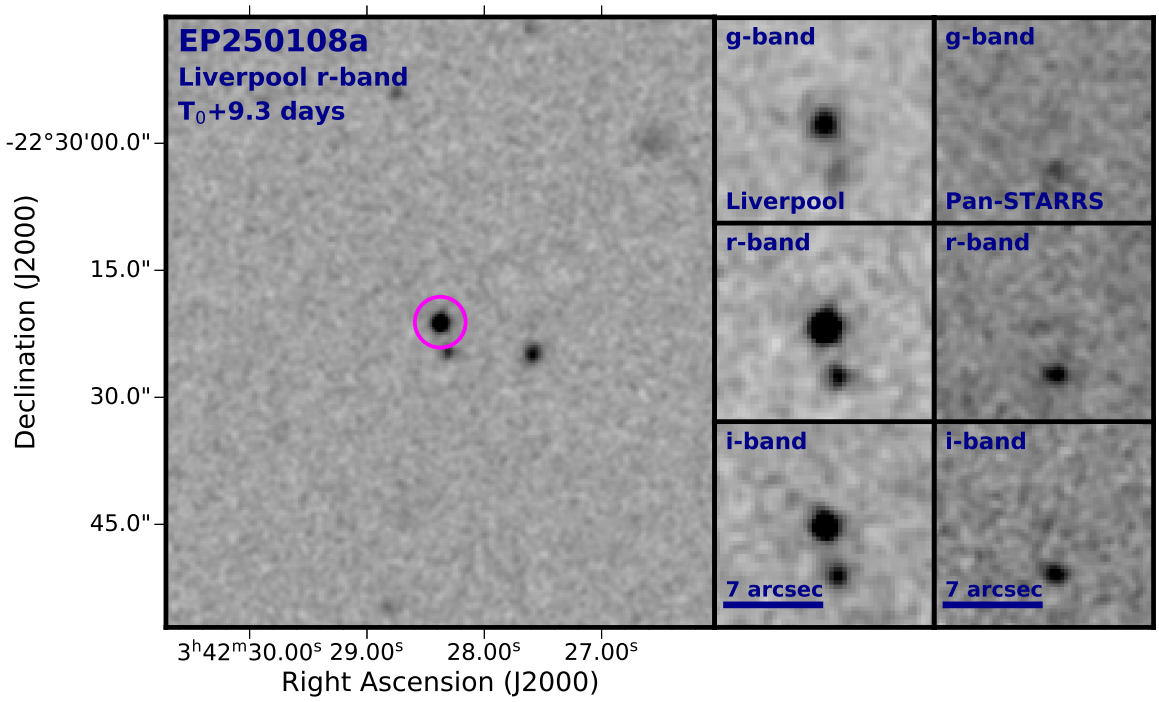

Figure 6.1: LT images of EP 250108a/SN 2025kg The left, large panel shows the wider field of view of EP 250108a, in r band 9.3 days after T_0. The right panels show the observations taken in the g, r, and i bands, as well as the Pan-STARRS1 templates used for photometry. The host galaxy is faint ($r \sim 23.2$; Dey et al. 2019), so image subtraction is not necessary until the final epoch. Images have been smoothed for display purposes.

stacked using the `SWarp` software (Bertin, 2010b). PSF photometry on obtained stacks was performed with the use of `SExtractor` (Bertin & Arnouts, 1996b) and `PSFex` (Bertin, 2013), relative to the Panoramic Survey Telescope and Rapid Response System 1 (Pan-STARRS1) catalogue (Chambers et al., 2016b). in Figure 6.1, we show the LT images from 9.3 days after the explosion time, along with Pan-STARRS1 reference images.

6.2.3 NOT

The AUTOPHOT (Brennan & Fraser, 2022) pipeline was employed to perform photometric measurements on NOT/ALFOSC images. For each image, the World Coordinate System

(WCS) values were verified using ASTROMETRY.NET (Lang et al., 2010b). An effective point spread function (ePSF) model was constructed using bright, isolated sources in the image with the `Photutils` package (Bradley et al., 2024). Zeropoints were calibrated against sequence sources in the ATLAS All-Sky Stellar Reference Catalog (REFCAT2; Tonry et al., 2018) for sloan- $griz$ images.

Science and reference images from Pan-STARRS1 were aligned using `SWarp`, and reference image subtraction was performed utilizing the saccadic fast Fourier transform (`SFFT`) algorithm (Hu et al., 2022) to isolate transient flux.

6.2.4 IMACS

We observed one epoch of Sloan-g, r, and i band images of SN 2025kg with the Inamori-Magellan Areal Camera and Spectrograph (IMACS; Dressler et al. 2011) on 05 February 2025. The images were reduced using standard procedures, including bias subtraction and flat fielding. We performed PSF photometry on the reduced images and calibrated the photometry relative to the Pan-STARRS1 catalogue (Chambers et al., 2016b).

6.2.5 GHTS

We obtained two epochs of longslit spectroscopy of SN 2025kg with the Goodman High throughput Spectrograph (GHTS; Clemens et al. 2004) mounted on the Southern Astrophysical Research (SOAR) telescope on 18 January 2025 and 23 January 2025. The observations consisted of 6 $\times$ 600 seconds of exposures. Both observations were taken with a grating of 400 lines/mm and a 1.0" wide slit mask in the M1 spectroscopic setup (hereafter 400M1) with 2×2 binning

using the GHTS Red Camera. The 400M1 spectra cover a wavelength range of 3800 – 7040 $\AA$.

The spectra were reduced using `pypeit` (Prochaska et al., 2020b,c), using arcs taken immediately before and/or after target observation and calibration images from the same night. Flux calibration was performed using standard stars observed on the night of the observations with an identical 400M1 setup and 2×2 binning.

We also imaged the location of SN 2025kg on 23 and 31 January 2025 with SOAR/GHTS in imaging mode. We took three 60 s exposures each in g and r-band on the first epoch and six, 90 s exposures each in g and r-band on the second epoch. After bias-correction, flat fielding, background subtraction and astrometric correction using ASTROMETRY.NET (Lang et al., 2010b), the images were stacked with SWARP (Bertin, 2010b). We performed image subtraction on the stacked images using `SFFT` with an archival template from the DECam Legacy Survey (Dey et al., 2019). Aperture photometry was conducted with SEXTRACTOR (Bertin & Arnouts, 1996b) and zeropoints were measured from the Pan-STARRS1 catalogue (Chambers et al., 2016b).

6.2.6 LRIS

We obtained one epoch of longslit spectroscopy of SN 2025kg on 25 January 2025 with the Keck Observatory Low Resolution Imaging Spectrometer (LRIS) (Oke et al., 1995b). This observation consisted of 3 $\times$ 900 second exposures on both blue and red sides using a 1.0" slit mask. We used the 400/3400 grating for blue exposures and the 400/8500 grating for the red exposures, and the spectrum had wavelength coverage 3000 – 9300 $\AA$. These observations were reduced using LPipe (Perley, 2019a).

6.2.7 Binospec

We obtained one epoch of long-slit spectroscopy of SN 2025kg with Binospec (Fabricant et al., 2019) on the MMT Observatory 6.5-m telescope on 03 February 2025. The observation consisted of 3 $\times$ 900 second exposures. The data were acquired with a grating of 270 lines per mm and a 1.0" slit mask. The basic data processing (bias subtraction, flat fielding) is done using the Binospec pipeline (Kansky et al., 2019). The processed images are downloaded from the MMTO queue observation data archive. The spectra are reduced with IRAF, including cosmic-ray removal, wavelength calibration (using arc lamp frames taken immediately after the target observation), and relative flux calibration with archived spectroscopic standards observation. The Binospec spectrum has a wavelength coverage of 3900–9240 $\mathring{A}$.

6.2.8 GMOS

SN 2025kg was observed using GMOS (Gimeno et al., 2016; Hook et al., 2004) long-slit at the Gemini South telescope in Cerro Pachon, Chile, on the nights of 2025 January 13, 23, and 29. The grating B480 was used at central wavelength 5400/5450 $\mathring{A}$ with 2 $\times$ 2 binning, giving wavelength coverage of around 3800–7500 $\mathring{A}$ at $R \sim 1400$. The observations consisted of 4 $\times$ 600 s exposures, except for January 29 (4 $\times$ 420 s). Standard data reduction process was performed using the Gemini DRAGONS package (Labrie et al., 2023), resulting in wavelength and flux-calibrated spectra.

6.2.9 VLA

We observed the location of EP250108A with NSF's Karl G. Jansky Very Large Array (VLA) on 15 January 2025 at a mid-time of 00:53 UT ($\delta t = 6.5$ days post discovery) at a mid-frequency of 10 GHz (4 GHz bandwidth), for a total of 0.6 hours on source (Program 25A-374, PI Perley). We used J0329-2357 for phase and gain calibration and 3C147 for flux and bandpass calibration. Data reduction and imaging was performed using the Common Astronomy Software Applications (CASA; McMullin et al. 2007b) VLA Calibration Pipeline[3] and the VLA Imaging Pipeline[4]. No source was detected at or near the position of EP250108a/SN 2025kg in this observation. We used the program `pwkit/imtool` (Williams et al., 2017) to measure the rms of the image, and determine a 3σ upper limit on a radio counterpart of $F_\nu \lesssim 13.5$ μJy (Schroeder et al., 2025a). We initiated three additional VLA epochs at $25.6, 47.5, 52.5$ days, and do not detect any sources at the position of EP250108a/SN2025kg. A summary of these observations is presented in Table E.3.

6.3 Analysis

6.3.1 Light Curve Analysis

We show the gri light curve of EP250108a/SN 2025kg in Figure 6.2. The light curve clearly has two peaks. The first peak rises on the timescale of less than a day after T_0 and displays blue colors ($g-r = -0.4$ mag), and then declines until 5 days after T_0 (though this decline extends till day 8 in g band). Initially, the rapid rise, blue colors, and luminous ($M_g \sim -19.5$ mag) emission

[3] `https://science.nrao.edu/facilities/vla/data-processing/pipeline`
[4] `https://science.nrao.edu/facilities/vla/data-processing/pipeline/vipl`

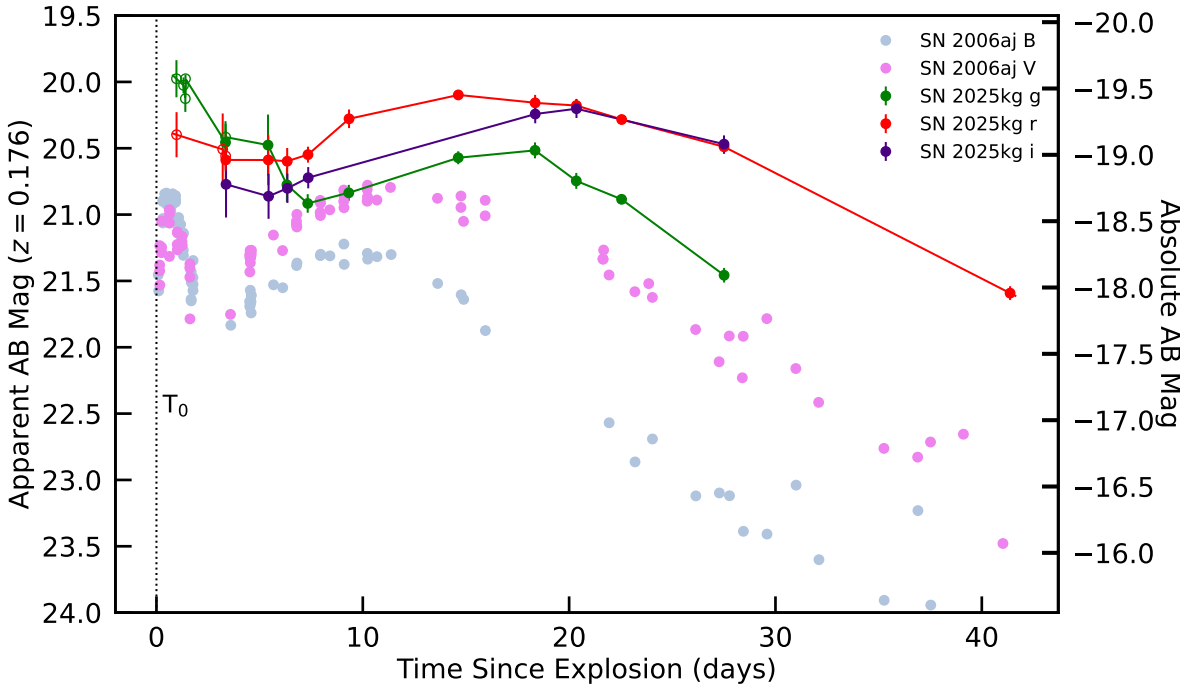

Figure 6.2: Light curve of SN 2025kg in g, r, and i bands connected with a curve, where all measurements have been corrected for MW extinction and times are in the observer frame. Hollow circles are photometry points taken from GCNs, while filled circles are photometry taken from our observations. For comparison, we show the B and V-band light curves of SN 2006aj (Bianco et al., 2014; Brown et al., 2014; Modjaz et al., 2006) also corrected for MW extinction, transformed to the redshift of SN 2025kg ($z = 0.176$). We also show the absolute magnitudes on the right axes. SN 2025kg's light curve displays very similar features to SN 2006aj, though it is more luminous and evolves more slowly.

led some authors to draw a connection with LFBOTs (Zhu et al., 2025d). However, there was a transition to red colors along with a slower rise after the initial decline, behavior which has never been seen in an LFBOT, but has been seen in certain SNe with early shock-powered peaks.

We spectroscopically confirm a SN Ic-BL classification during the later phase of the optical light curve in §6.3.3. The SN Ic-BL, SN 2025kg (Agui Fernandez et al., 2023a), rises to maximum light during its second peak on a timescale of $\sim$ 15 days in r band, and 18 days in g band. The peak absolute magnitudes ($M_r = -19.39 \pm 0.02$, $M_g = -18.95 \pm 0.06$) are brighter than the

average SNe Ic-BL population ($M_r = -18.5 \pm 0.9$ mag, Srinivasaragavan et al. 2024b; Taddia et al. 2019a), but still are within the overall range seen for SNe Ic-BL in the literature (-16.86 to -20.9 mag, Srinivasaragavan et al. 2024b; Taddia et al. 2019a), and consistent with GRB-SNe (e.g., GRB 980425/SN 1998bw: $M_R = -19.36 \pm 0.05$, Galama et al. 1998; GRB 230812B/SN 2023pel: $M_r = -19.46 \pm 0.18$ mag, Srinivasaragavan et al. 2024a).

Das et al. (2024) found an empirical correlation between the first peak and second peak in a sample of stripped-envelope SNe (which included 2 SNe Ic-BL) where the mechanism used to describe the first peak was shock cooling emission from SN ejecta interacting with an extended CSM (Piro et al., 2021). This correlation is $M_2 = 0.8 \times M_1 - 4.7$, where M_1 and M_2 are the absolute magnitudes of the first and second peak, respectively, in r band. Utilizing this expression, given the brightness of the second peak, we expect the first peak to have a brightness of $M_r \sim -18.4$ mag. The first peak is brighter than expected from the correlation, with $M_r \sim -19.1$ mag. This is not surprising, as only 2 SNe Ic-BL were in the sample that Das et al. (2024) used to create this correlation. However, it is notable that the overall trend is still followed, where the first peak is more luminous than the second peak.

In Figure 6.2, we also show the light curve of SN 2006aj (Bianco et al., 2014; Brown et al., 2014; Modjaz et al., 2006), shifted to the redshift of SN 2025kg, with the cosmological correction for redshift implemented on the magnitudes. SN 2006aj is a SN Ic-BL linked to the low luminosity (LL) GRB 060218 that shows a similar double-peaked optical light curve and soft X-ray prompt emission (Campana et al., 2006; Ferrero et al., 2006; Mirabal et al., 2006; Pian et al., 2006; Soderberg et al., 2006a; Sollerman et al., 2006) as EP250108a/SN 2025kg. Though we do not show the light curve in the Figure for visual purposes, we also compare the light curve to that of SN 2020bvc (Ho et al., 2020e). SN 2020bvc is a SN Ic-BL found independently of

a high-energy trigger (Ho et al., 2020e; Izzo et al., 2020; Rho et al., 2021), that also displays a similar double-peaked light curve, and possesses X-ray and radio emission similar to other LLGRBs.

SN 2006aj's and SN 2020bvc's first peak fades on the timescale of around one day, which is significantly faster than the fading timescale for SN 2025kg. Furthermore, the peak absolute magnitudes of this first peak are significantly fainter for SN 2006aj ($M_B \sim -18.5$ mag) and SN 2020bvc ($M_g \sim -18.1$ mag). We note here that the first peaks derived for both SN 2025kg and SN 2020bvc may not be the true "peak", as both events are fading after their first detection. Therefore, the true peak might be more luminous, and be earlier than the first detection. The second peaks are also fainter, as SN 2006aj possesses a peak $M_V \sim -18.8$ mag (Ferrero et al., 2006), and SN 2020bvc possesses a peak $M_r \sim -18.7$ mag.

Later on the text, we also compare SN 2025kg's properties to those of iPTF16asu (Whitesides et al., 2017) and SN 2018gep (Ho et al., 2019b; Leung et al., 2021b; Pritchard et al., 2021). These SNe were SNe Ic-BL found independent of high energy triggers and did not display a clear double-peak in their light curves. However, their quick rise times, luminous peaks, and blue colors at peak indicate a likely additional powering mechanism making contributions to the early-time light curve (more in §6.4), justifying the comparison with SN 2025kg.

6.3.2 Bolometric Luminosity Light Curve

We create SN 2025kg's bolometric luminosity light curve through utilizing bolometric correction (BC) coefficients (Lyman et al., 2014a, 2016a). We have sparse i-band photometric coverage of SN 2025kg (see Figure 6.2), but have sufficient coverage in the g and r bands over

numerous epochs. Therefore, we can utilize the BC coefficients, which depend on $g-r$ colors, to compute a bolometric luminosity light curve. These coefficients were measured by fitting the SEDs of a large sample of stripped-envelope SNe with broadband coverage across the ultraviolet, optical, and infrared wavelengths, and can be utilized to convert between $g-r$ colors and an absolute bolometric magnitude. We note that SNe Ic-BL may have slightly different color evolution than that of other stripped-envelope SNe; however the BC coefficients were calculated with a few SNe Ic-BL in the overall dataset (Lyman et al., 2014a), and most sample papers of SNe Ic-BL (Anand et al., 2023; Corsi et al., 2023; Srinivasaragavan et al., 2024b; Taddia et al., 2019a) use this method to calculate bolometric luminosity LCs.

We use two different BC coefficients in our analysis - one for the shock cooling phase, and one for the radioactive decay phase, both from Lyman et al. (2014a). The BC coefficient for the shock cooling phase is described as

$$\mathrm{BC}_g = -0.146 + 0.479 \times (g-r) - 2.257 \times (g-r)^2. \tag{6.1}$$

We note that this coefficient was not calculated specifically for stripped envelope SNe, as there was a lack of sufficient events to do so. The BC coefficient for stripped envelope SNe in the radioactive decay phase is

$$\mathrm{BC}_g = 0.054 - 0.195 \times (g-r) - 0.719 \times (g-r)^2, \tag{6.2}$$

with $-0.3\ \mathrm{mag} < g-r < 1.0\ \mathrm{mag}$. We note that we have one r-band point at $T_0 + 41$ days that does not have an accompanying g band point. We extrapolate the g-band light curve using

the `scipy.interp1d` package to obtain a g-band photometric point to use for the creation of a bolometric luminosity at late times. We then calculate the $\mathrm{BC_g}$ coefficient for every epoch in our sample where we have simultaneous r and g-band observations. Finally, using the definition of BC coefficients:

$$\mathrm{BC}_x = M_{\mathrm{bol}} - M_x, \tag{6.3}$$

we calculate the absolute bolometric magnitude light curve, and convert to a bolometric luminosity light curve given the distance luminosity at $z = 0.176$.

We present the bolometric luminosity light curve in Figure 6.3, and compare it to SN 2006aj, SN 2020bvc, and SN 2018gep. Similar to the photometry in Figure 6.2, the peak bolometric luminosity of the first peak and second peak are significantly larger than those of the other two compared events, while evolving on slower timescales. SN 2018gep does not display a double peaked LC, and has a more luminous peak, though its luminosity declines much more rapidly than the other three events.

6.3.3 Spectral Analysis

We obtained 7 spectra of SN 2025kg up to 26 days after T_0 and present them in Figure 6.4. Here we discuss the spectroscopic evolution, along with comparisons to other similar events.

A close-up of the first spectrum is shown in Figure 6.5, along with spectra of SN 2006aj (Modjaz et al., 2006) and SN 2020bvc (Ho et al., 2020e) at similar epochs. The spectrum displays an underlying blue continuum, and is best fit with a blackbody with $L_{\mathrm{bol}} = (1.60 \pm 0.31) \times 10^{43}\,\mathrm{erg\,s^{-1}}$, $T_{\mathrm{BB}} = (13.69 \pm 3.64) \times 10^3\,\mathrm{K}$, and $R_{\mathrm{BB}} = (1.11 \pm 0.10) \times 10^{15}\,\mathrm{cm}$. SN 2025kg

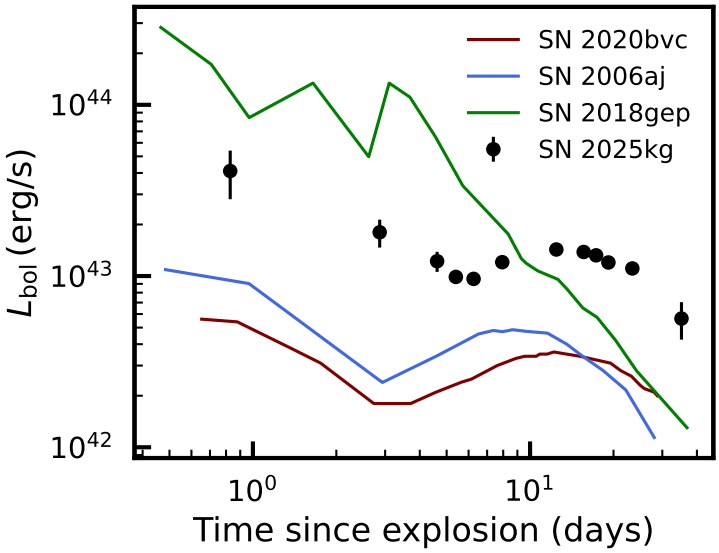

Figure 6.3: Bolometric luminosity LC of SN 2025kg, compared to SN 2006aj (Bianco et al., 2014; Brown et al., 2014; Modjaz et al., 2006), SN 2020bvc (Ho et al., 2020e), and SN 2018gep (Ho et al., 2019b; Leung et al., 2021b; Pritchard et al., 2021), with times in the rest frame. SN 2025kg's bolometric luminosity LC has a very similar shape to that of SN 2006aj and SN 2020bvc, while being more luminous and evolving on a slightly slower timescale. SN 2018gep does not have a double peak, and has a higher initial luminosity, but has a more rapid decline in luminosity over time.

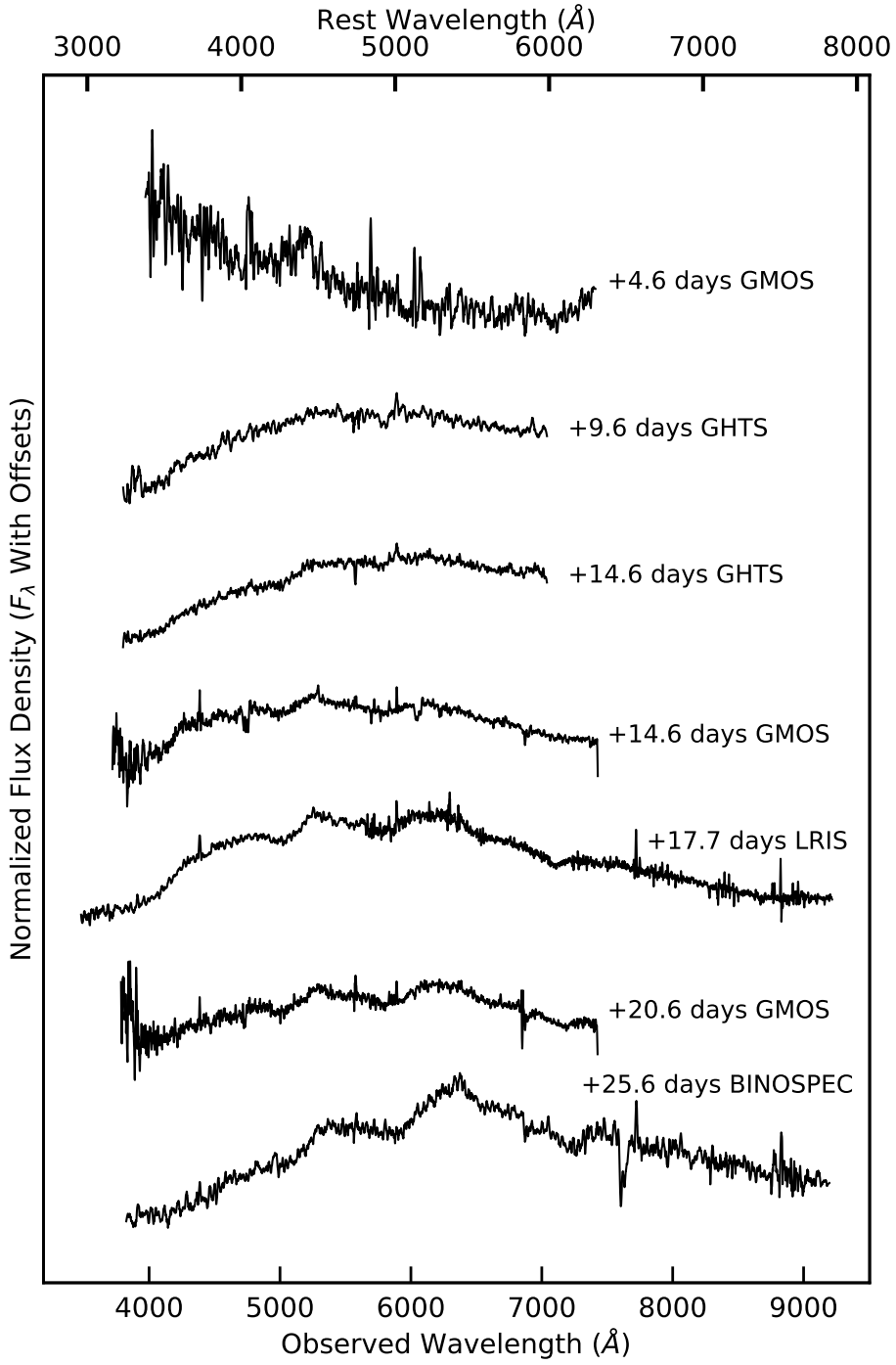

Figure 6.4: Optical spectra of SN 2025kg. The phases are relative to the time of the accompanying X-ray transient EP 250108a's detection. The spectra starts dominated by a blue underlying continuum, though broad features already are beginning to develop in the first epoch. The spectra reddens with time and strongly resembles a SN Ic-BL.

Time (days)	$v_{\rm ph}$ ($\rm km\,s^{-1}$)
4.6	$32440 \pm 3388^{*}$
14.6	17128 ± 2389
17.7	14779 ± 2837
20.6	13043 ± 2069
25.6	10816 ± 2373

Table 6.1: Photospheric velocity measurements of SN 2025kg. *The first measurement must be treated with caution, due to the uncertainty of a Fe II feature in the first spectra (see §6.3.3 for details).

is significantly hotter than SN 2006aj and SN 2020bvc at similar phases. Since the initial radius of the progenitor is $<< R_{\rm BB}$, the mean velocity over the first 3.9 (rest-frame) days is therefore $1.1 \times 10^{15}\,{\rm cm}/3.9 \sim 0.1c$. This is the same mean velocity that was derived for SN 2020bvc during the first 1.8 days (Ho et al., 2020e). Therefore, since the photospheric velocity slows with time, this means that SN 2025kg has relatively faster moving ejecta than SN 2020bvc at earlier times (which we also later confirm with explicit velocity measurements).

Furthermore, we also identify a possible broad absorption feature in SN 2025kg's first spectrum centered around 4100 $\mathring{A}$ that peaks at 4500 $\mathring{A}$, which could be due to a blue shifted Fe II absorption feature (rest-frame 5169 $\mathring{A}$), commonly seen in SNe Ic-BL. The photospheric velocity inferred from this feature is $\sim 0.1c$ (see Table 6.1), which is consistent with the speed derived from the blackbody fitting. This feature is also present in SN 2006aj's and SN 2020bvc's spectra.

However, this line identification is not robust, for multiple reasons. First, there is an emission feature around 4100 $\mathring{A}$, that we determine is not a real feature, as it is due to noisy spikes in the spectra. Therefore, the slight undulation between 3800 and 4800 $\mathring{A}$ must be interpreted with caution. Furthermore, at the blackbody temperature that we derive (> 13000 K), Fe has mostly transitioned from Fe II to Fe III (Nugent et al., 1995). In addition, at the high velocities

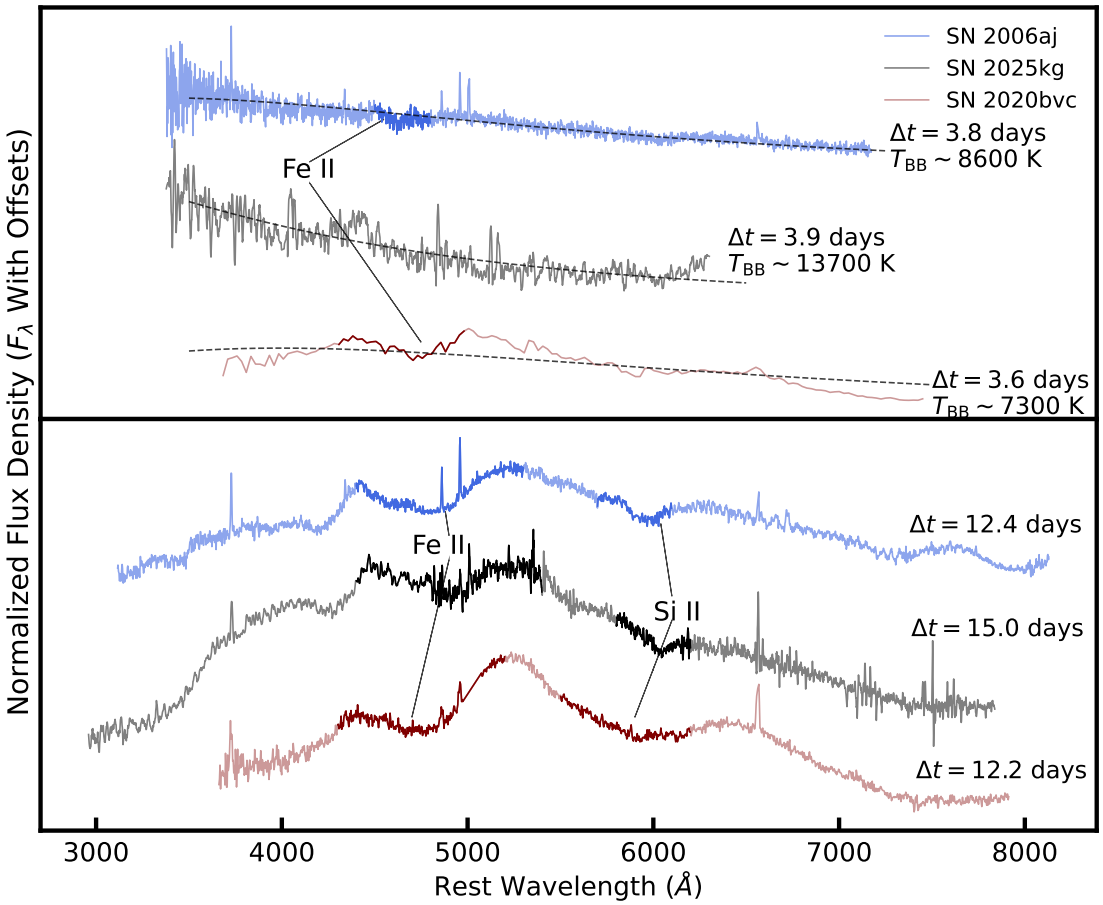

Figure 6.5: Spectra of SN 2025kg compared to spectra of SN 2006aj (Modjaz et al., 2006) and SN 2020bvc (Ho et al., 2020e) at similar epochs, with times shown in the rest frame. Some host galaxy lines are clipped for display purposes. The top panel shows the earliest spectrum we have of SN 2025kg along with comparison spectra, and we fit a blackbody to each spectrum to derive temperatures. We find that SN 2025kg has the highest temperature, and a possible broad Fe II feature is beginning to emerge in the spectrum (though we must interpret this with caution, more in §6.3.3, therefore we do not bold it in the Figure), and also show blueshifted Fe II features in SN 2006aj and SN 2020bvc's early time spectra. The bottom panel shows a spectrum taken at the time of the peak of SN 2025kg in r band, along with comparison spectra. We see clear blueshifted Fe II and Si II absorption features enabling a SN Ic-BL classification, labeled and shown in bold for SN 2025kg and for SN 2006aj and SN 2020bvc.

that we derive for the Fe II feature later in this Section, the Fe II 5169 $\mathring{A}$ feature may be blended with the Fe II features at 5018 and 4924 $\mathring{A}$. Finally, in §6.4 we show that the optical flux during the time of the first spectral epoch (4.6 days) has contributions from an additional component (CSM interaction, or a shocked cocoon), than just the radioactive decay of Nickel. If the flux is dominated by this additional component, it is surprising that a photospheric Fe line would be a dominant feature in the spectra; however, there are still strong contributions from the radioactive decay of Nickel during this epoch, so the possibility that a photospheric Fe line exists is still relevant. There is also a possible emission feature at around 4500 $\mathring{A}$, which may be due to [Mg I] at 4571 $\mathring{A}$, though this feature is usually strong at later phases. However, due to the noise in the spectra, this interpretation must also be taken with caution.

Maeda et al. (2023) compute synthetic spectra of engine-driven explosions with brief energy injection from the central engine, and find in their models that a peak in the early-time (< 7 days after explosion) spectrum at 4500 $\mathring{A}$ and the lack of a peak between 5500 and 6000 $\mathring{A}$ is indicative of a higher velocity component in the ejecta ($> 60{,}000\ \mathrm{km\,s^{-1}}$), that is greater than the normal photospheric velocity at the time. We see this same behavior in SN 2025kg, which points towards a higher velocity component at early-times, giving evidence that a collapsar jet-driven system may be necessary to explain SN 2025kg's properties (more in §7.6).

SN 2025kg's spectra turn redder with time, and further broad absorption features develop like Si II (rest-frame 6347 $\mathring{A}$), along with the continued lack of H and He features. We run the GHTS spectrum 9.6 days after T_0 in the Supernova Identification Code (Blondin & Tonry, 2007b), and find the best-fit spectrum is SN Ic-BL 2002ap (Mazzali et al., 2002), and the spectra at later phases continue to show SN Ic-BL matches, allowing for a classification. We also show a spectrum 15 days after T_0, during the SN's peak light in r band in Figure 6.5, along with SN

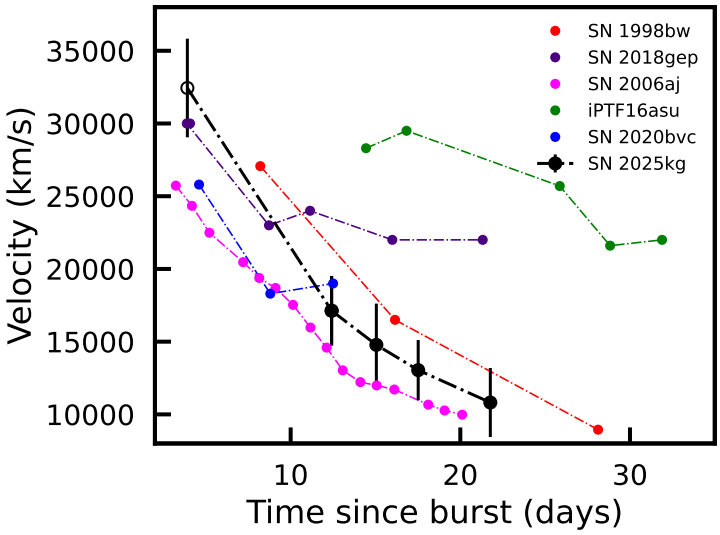

Figure 6.6: Photospheric velocity evolution for SN 2025kg, compared to other prominent LL-GRB SNe (SN 1998bw, Iwamoto et al. 1998a; SN 2006aj, Mazzali et al. 2006a) and other SNe Ic-BL that likely have different powering mechanisms than just radioactive decay (iPTF16asu, Whitesides et al. 2017; SN 2018gep, Ho et al. 2019b; SN 2020bvc, Ho et al. 2020e), with times in the rest frame. SN 2025kg's $v_{\rm ph}$ evolves very similarly to SN 2006aj. The first measurement is shown with an open circle due to the uncertainty in the identification of a Fe II feature (see §6.3.3 for details).

2006aj's and SN 2020bvc's spectra at similar phases. We see clear broad absorption features in the spectrum blueshifted with characteristic velocities. We label the Fe II and Si II features, which are good indicators of the photospheric velocity (Modjaz et al., 2016). By eye, we see that the absorption troughs for the Fe II feature in both SN 2025kg and SN 2006aj are centered around 5000 $\mathring{A}$, and around 4800 $\mathring{A}$ for SN 2020bvc. This indicates that SN 2020bvc has a higher photospheric velocity near peak, even though it had a slower velocity at earlier times.

We then measure the equivalent width (EW) of the Na I absorption doublet (5890, 5896 $\mathring{A}$), using the LRIS spectrum at 17.7 days after T_0. This feature is known to be a proxy for the amount of host-galaxy extinction present in systems (Stritzinger et al., 2018). We can convert the EW to a host-galaxy extinction value through the relation from Stritzinger et al. (2018): $A_{\rm V}^{\rm host}[\rm mag] = 0.78(\pm0.15) \times \rm EW_{Na\,I}$. But, Poznanski et al. (2011) showed that when using low-resolution

spectra, a large scatter exists in the correlation between the two parameters, and quantitative relations found using the correlation, such as that of Stritzinger et al. (2018), must be viewed conservatively. Therefore, following the methodology used in Srinivasaragavan et al. (2024b) in their sample of SNe Ic-BL, we compute a conservative upper limit on the amount of host-galaxy extinction for SN 2025kg utilizing this relation. We measure an EW of $EW_{\rm Na\,I} = 0.38 \pm 0.13$, which corresponds to an upper limit on the host-galaxy extinction of $A_{\rm V}^{\rm host}[{\rm mag}] < 0.47$. We note that (Rodríguez et al., 2023b) present a different relation between $EW_{\rm Na\,I}$ and $A_{\rm V}^{\rm host}$, with $A_{\rm V}^{\rm host}[{\rm mag}] = 0.02 + 0.73 \times {\rm EW}_{\rm Na\,I} \pm 0.29$. Using this relation, we would derive $A_{\rm V}^{\rm host}[{\rm mag}] < 0.60$. The difference between these two values is negligible, and we use the methodology from Stritzinger et al. (2018) to be consistent with the SNe Ic-BL sample in (Srinivasaragavan et al., 2024b).

We measure the velocity of the Fe II line at 5169 $\mathring{A}$ for each spectrum taken using the open source code SESNspectraLib[5] (Liu et al., 2016; Modjaz et al., 2016), which has been shown to be a good proxy for the photospheric expansion velocity $v_{\rm ph}$ (Modjaz et al., 2016). In order to do so, we first remove narrow galaxy emission lines and artifacts from bad pixels using the IRAF-based tool WOMBAT, and then smooth the spectra using SESNspectraPCA[6]. SESNspectraLib calculates the blueshift of the Fe II line at 5169$\mathring{A}$ relative to a standardized SN Ic spectroscopic template at the same phase. We estimate the uncertainty on the velocity by adding the uncertainty on the mean SN Ic template velocity in quadrature with the uncertainty on the relative blue-shift. We note that the velocity derived for the first epoch at 4.6 days must be treated with caution, as the broad feature between 3800 and 4800 $\mathring{A}$ was not confirmed as being due to Fe II, as mentioned

[5]https://github.com/metal-sn/SESNspectraLib
[6]https://github.com/metal-sn/SESNspectraPCA

earlier.

In Figure 6.6, we compare $v_{\rm ph}$ for SN 2025kg to LLGRB 980425/SN 1998bw (Iwamoto et al., 1998a), SN 2006aj (Mazzali et al., 2006a), SN 2020bvc (Ho et al., 2020e; Izzo et al., 2020; Rho et al., 2021), iPTF16asu (Whitesides et al., 2017) and SN 2018gep (Ho et al., 2019b; Leung et al., 2021b; Pritchard et al., 2021). We find that SN 2025kg's $v_{\rm ph}$ evolves very similarly to SN 1998bw and SN 2006aj, and its velocity is in between the two events. SN 2020bvc's $v_{\rm ph}$ is slower at early times, but then flattens out and becomes consistent at around day 12. SN 2018gep's $v_{\rm ph}$ is similar and shows a similar evolution at early times, but then flattens out and is significantly faster than SN 2025kg at later epochs. There are no early time constraints on iPTF16asu's $v_{\rm ph}$, but it also is significantly faster than SN 2025kg at later times, along with possessing a flatter evolution.

6.3.4 Radio Analysis

Historically, the majority of SNe associated with GRBs have been SNe Ic-BL, similar to SN 2025kg (Cano et al., 2017a; Modjaz et al., 2016). Therefore, the association of a Ic-BL SN with EP 250108A may indicate that the initial X-ray activity of EP 250108A is actually a LLGRB or a GRB observed off-axis (Urata et al., 2015; Yamazaki et al., 2003). Here, we use our radio observations to explore the possibility of a GRB progenitor for EP 250108A.

The VLA observations of EP 250108A allow us to place limits on the 10 GHz luminosity of $\lesssim 10^{28}$ erg s^{-1} Hz^{-1} (assuming $z = 0.176$), at rest-frame times of $\sim 5.5 - 44.7$ days (Figure 6.7). Our radio limits are ~ 3 orders of magnitude lower than the radio luminosity of typical on-axis long GRBs (e.g. Chandra & Frail, 2012), effectively ruling out a standard on-axis long GRB.

Similarly, the radio emission observed following the X-ray flash (XRF) 020903 is ruled out, as the radio luminosity of XRF 020903 is $\sim$ 2 orders of magnitude higher at a similar rest frame time (Soderberg et al., 2004). The canonical low-luminosity GRB is LLGRB 980425/SN 1998bw (Galama et al., 1998). Our radio observations of EP 250108A are $\sim$ 2–7 $\times$ deeper than the radio emission observed following LLGRB 980425/SN 1998bw, ruling out 1998bw-like emission (Kulkarni et al., 1998; Waxman et al., 1998). However, our limits cannot rule out fast-fading radio emission similar to the low-luminosity event LLGRB 060218/SN 2006aj (Soderberg et al., 2006a), or the nearby SN Ic-BL 2020bvc (Ho et al., 2020e). Late-rising AT2018cow-like emission is ruled out by our final VLA observation (Margutti et al., 2019).

Next, we explore whether EP 250108A could originate from an off-axis GRB, where the expectation is that the afterglow could become detectable at late times as the jet of the GRB decelerates and the beaming angle opens into our line of sight. (e.g., Eichler & Levinson 1999; Nakar et al. 2002; van Eerten et al. 2010). Many searches for late-rising afterglows have been conducted following SNe Ic-BL, with no definitive off-axis candidates to date (e.g. Berger et al., 2003b; Corsi et al., 2016, 2023; Soderberg et al., 2006a), though an off-axis model was favored for SN 2020bvc by Izzo et al. (2020). We test whether our radio limits could be consistent with an off-axis afterglow by generating model light curves using the `FIREFLY` code (Dastidar & Duffell, 2024). We set the power-law electron distribution to $p = 2.133$, the jet opening angle to $\theta_{\rm j} = 7^{\circ}$, and the energy imparted onto the electrons and magnetic field to $\epsilon_{\rm e} = 0.1$ and $\epsilon_{\rm B} = 0.01$ (similar to the values found for LGRBs e.g. Cenko et al., 2010, 2011; Kangas & Fruchter, 2021; Panaitescu & Kumar, 2002a; Ryan et al., 2015; Schroeder et al., 2022; Yost et al., 2003), and we vary the total energy of the GRB jet (E) and the circumburst density (n). We note that we assume a constant density ISM environment – see Eyles-Ferris et al. (2025) for models presented in a

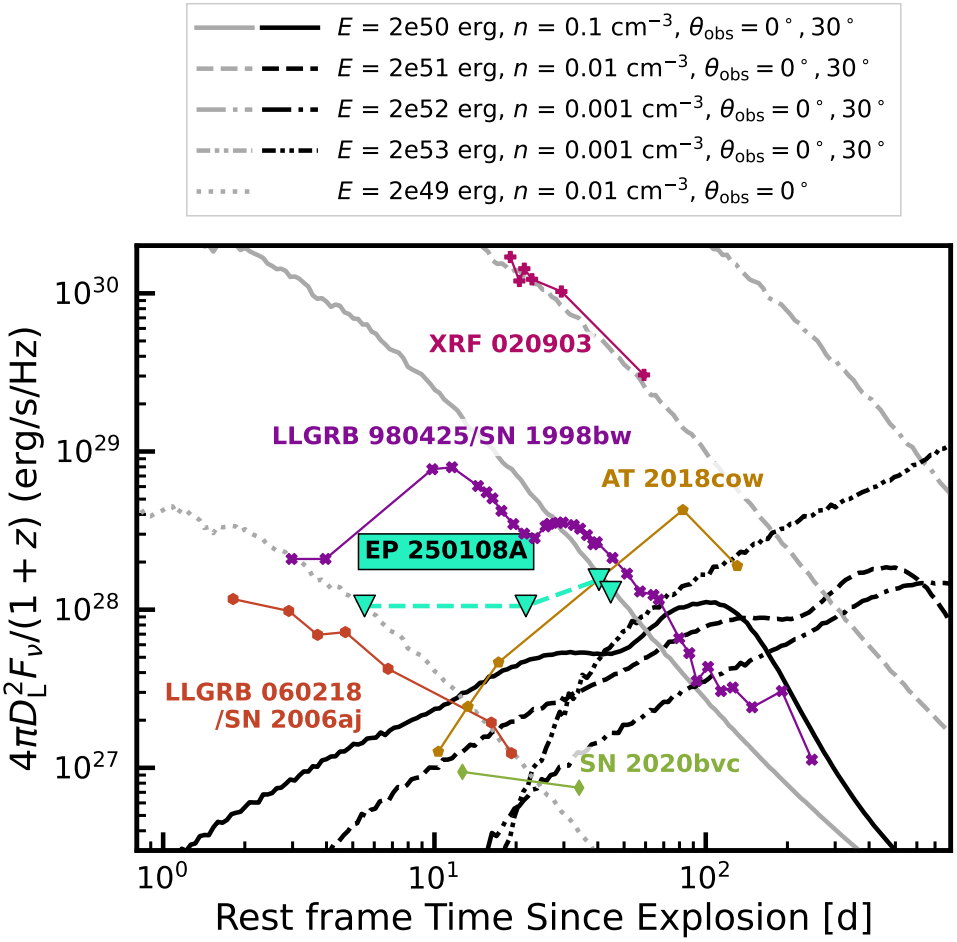

Figure 6.7: The 10 GHz radio light curve of our VLA non-detections of EP 250108A (green triangles). Also shown are the 8–12 GHz light curves of LLGRB 980425/SN 1998bw (purple, Kulkarni et al., 1998; Waxman et al., 1998), XRF 020903(pink, Soderberg et al., 2004), LLGRB 060218/SN 2006aj (orange, Soderberg et al., 2006a), SN 2020bvc (green, Ho et al., 2020e), and AT 2018cow (yellow, Margutti et al., 2019). We additionally plot afterglow models for several pairs of total GRB jet energy (E) and circumburst density (n), generated with the `FIREFLY` code (Dastidar & Duffell, 2024) for an on-axis ($\theta_{obs} = 0°$, grey) and off-axis ($\theta_{obs} = 30°$, black) jet. We cannot rule out radio emission similar to LLGRB 060218/SN 2006aj and SN 2020bvc.

wind-like medium. Though it may be expected that LGRBs occur in a stellar wind medium due to their massive star progenitors, multiple works show that a constant density ISM environment approximation is able to model LGRB emission well in many cases (e.g., Panaitescu & Kumar 2002b, Schulze et al. 2011, Gompertz et al. 2018). Furthermore Irwin & Hotokezaka (2024) found that LLGRB 060218 was more consistent with a constant density ISM at a large radius than a wind environment, and throughout this work we find similarities between EP250108a and LLGRB 060218.

We show a sample of allowed models for an off-axis observing angle of $\theta_{\rm obs} = 30^\circ$ in Figure 6.7, compared to their on-axis analogs ($\theta_{\rm obs} = 0^\circ$). Overall, our non-detections require either a low circumburst density environment ($\lesssim 6 \times 10^{-3}$ cm^{-3}) for a canonical $\sim 10^{52}$ erg GRB viewed $\gtrsim 30^\circ$ off-axis, a low energy GRB ($\lesssim 10^{50}$ erg) for a moderate circumburst density environment ($\sim 10^{-1}$ cm^{-3}) viewed $\gtrsim 30^\circ$ off-axis, or a highly off-set jet for a canonical GRB ($E \sim 10^{52}$ erg and $n \sim 1$ cm^{-3}) viewed $\gtrsim 60^\circ$ off-axis. The off-axis models typically peak $\sim 10^2$–10^3 days (rest-frame) after the GRB, and therefore continued radio monitoring should be performed to search for any late-rising emission.

In addition to some of the off-axis models, we also show the model of an on-axis, extremely low-energy GRB similar to LLGRB 060218 ($E \sim 5 \times 10^{49}$ erg, Ferrero et al. 2006), with $E \sim 10^{50}$ in a moderate circumburst density enviroment ($n \sim 10^{-1}\,{\rm cm}^{-1}$). We find that the model fits just under EP250108a's first radio non-detection, and is consistent with the rest of the radio non-detections. Therefore, an on-axis, extremely sub-energetic jet is consistent with the radio observations. This is consistent with the conclusions from Eyles-Ferris et al. (2025), and we discuss this more in §6.4.

6.3.5 X-ray Analysis

The prompt X-ray emission of EP 250108A detected by EP's WXT in combination with its lack of associated γ-ray emission further shows its possible association to LLGRBs and XRFs. LLGRB 060218/SN 2006aj's peak X-ray luminosity was $\sim 2.8 \times 10^{46}\,\mathrm{erg\,s^{-1}}$. Though it peaked at 4.9 keV (Campana et al., 2006) which is outside EP's WXT spectral range, this is very similar to the peak X-ray luminosity reported in §6.2.1 of $\sim 1.3 \times 10^{46}\,\mathrm{erg\,s^{-1}}$. Furthermore, the timescale for the prompt emission is similar, as LLGRB 060218 had prompt emission that lasted 2100 seconds (Campana et al., 2006), which is the same as the rest-frame time scale of EP250108a's prompt emission.

Follow-up X-ray observations (described in §7.2.1) of EP 250108A did not detect any emission in the 0.3 – 10 keV bands. In Figure 6.8, we place the X-ray upper limits of EP250108a in the context of other X-ray transients. The upper limits rule out emission as bright as classical GRB 230812B/SN 2023pel (Hussenot-Desenonges et al., 2023; Srinivasaragavan et al., 2024a), which we show as a comparison to demonstrate how under-luminous the rest of the transients shown in the Figure are in X-rays to classical GRBs. We are not able to rule out emission similar to AT 2018cow (Rivera Sandoval et al., 2018), LLGRB 060218a/SN 2006aj (Campana et al., 2006), LLGRB 980425/SN 1998bw (Kouveliotou et al., 2004) and SN 2020bvc (Ho et al., 2020e).

6.4 Light curve Modeling

There have been numerous stripped-envelope SNe of varying types that display double peaks in their light curves. The radioactive decay of ^{56}Ni (Arnett, 1982) produces the second peak

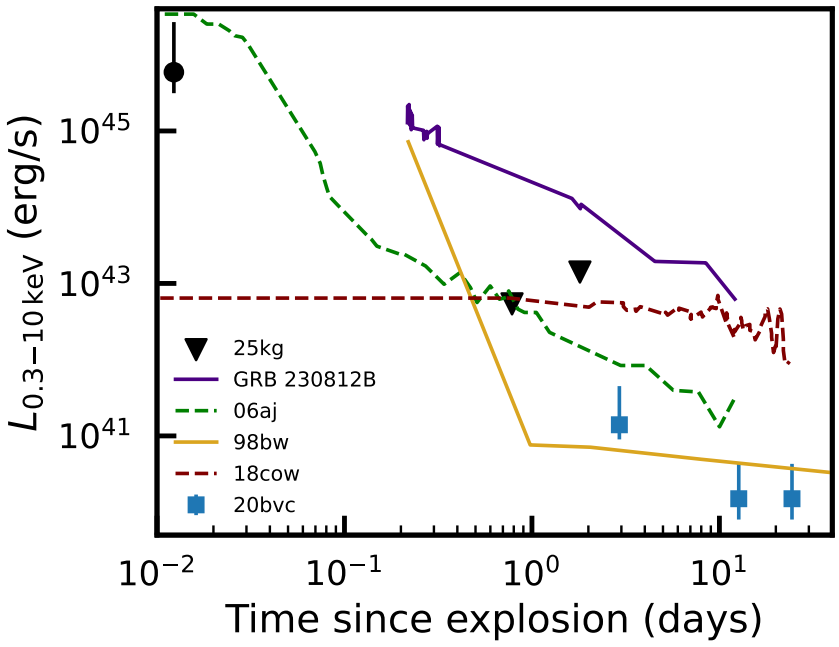

Figure 6.8: Comparison of 0.3 – 10 keV X-ray upper limits of EP 250108a/SN 2025kg to the X-ray light curves of GRB 230812B/SN 2023pel (Hussenot-Desenonges et al., 2023; Srinivasaragavan et al., 2024a), LLGRB 060218a/SN 2006aj (Campana et al., 2006), LLGRB 980425/SN 1998bw (Kouveliotou et al., 2004), double-peaked SN Ic-BL SN 2020bvc (Ho et al., 2020e), and LFBOT AT 2018cow (Rivera Sandoval et al., 2018), with times in the rest frame. The WXT detection is also shown, though we show the luminosity in the 0.5 – 4 keV range. We cannot rule out X-ray emission similar to SN 2006aj, or SN 2020bvc.

in nearly all of these systems, and drives the majority of SN emission during the photospheric phase.

However, the origin of the first peak is not as certain. Shock cooling emission (SCE; Chevalier 1992; Das et al. 2024; Falk & Arnett 1977; Grasberg & Nadezhin 1976; Nakar & Sari 2010; Piro et al. 2010; Rabinak & Waxman 2011) from SN ejecta interacting with an extended CSM is one possible explanation. In this scenario the progenitor star has a compact core and a low-mass extended shell M_e, which extends out to a radius R_e (Bersten et al. 2012; Nakar & Piro 2014; Piro et al. 2010, but see Sapir & Waxman 2017 for an alternative interpretation). After the initial shock breakout from the surface of the progenitor explodes through the outer, low-mass shell (which lasts on the timescales of hours), this material eventually expands and cools over the following days, producing a luminous, blue first peak. Unlike in Type IIb SNe, where M_e is thought to be the outer stellar envelope of the progenitor star, M_e in SNe Ic-BL is theorized to be from material ejected in mass loss episodes, perhaps due to binary interactions (Chevalier, 2012), or stellar winds (Quataert & Shiode, 2012).

The presence of prompt X-ray emission and the similarities to LLGRB 060218/SN 2006aj across different wavelengths motivates the testing of collapsar jet-driven models to explain the first peak. The blue peak contrasts with the expected non-thermal emission of classical GRBs, but can be explained by the cooling of a shocked cocoon (Nakar & Piran, 2017; Piro & Kollmeier, 2018). In this model, the GRB jet creates a cocoon as it propagates through the stellar atmosphere, and imparts a significant amount of energy (10^{51} - 10^{52} erg) into it. This cocoon radiates as it expands and cools within the stellar envelope, generating thermal emission. Another possible scenario is the interaction of this cocoon with an extended CSM, where emission is generated from cooling with the surrounding CSM (Nakar, 2015).

In this section, we present modeling of the optical LC, where we first fit the second peak of the LC beginning at T_0+8 day to the radioactive decay model, in order to derive the SN explosion parameters. We then simultaneously fit the first peak and second peak to a combined radioactive decay model with each of the three models presented above. Hereafter, these scenarios are referred to as:

- **(a) SN Ejecta – CSM**: emission is generated from interaction of the SN ejecta with an extended CSM (Piro et al., 2021).
- **(b) Collapsar Jet-Driven Shocked Cocoon**: emission is powered by emission from the cocoon of a collapsar-powered jet choked in its stellar envelope (Nakar & Piran, 2017; Piro & Kollmeier, 2018).
- **(c) Collapsar Jet-Driven Shocked Cocoon – CSM**: emission is powered by emission from the cocoon of a collapsar-powered jet choked with an extended CSM (Nakar, 2015).

The fitting of the second peak of the LC independent from the first peak is justified, as any contributions from shock cooling or jet-driven models will be negligible during these time periods. This is also the treatment used in Rastinejad et al. (2025). However, in order to derive the parameters of the first peak accurately, we believe a combined treatment of the radioactive decay model and a model describing the first peak is necessary. This is because the photometry between days 4 and 7 likely has contributions from both models, during the transition from the end of the first peak to the beginning of the radioactive decay peak. This differs from the treatment in Eyles-Ferris et al. (2025), and is likely a major reason for some discrepancies in parameters derived.

Below, we present descriptions of each of the models. We perform the fits for all the models through their implementations in REDBACK (Sarin et al., 2024), an open-source electromagnetic transient Bayesian inference software (Sarin et al., 2024). In order to derive posteriors and perform the sampling, we utilize `bilby` (Ashton et al., 2019) and `Dynesty` (Speagle, 2020). We perform the radioactive decay fit to the bolometric luminosity LC, while performing the fits of model (a), (b), and (c) combined with the radioactive decay model on the photometry. We fit the bolometric luminosity LC to derive the SN explosion parameters for consistency with the literature, as most SNe Ic-BL have their parameters derived through fitting the Arnett (1982) model to their bolometric luminosity LCs (Srinivasaragavan et al., 2024b; Taddia et al., 2019a). Furthermore, the BC coefficients used to derive the bolometric luminosity LC (Lyman et al., 2014a) are well defined for stripped-envelope SNe in the radioactive decay phase.

However, these BC coefficients are not as well defined for stripped-envelope SNe in the shock cooling phase (described in §6.3.2) so there are likely significant systematic uncertainties that would dominate fitting the bolometric light curve first peak with our models. Furthermore, Eyles-Ferris et al. (2025) fit the first peak using photometry, so this allows for consistent comparisons between our work. Similarly to Eyles-Ferris et al. (2025), we fit the models assuming a Gaussian likelihood with a systematic error added in quadrature to the statistical errors on the photometry, $\sigma_{\rm sys}$, to capture systematic uncertainties in the photometry, as well as the priors used. Eyles-Ferris et al. (2025) set this error equivalent to 0.15, but we let it vary as a free parameter in our fits. We also allow the host-galaxy extinction A_V to vary in our photometry fits as a free parameter, with a prior between 0 and 0.47 mag (the upper limit we found in §6.3.3).

6.4.1 Radioactive Decay Model

First, we describe the Arnett (1982) model, that we use to fit the second peak, as well as utilize in combination with cases (a), (b), and (c) to derive the first peak's parameters. The radioactive decay model of Arnett (1982) assumes that the instantaneous heating rate from the decay of ^{56}Ni and ^{56}Co equals the peak bolometric luminosity of the SN. This model assumes spherical symmetry and further radioactive inputs (Valenti et al., 2008). We do not assume full gamma-ray trapping, and account for gamma-ray leakage in the late-time LC (Clocchiatti & Wheeler, 1997). The model's main free parameters are the nickel mass ($M_{\rm Ni}$) and characteristic photon diffusion time scale (τ_m), where $M_{\rm Ni}$ sets the peak of the bolometric light curve and τ_m is a proxy for the rise time of the SN and relates to the kinetic energy ($E_{\rm KE}$) and ejecta mass ($M_{\rm ej}$) of the SN, through

$$M_{\rm ej} = \frac{\tau_{\rm m}^2 \beta c v_{\rm sc}}{2\kappa_{\rm opt}}, \tag{6.4}$$

and

$$E_{\rm KE} = \frac{3 v_{\rm sc}^2 M_{\rm ej}}{10}, \tag{6.5}$$

where $\beta = 13.8$ (Valenti et al., 2008), c is the speed of light, $\kappa_{\rm opt}$ is a constant, average optical opacity, and $v_{\rm sc}$ is the photospheric velocity $v_{\rm ph}$ at peak light. In our fitting procedure, the free parameters we use are $M_{\rm ej}$, the fraction of Nickel in the ejecta $f_{\rm Ni}$, $v_{\rm ej}$ which is a representative of the initial ejecta velocity, $\kappa_{\rm opt}$, the gamma-ray opacity κ_γ, and the temperature where the photosphere begins to recede, $T_{\rm floor}$. All of these parameters have broad, uninformed priors in the

fitting. These are the same parameters used in the one-zone model used in Rastinejad et al. (2025) who fit their photometry, except we do not include the host-galaxy extinction, A_V. We do not include this in our fitting procedure as REDBACK cannot incorporate extinction into its luminosity fits. However, this is justified as we showed in §6.3.3 that the host extinction is minimal. We note that Rastinejad et al. (2025) also test a Nickel mixing model (Sarin in prep.), and find significant evidence of mixing, where $M_{\rm Ni}$ is distributed into $\sim 60\%$ of the outer mass layers. We do not test this model, as we do not have sufficient late-time, multi-band photometry to get good constraints on the amount of nickel mixing present.

We report the 1D marginalized posterior median and 68% credible interval of the major parameters in Table 6.2. We derive $M_{\rm Ni} \sim 0.6 {\rm M}_\odot$ and $M_{\rm ej}$ $1.7\,{\rm M}_\odot$. Using the photospheric velocity derived in §6.3.3 of $\sim 17000\,{\rm km\,s^{-1}}$ around peak light, we derive $E_{\rm KE} \sim 2.8 \times 10^{51}$ erg. All values that we derive are consistent with those found in (Rastinejad et al., 2025) from their one-zone modeling, and the ejecta mass and kinetic energy are consistent with the overall SNe Ic-BL population (Srinivasaragavan et al., 2024b; Taddia et al., 2019a). The Nickel mass is slightly outside the 1σ range of Taddia et al. (2019a), but the range they report is for "ordinary" SNe Ic-BL after removing two outlier events from their sample (iPTF15eov and iPTF16asu). When including these two events, the Nickel mass is consistent with their median, and is also consistent with the sample from Srinivasaragavan et al. (2024b), who do not remove any events when calculating median values.

The Nickel mass we derive is significantly higher than that of SN 2006aj ($M_{\rm Ni} = 0.2 \pm 0.1\,{\rm M}_\odot$, Cano et al. 2017a) and SN 2020bvc ($M_{\rm Ni} = 0.4\,{\rm M}_\odot$, Rho et al. 2021), but similar to SN 1998bw ($M_{\rm Ni} = 0.3 - 0.9\,{\rm M}_\odot$, Sollerman et al. 2000). This is consistent with the relative brightness of each of these events, as SN 2025kg possesses a significantly higher peak absolute

Parameter	Median
$M_{\rm Ni}$ $(M_\odot)$	$0.57^{+0.60}_{-0.30}$
$E_{\rm KE}$ $(10^{51}$ erg)	$2.91^{+1.36}_{-0.86}$
$M_{\rm ej}$ $(M_\odot)$	$1.66^{+0.79}_{-0.49}$

Table 6.2: Explosion properties of SN 2025kg's radioactive decay (second) peak from LC modeling.

magnitude than SN 2006aj and SN 2020bvc, and a similar peak magnitude to SN 1998bw. We note that the true Nickel mass is likely lower than the value we derive, as Rastinejad et al. (2025) find significant evidence of Nickel mixing throughout the outer ejecta, but we do not test this model.

6.4.2 Model (a): SN Ejecta – CSM

We fit individual band LCs to a combination of the SCE model from Piro et al. (2021) and radioactive decay model from Arnett (1982). Here we summarize the major equations needed to describe model (a). The SCE luminosity is described as

$$L(t) \approx \frac{\pi(n-1)}{3(n-5)} \frac{cR_e v_t^2}{\kappa} \frac{t_d}{t}^{4/(n-2)}, \quad t \leq t_d. \tag{6.6}$$

and

$$L(t) = \frac{\pi(n-1)}{3(n-5)} \frac{cR_e v_t^2}{\kappa} \exp -\frac{1}{2}\frac{t^2}{t_d^2} - 1, \quad t \geq t_d, \tag{6.7}$$

where t_d is the time where the diffusion reaches a characteristic velocity v_t of the shock, or

$$t_d = \frac{3\kappa K M_e}{(n-1)v_t c}^{1/2}. \tag{6.8}$$

n is a power-law index that describes the density of the outer region of the ejecta with respect to radius, and its typical value is $n \approx 10$. Similarly, δ is a power-law index that describes the density of the inner region of the ejcta with respect to radius, and its typical value is $\delta \approx 1.1$. K is a constant set by mass conservation, represented as

$$K = \frac{(n-3)(3-\delta)}{4\pi(n-\delta)}. \tag{6.9}$$

For typical values, $K = 0.119$. M_e is the mass of the extended envelope, R_e is the radius of the envelope, and κ is a constant opacity. We fit a combination of the Arnett (1982) model and model (a) to SN 2025kg's photometry, where the major free parameters for model (a) are $M_{\rm e}$, $R_{\rm e}$, and $E_{\rm e}$ (the energy in the envelope), all with broad, uninformed priors. As we are fitting the two models simultaneously, we also invoke a condition between $E_{\rm e}$ and $E_{\rm KE}$, presented in Piro et al. (2021), where only a fraction of the total energy of the SN is allowed to be injected into the extended envelope:

$$E_e \approx 2 \times 10^{49} E_{51} \left(\frac{M_c}{3\,M_\odot}\right)^{-0.7} \left(\frac{M_e}{0.01\,M_\odot}\right)^{0.7}, \tag{6.10}$$

where E_{51} is $E_{\rm KE}/10^{51}$ (which we fix to the value derived in §6.4.1), and M_c is the mass of the helium core, which is $\sim M_{\rm ej}$.

We show the results of the fitting for the major parameters in Table 6.3, where we report the 1D marginalized posterior median and 68% credible interval. In Figure 6.9 we show the maximum likelihood estimate of the joint fit to the photometry, along with the 90% credible interval of the posteriors on the joint fit. We find $M_{\rm e} \sim 0.04{\rm M}_\odot$, $R_{\rm e} \sim 3.5 \times 10^{14}$ cm, and

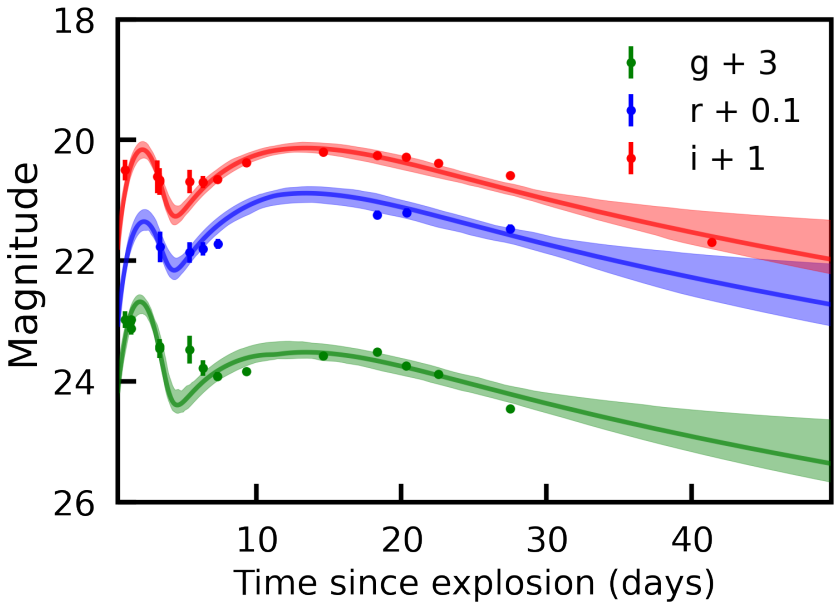

Figure 6.9: Fitting of model (a) (SN ejecta – CSM) and the radioactive decay model of Arnett (1982) in combination to the photometry of SN 2025kg. We show the maximum likelihood fit and the 90% credible interval.

$E_{\rm e} \sim 2.3 \times 10^{50}$ erg, and that this model can describe the optical LC well.

The parameters we derive are significantly different than those derived in Eyles-Ferris et al. (2025). They also test the Piro et al. (2021) model and find $M_{\rm e} > 6\,{\rm M}_{\odot}$ and $E_{\rm e} > 10^{52}$ erg for the Piro et al. (2021) model, which are inconsistent with our results. We believe the large discrepancy is due to the difference in fitting methods – we account for contributions from the radioactive decay component during the first 6 days, while Eyles-Ferris et al. (2025) do not. Therefore, we believe this leads them to derive larger parameters than needed when including the contribution from radioactive decay, particularly during days 4 – 6 after T_0. It also may be due to the difference in treatment of the systematic error $\sigma_{\rm sys}$, which we allowed to vary in our fits. They also test a dense-CSM model with an abrupt drop in density (Margalit, 2022) and find that these parameters are more consistent with the expected emission. However, we do not invoke this model, as the treatment of Piro et al. (2021) provided reasonable parameters.

Parameter	Median
$M_{\rm e}\,(M_\odot)$	0.04 ± 0.01
$R_{\rm e}\,(10^{13}\,{\rm cm})$	$34.67^{+31.40}_{-17.30}$
$E_{\rm e}\,(10^{51}\,{\rm erg})$	$0.23^{+0.27}_{-0.13}$

Table 6.3: Properties of model (a) for SN 2025kg (first peak) from LC modeling

6.4.3 Model (b): Collapsar Jet-Driven Shocked Cocoon

Next, we fit a shocked cocoon model following Nakar & Piran (2017) and Piro & Kollmeier (2018), in addition to the Arnett (1982) radioactive decay model. In this model, the GRB jet propagates through the stellar atmosphere, which possesses a mass profile

$$m(>v) = M\left(\frac{v}{v_0}\right)^{(-\eta+1)}, \tag{6.11}$$

where M is the total ejecta mass, v_0 is the minimum velocity of the ejecta, and η is a power-law index, and the profile extends out to a radius R cm. There are two components to the shocked cocoon here – an inner shocked jet cocoon that produces high-energy emission, and an outer stellar shocked cocoon, whose cooling emission produces optical emission (see Figure 1 in Nakar & Piran 2017 for a schematic of this model). Here, we model the emission from the shocked stellar cocoon. The luminosity an observer sees originates from the optical depth where the diffusion time ($t_{\rm diff}$) is equal to the observation time, and the energy at that depth goes as $E \propto \frac{MvR}{t}$, along with the corresponding luminosity, $L(t) \sim E(t)/t_{\rm diff}$ (see Nakar & Piran 2017; Piro & Kollmeier 2018 for full detailed equations). In our modeling, we assume that the shocked ejecta is confined within $\theta_{\rm cocoon}$. The additional major free parameters in the fitting, which we fit in conjunction to the radioactive decay model, are the mass of the cocoon $M_{\rm cocoon}$, its velocity

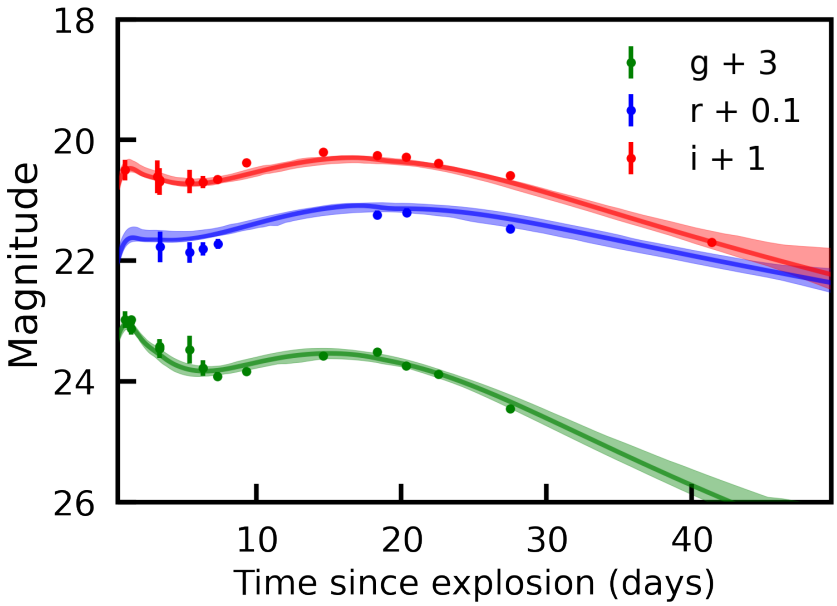

Figure 6.10: Fitting of model (b) (Collapsar Jet-Driven Shocked Cocoon) and radioactive decay model of Arnett (1982) in combination to the photometry of SN 2025kg. We show the maximum likelihood fit and the 90% credible interval.

$v_{\rm cocoon}$, η, the time the shock lasts $t_{\rm shock}$, and the fraction of the ejecta mass that is in the shocked cocoon $f_{\rm shocked}$. To derive the true mass of the shocked ejecta, we must correct for the geometry of the cocoon, so $M_{\rm shocked} \sim \frac{f_{\rm shocked} M_{\rm cocoon} \theta^2}{2}$ (Piro & Kollmeier, 2018). We note that for the optical emission, we are modeling the cooling emission from the stellar shocked cocoon.

We report the 1D marginalized posterior median and 68% credible interval of the major parameters in Table 6.4. In Figure 6.4.3 we show the maximum likelihood estimate of the joint fit to the photometry, along with the 90% credible interval of the posteriors on the joint fit. We find that the mass of shocked ejecta is $\sim 0.05\,M_\odot$, it is confined within $\sim 20^\circ$, in a shock radius of $\sim 2\,R_\odot$ cm, resulting in a kinetic energy of $\sim 4 \times 10^{50}$ erg, and that this model can describe the optical LC well. Our parameters are all overall consistent with what Eyles-Ferris et al. (2025) found fitting the same model, though on the lower end of what they derived.

Parameter	Median
$M_{\rm cocoon}\,(M_\odot)$	$1.19^{+0.49}_{-0.46}$
$v_{\rm cocoon}(c)$	$0.08^{+0.02}_{-0.02}$
$f_{\rm shocked}$	$0.63^{+0.16}_{-0.17}$
$t_{\rm shocked}$ (s)	$63.88^{+22.60}_{-20.16}$
$\theta_{\rm cocoon}$	$19.95 \pm 5.89^\circ$

Table 6.4: Properties of model (b) for SN 2025kg from LC modeling

6.4.4 Model (c): Collapsar Jet-Driven Shocked Cocoon – CSM

We then fit a model in which the GRB progenitor (a stripped-envelope Wolf-Rayet star) is surrounded by an extended CSM (Nakar, 2015), generated via mass loss prior to core collapse, in addition to the Arnett (1982) radioactive decay model. This scenario is motivated by growing observational evidence for extended CSM around stripped-envelope core-collapse SNe (e.g., Foley et al. 2007; Pastorello et al. 2007, 2008; Pellegrino et al. 2024), and the striking similarity between EP250108a and the LLGRB 060218, which has been interpreted as a failed GRB jet in an extended CSM (Nakar, 2015). We thus consider a GRB jet launched from the stellar core that propagates through the extended CSM, producing a hot cocoon that emits cooling radiation.

We solve the jet propagation through the CSM and derive the resulting jet-cocoon properties as a function of the CSM mass ($M_{\rm CSM}$), radius ($R_{\rm CSM}$), and central engine energy ($E_{\rm eng}$). We assume a wind-like CSM density profile, $\rho \propto r^{-2}$, corresponding to constant mass loss. The central engine is modeled with a constant jet power ($= E_{\rm eng}/t_{\rm eng}$) over $t_{\rm eng} \sim 100\,{\rm s}$, comparable to the progenitor's free-fall timescale (Matzner, 2003). A typical LGRB jet opening angle of 10° is adopted. The jet-cocoon dynamics are modeled analytically (Bromberg et al., 2011; Hamidani & Ioka, 2021, 2023a; Hamidani et al., 2025a; Harrison et al., 2018), yielding the breakout time and the cocoon's mass and energy. Post-breakout, the cocoon expands homologously, with

Parameter	Median
$M_{\rm CSM}$ ($M_\odot$)	$0.07^{+0.06}_{-0.04}$
$R_{\rm CSM}$ (10^{13} cm)	$3.71^{+8.58}_{-2.13}$
$E_{\rm eng}$ (10^{51} erg)	$5.75^{+20.00}_{-4.96}$

Table 6.5: Properties of model (c) for SN 2025kg from LC modeling

a velocity structure set by mass and energy conservation. We adopt $dE_{\rm c}/d\log(\Gamma\beta) \sim$ const. (Eisenberg et al., 2022a; Nakar & Piran, 2017), resulting in a density profile $\rho \propto v^{-5}t^{-3}$ (Suzuki et al., 2024), and internal energy evolution $E_{\rm c,i} \propto t^{-1}$ due to adiabatic cooling.

Thermal photons escape via diffusion, with emission originating near the shell where $\tau \sim c/(v_{\rm out} - v)$ (Hamidani & Ioka, 2023b; Kisaka et al., 2015). The bolometric luminosity is computed from the inward motion (in Lagrangian coordinates) of this diffusion front, and the effective temperature is derived using the Stefan–Boltzmann law, assuming gray opacity $\kappa \sim 0.1$–$0.2\,{\rm cm^2\,g^{-1}}$, consistent with Thomson scattering.

We report the 1D marginalized posterior median and 68% credible interval of the major parameters in Table 6.5. In Figure 6.11 we show the maximum likelihood estimate of the joint fit to the photometry, along with the 90% credible interval of the posteriors on the joint fit. We find $M_{\rm CSM} \sim 0.1\,M_\odot$, $R_{\rm CSM} \sim 4 \times 10^{13}$ cm, and $E_{\rm eng} \sim 6 \times 10^{51}$ erg, and that this model can describe the optical LC well. Eyles-Ferris et al. (2025) do not test this model, so we cannot make any comparisons.

6.5 Expected X-ray Emission

In §6.4, we found that all three models can describe the optical LC well, when combined with a radioactive decay model. Here we compare the expected X-ray emission from models (a),

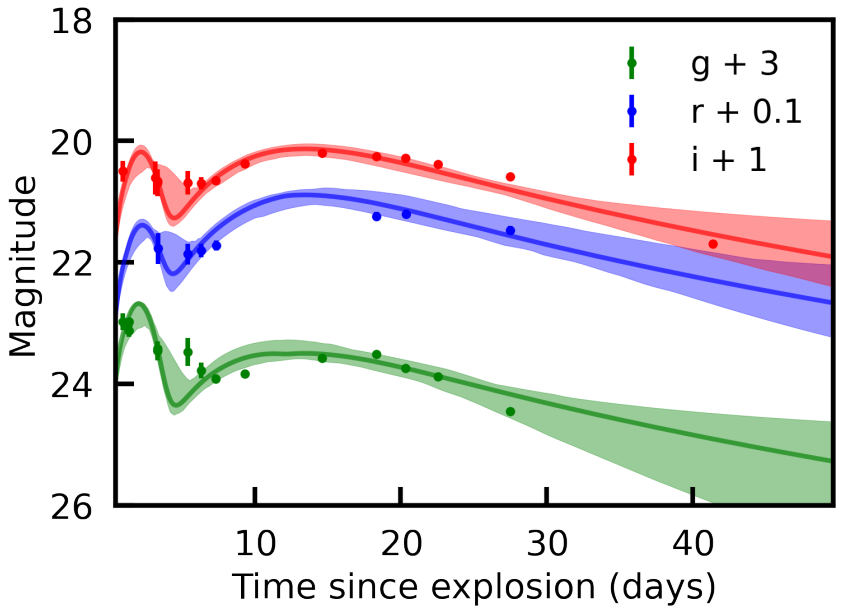

Figure 6.11: Fitting of model (c) (Collapsar Jet-Driven Shocked Cocoon in Extended CSM) and radioactive decay model of Arnett (1982) in combination to the photometry of SN 2025kg. We show the maximum likelihood fit and the 90% credible interval.

(b), and (c) in the WXT band pass of 0.5 – 4 keV, to the prompt emission detection described in §6.2.1.

6.5.1 Model (a): SN Ejecta – CSM

We use the same treatment as in Haynie & Piro (2021), who present an analytic method to calculate shock breakout emission in an extended CSM, followed by the calculation of the observed temperature from Waxman & Katz (2017).

Given the average 0.5 – 4 keV luminosity of $L_{\mathrm{X-ray}} \sim 6 \times 10^{45}\,\mathrm{erg\,s^{-1}}$, and the prompt emission timescale of 2500 seconds, this corresponds to an energy of the shock breakout $E_{\mathrm{SBO}} \sim 1.5 \times 10^{49}\,\mathrm{erg}$. The timescale of the breakout is dependent on whether the dominant rate-limiting process for the rise of the SBO is due to diffusion, or due to the light travel time. If the rise time of the SBO luminosity set by diffusion is longer than the light travel time, then diffusion will

dominate. The rise time is

$$t_r = \frac{R_e^2}{R_d v_t} \tag{6.12}$$

where we use the median $R_e \sim 5 \times 10^{13}$ cm and $v_t \sim 0.2c$. R_d is

$$R_d = \frac{\kappa D v_t}{c} \tag{6.13}$$

where κ is the opacity, and D is the mass loading factor,

$$D = \frac{\dot{M}}{4\pi v_t}. \tag{6.14}$$

Integrating this expression with respect to the mass, where we use $M_e \sim 4\pi R_e D$, and substituting into the expression for R_d, we get

$$R_d = \frac{\kappa v_t}{c} \frac{M_e}{4\pi R_e}. \tag{6.15}$$

Therefore, substituting this into the expression for t_r, we find

$$t_r = \frac{4\pi R_e^3 c}{\kappa M_e v_t^2}. \tag{6.16}$$

The light travel time t_l is simply $\frac{R_e}{c}$. Therefore, we have the inequality

$$\frac{4\pi R_e^3 c}{\kappa M_e v_t^2} > \frac{R_e}{c}, \tag{6.17}$$

for diffusion to dominate. Rearranging, we derive

$$M_e < \frac{4\pi R_e^2}{\kappa}\left(\frac{c}{v_t}\right)^2. \tag{6.18}$$

Therefore, we find that the diffusion time only dominates if $M_e < 1.1\mathrm{M}_\odot$, and we find $M_e \sim 0.04\,\mathrm{M}_\odot$ from our modeling. Therefore, we are in the diffusion dominated regime, and the luminosity of SBO in this scenario is

$$L_{\rm SBO} = \frac{E_{\rm SBO}}{t_r} \approx 4\pi D v_t^3, \tag{6.19}$$

which is $\sim 3 \times 10^{45}\,\mathrm{erg\,s^{-1}}$ for our parameters. This is less than the observed 0.5 – 4 keV X-ray luminosity of $\sim 10^{46}\,\mathrm{erg\,s^{-1}}$, even without accounting for the fact that only a fraction of this luminosity will go to 0.5 – 4 keV X-rays.

Furthermore, we compare t_r to the timescale of the prompt emission, as these two timescales should be approximately equal for model (a) to produce the prompt emission. Substituting known values into Eq. 6.16, we find $t_r \sim 1$ day. This is much longer than the prompt emission timescale. Therefore, we find that though model (a) can reproduce the optical emission, it cannot reproduce the observed prompt X-ray emission, and we therefore disfavor this model in our analysis.

6.5.2 Model (b): Collapsar Jet-Driven Shocked Cocoon

In §6.4.3, we focus on the thermal cooling emission from the shocked stellar cocoon, that generates the optical emission. The shocked cocoon model we use is also expected to produce high-energy X-ray and gamma-ray emission, through non-thermal emission mechanisms, primar-

ily from the shocked jet component. However, the precise details of such emission are sensitive to uncertain assumptions such as the degree of mixing between the jet and stellar material and the mass/momentum profiles (e.g., Nakar & Piran, 2017). Such calculations are beyond the scope of this work but we use fiducial estimates in Nakar & Piran (2017) to compare to observations. Assuming no mixing, they find a γ-ray/hard X-ray signal that lasts on the order of seconds, with a spectrum peaking around 100 keV, which is inconsistent with the prompt detection from WXT.

We also compare the timescales between the optical emission and the prompt emission. In this case, the optical emission is highly independent of the X-ray emission, as the optical emission comes from the cooling of the stellar cocoon, and largely ignores the contributions from the shocked jet cocoon, which produces the X-rays. This is why the timescales for the two processes are very different – the shock crossing timescale for the stellar cocoon is ~ 63 s, while the prompt emission timescale is more than an order of magnitude larger.

In the X-ray regime, emission is possible if there is partial mixing, and the shocked jet cocoon energy is deposited in mildly-relativistic material with $\Gamma < 10$. They find that this emission would peak a day after the prompt burst, with a luminosity of $\sim 10^{44} \mathrm{erg\,s^{-1}}$. As the precise peak timescales and luminosities are sensitive to the various assumptions and different parameters, it is reasonable that this emission is consistent with the X-ray non-detections reported in §6.3.5. Eyles-Ferris et al. (2025) report that the parameters derived from this model in their analysis are consistent with the X-ray non-detections. However, the prompt X-ray emission is not obviously reproducible through model (b) for the fiducial choice of parameters and assumptions in Nakar & Piran (2017).

In order to describe the X-ray prompt emission, Eyles-Ferris et al. (2025) invoke a model somewhat independent of model (b), but consistent with the physical picture, utilizing models

developed in Fryer et al. (in prep.). In this model, bremsstrahlung emission arises from a failed jet propagating through the star or clumpy stellar wind, forming a semi-relativistic cocoon. They find that this model can successfully explain the X-ray prompt emission. Therefore, it is possible that this model combined with model (b) can explain the X-ray prompt emission and first peak in the optical LC.

6.5.3 Model (c): Collapsar Jet-Driven Shocked Cocoon – CSM

As discussed in § 6.4.4, a GRB-jet propagating into an extended CSM can explain the observed early optical light curve. In this scenario, the extended CSM causes the jet to fail, forming a hot cocoon that expands through the surrounding material. The breakout of the cocoon from the CSM can also power X-ray emission via the shock breakout emission (e.g., Irwin & Hotokezaka 2024; Nakar 2015; Waxman & Katz 2017).

We estimate the X-ray luminosity using our median jet/CSM parameters that reproduce the optical light curve: $E_{\rm eng} \sim 6 \times 10^{51}\,{\rm erg}$, $R_{\rm CSM} \sim 4 \times 10^{13}\,{\rm cm}$, and $M_{\rm CSM} \sim 0.1\,M_{\odot}$. We adopt an opacity of $\kappa \sim 0.1\,{\rm cm^2\,g^{-1}}$.

The typical cocoon velocity can be found as $\overline{v} \sim \sqrt{2E_{\rm eng}/M_{\rm CSM}} \sim 0.25\,c$. This is a lower limit for the shock breakout velocity. Considering that the outer part of the cocoon is slightly faster, we approximately take:

$$v_{\rm SBO} \sim 0.3\,c. \tag{6.20}$$

The bolometric luminosity of the shock breakout is given by:

$$L_{\rm SBO} \sim 4\pi R_{\rm CSM}^2 \rho_{\rm SBO} v_{\rm SBO}^3. \tag{6.21}$$

The optical depth gives $\tau \sim \kappa \rho_{\rm SBO} R_{\rm CSM} \sim c/v_{\rm SBO}$. Hence, the shock breakout luminosity can be found as:

$$L_{\rm SBO} \sim 1.2 \times 10^{46}\,{\rm erg\,s^{-1}}, \tag{6.22}$$

and the observed timescale is set by the shock crossing time as:

$$t_{\rm obs} \sim 10^{3}\,{\rm s}. \tag{6.23}$$

Both the total luminosity, and observed timescale are broadly consistent with the observed prompt emission. However, only a fraction of the luminosity will be seen in the 0.5 – 4 keV bands, so here we calculate how much luminosity is generated in the observed frame of the prompt emission.

The effective temperature of the breakout emission given in Waxman & Katz (2017) is

$$T_{\rm eq} = 66 \rho_{-9}^{1/4} v_{t,9}^{1/2} {\rm eV}, \tag{6.24}$$

where ρ_{-9} is the density in terms of $10^{-9}\,{\rm g\,cm^{-3}}$, and $v_{t,9}$ is v_t in terms of $10^{9}\,{\rm km\,s^{-1}}$. Therefore, we find the effective temperature $T_{\rm eq} = 0.16$ keV.

However, this temperature only holds if the system is in true thermal equilibrium. In order to test this, we compute the thermal coupling coefficient in an expanding gas from Nakar & Sari (2010),

$$\eta \approx \frac{7 \cdot 10^{5}\,{\rm s}}{\min\{t, t_d\}} \left(\frac{\rho}{10^{-10}{\rm g/cm^3}}\right)^{-2} \left(\frac{kT_{eq}}{100eV}\right)^{7/2},$$

where k is the Boltzmann constant, and $\min\{t_l, t_d\}$ is the minimum time between the light travel time and the diffusion time. Since we already determined we are in the light-travel regime, t_d is the minimum value. If $\eta < 1$, then the system is thermalized and we can estimate the emission using the observed temperature $T = T_{\rm eq}$ as the blackbody temperature. However, if $\eta > 1$, then the spectrum transitions to an optically thin regime dominated by free-free emission, which is also modified by the Comptonization of these photons by the neighboring electrons (Nakar & Sari, 2010). In this regime, the spectrum is a Wien spectrum at high energies, where the temperature is determined by

$$T\xi(T)^2 = T_{\rm eq}\eta^2 \tag{6.25}$$

where $\xi(T)$ is the Comptonization correction factor, given by

$$\xi(T) \approx \max\left\{1, \frac{1}{2}\ln[y_{max}]\left(1.6 + \ln[y_{max}]\right)\right\}, \tag{6.26}$$

where $y_{\rm max}$ is the Compton parameter,

$$y_{max} \equiv \frac{kT}{h\nu_{min}} = 3\left(\frac{\rho}{10^{-9}\ {\rm g/cm^{-3}}}\right)^{-1/2}\left(\frac{T}{100{\rm eV}}\right)^{9/4}. \tag{6.27}$$

$y_{\rm max} < 1$ implies that comptonization does not play a significant role, so $\xi = 1$, and $T = T_{\rm eq}\eta^2$. Therefore, we solve Equation 6.25 for T, substituting our known values, incorporating the fact that the density ρ will be a factor of 7 larger due to the shock compressing the gas (Nakar & Sari, 2010), we find $\eta = 70$. Then, solving Equation 7.8 to find the the observed temperature, and we find $T = 1.2$ keV. Therefore, the majority of $L_{\rm SBO} \sim 10^{46}\,{\rm erg\,s^{-1}}$ will be seen in the 0.5 – 4 keV

bands, which is consistent with the WXT prompt emission detection.

6.6 Discussion

Here we discuss the implications of our analysis and make inferences about the progenitor system of EP250108a/SN 2025kg. We focus our discussion on model (c), as we found that this model self-consistently reproduce both the X-ray prompt emission and first optical peak, and therefore favor it in this work. We note that we do not rule out model (b), and we refer the reader to Eyles-Ferris et al. (2025) for more discussion on this model. There are additional models invoked to explain the emission in Li et al. (2025c), including an on-axis slow jet and a magnetar model to explain the SN emission, and we direct the reader to this work for more discussion on these models.

6.6.1 The Extended CSM Properties

Model (c) invokes an extended CSM, where cooling emission is generated from the interaction of the SN shock with the CSM. The invocation of an extended CSM is supported by detailed spectral analysis in Rastinejad et al. (2025), as they find evidence of a broadened Hα feature in an optical spectrum 42.5 days after T_0, as well as a He feature in a near-infrared spectrum taken near peak light. They conclude that the Hα feature is due to a detached Hydrogen shell $\sim 10^{16}$ cm away from the progenitor, while the He feature is an indication of a Helium shell $< 0.5\,\mathrm{M}_\odot$, which they argue could be consistent with the dense CSM model invoked in Eyles-Ferris et al. (2025), at an extended radius $R_e \sim 7 \times 10^{14}$. Therefore, though the details of our modeling and results differ, our work agrees that an extended CSM is likely present in this system.

Event	M_e ($M_\odot$)	R_e (10^{13} cm)	Reference
EP250108a/SN 2025kg	~ 0.1	~ 3.7	This work
LLGRB 060218/SN 2006aj	$\sim 0.01 - 0.1$	~ 4	Irwin & Hotokezaka (2024)
SN 2020bvc	~ 0.1	~ 10	Rho et al. (2021)
iPTF16asu	~ 0.45	~ 0.17	Whitesides et al. (2017)
SN 2018gep	~ 0.3	~ 7.7	Leung et al. (2021b)
EP240414a/SN 2024gsa	~ 0.33	~ 24	Sun et al. (2024)

Table 6.6: CSM Parameters for SNe Ic-BL in the literature.

Now, we compare the extended CSM properties for SN 2025kg to other SN Ic-BL that show evidence of having CSM interaction in the literature, and show the masses and radii of the extended envelopes in Table 6.6. We include EP240414a/SN 2024ga in the Table, as Sun et al. (2024) model the second red peak at $M_r = -21$ mag, after the initial afterglow emission but prior to the SN's radioactive decay peak as SCE of dense, extended material at a large radius. We see that overall, the envelope masses in these systems range between 0.1 and 0.45 $M_\odot$, while the radii ranges from 1.7×10^{12} to 2.4×10^{14} cm. SN 2006aj has the most similar CSM parameters to SN 2025kg. However, SN 2025kg has a brighter initial peak, and the peak takes longer to decline before transitioning to the radioactive decay component (see §6.3.1. This suggests a larger energy budget and larger envelope mass for SN 2025kg than SN 2006aj, which is supported by our modeling.

Though there is clear diversity in the observational properties of SNe Ic-BL that display SCE due to extended CSMs, understanding the landscape of the diversity of their progenitor systems is a complicated task. There are many degeneracies that exist between different parameters in these systems. The rise time and peak luminosity are dependent on the shock velocity and the radius of the extended envelope, while the shock velocity in turn is dependent on the density profile of the progenitor and the energy of the explosion, which in turn is dependent on the

mass of the extended envelope. Therefore, it is difficult to pin-point how important of a role each of these different parameters play in producing the range of observed SNe Ic-BL with extended CSM interaction.

The structure of the CSM surrounding SNe Ic-BL progenitors is also likely diverse, determined by the origin of the mass-loss prior to the star's death, i.e. presence of a binary, stellar outbursts, or winds (Fuller, 2017; Wu & Fuller, 2021). Different circumstellar material structures, especially asymmetric structures, can give rise to different SCE. In addition to the diversity of their progenitor systems, viewing angle effects may also play a role, as events viewed along their poles (SNe Ic-BL are expected to have asymmetric, bipolar emission) will have brighter SCE than events viewed off-axis to these poles (Ho et al., 2020e). Large sample studies of double-peaked SNe Ic-BL from a systematic perspective will be integral to understanding this landscape, and that will be the subject of a forthcoming paper (Vail et al. in preparation).

6.6.2 Understanding the X-ray and Radio Emission

In §6.5, we determined that model (c) can self-consistently recreate the X-ray prompt emission. The inability of model (a) to reproduce the X-ray emission is consistent to what Eyles-Ferris et al. (2025) found in their work. Using a a convective engine model for the progenitor from Fryer et al. (in prep.), where high-velocity ejecta is produced as the shock propagates out of the stellar edge, they found that they could only reproduce the X-ray observations in extreme cases, under the assumption that the supernova energy exceeds current models, or we have an extreme mass and energy distribution with respect to the ejecta velocity (Eyles-Ferris et al., 2025). This method is different than the method we provide in §6.5, where we use an analytic calculation to compute

the luminosity of shock breakout in an extended CSM. The fact that two independent methods arrive at the same conclusion, that model (a) cannot reproduce the X-ray prompt emission, gives further evidence that model (a) should be disfavored.

A collapsar-driven jet model is a more natural explanation for EP250108a/SN 2025kg, given its similarities to LLGRB 060218/SN 2006aj, which is consistent with what Eyles-Ferris et al. (2025) found from their X-ray modeling of a collapsar jet-driven explosion. In model (c), we have a GRB jet that gets choked, depositing energy in a hot cocoon, that breaks out quasi-spherically and interacts with an extended CSM.

There are differing opinions on how dense of a CSM is needed to truly "choke" a jet – analytic works like Hamidani et al. (2025a) show that jets can fail from interacting with an extended CSM at radius $R_e > 10^{13}$, running into just $\sim 0.1\,\mathrm{M}_\odot$ of material, and some simulations show this holds true (Suzuki & Maeda, 2022). If this is the case, this is a natural explanation for systems like LLGRB 060218/SN 2006aj. However, other simulations done by Duffell & Ho (2020) show that more than a few $\mathrm{M}_\odot$ of material is necessary within 10^{13} cm to truly "choke" a jet. They found that with CSM parameters like those derived for SN 2006aj (as well as SN 2025kg), that the CSM could not have fully choked the jet – it could just slow it down enough such that it spreads to a larger angle, but the shock breakout from the CSM would not be quasi-spherical as models suggest for SN 2006aj (e.g., Nakar 2015).

One way to reconcile these differences is to have a jet that is choked within its own stellar envelope, that then goes on to interact with an extended CSM. If this were to occur, then we would still see a quasi-spherical shock breakout from the cocoon, and shock cooling interaction with the extended CSM after the fact where the emission is dependent on the CSM parameters, and the physics of Nakar (2015)'s model we use in model (c) would still be accurate to describe the

system. In order to have a jet choked at the stellar envelope (assuming a Wolf-Rayet progenitor, $R \sim 10^{12}$ cm), an intrinsically weak jet, short engine duration, or dense stellar envelope is necessary. Eyles-Ferris et al. (2025) argues that a failed jet through the stellar interior, or a clumpy stellar wind can reproduce the prompt X-ray emission, which is similar to the above argument.

Both of these scenarios – where the jet is choked within its stellar envelope before interacting with an extended CSM, or is choked by an extended CSM, are consistent with the radio non-detections. In §6.3.4 we showed that the only viable on-axis solution was a very energetically weak jet. It has been shown that the choking of the jet by the CSM leads to a weakening of the jet's energy (Margutti et al., 2015; Nakar, 2015), and an intrinsic low-energy jet is also a natural explanation for why it may have been choked in its stellar envelope. Furthermore, model (c) is also consistent with the subsequent X-ray non-detections, as the X-ray emission duration is expected to match the shock crossing timescale, lasting for $t_{\rm obs} \sim 10^3$ s (see Equation 6.23 in §6.5.3) before fading. This timescale is consistent with the later-time upper limits.

Rastinejad et al. (2025) argue that the He and Hα features detected in the spectra indicate the presence of at least a binary system, and maybe a tertiary system, where the Helium shell was ejected in a common envelope phase, while Hydrogen was either ejected in a previous asymmetric common envelope phase or through interactions with a third star. Fryer et al. (2024a) argues that LGRBs arise from tight binary systems, and LLGRBs arise from wider binaries, with lower-mass BH-forming stars in the 20 – 30 $M_\odot$ range. If the He shell found in Rastinejad et al. (2025) is due to a common envelope phase, that necessitates a tight binary system. However, Rastinejad et al. (2025) also find that the zero age main sequence mass of the progenitor of SN 2025kg is between 19 and 30 $M_\odot$, if the central engine is a black hole. Lower mass progenitors produce weaker jets

(Fryer et al., 2024a), and that gives an explanation to how the jet may have been choked in its stellar envelope, though the proximity of a nearby companion would be a competing effect.

Including EP250108a/SN 2025kg, EP has already found three SNe Ic-BL associated with EFXTs (EP240414a/SN 2024gsa, Srivastav et al. 2025; Sun et al. 2024; van Dalen et al. 2025 and EP 250304, Izzo et al. 2025), in its first year of operations. Rastinejad et al. (2025) report that the volumetric rates of such events are around $\sim 10 - 100$ Gpc^{-3} yr^{-1}. This is significantly higher than the rates of classical, on-axis GRBs ($\sim 0.1 - 1$ Gpc^{-3} yr^{-1}, e.g., Liang et al. 2007; Schmidt 2001; Sun et al. 2015), on the lower end of the rate of LLGRBs ($\sim 100 - 1000$ Gpc^{-3} yr^{-1}, e.g., Guetta & Della Valle 2007; Liang et al. 2007; Virgili et al. 2009b), and much lower than the rate of SNe Ic-BL (~ 1000 Gpc^{-3} yr^{-1}; Li et al. 2011; Shivvers et al. 2017). However, it is very similar to the rate of bursts detected by HETE-2, whose three onboard instruments operated from 2 – 400 keV (Sakamoto et al., 2005). Pélangeon et al. (2008) derive a rate of ~ 10 Gpc^{-3} yr^{-1}, though they stress this is a lower limit as HETE-2 may have missed GRBs with peak energies less than 2 keV. They infer the difference in their rate to those derived in other works that find $\sim 0.1 - 1$ Gpc^{-3} yr^{-1} is the existence of XRFs in their sample.

Therefore, though there have only been a few events thus far, there is evidence that the SNe Ic-BL population associated with EFXTs are rarer than the normal SNe Ic-BL population, but less rare than classical LGRBs. Furthermore, their rates may be comparable to those of LLGRBS, and are broadly consistent with the rate of GRBs detected by HETE-2, which included a significant number of XRFs. This points towards a possible similar progenitor system between SNe Ic-BL associated with EP EFXTs, LLGRBs, and XRFs. However, the rate of EP EFXTs derived by Rastinejad et al. (2025) is just an estimate, and a more robust calculation with more discovered events is necessary to draw any firm conclusions.

6.7 Conclusions

In this Letter, we present optical, X-ray, and radio observations of EP 250108a/SN 2025kg, a SN Ic-BL associated with a EFXT discovered by EP. Our main findings are:

- SN 2025kg possesses a double-peaked light curve. Its first peak is blue and has an absolute magnitude $M_g \sim -19.5$ mag, while the second peak has an absolute magnitude $M_r \sim -19.4$. Its light curve is very similar to LLGRB 060218/SN 2006aj, though both of its peaks are more luminous, while evolving on slower timescales.

- SN 2025kg's spectral sequence transitions from a blue underlying continuum at early times with hints of broad absorption features, to a redder continuum with multiple clear broad absorption features and a lack of H or He features, characteristic of SNe Ic-BL. Its spectral evolution is very similar to that of SN 2006aj.

- We analyze its X-ray prompt detection, and subsequent X-ray and radio upper limits, and determine that both radio and X-ray emission similar to LLGRB 060218A/SN 2006aj cannot be ruled out. We also find that the radio limits are consistent with various off-axis afterglow models, viewed at $\theta_{\rm obs} \gtrsim 30^\circ$. Future radio observations at $\sim$ 100–1000 days will constrain the presence of late-rising radio emission from a possible off-axis jet. We also find that an on-axis, very sub-energetic GRB ($E \sim 10^{49}$) erg, in a moderate density circumburst medium ($n \sim 10^{-1}\,{\rm cm}^{-3}$) is also consistent with the radio upper limits.

- We model the second peak using the Arnett (1982) radioactive decay model to fit the bolometric luminosity light curve. We find that the SN parameters derived are overall consistent with the SNe Ic-BL population.

- We model the photometry with a combination of the Arnett (1982) radioactive decay model, and three different models to describe the first peak. These are (a) SN ejecta interacting with an extended CSM, (b) the shocked cocoon of a collapsar jet choked in its stellar envelope, and (c) the shocked cocoon of a collapsar jet choked by an extended CSM. The three models can all reproduce the optical LC well.

- We estimate the X-ray prompt emission generated in model (a), (b), and (c), and find that model (c) can reproduce the prompt emission detected by WXT self-consistently, and we therefore favor this model in this work. Model (b) is expected to produce high energy X-ray emission; however, using the fiducial choice of parameters and assumptions from the model's paper (Nakar & Piran, 2017), the prompt emission is not obviously reproducible. A combination of model (b) with another prompt emission model can explain EP250108a/SN 2025kg's properties well and we do not rule it out (see Eyles-Ferris et al. (2025) for this interpretation).

- In model (c), we find evidence that EP250108a/SN 2025kg possesses an extended CSM, with an envelope mass of $\sim 0.1 \mathrm{M}_{\odot}$ and radius of $\sim 4 \times 10^{13}$ cm. We place these parameters in the context of other SNe Ic-BL that show evidence of possessing an extended CSM, and find that its parameters are most consistent with LLGRB 060218/SN 2006aj. The overall properties of EP250108a/SN 2025kg make it a close analog of LLGRB 060218/SN 2006aj.

Therefore, we conclude that EP250108a/SN 2025kg shows evidence of extended CSM interaction. EP has opened a new discovery space for discovering SNe Ic-BL in tandem with EFXTs, providing a novel avenue for understanding their multiwavelength emission, as well as probing their surrounding CSM. Understanding the landscape of these unique SNe Ic-BL, along

with their relation to LLGRBs, EFXTs, XRFs, LFBOTs, and other known classes of relativistic transients, is essential for furthering our understanding of the continuum of relativistic stellar explosions and the various open questions that exist along that continuum.

Acknowledgements

G.P.S. thanks Jillian Rastinejad and Rob Eyles-Ferris for useful discussions about the nature of this source. G.P.S. thanks Kaustav K. Das for useful insight about the relationship between the peaks in double-pekaed SNe. G.P.S. thanks Ehud Nakar for useful discussions regarding the interpretaion of this source. G.P.S. thanks Simi Bhullar for her moral support during the paper writing process. B. O. is supported by the McWilliams Fellowship at Carnegie Mellon University. K. Maeda acknowledges support from JSPS KAKENHI grants JP24KK0070 and JP24H01810, and from JSPS Bilateral Joint Research Project (JPJSBP120229923). H.K. was funded by the Research Council of Finland projects 324504, 328898, and 353019.

The observations by Gemini-S (S24B-041, GS-2024B-Q-101, GS-2024B-Q-102, PI: K. Maeda) were carried out within the framework of Subaru-Keck/Subaru-Gemini time exchange program which is operated by the National Astronomical Observatory of Japan. We are honored and grateful for the opportunity of observing the Universe from Maunakea, which has the cultural, historical and natural significance in Hawaii. The Liverpool Telescope is operated on the island of La Palma by Liverpool John Moores University in the Spanish Observatorio del Roque de los Muchachos of the Instituto de Astrofisica de Canarias with financial support from the UK Science and Technology Facilities Council. Some of the data presented herein were obtained at the W.M. Keck Observatory, which is operated as a scientific partnership among the California

Institute of Technology, the University of California and the National Aeronau- tics and Space Administration. The Observatory was made possible by the generous financial support of the W.M. Keck Foundation. The authors wish to recognize and acknowledge the very significant cultural role and reverence that the summit of Mauna Kea has always had within the indigenous Hawaiian community. We are most fortunate to have the opportunity to conduct observations from this mountain. Observations reported here were obtained at the MMT Observatory, a joint facility of the Smithsonian Institution and the University of Arizona. This work was also based on observations made with the Nordic Optical Telescope, owned in collaboration by the University of Turku and Aarhus University, and operated jointly by Aarhus University, the University of Turku and the University of Oslo, representing Denmark, Finland and Norway, the University of Iceland and Stockholm University at the Observatorio del Roque de los Muchachos, La Palma, Spain, of the Instituto de Astrofisica de Canarias. This work makes use of observations from the Las Cumbres Observatory global telescope network. Based on observations obtained at the Southern Astrophysical Research (SOAR) telescope, which is a joint project of the Ministério da Ciência, Tecnologia e Inovações (MCTI/LNA) do Brasil, the US National Science Foundation's NOIRLab, the University of North Carolina at Chapel Hill (UNC), and Michigan State University (MSU). The National Radio Astronomy Observatory and Green Bank Observatory are facilities of the U.S. National Science Foundation operated under cooperative agreement by Associated Universities, Inc.

Chapter 7: EP250827b/SN 2025wkm: An X-ray Flash-Supernova Powered by a Central Engine and Circumstellar Interaction

7.1 Introduction

Unlike gamma-ray bursts (GRBs), whose populations are relatively well characterized (Berger, 2014; Piran, 2004; Woosley, 1993), the origins of extragalactic fast X-ray transients (EFXTs) are still a mystery. EFXTs are short flashes of soft X-ray emission ranging from minutes to hours, discovered in the energy range 0.3 – 10 keV. The majority of historical satellites (e.g., *Swift*, *Fermi*) focused on studying the gamma-ray sky, resulting in the under-exploration of the EFXT discovery space. The few historical satellites sensitive to soft X-rays (HETE-2, $\sim 0.5 - -10$ keV; Beppo-Sax, $\sim$ 2 – 25 keV; MAXI, $\sim$ 0.5 – 30 keV) found a small number of EFXTs (Heise et al., 2001; Negoro et al., 2016; Sakamoto et al., 2005), but studies determined their intrinsic rates are likely comparable to those of classical GRBs (Heise et al., 2001; Sakamoto et al., 2005). Additional EFXTs were discovered through searches of historical archives (Quirola-Vásquez et al., 2022), but the lack of real-time follow-up made their characterizations difficult.

Many EFXTs have accompanying high-energy gamma-ray emission; however, some have intrinsic peak energies $\lesssim 25$ keV, which is lower than those of classical GRBs (hundreds of keV) and higher than those of supernovae (SNe; tens of eV). These EFXTs with low peak energies

are known as X-ray Flashes (XRFs), and the characteristics of their progenitor systems are a major open question. Some possibilities include high-z (Heise et al., 2001) or off-axis (Mészáros et al., 1998; Rhoads, 1997) GRBs, baryon-loaded GRBs with low Lorentz factors known as "dirty fireballs" (Dermer et al., 1999), supernova (SN) shock breakout or cooling (Balberg & Loeb, 2011; Colgate, 1974), tidal disruption events (TDEs; Quirola-Vásquez et al. 2022), off-axis GRBs (Sarin et al., 2021), magnetars after binary neutron star mergers (Lin et al., 2022; Quirola-Vásquez et al., 2024; Sun et al., 2017; Xue et al., 2019; Zhang, 2013), or new, never-before-seen classes of transient phenomena.

The Einstein Probe (EP; Yuan et al. 2022b, 2025), or Tianguan mission is changing the landscape of EFXT and XRF science, with its wide-field, soft X-ray capabilities. EP's all sky monitor (ASM) Wide-field X-ray Telescope (WXT) has an instantaneous field of view of 3850 deg^2 and operates from 0.5 to 4 keV. With over 10 times the field of view and more than one order of magnitude greater sensitivity than MAXI (Matsuoka et al., 2009), the only other currently operational X-ray ASM, EP has revolutionized the study of the soft X-ray time-domain sky. EP also possesses two conventional X-ray focusing telescopes (Follow-up X-ray Telescope, FXT) operating from 0.3 – 10 keV that can provide arcsecond localizations.

In its first 1.5 years of operations, EP has already discovered numerous EFXTs, as well as a smaller sample of XRF candidates. EP240801a was a confirmed XRF with $E_{\rm peak} \sim 15$ keV and was interpreted as either an off-axis or intrinsically weak jet (Jiang et al., 2025). EP241021a had no accompanying γ-ray emission (Shu et al., 2025), along with a luminous optical and radio counterpart (Busmann et al., 2025; Gianfagna et al., 2025; Quirola-Vásquez et al., 2025; Shu et al., 2025; Wu et al., 2025; Yadav et al., 2025). There are many proposed interpretations for EP241021a, including afterglow emission from wobbling jets (Gottlieb, 2025; Gottlieb et al.,

2022), refreshed GRB shocks accompanying a low-luminosity GRB (Busmann et al., 2025), a compact star merger producing a compact object or binary compact object system (Sun et al., 2025; Wu et al., 2025), an intermediate mass black hole tidal disruption event (Shu et al., 2025), a collapsar origin with extra energy input from a central engine (Quirola-Vásquez et al., 2025), or an off-axis jet (Gianfagna et al., 2025).

An even smaller subset of XRFs have detected associated SNe (XRF-SNe). These events are very important probes of the massive stellar deaths accompanying XRFs, giving a stronger indication of their progenitor system characteristics. Prior to EP, there were five such events – XRF020903 (Bersier et al., 2006; Soderberg et al., 2005), XRF030723 (Fynbo et al., 2004; Tominaga et al., 2004), XRF060218/SN 2006aj (e.g., Campana et al. 2006; Mazzali et al. 2006a; Sollerman et al. 2006), XRF080109/SN 2008D (e.g., Chevalier & Fransson 2008; Maund et al. 2009; Mazzali et al. 2008), and XRF100316D/SN 2010bh (e.g., Bufano et al. 2012; Cano et al. 2011). Although GRB-SNe have relatively uniform properties (Cano et al., 2017a; Srinivasaragavan et al., 2024a), studies of these XRF-SNe indicated they were diverse, giving more evidence that they may originate from different progenitors than classical GRBs. In addition, though all historical spectroscopically confirmed GRB-SNe and XRF-SNe were broad-lined Type Ic SNe (SNe Ic-BL; Cano et al. 2017a; Galama et al. 1998; Hjorth et al. 2003), the one exception was XRF080109/SN 2008D (e.g., Chevalier & Fransson 2008; Maund et al. 2009; Mazzali et al. 2008), which showed strong He features leading to a Type Ib SN classification. This diversity within the XRF-SN population may be due to a variety of factors - differing surrounding CSM environments implying heterogenous mass-loss histories (e.g., Soderberg et al. 2008; Srinivasaragavan et al. 2025a, the existence of binary or tertiary systems (Rastinejad et al., 2025), along with varying central engine powering mechanisms (e.g., Quirola-Vásquez et al. 2025; Sun et al. 2025)

have all been theorized to be the source of this diversity. However, no statistically robust conclusions have been made to date due to the small sample size of events.

EP has already found three speectroscopically confirmed XRF-SNe, dramatically increasing the rate of XRF-SN discoveries. EP250304a possessed no associated γ-ray emission (Ravasio et al., 2025a), and showed spectroscopic evidence that its optical counterpart was a SN Ic-BL (Izzo et al., 2025). Two other EP XRF-SNe have been studied in detail in the literature. EP240414a/SN 2024gsa (Hamidani et al., 2025b; Srivastav et al., 2025; Sun et al., 2025; van Dalen et al., 2025; Zheng et al., 2025) has $E_{\rm peak} < 1.3$ keV (Sun et al., 2025), making it an XRF. Its optical counterpart was a SN Ic-BL that possessed a mysterious early red peak. The origin of this peak had several theories in the literature, some of which included interaction of a GRB jet with a dense circumstellar medium (van Dalen et al., 2025), shock cooling emission following interaction with a dense circumstellar medium (Sun et al., 2025), an afterglow from a mildly relativistic cocoon (Hamidani et al., 2025b) or off-axis jet (Zheng et al., 2025), afterglow emission from wobbling jets (Gottlieb, 2025; Gottlieb et al., 2022), or refreshed shocks from a GRB (Srivastav et al., 2025). In addition, van Dalen et al. (2025) suggested that EP240414a had resemblances to luminous fast blue optical transients (LFBOTS; Drout et al. 2014; Ho et al. 2023; Margutti et al. 2019; Perley et al. 2019; Prentice et al. 2018; Pursiainen et al. 2018) due to its rise time, though its red colors indicate otherwise.

EP250108a/SN 2025kg was also an XRF, with $E_{\rm peak} < 1.8$ keV (Li et al., 2025c), and its associated SN 2025kg was a SN Ic-BL (Rastinejad et al., 2025; Srinivasaragavan et al., 2025a) that possessed a blue peak prior to the SN peaking. Similary to EP240414a/SN 2024gsa, there were varying interpretations for the progenitor system of this event, including cooling emission of black hole disk outflows (Gottlieb, 2025), a black hole-driven jet that is stifled by its progenitor

star's envelope, leading to a shocked cocoon (Eyles-Ferris et al., 2025), a similar shocked cocoon interacting with an extended circumstellar medium (CSM; Srinivasaragavan et al. 2025a), and a magnetar-powered explosion (Li et al., 2025c; Roman Aguilar & Bersten, 2025; Zhu et al., 2025a).

Recently, Quirola-Vásquez et al. (2025) argues that the late-time emission of EP241021a may be consistent with SNe Ic-BL, though no SN features were found in the spectrum at late-times, and the emission peaks at an order of magnitude higher than what is expected for SNe Ic-BL. We direct the readers to Quirola-Vásquez et al. (2025) for a further discussion of EP241021a as a possible XRF-SN, but do not consider it as an XRF-SN for the rest of this work.

In this Letter, we present the discovery EP250827b/SN 2025wkm at $z = 0.1194$, the fourth XRF-SN discovered by EP, and the third studied in detail in the literature. We note that EP250827b/SN 2025wkm was discovered through a different method than the previous three XRF-SNe, made possible by the Zwicky Transient Facility's (ZTF; Bellm et al. 2019; Dekany et al. 2020a; Graham et al. 2019; Masci et al. 2019) shadowing of EP's public observing schedule, which resulted in an optical counterpart association to a subthreshold EFXT (see §7.2.5.1 for more details). We discovered both the EFXT EP250827b as well as its optical counterpart SN 2025wkm, but note that Corcoran et al. (2025) reported the first classification as a SN Ic-BL.

The Letter is structured as follows: in §7.2 we present the observations of EP250827b/SN2025 wkm; in §7.3 we present analysis of the X-ray prompt emission, associated SN, and radio observations; in §7.4 we present analytical arguments to describe the X-ray prompt emission, in §7.5 we present light curve (LC) modeling used to characterize the SN LC; in §7.6 we discuss the implications our results; and in §7.7 we summarize our findings. Throughout this paper we utilize a flat ΛCDM cosmology with $\Omega_{\rm m} = 0.315$ and $H_0 = 67.4$ km s^{-1} Mpc^{-1} (Planck Col-

laboration et al., 2020) to convert the redshift to a luminosity distance and correct for the Milky Way extinction of $E(B-V)_{\rm MW} = 0.05$ mag (Schlafly & Finkbeiner, 2011a), using the Cardelli et al. (1989c) extinction law with $R_v = 3.1$.

7.2 Observations

In this section, we present the discovery and observations of EP250827b/SN 2025wkm.

7.2.1 X-ray Prompt Emission

EP250827b/SN 2025kg was detected by the WXT at RA = 36.581°, Dec = 37.499° (J2000; Schroeder et al. 2025c), with a positional uncertainty of 2.4 arcminutes in radius at 90% confidence level, incorporating both statistical and systematic errors, and reported by the offline archive search pipeline; see the WXT image in left panel of Figure 7.1. The source was not reported to the public NASA General Coordinates Network (GCN), as was the case for every other XRF-SN discovery. This is because the X-ray transient was not an onboard trigger, and was flagged as a subthreshold event in the EP data stream. Its confirmation as a real EFXT was only done after ZTF discovered its optical counterpart (see §7.2.5.1).

The WXT data were processed using the WXT Analysis Software (WXTDAS; Liu et al., in prep) with the latest calibration database (WXTCALDB V2.35). The CALDB was initially constructed from ground calibration experiments (Cheng et al., 2025) and subsequently refined through a series of in-flight calibration campaigns[1] conducted after launch (Cheng et al., in prep).

[1]In particular, the in-orbit effective area if found to be broadly consistent with the ground calibration result, showing systematic uncertainty arounf 10% (90% C.L). The energy response of the CMOS detector (i.e. the gain coefficient and energy resolution) is also in line with ground measurement, with slight variation of (1-2)%. No significant degradation in these parameters has been detected after nearly two years of on-orbit operations.

Photon positions were reprojected onto the celestial coordinate system, and the pulse-invariant value—representing energy in channel units—was computed for each event based on the bias and gain parameters stored in the CALDB. After flagging bad and flaring pixels and assigning event grades, we selected events with grades 0–12 and no anomalous flags to generate a cleaned event list and a corresponding image in the 0.5–4 keV band for subsequent source detection. The light curve and spectrum of the source and background within a specified time interval were extracted using a circular source region with a radius of 9 arcmin and an annular background region with inner and outer radii of 18 arcmin and 36 arcmin, respectively.

The temporal properties of the source, including the start time (t_0), total duration (T_{100}), and the T_{90} duration, were derived following a standard analysis procedure adapted for EP fast X-ray transients (Wu et al. in prep.). The start time of the transient was objectively determined by applying the Bayesian block algorithm to the net light curve, defined as the beginning of the first time bin with a signal-to-noise ratio (SNR) greater than 3. The redefined start time of the event is 2025-08-27T06:23:02.5 (UTC), which we refer to hereafter as t_0. The T90 duration was calculated as the time interval containing 90% of the total net counts (from 5% to 95% of the cumulative counts). The uncertainty on T90 was estimated using a Monte Carlo approach, wherein the net counts in each light-curve bin were independently resampled based on their Poisson statistics to generate multiple realizations of the net light curve. For each realization, T90 was recomputed from the accumulated counts, and the final uncertainty was derived from the distribution of the resulting T90 values. The measured T_{90} for EP250827b is $T_{90} = 1203.6^{+48.0}_{-55.5}$ s. Furthermore, inspection of the light curve, as shown in the right panel of Figure 7.1, indicates that the flare was still in progress at the end of the observation. Consequently, the derived duration is likely a lower limit, underestimating the true event duration.

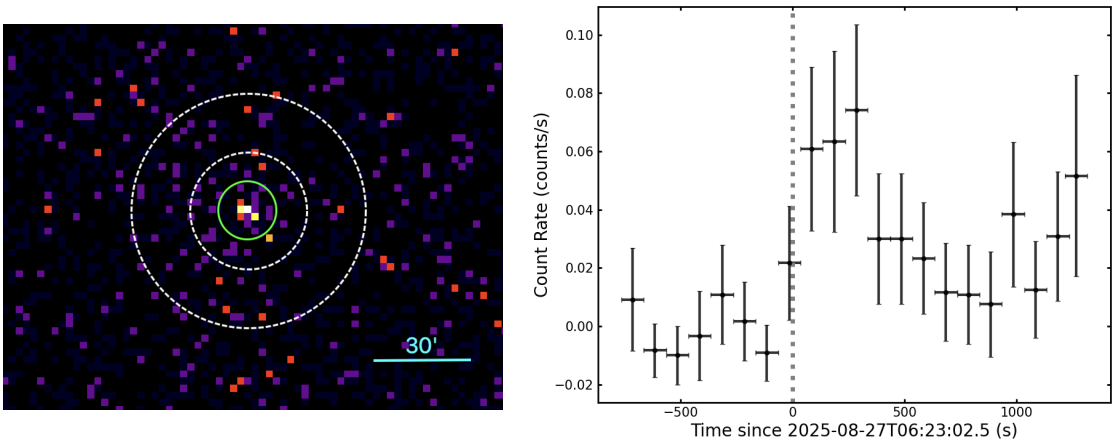

Figure 7.1: *Left*: The WXT image of EP250827b. The green circle represents the 9 arcmin aperture used for extracting the spectrum and the light curve of EP250827b. The dashed annulus with inner and outer radius of 18 arcmin and 36 arcmin indicates the background region. *Right:* The EP-WXT light curve of EP250827b. The vertical dashed line indicate the start time of the flare derived with the Bayesian block method.

7.2.2 X-ray Follow-up Observations

7.2.2.1 *Swift*-XRT

The *Neil Gehrels Swift Observatory* X-ray Telescope (Burrows et al., 2005) observed SN 2025wkm on 2025-08-31 (PI: M. Coughlin), 2025-09-05, and 2025-09-09 (PI: X. Hall; Table F.1), but did not detect any source (Hall et al., 2025). We used the Living Swift XRT Point Source Catalogue (LSXPS; Evans et al., 2022) upper limit server[2] to derive 3σ upper limits, shown in Table F.1, in the energy range of 0.3 – 10 keV, assuming a photon index $\Gamma = 2$.

7.2.2.2 Einstein Probe FXT

Follow-up observations were conducted with the EP-FXT instrument over a period spanning from 4.8 to 26.8 days after the trigger. The FXT, one of the primary payloads aboard EP,

[2] https://www.swift.ac.uk/LSXPS/ulserv.php

operates in the 0.3–10 keV energy band. It comprises two co-aligned modules (FXT-A and FXT-B), each equipped with 54 nested Wolter-I paraboloid–hyperboloid mirror shells. The source and background regions in the FXT data were processed using dedicated FXT data analysis software. A summary of the EP observations is provided in Table F.1. No X-ray sources were detected in any of the four EP-FXT observations. We estimated the 90% confidence upper flux limits assuming the same spectral model as used in the WXT analysis, shown in table F.1.

7.2.3 Gamma-Ray Constraints

There was no Fermi-GBM (Meegan et al., 2009) onboard trigger around t_0, and during the duration of the event. While the location of the transient was visible above Earth to Fermi/GBM for this full duration, Fermi entered the South Atlantic Anomaly about 100 s after t_0 and thus has no data after this time. The GBM targeted search (Goldstein et al., 2019), developed to search for GRB-like signals between 64 ms and 32.768 s in duration, was run in the time interval [t_0-50; t_0+100] s, finding no signal consistent with the EP transients, neither temporally nor spatially. Using the "soft" spectral template (Band function with $E_{\rm p}$ = 70 keV, α = -1.9, β = -3.7), we derived a flux upper limit of 3.52×10^{-9} erg cm^{-2} s^{-1}, in the energy band 10-1000 keV.

7.2.4 Radio Observations

We observed the field of EP250827b/SN 2025wkm with the NSF's Karl G. Jansky Very Large Array (VLA) on 2025-09-13 at a mid time of 13:03:23 UT ($\sim$ 17.3 days post burst) at a mid frequency of 10 GHz (4 GHz bandwidth) under program 25B-363 (PI Perley). We used J0251+4315 for complex phase calibration and 3C48 for flux and gain calibration. We reduced

and imaged the data using the Common Astronomy Software Applications (CASA; McMullin et al., 2007b) VLA Calibration Pipeline[3] and VLA Imaging Pipeline[4]. At the location of SN 2025wkm, we detect a $\sim 6\sigma$ source. We measure the flux density of the source using the `imtool` tool from `pwkit` (Williams et al., 2017), and find $F_\nu = 28 \pm 5$ μJy (beam size of $0.7'' \times 0.6''$).

We initiated an additional epoch at 10 GHz on 2025 September 25 at a mid-time of 04:24:50 UT (~ 28.9 days post burst), and measure the flux density of the source to be $F_\nu = 29 \pm 5$ μJy (beam size of $1.1'' \times 0.6''$). Given the lack of evolution of the radio source, we do not associate this source with SN 2025wkm, and rather assume the radio emission arises from the host galaxy (see §7.3.5 and Figure 7.12 for estimates on how radio emission from the transient would result in temporal evolution over the two epochs). If the radio emission can be attributed solely to star formation, this would indicate a radio star formation rate of $\mathrm{SFR}_{\mathrm{radio}} \approx 3\ M_\odot\ \mathrm{yr}^{-1}$, similar to the optically derived SFR of $2.83 \pm 0.04\ M_\odot\ \mathrm{yr}^{-1}$ (§ 7.3.4). Given that the beam sizes of the images are similar to the apparent size of the host galaxy, we cannot disentangle whether any excess radio emission is present at the location of EP250827b/SN 2025wkm. Thus, we use our host galaxy detections as upper limits on the radio emission associated with EP250827b/SN 2025wkm for subsequent analysis (§ 7.3.5).

7.2.5 Photometric Observations

Here we present the photometric observations of EP250827b/SN 2025wkm. A full log of photometric and spectroscopic observations are presented in the Appendix, in Tables F.2 and F.3. Photometric uncertainties reported include both statistical (Poisson) errors and systematic errors

[3] `https://science.nrao.edu/facilities/vla/data-processing/pipeline`
[4] `https://science.nrao.edu/facilities/vla/data-processing/pipeline/vipl`

from template subtraction

7.2.5.1 ZTF Detection of Optical Counterpart

Starting in March 2025, ZTF began using its wide field of view (47 deg^2) to shadow the regions observed by the EP's WXT (Ahumada et al., 2025). The EP observing schedule is publicly available, and after requesting the corresponding fields, the ZTF scheduler adds to its plan those areas that have two or more EP observations.

The goal of this project is to co-discover sources detected by EP by crossmatching them with ZTF alerts, which includes sources reported publicly to GCNS, along with subthreshold sources only available to the ZTF+EP collaboration team. Using Kowalski (Duev et al., 2019) and Fritz, the SkyPortal (Coughlin et al., 2023; van der Walt et al., 2019a) instance of ZTF, the alerts are crossmatched within the EP detection error circles and sent to human scanners, who evaluate the temporal and spatial differences to assess whether the crossmatches are plausible optical counterparts.

On August 27th, 2025 (MJD 60914.4), during routine scanning of the ZTF-EP crossmatches, ZTF25abmpngy/SN 2025wkm was discovered. The spatial and temporal offsets from EP250827b were 0.27 arcmin and 0.23 days, respectively. It was originally detected in the r band at r = 20.33 $\pm$ 0.1 mag (Schroeder et al., 2025c), and subsequent detections showed a persistent optical source. The last upper limit from ZTF at the position of the transient was obtained on MJD 60913.42, 0.98 days before the first detection, with g $>$ 21.37 mag. The EP team reported that the associated EFXT was a subthreshold detection, and they confirmed that it was a real transient after the detection of the possible optical counterpart. This is why there was a 5 day

latency between the reported GCN (Schroeder et al., 2025c) and the detection of the EFXT. The relationship between latency of EFXT detections and the discovery of optical counterparts and spectroscopic redshift measurements is explored in O'Connor et al. (2025b).

7.2.5.2 The Spectral Energy Distribution Machine (SEDM)

We performed observations with the Spectral Energy Distribution Machine (SEDM; Blagorodnova et al., 2018c; Rigault et al., 2019a), mounted on the 60-inch telescope at Palomar Obsevatory. We took images in the g, r, and i-band throughout the duration of our campaign. Standard reduction techniques were applied to the data (Kim et al., 2022b). We used the Pan-STARRS1 catalog (PS1; Chambers et al., 2016b; Flewelling et al., 2020c) for photometric calibration. We performed image subtraction with FPipe (Fremling et al., 2016) which uses templates from PS1 imaging (Chambers et al., 2016b; Flewelling et al., 2020c).

7.2.5.3 Fraunhofer Telescope at Wendelstein Observatory (FTW)

We performed observations with the Three Channel Imager (3KK; Lang-Bardl et al. 2016) instrument mounted on the FTW (Hopp et al., 2014) in the g', r', i', z', and J bands. The optical CCD and NIR CMOS data were reduced using a custom pipeline developed at Wendelstein Observatory (Busmann et al., 2025; Gössl & Riffeser, 2002). For the astrometric calibration of the images, we used the Gaia EDR3 catalog (Gaia Collaboration, 2020; Gaia Collaboration et al., 2021; Lindegren et al., 2021). We used the Pan-STARRS1 catalog (PS1; Chambers et al., 2016b; Flewelling et al., 2020c) for the optical photometric calibration and the 2MASS catalog (Skrutskie et al., 2006) for the J band. Tools from the AstrOmatic software suite (Bertin, 2006; Bertin

& Arnouts, 1996b; Bertin et al., 2002) were used for the coaddition of each epoch's individual exposures. We used the Saccadic Fast Fourier Transform (SFFT; Hu et al. 2019) algorithm for image subtraction. For subtraction templates we use PS1 imaging for the g, r, i, and z bands (Chambers et al., 2016b; Flewelling et al., 2020c). For the J band, we use a synthetic host subtraction using `GALSYNTHSPEC`[5] with host modeling performed using Prospector (Johnson et al., 2021a).

7.2.5.4 TRT

We performed observations with the 70cm telescope of Thai-Robotic Telescope located at Sierra Remote Observatories, California, United States (TRT-SRO). Images observed were processed through standard procedures and combined using the Image Reduction and Analysis Facility (`IRAF;` Tody, 1986). The result flux was calibrated with nearby Pan-STARRS1 field stars (Chambers et al., 2019), with the correction from ref [6]. The logs of photometric observations and results are listed in Table F.2 in the Appendix.

7.2.5.5 ALT

We performed observations with the 100cm A, B and C telescopes of the JinShan project, located at Altay, Xinjiang, China (ALT-100A, ALT-100B and ALT-100C). The data were processed using standard procedures with the Image Reduction and Analysis Facility (`IRAF;` Tody, 1986). Aperture photometries were then conducted on the stacked images subtracting Pan-STARRS1 field images (Chambers et al., 2019), with zero points measured using the nearby

[5] `https://github.com/robertdstein/galsynthspec`
[6] `https://classic.sdss.org/dr4/algorithms/sdssUBVRITransform.php`

Pan-STARRS1 catalogs.

7.2.5.6 NOT

We performed observations using the Alhambra Faint Object Spectrograph and Camera (ALFOSC[7]) mounted on the 2.56 m Nordic Optical Telescope (NOT) located at the Roque de los Muchachos Observatory on La Palma (Spain). The data were processed using standard procedures with the Image Reduction and Analysis Facility (`IRAF`; Tody, 1986). Aperture photometries were then conducted on the stacked images subtracting Pan-STARRS1 field images (Chambers et al., 2019), with zero points measured using the nearby Pan-STARRS1 catalogs.

7.2.5.7 LCO

Through the Global Supernova Project (Howell & Global Supernova Project, 2017), we obtained the *BVgri*-band images with the network of 1.0 m telescopes of the Las Cumbres Observatory (LCO) (Brown et al., 2013). *BV* and *gri* point-spread function (PSF) photometry was calibrated to Vega and AB magnitudes, respectively. PSF photometry was performed using AutoPhot (Brennan & Fraser, 2022).

7.2.5.8 LT

We performed observations with the Liverpool Telescope (LT; Steele et al. 2004) IO:O camera in SDSS *ugriz* filters. Raw data was processed by the automatic LT IO:O reduction pipeline. For images in *griz* filters, image subtraction and PSF photometry was conducted using a custom pipeline, using Pan-STARRS1 as reference and for image calibration. *u*-band images

[7]http://www.not.iac.es/instruments/alfosc

were calibrated using the SDSS Extended Northern+Equatorial u'g'r'i'z' Standards [8] taken on each night of the observations. The *u*-band magnitudes were obtained via aperture photometry, and corrected to AB magnitude system [9]; host subtraction was not performed.

7.2.5.9 TNOT

We performed observations with the Tsinghua–Nanshan Optical Telescope (TNOT), an equatorial-mount telescope located at the Nanshan Station of the Xinjiang Astronomical Observatory (XAO), Chinese Academy of Sciences (CAS). The system comprises an 80 cm ASA800 Ritchey–Chrétien optical tube mounted on an ASA DDM500 premium equatorial mount. The field of view is $26.5' \times 26.5'$. Multi-band follow-up observations of EP250827b/SN 2025wkm were obtained with TNOT and reduced with IRAF (bias subtraction and flat-fielding). Instrumental magnitudes were measured with AutoPhot (Brennan & Fraser, 2022) and calibrated against the Gaia Synthetic Photometry catalog (Gaia Collaboration et al., 2023).

7.2.5.10 Swift-UVOT

We observed with the Ultra-violet Optical Telescope (Roming et al., 2005b), on board the *Neil Gehrels Swift Observatory*. Observations were conducted in three epochs, across all UV filters (U, UVW1, UVM2, UVW2). The data were reduced through `uvotredux`[10], using the standard `HEASOft` tools (Nasa High Energy Astrophysics Science Archive Research Center (Heasarc), 2014). We performed a synthetic host subtraction using `GALSYNTHSPEC`[11], with host

[8] `https://www-star.fnal.gov`
[9] `https://www.sdss4.org/dr17/algorithms/fluxcal`
[10] `https://github.com/robertdstein/uvotredux`
[11] `https://github.com/robertdstein/galsynthspec`

modeling performed using Prospector (Johnson et al., 2021a).

7.2.6 Spectroscopic Observations

Here we present the spectroscopic observations of EP250827b/SN 2025wkm.

7.2.6.1 Gemini

We performed observations with the Gemini Multi-Object Spectrographs (GMOS) at Gemini North under programs GN-2025B-Q-130 (PI: A. Ho), GN-2025B-FT-104 (PI: B. O'Connor), and GN-2025B-Q-125 (PI: G. Srinivasaragavan). Longslit spectroscopy of the optical transient was acquired on 2025-08-31, 2025-09-02, 2025-09-04, 2025-09-07, 2025-09-12, and 2025-10-03. We made use of both the B480 and R400 gratings. The data were reduced and analyzed using the `DRAGONS` software (Labrie et al., 2019).

7.2.6.2 NGPS

We performed observations with the Next Generation Palomar Spectrograph (NGPS; Jiang et al., 2018; Kasliwal et al., 2024) located on the Palomar Observatory 200-inch telescope. Spectra were obtained on 2025-09-02, 2025-09-17, 2025-09-24, and 2025-10-08. On UT 2025-09-02, 2025-09-17, and 2025-10-08 spectra were obtained with a 1.5" wide slit and 2x3 spatial $\times$ spectral binning. On UT 2025-09-24 the spectrum was obtained with a 1.0" wide slit and 2x2 spatial $\times$ spectral binning. While NGPS will eventually have four arms and obtain data from 310 nm-1040 nm at the time of these observations only the R and I channels (555nm-1040nm) were available. The data were reduced using standard methods with a custom pipeline developed for

NGPS.

7.2.6.3 NOT

We performed observations using the Alhambra Faint Object Spectrograph and Camera (ALFOSC[12]) mounted on the 2.56 m Nordic Optical Telescope (NOT) located at the Roque de los Muchachos Observatory on La Palma (Spain), one under the program P71-812 (PI: J.P.U.Fynbo) and two under the program NOIRLab-20255B-353868 (PI: T. Ahumada). The first spectrum under program P71-812 was obtained with a $1.3''$ wide slit, and the later two spectra under program NOIRLab-20255B-353868 were obtained with a 1.0“ wide slit, all using grism #4. The observations were taken on 2025-09-03, 2025-09-17 and 2025-09-27, respectively. The first spectrum was reduced using a standard procedure with the Image Reduction and Analysis Facility (`IRAF`; Tody, 1986), and the later two spectra were reduced in a standard manner using a custom fork of `PypeIt` (Prochaska et al., 2020b,c; Prochaska et al., 2020).

7.2.6.4 The Low Resolution Imaging Spectrometer (LRIS)

We performed observations using LRIS (Oke et al., 1995), mounted in the Keck I telescope, to acquire spectroscopy on 2025-10-22. We utilized the 400/8500 red grating and the long 1.0“ slit, with blue grism 400/3400. We then processed these data using `lpipe` (Perley, 2019b).

[12]http://www.not.iac.es/instruments/alfosc

7.3 Analysis

In this section we present analysis of EP250827b's X-ray emission, SN 2025wkm's LC, and the radio observations of the source.

7.3.1 X-ray Analysis

The WXT spectrum was analyzed with `XSPEC` (v12.14.0; Arnaud, 1996) using an absorbed power-law (`tbabs * ztbabs * powerlaw`, Wilms et al. 2000b). In this model, the `tbabs` component accounts for the fixed Galactic absorption (5.6 $\times 10^{20}$ cm^{-2}) and `ztbabs` represents intrinsic absorption ($N_{\rm H,ins}$) at the redshift of $z = 0.1194$. The `powerlaw` represents a power-law spectrum of the form $N(E) = K \times (E/1\ {\rm keV})^{\alpha}$, where K is the normalization and α is the photon index. This fit yielded a photon index of $\alpha = -3.3^{+1.0}_{-1.7}$, and the intrinsic absorption cannot be well constrained ($N_{\rm H,ins} < 7.1 \times 10^{21}{\rm cm}^{-2}$; 90% confidence) with an acceptable fit statistic of CSTAT/d.o.f. = 27.8/28 (Cash, 1979). The corresponding average unabsorbed flux in the 0.5-4.0 keV band is $3.4^{+6.0}_{-1.2} \times 10^{-11}$, while the peak flux reaches $1.5^{+0.8}_{-0.8} \times 10^{-10}$. The best-fit results are shown in Figure 7.2.

For comparison, an absorbed blackbody model (`tbabs * ztbabs * bbody`) was also tested. With this model, this did not significantly improve the fit and similarly gave poorly constrained intrinsic absorption, with a 90% upper limit of $N_{\rm H,ins} < 2.1 \times 10^{21}$ cm^{-2} and a temperature of 0.22 ± 0.03 keV.

The soft spectrum, as characterized by the single power-law model, suggests a spectral peak energy ($E_{\rm peak}$) near or below the WXT's lower energy bound of 0.5 keV. To quantify this, we used an absorbed broken power-law model (`tbabs * ztbabs * bknpower`), fixing the

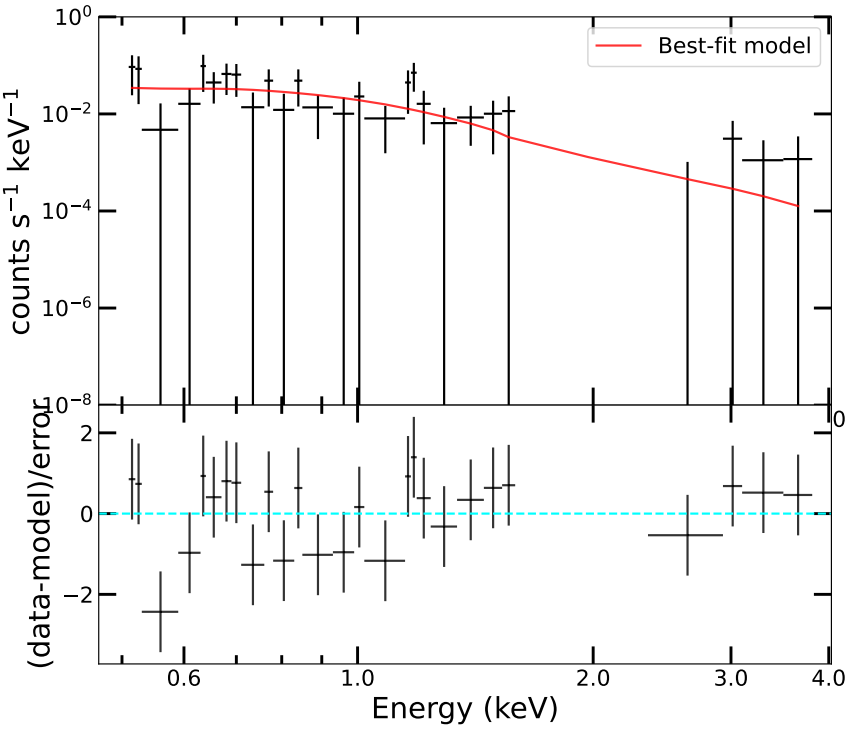

Figure 7.2: The EP-WXT observed spectrum and the predicted best-fit absorbed power-law model. Data are presented as the count rate spectrum with 1σ uncertainties.

first power-law index ($\alpha_{\rm X}$) to the typical GRB value of -1, motivated by the possible connection between EP X-ray transients and GRBs (Aryan et al., 2025). The second index ($\beta_{\rm X}$) was fitted to be $-3.3^{+1.1}_{-1.7}$, consistent with the single power-law model. While the $E_{\rm peak}$ itself could not be well constrained, we obtained a 90% confidence upper limit of $E_{\rm peak} < 1.5$ keV [13]. This model provided a comparable fit statistic to the single power-law (CSTAT/(d.o.f.) = 27.7/28), despite the additional free parameter. All fitting results are summarized in Table 7.1.

In Figure 7.3, we show the X-ray light curve of EP250827b compared to other XRF-SNe, along with SN 2020bvc (Ho et al., 2020e; Izzo et al., 2020), which was a similar double-peaked SN Ic-BL that was discovered optically, without the use of a high-energy trigger. We also show

[13] We attempted to fit the spectrum using the absorbed broken power-law model, fixing the $\alpha_{\rm X}$ to values between -0.8 and -1.2. Under these assumptions, the derived 90% confidence upper limits on $E_{\rm peak}$ fall within the range of -1.4 keV to -1.7 keV.

Model	$\alpha_{\rm X}$	$\beta_{\rm X}$	$E_{\rm peak}$ (keV)	T_{BB} (keV)	$N_{\rm H,int}$ (10^{21} cm^{-2})	$F_{\rm unabs}$ 0.5 – 4 keV (10^{-11} erg cm^{-2} s^{-1})	CSTAT/(d.o.f)
Power-law	$-3.3^{+1.0}_{-1.7}$	-	-	-	<7.1	$3.4^{+6.0}_{-1.2}$	27.8/28
Blackbody	-	-	-	$0.22^{+0.03}_{-0.03}$	<2.1	$1.9^{+0.3}_{-0.3}$	28.3/28
Broken Power-law	-1 (Fixed)	$-3.3^{+1.1}_{-1.7}$	<1.5	-	<7.0	$3.4^{+5.8}_{-1.2}$	27.8/28

Table 7.1: Spectral results of X-ray observations of EP250827b/SN 2025wkm. Errors represent the 1σ uncertainties. The upper limits are at the 90% confidence level.

the X-ray afterglow emission from a highly energetic, classical long GRB (Srinivasaragavan et al., 2024a) as reference. We see that EP250827b's prompt emission is fainter than that of XRF060218, and on the lower end of EP250108a's error bars. The upper limits following the prompt emission are consistent with XRF060218's X-ray afterglow LC, as well as detections corresponding to SN 2020bvc.

7.3.2 Ultraviolet, Optical, and Near-Infrared Light Curve Analysis

We show the light curve (LC) of EP250827b/SN 2025wkm in Figure 7.4, in the UVM2, UVW1, and $grizJ$ bands. We constructed the LC by combining all available photometry from all facilities, retaining each instrument's native pass-band. We removed outliers by discarding measurements more than 2σ from the data distribution by comparing the observed data point to the nearest two points. When a single facility obtained multiple measurements within the same night, we consolidated them into one nightly point per band using an inverse variance weighted average. This occurred most frequently for ZTF, where chip-gap coverage often produces repeated visits within a night. In the following analysis, we account for the Milky Way extinction of $A_{\rm V} = 0.155$ mag. We describe constraints on the host galaxy extinction in §7.3.4, but do not account for it in our analysis, as we only derive an upper limit.

The LC possesses a clear initial peak in the gri bands at ~ 2 days after t_0, assumed to be the

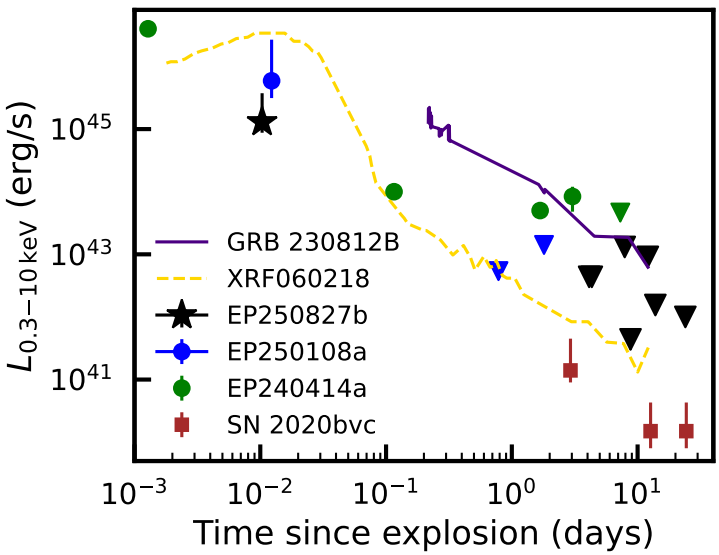

Figure 7.3: Comparison of 0.3 – 10 keV X-ray upper limits of EP250827b/SN 2025kg (black points) to the X-ray LCs of GRB 230812B/SN 2023pel (Hussenot-Desenonges et al., 2023; Srinivasaragavan et al., 2024a), LLGRB 060218a/SN 2006aj (Campana et al., 2006), EP250108a/SN 2025kg (Srinivasaragavan et al., 2025a), EP240414a/SN 2024gsa (Sun et al., 2025), and double-peaked SN Ic-BL SN 2020bvc (Ho et al., 2020e), with times in the rest frame. The WXT detections for the three EP events are also shown, though we show the luminosity in the 0.5 – 4 keV range, where the time of detection is estimated as the end-time of the X-ray detection.

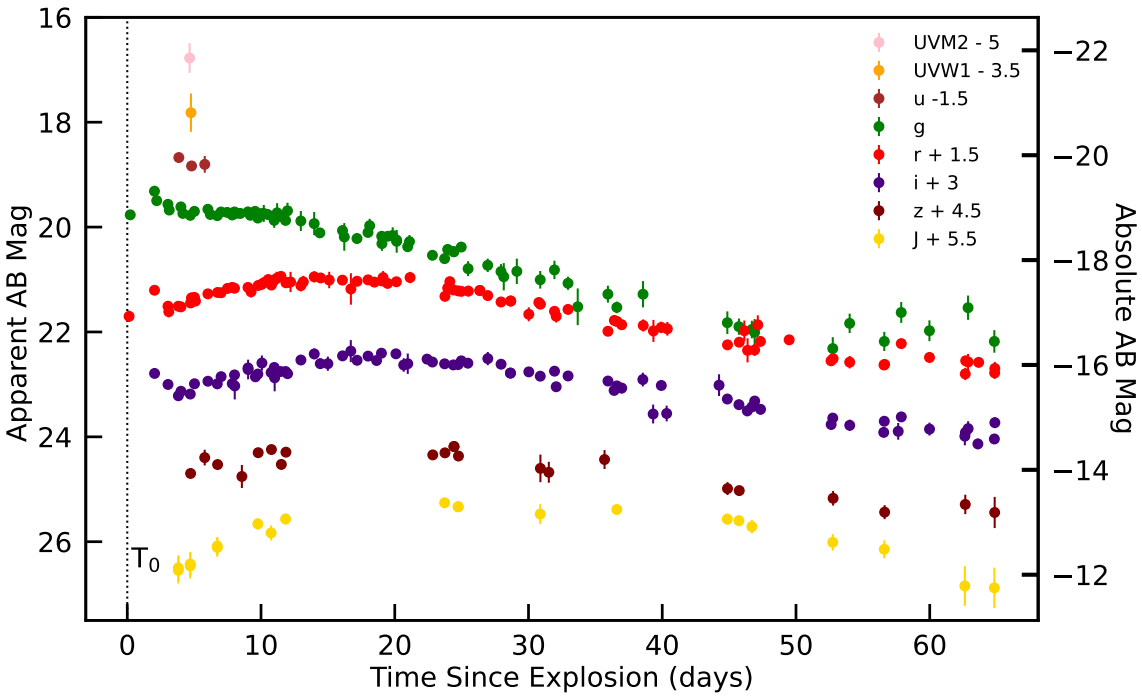

Figure 7.4: Light Curve of EP250827b/SN 2025wkm in UVM2, UVW1, and $grizJ$ bands, corrected for Milky Way extinction. We show the time of explosion t_0 with a vertical dotted line. In addition, we show the LC of EP250108a/SN 2025kg (Srinivasaragavan et al., 2025a) for comparison. The photometry is compiled using multiple different telescopes, and the process used to compile the LC is described in §7.3.2. A full table of the photometric observations, along with the different telescopes used for every epoch is presented in Table F.2 in the Appendix.

time of explosion for the rest of this work. The LC then declines in every band, and peaks again at progressively later times in the $grizJ$ bands, though sparser coverage in the z and J bands do not make it clear where the exact time of the peak is. The first optical detections in r and g band are 3.2 hours after t_0 in the observer frame, allowing for constraints on the rise of the initial first peak, unlike the LC for EP250108a/SN 2025kg (Eyles-Ferris et al., 2025; Li et al., 2025c; Srinivasaragavan et al., 2023), whose first optical photometry point was during the decline phase.

After the second photometry point in r and g band at t_0+2 days, the LC is already declining, and the decline continues until $\sim t_0 + 3$ days. Therefore, the LC most likely peaks prior to $t_0 + 2$ days. This corresponds to a lower limit on the absolute magnitude of the first peak of $M_g = -19.31 \pm 0.06$ and $M_r = -18.93 \pm 0.03$. The first peak has clear blue colors, where $g - r \sim -0.4$ mag. The luminosity and colors of the first peak are very similar to those of EP250108a/SN2025kg (Eyles-Ferris et al., 2025; Srinivasaragavan et al., 2025a), though the first peak declines on a much quicker timescale than for EP250108a/SN 2025kg ($\sim$ 5 days in r band and $\sim$ 8 days in g band).

We spectroscopically confirm a SN Ic-BL classification during the second phase of the optical LC (more details in §7.3.4). SN 2025wkm rises to maximum light during its second peak on a timescale of $\sim$ 14 days at an absolute magnitude of $M_r \sim -19.2$ mag, which again is similar to the r-band peak properties of SN 2025kg (Li et al., 2025c; Rastinejad et al., 2025; Srinivasaragavan et al., 2025a). However, the second peak in g band is not as pronounced, and the g band LC plateaus until around $\sim$ 12 days at $M_g \sim -19$ mag before it starts declining. This is unlike SN 2025kg, whose g band LC had a clear peak 18 days after explosion, with $M_g = -18.95 \pm 0.06$. In Figure 7.5, we show the g and B-band LCs of double-peaked SNe Ic-BL in the literature. SN 2025wkm clearly has a broader second peak than every other event

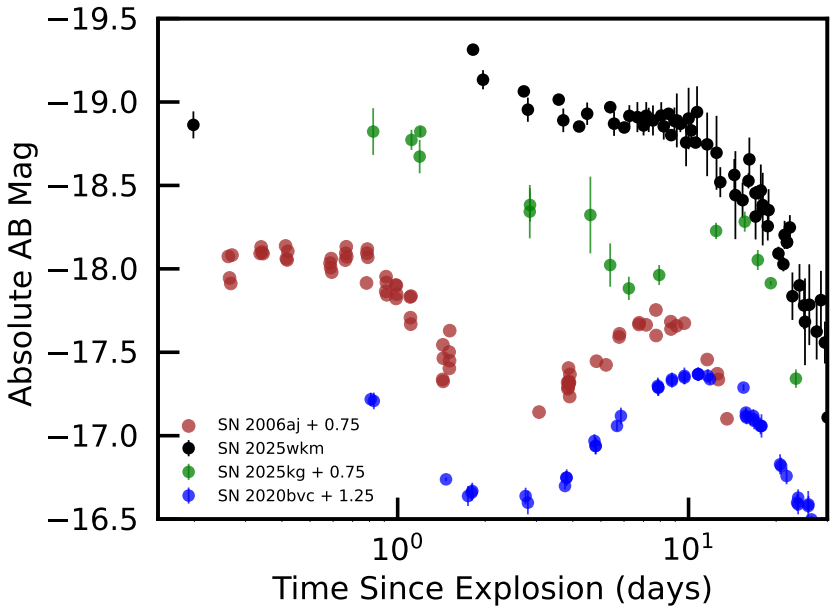

Figure 7.5: g-band LC of SN 2025wkm, in comparison to other double-peaked SN Ic-BL, including the g-band LCs of EP250108a/SN 2025kg (Srinivasaragavan et al., 2025a), SN 2020bvc (Ho et al., 2020e), and the B-band LC of XRF060218/SN 2006aj (Modjaz et al., 2006).

that has been observed, with a pronounced plateau rather than a decline into a second rise. The peak magnitude in r band corresponding to the second peak is within the median range reported for SNe Ic-BL in sample papers ($M_r = -18.5 \pm 0.9$; Srinivasaragavan et al. 2024b; Taddia et al. 2019a), and is consistent with the average seen in the GRB-SN population (Cano et al., 2017a).

An empirical correlation between the first peak and second peak in double-peaked stripped-envelope SNe exists – $M_2 = 0.8 \times M_1 - 4.7$, where M_1 and M_2 are the absolute magnitudes of the first and second peak, respectively, in r band (Das et al., 2024). Substituting M_1 into the expression, the second peak should have a brightness $M_2 \sim -19.3$ mag. This is consistent with the observed second peak brightness. In the sample of 54 stripped-envelope SNe this relation was tested on, only two were SNe Ic-BL (Das et al., 2024). The mechanism used to describe the first peak in these SNe was shock cooling emission from SN ejecta interacting with an extended CSM (Piro et al. 2021). EP250108a/SN 2025kg did not follow this correlation, though it still followed

the overall trend, where the first peak is more luminous than the second peak (Srinivasaragavan et al., 2025a).

7.3.3 Bolometric Luminosity Light Curve

Due to exquisite gri-band photometric coverage across the LC, along with the supplementation of one UV epoch, and multiple epochs in z and J band, we are able to construct a bolometric luminosity LC through fitting a blackbody model across different epochs. We bin the data every 0.5 days, and fit a blackbody to bins with at least 3 photometric band measurements. We do not compute bolometric luminosities for epochs where there are less than 3 photometric band measurements. We utilize the blackbody fitting tool in `Redback` (Sarin et al., 2024) to perform this analysis, and show the bolometric luminosity LC in Figure 7.6, along with the derived temperatures and radii in Figure 7.7.

We also show comparisons to the bolometric LCs of EP250108a/SN 2025kg, and XRF060218/SN 2006aj (Bianco et al., 2014; Brown et al., 2014; Modjaz et al., 2006). We note that the bolometric LC of EP250108a/SN2025 kg was computed using a different method, as there was only sparse i band coverage, and no coverage in any other bands. Srinivasaragavan et al. (2025a) utilized bolometric correction coefficients from Lyman et al. (2014a) to compute the bolometric luminosity LC, which were measured by fitting the SEDs of a large sample of stripped-envelope SNe with broadband coverage. The bolometric luminosity LC of XRF060218/SN 2006aj was computed using a similar method that we used, utilizing blackbody fits to photometry.

We find that the shape of the bolometric luminosity LC differs from those of SN 2006aj and SN 2025kg. Both SN 2006aj and SN 2025kg display a decline at the beginning of the

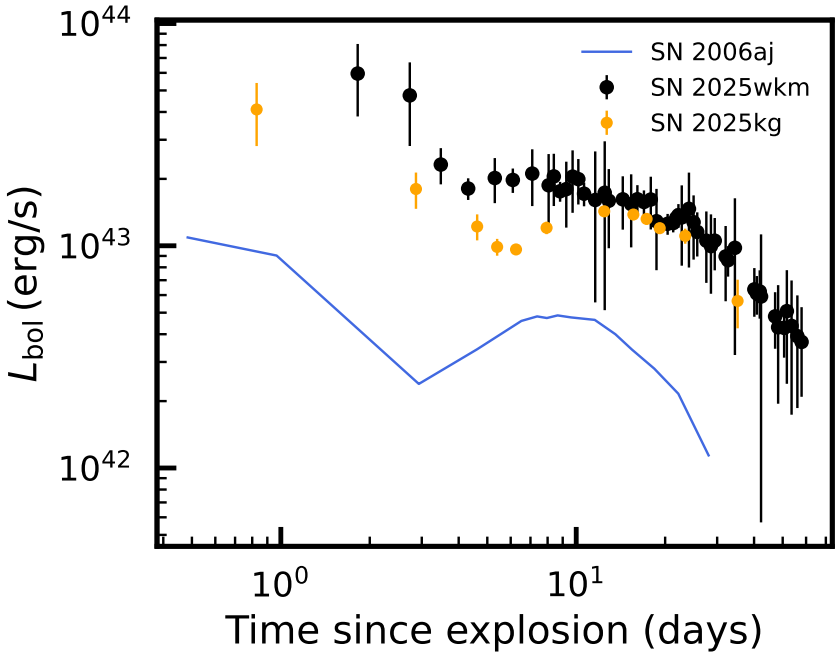

Figure 7.6: Bolometric luminosity LC of SN 2025wkm, computed through fitting blackbodies to SEDs binned every 0.75 days. We also show the bolometric luminosity LCs of SN 2025kg (Srinivasaragavan et al., 2025a) and SN 2006aj (Modjaz et al., 2006).

LC, which transitions into a clear rise that peaks at around 10 days after explosion and ends with a second decline. SN 2025wkm follows the trend of a decline at the beginning of the LC; however, there is not a clear second rise and decline like the other two events. Instead, the bolometric luminosity LC plateaus until $\sim$ 20 days, and then declines at a similar rate to the other two events. We note that we only have a r and g band point 2 hours after t_0, which does not allow us to compute a bolometric luminosity point at the beginning of the LC to capture the rise. Therefore, the peak bolometric lumonisity we derive during the first peak is a lower limit, which is $L_{\rm bol,peak} = 5.38 \pm 1.74 \times 10^{43}\,{\rm erg\,s^{-1}}$. This is comparable to the peak luminosity of SN 2025kg, but higher than SN 2006aj by a factor of ~ 5.

In Figure 7.7, we find that the blackbody temperature plateaus over the first $\sim$ 3 days and peaks at $\sim 20,000$ K, declines until $\sim$ 20 days, and plateaus around 5000 K for the remaining

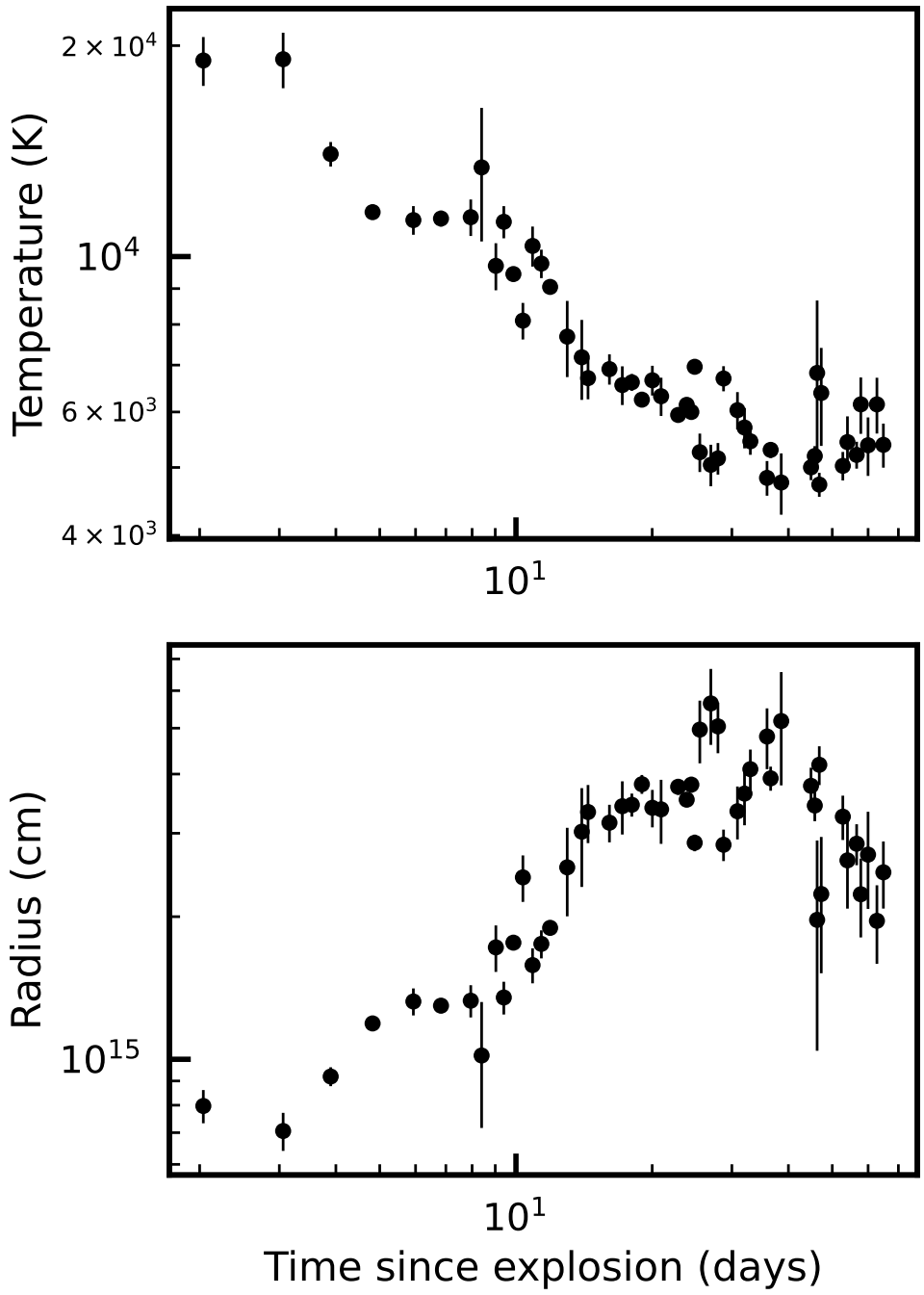

Figure 7.7: Temperature and Radius evolution as a function of time, from fitting blackbodies to SEDs binned every 0.5 days.

epochs. The blackbody radius decreases over the first ~ 3 days, increases around ~ 20 days, and then plateaus around 4×10^{15} cm. The decline in temperature until ~ 6 days after peak light is very similar to the behavior exhibited by samples of SNe Ic-BL presented in Taddia et al. (2019a) and Srinivasaragavan et al. (2024b). However, the radii of the SNe in these samples exhibited a decline after ~ 10 days after peak light, while the radius plateaus in SN 2025wkm.

In addition, the early-time behavior within the three days is unlike what is seen for most SNe Ic-BL. The plateau in temperature and decline in radius may be an artifact of the fitting procedure due to degeneracies between the blackbody temperature and radius. However, it is physically possible if a central engine is heating up inner parts of the ejecta, while outer parts are already optically thin. In this scenario, we expect the temperature to increase while the radius recedes. This scenario is consistent with progenitor scenarios we test in §7.5. The blackbody radius we derive at ~ 2 days is around 7.9×10^{14} cm, which corresponds to an average velocity over the first 2 days of $\sim 0.15c$. This is comparable to the average velocity of EP250108a/SN 2025kg of $\sim 0.1c$ over the first 3.9 days.

7.3.4 Spectral Analysis

We obtained ten spectra of EP250827b/SN 2025wkm up to $t_0 + 37.3$ days and present them in Figure 7.8, with host emission lines clipped. The early-time spectra up to $t_0 + 8.2$ days display a clear hot, blue continuum. A close-up of the first spectrum is shown in Figure 7.9, along with a comparison to spectra of XRF060218/SN 2006aj (Modjaz et al., 2006) and EP250108a/SN 2025kg (Srinivasaragavan et al., 2025a) at a similar rest-frame phase. We fit a blackbody to each of the spectra, and find that SN 2025wkm possesses a much higher temperature than the other

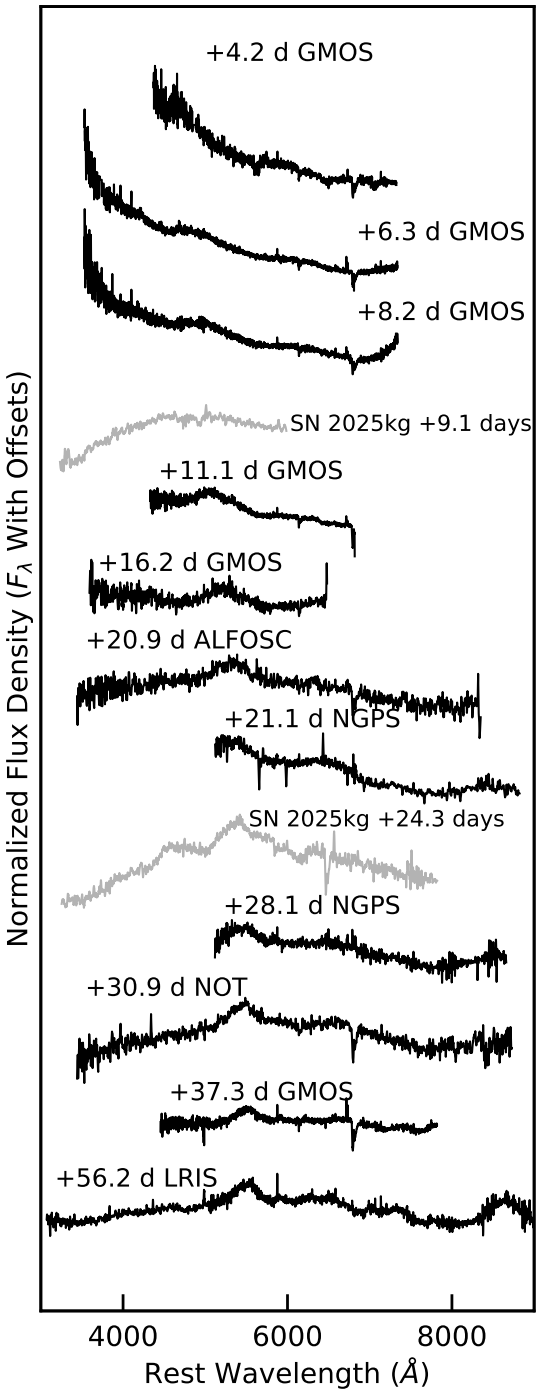

Figure 7.8: Spectra series of EP250827b/SN 2025wkm, with host galaxy emission lines clipped, along with the phase of the spectrum and the instrument it was taken on. The spectra start as a blue, mostly featureless continuum, and then evolve to redder SN spectra, with clear, broad absorption features. The lack of H and He and broad features allow for a classification of SN Ic-BL. We also show selected spectra of EP250108a/SN 2025kg at certain phases from Srinivasaragavan et al. (2025a). Some spectra have been smoothed for viewing purposes. The GMOS and ALFOSC spectra are not corrected for telluric features.

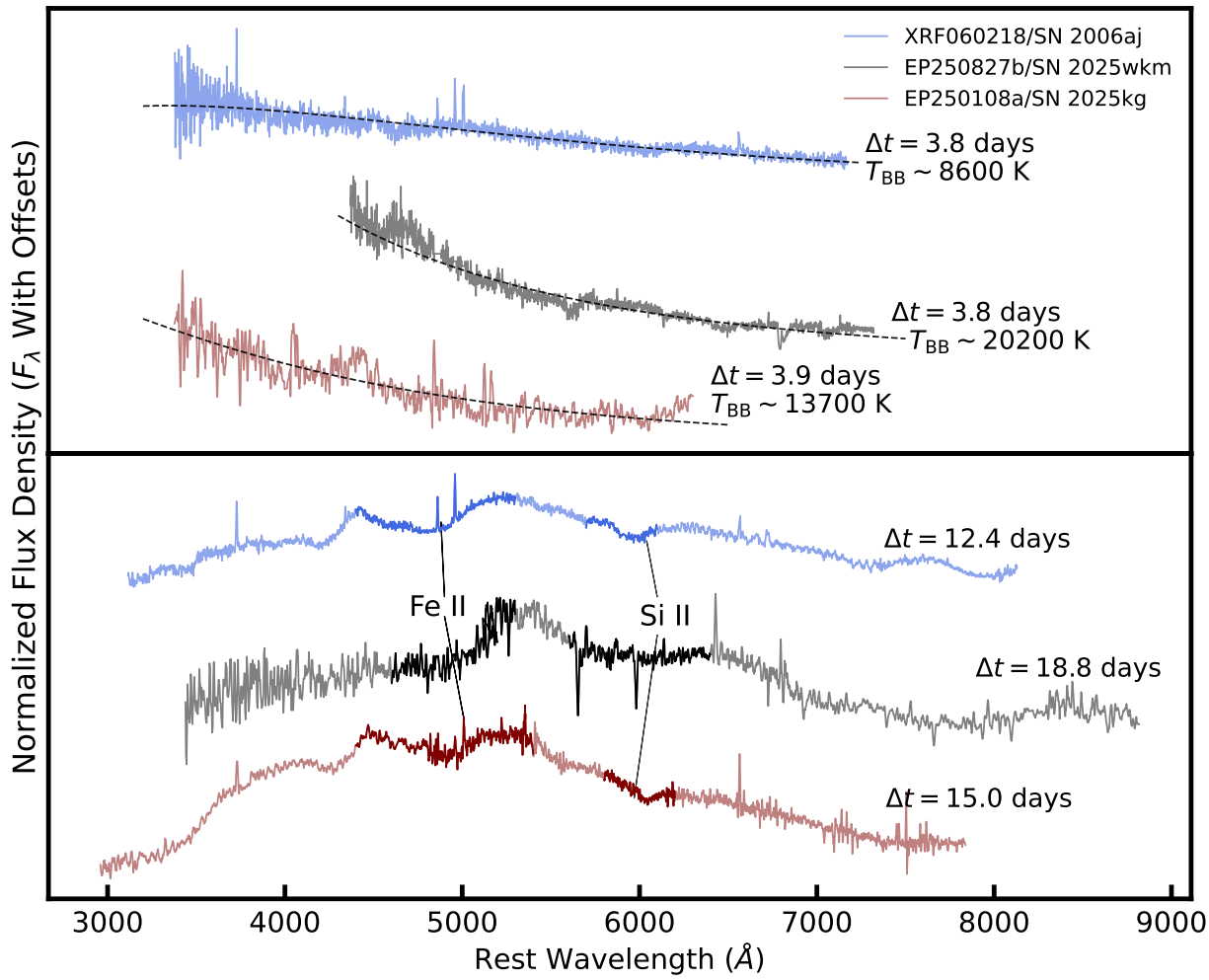

Figure 7.9: Close-up spectra of EP250827b/SN 2025wkm at 3.8 days and 18.8 days $+t_0$ (rest-frame). Comparison spectra of XRF060218/SN 2006aj (Modjaz et al., 2006) and EP250108a/SN 2025kg (Srinivasaragavan et al., 2025a) are also shown, at similar phases. Some host galaxy emission lines are clipped for viewing purposes. In the top panel, we also fit a blackbody spectrum to each of the spectra, and show the derived blackbody temperature ($T_{\rm BB}$). EP250827b/SN 2025wkm displays an extremely blue continuum in its first spectrum, along with a broad absorption feature $\sim 4500\mathring{A}$ corresponding to blueshifted Fe II at $\sim 40,000\,{\rm km\,s^{-1}}$. The blackbody temperature derived is $T_{\rm BB} \sim 20,200$ K, which is significantly hotter than $T_{\rm BB}$ for the compared events. In the bottom spectra, we see clear broad absorption features corresponding to blueshifted Fe II and Si II, and the lack of clear H and He absorption allow for a SN Ic-BL classification. We also show the Fe II and Si II absorption features bolded in the comparison spectra as reference.

two events, with $T_{\rm BB} = (2.2 \pm 0.6) \times 10^3$ K, which is consistent with the temperature found from fitting the SED at a similar phase in §7.3.3. Therefore, we find that SN 2025wkm stays blue for a longer time period than SN 2025kg. Figure 7.8 shows a spectrum of SN 2025kg 9.1 days after explosion if it exploded at $z = 0.1194$, and the spectrum shows a much redder continuum than SN 2025wkm does at $t_0 + 8.2$ days.

By the fourth spectrum at $t_0 + 11.1$ days, we find that the continuum reddens significantly, and broad absorption features in the spectra clearly develop, corresponding to blueshifted Fe II and Si II. We show a closer look at the SN spectra in Figure 7.9, and show the broad Fe II and Si II absorption features in bold. These features, along with a lack of H and He features, indicate that SN 2025wkm is a SN Ic-BL. We run the spectrum obtained at $t_0 + 11.1$ days through the SuperNova Indentification Code (Blondin & Tonry, 2007b), and find that the best-match spectrum is SN Ic-BL 1998bw, 7.8 days after explosion, allowing us to confirm its classification as a SN Ic-BL.

We then measure the velocity of the 5169 $\mathring{A}$ Fe II line for every spectrum using the open source code SESNspectraLib[14] (Liu et al., 2016; Modjaz et al., 2016). The Fe II line is a good proxy for the photospheric expansion velocity $v_{\rm ph}$ (Modjaz et al., 2016). We smooth each of the spectra using SESNspectraPCA[15]. SESNspectraLib then calculates the blueshift of the Fe II line at 5169 $\mathring{A}$ relative to a standardized SN Ic spectroscopic template at a similar phase. The uncertainty is estimated through adding the uncertainty on the velocity of the mean SN Ic template in quadrature with the uncertainty on the relative blue-shift. The uncertainty is dominated by the strength of the blueshifted Fe II absorption feature relative to the continuum.

[14]https://github.com/metal-sn/SESNspectraLib
[15]https://github.com/metal-sn/SESNspectraPCA

Time (days)	$v_{\rm ph}$ (km s^{-1})
4.2	40200 ± 14000
6.3	32700 ± 4800
8.2	27800 ± 4800
11.1	19600 ± 4800
20.9	15900 ± 2800
30.9	11900 ± 2700
57.2	8300 ± 2000

Table 7.2: Photospheric velocity measurements of SN 2025wkm.

We derive velocity measurements for 6 out of the 10 spectra, and they are presented in Table 7.2. In addition, we show the velocity evolution over time in Figure 7.10, compared to SN 2006aj (Modjaz et al., 2006), SN 2025kg (Srinivasaragavan et al., 2025a), as well as SN 2020bvc (Ho et al., 2020e; Izzo et al., 2020). We see that SN 2025wkm possesses much higher velocities at early times than all of the other comparable objects, though at later times, the velocity evolution flattens out and reaches broadly consistent values with the rest of the events.

Srinivasaragavan et al. (2025a) recognized a possible blueshifted Fe II feature in their spectrum of EP250108a/SN 2025kg taken at 3.9 rest-frame days after explosion (shown in Figure 7.9), corresponding to a velocity of $\sim 30,000$ km s^{-1}. However, they stressed that this line identification was not robust, in part due to low signal-to-noise in their spectra. In addition, they discussed that at the blackbody temperature they derived $\sim$ 13,700 K, Fe has mostly transitioned from Fe II to Fe III. In addition, the optical LC during the time of the spectral epoch had significant contributions from a component not dominated by radiaoctive decay (Eyles-Ferris et al., 2025; Li et al., 2025c; Srinivasaragavan et al., 2025a), which would make it surprising that a photospheric Fe II line was present in the spectrum.

However, our identification of a blueshifted Fe II feature in the spectrum of EP250827b/SN 2025wkm at $t_0 + 4.2$ days (a close-up shown in Figure 7.9) is more robust. Though the temper-

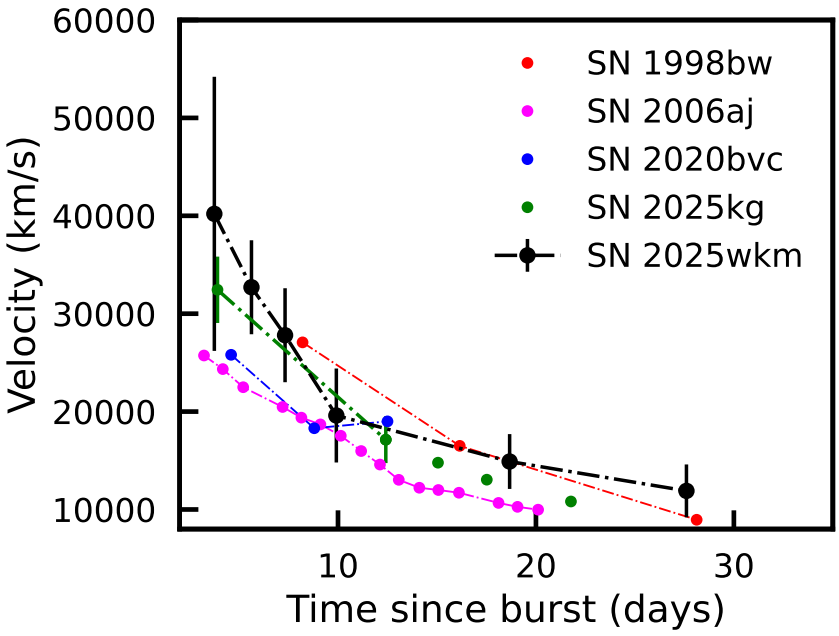

Figure 7.10: Photospheric velocity evolution for SN 2025wkm, compared to other prominent XRF and GRB–SNe (SN 1998bw, Iwamoto et al. 1998a; SN 2006aj, Mazzali et al. 2006a; SN 2025kg, Srinivasaragavan et al. 2025a) and double-peaked SN Ic-BL 2020bvc, Ho et al. 2020e), with times in the rest frame.

ature that we derive is still extremely high $\sim 20,200$ K, the signal-to-noise is much higher than that of the spectrum of EP250108a/SN 2025kg taken at a similar epoch, and the broad absorption feature at the beginning of the spectrum is seen much more clearly. A similar broad absorption feature at slightly redder wavelengths is also seen in XRF060218/SN 2006aj's early-time spectrum shown in the same Figure. Figure 7.8 shows that this absorption feature clearly shifts to redder wavelengths over time. In addition, though SN 2025wkm also displays an inital first peak in its LC not due to radioactive decay, the first peak declines much more rapidly than in SN 2025kg (see Figure 7.6), and it is therefore plausible that a photospheric line may be present at this stage in the LC's evolution.

We then try to estimate the host-galaxy extinction by measuring the equivalent width (EW) of the Na I absorption doublet (5890, 5896 $\AA$), using the NGPS spectrum at $t_0 + 28.1$ days. This

feature is a proxy for the amount of host-galaxy extinction, with various relations presented in the literature (Rodríguez et al., 2023b; Stritzinger et al., 2018). We use the relation from Rodríguez et al. (2023b), where $A_{\rm V}^{\rm host}[{\rm mag}] = 0.02 + 0.73 \times {\rm EW}[\text{Å}]_{\rm Na\,I} \pm 0.29$. However, Poznanski et al. (2011) showed that a large scatter exists in these correlations when using low-resolution spectra, and quantitative relations must be viewed conservatively. Therefore, we use the value derived through this method as a conservative upper limit for the host-galaxy extinction. We find $A_{\rm V}^{\rm host} < 0.73$ mag. This value is consistent with the extinction inferred from the Balmer decrement (Osterbrock, 1989) as well. If the host extinction is close to this upper limit and is significant, then the analysis performed in 7.3.2 would be impacted as the overall brightness of the LC would increase. For example, if $A_{\rm V,host} \sim 0.5$ mag, M_g would decrease by ~ 0.6 mag and M_r would decrease by ~ 0.4 mag, making EP250827b/SN 2025wkm brighter than EP250108a/SN 2025kg (Rastinejad et al., 2025; Srinivasaragavan et al., 2025a). However, given the lack of additional constraints, we do not try to further quantify the impact that host galaxy extinction may have on our analysis.

We also show the Keck LRIS spectrum obtained at $t_0 + 56.2$ days, without host-galaxy emission lines clipped, in Figure 7.11. The host galaxy has an abundance of nebular and recombination features characteristic of a star-forming galaxy: the [O II] doublet at $\lambda\lambda 3726, 3729$; Balmer lines from H$\eta$ through Hα (Hη 3835, Hζ 3889, Hϵ 3970, Hδ 4102, Hγ 4340, Hβ 4861, Hα 6563); He I at $\lambda\lambda 3889, 5876, 6678, 7065$; high-excitation [Ne III] at $\lambda\lambda 3869, 3967$; [O III] including the auroral line near $\lambda 4363$ and the strong nebular lines at $\lambda\lambda 4959, 5007$; [N II] $\lambda 6583$ adjacent to Hα; the [S II] doublet at $\lambda\lambda 6716, 6731$; and [Ar III] $\lambda 7136$. These emission lines allowed us to make a redshift measurement of $z = 0.1194 \pm 0.0002$. Additional narrow lines are shown in Figure 7.11. We estimate the star formation rate using the equivalent width of the

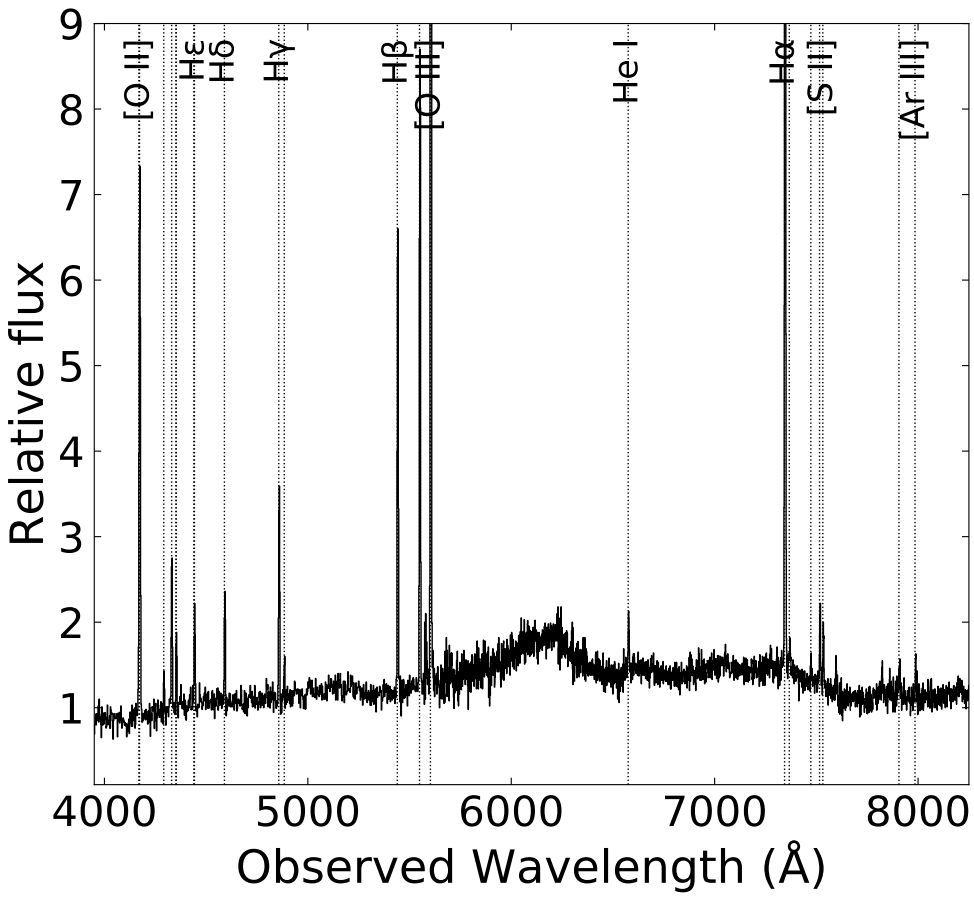

Figure 7.11: Late-time Keck LRIS spectrum on 2025-10-22 (corresponding to 56.2 days). We identify numerous narrow emission lines produced by star formation within the host galaxy. These lines yield a redshift of $z = 0.1194$. We note that the narrow galaxy lines are clipped in Figure 7.8.

observed Hα line (Kennicutt, 1998), and find a $\mathrm{SFR}_{\mathrm{H}\alpha} = 2.83 \pm 0.04\,\mathrm{M}_{\odot}\,\mathrm{yr}^{-1}$. This is consistent with the SFR derived from radio observations in §7.2.4.

7.3.5 Radio Analysis

The detection of EP250827b in conjunction with the discovery of the SN 2025wkm is reminiscent of nearby GRBs with associated SNe Ic-BL (Campana et al., 2006; Cano et al., 2017a; Modjaz et al., 2016; Soderberg et al., 2006a; Woosley & Bloom, 2006), and could imply that EP250827b was a GRB, either on-axis or moderately off-axis. With this context as a backdrop,

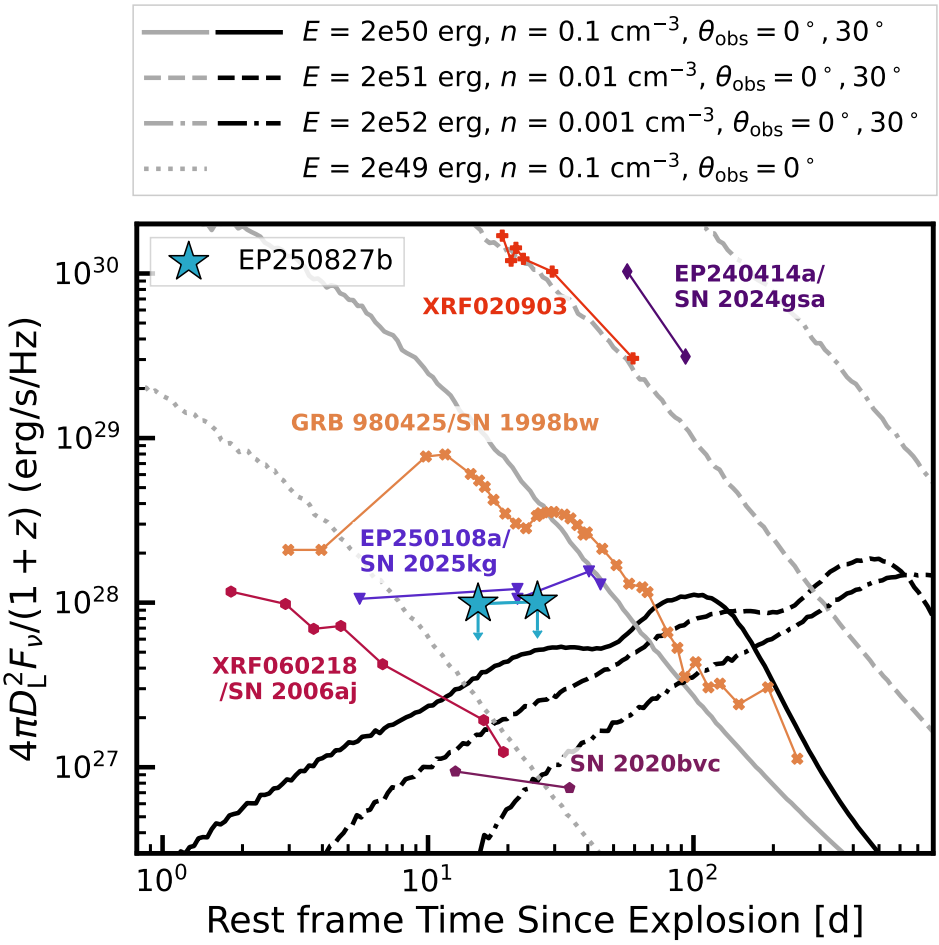

Figure 7.12: The 10 GHz radio light curve of EP250827b (blue stars), where we use the detection of the host galaxy as upper limits on the radio emission. Also shown are the radio light curves of LLGRB 980425/SN 1998BW (Kulkarni et al., 1998; Waxman et al., 1998), XRF060218/SN 2006aj (Soderberg et al., 2006b), XRF 020903 (Soderberg et al., 2004), the SNe Ic-BL 2020bvc (Ho et al., 2020f), and EP events EP240414A/SN 2024gsa (Bright et al., 2025) and EP250108a/SN 2025kg (Srinivasaragavan et al., 2025a). Lines represent predicted radio emission for an on-axis ($\theta_{obs} = 0°$, grey) or off-axis ($\theta_{obs} = 30°$, black) afterglow generated with the `FIREFLY` code (Dastidar & Duffell, 2024), for various pairs of jet energy E and circumburst density n.

we explore what constraints our radio observations can place on the progenitor of EP250827b.

The lack of detected radio emission associated with EP250827b/SN 2025wkm results in luminosity limits of $\sim 10^{28}$ erg s^{-1}Hz^{-1} (Figure 7.12), ~ 3 orders of magnitude lower than typical on-axis GRBs (Chandra & Frail, 2012), indicating that EP250827b was not produced by a typical on-axis GRB. We are also able to rule out emission similar to XRF 020903 (Soderberg et al., 2004) as well as EP240414A/SN 2024gsa (Bright et al., 2025), as our limits are ~ 2 orders of magnitude lower. However, many of the nearby ($z < 0.3$) GRB-SNe have belonged to the class of low-luminosity GRBs (LLGRB) and XRFs, such as the prototypical GRB-SN LLGRB 980425/SN 1998bw (Galama et al., 1998), and often have much lower radio luminosities than typical GRBs. Our luminosity limits are ~ 3–$5\times$ lower than the radio emission associated with LLGRB 980425/SN 1998bw at a similar frequency and epoch (Kulkarni et al., 1998; Waxman et al., 1998). However, we are unable to rule out low-luminosity ($\sim 10^{27}$ erg s^{-1}Hz^{-1}), fast-fading radio emission, such as that associated with XRF060218/SN 2006aj (Soderberg et al., 2006b) and the double-peaked SN Ic-BL 2020bvc (Ho et al., 2020e), at a similar frequency and epoch. Similar luminosity limits, and as a result constraints, were achieved for the recent EP250108a/SN 2025kg (Srinivasaragavan et al., 2025a).

If EP250827b was the result of an off-axis GRB, we may expect to see late-rising radio emission as the GRB jet decelerates and spreads. Several studies searching for late-rising radio emission following SNe Ic-BL have been performed, with some promising candidates (Berger et al., 2003a; Corsi et al., 2016, 2023; Schroeder et al., 2025b; Soderberg et al., 2006a). We compare our limits to GRB afterglow models generated by the `FIREFLY` code (Dastidar & Duffell, 2024), where we assume a jet opening angle of $\theta_{\rm j} \approx 7^{\circ}$, electron powerlaw index $p = 2.133$, and fractions of energy imparted on the electrons and magnetic field of $\epsilon_{\rm e} = 0.1$ and $\epsilon_{\rm B} = 0.01$,

respectively. We vary the values of the total jet energy E and circumburst density n to determine what combinations are compatible with our radio limits.

Based on these generated models, we find that our limits are consistent with a GRB observed $\theta_{\rm obs} \approx 30^\circ$ off-axis with typical GRB energies of $E \approx 10^{50}$–10^{52} erg (e.g. Bloom et al., 2003; Frail et al., 2001; Granot & van der Horst, 2014b), assuming the circumburst density is $n \approx 10^{-3}$–10^{-1} cm^{-3}, with higher energies requiring lower densities to be consistent with our limits. Additionally, a low energy on-axis ($\theta_{\rm obs} = 0^\circ$) GRB ($E \approx 10^{49}$ erg) is still consistent with our limits, even within a moderately high density environment ($n \approx 0.1$ cm^{-3}), as such emission is expected to fade beyond detection prior to our first observation. Given the radio brightness of the host galaxy, in order to confidently detect a late rising radio afterglow, the emission must rise above ~ 45 μJy ($\sim 2 \times 10^{28}$ erg s^{-1}Hz^{-1}), which we predict will occur $\gtrsim 1$ year post burst for energies $E \gtrsim 10^{51}$ erg.

Overall, EP250827b is not consistent with a a typical on-axis GRB with a radio afterglow luminosity of $\sim 10^{31}$ erg s^{-1}Hz^{-1} and energy of 10^{50}–10^{52} erg. However, a lower energy on-axis jet ($\sim 10^{49}$ erg) or a higher energy ($\sim 10^{50}$–10^{52} erg) off-axis ($\theta_{\rm obs} \sim 30^\circ$) GRB is still consistent with our non-detections. Deep, late-time ($\gtrsim 1$ year) radio follow-up of EP250827b may reveal a rising radio component, which would support the off-axis GRB scenario.

In addition, we note here that a magnetar central engine is favored by the optical light curve analysis (see §7.5.1.2). Radio emission from an embedded magnetar wind nebula is expected to arise in these systems (e.g., Metzger et al. 2014; Murase et al. 2016; Omand et al. 2018). However, the emission is expected to be strongly absorbed by the SN ejecta at ∼weeks (Eftekhari et al., 2021; Metzger et al., 2014), and thus our 10 GHz limits primarily constrain external-shock scenarios from jets or cocoons, while meaningful wind magnetar nebula constraints require

higher frequency or later epoch observations.

7.4 Estimating the X-ray Prompt Emission

In this section, we test two different models to see if they can reproduce the X-ray prompt emission described in §7.2.1. In particular, we check if the parameters needed to reproduce a luminosity of $\sim 10^{45}\,\mathrm{erg\,s^{-1}}$, timescale of $\gtrsim 1000$ seconds, and peak energy < 1.5 keV are reasonable for the system.

7.4.1 Cocoon Shock Breakout

We consider whether a mildly-relativistic ($\beta > 0.4$) cocoon shock breakout (from a stellar surface or from an extended circumstellar medium, CSM) can explain an X-ray transient with characteristic photon energy ~ 1 keV, luminosity $L_X \sim 10^{45}\,\mathrm{erg\,s^{-1}}$, and duration $\Delta t \gtrsim 10^3$ s. We show that neither the cocoon of a successful jet nor a choked jet-cocoon can satisfy all observables simultaneously.

In relativistic, radiation-mediated shocks, the photon spectrum is pair-regulated: copious $e^{\pm}$ pairs set the comoving temperature at $T \gtrsim 50\,\mathrm{keV}$, almost independently of the breakout conditions (Budnik et al., 2010; Nakar & Sari, 2012), as long as the shock is not in thermal equilibrium, meaning that the electrons and ions are decoupled. Weaver (1976) and Katz et al. (2010) showed that for mildly relativistic shocks ($\beta > 0.6$), there is not enough time for the plasma to generate blackbody photons in the downstream portion of the shock, meaning that cocoon must be out of thermal equilibrium.

The observed temperature is then Doppler-boosted by a factor of order the shock Lorentz

factor, giving $T_{\rm obs} \gtrsim 50\,\Gamma\,{\rm keV}$. A mildly relativistic shock, as expected for a cocoon (Gottlieb et al., 2018b), is therefore pair-regulated and would produce shock breakout emission with $T_{\rm obs} \gtrsim 100\,{\rm keV}$, about ~ 2 orders of magnitude higher than the observed emission. Off-axis viewing or de-boosting cannot rescue this picture, as the Doppler factor that would lower the apparent temperature also suppresses the luminosity by orders of magnitude, yielding values far below the measured $L_X \sim 10^{45}\,{\rm erg\,s^{-1}}$. For a shock velocity of $\beta \sim 0.35$ in the relevant density range, the downstream temperature may reach the observed value of $\sim 1\,{\rm keV}$ (e.g., Irwin & Hotokezaka, 2025; Ito et al., 2020; Levinson & Nakar, 2020). We calculate the shock breakout emission from the subrelativistic ejecta in §7.4.2.

We emphasize that a choked-jet cocoon, although it may be subrelativistic by the time of breakout, is unlikely to be the source of the observed subrelativistic X-ray emission. Observations of SNe Ic-BL indicate that the subrelativistic ejecta component cannot originate from the jet-cocoon system itself and instead requires an additional component that dominates the energy budget, regardless of whether the jet successfully escapes or becomes choked (Eisenberg et al., 2022b). Gottlieb (2025) demonstrated that this component is naturally produced by the remnant accretion disk that accompanies jet launching and provides the bulk of the energy at subrelativistic velocities, although a subrelativistic magnetar wind could yield a similar outcome. In systems where the jet is choked, this conclusion becomes even stronger: the weaker jet generates a weaker cocoon, while the accretion disk or magnetar continues to power a massive, wide-angle outflow. The disk or magnetar-driven wind, therefore, inevitably dominates both the subrelativistic ejecta and the associated breakout-like X-ray emission.

7.4.2 SN Ejecta Shock Breakout With an Extended CSM

Here we use the same treatment presented in Haynie & Piro (2021) to calculate subrelativistic shock breakout emission of ejecta in an extended CSM environment. We assume that diffusion is the dominant rate-limiting process. The rise time of the breakout emission is

$$t_r = \frac{R_{\rm e}^2}{R_d v_t} \tag{7.1}$$

where $R_{\rm e}$ is the radius of the extended CSM and v_t is the characteristic velocity of the shock. R_d is

$$R_d = \frac{\kappa D v_t}{c} \tag{7.2}$$

where κ is the opacity, and D is the mass loading factor,

$$D = \frac{\dot{M}}{4\pi v_t}. \tag{7.3}$$

After integrating this expression with respect to the mass, using $M_{\rm e} \sim 4\pi R_{\rm e} D$ we substitute this into the expression for R_d and get

$$R_d = \frac{\kappa v_t}{c}\frac{M_{\rm e}}{4\pi R_{\rm e}}. \tag{7.4}$$

Then substituting this expression into t_r, we find

$$t_r = \frac{4\pi R_{\rm e}^3 c}{\kappa M_{\rm e} v_t^2}. \tag{7.5}$$

In the diffusion dominated regime, the luminosity of the shock breakout is

$$L_{\rm SBO} = \frac{E_{\rm SBO}}{t_r} \approx 4\pi D v_t^3, \tag{7.6}$$

where $E_{\rm SBO}$ is the energy of the shock breakout.

The rise time of the shock breakout should be similar to the rest-frame timescale of the observed prompt emission, if the prompt emission is generated through this mechanism. Therefore, we solve Equations 5 and 6 in parallel, for $R_{\rm e}$ and $M_{\rm e}$, taking a characteristic value of $\kappa = 0.2\,{\rm cm^2\,g^{-1}}$, and $v_t \sim 0.35c$, below the threshold where pair production begins to affect the emission. This velocity is consistent with the high ejecta velocity inferred from the optical spectra at early times ($\sim 0.15c$ at $t_0 + 3.8$ days). It further supports, on one hand, the absence of a relativistic jet (consistent with the lack of a bright X-ray afterglow or radio detection), and, on the other hand, the presence of a central engine, such as a magnetar or an accretion disk. Solving Equations 6 and 9, we derive $R_{\rm e} \sim 1 \times 10^{13}$ cm and $M_{\rm e} \sim 6 \times 10^{-6}\,{\rm M_\odot}$.

This is a very low-density CSM at $R_{\rm e} \sim 10^{13}$ cm, of $\sim 3 \times 10^{-12}$ g cm^{-3}. Qualitatively, this is consistent with the upper limit on the peak energy of the X-ray prompt emission, as it would take a very low-density CSM to push the prompt emission peak energy less than 1.5 keV, given such a high initial shock velocity of $0.35c$. Shiode & Quataert (2014) determined that in compact Wolf-Rayet stars (the progenitors of SNe Ic-BL), wave excitation and damping during the Si burning phase in the months – decades before collpase can inflate $10^{-3} - 1\,{\rm M_\odot}$ of material to $\sim$ 100's of ${\rm R_\odot}$. The extended radius we derive is consistent with their predictions, though EP250827b/SN 2025wkm's mass-loss rate is significantly lower than predicted by the models presented in Shiode & Quataert (2014).

We now compute the expected peak energy from this breakout emission to check if it is consistent with the observed peak energy upper limit. If the radiation is thermalized, we expect the shock breakout spectrum to resemble a blackbody, where

$$T_{\rm BB} \approx \left(\frac{L_{\rm SBO}}{4\pi R_{\rm e}^2 \sigma_{\rm SB}} \right)^{1/4} \tag{7.7}$$

where $\sigma_{\rm SBO}$ is the Stefan-Boltzmann constant. Substituting our known values into this expression, we find $T_{\rm BB} \sim 3.5 \times 10^5$ K, or a peak energy of 0.03 keV. However, this temperature only holds if the radiation is thermalized and in true thermal equilibrium. To see if this is the case, we compute the thermal coupling coefficient in an expanding gas from Nakar & Sari (2010),

$$\eta \approx \frac{7 \cdot 10^5 \text{ s}}{\min\{t, t_d\}} \left(\frac{\rho}{10^{-10} \text{g/cm}^3} \right)^{-2} \left(\frac{kT_{BB}}{100eV} \right)^{7/2},$$

where k is the Boltzmann constant, and $\min\{t, t_d\}$ is the minimum time between the time we are computing the coefficient and the diffusion time. We compute this coefficient at the end of the prompt emission timescale of $t \sim 1000$ s. If $\eta < 1$, then the system can be approximated as being in thermal equilibrium, and the observed temperature $T = T_{\rm BB}$. But, if $\eta > 1$, then free-free emission will dominate the emission, and the spectrum will transition to an optically thin regime that is also modified by Comptonization of photons by neighboring electrons (Nakar & Sari, 2010). Substituting our known values, taking into account that the density is increased by a factor of seven due to compression of the shock (Waxman & Katz, 2017), we derive $\eta = 234$. Therefore, free-free emission dominates, and a Wien spectrum can be used to represent this

system at high energies, where the true temperature becomes determined by

$$T\xi(T)^2 = T_{\rm eq}\eta^2 \tag{7.8}$$

where $\xi(T)$ is the Comptonization correction factor, given by

$$\xi(T) \approx \max\left\{1, \frac{1}{2}\ln[y_{max}]\,(1.6 + \ln[y_{max}])\right\}, \tag{7.9}$$

where $y_{\rm max}$ is the Compton parameter,

$$y_{max} \equiv \frac{kT}{h\nu_{min}} = 3\left(\frac{\rho}{10^{-9}\ {\rm g/cm^{-3}}}\right)^{-1/2}\left(\frac{T}{100{\rm eV}}\right)^{9/4}. \tag{7.10}$$

Therefore, we solve Equation 7.8 for T, substituting our known values find $T \sim 0.7$ keV. This is consistent with the peak energy upper limit derived in §7.4, making the SN ejecta shock breakout in an extended CSM scenario self-consistent over all observables. We note that if we had obtained spectroscopy of the transient at < 4 days after t_0, we could have searched for signatures of CSM interaction in the spectra (e.g., broad Hα, flash ionization features) to confirm the scenario we hypothesize here. This highlights the need to obtain very early-time spectroscopy of XRF-SNe in order to characterize their progenitor systems with accuracy.

7.5 Modeling the Optical Emission

Here we utilize numerical techniques to test different models that can reproduce the optical LCs of EP250827b/SN2025wkm. As described in §7.3.2, the LC displays a prominent first peak

whose origin is not known, and a second peak/plateau that is due to the the late-time SN emission.

7.5.1 Modeling the Late-time SN Emission

In order to model the late-time SN emission, we fit two different models to the LC after ~ 7 days, when different emission mechanisms that contribute to the first peak are neglible when compared to the SN emission. The two models are a radioactive decay model from Arnett (1982), commonly used to model SNe Ic-BL (Srinivasaragavan et al., 2024b; Taddia et al., 2019a), and a magnetar model, where the spindown of a magnetar powers the SN (Omand & Sarin, 2024a). We perform the fits for these models through their implementations in REDBACK (Sarin et al., 2024), which is an open-source electromagnetic transient Bayesian inference software. We utilize `bilby` (Ashton et al., 2019) and `Dynesty` (Speagle, 2020) to perform the sampling and derive posteriors. We also fit the models assuming a Gaussian likelihood with a systematic error added in quadrature to the statistical errors on the photometry, $\sigma_{\rm sys}$, to capture systematic uncertainties from combining photometry from multiple telescopes. We also allow the host-galaxy extinction $A_{V,\rm host}$ to vary as a free parameter, with a prior between 0 and 0.72 mag (the upper limit found in §7.3.4).

7.5.1.1 Radioactive Decay Model

We begin by fitting the second peak of the LC to the Arnett (1982) radioactive decay model. This model assumes that the peak bolometric luminosity of the SN is equal to the instantaneous heating rate from the decay of ^{56}Ni and ^{56}Co, assuming spherical symmetry and further radioactive inputs (Valenti et al., 2008). We account for gamma-ray leakage in the late-time LC (Clocchi-

atti & Wheeler, 1997), and therefore do not assume full gamma-ray trapping. The main parameters in this model that describe the bolometric LC are the nickel mass ($M_{\rm Ni}$) and characteristic photon diffusion time scale (τ_m). $M_{\rm Ni}$ sets the peak luminosity, while τ_m relates to the rise ande decline time of the SN. The kinetic energy ($E_{\rm KE}$) and ejecta mass ($M_{\rm ej}$) of the SN are related through

$$M_{\rm ej} = \frac{\tau_{\rm m}^2 \beta c v_{\rm sc}}{2\kappa_{\rm opt}}, \tag{7.11}$$

and

$$E_{\rm KE} = \frac{3 v_{\rm sc}^2 M_{\rm ej}}{10}, \tag{7.12}$$

where $\beta = 13.8$ (Valenti et al., 2008), c is the speed of light, $\kappa_{\rm opt}$ is a constant, average optical opacity, and $v_{\rm sc}$ is the photospheric velocity $v_{\rm ph}$ at peak light.

The free parameters in our fit are $M_{\rm ej}$, the fraction of Nickel in the ejecta $f_{\rm Ni}$, the ejecta velocity $v_{\rm ej}$, the optical opacity $\kappa_{\rm opt}$, the gamma-ray opacity κ_γ, and the temperature where the photosphere begins to recede $T_{\rm floor}$. These parameters all have broad uniformed priors in the fitting procedure. We report the main explosion properties in Table 7.3. The full corner plots are presented in the Appendix. We derive an extremely high $f_{\rm Ni} \sim 0.6$ from our modeling, which is not physically well motivated - it is expected that events powered purely by radioactive decay possess $f_{\rm Ni} < 0.5$ (Kasen & Bildsten, 2010). Events that have a higher $f_{\rm Ni}$ must be powered by an additional mechanism. In Figure 7.13, we show the maximum likelihood fit and 90% confidence interval along with the observed photometry when setting the Nickel fraction to a reasonable value $f_{\rm Ni} = 0.3$.

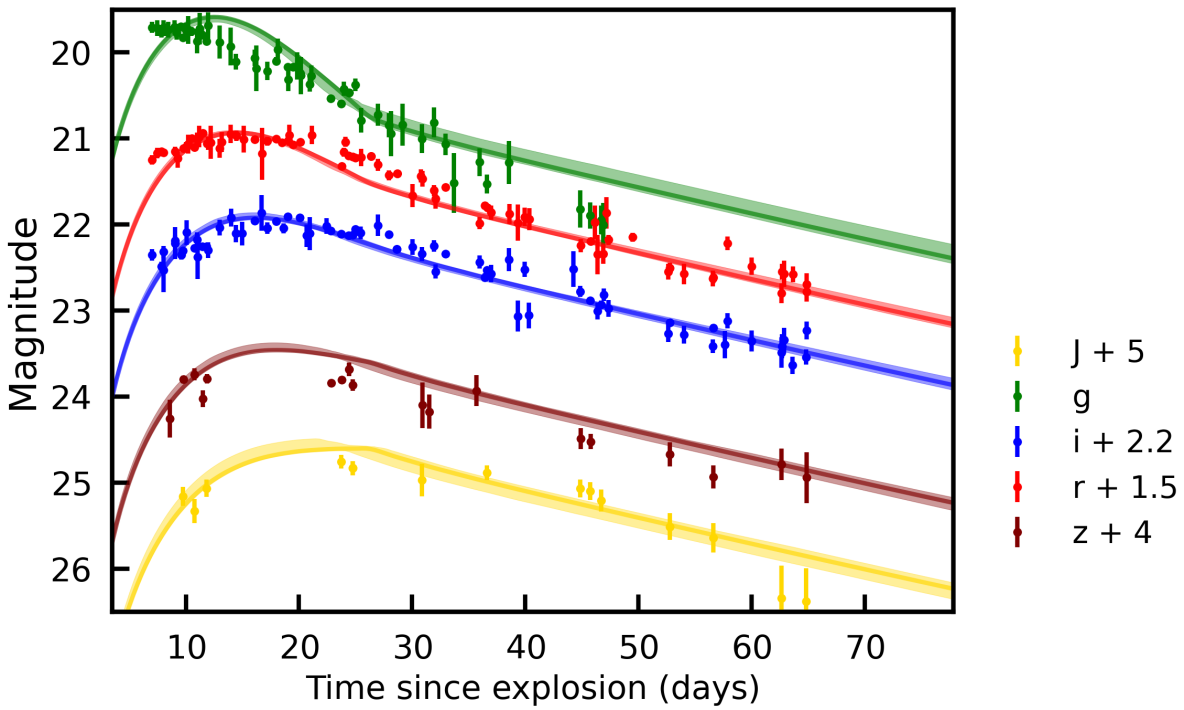

Figure 7.13: Fitting of radioactive decay model of Arnett (1982) to the photometry of SN 2025wkm after 7 days, with the Nickel fraction set to a physically reasonable value $f_{\rm Ni} = 0.3$. We show the maximum likelihood fit and the 90% credible interval.

Parameter	Median
$M_{\rm Ni}$ $(M_\odot)$	$0.65^{+0.17}_{-0.14}$
$E_{\rm KE}$ $(10^{51}$ erg)	$2.12^{+0.47}_{-0.39}$
$M_{\rm ej}$ $(M_\odot)$	$1.04^{+0.18}_{-0.08}$

Table 7.3: Explosion properties of SN 2025wkm from the Arnett (1982) model

Some caution should be used in using the inferred explosion properties from simplified models using the Arnett model (designed for thermonuclear supernovae) on type Ib/c supernovae (Arnett et al., 2017). Niblett et al. (2025) ran a series of radiation-transport models studying Type Ic supernovae. The models assumed a velocity distribution for the ejecta based on a single model from a 1-dimensional hydrodynamic explosion (Fryer et al., 2018). The light-curve calculations mapped this 1-dimensional hydrodynamics explosion into calculations assuming ballistic (i.e. homologous) outflow conditions. A prescription to incorporate shock heating from the forward shock that converts kinetic energy to thermal energy was added to this basic homologous transport calculations.

The series of models in Niblett et al. (2025) did not form a broad grid varying all the explosion conditions. Models studied the amount of ^{56}Ni and its level of mixing. A smaller set of models studied the role of ejecta mass and total energy. A small number of shock heating models were also included. But this suite of models did not include many other initial condition properties. For example, these models use a single explosion profile describing the velocity distribution with ejecta mass. As has been seen in kilonova explosions, this velocity profile can have a dramatic effect on the observed light-curves (Fryer et al., 2024b). In addition, the sparsity of the suite of models from Niblett et al. (2025) was not sufficient to identify direct fits to the our broadband light-curve. But we did find reasonable fits with total ejecta mass of $2-4.5\,M_\odot$ and a total ^{56}Ni yield of $0.2\,M_\odot$: e.g. models ni0.2f1m0.5, ni0.2f0.25m0.5, ni0.2f1m1, ni0.2f0.25m1, ni0.2f1m1sig0.93 - see Niblett et al. (2025) for the detailed description of these models. For larger ^{56}Ni masses, these radiation transport models predict a too-bright late-time light curve. With a modest amount of shock heating, the required ^{56}Ni mass could be below $< 0.2\,M_\odot$.

7.5.1.2 Magnetar-powered Model

Some SNe Ic-BL possess explosion energies ~ 10 times higher than normal SNe, or a Nickel fraction with respect to the $M_{\rm ej}$ of $f_{\rm Ni} > 0.5$ (Srinivasaragavan et al., 2024b; Taddia et al., 2019a). These SNe Ic-BL cannot be modeled purely by the radioactive decay of ^{56}Ni. A popular model that has been invoked is the magnetar model, where the spindown of a magnetar remnant left behind after core-collapse powers part of the SN LC (Kasen & Bildsten, 2010; Woosley, 2010). We direct the readers to those papers for more details on the model, but describe the basic picture here, following the description presented in Omand & Sarin (2024a). The spin-down energy gets emitted as a particle wind that is highly magnetized. This wind expands relativistically and creates a shock when it collides with the inner ejecta, and the reverse shock bounces back and shocks the expanding wind itself. This reverse shock accelerates the particles in the wind to extremely high, ultrarelativistic velocities. These particles then emit non-thermal radiation, mostly synchrotron and inverse Compton scattering (Gaensler & Slane, 2006), and is known as a pulsar wind nebula. The pulsar wind nebula then accelerates the SN ejecta, and the winds get mixed with the SN ejecta. This leads to the winds thermalizing, increasing the temperature and therefore the bolometric luminosity (Kasen & Bildsten, 2010).

This magnetar model has historically been invoked to describe superluminous SNe (SLSNe; Nicholl et al. 2017). Omand & Sarin (2024a) relax the assumptions made in previous parameter estimation codes using this model and present a semi-analytic magnetar model based on previous magnetar-driven kilonova models (e.g., Metzger 2019; Sarin et al. 2022; Yu et al. 2013), with an aim of uniting SNe Ic-BL and SLSNe under one theoretical framework. We use the implementation of this model in `Redback` to fit the main SN LC after 7 days. We direct the reader to Omand

& Sarin (2024a) for the full set of equations describing this model. The main free parameters are L_0 , the initial spin-down luminosity of the magnetar, and $t_{\rm SD}$, the spin down time. Using these parameters, we can derive the initial magnetic field of the magnetar B, along with the spin period P_0 through the relations

$$L_0 = 2.0 \times 10^{47} P_{0,-3}^{-4} B_{14}^{2} \, {\rm erg \, s^{-1}}, \tag{7.13}$$

$$t_{\rm SD} = 1.3 \times 10^{5} P_{0,-3}^{2} B_{14}^{-2} \left(\frac{M_{\rm NS}}{1.4 M_{\odot}} \right) \, {\rm s}, \tag{7.14}$$

where $P_{0,-3} = P_0/10^{-3}$ in seconds and $B_{14} = B/10^{14}$ in Gauss (Omand & Sarin, 2024a). $M_{\rm NS}$ is the mass of the neutron star, which we assume is 1.4 $\rm M_{\odot}$. We also assume a moment of inertia of $1.3 \times 10^{45} \, {\rm g \, cm^2}$ (see Omand & Sarin 2024a for a more detailed description of these assumptions). We show the maximum likelihood fit and 90% confidence interval along with the observed photometry in Figure 7.14, and report the main explosion properties in Table 7.4. The full corner plots are presented in the Appendix. We note that this model also takes into account extra contributions from the radioactive decay of Nickel in combination with the spin-down of the magnetar powering the LC, and we also report $f_{\rm Ni}$ and $M_{\rm ej}$. We derive a magnetar spin period of ~ 1.9 ms, and a magnetic field strength of $\sim 5 \times 10^{14}$ Gauss, along with a new, much more reasonable $f_{\rm Ni} \sim 0.2$. The ejecta mass we derive of $M_{\rm ej} = 1.73^{+1.48}_{-0.18}$ is within the median range of SNe Ic-Bl presented in Taddia et al. (2019a) ($1 - 7 \, \rm M_{\odot}$) and Srinivasaragavan et al. (2024a) ($2 - 3 \, \rm M_{\odot}$). The magnetar parameters that we derive are in the range of parameters derived in different works invoking a magnetar to explain the LC of EP250108a/SN 2025kg (Li et al., 2025c; Roman Aguilar & Bersten, 2025; Zhu et al., 2025a).

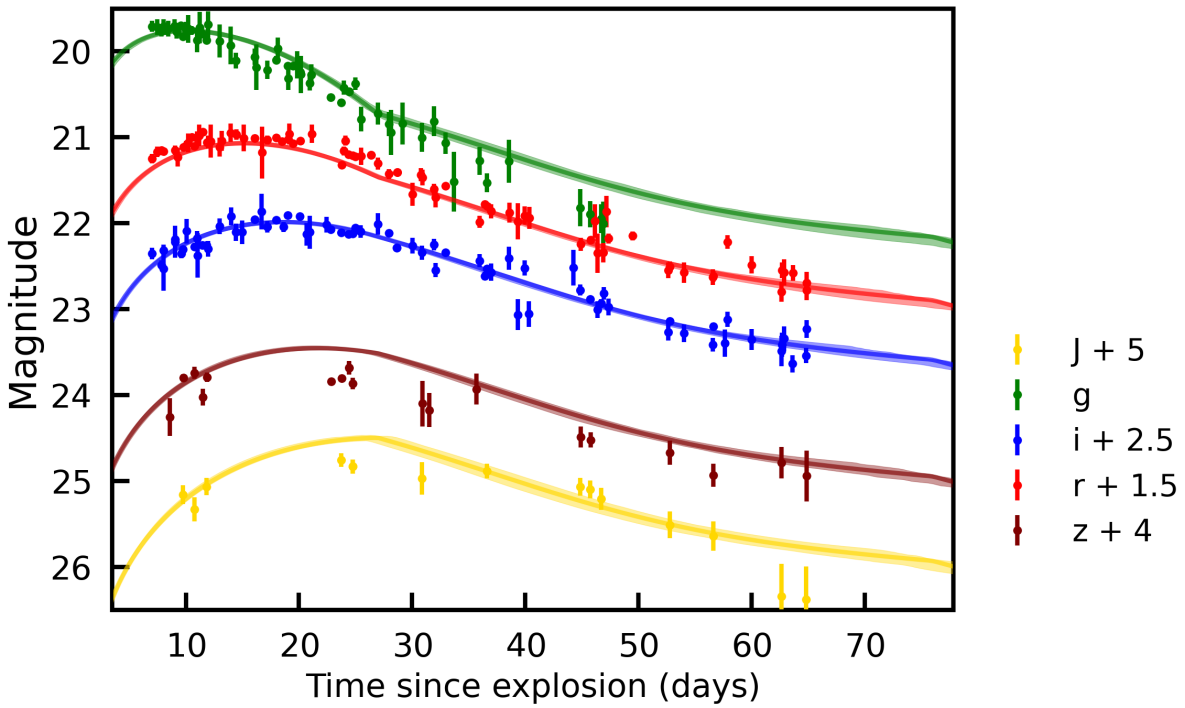

Figure 7.14: Fitting of the magnetar model from Omand & Sarin (2024a) to the photometry of SN 2025wkm after 7 days. We show the maximum likelihood fit and the 90% credible interval.

Parameter	Median
$L_0\,(10^{47}\,\mathrm{erg\,s^{-1}})$	$3.54^{+4.21}_{-1.64}$
$t_{\mathrm{SD}}\,(10^4\,\mathrm{s})$	$2.59^{+1.99}_{-2.00}$
f_{Ni}	$0.29^{+0.04}_{-0.05}$
$M_{\mathrm{ej}}\,(\mathrm{M}_\odot)$	$1.73^{+1.48}_{-0.18}$

Table 7.4: Explosion properties of SN 2025wkm from the magnetar model (Omand & Sarin, 2024a).

In addition, we perform a Bayesian statistical comparison between the radioactive decay model, where $f_{\rm Ni}$ is set to a physically reasonable value of 0.3, and the magnetar-driven model presented above. We calculate the Bayesian Information Criterion (BIC) for the two models, which is a parameter that accounts for the fit to the data, along with overfitting corrections to the use of extra parameters. The BIC is

$$\mathrm{BIC} = k\ln(n) - 2\ln(L), \tag{7.15}$$

where k is the number of parameters used in the fit, n is the number of data points, and L is the maximum log-likelihood of the fit. The radioactive decay model has 8 free parameters, while the magnetar model has 12 free parameters. A lower BIC corresponds to the model that is more preferred. We compute $\mathrm{BIC}_{\rm arnett} = -100.35$, and $\mathrm{BIC}_{\rm magnetar} = -160.46$. Therefore, we prefer the magnetar model over the radioactive decay model to explain the second peak of EP250827b/SN 2025wkm. We note that late-time optical observations of the tail of the LC at $\sim 1-2$ years after explosion can confirm whether SN 2025wkm has an additional powering source to radioactive decay, as magnetar-powered LCs are expected to decay as power-laws (Wang et al., 2015), while radioactive decay-powered LCs decay exponentially (Arnett, 1982).

We note here that there are alternative models that can explain a central engine pumping energy into the system, such as fallback accretion onto a black hole (e.g., Moriya et al. 2019; Rodríguez et al. 2024b). We do not test this model in detail in this work, as for the typical accretion scenario, it is difficult to power an engine longer than 10^4 seconds (Rodríguez et al., 2024b), which is too short of a timescale to power the late-time SN LC.

In addition, the models presented in Rodríguez et al. (2024b) assume a progenitor star

radius of $\sim 10^{13}$ cm, and that most of the ejecta mass is roughly at that radius prior to explosion. However, the progenitors of SNe Ic-BL are likely Wolf-Rayet stars with much smaller radii (Woosley & Bloom, 2006). The derived CSM radius for SN 2025wkm is $\sim 10^{13}$ cm, making it clear that the progenitor radius must be much smaller, and that the models presented in Rodríguez et al. (2024b) are not directly applicable to this work. However, there is a wide range of accretion parameters and more complex fallback accretion models that can be tested, which is outside of the current scope of this work. Therefore, we do not say for certain that a magnetar central engine powers this system – we simply prefer it in our analysis.

7.5.2 Modeling the First Peak

A handful of SNe Ic-BL possess double-peaked LCs, or LCs that peak too early to be described purely by radioactive decay (Ho et al., 2019b, 2020e; Modjaz et al., 2006; Rastinejad et al., 2025; Srinivasaragavan et al., 2025a; Whitesides et al., 2017). Shock cooling emission (Chevalier 1992; Das et al. 2024; Falk & Arnett 1977; Grasberg & Nadezhin 1976; Nakar & Sari 2010; Piro et al. 2010; Rabinak & Waxman 2011) from SN ejecta interacting with an extended CSM is the usual explanation for this initial peak in most stripped-envelope SNe that display double peaks. In this picture, the radius of the star does not set the photosphere. Instead, it is set by an extended shell with mass $M_{\rm e}$ and radius $R_{\rm e}$ (Bersten et al. 2012; Nakar & Piro 2014; Piro et al. 2010). The shock needs to travel through the outer low-mass shell, and the emission from the breakout itself is described in §7.4. Afterwards, the material expands and cools over the timescales of $\sim$ days, which can produce a luminous, blue peak, due to the ejecta being extremely hot. The origin of the extended CSM in these systems is still an open question, but

a likely explanation is material ejected in mass loss episodes, perhaps due to binary interactions (Chevalier, 2012), or stellar winds (Quataert & Shiode, 2012).

The large kinetic energies and high velocities of the ejecta in SNe Ic-BL suggest that, unlike ordinary core-collapse SNe, their ejecta require sustained central-engine activity (e.g., Rodríguez et al., 2024a). Indeed, in EP250827b, the inferred velocity at $\sim 4.2\,\mathrm{days}$ is $\beta \approx 0.13$ (see §7.4.2), indicating faster ejecta than what neutrino-driven shocks can produce (Janka, 2017).

Eyles-Ferris et al. (2025) and Srinivasaragavan et al. (2025a) find that cooling from a jet-driven shocked cocoon (Hamidani et al., 2025a; Nakar & Piran, 2017), either interacting with its stellar envelope or an extended CSM, might be able to explain the first optical peak for EP250108a/SN 2025kg (see however Gottlieb, 2025). However, we showed in §7.4 that a shocked cocoon model cannot recreate the prompt emission; therefore, we do not test the cooling emission from a shocked cocoon model in our work. The first peak may also be due to the presence of a bright optical afterglow; however, in §7.3.5, we showed that an energetic, on-axis jet is not consistent with the radio upper limits, and we therefore do not test any on-axis optical afterglow models. Though we could not rule out a very off-axis jet from the radio upper limits, the optical emission from such a system would be too faint, and occur at too late of a time to be relevant for the emission seen in the LC, so we also do not test an off-axis optical afterglow either.

The first peak can also be from purely shock cooling emission of the SN shock without central engine contributions (Piro et al., 2021), but we find that the CSM parameters we derive in §7.4 needed to describe the prompt emission cannot recreate the luminosity of the first peak. We therefore remain with two engine-powered outflows that are likely to play a role in collapsars, whose cooling emission can reproduce the first peak in the LC:

(i) *Accretion disk outflows*: A defining feature of collapsars is their high angular momentum, which facilitates the formation of an accretion disk. In the presence of dynamically important magnetic fields, as expected around compact objects that launch jets, these disks power their own magnetically driven, subrelativistic outflows (Bopp & Gottlieb, 2025; Issa et al., 2025). Such disks may power ejecta with isotropic equivalent energies of $E_{\rm iso} \sim 10^{52}\,{\rm erg}$, dominating over other subrelativistic outflows at velocities $\beta \lesssim 0.3$ (Gottlieb, 2025), and consistent with the energies inferred for Type Ic-BL SNe (Bopp & Gottlieb, 2025; Dean & Fernández, 2024a,b; Fujibayashi et al., 2024, 2023).

(ii) *Magnetar outflows*: A proto–neutron star inevitably forms during core collapse prior to black hole formation. If the proto-neutron star possesses sufficient angular momentum, an α–Ω dynamo can amplify its magnetic field, giving rise to a protomagnetar (Duncan & Thompson, 1992; Thompson & Duncan, 1993) that launches magnetically driven winds. The properties and impact of protomagnetar outflows in this regime remain poorly constrained, partly due to the scarcity of global simulations that capture both the proto-neutron star's interior and the extended stellar envelope. Nevertheless, existing magnetorotational core-collapse simulations have shown that, during the first few seconds after core bounce, the protomagnetar drives strong, magnetically dominated winds (e.g., Aloy & Obergaulinger, 2021; Kuroda et al., 2020; Mösta et al., 2015, 2018, 2014; Obergaulinger & Aloy, 2022). These early outflows, however, experience intense hydrodynamic mixing and interact with the infalling stellar mantle, resulting in weak collimation and subrelativistic velocities. Protomagnetars are expected to inject $\gtrsim 10^{52}\,{\rm erg}$ into the collapsing star (Gottlieb et al., 2024; Metzger et al., 2015; Omand & Sarin, 2024a; Shankar et al., 2021; Suzuki & Maeda, 2017; Woosley, 2010), suggesting that their wind energy and characteristic velocities are comparable to those of disk-driven outflows.

The characteristics (velocity and energy) of protomagnetar-driven and disk-driven outflows may be similar to each other, and their morphology is shaped primarily by turbulent mixing, which is largely independent of the detailed nature of the energy source. Therefore, due to the challenge of distinguishing between the contributions of the two sources, we fit the early cooling emission by considering a general outflow, modeled by an energy distribution with a broken power law, $E(\beta_{\rm min} < \beta < \beta_{\rm max})$, where $\beta_{\rm min}$ is the minimum velocity of the cooling phase, estimated to be $\beta_{\rm min} \approx 0.13$, and the shock breakout velocity $\beta_{\rm max} \sim 0.35$ (see §7.4.2). The outflow escapes from an environment of $R_{\rm e} \sim 10^{13}$ cm, derived in §7.4.2, and expands adiabatically to power cooling emission.

At each observed time, the trapping radius of the ejecta is a shell moving with dimensionless velocity β, mass m, and thermal energy $E_{\rm th}$, assumed to be in equipartition with the kinetic component $E = m(\beta c)^2/2$ upon breakout. The shell radiates its emission at an observed time (Bopp & Gottlieb, 2025; Gottlieb et al., 2023)

$$t = \sqrt{\frac{\kappa_{\rm opt} m (1-\beta)^3}{4\pi \beta c^2}} \,. \tag{7.16}$$

The total power emitted by this shell is thus

$$L(t) \sim E_{\rm th} \left(\frac{R_{\rm e}}{\beta c t^4} \right)^{1/3} \,. \tag{7.17}$$

For each shell, we determine the photospheric radius and assume a blackbody temperature to compute the spectral luminosity. We fit the spectral luminosities as well as the observed temperature $T \approx 2 \times 10^4\,{\rm K}$ at $\sim 4.2\,{\rm days}$ (from §7.3.4).

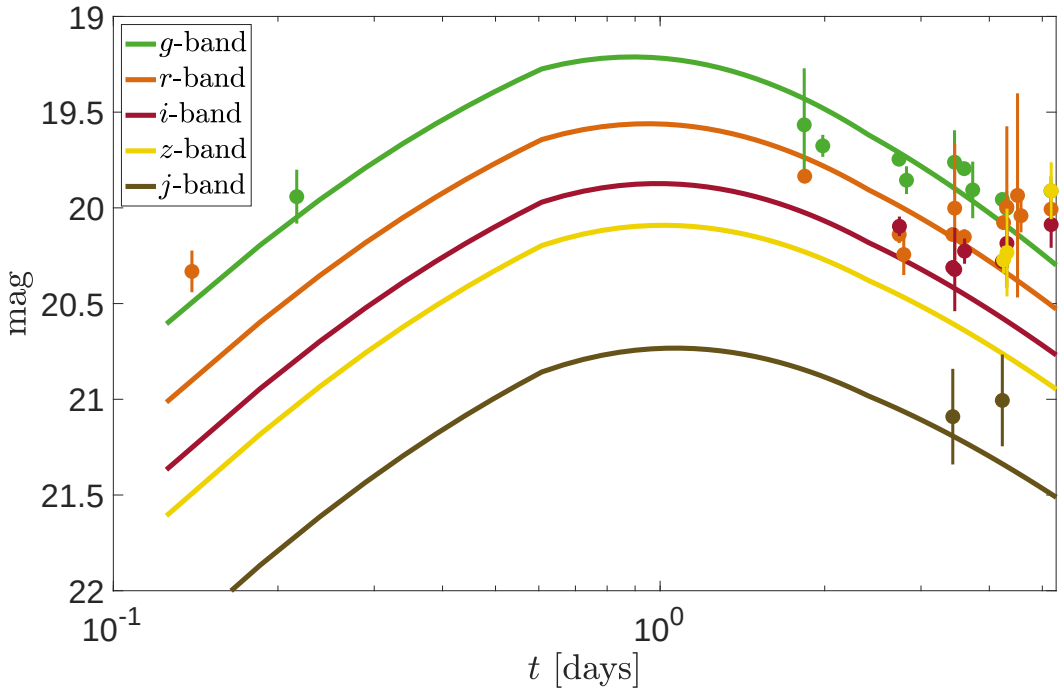

Figure 7.15: Semi-analytic fit of a subrelativistic energy distribution to the early time data up to $t \approx 3.5$ days.

Figure 7.15 depicts our fit to the optical data at $t \lesssim 3.5\,\mathrm{days}$. Our best-fit parameters imply a total (kinetic and thermal) ejecta energy of $E \approx 2 \times 10^{52}\,\mathrm{erg}$, typical for SNe Ic-BL and $\kappa_{\rm opt} = 0.5\,\mathrm{cm^2\,g^{-1}}$. We find that the energy distribution is flat at $\beta \gtrsim 0.23$, and rises linearly with β at lower velocities. This profile indicates the presence of two mixed components with comparable energies of $\sim 5 \times 10^{51}\,\mathrm{erg}$ each. Since such energies exceed those expected from choked jet cocoons or neutrino-driven explosions, the two components may correspond to magnetar and accretion-disk outflows. The opacity that we derive is slightly higher than values usually assumed for SNe Ic-BL ($\kappa_{\rm opt} \sim 0.1\,\mathrm{cm^2\,g^{-1}}$; Srinivasaragavan et al. 2024b; Taddia et al. 2019a), though slightly higher opacities are plausible if heavier elements are mixed into the outer ejecta.

We show an artistic depiction of the model we invoke in Figure 7.16. We note that we

do not perform a joint fit of the first peak and late-time SN emission, due to the difference in modeling procedures used – numerical techniques were used in modeling the late-time emission, while we used a semi-analytic model to describe the first peak, with only a narrow range of free parameters that should be expanded in future works. This semi-analytic model (described in more detail in Gottlieb 2025) will be incorporated into `Redback` in the future, where the joint fits can be accurately represented through evolving a co-moving photosphere with a shared temperature floor.

7.6 Discussion

Here we discuss some implications of the modeling done in §7.4 and §7.5, and present discussion on the current landscape of XRF-SNe.

7.6.1 Invocation of Circumstellar Interaction

In §7.4, we showed that all three observables corresponding to the X-ray prompt emission – the observed timescale of $\gtrsim 1000$ s, the average 0.5 - 4 keV luminosity of $\sim 10^{45}\,\mathrm{erg\,s^{-1}}$, and peak energy < 1.5 keV – were reproducible in a model where the X-ray emission originates from SN ejecta breaking out of an extended CSM environment. However, is the invocation of an extended CSM necessary to describe the observables in this system? Waxman & Katz (2017) describe the energy of the shock breakout from a stellar envelope as

$$E_{\rm SBO} \sim 10^{46} v_{\rm s,9} R_{13}^2 \kappa_{0.34}^{-1}. \tag{7.18}$$

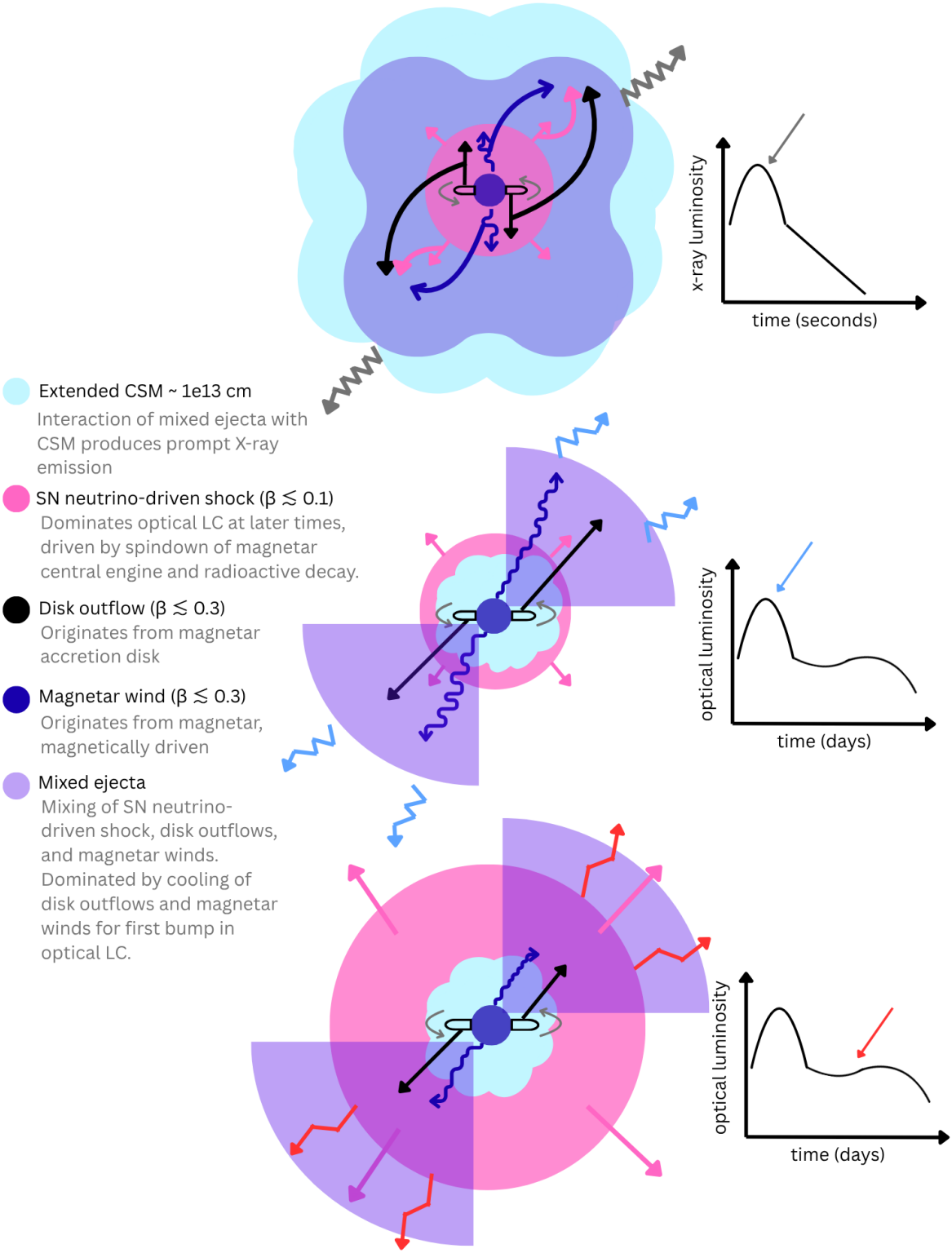

Figure 7.16: Artistic depiction of the magnetar-driven disk cooling model presented in §7.5.2.

Assuming a Wolf-Rayet progenitor with $R \sim 10^{12}$ cm, $v_s \sim 0.35c$, and $\kappa = 0.2\,\mathrm{cm^2\,g^{-1}}$, we find $E_{\mathrm{SBO}} \sim 2 \times 10^{45}\,\mathrm{erg}$, which is three orders of magnitude less than the observed prompt emission energy of $\sim 10^{48}\,\mathrm{erg}$. Therefore, it is clear that a shock breakout from the stellar surface of a Wolf-Rayet star cannot reproduce the X-ray prompt emission, and it is natural to invoke the presence of an extended CSM. This is consistent with stellar evolution models that show that Wolf-Rayet stars eject significant material from their envelopes prior to collapse, from binary interactions (Chevalier, 2012) or stellar winds (Quataert & Shiode, 2012).

Recent semi-analytic models presented by Fryer et al. (in prep) describe the thermal, free-free emission from shock breakout emission under a variety of different initial conditions arising from shock heating as the SN exits the stellar photosphere. This model was invoked to describe the prompt emission from EP250108a/SN 2025kg in Eyles-Ferris et al. (2025). When investigating the models in Fryer et al. (in prep.) obtained through internal communication, we find that for a range of parameters corresponding to the power-law decay index of the energy distribution with respect to velocity $E(\beta) = \beta^{-p}$ and maximum Lorentz factor Γ_{max}, that sustained emission on the order of ~ 1000 s at a luminosity of $\sim 10^{45}\,\mathrm{erg\,s^{-1}}$ that peaks at < 1 keV is not possible. Each of these models drop off to luminosities lower than $\sim 10^{44}\,\mathrm{erg\,s^{-1}}$ by ~ 250 s. However, when invoking the presence of an extended CSM environment, where additional energy is injected into the CSM from expansion during the time of shock heating, models are able to sustain $10^{45}\,\mathrm{erg\,s^{-1}}$ luminosities on the order of 1000's of seconds.

We can estimate the mass-loss rate of SN 2025wkm's progenitor star utilizing our derived

CSM parameters. We begin with

$$M_{\rm e} = 4\pi \int_{R_{\rm in}}^{R_{\rm out}} \rho(r) r^2 \, dr \tag{7.19}$$

where we are integrating over the inner and outer radii of the CSM, and $\rho(r)$ is the density profile of the CSM. Assuming that the CSM is a constant density shell, and a Wolf-Rayet progenitor whose wind velocity is $v_w \sim 4000\,{\rm km\,s^{-1}}$ (Nugis & Lamers, 2000), we can estimate the mass-loss rate $\dot{M}$ as

$$\dot{M} \approx 4\pi R^2 \frac{M_{\rm e}}{4\pi R^2 R_{\rm e}} v_w = \frac{M_{\rm e} v_w}{R_{\rm e}}. \tag{7.20}$$

Therefore, substituting our derived values for $R_{\rm e}$ and $M_{\rm e}$, we find $\dot{M} \sim 10^{-4}\,{\rm M_\odot\,yr^{-1}}$. This is consistent with expected mass-loss rates from Wolf-Rayet stars (Nugis & Lamers, 2000).

The radius derived for the extended CSM in §7.4 is $R_{\rm e} \sim 10^{13}$ cm, which is similar to the radius derived for EP250108a/SN 2025kg of 3.7×10^{13} cm (Srinivasaragavan et al., 2025a), and XRF060218/SN 2006aj of 4×10^{13} cm (Irwin & Hotokezaka, 2025). Srinivasaragavan et al. (2025a) hypothesize that the X-ray emission and first optical peak in EP250108a was due the breakout and cooling emission of a shocked cocoon formed from a collapsar jet (Hamidani et al., 2025b; Nakar & Piran, 2017), while XRF060218/SN 2006aj has also been modeled as a failed jet within an extended CSM (Nakar, 2015). In addition, Sun et al. (2025) hypothesize that the first optical peak of EP240414a/SN 2024gsa was due to shock cooling emission with a very dense CSM of $R_{\rm e} \sim 2 \times 10^{14}$ cm, though the X-ray emission is due to synchrotron radiation from a weak, but successful relativistic jet. Rho et al. (2021) also find that the first optical peak for SN 2020bvc is likely from shock cooling emission at a CSM radius $R_{\rm e} \sim 10^{14}$ cm. Its radio

properties were well described from synchrotron emission from a mildly relativistic jet, though its X-ray properties show excess flux that isn't consistent with the radio synchrotron spectrum (Ho et al., 2020a).

There are also additional SNe Ic-BL (iPTF16asu, SN 2018gep) in the literature that do not have clear double-peaked optical LCs, but display an early, luminous peak which is likely due to the combination of radioactive decay and shock cooling within an extended CSM environment (Ho et al., 2019b; Whitesides et al., 2017). Both of these events do not have reported X-ray emission. In addition, Nakar & Sari (2012) reported that the X-ray prompt emission of XRF100316D/SN 2010bh was from a relativistic shock breakout at $R_{\rm e} > 6 \times 10^{13}$. This event possessed similar X-ray properties to XRF060218/SN 2006aj with a slightly higher peak energy of $E_p \sim 30$ keV (Starling et al., 2011), though the associated SN Ic-BL did not possess a double-peaked LC (Chornock et al., 2010).

Therefore, it is clear that interaction with an extended CSM plays a significant role in powering at least a subset of SNe Ic-BL. More significantly, every confirmed Ic-BL XRF-SN (XRF060218/SN 2006aj, XRF10316D/SN 2010bh, EP240414a/SN 2024gsa, EP250108a/SN 2025kg, and EP250827b/SN 2025wkm) shows evidence of this extended CSM interaction, whether that interaction produces the prompt X-ray emission or the first peak in the optical LC. Qualitatively, this gives evidence that XRF-SNe may have a more extended CSM surrounding their progenitors than normal SNe Ic-BL. Interestingly, Chevalier & Fransson (2008) also hypothesize that the late-time optical emission of XRF080109/SN 2008D, a Type Ib SN, is powered by CSM interaction. The fact that the late-time emission in this system is dominated by CSM interaction. This is in contrast to the early-time emission being dominated by CSM interaction in SNe Ic-BL XRF-SNe, which is likely due to the presence of the progenitor's He envelope, delaying the timescale

of CSM interaction.

In Table 7.5, we present the peak energies and CSM properties for the three EP XRF-SN studied in detail thus far. All three events have similar peak energy constraints; however, their CSM parameters vary to a wide degree, giving evidence that the CSM environments surrounding XRF-SN likely are not homogeneous. The extremely low $M_{\rm e}$ for EP250827b/SN 2025wkm stands out with respect to the other two events, giving evidence that its progenitor's mass-loss history may be less extreme than when compared to the other two events.

Margutti et al. (2015) report an association between LGRBs with long durations (> 1000s), large intrinsic absorptions ($N_{\rm H,int} > 6 \times 10^{21}\,{\rm cm}^{-2}$), and very soft photon indices ($\alpha_{\rm X} > 3$). They report that chance association between these three properties is extremely statistically unlikely, and they theorize that these properties arise from very turbulent mass-loss history of the progenitor star prior to collapse, enriching the surrounding CSM. EP250827b possesses a long duration and soft photon index, and the constraint on its intrinsic absorption does not rule out $N_{\rm H,int} > 6 \times 10^{21}\,{\rm cm}^{-2}$. As the sample of XRF-SNe grows, it will be interesting to note if they also share these associations, which would provide more evidence that the CSM environmnts around XRFs play a significant role affeting their observed emission.

The densities of these extended CSM environments for the majority of Ic-BL XRF-SNe are $\sim 10^{-11}\,{\rm g\,cm}^{-3}$ (Srinivasaragavan et al., 2025a), while we derive a density for EP250827b/SN 2025wkm of $\sim 3 \times 10^{-12}\,{\rm g\,cm}^{-3}$, around an order of magnitude smaller. As mentioned in §7.4, this low-density environment is necessary to explain the high speeds and temperature of the ejecta at early-times in combination with the low peak energy of the X-ray prompt emission.

Detailed spectral analysis of EP250108a/SN 2025kg done in Rastinejad et al. (2025) finds evidence of a He feature in a near-infrared spectrum taken near peak light, along with a broad

Event	$E_{\rm p}$	$M_{\rm e}$ ($M_\odot$)	$R_{\rm e}$ (10^{13} cm)	Reference
EP240414a/SN 2024gsa	< 1.8 keV	~ 0.33	~ 24	Sun et al. (2025)
EP250108a/SN 2025kg	< 1.3 keV	~ 0.1	~ 3.7	Srinivasaragavan et al. (2025a)
EP250827b/SN 2025wkm	< 1.5 keV	6×10^{-6}	1	This work

Table 7.5: Peak Energy and CSM Parameters for EP XRF-SNe.

Hα feature in an optical spectrum 42.5 days after explosion. These features are consistent with the presence of an extended CSM, due to detached He and H shells at radii $\sim 10^{15} - 10^{16}$ cm. These features in the spectra indicate the presence of a binary system, and even possibly a tertiary system when other properties are considered (Rastinejad et al., 2025).

We do not have any near-infrared spectra of EP250827b/SN 2025wkm, so we cannot confirm or rule out the presence of a similar He feature. We do not find any evidence for this broad Hα feature in our spectra of EP250827b/SN 2025wkm. However, this feature quickly disappeared in EP250108a/SN 2025kg's spectra taken at 47.7 days (Rastinejad et al., 2025), so we cannot rule out that a similar situation may have occurred for EP250827b. Future theoretical studies looking at the impact that binary and tertiary companions have on the surrounding CSM environments of Wolf-Rayet stars will be key to understanding the CSM structure in more detail surrounding the progenitors of XRF-SNe.

7.6.2 The Progenitor System Landscape for XRF-SNe

This is now the third XRF-SNe discovered by EP that has been studied in detail, and the fourth overall discovered by the mission. In Figure 7.17, we show the LCs for the three EP XRF-SNe presented in the literature, along with XRF060218/SN 2006aj, the most similar XRF-SN to these EP events. The LCs show clear diversity, ranging four orders of magnitude with respect to their optical lumnosities. In addition, though each of these LCs display at least two peaks, the rise

and fall times of these peaks vary. In addition, EP240414a displays three possible peaks, where the initial peak has been attributed to a GRB-like afterglow (Gottlieb, 2025; Srivastav et al., 2025; Sun et al., 2025; van Dalen et al., 2025).

In Figure 7.18, we show the Amati et al. (2002) relation between the peak energies and isotropic equivalent energies of GRBs, using the sample of events from Minaev & Pozanenko (2020). Most LGRBs and SGRBs in the figure follow the correlation well; however, the EP XRF-SNe seem to deviate from this relation. From a physical perspective, the reason for the deviation from the Amati et al. (2002) relation is likely due to the prompt emission of EP XRF-SNe originating from a different powering source than the prompt emission of GRBs. This may be due to a variety of factors - differing CSM environments, central engine powering sources, and geometric viewing effects may all play a role.

Though not a SN Ic-BL, XRF080109/SN 2008D represents the extreme end of this different powering source. Its X-ray prompt luminosity was orders of magnitude smaller than what has been observed for Ic-BL XRF-SNe, of $\sim 10^{43}\,\mathrm{erg\,s^{-1}}$ (Mazzali et al., 2008; Soderberg et al., 2008). The presence of He in the SN spectra (Malesani et al., 2009; Modjaz et al., 2009) indicates that the progenitor star retained its He envelope, meaning that even if a collapsar formed and launched a relativistic jet (as hypothesized by Mazzali et al. 2008 for this system), it must have been fully choked and stifled before reaching the stellar envelope. On the other hand, EP240414a/SN 2024gsa's prompt emission had properties that skewed more similar to classical LGRBs, with a duration of ~ 150 s and a luminosity of $\sim 10^{47}\,\mathrm{erg\,s^{-1}}$ (Sun et al., 2025). In addition, its optical LC showed an afterglow-like component at early times that displayed red colors and decayed rapidly (Srivastav et al., 2025; Sun et al., 2025; van Dalen et al., 2025), giving evidence that a jet was successfully launched and likely formed a cocoon, which played some

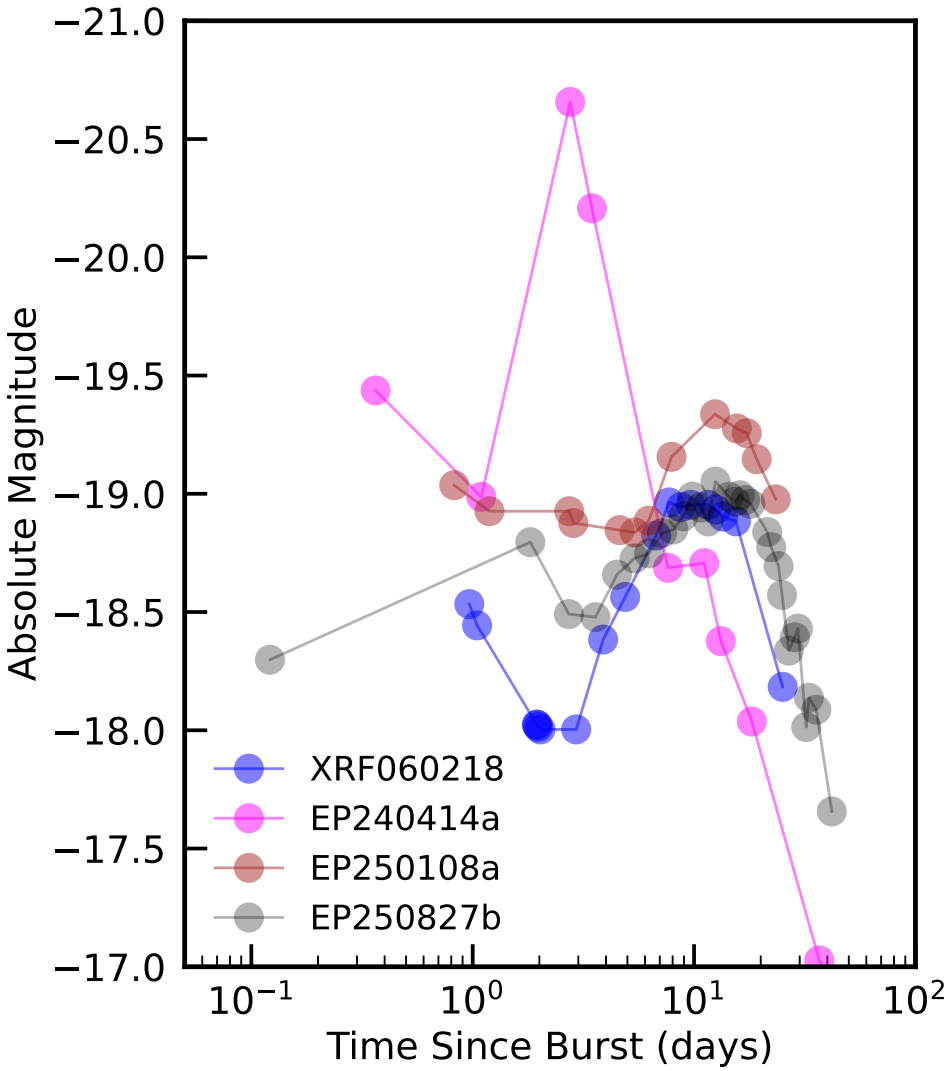

Figure 7.17: r-band rest-frame LCs of EP XRF-SNe (Srinivasaragavan et al., 2025a; van Dalen et al., 2025), along with XRF060218 (Modjaz et al., 2006). The LCs show clear diversity in shape and brightness, ranging four orders of magnitude.

role in creating the prompt emission.

These two events seem to represent the current extremes of the XRF-SN landscape – and there likely is not a standard, common progenitor system that can describe the multi-wavelength emission of XRFs. This contrasts to the story for LGRBs, where a collapsar forming an accretion disk launching a successful, relativistic jet can describe the vast majority of observed events. Indeed, it is not even clear whether a collapsar is necessary for XRF-SNe, since XRF080109/SN 2008D was a Type Ib SNe. However, for Ic-BL XRF-SNe, the formation of a collapsar must be a common feature – the high velocities observed in the early optical spectra of SNe Ic-BL are not possible in a system described solely by a neutrino-driven shock (Rodríguez et al., 2024a).

From the three EP XRF-SNe studied in detail thus far, it is clear that the degree of success for a jet launched from collapsars is not consistent – EP240414a likely had a successful jet (Sun et al., 2025), EP250108a likely had a failed jet that transformed into a cocoon (Eyles-Ferris et al., 2025; Srinivasaragavan et al., 2025a), while EP250827b either did not launch a jet at all, or had a jet that was stifled deep in the layers of the explosion, where any cocoon formed was not energetic enough to impact the observed emission.

In addition, the central engine powering mechanism in these systems is also not homogenous – EP250108a/SN 2025kg has also been shown to possibly be powered by a magnetar (Sun et al., 2025; Zhu et al., 2025a), though other works hypothesize it is powered by a black hole (Eyles-Ferris et al., 2025; Srinivasaragavan et al., 2025a). Works have shown EP240414a is also likely powered by a black hole (Srivastav et al., 2025; van Dalen et al., 2024). This heterogeneity of XRF-SNe is an important distinction that must be considered in future sample studies. XRF-SNe are important events that can shed light on the central engine populations in collapsing massive stars, motivating the need for detailed, multi-wavelength follow-up studies on every new

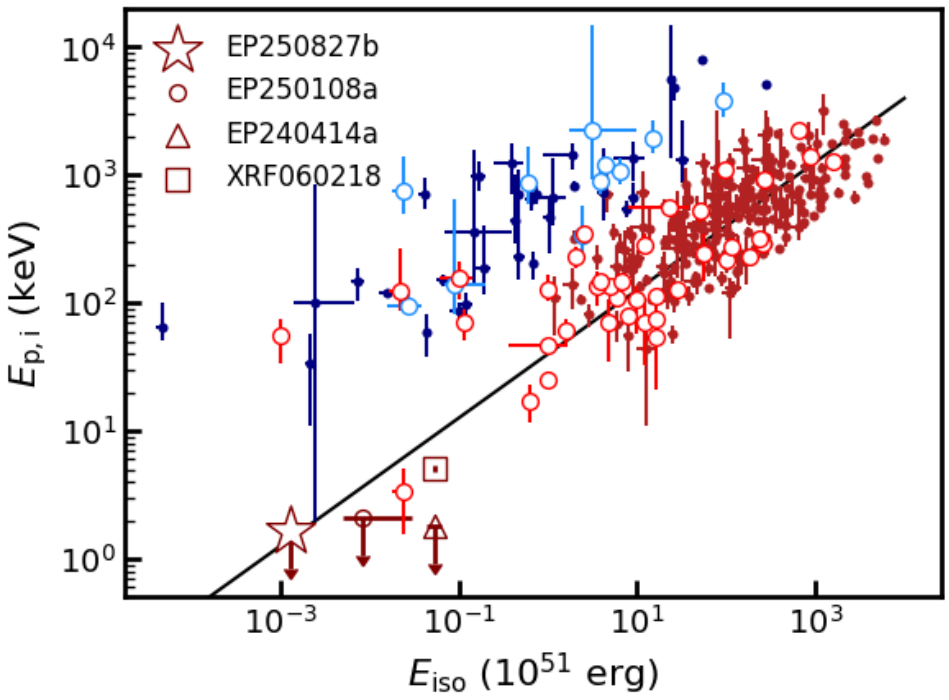

Figure 7.18: The Amati et al. (2002) relation, or peak energies ($E_{p,i}$) of GRBs and XRFs plotted against their rest-frame isotropic equivalent (E_{iso}). GRBs are categorized into LGRBs (red), GRB-SNe (red with open circles), short GRBs (blue), short GRBs with extended emission (blue with open circles), and EP XRF-SNe (maroon) and XRF060218. The sample is created from Minaev & Pozanenko (2020). The relation is explicitly shown for LGRBs with the black solid line.

discovery.

7.7 Conclusion

In this Letter, we present X-ray, ultraviolet, optical, near-infrared, and radio observations of EP250827b/SN 2025wkm, an EP XRF with a SN Ic-BL counterpart. Our major findings are:

- EP250827b's X-ray prompt emission lasted at least $\sim$ 1000 seconds and has an average 0.5–4 keV luminosity of $\sim 10^{45}\,\mathrm{erg\,s^{-1}}$. In addition, we derive an upper limit on its peak energy of < 1.5 keV, allowing for an XRF classification. There is no subsequent X-ray

emission detected after the prompt emission. The X-ray properties for this event are similar to those of XRF060218/SN 2006aj (Mazzali et al., 2006a) and EP250108a/SN 2025kg (Li et al., 2025c).

- EP250827b's optical counterpart is SN 2025wkm, which was found through the ZTF–EP experiment (Ahumada et al., 2025). SN 2025wkm possesses a clear double-peaked optical LC, with its first peak possessing an absolute magnitude of at least $M_g \sim -19.3$ mag, and blue colors ($g - r \sim 0.4$). Its second peak has a peak absolute magnitude of $M_r \sim -19.2$ mag. However, its bolometric luminosity LC does not display a clear second peak, and instead plateaus until $t_0 + 20$ days before declining. This makes EP250827b/SN 2025wkm the first EP XRF-SN with a plateau in its bolometric luminosity LC, providing evidence for an extra central engine powering source.

- SN 2025wkm's spectrum evolve from an extremely hot ($T \sim 20,000$ K) and blue continuum at early times, to a red continuum by $t_0 + 11.1$ days, with clear broad Fe II and Si II absorption features, along with a lack of H and He features. This allowed for classification of SN 2025wkm as a SN Ic-BL. We derive extremely high ejecta velocities $\sim 40,000\,\mathrm{km\,s^{-1}}$ at $t_0 + 4.2$ days. The host galaxy spectrum shows an abundance of star-formation lines.

- We do not detect variable radio emission from the source location of EP250827b – therefore, we determine the radio observations are from the host galaxy, produced by a SFR of $\sim 3\,\mathrm{M_\odot/yr}$. The radio upper limits rule out a classical, on-axis jet being successfully launched in this system, but do not rule out an extremely low-energetic jet of $E \sim 2 \times 10^{49}$ erg, or extremely off-axis jets with $\theta_{\rm obs} \geq 30^\circ$. The radio upper limits we derive are similar to those derived for EP250108a (Srinivasaragavan et al., 2025a), and radio emission similar

to XRF060218 (Soderberg et al., 2006b) cannot be ruled out.

- We determine that a failed jet transforming into a shocked cocoon cannot describe the X-ray prompt emission characteristics of EP250827b, due to the low peak energy constraint in combination with the high velocities and temperatures at early times. We determine that the X-ray prompt emission is likely due to disk- or magnetar-driven fast ejecta breaking out and interacting with an extended CSM environment, at a radius $R_{\rm e} \sim 10^{13}$ cm. We also derive a very low CSM density of $\sim 3 \times 10^{-12} {\rm gcm}^{-3}$. This gives evidence that EP250827b/SN 2025wkm's progenitor star had a less extreme mass-loss history in comparison to other XRF-SNe that show evidence of interacting with an extended CSM.

- The Arnett (1982) radioactive decay of ^{56}Ni model that is usually used to describe the emission of stripped-envelope SNe cannot describe the late-time SN LC, as the necessary Nickel fraction with respect to the total ejecta mass is unphysical ($f_{\rm Ni} > 0.5$). Comparisons with radiation-transport models suggest that the required ^{56}Ni fraction may be more reasonable ($f_{\rm Ni} \sim 0.1$). Shock heating can also contribute to this late-time light-curve. We also determine that a central engine is likely pumping additional energy into the system. We test a model where the spindown of a millisecond magnetar powers the LC in combination with the radioactive decay of ^{56}Ni (Omand & Sarin, 2024a), and find that it provides a reasonable fit to the data. We derive a magnetar magnetic field strength of $B_0 \sim 5 \times 10^{14}$ Gauss and spin period of ~ 1.9 ms.

- In order to describe the first peak of the SN LC, we test a semi-analytic model from Gottlieb (2025) that is consistent with the picture of fast ejecta breaking out of an extended CSM for the X-ray prompt emission, and a magnetar powering the late-time SN LC. This model

invokes magnetar winds and/or disk outflows, with maximum velocities $\sim 0.35c$. The mixing of these disk outflows, magnetar winds, and neutrino-driven shock ejecta breaking out of the extended CSM produces the X-ray prompt emission, while the cooling emission of the disk outflows and magnetar winds produce the first peak in the SN LC. At later times, the spin-down of the magnetar remnant in combination with the radiocactive decay of ^{56}Ni powers the late-time SN LC.

In §7.6, we provide a detailed discussion on the implications of our major findings, and discuss the landscape of the XRF-SN field. EP is dramatically increasing the discovery rate of XRF-SNe. Every new event has provided the community with unprecedented opportunities to understand the amount of diversity regarding SNe explosion mechanisms, relativistic jet formation, central engine activity, and CSM properties surrounding massive stars. We are just now beginning to uncover this rich landscape. Future time-domain missions such as ULTRASAT (Shvartzvald et al., 2024), LSST (Ivezić et al., 2019b), the La Silla Southern Sky Survey (Miller et al., 2025), and UVEX (Kulkarni et al., 2021) will continue to probe this landscape even more, unveiling major open questions surrounding the physics of some of nature's most powerful and mysterious explosions.

Acknowledgements

G.P.S. acknowledges Kaustav K. Das for useful conversations about understanding CSM interaction in stripped-envelope SNe, and Jillian Rastinejad for compiling the LCs presented in Figure 15. G.P.S. thanks the ZTF and EP publication boards for their useful comments on the manuscript prior to submission. G.P.S. acknowledges Simi Bhullar for her moral support through

the paper writing process and through G.P.S's postdoc application season. Though she is an attorney and not a scientist in the field, she is on the author list for bringing to life the artistic depiction shown in Figure 16. G.P.S. acknowledges the players on the Caltech Men's Basketball team - Josh Balami, Finnegan Fancher, Stuart Florescu, Ido Geffen, Dagemawi Getachew, Dorian Glogovac, Pranit Gunjal, Noah Hicks, Robert Jackson, Andrew Koclanes, Ryan Rodrigue, Chase Williamson, and coaches Dr. Oliver Eslinger and Seamus McKiernan. Their energy and commitment during the beginning of the 2025-2026 season made practices a welcome outlet for assistant coach G.P.S. to recharge after long days and nights of paper writing and postdoc applications.

The material is based upon work supported by NASA under award number 80GSFC24M0006. O.G. is supported by the Flatiron Research Fellowship. B. O. is supported by the McWilliams Postdoctoral Fellowship in the McWilliams Center for Cosmology and Astrophysics at Carnegie Mellon University. M.E.R. is supported by the European Union (ERC, Starstruck, 101095973, PI Jonker). Views and opinions expressed are however those of the author(s) only and do not necessarily reflect those of the European Union or the European Research Council Executive Agency. Neither the European Union nor the granting authority can be held responsible for them. AA acknowledges the Yushan Young Fellow Program by the Ministry of Education, Taiwan (MOE-111-YSFMS-0008-001-P1) and National Science and Technology Council, Taiwan (NSTC grant 114-2112-M-008-021-MY3) for the financial support. M. B. is a recipient of a Student Grant from the Wübben Stiftung Wissenschaft. CJ acknowledges the National Natural Science Foundation of China through grant 12473016, and the support by the Strategic Priority Research Program of the Chinese Academy of Sciences (Grant No. XDB0550200). Funded in part by the Deutsche Forschungsgemeinschaft (DFG, German Research Foundation) under Germany's Excellence Strategy – EXC-2094 – 390783311. WXL is supported by NSFC (12120101003 and

12373010), the National Key R&D Program (2022YFA1602902 and 2023YFA1607804), and Strategic Priority Research Program of CAS (XDB0550100 and XDB0550000). X.W. is supported by the National Natural Science Foundation of China (NSFC) under grants 12288102 and 12033003. This work makes use of observations from the Las Cumbres Observatory network. The LCO team is supported by NSF grants AST-2308113 and AST-1911151.

The detection of the prompt X-ray emission is based on data obtained with Einstein Probe, a space mission supported by the Strategic Priority Program on Space Science of Chinese Academy of Sciences, in collaboration with the European Space Agency, the Max-Planck-Institute for extraterrestrial Physics (Germany), and the Centre National d'Études Spatiales (France).

Based on observations obtained with the Samuel Oschin Telescope 48-inch and the 60-inch Telescope at the Palomar Observatory as part of the Zwicky Transient Facility project. ZTF is supported by the National Science Foundation under Award #2407588 and a partnership including Caltech, USA; Caltech/IPAC, USA; University of Maryland, USA; University of California, Berkeley, USA; University of Wisconsin at Milwaukee, USA; Cornell University, USA; Drexel University, USA; University of North Carolina at Chapel Hill, USA; Institute of Science and Technology, Austria; National Central University, Taiwan, and OKC, University of Stockholm, Sweden. Operations are conducted by Caltech's Optical Observatory (COO), Caltech/IPAC, and the University of Washington at Seattle, USA. The Liverpool Telescope is operated on the island of La Palma by Liverpool John Moores University in the Spanish Observatorio del Roque de los Muchachos of the Instituto de Astrofisica de Canarias with financial support from the UK Science and Technology Facilities Council. SED Machine is based upon work supported by the National Science Foundation under Grant No. 1106171. The Gordon and Betty Moore Foundation, through both the Data-Driven Investigator Program and a dedicated grant, provided critical

funding for SkyPortal.

TRT Data Based on observations made with the Thai Robotic Telescopes under program ID TRTC12C_001, which is operated by the National Astronomical Research Institute of Thailand (Public Organization). Based on observations obtained at the international Gemini Observatory, a program of NSF's OIR Lab, which is managed by the Association of Universities for Research in Astronomy (AURA) under a cooperative agreement with the National Science Foundation on behalf of the Gemini Observatory partnership: the National Science Foundation (United States), National Research Council (Canada), Agencia Nacional de Investigación y Desarrollo (Chile), Ministerio de Ciencia, Tecnología e Innovación (Argentina), Ministério da Ciência, Tecnologia, Inovações e Comunicações (Brazil), and Korea Astronomy and Space Science Institute (Republic of Korea). The authors wish to recognize and acknowledge the very significant cultural role and reverence that the summit of Maunakea has always had within the indigenous Hawaiian community. The data were acquired through the Gemini Observatory Archive at NSF NOIRLab and processed using DRAGONS (Data Reduction for Astronomy from Gemini Observatory North and South). This paper contains data obtained at the Wendelstein Observatory of the Ludwig-Maximilians University Munich. Funded by the Deutsche Forschungsgemeinschaft (DFG, German Research Foundation) under Germany's Excellence Strategy – EXC-2094 – 390783311. Sponsored by the Natural Science Foundation of Xinjiang Uygur Autonomous Region under No.2024D01D32, Tianshan Talent Training Program grant 2023TSYCLJ0053the National Natural Science Foundation of China NSFC No.12373038.

The National Radio Astronomy Observatory and Green Bank Observatory are facilities of the U.S. National Science Foundation operated under cooperative agreement by Associated Universities, Inc. Based in part on observations made with the Nordic Optical Telescope, owned

in collaboration by the University of Turku and Aarhus University. The data presented here were obtained with ALFOSC, which is provided by the Instituto de Astrofisica de Andalucia (IAA) under a joint agreement with the University of Copenhagen and NOT.

Chapter 8: A Look to the Future

...and there goes the buzzer! A huge thank you to readers for making it this far and completing all four quarters. In my dissertation, I presented six observational studies of stellar engine-driven transients, divided into four parts based on the various classes of events. If I had to summarize the most important discoveries of every class in a single sentence, it would go as follows:

- The physics powering stellar collapse is decoupled from the mechanisms that launch relativistic jets in LGRB-SNe.
- Optical data is not a sufficient discriminant to determine the presence of relativistic ejecta in SNe Ic-BL.
- Some orphan afterglows lack gamma-ray counterparts due to possessing structured jets being viewed off-axis.
- Interaction with an extended CSM can suppress gamma-ray emission in XRF-SNe and magnetars are viable progenitors for XRF-SNe.

Looking forward, there has never been a more fruitful time to uncover the full landscape of stellar engine-driven transients. A new generation of facilities is enabling this frontier. In addition to the previously discussed missions (e.g., ZTF, Einstein Probe, and SVOM), the *James Webb*

Space Telescope (*JWST*) is enabling spectroscopy in the near-infrared bands and to later times, resulting in direct probes of chemical composition; the upcoming La Silla Schmidt Southern Survey (LS4; a Southern Sky Survey similar to ZTF; Miller et al. 2025) and Rubin Observatory will continue to expand our ability to discover optical transients across the entire sky; the future NASA missions ULTRASAT (Shvartzvald et al., 2024) and the Ultraviolet Explorer (UVEX; Kulkarni et al. 2021) will open a new discovery space in the UV time-domain sky; and future radio facilities such as the next-generation VLA (Di Francesco et al., 2019) and Deep Sypnotic Array-2000 (Hallinan et al., 2019) will probe new parameter spaces in the radio time-domain sky, both with respect to sensitivity and temporal coverage.

Modeling efforts are also improving. As highlighted throughout this dissertation, observations hint towards diverse progenitor systems such as choked jets suppressed by stellar envelopes or dense circumstellar media (Gottlieb et al., 2018a), dirty fireballs (Dermer et al., 1999), structured jets viewed off-axis (Gottlieb et al., 2021), and more. Historical light curve (LC) modeling software could not fully reproduce the multi-wavelength emission of these complex systems; however, new LC modeling software such as `Redback` (Sarin et al. 2024; which I used extensively during this dissertation) are changing this. These new software are beginning to incorporate recent theoretical advances in jet dynamics, geometries, and CSM interaction into their models, significantly enhancing our ability to model stellar engine-driven transient emission and infer their physical features.

Therefore, the future is extremely bright for stellar engine-driven transient science. Through the process of writing this dissertation, I began thinking about what this future holds and what new questions have as a result arisen in the field. Though my dissertation features extensive analysis and characterization of the *emission* associated with stellar engine-driven phenomena,

I realized that it was only in the latter parts of my dissertation, specifically Chapters 5–7, that I truly began to probe their *progenitor systems* to a large degree. Major open questions regarding these progenitor systems remain. For example, what physical conditions are necessary to successfully launch jets? How do binary companions and circumstellar environments regulate jet breakout? What fraction of engines are neutron stars versus black holes? Addressing these questions informs not only the origins of stellar engine-driven phenomena, but also stellar evolution, galaxy feedback, the progenitors for gravitational-wave systems, and more.

The upcoming observational revolution of time-domain facilities makes the upcoming years the perfect time to pursue answers to these sorts of questions. After much thought, my future research will utilize this new generation of facilities to target the population of stellar engine-driven transients that escape traditional gamma-ray detection, which includes classes I have previously studied such as orphan afterglows and XRFs. By systematically studying their emission across the electromagnetic spectrum and connecting to theoretical models, I aim to build a comprehensive mapping between their observable emission and the properties of their progenitor systems.

This was just Game 1...I will be back soon, this time as a CIERA Postdoctoral Fellow at Northwestern University, to continue my pursuit of stellar engine driven transient science. It is shaping up to be a great series...only time will tell if the Universe can keep its secrets of nature's most explosive and energetic phenomena hidden from us for much longer.

Appendix A: Supplementary Materials for Chapter 2

Below we provide the optical photometry of GRB 221009A.

$t_{\rm obs} - T_0$ (days)	Telescope	Filter	AB mag	Uncertainty
0.13	GIT	g′	17.66	0.08
0.13	GIT	r′	16.16	0.07
0.13	GIT	i′	15.17	0.03
0.14	GIT	z′	14.50	0.04
0.14	GIT	g′	17.69	0.07
0.14	GIT	r′	16.26	0.05
0.15	GIT	i′	15.28	0.03
0.15	GIT	z′	14.57	0.05
0.16	GIT	g′	17.99	0.10
0.16	GIT	r′	16.32	0.05
0.16	GIT	i′	15.34	0.04
0.17	GIT	z′	14.64	0.06
0.17	GIT	g′	17.94	0.11
0.17	GIT	r′	16.40	0.05
0.18	GIT	i′	15.41	0.04

0.18	GIT	z′	14.71	0.07
0.19	GIT	g′	18.11	0.16
0.19	GIT	r′	16.49	0.05
0.19	GIT	i′	15.47	0.05
0.19	GIT	z′	14.72	0.06
1.00	GIT	g′	20.21	0.23
1.00	GIT	z′	16.75	0.05
1.00	GIT	z′	16.73	0.06
1.00	GIT	i′	17.48	0.04
1.00	GIT	i′	17.49	0.03
1.00	GIT	i′	17.52	0.04
1.10	GIT	r′	18.58	0.06
1.10	GIT	r′	18.55	0.05
1.10	GIT	g′	20.50	0.16
1.10	GIT	z′	16.90	0.15
1.10	GIT	r′	18.66	0.08
1.14	GIT	z′	17.06	0.08
1.15	GIT	z′	17.01	0.15
2.12	GIT	r′	19.77	0.14
2.14	GIT	z′	17.99	0.15
3.00	GIT	i′	19.20	0.14
3.00	GIT	r′	20.41	0.15

3.00	GIT	z′	18.57	0.16
4.03	GIT	i′	19.68	0.14
4.03	GIT	r′	20.83	0.16
4.03	GIT	z′	18.82	0.17
5.08	GIT	r′	20.91	0.21
5.08	GIT	i′	19.85	0.19
5.08	GIT	z′	18.93	0.17
6.10	GIT	i′	20.43	0.18
6.10	GIT	z′	19.41	0.19
3.6	LDT	g′	22.06	0.04
3.6	LDT	r′	20.44	0.04
3.6	LDT	i′	19.37	0.01
3.6	LDT	z′	18.67	0.01
9.5	LDT	r′	21.5	0.08
9.5	LDT	i′	20.75	0.05
9.5	LDT	z′	20.01	0.03
18.5	LDT	g′	24.71	0.15
18.5	LDT	r′	22.71	0.06
18.5	LDT	i′	21.83	0.15
18.5	LDT	z′	20.97	0.05
21.5	LDT	r′	22.91	0.06
21.5	LDT	i′	21.82	0.02

21.5	LDT	z′	21.37	0.04
28.5	LDT	r′	23.55	0.15
28.5	LDT	i′	22.07	0.09
28.5	LDT	z′	21.45	0.07
36.53	LDT	r′	23.64	0.11
36.53	LDT	i′	22.45	0.05
36.53	LDT	z′	21.82	0.07
52.53	LDT	i′	22.73	0.15
4.4	Gemini-South	i′	19.78	0.02
17.4	Gemini-South	i′	21.71	0.05

Table A.1: Optical photometry and associated 1σ errors of GRB 221009A, which includes contributions from its afterglow, host galaxy, and associated SN 2022xiw. All times are in the observer frame. The magnitudes are not corrected for Galactic extinction. The photometry here was obtained by members of our collaboration.

$t_{\rm obs} - T_0$ (days)	Filter	AB mag	Uncertainty
0.128349	g	17.66	0.07
0.211	g	18.22	0.33
1.134	g	20.43	0.2
1.152193	g	20.13	0.08
1.165	g	20.53	0.11
2.166539	g	21.15	0.21
1.02802141	g	20.037	0.205

1.03149415	g	20.248	0.234
1.12791174	g	20.228	0.339
1.13782442	g	20.299	0.363
1.1412292	g	20.634	0.469
1.27027935	g	20.33	0.06
1.39404935	g	20.41	0.12
2.29360935	g	21.05	0.12
3.28066935	g	21.61	0.19
6.09	g	22.61	0.12
11.55024	g	23.7	0.2
0.131049	r	16.16	0.07
0.211	r	16.76	0.08
0.43625	r	17.36	0.12
1.136	r	18.57	0.05
1.159669	r	18.65	0.02
1.168	r	18.64	0.03
1.172	r	18.43	0.11
1.2568	r	18.74	0.12
1.301	r	18.96	0.1
1.314699	r	18.81	0.05
2.138926	r	19.53	0.04
2.306539	r	19.67	0.11

3.156539	r	20.03	0.06
3.176539	r	19.97	0.08
3.206539	r	20.07	0.19
3.226539	r	20.32	0.17
3.2459	r	20.23	0.09
3.266539	r	20.17	0.12
3.296539	r	20.26	0.16
3.316539	r	20.24	0.19
4.146539	r	20.53	0.09
4.176539	r	20.63	0.09
4.196539	r	20.71	0.15
4.216539	r	20.54	0.1
4.236539	r	20.55	0.12
4.266539	r	20.74	0.16
4.286539	r	20.9	0.23
4.306539	r	20.86	0.27
4.674099	r	20.92	0.05
5.7	r	21.13	0.06
0.214	i	15.58	0.03
1.154	i	17.56	0.05
1.167041	i	17.52	0.01
1.17	i	17.58	0.01

1.322576	i	17.69	0.02
1.48	i	17.92	0.11
2.14674	i	18.4	0.02
2.316539	i	18.49	0.04
3.146539	i	18.82	0.03
3.176539	i	19.02	0.07
3.196539	i	19.09	0.1
3.216539	i	18.95	0.07
3.236539	i	18.93	0.04
3.2459	i	18.91	0.11
3.266539	i	18.93	0.04
3.286539	i	18.92	0.04
4.156539	i	19.51	0.06
4.176539	i	19.41	0.05
4.206539	i	19.52	0.05
4.226539	i	19.44	0.04
4.246539	i	19.45	0.05
4.266539	i	19.43	0.05
4.296539	i	19.48	0.06
4.316539	i	19.5	0.07
4.45	i	19.89	0.05
4.671579	i	19.88	0.02

5.7	i	20.01	0.05
6.07	i	20.01	0.04
0.216667	z	14.89	0.03
1.166	z	16.93	0.05
1.171	z	16.87	0.05
1.174389	z	16.81	0.01
1.330626	z	16.99	0.01
1.48	z	16.92	0.11
2.154231	z	17.69	0.02
2.326539	z	17.72	0.03
3.166539	z	18.2	0.04
3.186539	z	18.19	0.05
3.206539	z	18.4	0.08
3.236539	z	18.26	0.03
3.2459	z	18.35	0.13
3.256539	z	18.23	0.03
3.276539	z	18.23	0.04
3.306539	z	18.3	0.04
3.326539	z	18.18	0.04
4.166539	z	18.63	0.05
4.186539	z	18.76	0.05
4.191	z	18.8	0.1

4.206539	z	18.69	0.04
4.236539	z	18.75	0.04
4.256539	z	18.74	0.05
4.276539	z	18.83	0.05
4.306539	z	18.74	0.05
4.326539	z	18.71	0.06
4.670249	z	19.21	0.02
5.7	z	19.39	0.05

Table A.2: Optical photometry and 1σ errors of GRB 221009A, including contributions from its afterglow, host galaxy, and associated SN 2022xiw, from publicly available GCNs. All times are in the observer frame. The magnitudes are not corrected for Galactic extinction.

Appendix B: Supplementary Materials for Chapter 3

Optical photometry obtained of GRB 230812B.

$t_{\rm obs} - T_0$ (days)	Telescope	Filter	AB mag	Uncertainty
0.359	ZTF	r	18.85	0.04
0.359	ZTF	r	18.85	0.04
0.359	ZTF	r	18.83	0.02
0.377	ZTF	r	18.95	0.03
0.377	ZTF	r	18.95	0.03
0.377	ZTF	r	18.96	0.01
0.393	ZTF	g	19.19	0.03
0.393	ZTF	g	19.19	0.03
0.393	ZTF	g	19.21	0.01
0.411	ZTF	g	19.22	0.03
0.411	ZTF	g	19.22	0.03
0.411	ZTF	g	19.29	0.03
0.446	ZTF	r	19.16	0.04
0.446	ZTF	r	19.16	0.04
0.446	ZTF	r	19.16	0.02

0.451	SEDM	u	19.84	0.2
0.455	SEDM	g	19.52	0.13
0.455	SEDM	g	19.52	0.13
0.457	SEDM	r	19.28	0.04
0.46	ZTF	r	19.3	0.09
0.46	SEDM	i	19.1	0.05
0.463	SEDM	r	19.28	0.16
0.489	ZTF	r	19.14	0.12
0.489	ZTF	r	19.14	0.12
0.489	ZTF	r	19.15	0.06
0.49	SEDM	u	19.69	0.23
0.494	SEDM	g	19.68	0.14
0.497	SEDM	r	19.29	0.04
0.497	ZTF	r	19.24	0.16
0.497	ZTF	r	19.24	0.16
0.497	ZTF	r	19.27	0.07
0.5	SEDM	i	19.15	0.05
0.518	ZTF	r	19.28	0.1
0.518	ZTF	r	19.28	0.1
0.518	ZTF	r	19.26	0.07
0.53	ZTF	r	19.26	0.12
0.53	ZTF	r	19.21	0.06

0.531	SEDM	g	19.89	0.13
0.534	SEDM	r	19.4	0.03
0.536	SEDM	i	19.32	0.04
0.832	GIT	r	19.98	0.05
0.85	GIT	g	20.34	0.06
0.868	GIT	i	19.71	0.06
1.368	SEDM	g	21.09	0.15
1.372	SEDM	r	20.76	0.07
1.376	SEDM	i	20.79	0.12
1.86	GIT	r	21.38	0.05
2.125	LT	g	21.77	0.24
2.127	LT	r	21.16	0.14
2.129	LT	i	21.15	0.18
3.009	HCT	r	21.77	0.16
4.1	LT	r	21.96	0.19
4.103	LT	i	22.47	0.3
6.907	HCT	r	22.04	0.18
6.91	GIT	r	22.06	0.1
6.945	HCT	i	22.04	0.15
9.427	SEDM	i	21.67	0.23
9.916	HCT	r	22.02	0.14
11.979	HCT	r	21.84	0.15

13.445	LDT	r	22.14	0.08
13.45	LDT	i	21.76	0.11
15.436	LDT	r	22.22	0.1
15.439	LDT	i	21.86	0.11
18.43	LDT	r	22.22	0.11
18.438	LDT	i	21.8	0.07
23.074	LT	r	22.49	0.22
24.382	LDT	r	22.6	0.07
24.388	LDT	i	21.94	0.09
27.384	LDT	r	22.85	0.1
27.394	LDT	i	22.21	0.08
37.385	LDT	r	> 24.29	-
37.390	LDT	i	22.86	0.06
38.340	LDT	r	> 24.12	-
38.351	LDT	i	22.96	0.1

Table B.1: Optical photometry and 1σ errors of GRB 230812B/SN 2023pel. The photometry includes contributions from the afterglow and associated SN, and are all image-subtracted to correct for the host galaxy contribution. All times are in the observer frame, and the magnitudes are not corrected for Galactic extinction.

Appendix C: Supplementary Materials for Chapter 4

C.1 Discovery Paragraphs

Below we present the discovery paragraphs for every event. We note here that the first ZTF photometry reported is not from forced photometry, but from ZTF's nightly alerts that are reported to TNS.

C.1.1 SN 2018bvw

We refer the reader to Ho et al. (2020b) for details about this event.

C.1.2 SN 2018ell

The first ZTF photometry of SN 2018ell (ZTF18abhhnnv) was obtained on 2018 July 17 (JD $= 2458316.72$). This first detection was in the r band with a host-subtracted magnitude of 20.09 ± 0.19, at $\alpha = 16^h49^m57.02^s$, $\delta = +27°38'26.94''$ (J2000.0, throughout). The discovery was reported to TNS (Fremling, 2018a) two days later on 2018 July 19, with a note saying the latest non-detection from ZTF was five days prior to discovery (July 12, $g > 20.81$). The event was first classified as a Type Ia SN based on a P60 SEDM spectrum obtained on 2018 July 31 (Fremling, 2018a), but was reclassified two years later as a Type Ic-BL SN (Dahiwale & Fremling,

2020a). The SN exploded in the outskirts of the spiral galaxy WISEA J164957.78+273828.3, with a well-established redshift of $z = 0.0638$.

C.1.3 SN 2018gep

We refer the reader to Ho et al. (2019a); Leung et al. (2021a); Pritchard et al. (2021) for details about this event.

C.1.4 SN 2018hsf

The first ZTF photometry of SN 2018hsf (ZTF18acbvpzj) was obtained on 2018 October 31 (JD $= 2458422.83$). This first detection was in the r band, with a host-subtracted magnitude of 19.58 ± 0.16 at $\alpha = 02^h40^m12.78^s$, $\delta = -19°58'44.94''$.The discovery was reported to TNS (Fremling, 2018b), with no prior non-detection from ZTF. The transient was classified as a Type Ic-BL event based on a LRIS spectrum obtained on 2018 December 4 (Fremling et al., 2018). The SN exploded in the plane of spiral galaxy PSO J040.0536-19.9798, and a redshift of $z = 0.119$ was determined through narrow host lines from the LRIS spectrum.

C.1.5 SN 2018keq

The first ZTF photometry of SN 2018keq (ZTF18acxgoki) was obtained on 2018 December 17 (JD $= 2458469.59$). This first detection was in the r band with a host-subtracted magnitude of 19.03 ± 0.10, at $\alpha = 23^h22^m41.97^s$, $\delta = +21°00'43.17''$. The discovery was reported to TNS (Fremling, 2020a) two days later on 2018 December 19, with a note saying the latest non-detection from ZTF was 4 days prior to discovery ($r > 20.2$ mag). The event was classifed as a

Type Ic-BL SN (Fremling et al., 2019c) based on a spectrum obtained by LRIS on 2019 January 04. The SN exploded in the spiral galaxy SDSS J232241.80+210042.6, with a well-established redshift of $z = 0.038$.

C.1.6 SN 2019hsx

We refer the reader to Anand et al. (2024) for details about this event.

C.1.7 SN 2019gwc

We refer the reader to Anand et al. (2024) for details about this event.

C.1.8 SN 2019lci

The first ZTF photometry of SN 2019lci (ZTF19abfsxpw) was obtained on 2019 July 11 (JD $= 2458675.79$) with the P48. This first detection was in the g band, with a host-subtracted magnitude of 19.15 ± 0.12, at $\alpha = 16^h31^m01.62^s$, $\delta = 8°2823.74''$. The discovery was reported to TNS (Nordin et al., 2019) three days later on 2019 July 14, with a note saying that the latest non-detection was two hours prior to discovery ($g > 20.0$ mag). The transient was classified as a Type Ic-BL event based on a P60 SEDM spectra obtained on 2019 July 16 (Dugas et al., 2019). The SN exploded in the outskirts of spiral galaxy WISEA J163101.63+082829.7, with a well-established redshift of $z = 0.0292$.

C.1.9 SN 2019moc

We refer the reader to Anand et al. (2024) for details about this event.

C.1.10 SN 2019oqp

The first ZTF photometry of SN 2019oqp (ZTF19abqshry) was obtained on 2019 August 21 (JD $= 2458716.66$). This first detection was in the r band, with a host-subtracted magnitude of 20.20 ± 0.15, at $\alpha = 16^h49^m57.02^s$, $\delta = 27°38'26.94''$. The discovery was first reported to TNS by ATLAS (Tonry et al., 2019) on 2021 August 25 ($c = 19.32$). The transient was classified as a Type Ic-BL event based on a DBSP spectrum obtained on 2019 August 27 (Fremling et al., 2019b). The SN exploded in the outskirts of the spiral galaxy MCG +08-30-042 with a redshift of $z = 0.0308$.

C.1.11 SN 2019pgo

The first ZTF photometry of SN 2019pgo (ZTF19abupned) on 2019 August 30 (JD $=$ 2458725.89). The first detection was in the g band, with a host-subtracted magnitude of 20.69 ± 0.22 at $\alpha = 23^h53^m00.05^s$, $\delta = 25°07'16.46''$. The discovery was reported by the Tsinghua-NAOC Transient Survey to TNS two days later (Zhang et al., 2019) on 2019 September 1. The transient was classified as a Type Ic-BL event based on a spectrum obtained on 2019 September 18 (Fremling et al., 2019a) with SPRAT on the Liverpool Telescope. The SN exploded in the galaxy WISEA J235300.28+250717.2. The galaxy does not have a well-established redshift, but a redshift of $z = 0.0500$ was determined through narrow host lines from a Liverpool Telescope spectrum.

C.1.12 SN 2019qfi

We refer the reader to Anand et al. (2024) for details about this event.

C.1.13 SN 2020zg

The first ZTF photometry of SN 2020zg (ZTF20aafmdzj) was obtained on 2020 January 15 (JD $= 2458863.63$). The first detection was in the g band, with a host-subtracted magnitude of $g = 17.91 \pm 0.02$ at $\alpha = 4^h02^m36.40^s$, $\delta = -16°11'54.33''$. The discovery was reported to TNS (Forster et al., 2020a) with a note saying the latest not-detection by ZTF was two days prior to discovery on 2020 January 13 ($g > 19.32$). The transient was classified as a Type Ic-BL event (Dahiwale & Fremling, 2020b) based on a DBSP spectrun obtained on on 2020 Feburary 26. The SN exploded in the edge of galaxy WISEA J040236.46-161152.0. The galaxy does not have a well-established redsift, but a redshift of $z = 0.0557$ was determined through narrow host lines from the DBSP spectrum.

C.1.14 SN 2020ayz

The first ZTF photometry of SN 2020ayz (ZTF20aaiqiti) was obtained on 2020 January 26 (JD $= 2458874.83$). The first detection was in the r band, with a host-subtracted magnitude of $r = 19.77 \pm 0.13$ at $\alpha = 12^h12^m04.90^s$, $\delta = 32°44'01.73''$. The discovery was reported to TNS (Forster et al., 2020b) on the same day ($g = 20.0$) with a note saying the latest non-detection by ZTF was three days prior to discovery on 2020 January 23 ($g > 20.23$). The transient was classified as a Type Ic-BL event (Dahiwale & Fremling, 2020b) based on a SEDM spectrum obtained on 2020 Feburary 03. The SN exploded in the center of the spiral galaxy MCG+06-27-025, with a well-established redshift of $z = 0.025437$.

C.1.15 SN 2020bvc

We refer the reader to Ho et al. (2020c); Izzo et al. (2020); Li et al. (2023); Rho et al. (2021) for details about this event.

C.1.16 SN 2020dgd

We refer the reader to Anand et al. (2024) for details about this event.

C.1.17 SN 2020hes

The first ZTF photometry of SN 2020hes (ZTF20aaurexl) was obtained on 2020 April 14 (JD $= 2458953.93$). The first detection was in the g band, with a host-subtracted magnitude of $g = 18.62 \pm 0.07$ at $\alpha = 17^h47^m05.71^s$, $\delta = 42°46'39.72''$. The discovery was reported to TNS (Forster et al., 2020c) with a note saying the latest non-detection by ZTF was ten days prior to discovery on 2020 April 04 ($g > 20.60$). The transient was classified as a Type Ic-BL event (Dahiwale & Fremling, 2020c) based on a SEDM spectrum obtained on 2020 April 25. The SN exploded in the galaxy WISEA J174706.10+424640.5. The galaxy does not have a well-established redsift, but a redshift of $z = 0.0700$ was determined through narrow host lines from a DBSP spectrum.

C.1.18 SN 2020hyj

The first ZTF photometry of SN 2020hyj (ZTF20aavcvrm) was obtained on 2020 April 16 (JD $= 2458955.92$). This first detection was in the g band, with a host-subtracted magnitude of 20.33 ± 0.21 at $\alpha = 16^h23^m47.22^s$, $\delta = 29°58'58.38''$. The discovery was reported to TNS

(Nordin et al., 2020) on 2020 April 16 with a note saying the latest non-detection by ZTF was two days prior to discovery on 2020 April 14 ($g > 20.32$). The transient was classified as a Type Ic-BL event (Dahiwale & Fremling, 2020d) based on a SEDM spectrum obtained on on 2020 April 29. No host galaxy was found upon inspection of archival images through NED. The redshift of $z = 0.055$ was determined through narrow host lines from the SEDM spectrum.

C.1.19 SN 2020jqm

We refer the reader to Corsi et al. (2023) for details about this event.

C.1.20 SN 2020lao

We refer the reader to Anand et al. (2024) for details about this event.

C.1.21 SN 2020rfr

The first ZTF photometry of SN 2020rfr (ZTF20abrmmah) was obtained on 2020 August 12 (JD $= 2459073.84$). This first detection was in the g band, with a host-subtracted magnitude of 19.67 ± 0.15 at $\alpha = 22^h39^m49.30^s$, $\delta = -06°26'15.92''$. The discovery was reported to TNS (Forster et al., 2020d) with a note saying the latest non-detection by ZTF was four days prior to discovery on 2020 August 08 ($r > 19.96$). The transient was classified as a Type Ic-BL event (Dahiwale & Fremling, 2020e) based on a LRIS spectrum obtained on on 2020 September 20. The SN exploded in spiral galaxy WISEA J223949.24-062616.9. The galaxy does not have a well-established redshift, but a redshift of $z = 0.073$ was determined through narrow host lines from the LRIS spectrum.

C.1.22 SN 2020rph

We refer the reader to Anand et al. (2024) for details about this event.

C.1.23 SN 2020tkx

We refer the reader to Anand et al. (2024) for details about this event.

C.1.24 SN 2020wgz

Our first ZTF photometry of SN 2020wgz (ZTF20achvlbs) was obtained on 2020 October 08 (JD $= 2459130.99$). This first detection was in the r band, with a host-subtracted magnitude of 20.08 ± 0.24 at $\alpha = 08^h57^m33.32^s$, $\delta = 62°34'00.07''$, The discovery was reported to TNS (Fremling, 2020b) with a note saying the latest non-detection by ZTF was one hour prior to the first detection. The SN has no visible galaxy counterpart, and a redshift of $z = 0.1785$ was determined through narrow host lines from a DBSP spectrum obtained on 2020 October 21.

C.1.25 SN 2020abxl

The first ZTF photometry of SN 2020abxl (ZTF20acvcxkz) was obtained on 2020 December 05 (JD $= 2459188.79$). This first detection was in the r band, with a host-subtracted magnitude of 19.48 ± 0.16 at $\alpha = 05^h04^m22.76^s$, $\delta = -14°02'46.42''$. The discovery was reported to TNS (Tonry et al., 2020) by ATLAS on 2020 December 07 ($o = 19.65$) with a note saying the latest non-detection by ATLAS was one day prior to discovery on 2020 December 06 ($o > 19.33$). The transient was classified as a Type Ic-BL event (Anderson et al., 2020) based on a spectrum obtained by the EFOSC2-NTT on the ESO New Technology Telescope on 2020 December 11.

The SN exploded in spiral galaxy SDSS J223949.25-062616.3. The galaxy does not have a well established redshift, but a redshift of $z = 0.0815$ was determined through narrow host lines from the NTT spectrum.

C.1.26 SN 2020abxc

Our first ZTF photometry of SN 2020abxc (ZTF20acvmzfv) was obtained on 2020 December 07 (JD $= 2459190.65$). This first detection was in the r band, with a host-subtracted magnitude of 19.22 ± 0.09 at $\alpha = 01^h00^m34.04^s$, $\delta = -08°07'00.67''$. The discovery was reported to TNS (Forster et al., 2020e) with a note saying the latest non-detection by ZTF was two days prior to discovery on 2020 December 05 ($g > 20.03$). The transient was classified as a Type Ic-BL event (Cartier et al., 2020) based on a spectrum obtained by the IMACS instrument on the Walter Baade Magellan 6.5-m telescope on 2020 December 08. The SN exploded in the spiral galaxy WISEA J010033.88-080656.9. The galaxy does not have a well-established redshift, but a redshift of $z = 0.0600$ was determined through narrow host lines from the IMACS spectrum.

C.1.27 SN 2020adow

Our first ZTF photometry of SN 2020adow (ZTF20adadrhw) was obtained on 2020 December 27 (JD $= 2459210.7560$). This first detection was in the g band, with a host-subtracted magnitude of 15.84 ± 0.03, at $\alpha = 08^h33^m42.26^s$, $\delta = +27°42'43.8''$. The transient was discovered by ASASSN already the day before, on 2020 December 26 (Stanek & Kochanek, 2020). The transient was classified as a Type Ic-BL on December 27 (Zheltoukhov et al., 2020) from a spectrum obtained on the Liverpool Telescope. The SN exploded in the spiral galaxy KUG

0830+278, with a well-established redshift of $z = 0.0075$.

C.1.28 SN 2021bmf

We refer the reader to Anand et al. (2024) for details about this event.

C.1.29 SN 2021epp

We refer the reader to Corsi et al. (2023) for details about this event.

C.1.30 SN 2021fop

The first ZTF photometry of SN 2021fop (ZTF21aapecxb) was obtained on 2021 March 17 (JD $= 2459290.71$). This first detection was in the g band, with a host-subtracted magnitude of 18.61 ± 0.05 at $\alpha = 07^h46^m42.91^s$, $\delta = 07°12'38.70''$. The discovery was reported to TNS (Tonry et al., 2021a) on 2021 March 15 by ATLAS ($o = 18.63$) with a note saying the latest non-detection by ATLAS was eight days prior to discovery on 2021 March 07 ($o > 19.76$). The transient was classified as a Type Ic-BL event (Tucker, 2021a) based on a spectrum obtained by the SNIFS instrument on the UH 88 inch telescope on 2021 March 20. The SN exploded in the spiral galaxy WISEA J074642.81+071238.0. The galaxy does not have a well established redshift, but a redshift of $z = 0.077$ was determined through narrow host lines from a spectrum on 2021 March 18 obtained by the SPRAT instrument aboard the Liverpool Telescope.

C.1.31 SN 2021hyz

We refer the reader to Corsi et al. (2023) for details about this event.

C.1.32 SN 2021ktv

The first ZTF photometry of SN 2021ktv (ZTF21aaxxihx) was obtained on 2021 May 01 (JD $= 2459335.69$). This first detection was in the r band, with a host-subtracted magnitude of 19.38 ± 0.13 at $\alpha = 11^h03^m03.89^s$, $\delta = 08°51'39.75''$. The discovery was reported to TNS (Tonry et al., 2021b) on the same day by ATLAS ($o = 19.50$) with a note saying the latest non-detection by ATLAS was two days prior to discovery on 2021 April 30 ($o > 19.4$). The transient was classified as a Type Ic-BL event (Tucker, 2021b) based on a spectrum obtained by the SNIFS instrument on the UH 88 inch telescope on 2021 May 19. The SN exploded in galaxy WISEA J110303.81+085140.9. The galaxy does not have a well-established redshift, but a redshift of $z = 0.07$ was determined through narrow host lines from a spectrum taken by DBSP on 2021 June 04.

C.1.33 SN 2021ncn

The first ZTF photometry of SN 2021ncn (ZTF21abchjer) was obtained on 2021 May 23 (JD $= 2459357.97$). This first detection was in the r band, with a host-subtracted magnitude of 18.58 ± 0.06 at $\alpha = 22^h36^m32.93^s$, $\delta = 25°45'40.58''$. The discovery was reported to TNS (Forster et al., 2021) with a note saying the latest non-detection by ZTF was three days prior to discovery on 2021 May 20 ($g > 19.64$). The transient was classified as a Type Ic-BL event (Dahiwale & Fremling, 2021) based on a spectrum obtained by the SEDM on 2021 May 30. The SN exploded in the outskirts of spiral galaxy IC 5233, with a well-established redshift of $z = 0.0246$.

C.1.34 SN 2021qjv

The first ZTF photometry of SN 2021qjv (ZTF20abcjdwu) was obtained on 2021 June 18 (JD $= 2459383.72$). This first detection was in the r band, with a host-subtracted magnitude of 19.38 ± 0.18 at $\alpha = 15^h10^m47.04^s$, $\delta = 49°12'18.14''$. The discovery was reported to TNS (De, 2021) two days earlier on 2021 June 16 ($g = 19.67$) with a note saying the latest non-detection by ZTF was two days prior to discovery on 2021 May 20 ($r > 20.57$). The transient was classified as a Type Ic-BL event (Chu et al., 2021) based on a spectrum obtained by LRIS on 2021 July 09. Two galaxies, WISEA J151047.04+491218.1 and SDSS J151046.89+491215.4 are spatially consistent with the location of the SN, both with a redshift of $z = 0.0383$

C.1.35 SN 2021too

We refer the reader to Anand et al. (2024) for details about this event.

C.1.36 SN 2021ywf

We refer the reader to Anand et al. (2024) for details about this event.

C.2 Spectral Sequences

Spectra are all shown at their rest wavelengths, and fluxes have been normalized to the median of the spectrum. The rest frame phase of the spectrum with respect to the r-band peak is also shown to the right of each individual spectrum. We show a log of the spectroscopic observations in Table F.3.

ZTF name	SN name	Spectrum Phase	Instrument
ZTF18abhhnnv	SN 2018ell	0.7	SEDM
ZTF18acbvpzj	SN 2018hsf	-7.5	SEDM
		22.1	LRIS
ZTF18acxgoki	SN 2018keq	0.8	SEDM
		12.3	LRIS
		186.6	LRIS
ZTF19aawqcgy	SN 2019hsx	-3.2	SEDM
		0.7	SEDM
		18.4	DBSP
		103.6	LRIS
ZTF19aaxfcpq	SN 2019gwc	-8.9	SEDM
		-7.0	SEDM
		-5.0	SEDM
		-0.2	SEDM
		4.6	SEDM
		8.5	SEDM
		15.2	DBSP
		20.0	SEDM
		45.1	DBSP
ZTF19abfsxpw	SN 2019lci	-13.8	SEDM
		-12.8	SEDM

		-9.0	SEDM
		1.7	SEDM
		6.6	DBSP
		12.4	SEDM
		21.2	NOT
ZTF19ablesob	SN 2019moc	-13.6	SEDM
		-9.8	SEDM
		-8.9	DBSP
		-6.0	SEDM
		7.2	DBSP
		65.0	LRIS
ZTF19abqshry	SN 2019oqp	-17.7	SEDM
		-13.8	DBSP
		-10.9	NOT
		-8.0	DBSP
ZTF19abupned	SN 2019pgo	-9.0	SEDM
		-6.1	SEDM
		1.5	SPRAT
		1.5	SEDM
		38.7	LRIS
ZTF19abzwaen	SN 2019qfi	-5.2	SEDM
		4.6	SEDM

		13.3	SEDM
		29.9	LRIS
ZTF20aafmdzj	SN 2020zg	10.2	SEDM
		13.0	SEDM
		23.5	SEDM
ZTF20aaiqiti	SN 2020ayz	-8.3	SEDM
		-6.3	SEDM
		7.4	SEDM
		18.1	DBSP
		133.2	LRIS
ZTF20aapcbmc	SN 2020dgd	-7.3	SEDM
		-0.5	SEDM
		0.4	SEDM
		16.0	LRIS
		28.6	SEDM
		106.1	LRIS
ZTF20aaurexl	SN 2020hes	-7.9	SEDM
		0.5	SEDM
		7.0	SPRAT
ZTF20aavcvrm	SN 2020hyj	-0.4	SEDM
		2.4	SEDM
		4.3	SEDM

ZTF20aazkjfv	SN 2020jqm	-0.4	SEDM
		1.6	SEDM
		4.4	SEDM
		10.2	NOT
		21.8	SEDM
ZTF20abbplei	SN 2020lao	-8.2	SEDM
		-7.2	DBSP
		-4.3	SEDM
		0.5	SEDM
		9.3	SEDM
		14.1	SEDM
		16.1	SPRAT
ZTF20abcjdwu	SN 2021qjv	-1.3	SEDM
		4.5	SPRAT
		15.1	LRIS
ZTF20abrmmah	SN 2020rfr	2.5	SEDM
		3.4	SEDM
		7.1	SEDM
		28.6	DBSP
		32.3	LRIS
ZTF20abswdbg	SN 2020rph	-6.2	SEDM
		-5.2	SEDM

		-0.4	NOT
		-0.4	SEDM
		5.3	SEDM
		47.5	LRIS
		78.2	LRIS
ZTF20abzoeiw	SN 2020tkx	-5.2	SPRAT
		-2.3	SEDM
		-0.4	SEDM
		6.4	SEDM
		14.2	SEDM
		20.1	SEDM
		24.9	SEDM
		50.3	SEDM
		54.2	SEDM
ZTF20achvlbs	SN 2020wgz	-0.4	SEDM
		3.8	DBSP
		21.6	DBSP
ZTF20acvcxkz	SN 2020abxl	-5.1	ePESSTO+
ZTF20acvmzfv	SN 2020abxc	-2.1	SEDM
ZTF20adadrhw	SN 2020adow	-6.4	SPRAT
ZTF21aagtpro	SN 2021bmf	-11.4	P200
		55.5	SEDM

		96.8	P200
		137.1	LRIS
		172.5	LRIS
ZTF21aaocrlm	SN 2021epp	-5.1	ePESSTO+
ZTF21aapecxb	SN 2021fop	-0.2	SEDM
ZTF21aartgiv	SN 2021hyz	-7.0	SEDM
		0.7	SEDM
		15.0	SEDM
ZTF21aaxxihx	SN 2021ktv	6.3	SEDM
		7.3	SPRAT
		23.3	DBSP
ZTF21abchjer	SN 2021ncn	-5.3	SEDM
		0.5	SEDM
		2.5	SEDM
ZTF21abmjgwf	SN 2021too	-0.4	DBSP
		5.4	LRIS
ZTF21acbnfos	SN 2021ywf	-5.3	SEDM
		-0.4	DBSP
		2.5	DBSP
		15.1	DBSP
		125.0	LRIS

Table C.1: Spectral log of observations. Spectrum phase is in rest-frame with respect to r-band maximum

C.3 Multiwavelength Modeling

We use the open-source electromagnetic transient Bayesian fitting software package `redback` (Sarin et al., 2023) to perform multiwavelength modeling of three events to determine if it is possible that these events had an associated relativistic jet, through modeling the optical, radio, and X-ray data simultaneously in flux density space. We use the `arnett + tophat` model in `redback`, which utilizes a combination of radioactive decay of Nickel from Arnett (1982), along with a synchrotron component from an accompanying top-hat jet generated from the software package `afterglowpy` (Ryan et al., 2020b), to model SN emission with an off-axis accompanying relativistic jet with a jet half-opening angle of 0.1 radian.

We compare the Bayesian evidences for this model to those of the synchrotron self-absorption (SSA) model for radio SNe (Eq. 4 from Chevalier 1998), to compute a Bayes factor and determine which model can better explain the multiwavelength observations. We report the free fitting parameters for each of the models and the priors used in Tables C.2 and C.3. Below we report the results for each of the events. Because there are only a few radio and X-ray detections/non-detections available for each event, we note that these results must be taken with a grain of salt, and therefore present them in the Appendix.

C.3.0.1 SN 2020tkx

SN 2020tkx has two radio detections and one X-ray non-detection reported in Corsi et al. (2023). Because v_{ph} for this event was measured from a spectrum 53 days after peak, we allow it to vary as a free parameter with uniform priors. Furthermore, the radio LC shown in Figure 11 in Corsi et al. (2023) shows a rise in time, and there are no significant constraints that can be put on the jet's energy or the ISM number density, so we allow both those parameters to vary with uniform priors in logarithmic space. The corner plots for the fitting are shown in the Appendix, and we find that the `Arnett + tophat` model is favored with a Bayes factor of $10^{23.0}$.

C.3.0.2 SN 2020adow

SN 2020adow has two radio detections and one X-ray detection, and was not reported in Corsi et al. (2023). There were two radio measurements obtained, at 5.3 days and 16.3 days after explosion, with flux densities of 28.5 ± 7.1 and 17.1 ± 7.6 μJy (Corsi et al., 2021). The X-ray measurement was obtained 42 days after explosion, with a 0.3 – 10 keV flux of $4.9^{+2.8}_{-2.1} \times 10^{-14}$ erg cm^{-2} s^{-1}. We convert the 0.3 – 10 keV flux to a flux density at 5 keV for the fitting, through assuming a power-law spectrum of photon index $\Gamma = 2$. We constrain v_{ph} as a prior to the value obtained in §7.3.4 (19,500 km s^{-1}), which utilized a spectrum taken 7 days before peak. We have no constraints on the jet energy or ISM number density for this object from previous works, so we allow both those parameters to vary with uniform priors in logarithmic space. The corner plots for the fitting are shown in the Appendix, and we find that the Radio + SSA model is favored qualitatively, though a conclusive Bayes factor was not able to be found for this event.

C.3.0.3 SN 2021ywf

SN 2021ywf has two radio detections and one X-ray detection reported in Corsi et al. (2023). We convert the 0.3 – 10 keV flux reported to a flux density at 5 keV for the fitting, through assuming a power-law spectrum of photon index $\Gamma = 2$. We constrain $\mathrm{v_{ph}}$ as a prior to the value obtained in §7.3.4 (12,000 km $\mathrm{s^{-1}}$), which utilized a spectrum taken 0.5 days after peak. Corsi et al. (2023) also was able to rule out top-hat jets with energies greater than 10^{49} erg and interstellar medium (ISM) number densities (n_0) greater than 0.1 $\mathrm{cm^{-3}}$ for this event, so we utilize these priors in the fitting procedure as well. The corner plots for the fitting are shown in the Appendix, and we find that the Radio SSA model is favored with a Bayes factor of $K_{\mathrm{Bayes}} = 10^{28.5}$.

Parameters	Description	Prior Boundaries
z	redshift	Set to values from Table 4.1
$\mathrm{v_{ph}}$	Peak photospheric expansion velocity	Set to values from Table 4.5
f_{Ni}	Nickel fraction	[0.001, 1] (in $\mathrm{Log_{10}}$ space)
$\mathrm{M_{ej}}$	Ejecta mass	[0.0001, 100] $\mathrm{M_\odot}$ (in $\mathrm{Log_{10}}$ space)
A_v	MW extinction	0 mag
κ	Optical opacity	0.07 $\mathrm{cm^2\,g^{-1}}$
κ_γ	Gamma-ray Opacity	[0.0001, 10000] $\mathrm{cm^2\,g^{-1}}$ (in $\mathrm{Log_{10}}$ space)
T_{floor}	Minimum temperature reached in early explosion	[1000, 100000] K (in $\mathrm{Log_{10}}$ space)
$\theta_{\mathrm{observer}}$	Observing angle of jet	Sine[0.2, 1.57]
θ_{core}	Jet opening angle	0.1
ϵ_e	$\mathrm{Log_{10}}$ fraction of thermal energy to electrons	0.1
ϵ_b	$\mathrm{Log_{10}}$ fraction of thermal energy to magnetic field	0.1
$\mathrm{E_0}$	$\mathrm{Log_{10}}$ on axis isotropic equivalent energy	See individual event subsections
n_0	$\mathrm{Log_{10}}$ ISM number density	See individual event subsections
p	Electron distribution power-law index	[2, 3]
ξ_N	Fraction of electrons that get accelerated	[0,1]
Γ_0	Initial Lorentz Factor	[100, 2000]

Table C.2: Model parameters, description, and priors used for the `arnett + tophat` model in the `redback` fitting.

Parameters	Description	Prior Boundaries
z	redshift	Set to values from Table 4.1
$\mathrm{v_{ph}}$	Peak photospheric expansion velocity	Set to values from Table 4.5
f_{Ni}	Nickel fraction	[0.001, 1] (in $\mathrm{Log_{10}}$ space)
$\mathrm{M_{ej}}$	Ejecta mass	[0.0001, 100] $\mathrm{M_\odot}$ (in $\mathrm{Log_{10}}$ space)
A_v	MW extinction	0 mag
κ	Optical opacity	0.07 $\mathrm{cm^2\,g^{-1}}$
κ_γ	Gamma-ray Opacity	[0.0001, 10000] $\mathrm{cm^2\,g^{-1}}$ (in $\mathrm{Log_{10}}$ space)
T_{floor}	Minimum temperature reached in early explosion	[1000, 100000] K (in $\mathrm{Log_{10}}$ space)
t_c	Time where emission has $\tau_{\mathrm{opt}} \sim 1$ at ν_c	[0, 1000] days
ν_c	Characteristic frequency to scale t_c	[10^7, 10^9] Hz (in $\mathrm{Log_{10}}$ space)
m	Power law index of emitting region expansion (R^m)	[$\frac{2}{3}$, 1]
γ	electron spectral index	[1, 4]
k	Flux-scaling Factor	[0.0001, 100] (in $\mathrm{Log_{10}}$ space)
β	Spectral power-law index	[0.5, 2]
β_{time}	Temporal power-law index	[0.5, 3]

Table C.3: Model parameters, description, and priors used for the Radio SSA model (Chevalier, 1998) in the `redback` fitting.

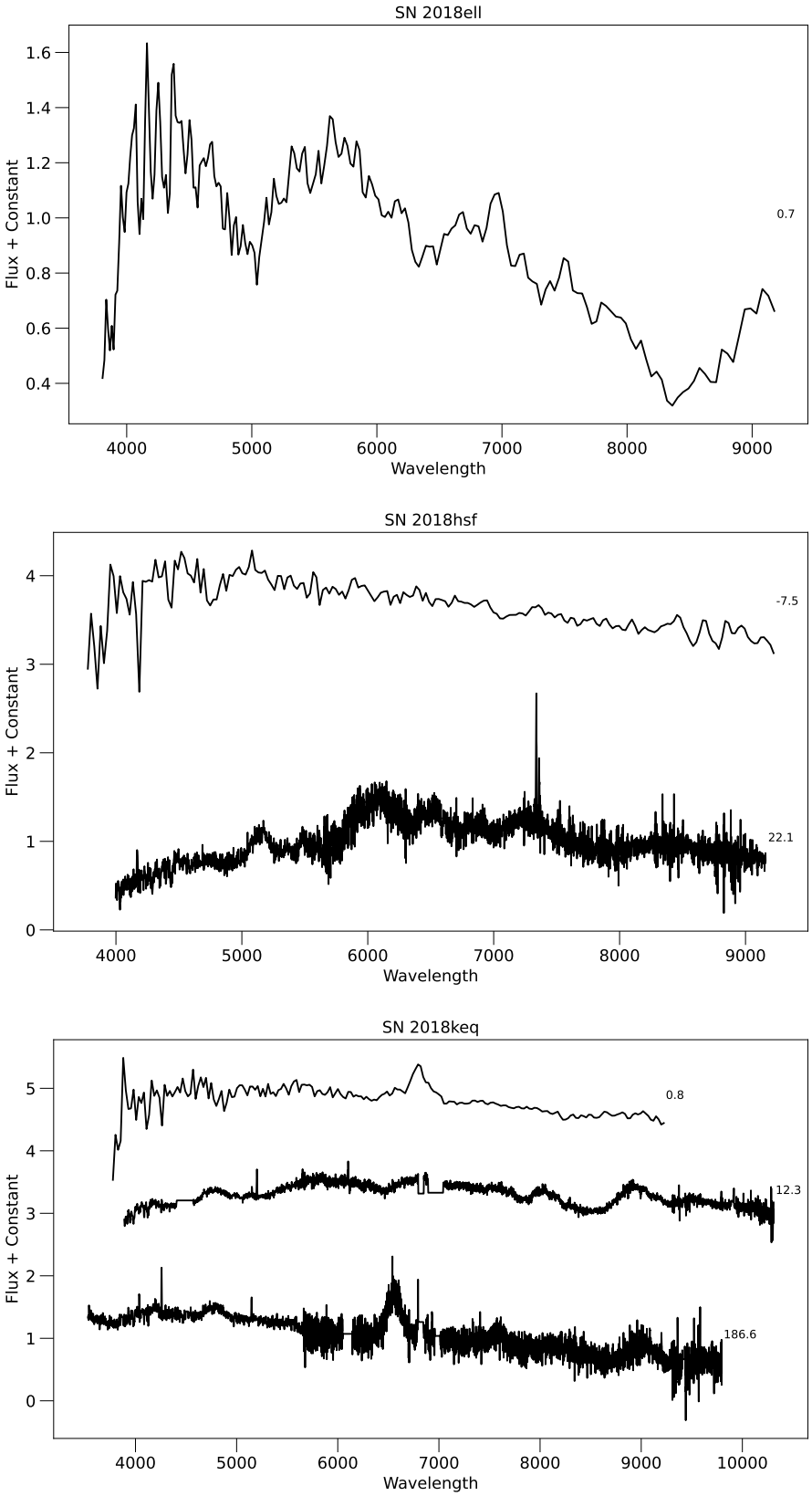

Figure C.1: Spectral sequences of SN 2018ell, SN 2018hsf, and SN 2018keq. The phases next to each spectrum are the rest-frame days since the maximum r-band flux from the GP processing. The spectra for the rest of the events except for those presented in single-object works (SN 2018bvw, SN 2018gep, and SN 2020bvc) are presented in a similar format below.

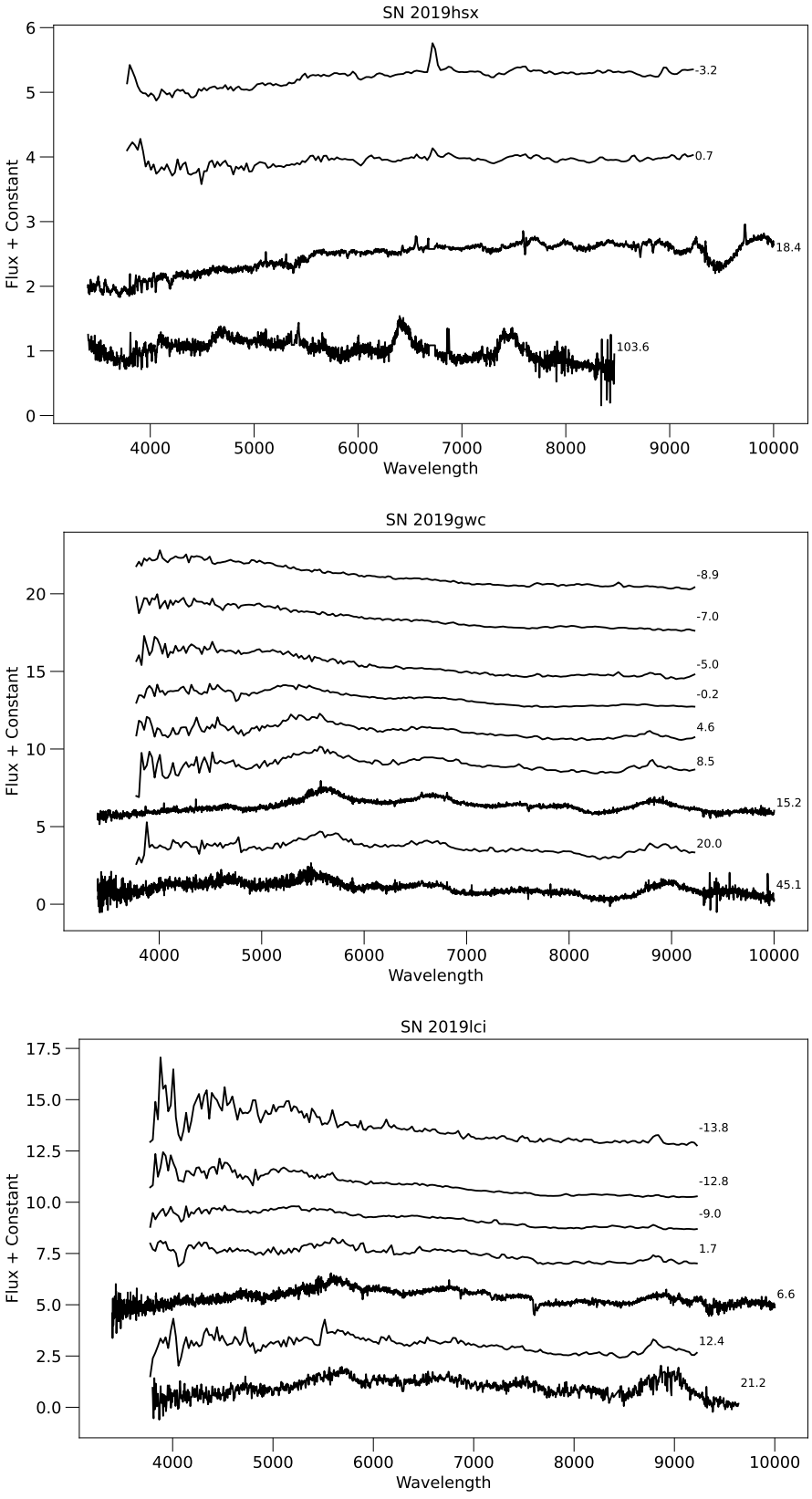

Figure C.2: Spectral sequences of SN 2019hsx, SN 2019gwc, SN 2019lci.

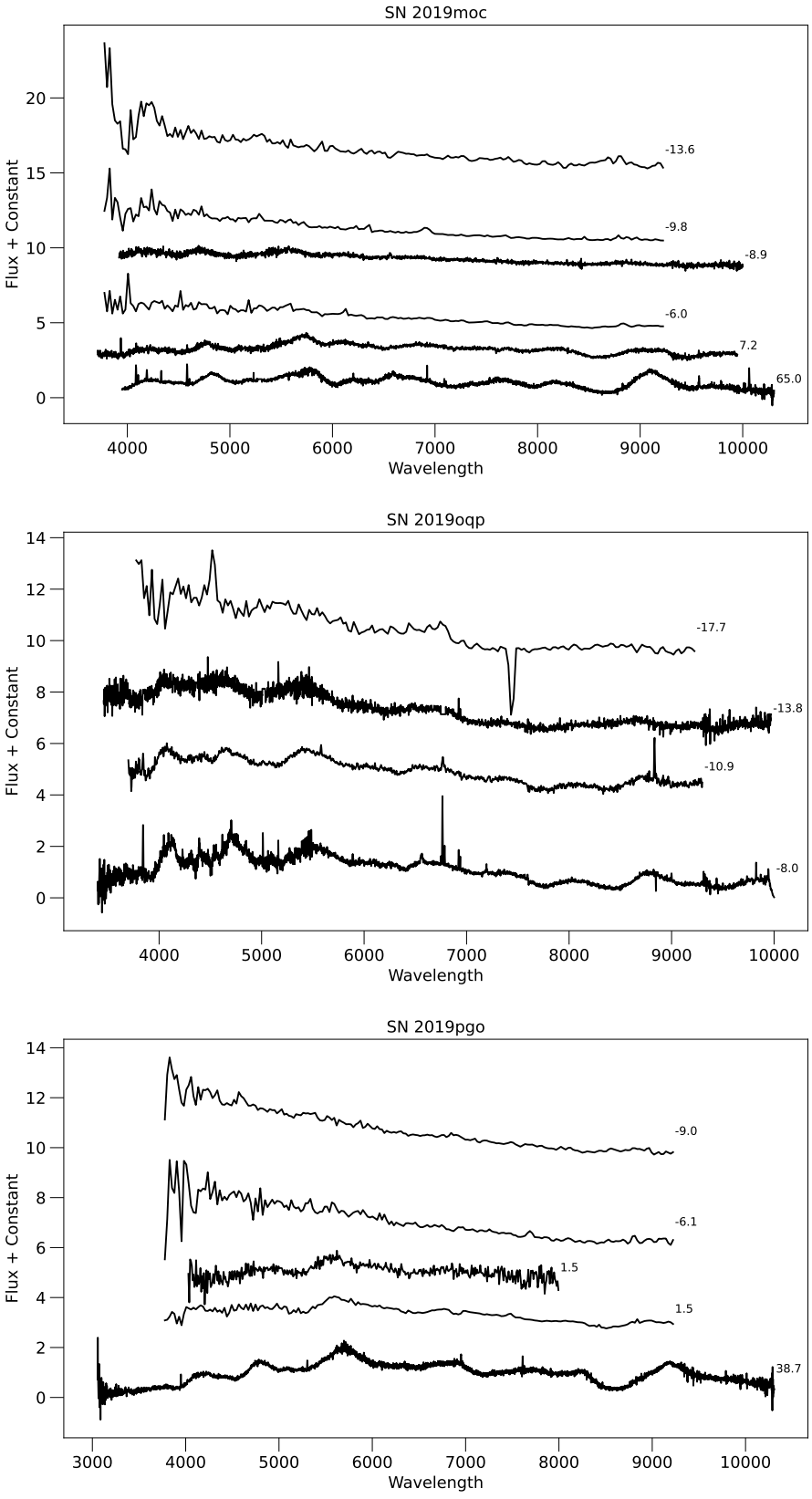

Figure C.3: Spectral sequences of SN 2019moc, SN 2019oqp, SN 2019pgo.

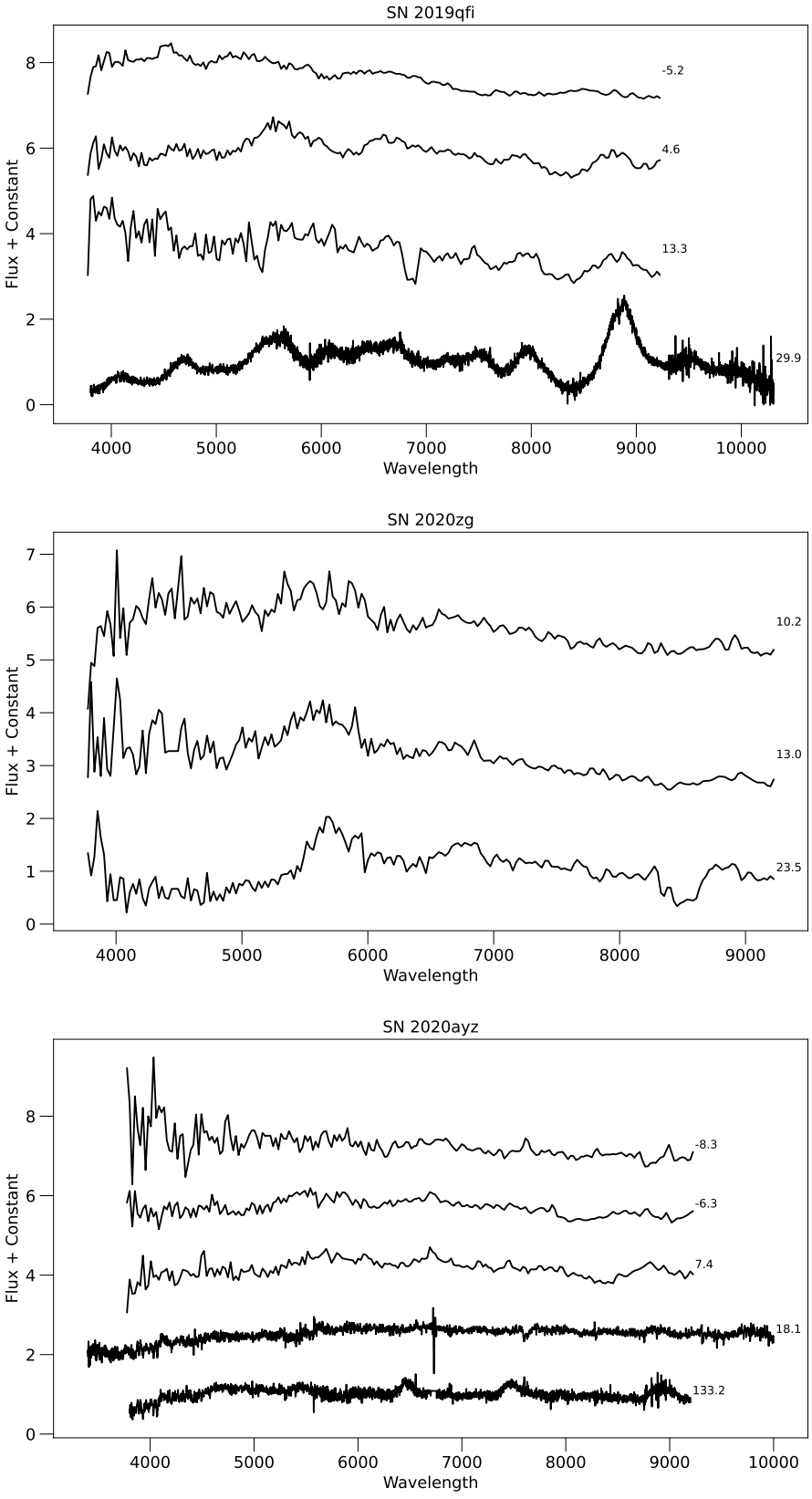

Figure C.4: Spectral sequences of SN 2019qfi, SN 2020zg, SN 2020ayz.

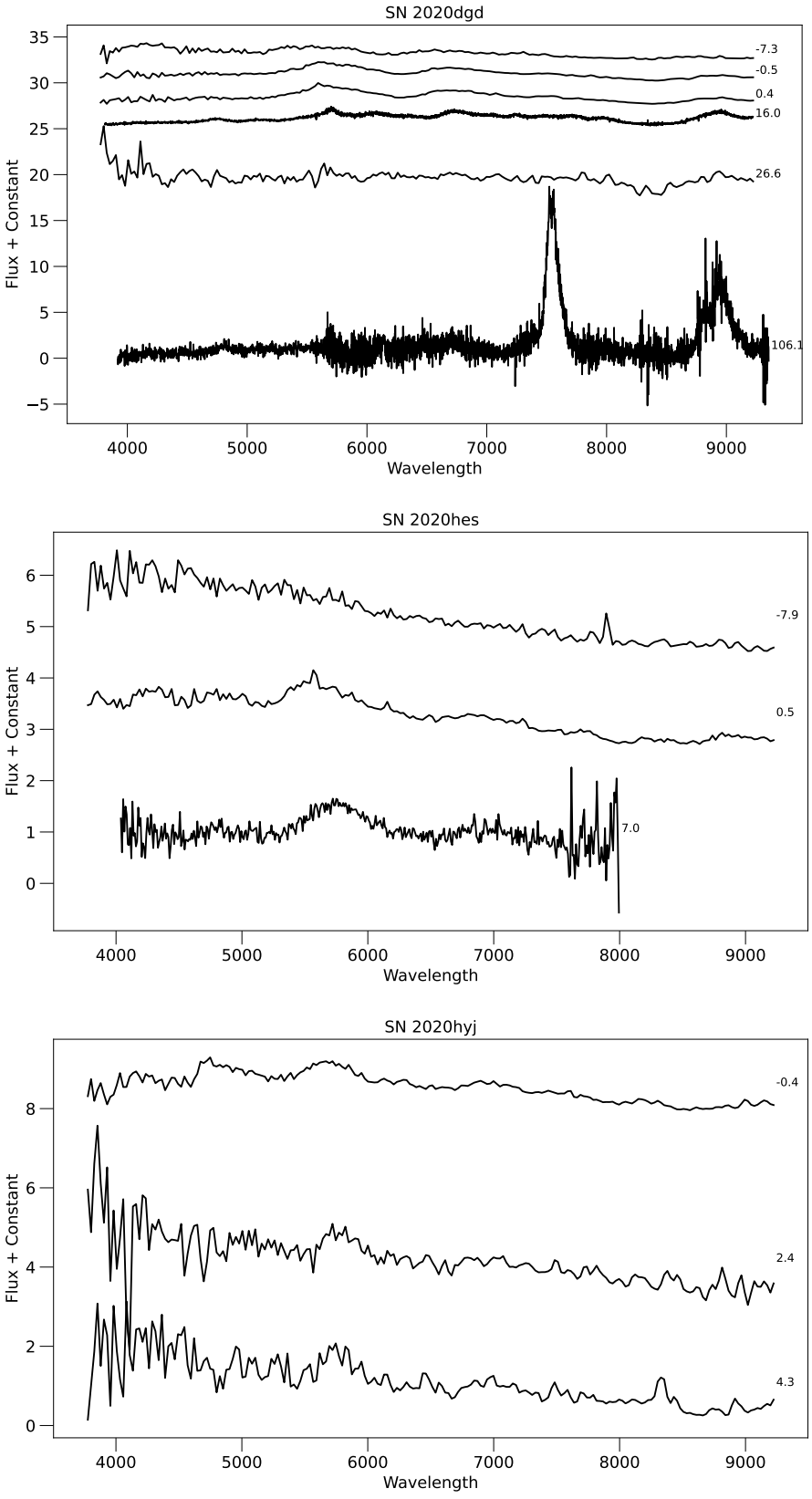

Figure C.5: Spectral sequences of SN 2020dgd, SN 2020hes, SN 2020hyj.

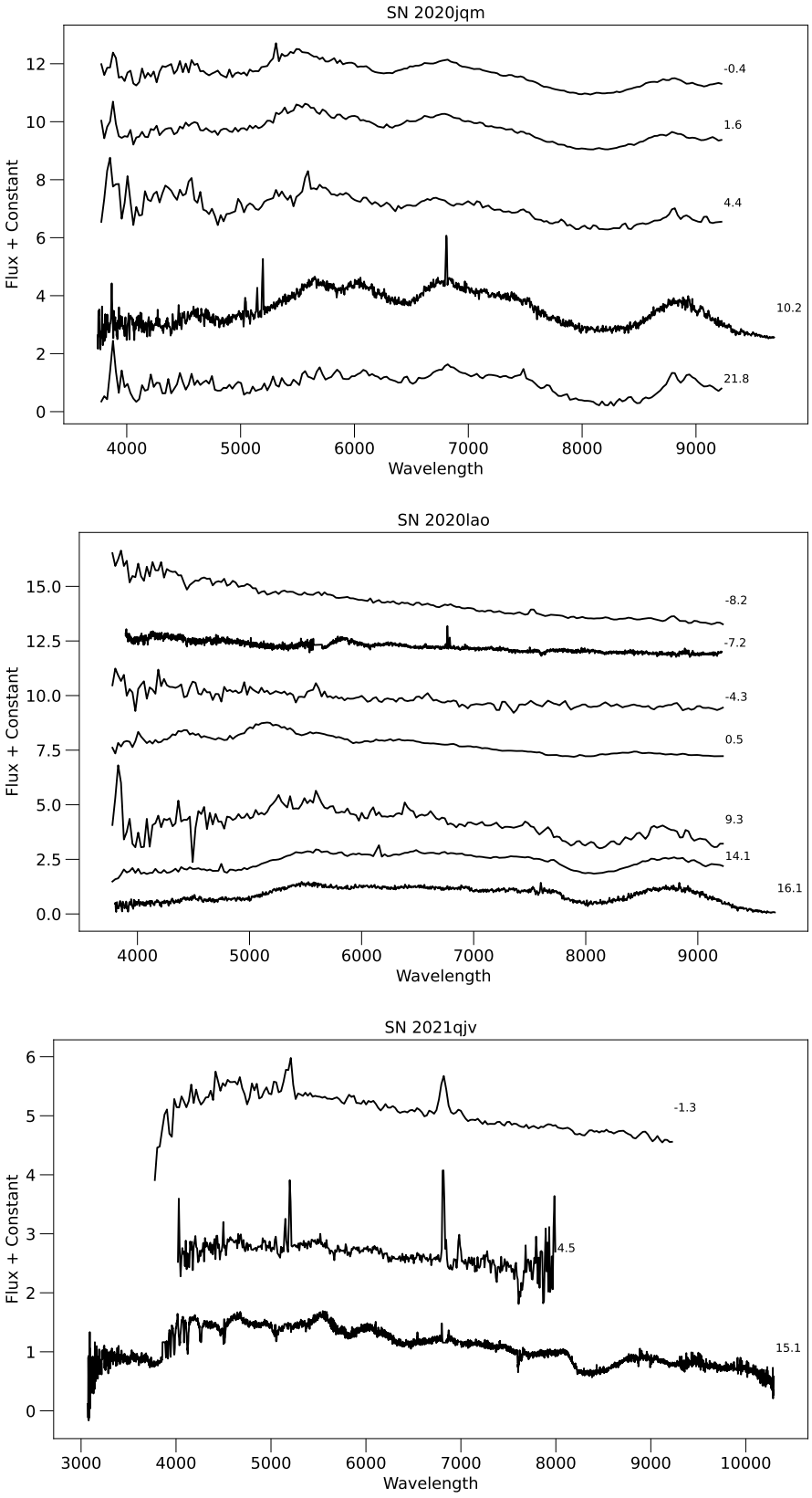

Figure C.6: Spectral sequences of SN 2020jqm, SN 2020lao, SN 2021qjv.

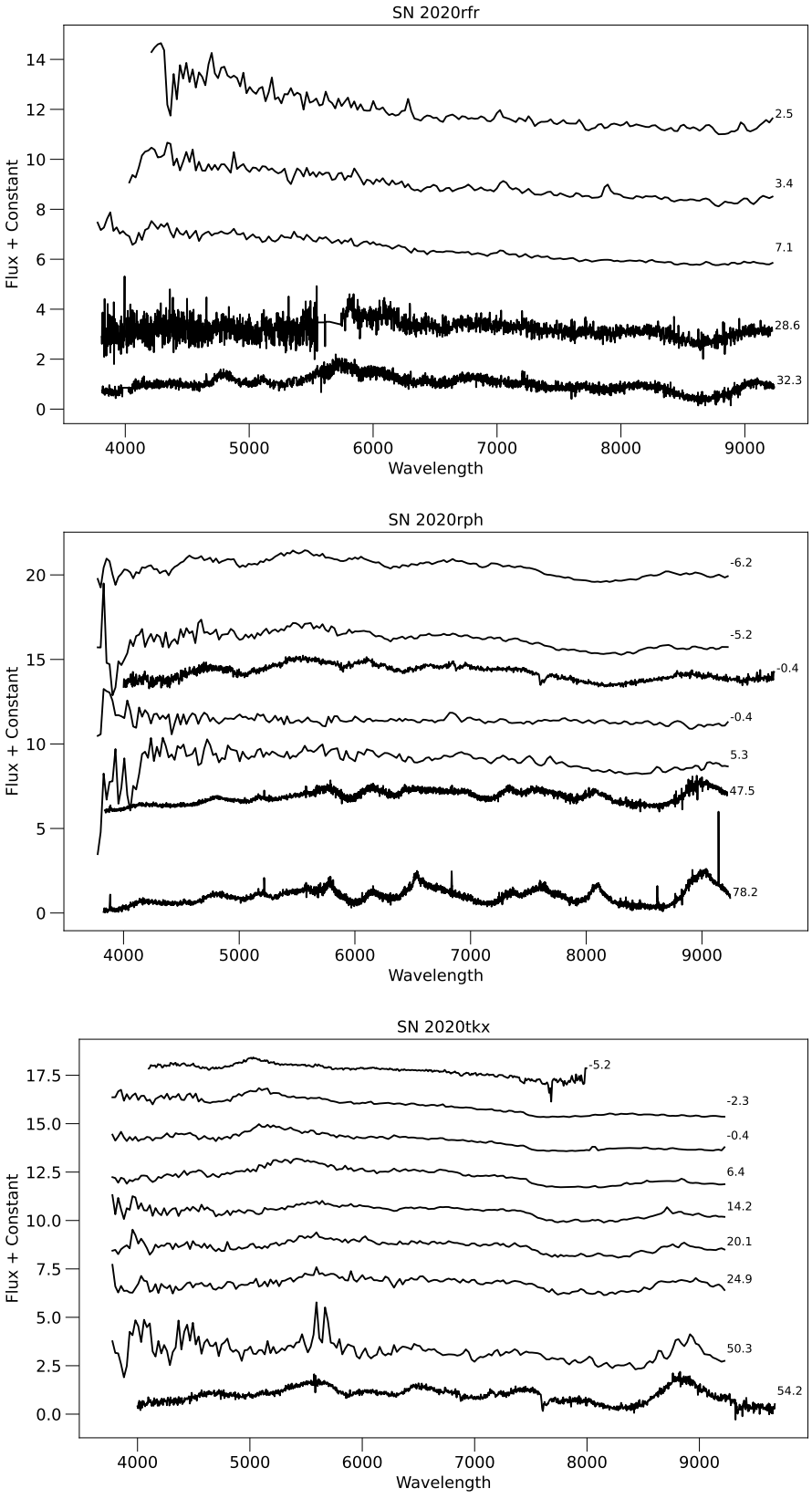

Figure C.7: Spectral sequences of SN 2020rfr, SN 2020rph, SN 2020tkx.

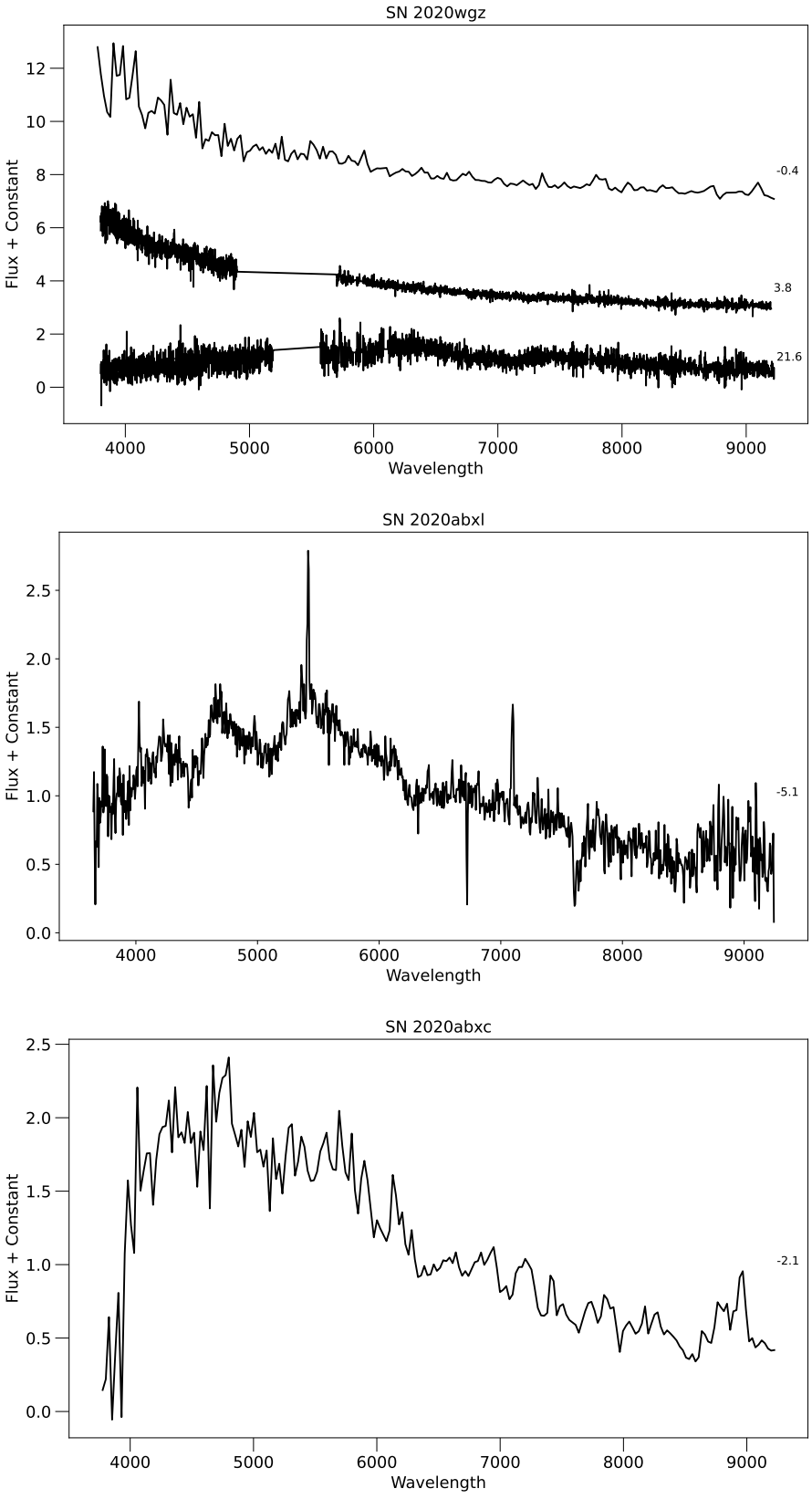

Figure C.8: Spectral sequences of SN 2020wgz, SN 2020abxl, SN 2020abxc.

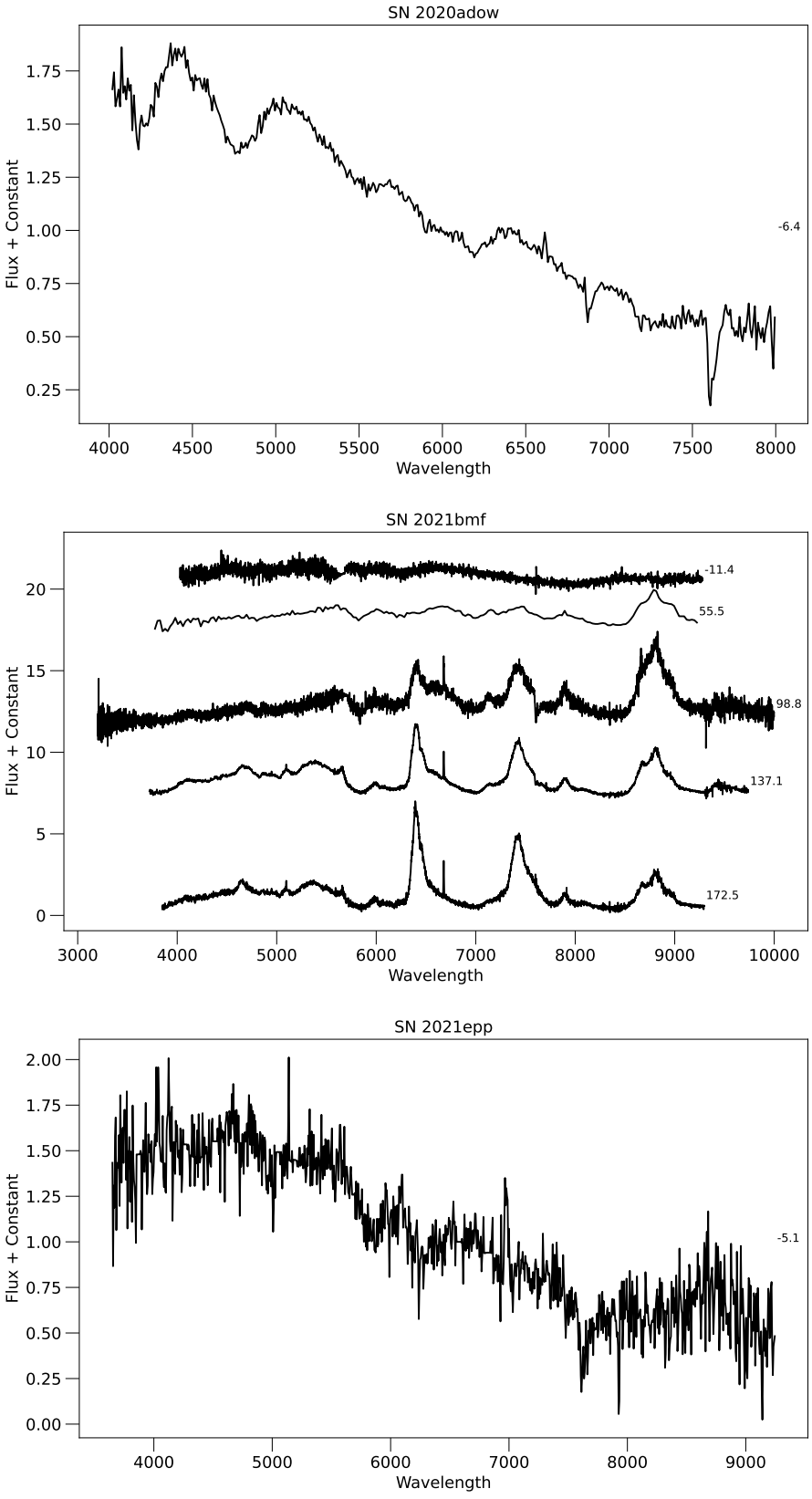

Figure C.9: Spectral sequences of SN 2020adow, SN 2021bmf, SN 2021epp.

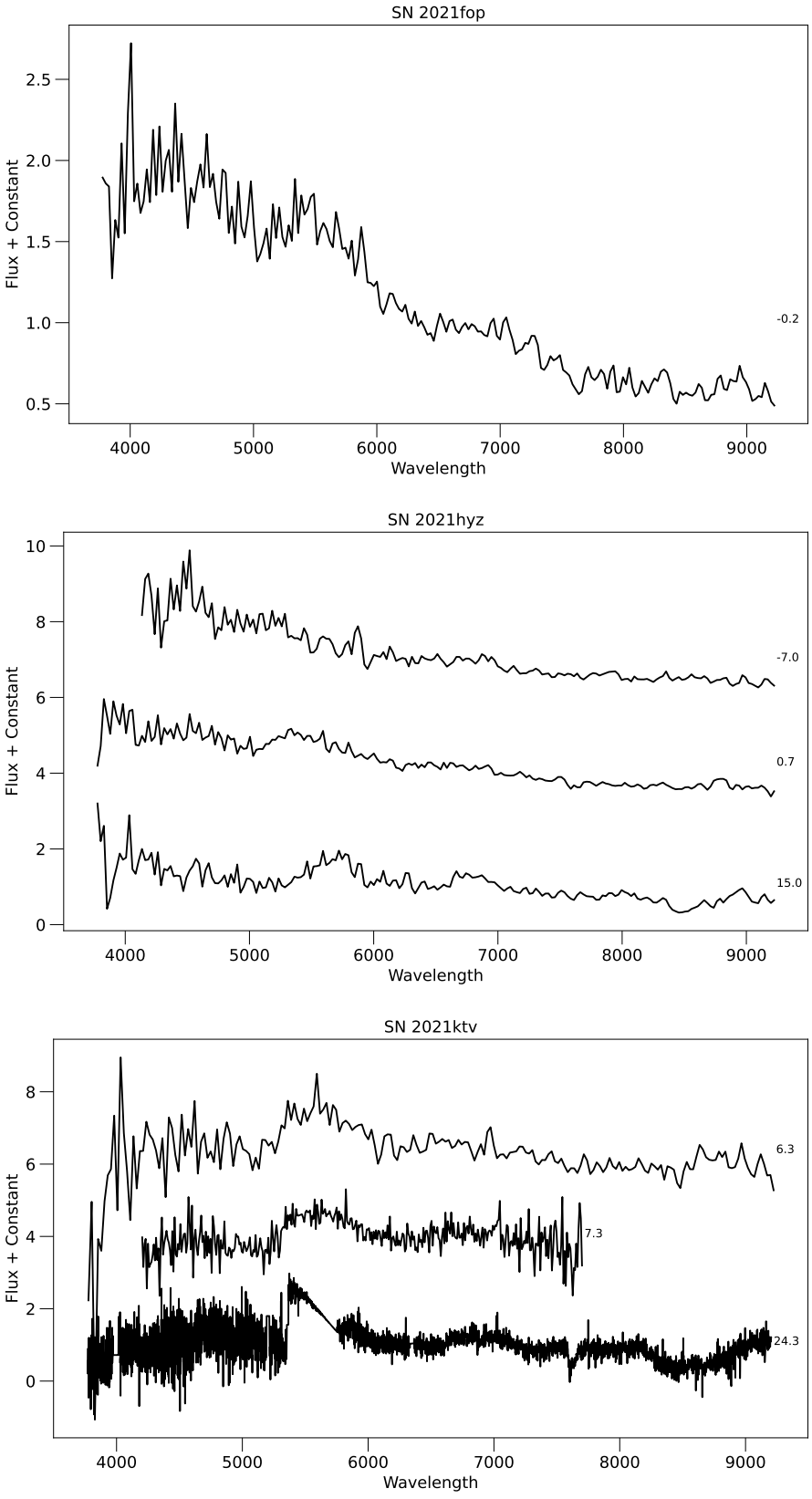

Figure C.10: Spectral sequences of SN 2021fop, SN 2021hyz, SN2021ktv.

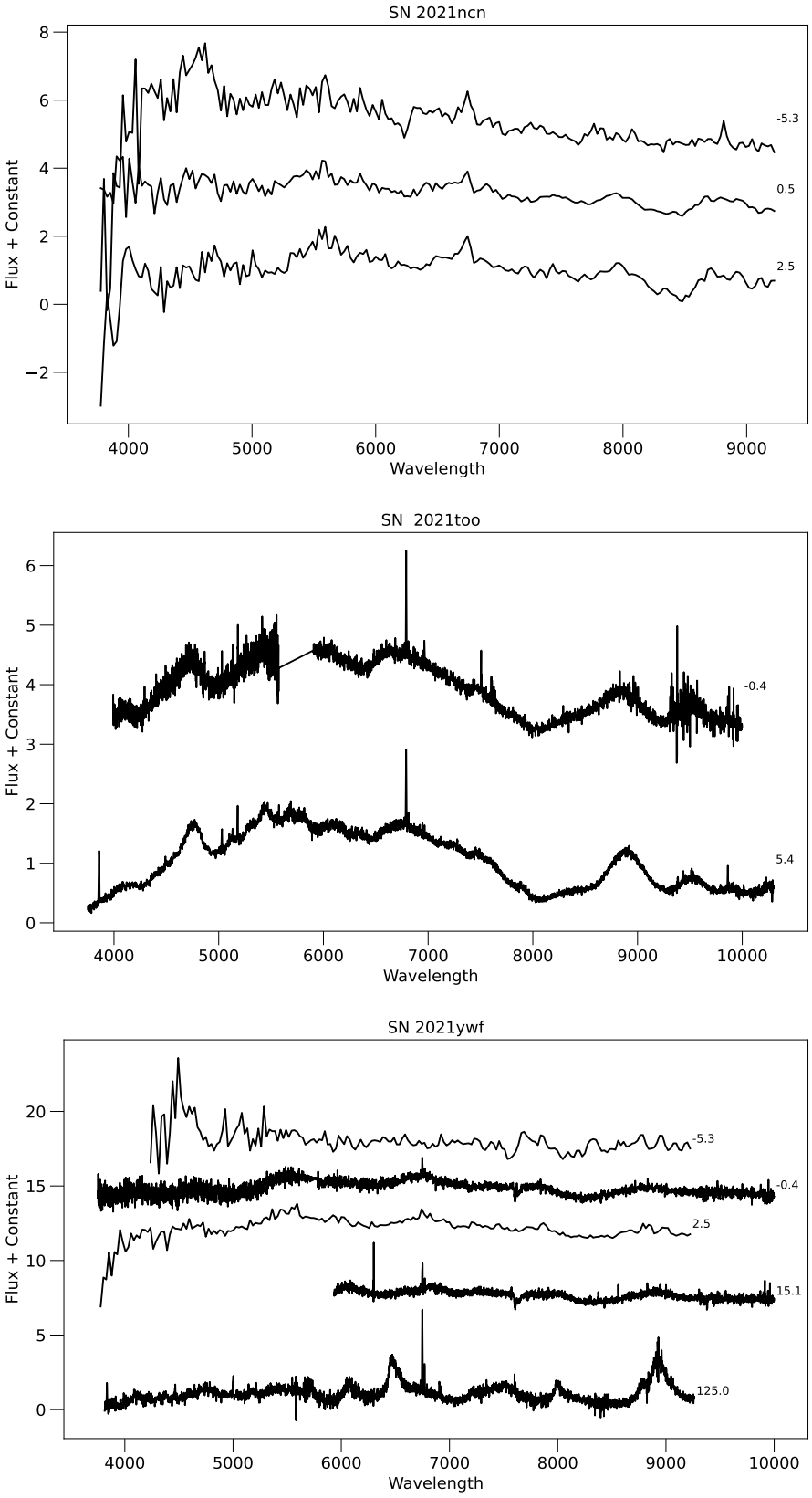

Figure C.11: Spectral sequences of SN 2021ncn, SN 2021too, SN 2021ywf.

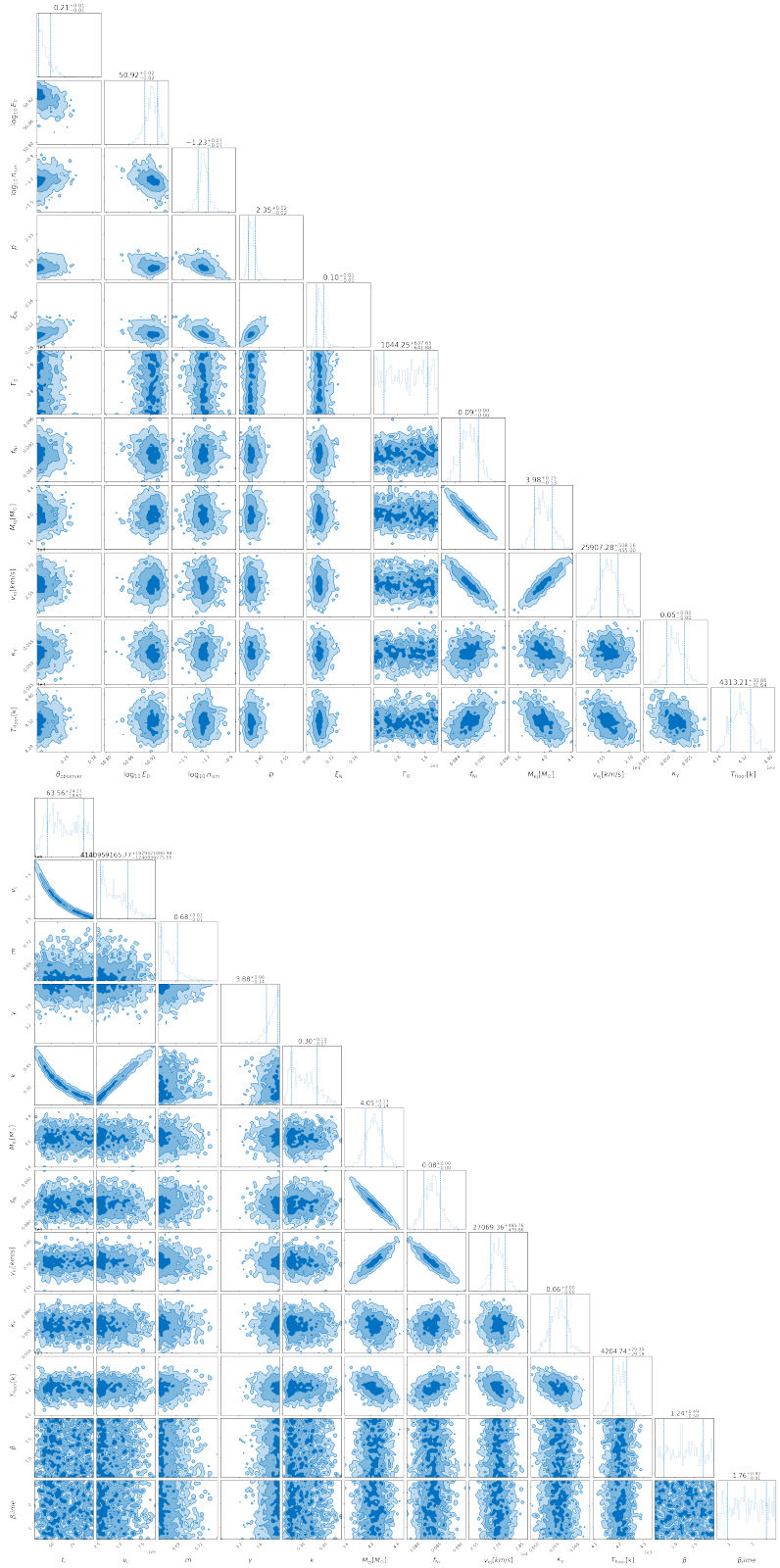

Figure C.12: `Redback` modeling results for SN 2020tkx, with the `arnett + tophat` model above and the Radio SSA model below.

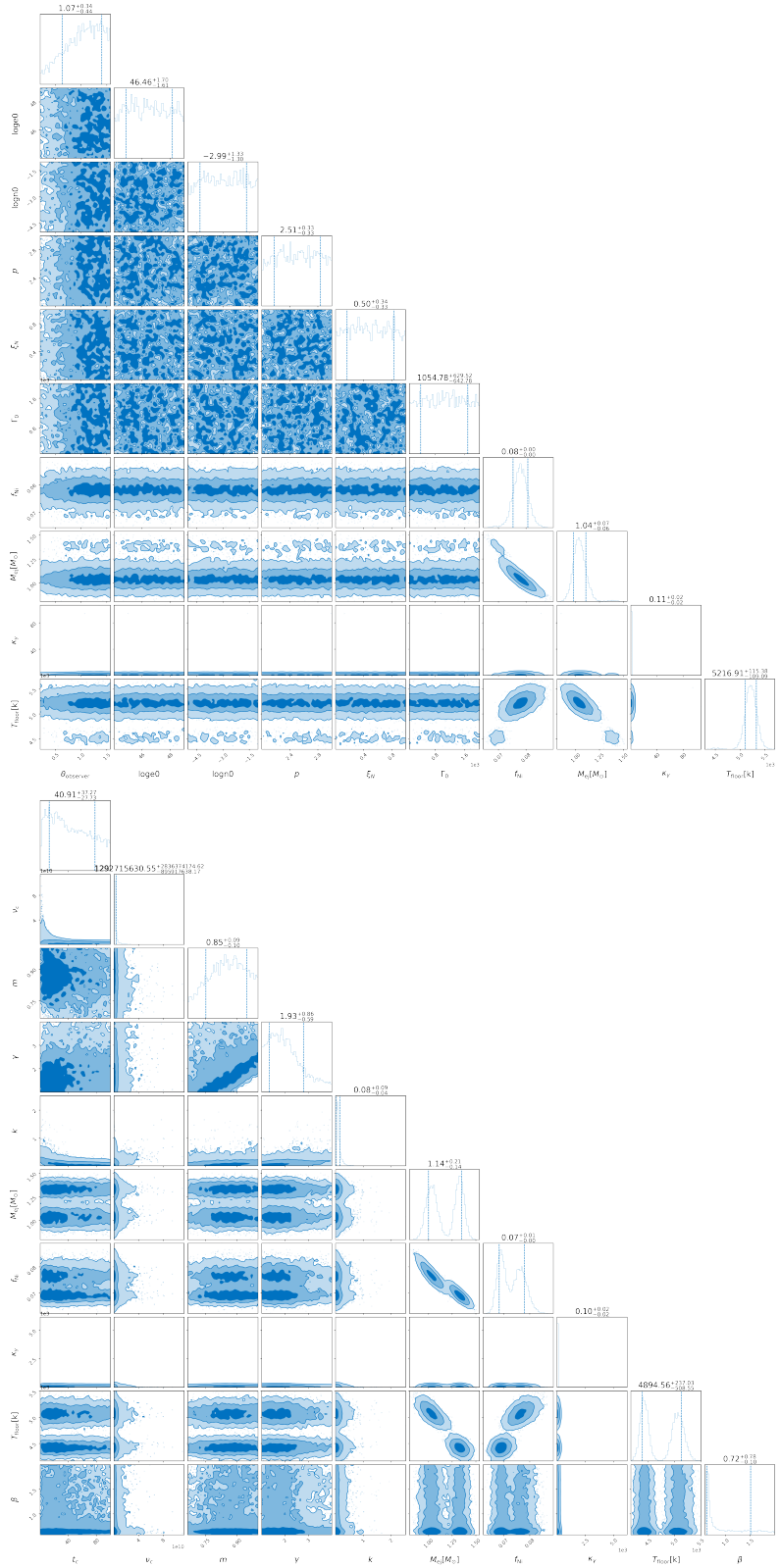

Figure C.13: `Redback` modeling results for SN 2021ywf, with the `arnett + tophat` model above and the Radio SSA model below.

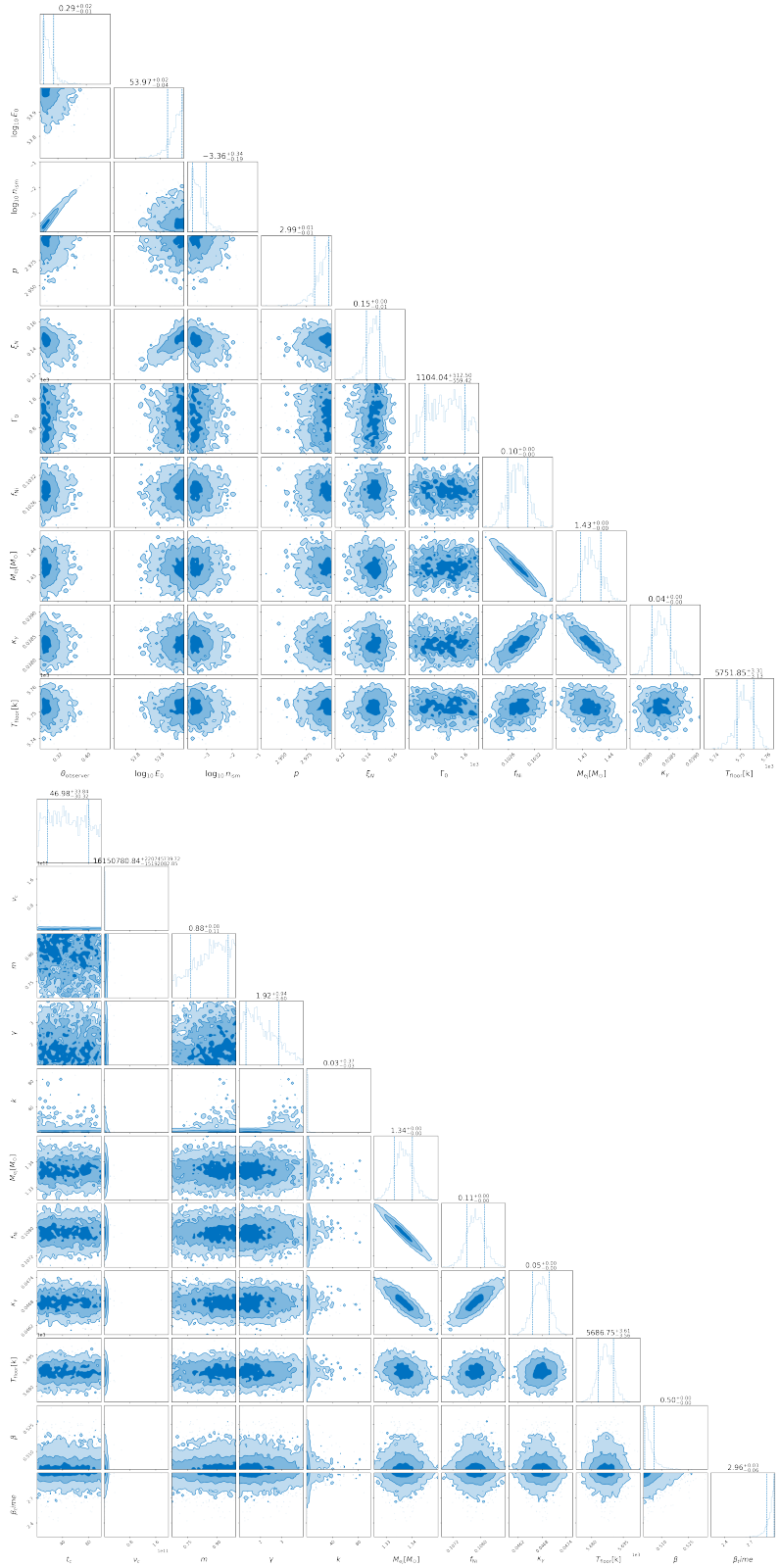

Figure C.14: `Redback` modeling results for SN 2020adow, with the `arnett + tophat` model above and the Radio SSA model below.

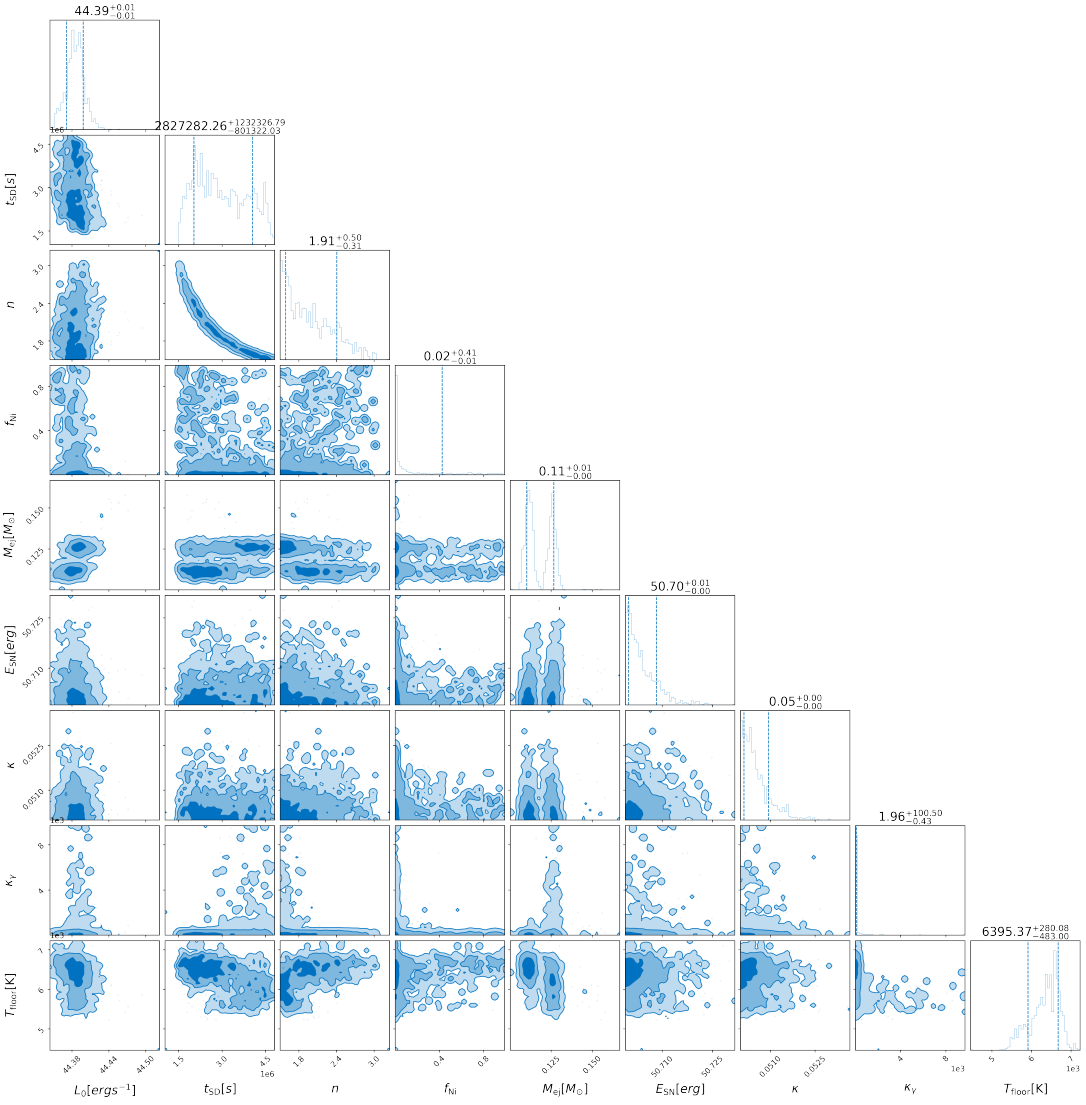

Figure C.15: `Redback` modeling results for SN 2020wgz, for the magnetar and nickel powered model.

Appendix D: Supplementary Materials for Chapter 5

D.1 Photometry and Radio observations of AT 2023sva

Here we present the photometric and radio observations of AT 2023sva in Tables D.1, D.2, and D.3.

ν (GHz)	F_ν (μJy)	σ (μJy)
Epoch 1 (MJD 60276.35)		
4.53	25.2	14
5.49	49.3	13
6.43	95.6	12
7.51	108.3	11
8.49	147	14
9.51	134	13
10.48	146	14
11.49	109	18
12.5	63	20
13.5	79	14
14.5	92	14

15.6	85	15
16.6	67	16
17.6	115	18
Epoch 2 (MJD 60282.00)		
8.5	139	11
9.5	112	11
10.5	100	12
11.5	66	15
12.5	99	14
13.5	72	11
14.5	84	11
15.5	72	12
16.5	86	11
17.5	82	17
31	63.8	13.9
35	51.7	16
Epoch 3 (MJD 60287.06)		
4.5	157	13
5.5	229	12
6.5	216	11
7.5	153	10
8.5	132	12

9.5	143	12
10.5	119	13
11.5	90	16
Epoch 4 (MJD 60335.10)		
2.25	127	45
2.75	145	20
3.25	210	15
3.75	141	15
4.5	119	11
5.5	110	11
6.5	111	10
7.5	68	9
8.5	100	13
9.5	50	11
10.5	67	12
11.5	41	13
13	36	13
15	24	8
Epoch 5 (MJD 60437.90)		
2.7	40	18
3.24	110	15
3.75	136	15

4.5	64.2	9.6
5.5	39	9.4
7	21.4	6.2
9	18.4	5.1
11	17	5.5
Epoch 6 (MJD 60537.30)		
3.5	47.5	6.6
5	35.7	6.2
7	21	5.1
9	17.3	4

MJD	Filter	AB mag	Uncertainty	Facility
60204.40175	*r*	17.71	0.05	ZTF
60204.40175	*r*	17.71	0.05	ZTF
60204.40175	*r*	17.68	0.02	ZTF
60204.42189	*r*	17.71	0.05	ZTF
60204.42189	*r*	17.71	0.05	ZTF
60204.42189	*r*	17.70	0.01	ZTF
60204.44532	*g*	18.45	0.06	ZTF
60204.44532	*g*	18.39	0.02	ZTF
60204.4458	*g*	18.52	0.02	ZTF
60204.4458	*g*	18.49	0.06	ZTF
60205.16078	*g*	20.33	0.07	SEDM
60205.16243	*r*	19.89	0.07	SEDM
60205.16408	*i*	19.38	0.05	SEDM
60205.30556	*g*	20.41	0.08	SEDM
60205.30721	*r*	19.79	0.06	SEDM
60205.30887	*i*	19.59	0.09	SEDM
60205.48597	*g*	20.73	0.10	SEDM
60205.48761	*r*	20.22	0.07	SEDM
60205.48925	*i*	19.72	0.07	SEDM
60205.8439	*r*	20.61	0.07	NOT
60205.8477	*g*	21.18	0.09	NOT
60206.16083	*g*	21.20	0.12	SEDM
60206.1649	*r*	21.10	0.15	SEDM
60206.7128	*r*	21.89	0.07	GIT
60206.8192	*g*	22.68	0.11	GIT
60208.3729	*r*	> 22.12	–	SEDM
60208.3666	*g*	> 22.13	–	SEDM

Table D.1: Optical photometry of AT 2023sva. The photometry in this table is not corrected for MW or host-galaxy extinction.

Table D.3: AMI radio observations of AT 2023sva, obtained at 15.5 GHz.

MJD	F_ν (μJy)	σ (μJy)
60206.11	220	41
60210.11	350	37
60216.01	522	106
60218.01	423	55
60221.01	455	52
60224.01	432	80
60232.91	348	33
60238.91	301	47
60240.61	392	90

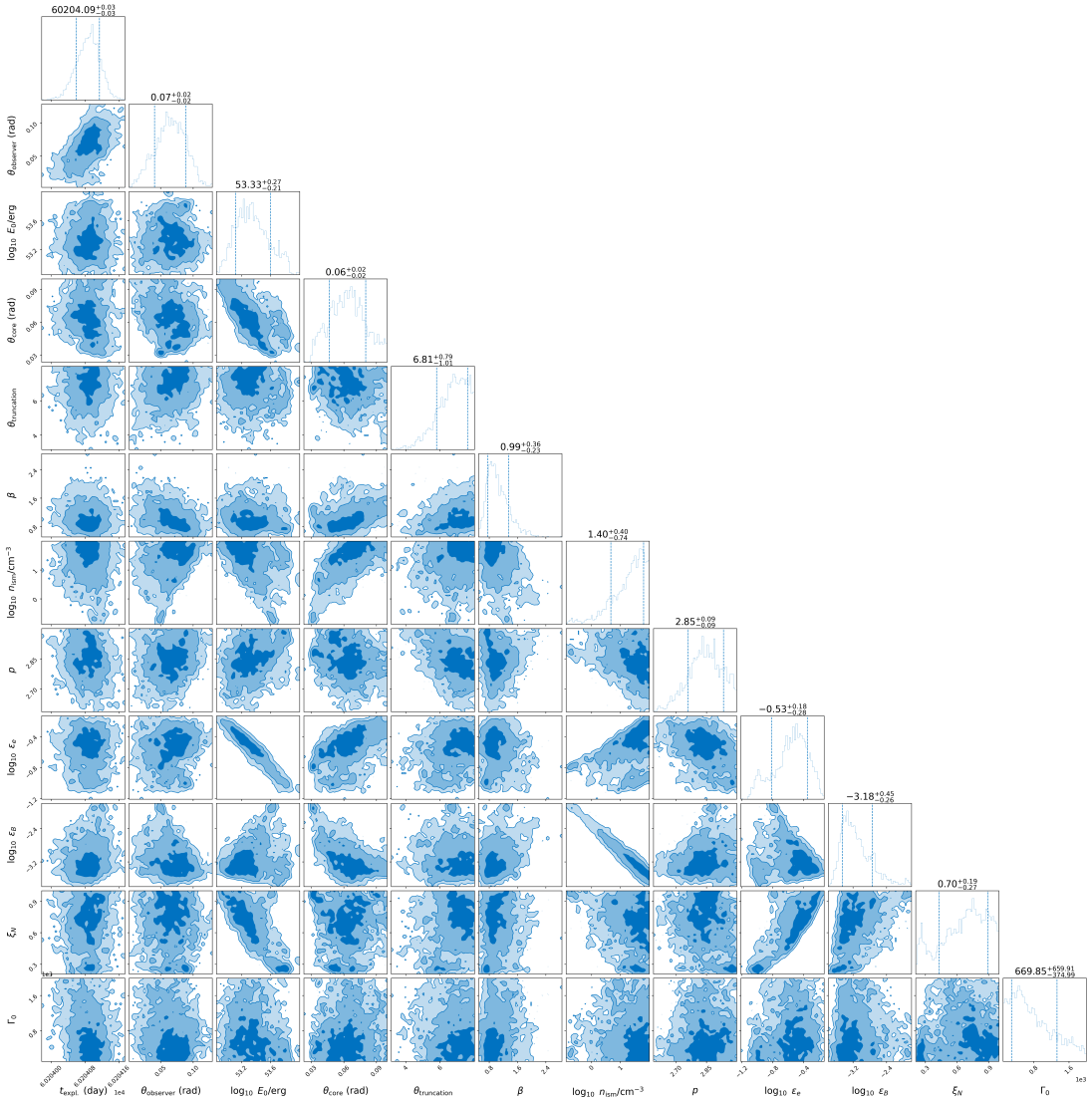

Figure D.1: Corner plot for the power-law structured jet model, generated through `redback`.

D.2 Corner Plots

Here we show the corner plots for the modeling described in §5.9, in Figures D.1, D.2, and D.3.

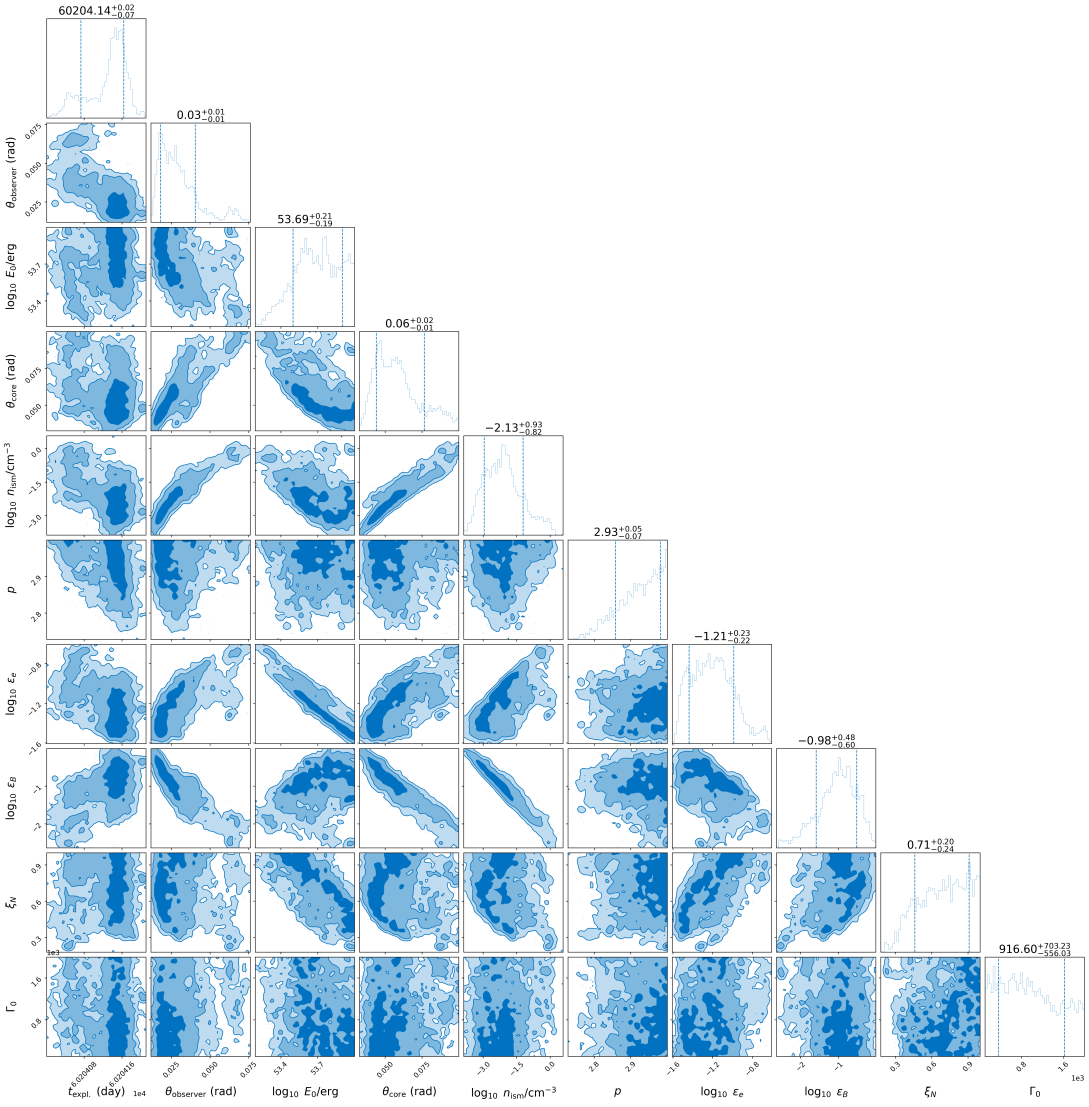

Figure D.2: Corner plot for the tophat model, generated through `redback`.

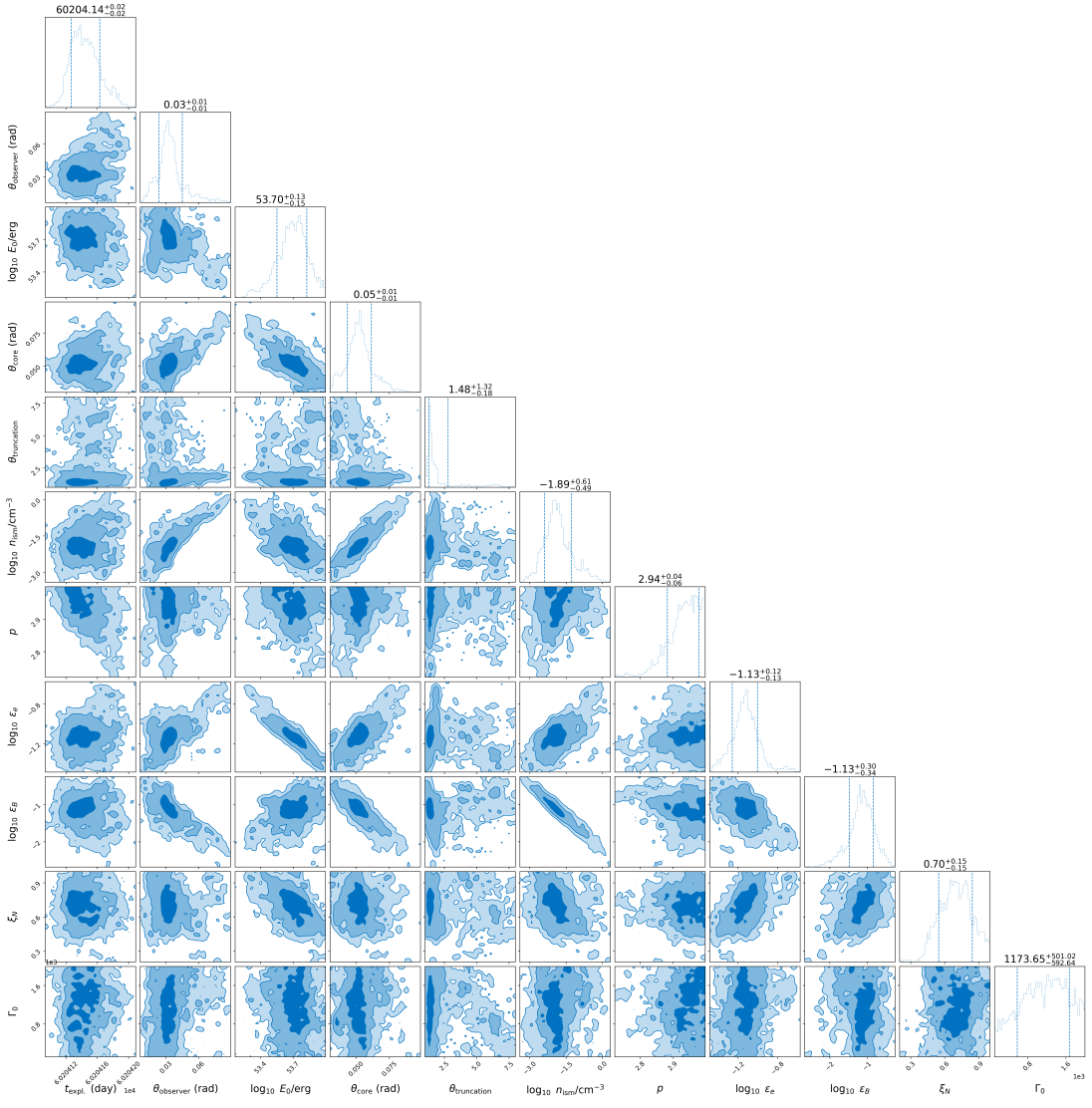

Figure D.3: Corner plot for the gaussian structured jet model, generated through `redback`.

Appendix E: Supplementary Materials for Chapter 6

E.1 Photometric, Spectroscopic, and Radio Observations

Here we provide a log of the photometric, spectroscopic, and radio observations of EP250108a/SN 2025kg in Tables E.2 and E.1, along with the corner plots associated with the LC modeling presented in §6.4 in Figures E.1, E.2, E.3, and E.4.

$t - T_0$	Telescope	Filter	AB Mag	Uncertainty
0.97	Memphisto (Zou et al., 2025)	g	20.05	0.14
0.97	Memphisto (Zou et al., 2025)	r	20.45	0.17
1.31	LT (Eyles-Ferris, 2025b)	g	20.10	0.06
1.40	LT (Kumar et al., 2025)	g	20.20	0.10
1.40	NOT (Zhu et al., 2025b)	r	20.05	0.03
3.21	SAO (Moskvitin et al., 2025)	r	20.56	0.27
3.35	LT	g	20.53	0.16
3.35	LCO (Izzo, 2025)	g	20.48	0.10
3.35	LCO (Izzo, 2025)	r	20.61	0.11
3.36	LT	r	20.64	0.22
3.37	LT	i	20.81	0.25
5.41	LT	g	20.55	0.23
5.42	LT	r	20.64	0.19
5.43	LT	i	20.9	0.17
6.32	LT	g	20.85	0.13
6.34	LT	r	20.65	0.1
6.35	LT	i	20.84	0.11
7.33	LT	g	20.99	0.07
7.34	LT	r	20.6	0.06
7.36	LT	i	20.76	0.08
9.32	LT	g	20.91	0.06
9.33	LT	r	20.33	0.07
14.63	SOAR	g	20.65	0.05
14.63	SOAR	r	20.15	0.02
18.35	LT	g	20.59	0.06
18.35	LT	r	20.21	0.06
18.36	LT	i	20.28	0.07
20.35	LT	g	20.82	0.06
20.35	LT	r	20.23	0.05
20.36	LT	i	20.24	0.07
22.54	SOAR	g	20.96	0.01
22.55	SOAR	r	20.34	0.02
27.51	IMACS	g	21.531	0.06
27.51	IMACS	r	20.541	0.06
27.51	IMACS	i	20.507	0.07
41.37	NOT	r	21.644	0.05

Table E.1: Optical photometry and 1σ errors of EP250108a/SN 2025kg. All times are in the observer frame, and the magnitudes are not corrected for Galactic extinction. Photometry obtained by GCNs is indicated with citations.

$t - T_0$	Tel.+Instr.	Exp. Time (s)	Wavelength Range ($\AA$)
4.6	Gemini+GMOS-South	4×600	3800 – 7500
9.6	SOAR+GHTS	6×600	3800 – 7040
14.6	SOAR+GHTS	6×600	3800 – 7040
14.6	Gemini+GMOS-South	4×600	3800 – 7500
17.7	Keck+LRIS	3×900	3000 – 9300
20.6	Gemini+GMOS-South	4×420	3800 – 7500
25.6	MMT+Binospec	3×900	3900 – 9240

Table E.2: Spectroscopic observations of EP250108a/SN 2025kg. Epochs are given in observer times since T_0.

$\delta t_{\rm obs}$ (d)	$\nu_{\rm obs}$ (GHz)	Beam Size (arcsec)	Beam Angle (deg)	VLA Configuration	$F_\nu{}^a$ (μJy)	Image RMS height (μJy)
6.5	10.0	0.41×0.17	-30.0	A	≤ 13.5	4.5
25.56	10.0	0.34×0.17	0.7	A	≤ 13.5	4.5
47.53	10.0	15.03×5.65	3.5	A$\rightarrow$D	≤ 19.8	6.6
52.51	10.0	10.75×5.41	8.7	D	≤ 16.5	5.5

Table E.3: Very Large Array observations of EP 250108A. Upper limits correspond to 3σ.

E.2 Corner Plots

Here we present corner plots associated with the modeling of EP250108a/SN 2025kg in Figures E.1, E.2, and E.3.

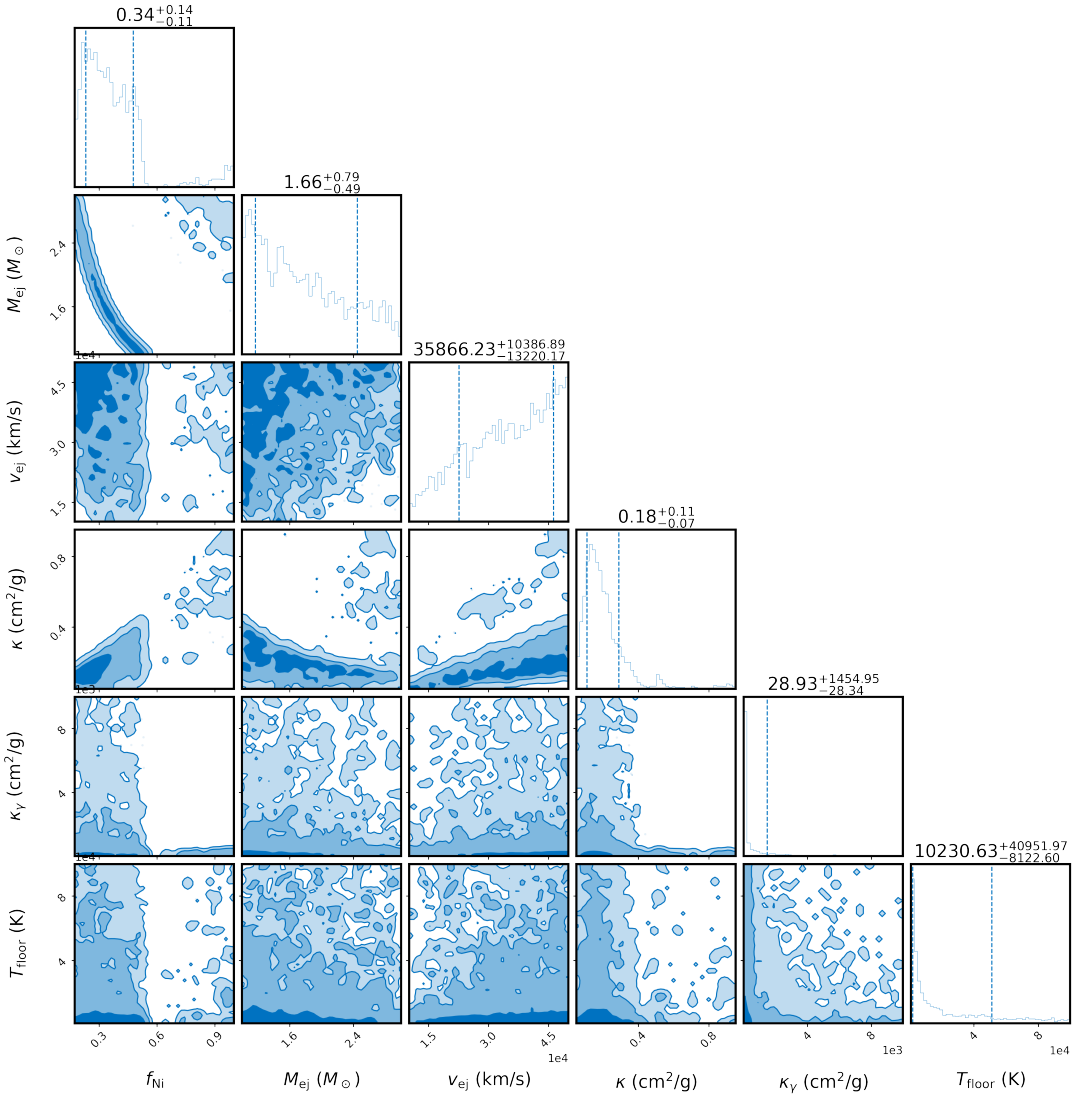

Figure E.1: Corner plots associated with fitting the Arnett (1982) radioactive decay model to the bolometric luminosity LC's second peak.

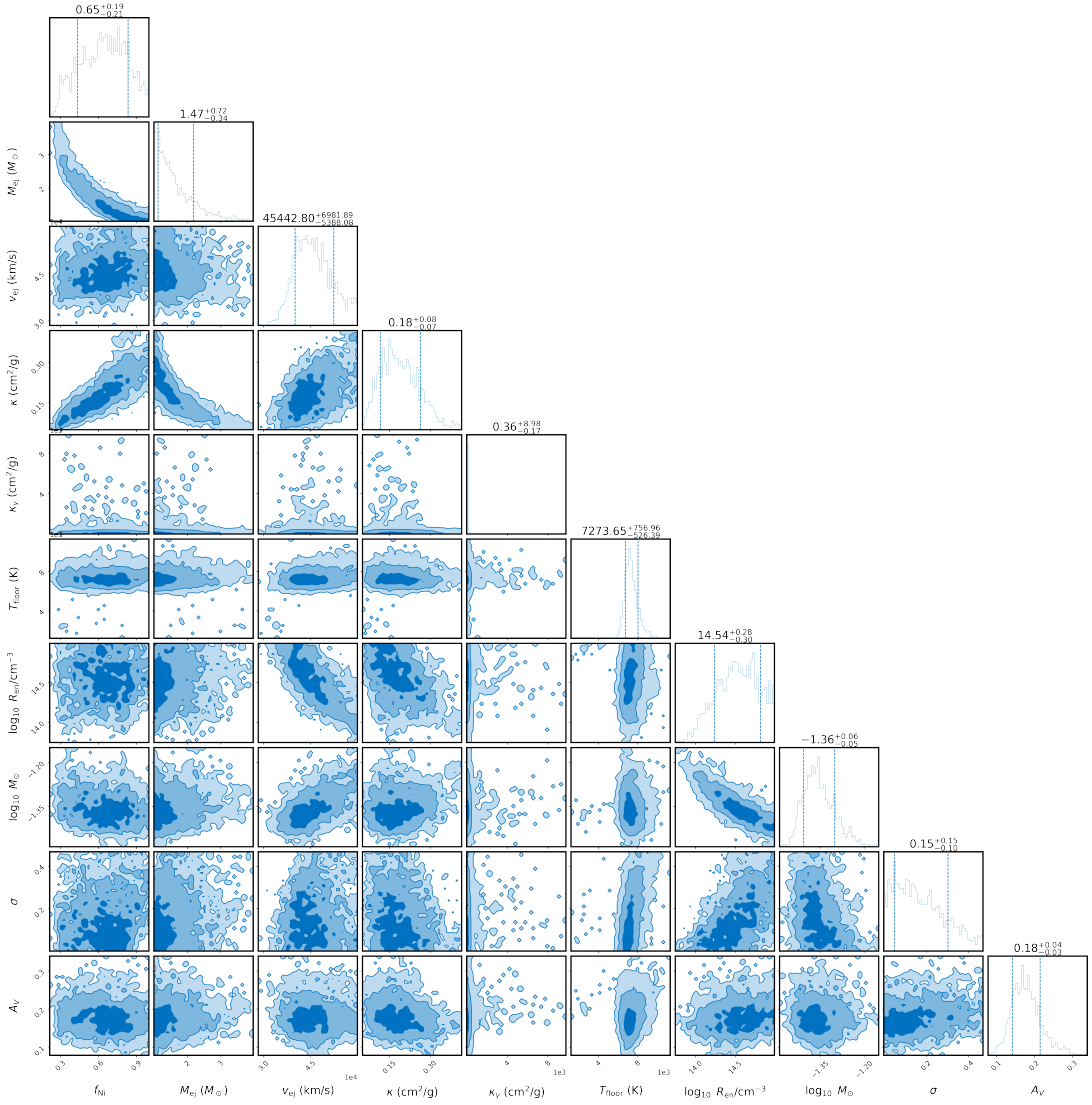

Figure E.2: Corner plots associated with fitting the combined SCE model from Piro et al. (2021) and radioactive decay model from Arnett (1982) to the photometry.

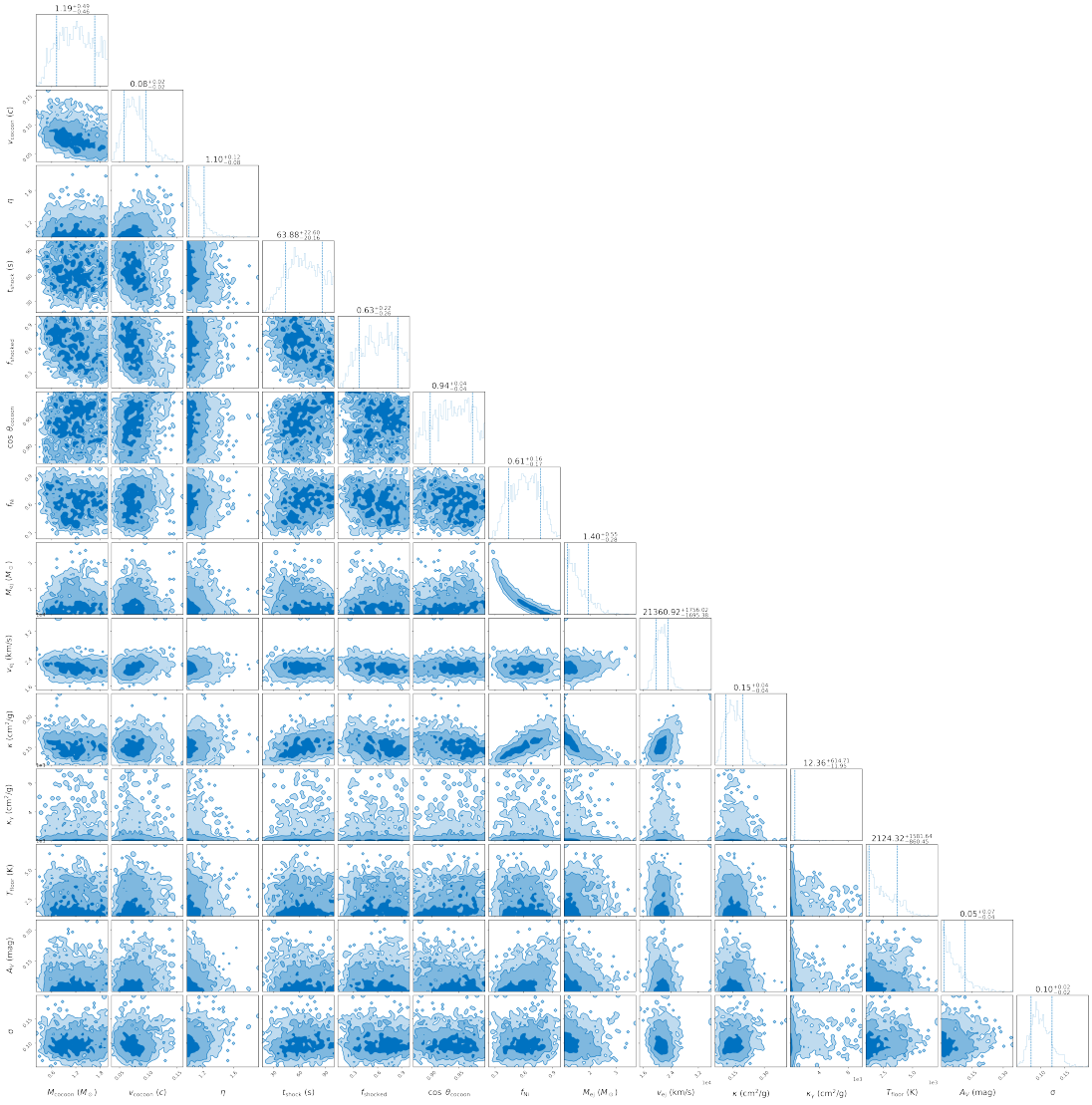

Figure E.3: Corner plots associated with fitting the combined shocked cocoon model from Nakar & Piran (2017) and radioactive decay model from Arnett (1982) to the photometry.

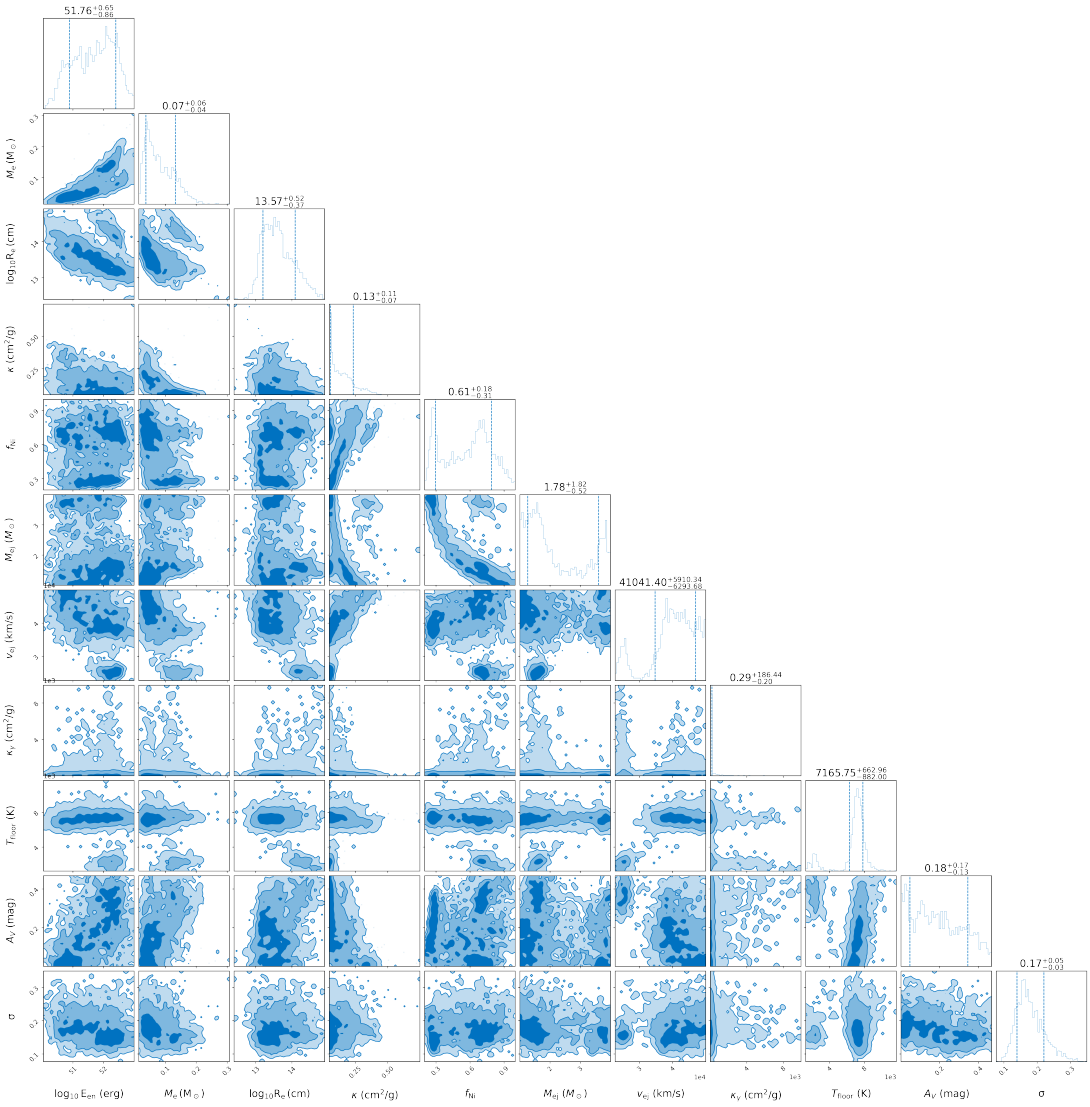

Figure E.4: Corner plots associated with fitting the combined shocked cocoon model in an extended CSM from Nakar (2015) and radioactive decay model from Arnett (1982) to the photometry.

Appendix F: Supplementary Materials for Chapter 7

Here we provide a log of the photometric, spectroscopic, and X-ray observations of EP250827b/SN 2025wkm in Tables F.1, F.2, and F.3.

F.1 Photometric, Spectroscopic and X-ray Observations

Time (days)	AB Magnitude	Error	Filter	Telescope
0.14	20.33	0.11	r	ZTF
0.22	19.95	0.08	g	ZTF
2.03	19.5	0.02	g	SEDM
2.04	19.83	0.03	r	SEDM
2.04	19.89	0.04	i	SEDM
2.2	19.68	0.06	g	ZTF
3.04	19.75	0.03	g	SEDM
3.04	20.14	0.04	r	SEDM
3.05	20.1	0.05	i	SEDM
3.1	20.24	0.11	r	ZTF
3.14	19.86	0.07	g	ZTF

3.82	20.31	0.03	i	Wendelstein 3KK
3.82	20.14	0.02	r	Wendelstein 3KK
3.82	21.04	0.24	J	Wendelstein 3KK
3.82	21.09	0.25	J	Wendelstein 3KK
3.86	20.42	0.08	u	IOO
4.01	19.8	0.03	g	SEDM
4.01	20.15	0.04	r	SEDM
4.01	20.23	0.07	i	SEDM
4.16	19.92	0.07	g	ZTF
4.66	22.25	0.28	uvm2	*Swift*-UVOT
4.71	20.28	0.03	i	Wendelstein 3KK
4.71	19.96	0.02	g	Wendelstein 3KK
4.71	20.97	0.23	J	Wendelstein 3KK
4.71	21.01	0.24	J	Wendelstein 3KK
4.73	20.08	0.02	r	Wendelstein 3KK
4.73	20.27	0.07	z	Wendelstein 3KK
4.76	21.66	0.37	uvw1	*Swift*-UVOT
4.8	19.98	0.1	r	IOO
4.81	20.58	0.07	u	IOO
5.02	19.88	0.07	g	SEDM
5.02	19.97	0.04	r	SEDM
5.03	20.08	0.06	i	SEDM

5.1	20.04	0.09	r	ZTF
5.79	19.97	0.15	z	IOO
5.79	20.55	0.16	u	IOO
6.03	19.84	0.04	g	SEDM
6.03	19.9	0.03	r	SEDM
6.03	20.03	0.05	i	SEDM
6.21	19.94	0.07	g	ZTF
6.73	20.08	0.03	i	Wendelstein 3KK
6.73	20.63	0.17	J	Wendelstein 3KK
6.73	20.65	0.18	J	Wendelstein 3KK
6.73	19.96	0.02	g	Wendelstein 3KK
6.75	19.88	0.02	r	Wendelstein 3KK
6.75	20.1	0.06	z	Wendelstein 3KK
7.01	19.89	0.06	g	SEDM
7.01	19.88	0.06	r	SEDM
7.02	19.95	0.07	i	SEDM
7.47	19.9	0.09	g	ALT
7.49	19.8	0.06	r	ALT
7.84	19.78	0.04	r	NOT
7.85	19.95	0.06	g	NOT
7.85	20.08	0.05	i	NOT
8.01	19.89	0.08	g	SEDM

8.02	19.8	0.05	r	SEDM
8.02	19.91	0.07	i	SEDM
8.04	20.12	0.26	i	ZTF
8.17	19.92	0.07	g	ZTF
8.45	19.92	0.09	g	ALT
8.57	20.33	0.22	z	ALT
9.02	19.89	0.08	g	SEDM
9.03	19.78	0.06	r	SEDM
9.03	19.78	0.06	i	SEDM
9.04	19.81	0.19	i	ZTF
9.2	19.96	0.08	g	ZTF
9.26	19.86	0.11	r	ZTF
9.56	19.88	0.03	g	ALT
9.58	19.95	0.05	i	ALT
9.76	20.01	0.02	g	Wendelstein 3KK
9.76	19.9	0.02	i	Wendelstein 3KK
9.76	20.2	0.11	J	Wendelstein 3KK
9.79	19.74	0.02	r	Wendelstein 3KK
9.79	19.88	0.05	z	Wendelstein 3KK
10.02	19.92	0.08	g	SEDM
10.02	19.73	0.05	r	SEDM
10.07	19.69	0.14	i	ZTF

10.19	19.7	0.11	r	ZTF
10.21	19.92	0.16	g	ZTF
10.5	19.94	0.05	g	ALT
10.54	19.63	0.04	r	ALT
10.75	20.38	0.14	J	Wendelstein 3KK
10.76	19.87	0.03	i	Wendelstein 3KK
10.78	19.82	0.07	z	Wendelstein 3KK
10.78	19.74	0.03	r	Wendelstein 3KK
10.98	20.05	0.14	g	SEDM
10.99	19.64	0.08	r	SEDM
10.99	19.77	0.09	i	SEDM
11.02	19.97	0.26	i	ZTF
11.16	19.61	0.13	r	ZTF
11.2	19.91	0.18	g	ZTF
11.44	19.98	0.05	g	ALT
11.46	19.85	0.04	i	ALT
11.49	19.57	0.03	r	ALT
11.52	20.1	0.1	z	ALT
11.84	20.05	0.03	g	Wendelstein 3KK
11.84	19.85	0.02	i	Wendelstein 3KK
11.84	20.11	0.1	J	Wendelstein 3KK
11.86	19.69	0.02	r	Wendelstein 3KK

11.86	19.87	0.06	z	Wendelstein 3KK
11.98	19.87	0.15	g	SEDM
11.98	19.69	0.07	r	SEDM
11.99	19.89	0.09	i	SEDM
12.21	19.68	0.19	r	ZTF
12.98	20.06	0.19	g	SEDM
12.98	19.75	0.11	r	SEDM
12.98	19.63	0.09	i	SEDM
13.16	19.67	0.11	r	ZTF
13.98	20.11	0.22	g	SEDM
13.98	19.58	0.1	r	SEDM
13.98	19.51	0.1	i	SEDM
14.4	20.29	0.09	g	ALT
14.43	19.7	0.1	i	ALT
14.45	19.6	0.06	r	ALT
15	19.7	0.14	i	SEDM
15.1	19.64	0.16	r	ZTF
16.09	19.64	0.04	r	SEDM
16.09	20.25	0.1	g	SEDM
16.1	19.55	0.04	i	SEDM
16.23	20.37	0.26	g	ZTF
16.71	19.46	0.21	i	IOO

16.72	19.81	0.3	r	IOO
17.18	20.4	0.11	g	SEDM
17.18	19.66	0.05	r	SEDM
17.18	19.64	0.07	i	SEDM
18	20.28	0.05	g	SEDM
18	19.64	0.02	r	SEDM
18	19.56	0.03	i	SEDM
18.12	20.15	0.13	g	ZTF
18.48	19.68	0.02	r	ALT
18.64	19.64	0.06	i	ALT
19	19.5	0.02	i	SEDM
19.02	20.36	0.04	g	SEDM
19.03	19.66	0.03	r	SEDM
19.04	20.5	0.14	g	ZTF
19.13	19.59	0.12	r	ZTF
19.46	19.7	0.03	r	ALT
19.49	20.35	0.04	g	ALT
19.85	20.34	0.16	g	IOO
20.09	19.51	0.03	i	SEDM
20.12	19.67	0.03	r	SEDM
20.14	20.43	0.05	g	SEDM
20.14	20.45	0.22	g	ZTF

20.67	19.72	0.13	i	ALT
20.97	20.55	0.09	g	SEDM
20.97	19.7	0.19	i	SEDM
21.1	20.46	0.13	g	ZTF
21.14	19.59	0.11	r	ZTF
22.42	19.61	0.09	i	ALT
22.82	20.72	0.04	g	Wendelstein 3KK
22.82	19.67	0.02	i	Wendelstein 3KK
22.84	19.92	0.05	z	Wendelstein 3KK
23.73	20.78	0.04	g	Wendelstein 3KK
23.73	19.7	0.02	i	Wendelstein 3KK
23.73	19.8	0.08	J	Wendelstein 3KK
23.75	19.95	0.02	r	Wendelstein 3KK
23.75	19.88	0.04	z	Wendelstein 3KK
23.96	20.61	0.08	g	SEDM
23.96	19.79	0.05	r	SEDM
24.12	19.67	0.06	r	ZTF
24.38	19.72	0.03	i	ALT
24.39	19.83	0.02	r	ALT
24.41	20.65	0.04	g	ALT
24.41	20.65	0.04	g	ALT
24.43	19.76	0.08	z	ALT

24.43	19.76	0.08	z	ALT
24.74	19.72	0.02	i	Wendelstein 3KK
24.74	19.85	0.02	r	Wendelstein 3KK
24.74	19.88	0.08	J	Wendelstein 3KK
24.74	19.88	0.08	J	Wendelstein 3KK
24.76	19.94	0.07	z	Wendelstein 3KK
24.97	20.56	0.07	g	SEDM
24.97	19.86	0.04	r	SEDM
24.97	19.65	0.04	i	SEDM
25.47	19.69	0.07	i	NOT
25.48	20.97	0.14	g	NOT
25.5	19.85	0.1	r	NOT
26.36	19.84	0.02	r	ALT
26.36	19.84	0.02	r	ALT
26.95	20.91	0.13	g	SEDM
26.95	19.94	0.07	r	SEDM
26.96	19.6	0.13	i	SEDM
27.94	21.03	0.14	g	SEDM
27.95	20.06	0.06	r	SEDM
27.95	19.71	0.05	i	SEDM
28.15	21.13	0.26	g	ZTF
28.65	19.88	0.03	i	ALT

28.65	19.88	0.03	i	ALT
28.67	20.04	0.03	r	ALT
28.67	20.04	0.03	r	ALT
29.13	21.02	0.24	g	ZTF
30.02	20.29	0.13	r	SEDM
30.02	19.86	0.09	i	SEDM
30.77	20.07	0.08	r	IOO
30.88	21.19	0.17	g	Wendelstein 3KK
30.88	19.94	0.08	i	Wendelstein 3KK
30.88	20.02	0.19	J	Wendelstein 3KK
30.89	20.18	0.26	z	Wendelstein 3KK
30.89	20.1	0.09	r	Wendelstein 3KK
31.52	20.25	0.2	z	ALT
31.94	21	0.18	g	SEDM
31.94	20.24	0.07	r	SEDM
31.94	19.84	0.07	i	SEDM
32.07	20.33	0.12	r	ALT
32.07	20.14	0.08	i	ALT
32.95	21.25	0.13	g	SEDM
32.96	20.2	0.03	r	SEDM
32.96	19.93	0.04	i	SEDM
33.68	21.7	0.35	g	IOO

35.69	20.01	0.18	z	IOO
35.94	21.46	0.16	g	SEDM
35.94	20.62	0.07	r	SEDM
35.94	20.03	0.08	i	SEDM
36.4	20.21	0.05	i	ALT
36.42	20.41	0.04	r	ALT
36.6	21.71	0.11	g	Wendelstein 3KK
36.6	20.12	0.03	i	Wendelstein 3KK
36.6	19.93	0.09	J	Wendelstein 3KK
36.63	20.43	0.04	r	Wendelstein 3KK
36.97	20.49	0.08	r	SEDM
36.97	20.17	0.1	i	SEDM
38.55	20	0.13	i	NOT
38.56	21.46	0.25	g	NOT
38.58	20.51	0.12	r	NOT
39.32	20.66	0.18	i	ALT
39.34	20.61	0.21	r	ALT
39.93	20.54	0.11	r	SEDM
39.93	20.12	0.09	i	SEDM
40.33	20.65	0.15	i	ALT
40.38	20.57	0.13	r	ALT
44.25	20.11	0.21	i	SEDM

44.87	22	0.22	g	Wendelstein 3KK
44.87	20.37	0.06	i	Wendelstein 3KK
44.87	20.11	0.1	J	Wendelstein 3KK
44.88	20.88	0.08	r	Wendelstein 3KK
44.88	20.56	0.12	z	Wendelstein 3KK
45.73	22.08	0.16	g	Wendelstein 3KK
45.73	20.48	0.03	i	Wendelstein 3KK
45.73	20.14	0.1	J	Wendelstein 3KK
45.76	20.83	0.04	r	Wendelstein 3KK
45.76	20.6	0.09	z	Wendelstein 3KK
46.14	20.61	0.2	r	ZTF
46.36	20.6	0.1	i	ALT
46.38	20.98	0.23	r	ALT
46.7	22.13	0.17	g	Wendelstein 3KK
46.7	20.52	0.05	i	Wendelstein 3KK
46.7	20.26	0.13	J	Wendelstein 3KK
46.91	22.19	0.25	g	SEDM
46.91	20.97	0.11	r	SEDM
46.91	20.41	0.07	i	SEDM
47.14	20.5	0.18	r	ZTF
47.34	20.81	0.06	r	ALT
47.35	20.57	0.1	i	ALT

49.49	20.78	0.05	r	ALT
52.62	21.18	0.09	r	ALT
52.63	20.86	0.1	i	ALT
52.75	22.5	0.22	g	Wendelstein 3KK
52.75	20.74	0.05	i	Wendelstein 3KK
52.75	20.56	0.16	J	Wendelstein 3KK
52.78	21.14	0.06	r	Wendelstein 3KK
52.78	20.75	0.14	z	Wendelstein 3KK
54.01	22.02	0.19	g	SEDM
54.02	21.21	0.12	r	SEDM
54.02	20.88	0.11	i	SEDM
56.56	21.01	0.08	i	ALT
56.58	21.26	0.09	r	ALT
56.6	22.36	0.18	g	Wendelstein 3KK
56.6	20.8	0.05	i	Wendelstein 3KK
56.6	20.69	0.17	J	Wendelstein 3KK
56.63	21.25	0.06	r	Wendelstein 3KK
56.63	21.01	0.13	z	Wendelstein 3KK
57.64	20.99	0.16	i	IOO
57.87	21.81	0.2	g	SEDM
57.87	20.85	0.08	r	SEDM
57.87	20.71	0.09	i	SEDM

59.98	22.16	0.2	g	SEDM
59.98	21.12	0.1	r	SEDM
59.98	20.95	0.12	i	SEDM
62.63	21.08	0.17	i	Wendelstein 3KK
62.63	21.39	0.38	J	Wendelstein 3KK
62.66	21.43	0.12	r	Wendelstein 3KK
62.66	20.86	0.18	z	Wendelstein 3KK
62.67	21.01	0.14	i	ALT
62.69	21.18	0.09	r	ALT
62.87	21.72	0.23	g	SEDM
62.87	21.2	0.15	r	SEDM
62.87	20.94	0.14	i	SEDM
63.6	21.23	0.1	i	ALT
63.66	21.21	0.09	r	ALT
64.83	22.36	0.21	g	Wendelstein 3KK
64.83	21.14	0.09	i	Wendelstein 3KK
64.83	21.42	0.39	J	Wendelstein 3KK
64.86	21.41	0.11	r	Wendelstein 3KK
64.86	21.02	0.3	z	Wendelstein 3KK
64.87	21.33	0.13	r	SEDM
64.87	20.82	0.1	i	SEDM

Table F.2: Photometry Log (magnitudes have not been corrected for Galactic Extinction $E(B - V) = 0.05$ mag.

ObsID	Start Time (UTC)	Exposure (s)	Flux ($\mathrm{erg\,cm^{-2}\,s^{-1}}$)
EP-WXT			
11916650962	2025-08-27 06:10:21	2063	$3.4^{+6.0}_{-1.2} \times 10^{-11}$
EP-FXT			
06800000865	2025-09-01 02:35:49	2995	$< 1.1 \times 10^{-13}$
06800000881	2025-09-06 02:29:39	5997	$< 1.1 \times 10^{-14}$
06800000898	2025-09-11 18:21:49	6027	$< 3.9 \times 10^{-14}$
06800000912	2025-09-23 02:09:59	4141	$< 2.6 \times 10^{-14}$
Swift			
03000057001	2025-08-31 21:09:31	4030	$< 1.1 \times 10^{-13}$
03000057002	2025-09-05 02:34:00	1160	$< 3.3 \times 10^{-13}$
03000057003	2025-09-09 18:20:00	1525	$< 2.3 \times 10^{-13}$

Table F.1: Log of X-ray observations

Time(days)	Tel.+Instr.	Wavelength Range ($\AA$)
4.2	Gemini+GMOS-North	4900–8200
6.3	Gemini+GMOS-North	4000-8200
7.9	NOT+ALFOSC	3900 – 9300
8.2	Gemini+GMOS-North	4000-8200
11.1	Gemini+GMOS-North	4800–7600
16.2	Gemini+GMOS-North	4000-7200
20.9	NOT+ALFOSC	3900 – 9300
21.2	P200+NGPS	5700–9900
28.1	P200+NGPS	5700–9700
30.9	NOT+ALFOSC	3900–9800
37.3	Gemini+GMOS-North	5000–8800
56.2	Keck I+LRIS	3400–10300

Table F.3: Spectroscopic observations of EP250827b/SN 2025kg. Epochs are given in observer times since t_0.

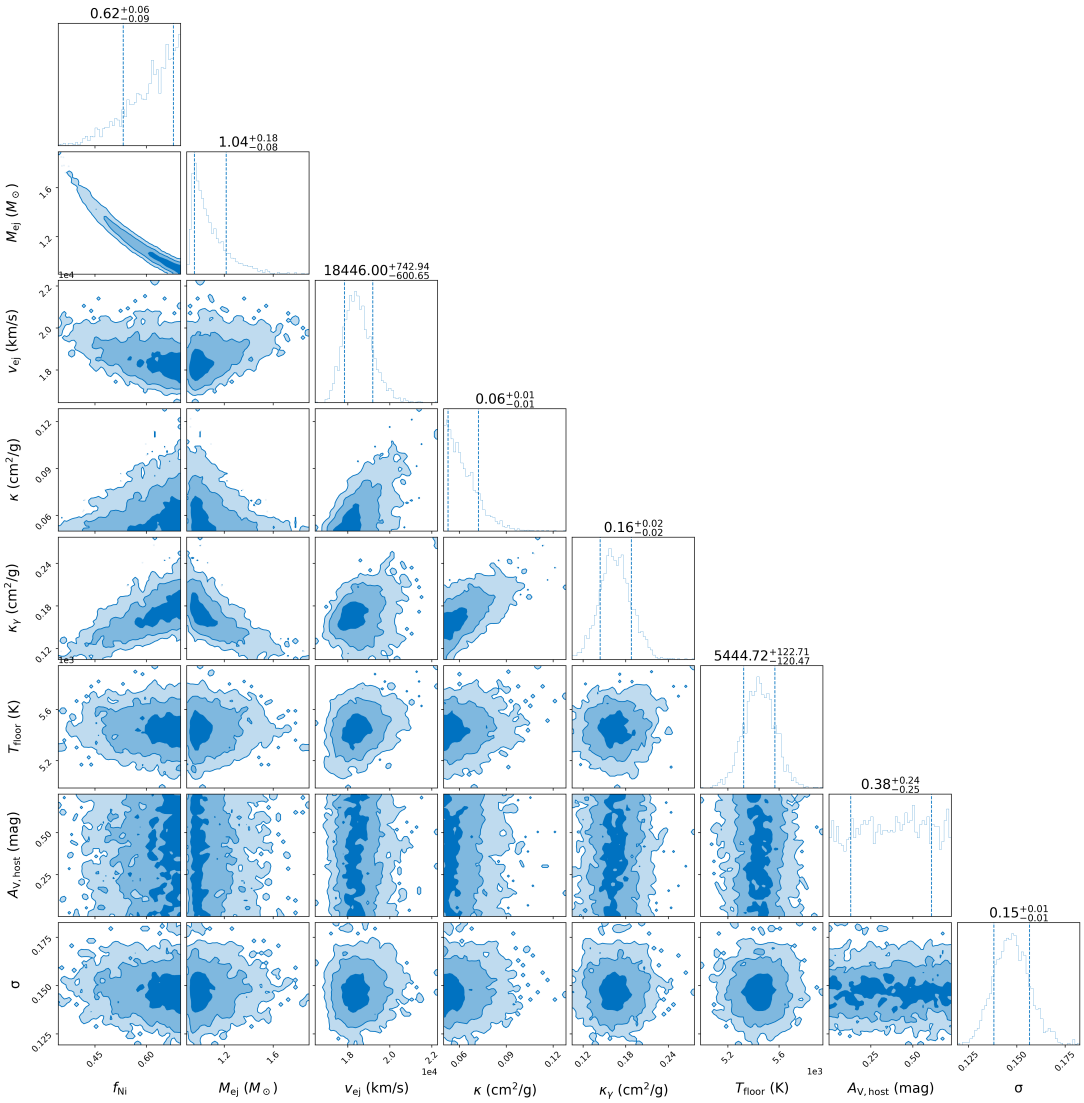

Figure F.1: Corner plot of fitting a Arnett (1982) radioactive decay model to the late-time SN LC at $t_0 + 7$ days.

F.2 Corner Plots

Here we present corner plots associate with the modeling of EP250827b/SN 2025wkm in Figures F.1 and F.2.

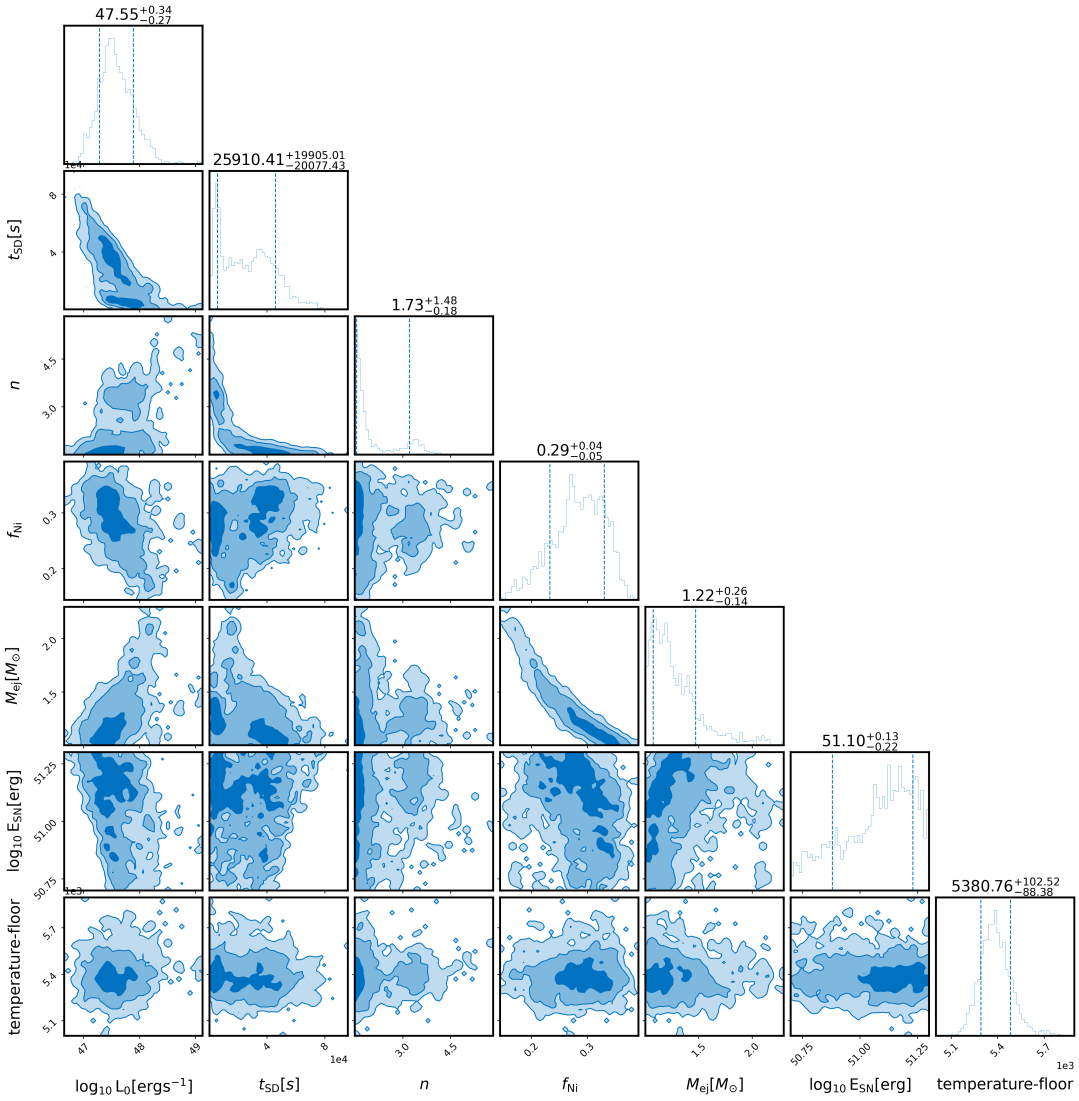

Figure F.2: Corner plot of fitting a combination of a Arnett (1982) radioactive decay model and spindown of a millisecond magnetar (Omand & Sarin, 2024a; Sarin et al., 2022) the late-time SN LC at $t_0 + 7$ days.

Appendix G: Facilities and Software Used in this Thesis

G.1 Facilities

1. ATLAS
2. DBSP
3. EP: WXT, FXT
4. Fermi: GBM
5. GTC
6. Gemini: GMOS
7. GIT
8. HCT
9. Keck-II: LRIS, DEIMOS, KCWI
10. Konus-Wind
11. Lick Observatory: KAST
12. LCO

13. LDT: LMI
14. LT: IO:O, SPRAT
15. NOT: ALFOSC
16. NGPS
17. SEDM
18. Swift: XRT, UVOT, BAT
19. TNOT
20. TRT
21. VLA
22. ZTF

G.2 Software

1. Astropy (Astropy Collaboration et al., 2013, 2018, 2022)
2. corner (Foreman-Mackey, 2016)
3. emcee (Foreman-Mackey et al., 2013b)
4. matplotlib (Hunter, 2007)
5. NumPy (Harris et al., 2020)
6. Pandas (pandas development team, 2020)

7. PypeIt (Prochaska et al., 2020a)

8. ppxf (Cappellari, 2023; Cappellari & Copin, 2003)

9. Prospector (Johnson et al., 2021b)

10. PSFEx (Bertin, 2011)

11. Redback (Sarin et al., 2024)

12. SciPy (Virtanen et al., 2020)

13. SciServer (Taghizadeh-Popp et al., 2020)

14. Source-Extractor (Bertin & Arnouts, 1996c)

15. specitils (Astropy-Specutils Development Team, 2019)

16. ztfquery (Rigault, 2018)

Bibliography

Abazajian, K. N., Adelman-McCarthy, J. K., Agüeros, M. A., et al. 2009, The Astrophysical Journal Supplement, 182, 543, doi: 10.1088/0067-0049/182/2/543

Abbott, B. P., Abbott, R., Abbott, T. D., et al. 2017, , 119, 161101, doi: 10.1103/PhysRevLett.119.161101

Agui Fernandez, J. F., de Ugarte Postigo, A., Thoene, C. C., et al. 2023a, GRB Coordinates Network, 34597, 1

—. 2023b, GRB Coordinates Network, 34597, 1

Ahumada, T., Singer, L. P., Anand, S., et al. 2021, Nature Astronomy, 5, 917, doi: 10.1038/s41550-021-01428-7

Ahumada, T., Anand, S., Coughlin, M. W., et al. 2022, The Astrophysical Journal, 932, 40, doi: 10.3847/1538-4357/ac6c29

Ahumada, T., Bellm, E. C., Yan, L., et al. 2025, GRB Coordinates Network, 39791, 1

Alexander, K. D., Laskar, T., Berger, E., et al. 2019, The Astrophysical Journal, 870, 67, doi: 10.3847/1538-4357/aaf19d

Almualla, M., Coughlin, M. W., Anand, S., et al. 2020, Monthly Notices of the Royal Astronomical Society, 495, 4366, doi: 10.1093/mnras/staa1498

Aloy, M. Á., & Obergaulinger, M. 2021, Monthly Notices of the Royal Astronomical Society, 500, 4365, doi: 10.1093/mnras/staa3273

Alp, D., & Larsson, J. 2020, The Astrophysical Journal, 896, 39, doi: 10.3847/1538-4357/ab91ba

Amati, L., Frontera, F., Tavani, M., et al. 2002, Astronomy and Astrophysics, 390, 81, doi: 10.1051/0004-6361:20020722

Ambikasaran, S., Foreman-Mackey, D., Greengard, L., Hogg, D. W., & O'Neil, M. 2015, IEEE Transactions on Pattern Analysis and Machine Intelligence, 38, 252, doi: 10.1109/TPAMI.2015.2448083

Anand, S., Barnes, J., Yang, S., et al. 2023, arXiv e-prints, arXiv:2302.09226, doi: 10.48550/arXiv.2302.09226

—. 2024, The Astrophysical Journal, 962, 68, doi: 10.3847/1538-4357/ad11df

Anderson, G. E., Russell, T. D., Fausey, H. M., et al. 2023, Monthly Notices of the Royal Astronomical Society, 523, 4992, doi: 10.1093/mnras/stad1635

Anderson, J. P., Pessi, P., Galbany, L., & Irani, I. 2020, Transient Name Server Classification Report, 2020-3755, 1

Andreoni, I., Coughlin, M. W., Kool, E. C., et al. 2021, The Astrophysical Journal, 918, 63, doi: 10.3847/1538-4357/ac0bc7

Andreoni, I., Coughlin, M. W., Perley, D. A., et al. 2022, Nature, 612, 430, doi: 10.1038/s41586-022-05465-8

Arcavi, I., Gal-Yam, A., Yaron, O., et al. 2011

Arnaud, K. A. 1996, in Astronomical Society of the Pacific Conference Series, Vol. 101, Astronomical Data Analysis Software and Systems V, ed. G. H. Jacoby & J. Barnes, 17

Arnett, W. D. 1980, The Astrophysical Journal, 237, 541, doi: 10.1086/157898

—. 1982, The Astrophysical Journal, 253, 785, doi: 10.1086/159681

Arnett, W. D., Fryer, C., & Matheson, T. 2017, The Astrophysical Journal, 846, 33, doi: 10.3847/1538-4357/aa8173

Aryan, A., Chen, T.-W., Yang, S., et al. 2025, The Astrophysical Journal Supplement, 281, 20, doi: 10.3847/1538-4365/adfc69

Ashall, C., Mazzali, P. A., Pian, E., et al. 2019, Monthly Notices of the Royal Astronomical Society, 487, 5824, doi: 10.1093/mnras/stz1588

Ashton, G., Hübner, M., Lasky, P. D., et al. 2019, The Astrophysical Journal Supplement, 241, 27, doi: 10.3847/1538-4365/ab06fc

Astropy Collaboration, Robitaille, T. P., Tollerud, E. J., et al. 2013, Astronomy and Astrophysics, 558, A33, doi: 10.1051/0004-6361/201322068

Astropy Collaboration, Price-Whelan, A. M., Sipőcz, B. M., et al. 2018, The Astronomical Journal, 156, 123, doi: 10.3847/1538-3881/aabc4f

Astropy Collaboration, Price-Whelan, A. M., Lim, P. L., et al. 2022, The Astrophysical Journal, 935, 167, doi: 10.3847/1538-4357/ac7c74

Astropy-Specutils Development Team. 2019, Specutils: Spectroscopic analysis and reduction, Astrophysics Source Code Library, record ascl:1902.012

Balberg, S., & Loeb, A. 2011, Monthly Notices of the Royal Astronomical Society, 414, 1715, doi: 10.1111/j.1365-2966.2011.18505.x

Barbarino, C., Sollerman, J., Taddia, F., et al. 2020, arXiv e-prints, arXiv:2010.08392, doi: 10.48550/arXiv.2010.08392

—. 2021, Astronomy and Astrophysics, 651, A81, doi: 10.1051/0004-6361/202038890

Barbary, K., Barclay, T., Biswas, R., et al. 2016, SNCosmo: Python library for supernova cosmology, Astrophysics Source Code Library, record ascl:1611.017. http://ascl.net/1611.017

Barkov, M. V., & Komissarov, S. S. 2011, Monthly Notices of the Royal Astronomical Society, 415, 944, doi: 10.1111/j.1365-2966.2011.18762.x

Barthelmy, S. D., Barbier, L. M., Cummings, J. R., et al. 2005, Space Science Reviews, 120, 143, doi: 10.1007/s11214-005-5096-3

Bazin, G., Palanque-Delabrouille, N., Rich, J., et al. 2009, Astronomy and Astrophysics, 499, 653, doi: 10.1051/0004-6361/200911847

Beardmore, A. P., Melandri, A., Sbarrato, T., et al. 2023, GRB Coordinates Network, 34400, 1

Belkin, S., Kim, V., Pozanenko, A., et al. 2022a, GRB Coordinates Network, 32769, 1

Belkin, S., Moskvitin, A., Kim, V., et al. 2022b, GRB Coordinates Network, 32818, 1

Belkin, S., Nazarov, S., Pozanenko, A., Pankov, N., & IKI GRB FuN. 2022c, GRB Coordinates Network, 32684, 1

Bellm, E. C., & Sesar, B. 2016, pyraf-dbsp: Reduction pipeline for the Palomar Double Beam Spectrograph, Astrophysics Source Code Library. http://ascl.net/1602.002

Bellm, E. C., Kulkarni, S. R., Graham, M. J., et al. 2019, Publications of the Astronomical Society of the Pacific, 131, 018002, doi: 10.1088/1538-3873/aaecbe

Beniamini, P., Duran, R. B., Petropoulou, M., & Giannios, D. 2020, The Astrophysical Journal Letters, 895, L33, doi: 10.3847/2041-8213/ab9223

Beniamini, P., & Nakar, E. 2019, Monthly Notices of the Royal Astronomical Society, 482, 5430, doi: 10.1093/mnras/sty3110

Bennett, C. L., Larson, D., Weiland, J. L., & Hinshaw, G. 2014, The Astrophysical Journal, 794, 135, doi: 10.1088/0004-637X/794/2/135

Berger, E. 2014, Annual Review of Astronomy and Astrophysics, 52, 43, doi: 10.1146/annurev-astro-081913-035926

Berger, E., Fong, W., & Chornock, R. 2013, The Astrophysical Journal Letters, 774, L23, doi: 10.1088/2041-8205/774/2/L23

Berger, E., Kulkarni, S. R., & Chevalier, R. A. 2002, The Astrophysical Journal Letters, 577, L5, doi: 10.1086/344045

Berger, E., Kulkarni, S. R., Frail, D. A., & Soderberg, A. M. 2003a, The Astrophysical Journal, 599, 408, doi: 10.1086/379214

Berger, E., Kulkarni, S. R., Pooley, G., et al. 2003b, Nature, 426, 154, doi: 10.1038/nature01998

Bersier, D., Fruchter, A. S., Strolger, L. G., et al. 2006, The Astrophysical Journal, 643, 284, doi: 10.1086/502640

Bersten, M. C., Benvenuto, O. G., Nomoto, K., et al. 2012, The Astrophysical Journal, 757, 31, doi: 10.1088/0004-637X/757/1/31

Bertin, E. 2006, in Astronomical Society of the Pacific Conference Series, Vol. 351, Astronomical Data Analysis Software and Systems XV, ed. C. Gabriel, C. Arviset, D. Ponz, & S. Enrique, 112

Bertin, E. 2010a, SWarp: Resampling and Co-adding FITS Images Together. http://ascl.net/1010.068

—. 2010b, SWarp: Resampling and Co-adding FITS Images Together, Astrophysics Source Code Library, record ascl:1010.068. http://ascl.net/1010.068

—. 2011, Astronomical Society of the Pacific Conference Series, Vol. 442, Automated Morphometry with SExtractor and PSFEx, 435

—. 2013, PSFEx: Point Spread Function Extractor, Astrophysics Source Code Library, record ascl:1301.001. http://ascl.net/1301.001

Bertin, E., & Arnouts, S. 1996a, Astronomy and Astrophysics, Supplement, 117, 393, doi: 10.1051/aas:1996164

—. 1996b, Astronomy and Astrophysics, Supplement, 117, 393, doi: 10.1051/aas:1996164

—. 1996c, Astronomy and Astrophysics, Supplement, 117, 393, doi: 10.1051/aas:1996164

Bertin, E., Mellier, Y., Radovich, M., et al. 2002, in Astronomical Society of the Pacific Conference Series, Vol. 281, Astronomical Data Analysis Software and Systems XI, ed. D. A. Bohlender, D. Durand, & T. H. Handley, 228

Bhalerao, V., Bhattacharya, D., Vibhute, A., et al. 2017, Journal of Astrophysics and Astronomy, 38, 31, doi: 10.1007/s12036-017-9447-8

Bianco, F. B., Modjaz, M., Hicken, M., et al. 2014, The Astrophysical Journal Supplement, 213, 19, doi: 10.1088/0067-0049/213/2/19

Bikmaev, I., Khamitov, I., Irtuganov, E., et al. 2022a, GRB Coordinates Network, 32743, 1

—. 2022b, GRB Coordinates Network, 32752, 1

Blagorodnova, N., Neill, J. D., Walters, R., et al. 2018a, Publications of the Astronomical Society of the Pacific, 130, 035003, doi: 10.1088/1538-3873/aaa53f

—. 2018b, Publications of the Astronomical Society of the Pacific, 130, 035003, doi: 10.1088/1538-3873/aaa53f

—. 2018c, Publications of the Astronomical Society of the Pacific, 130, 035003, doi: 10.1088/1538-3873/aaa53f

Blanchard, P. K., Nicholl, M., Berger, E., et al. 2019, The Astrophysical Journal, 872, 90, doi: 10.3847/1538-4357/aafa13

Blanchard, P. K., Villar, V. A., Chornock, R., et al. 2024, Nature Astronomy, 8, 774, doi: 10.1038/s41550-024-02237-4

Blondin, S., & Tonry, J. L. 2007a, The Astrophysical Journal, 666, 1024, doi: 10.1086/520494

—. 2007b, The Astrophysical Journal, 666, 1024, doi: 10.1086/520494

Bloom, J. S., Frail, D. A., & Kulkarni, S. R. 2003, The Astrophysical Journal, 594, 674, doi: 10.1086/377125

Bopp, J., & Gottlieb, O. 2025, The Astrophysical Journal Letters, 982, L56, doi: 10.3847/2041-8213/adbdcd

Bowers, R., & Wilson, J. R. 1982, The Astrophysical Journal, 263, 366, doi: 10.1086/160510

Bradley, L., Sipőcz, B., Robitaille, T., et al. 2024, astropy/photutils: 2.0.2, 2.0.2, Zenodo, doi: 10.5281/zenodo.13989456

Brennan, S. J., & Fraser, M. 2022, Astronomy and Astrophysics, 667, A62, doi: 10.1051/0004-6361/202243067

Bright, J. S., Carotenuto, F., Fender, R., et al. 2024, arXiv e-prints, arXiv:2409.19055, doi: 10.48550/arXiv.2409.19055

—. 2025, The Astrophysical Journal, 981, 48, doi: 10.3847/1538-4357/adaaef

Brivio, R., Ferro, M., D'Avanzo, P., et al. 2022, GRB Coordinates Network, 32652, 1

Bromberg, O., Nakar, E., Piran, T., & Sari, R. 2011, The Astrophysical Journal, 740, 100, doi: 10.1088/0004-637X/740/2/100

Brown, P. J., Breeveld, A. A., Holland, S., Kuin, P., & Pritchard, T. 2014, , 354, 89, doi: 10.1007/s10509-014-2059-8

Brown, T. M., Baliber, N., Bianco, F. B., et al. 2013, Publications of the Astronomical Society of the Pacific, 125, 1031, doi: 10.1086/673168

Buchner, J., Georgakakis, A., Nandra, K., et al. 2014, Astronomy and Astrophysics, 564, A125, doi: 10.1051/0004-6361/201322971

Budnik, R., Katz, B., Sagiv, A., & Waxman, E. 2010, The Astrophysical Journal, 725, 63, doi: 10.1088/0004-637X/725/1/63

Bufano, F., Pian, E., Sollerman, J., et al. 2012, The Astrophysical Journal, 753, 67, doi: 10.1088/0004-637X/753/1/67

Burbidge, G. R., Hoyle, F., Burbidge, E. M., Christy, R. F., & Fowler, W. A. 1956, Physical Review, 103, 1145, doi: 10.1103/PhysRev.103.1145

Burns, C. R., Stritzinger, M., Phillips, M. M., et al. 2011, The Astronomical Journal, 141, 19, doi: 10.1088/0004-6256/141/1/19

Burns, E., Svinkin, D., Fenimore, E., et al. 2023, The Astrophysical Journal Letters, 946, L31, doi: 10.3847/2041-8213/acc39c

Burrows, A., Dessart, L., Livne, E., Ott, C. D., & Murphy, J. 2007, The Astrophysical Journal, 664, 416, doi: 10.1086/519161

Burrows, D. N., Hill, J. E., Nousek, J. A., et al. 2005, Space Science Reviews, 120, 165, doi: 10.1007/s11214-005-5097-2

Busmann, M., O'Connor, B., Sommer, J., et al. 2025, arXiv e-prints, arXiv:2503.14588, doi: 10.48550/arXiv.2503.14588

Campana, S., Mangano, V., Blustin, A. J., et al. 2006, Nature, 442, 1008, doi: 10.1038/nature04892

Cano, Z. 2013, Monthly Notices of the Royal Astronomical Society, 434, 1098, doi: 10.1093/mnras/stt1048

—. 2014, The Astrophysical Journal, 794, 121, doi: 10.1088/0004-637X/794/2/121

Cano, Z., Johansson Andreas, K. G., & Maeda, K. 2016, Monthly Notices of the Royal Astronomical Society, 457, 2761, doi: 10.1093/mnras/stw122

Cano, Z., Wang, S.-Q., Dai, Z.-G., & Wu, X.-F. 2017a, Advances in Astronomy, 2017, 8929054, doi: 10.1155/2017/8929054

Cano, Z., Bersier, D., Guidorzi, C., et al. 2011, The Astrophysical Journal, 740, 41, doi: 10.1088/0004-637X/740/1/41

Cano, Z., Izzo, L., de Ugarte Postigo, A., et al. 2017b, Astronomy and Astrophysics, 605, A107, doi: 10.1051/0004-6361/201731005

Cappellari, M. 2023, Monthly Notices of the Royal Astronomical Society, 526, 3273, doi: 10.1093/mnras/stad2597

Cappellari, M., & Copin, Y. 2003, Monthly Notices of the Royal Astronomical Society, 342, 345, doi: 10.1046/j.1365-8711.2003.06541.x

Cardelli, J. A., Clayton, G. C., & Mathis, J. S. 1989a, The Astrophysical Journal, 345, 245, doi: 10.1086/167900

—. 1989b, The Astrophysical Journal, 345, 245, doi: 10.1086/167900

—. 1989c, The Astrophysical Journal, 345, 245, doi: 10.1086/167900

Cartier, R., Contreras, C., Pasten, A., & Fuentes, C. 2020, Transient Name Server Classification Report, 2020-3729, 1

Cash, W. 1979, The Astrophysical Journal, 228, 939, doi: 10.1086/156922

Castro-Tirado, A. J., Sanchez-Ramirez, R., Hu, Y. D., et al. 2022, GRB Coordinates Network, 32686, 1

Cenko, B. 2023, GRB Coordinates Network, 34633, 1

Cenko, S. B., Frail, D. A., Harrison, F. A., et al. 2010, The Astrophysical Journal, 711, 641, doi: 10.1088/0004-637X/711/2/641

—. 2011, The Astrophysical Journal, 732, 29, doi: 10.1088/0004-637X/732/1/29

Cenko, S. B., Kulkarni, S. R., Horesh, A., et al. 2013, The Astrophysical Journal, 769, 130, doi: 10.1088/0004-637X/769/2/130

Cenko, S. B., Urban, A. L., Perley, D. A., et al. 2015, The Astrophysical Journal Letters, 803, L24, doi: 10.1088/2041-8205/803/2/L24

Cepa, J., Aguiar, M., Escalera, V. G., et al. 2000, in Society of Photo-Optical Instrumentation Engineers (SPIE) Conference Series, Vol. 4008, Optical and IR Telescope Instrumentation and Detectors, ed. M. Iye & A. F. Moorwood, 623–631, doi: 10.1117/12.395520

Chambers, K. C., Magnier, E. A., Metcalfe, N., et al. 2016a, arXiv e-prints, arXiv:1612.05560. https://arxiv.org/abs/1612.05560

—. 2016b, arXiv e-prints, arXiv:1612.05560. https://arxiv.org/abs/1612.05560

Chambers, K. C., Magnier, E. A., Metcalfe, N., et al. 2019, The Pan-STARRS1 Surveys. https://arxiv.org/abs/1612.05560

Chandra, P., & Frail, D. A. 2012, The Astrophysical Journal, 746, 156, doi: 10.1088/0004-637X/746/2/156

Chandra, P., Cenko, S. B., Frail, D. A., et al. 2008, The Astrophysical Journal, 683, 924, doi: 10.1086/589807

Chandrasekhar, S. 1931, The Astrophysical Journal, 74, 81, doi: 10.1086/143324

Chatzopoulos, E., Wheeler, J. C., & Vinko, J. 2009, The Astrophysical Journal, 704, 1251, doi: 10.1088/0004-637X/704/2/1251

Chatzopoulos, E., Wheeler, J. C., Vinko, J., et al. 2011, The Astrophysical Journal, 729, 143, doi: 10.1088/0004-637X/729/2/143

Cheng, H., Zhang, C., Ling, Z., et al. 2025, Experimental Astronomy, 60, 15, doi: 10.1007/s10686-025-10025-9

Chevalier, R. A. 1992, The Astrophysical Journal, 394, 599, doi: 10.1086/171612

—. 1998, The Astrophysical Journal, 499, 810, doi: 10.1086/305676

—. 2012, The Astrophysical Journal Letters, 752, L2, doi: 10.1088/2041-8205/752/1/L2

Chevalier, R. A., & Fransson, C. 2008, The Astrophysical Journal Letters, 683, L135, doi: 10.1086/591522

Chornock, R., Berger, E., Levesque, E. M., et al. 2010, arXiv e-prints, arXiv:1004.2262, doi: 10.48550/arXiv.1004.2262

Chu, M., Dahiwale, A., & Fremling, C. 2021, Transient Name Server Classification Report, 2021-2534, 1

Chugai, N. N. 2000, Astronomy Letters, 26, 797, doi: 10.1134/1.1331160

Clemens, J. C., Crain, J. A., & Anderson, R. 2004, in Society of Photo-Optical Instrumentation Engineers (SPIE) Conference Series, Vol. 5492, Ground-based Instrumentation for Astronomy, ed. A. F. M. Moorwood & M. Iye, 331–340, doi: 10.1117/12.550069

Clocchiatti, A., Suntzeff, N. B., Covarrubias, R., & Candia, P. 2011, The Astronomical Journal, 141, 163, doi: 10.1088/0004-6256/141/5/163

Clocchiatti, A., & Wheeler, J. C. 1997, The Astrophysical Journal, 491, 375, doi: 10.1086/304961

Colgate, S. A. 1974, The Astrophysical Journal, 187, 333, doi: 10.1086/152632

Conti, P. S., & Walborn, N. R. 1976, The Astrophysical Journal, 207, 502, doi: 10.1086/154517

Corcoran, G., Levan, A. J., Malesani, D. B., et al. 2025, GRB Coordinates Network, 41670, 1

Corsi, A., Ho, A., Kulkarni, S., & Perley, D. 2021, Transient Name Server AstroNote, 47, 1

Corsi, A., Ofek, E. O., Gal-Yam, A., et al. 2014, The Astrophysical Journal, 782, 42, doi: 10.1088/0004-637X/782/1/42

Corsi, A., Gal-Yam, A., Kulkarni, S. R., et al. 2016, The Astrophysical Journal, 830, 42, doi: 10.3847/0004-637X/830/1/42

Corsi, A., Ho, A. Y. Q., Cenko, S. B., et al. 2022, arXiv e-prints, arXiv:2210.09536, doi: 10.48550/arXiv.2210.09536

—. 2023, The Astrophysical Journal, 953, 179, doi: 10.3847/1538-4357/acd3f2

Coughlin, M. W., Tao, D., Chan, M. L., et al. 2018, Monthly Notices of the Royal Astronomical Society, 478, 692, doi: 10.1093/mnras/sty1066

Coughlin, M. W., Antier, S., Corre, D., et al. 2019, Mon. Not. R. Astron. Soc., doi: 10.1093/mnras/stz2485

Coughlin, M. W., Bloom, J. S., Nir, G., et al. 2023, The Astrophysical Journal Supplement, 267, 31, doi: 10.3847/1538-4365/acdee1

Cunningham, V., Cenko, S. B., Ryan, G., et al. 2020, The Astrophysical Journal, 904, 166, doi: 10.3847/1538-4357/abc2cd

Curran, P. A., Evans, P. A., de Pasquale, M., Page, M. J., & van der Horst, A. J. 2010, The Astrophysical Journal Letters, 716, L135, doi: 10.1088/2041-8205/716/2/L135

Cutri, R. M., Wright, E. L., Conrow, T., et al. 2013, Explanatory Supplement to the AllWISE Data Release Products, Explanatory Supplement to the AllWISE Data Release Products

Dahiwale, A., & Fremling, C. 2020a, Transient Name Server Classification Report, 2020-1667, 1

—. 2020b, Transient Name Server Classification Report, 2020-688, 1

—. 2020c, Transient Name Server Classification Report, 2020-1130, 1

—. 2020d, Transient Name Server Classification Report, 2020-1186, 1

—. 2020e, Transient Name Server Classification Report, 2020-2954, 1

—. 2021, Transient Name Server Classification Report, 2021-1879, 1

Daigne, F., & Mochkovitch, R. 2007, Astronomy and Astrophysics, 465, 1, doi: 10.1051/0004-6361:20066080

Dalessi, S., Roberts, O. J., Meegan, C., & Fermi GBM Team. 2023, GRB Coordinates Network, 33411, 1

Das, K. K., Kasliwal, M. M., Sollerman, J., et al. 2024, The Astrophysical Journal, 972, 91, doi: 10.3847/1538-4357/ad595f

Dastidar, R. G., & Duffell, P. C. 2024, The Astrophysical Journal, 976, 252, doi: 10.3847/1538-4357/ad86bf

D'Avanzo, P., Ferro, M., Brivio, R., et al. 2022, GRB Coordinates Network, 32755, 1

De, K. 2021, Transient Name Server Discovery Report, 2021-2126, 1

De Pasquale, M., Page, M. J., Kann, D. A., et al. 2016, Monthly Notices of the Royal Astronomical Society, 462, 1111, doi: 10.1093/mnras/stw170410.48550/arXiv.1602.04158

de Ugarte Postigo, A., Agui Fernandez, J. F., Thoene, C. C., & Izzo, L. 2023a, GRB Coordinates Network, 34409, 1

de Ugarte Postigo, A., Izzo, L., Thoene, C. C., et al. 2022a, GRB Coordinates Network, 32800, 1

de Ugarte Postigo, A., Malesani, D. B., Agui Fernandez, J. F., Thoene, C. C., & Geier, S. 2023b, GRB Coordinates Network, 34740

de Ugarte Postigo, A., Fynbo, J. P. U., Thöne, C. C., et al. 2012, Astronomy and Astrophysics, 548, A11, doi: 10.1051/0004-6361/201219894

de Ugarte Postigo, A., Izzo, L., Pugliese, G., et al. 2022b, GRB Coordinates Network, 32648, 1

de Wet, S., Groot, P. J., & Meerlicht Consortium. 2022, GRB Coordinates Network, 32646, 1

Dean, C., & Fernández, R. 2024a, Physical Review D: Particles, Fields, Gravitation and Cosmology, 109, 083010, doi: 10.1103/PhysRevD.109.083010

—. 2024b, Physical Review D: Particles, Fields, Gravitation and Cosmology, 110, 083024, doi: 10.1103/PhysRevD.110.083024

Dekany, R., Smith, R. M., Riddle, R., et al. 2020a, Publications of the Astronomical Society of the Pacific, 132, 038001, doi: 10.1088/1538-3873/ab4ca2

—. 2020b, Publications of the Astronomical Society of the Pacific, 132, 038001, doi: 10.1088/1538-3873/ab4ca2

D'Elia, V., Pian, E., Melandri, A., et al. 2015a, Astronomy and Astrophysics, 577, A116, doi: 10.1051/0004-6361/201425381

—. 2015b, Astronomy and Astrophysics, 577, A116, doi: 10.1051/0004-6361/201425381

Della Valle, M., Chincarini, G., Panagia, N., et al. 2006, Nature, 444, 1050, doi: 10.1038/nature05374

Dermer, C. D., Chiang, J., & Böttcher, M. 1999, The Astrophysical Journal, 513, 656, doi: 10.1086/306871

Dessart, L., & Hillier, D. J. 2005, Astronomy and Astrophysics, 439, 671, doi: 10.1051/0004-6361:20053217

Dessart, L., Hillier, D. J., Waldman, R., Livne, E., & Blondin, S. 2012, Monthly Notices of the Royal Astronomical Society, 426, L76, doi: 10.1111/j.1745-3933.2012.01329.x

Dey, A., Schlegel, D. J., Lang, D., et al. 2019, The Astronomical Journal, 157, 168, doi: 10.3847/1538-3881/ab089d

Di Francesco, J., Chalmers, D., Denman, N., et al. 2019, in Canadian Long Range Plan for Astronomy and Astrophysics White Papers, Vol. 2020, 32, doi: 10.5281/zenodo.3765763

Dichiara, S., Gropp, J. D., Kennea, J. A., et al. 2022, GRB Coordinates Network, 32632, 1

Dressler, A., Bigelow, B., Hare, T., et al. 2011, Publications of the Astronomical Society of the Pacific, 123, 288, doi: 10.1086/658908

Drout, M. R., Soderberg, A. M., Gal-Yam, A., et al. 2011, The Astrophysical Journal, 741, 97, doi: 10.1088/0004-637X/741/2/97

Drout, M. R., Chornock, R., Soderberg, A. M., et al. 2014, The Astrophysical Journal, 794, 23, doi: 10.1088/0004-637X/794/1/23

Duev, D. A., Mahabal, A., Masci, F. J., et al. 2019, Monthly Notices of the Royal Astronomical Society, 489, 3582

Duffell, P. C., & Ho, A. Y. Q. 2020, The Astrophysical Journal, 900, 193, doi: 10.3847/1538-4357/aba90a

Dugas, A., Fremling, C., & Sharma, Y. 2019, Transient Name Server Classification Report, 2019-1215, 1

Duncan, R. C., & Thompson, C. 1992, The Astrophysical Journal Letters, 392, L9, doi: 10.1086/186413

Eastman, R. G., Schmidt, B. P., & Kirshner, R. 1996, The Astrophysical Journal, 466, 911, doi: 10.1086/177563

Eftekhari, T., Margalit, B., Omand, C. M. B., et al. 2021, The Astrophysical Journal, 912, 21, doi: 10.3847/1538-4357/abe9b8

Eichler, D., & Levinson, A. 1999, The Astrophysical Journal Letters, 521, L117, doi: 10.1086/312187

Eisenberg, M., Gottlieb, O., & Nakar, E. 2022a, Monthly Notices of the Royal Astronomical Society, 517, 582, doi: 10.1093/mnras/stac2184

—. 2022b, Monthly Notices of the Royal Astronomical Society, 517, 582, doi: 10.1093/mnras/stac2184

Evans, P. A., Page, K. L., Bearmore, A. P., et al. 2022, arXiv e-prints, arXiv:2208.14478. https://arxiv.org/abs/2208.14478

Evans, P. A., Beardmore, A. P., Page, K. L., et al. 2009, Monthly Notices of the Royal Astronomical Society, 397, 1177, doi: 10.1111/j.1365-2966.2009.14913.x

Eyles-Ferris, R. 2025a, Transient Name Server Discovery Report, 2025-151, 1

—. 2025b, GRB Coordinates Network, 38878, 1

Eyles-Ferris, R. A. J., Jonker, P. G., Levan, A. J., et al. 2025, arXiv e-prints, arXiv:2504.08886. https://arxiv.org/abs/2504.08886

Faber, S. M., Phillips, A. C., Kibrick, R. I., et al. 2003, in Society of Photo-Optical Instrumentation Engineers (SPIE) Conference Series, Vol. 4841, Instrument Design and Performance for Optical/Infrared Ground-based Telescopes, ed. M. Iye & A. F. M. Moorwood, 1657–1669, doi: 10.1117/12.460346

Fabricant, D., Fata, R., Epps, H., et al. 2019, Publications of the Astronomical Society of the Pacific, 131, 075004, doi: 10.1088/1538-3873/ab1d78

Falk, S. W., & Arnett, W. D. 1977, The Astrophysical Journal Supplement, 33, 515, doi: 10.1086/190440

Feroz, F., Hobson, M. P., & Bridges, M. 2009, Monthly Notices of the Royal Astronomical Society, 398, 1601, doi: 10.1111/j.1365-2966.2009.14548.x

Ferrero, P., Kann, D. A., Zeh, A., et al. 2006, Astronomy and Astrophysics, 457, 857, doi: 10.1051/0004-6361:20065530

Ferro, M., Brivio, R., D'Avanzo, P., et al. 2022, GRB Coordinates Network, 32804, 1

Filippenko, A. V. 1997, Annual Review of Astronomy and Astrophysics, 35, 309, doi: 10.1146/annurev.astro.35.1.309

Flesch, E. W. 2019, arXiv e-prints, arXiv:1912.05614. https://arxiv.org/abs/1912.05614

Flewelling, H. A., Magnier, E. A., Chambers, K. C., et al. 2020a, The Astrophysical Journal Supplement, 251, 7, doi: 10.3847/1538-4365/abb82d

—. 2020b, The Astrophysical Journal Supplement, 251, 7, doi: 10.3847/1538-4365/abb82d

—. 2020c, The Astrophysical Journal Supplement, 251, 7, doi: 10.3847/1538-4365/abb82d

Foley, R. J., Smith, N., Ganeshalingam, M., et al. 2007, The Astrophysical Journal Letters, 657, L105, doi: 10.1086/513145

Foreman-Mackey, D. 2016, The Journal of Open Source Software, 1, 24, doi: 10.21105/joss.00024

Foreman-Mackey, D., Hogg, D. W., Lang, D., & Goodman, J. 2013a, Publications of the Astronomical Society of the Pacific, 125, 306, doi: 10.1086/670067

—. 2013b, Publications of the Astronomical Society of the Pacific, 125, 306, doi: 10.1086/670067

Forster, F., Pignata, G., Bauer, F. E., et al. 2020a, Transient Name Server Discovery Report, 2020-141, 1

—. 2020b, Transient Name Server Discovery Report, 2020-263, 1

Forster, F., Bauer, F. E., Galbany, L., et al. 2020c, Transient Name Server Discovery Report, 2020-1027, 1

—. 2020d, Transient Name Server Discovery Report, 2020-2457, 1

Forster, F., Bauer, F. E., Pignata, G., et al. 2020e, Transient Name Server Discovery Report, 2020-3690, 1

Forster, F., Mourao, A., Bauer, F. E., et al. 2021, Transient Name Server Discovery Report, 2021-1769, 1

Frail, D. A., Waxman, E., & Kulkarni, S. R. 2000, The Astrophysical Journal, 537, 191, doi: 10.1086/309024

Frail, D. A., Kulkarni, S. R., Sari, R., et al. 2001, The Astrophysical Journal Letters, 562, L55, doi: 10.1086/338119

Frederiks, D., Svinkin, D., Lysenko, A. L., et al. 2023a, arXiv e-prints, arXiv:2302.13383, doi: 10.48550/arXiv.2302.13383

—. 2023b, The Astrophysical Journal Letters, 949, L7, doi: 10.3847/2041-8213/acd1eb

Freeburn, J., Cooke, J., Möller, A., et al. 2024, Monthly Notices of the Royal Astronomical Society, 531, 4836, doi: 10.1093/mnras/stae1489

Fremling, C. 2018a, Transient Name Server Discovery Report, 2018-1058, 1

—. 2018b, Transient Name Server Discovery Report, 2018-1674, 1

—. 2020a, Transient Name Server Discovery Report, 2020-3102, 1

—. 2020b, Transient Name Server Discovery Report, 2020-3102, 1

Fremling, C., Dahiwale, A., & Dugas, A. 2019a, Transient Name Server Classification Report, 2019-1855, 1

Fremling, C., Dahiwale, A., & Sharma, Y. 2019b, Transient Name Server Classification Report, 2019-1757, 1

Fremling, C., Dugas, A., & Sharma, Y. 2018, Transient Name Server Classification Report, 2018-1877, 1

—. 2019c, Transient Name Server Classification Report, 2019-32, 1

Fremling, C., Sollerman, J., Taddia, F., et al. 2016, Astronomy and Astrophysics, 593, A68, doi: 10.1051/0004-6361/201628275

Fremling, C., Miller, A. A., Sharma, Y., et al. 2020, The Astrophysical Journal, 895, 32, doi: 10.3847/1538-4357/ab8943

Fryer, C. L., Andrews, S., Even, W., Heger, A., & Safi-Harb, S. 2018, The Astrophysical Journal, 856, 63, doi: 10.3847/1538-4357/aaaf6f

Fryer, C. L., Burns, E., Ho, A. Y. Q., et al. 2024a, arXiv e-prints, arXiv:2410.10378, doi: 10.48550/arXiv.2410.10378

Fryer, C. L., Hungerford, A. L., Wollaeger, R. T., et al. 2024b, The Astrophysical Journal, 961, 9, doi: 10.3847/1538-4357/ad1036

Fujibayashi, S., Lam, A. T.-L., Shibata, M., & Sekiguchi, Y. 2024, Physical Review D: Particles, Fields, Gravitation and Cosmology, 109, 023031, doi: 10.1103/PhysRevD.109.023031

Fujibayashi, S., Sekiguchi, Y., Shibata, M., & Wanajo, S. 2023, The Astrophysical Journal, 956, 100, doi: 10.3847/1538-4357/acf5e5

Fuller, J. 2017, Monthly Notices of the Royal Astronomical Society, 470, 1642, doi: 10.1093/mnras/stx1314

Fulton, M. D., Smartt, S. J., Rhodes, L., et al. 2023, arXiv e-prints, arXiv:2301.11170, doi: 10.48550/arXiv.2301.11170

Fynbo, J. P. U., Sollerman, J., Hjorth, J., et al. 2004, The Astrophysical Journal, 609, 962, doi: 10.1086/421260

Fynbo, J. P. U., Watson, D., Thöne, C. C., et al. 2006, Nature, 444, 1047, doi: 10.1038/nature05375

Gaensler, B. M., & Slane, P. O. 2006, Annual Review of Astronomy and Astrophysics, 44, 17, doi: 10.1146/annurev.astro.44.051905.092528

Gaia Collaboration. 2020, VizieR Online Data Catalog, I/350

Gaia Collaboration, Brown, A. G. A., Vallenari, A., et al. 2021, Astronomy and Astrophysics, 649, A1, doi: 10.1051/0004-6361/202039657

Gaia Collaboration, Montegriffo, P., Bellazzini, M., et al. 2023, Astronomy and Astrophysics, 674, A33, doi: 10.1051/0004-6361/202243709

Gal-Yam, A. 2012, Science, 337, 927, doi: 10.1126/science.1203601

—. 2017a, in Handbook of Supernovae, ed. A. W. Alsabti & P. Murdin, 195, doi: 10.1007/978-3-319-21846-5_35

—. 2017b, Observational and Physical Classification of Supernovae, ed. A. W. Alsabti & P. Murdin, 195, doi: 10.1007/978-3-319-21846-5_35

Gal-Yam, A., Fox, D. B., Price, P. A., et al. 2006, Nature, 444, 1053, doi: 10.1038/nature05373

Galama, T. J., Frail, D. A., Sari, R., et al. 2003, The Astrophysical Journal, 585, 899, doi: 10.1086/346083

Galama, T. J., Vreeswijk, P. M., van Paradijs, J., et al. 1998, Nature, 395, 670, doi: 10.1038/27150

Gehrels, N., Chincarini, G., Giommi, P., et al. 2004, The Astrophysical Journal, 611, 1005, doi: 10.1086/422091

Gehrels, N., Chincarini, G., Giommi, P., et al. 2004, The Astrophysical Journal, 611, 1005, doi: 10.1086/422091

Ghirlanda, G., & Salvaterra, R. 2022, The Astrophysical Journal, 932, 10, doi: 10.3847/1538-4357/ac6e43

Ghirlanda, G., Nappo, F., Ghisellini, G., et al. 2018, Astronomy and Astrophysics, 609, A112, doi: 10.1051/0004-6361/201731598

Gianfagna, G., Piro, L., Bruni, G., et al. 2025, arXiv e-prints, arXiv:2505.05444, doi: 10.48550/arXiv.2505.05444

Gill, R., & Granot, J. 2023, Monthly Notices of the Royal Astronomical Society, 524, L78, doi: 10.1093/mnrasl/slad075

Gill, R., Granot, J., & Kumar, P. 2020, Monthly Notices of the Royal Astronomical Society, 491, 3343, doi: 10.1093/mnras/stz2976

Gillanders, J. H., Troja, E., Fryer, C. L., et al. 2023, arXiv e-prints, arXiv:2308.00633, doi: 10.48550/arXiv.2308.00633

Gillanders, J. H., Rhodes, L., Srivastav, S., et al. 2024, The Astrophysical Journal Letters, 969, L14, doi: 10.3847/2041-8213/ad55cd

Gimeno, G., Roth, K., Chiboucas, K., et al. 2016, in Society of Photo-Optical Instrumentation Engineers (SPIE) Conference Series, Vol. 9908, Ground-based and Airborne Instrumentation for Astronomy VI, ed. C. J. Evans, L. Simard, & H. Takami, 99082S, doi: 10.1117/12.2233883

Ginsburg, A., & Mirocha, J. 2011, PySpecKit: Python Spectroscopic Toolkit, Astrophysics Source Code Library, record ascl:1109.001. http://ascl.net/1109.001

Ginsburg, A., Sokolov, V., de Val-Borro, M., et al. 2022, The Astronomical Journal, 163, 291, doi: 10.3847/1538-3881/ac695a

Goldstein, A., Cleveland, W. H., & Kocevski, D. 2022, Fermi GBM Data Tools: v1.1.1. https://fermi.gsfc.nasa.gov/ssc/data/analysis/gbm

Goldstein, A., Hamburg, R., Wood, J., et al. 2019, arXiv e-prints, arXiv:1903.12597, doi: 10.48550/arXiv.1903.12597

Goldwasser, S., Yaron, O., Sass, A., et al. 2022, Transient Name Server AstroNote, 191, 1

Gompertz, B. P., Fruchter, A. S., & Pe'er, A. 2018, The Astrophysical Journal, 866, 162, doi: 10.3847/1538-4357/aadba8

Gössl, C. A., & Riffeser, A. 2002, Astronomy and Astrophysics, 381, 1095, doi: 10.1051/0004-6361:20011522

Gottlieb, O. 2025, The Astrophysical Journal Letters, 992, L3, doi: 10.3847/2041-8213/ae09af

Gottlieb, O., Liska, M., Tchekhovskoy, A., et al. 2022, The Astrophysical Journal Letters, 933, L9, doi: 10.3847/2041-8213/ac753010.48550/arXiv.2204.12501

Gottlieb, O., Nakar, E., & Bromberg, O. 2021, Monthly Notices of the Royal Astronomical Society, 500, 3511, doi: 10.1093/mnras/staa350110.48550/arXiv.2006.02466

Gottlieb, O., Nakar, E., & Piran, T. 2018a, Monthly Notices of the Royal Astronomical Society, 473, 576, doi: 10.1093/mnras/stx2357

Gottlieb, O., Nakar, E., Piran, T., & Hotokezaka, K. 2018b, Monthly Notices of the Royal Astronomical Society, 479, 588, doi: 10.1093/mnras/sty1462

Gottlieb, O., Renzo, M., Metzger, B. D., Goldberg, J. A., & Cantiello, M. 2024, The Astrophysical Journal Letters, 976, L13, doi: 10.3847/2041-8213/ad8563

Gottlieb, O., Issa, D., Jacquemin-Ide, J., et al. 2023, The Astrophysical Journal Letters, 953, L11, doi: 10.3847/2041-8213/acec4a

Graham, M. J., Kulkarni, S. R., Bellm, E. C., et al. 2019, Publications of the Astronomical Society of the Pacific, 131, 078001, doi: 10.1088/1538-3873/ab006c

Granot, J., & Ramirez-Ruiz, E. 2010, arXiv e-prints, arXiv:1012.5101, doi: 10.48550/arXiv.1012.5101

Granot, J., & Sari, R. 2002, The Astrophysical Journal, 568, 820, doi: 10.1086/338966

Granot, J., & van der Horst, A. J. 2014a, Publications of the Astronomical Society of Australia, 31, e008, doi: 10.1017/pasa.2013.44

—. 2014b, Publications of the Astronomical Society of Australia, 31, e008, doi: 10.1017/pasa.2013.44

Grasberg, E. K., & Nadezhin, D. K. 1976, , 44, 409, doi: 10.1007/BF00642529

Greiner, J., Krühler, T., McBreen, S., et al. 2009, The Astrophysical Journal, 693, 1912, doi: 10.1088/0004-637X/693/2/1912

Greiner, J., Mazzali, P. A., Kann, D. A., et al. 2015a, Nature, 523, 189, doi: 10.1038/nature14579

—. 2015b, Nature, 523, 189, doi: 10.1038/nature14579

Greisen, E. W. 2003, in Astrophysics and Space Science Library, Vol. 285, Information Handling in Astronomy - Historical Vistas, ed. A. Heck, 109, doi: 10.1007/0-306-48080-8_7

Groot, P. J., Vreeswijk, P. M., Ter Horst, R., et al. 2022, GRB Coordinates Network, 32678, 1

Guetta, D., & Della Valle, M. 2007, The Astrophysical Journal Letters, 657, L73, doi: 10.1086/511417

Gupta, R., Ror, A. K., Pandey, S. B., et al. 2022a, GRB Coordinates Network, 32811, 1

Gupta, R., Kumar, A., Pandey, S. B., et al. 2022b, Journal of Astrophysics and Astronomy, 43, 11, doi: 10.1007/s12036-021-09794-4

Hall, X. J., Ahumada, T., & Stein, R. 2025, GRB Coordinates Network, 41641, 1. https://ui.adsabs.harvard.edu/abs/2025GCN.41641....1H

Hallinan, G., Ravi, V., Weinreb, S., et al. 2019, in Bulletin of the American Astronomical Society, Vol. 51, 255, doi: 10.48550/arXiv.1907.07648

Hamidani, H., & Ioka, K. 2021, Monthly Notices of the Royal Astronomical Society, 500, 627, doi: 10.1093/mnras/staa3276

—. 2023a, Monthly Notices of the Royal Astronomical Society, 520, 1111, doi: 10.1093/mnras/stad041

—. 2023b, Monthly Notices of the Royal Astronomical Society, 524, 4841, doi: 10.1093/mnras/stad1933

Hamidani, H., Ioka, K., Kashiyama, K., & Tanaka, M. 2025a, arXiv e-prints, arXiv:2503.16242, doi: 10.48550/arXiv.2503.16242

Hamidani, H., Sato, Y., Kashiyama, K., et al. 2025b, arXiv e-prints, arXiv:2503.16243, doi: 10.48550/arXiv.2503.16243

Hamuy, M., Pinto, P. A., Maza, J., et al. 2001, The Astrophysical Journal, 558, 615, doi: 10.1086/322450

Harris, C. R., Millman, K. J., van der Walt, S. J., et al. 2020, Nature, 585, 357, doi: 10.1038/s41586-020-2649-2

Harrison, R., Gottlieb, O., & Nakar, E. 2018, Monthly Notices of the Royal Astronomical Society, 477, 2128, doi: 10.1093/mnras/sty760

Haynie, A., & Piro, A. L. 2021, The Astrophysical Journal, 910, 128, doi: 10.3847/1538-4357/abe938

Heger, A., Fryer, C. L., Woosley, S. E., Langer, N., & Hartmann, D. H. 2003, The Astrophysical Journal, 591, 288, doi: 10.1086/375341

Heger, A., Woosley, S. E., & Spruit, H. C. 2005, The Astrophysical Journal, 626, 350, doi: 10.1086/429868

Heise, J., Zand, J. I., Kippen, R. M., & Woods, P. M. 2001, in Gamma-ray Bursts in the Afterglow Era, ed. E. Costa, F. Frontera, & J. Hjorth, 16, doi: 10.1007/10853853_4

Hickish, J., Razavi-Ghods, N., Perrott, Y. C., et al. 2018, Monthly Notices of the Royal Astronomical Society, 475, 5677, doi: 10.1093/mnras/sty074

Hjorth, J. 2013, Philosophical Transactions of the Royal Society of London Series A, 371, 20120275, doi: 10.1098/rsta.2012.0275

Hjorth, J., & Bloom, J. S. 2012, in Chapter 9 in "Gamma-Ray Bursts, ed. C. Kouveliotou, R. A. M. J. Wijers, & S. Woosley, 169–190, doi: 10.48550/arXiv.1104.2274

Hjorth, J., Sollerman, J., Møller, P., et al. 2003, Nature, 423, 847, doi: 10.1038/nature01750

Ho, A. Y. Q., Goldstein, D. A., Schulze, S., et al. 2019a, The Astrophysical Journal, 887, 169, doi: 10.3847/1538-4357/ab55ec

—. 2019b, The Astrophysical Journal, 887, 169, doi: 10.3847/1538-4357/ab55ec

Ho, A. Y. Q., Corsi, A., Cenko, S. B., et al. 2020a, The Astrophysical Journal, 893, 132, doi: 10.3847/1538-4357/ab7f3b

—. 2020b, The Astrophysical Journal, 893, 132, doi: 10.3847/1538-4357/ab7f3b

Ho, A. Y. Q., Kulkarni, S. R., Perley, D. A., et al. 2020c, The Astrophysical Journal, 902, 86, doi: 10.3847/1538-4357/aba630

Ho, A. Y. Q., Perley, D. A., Beniamini, P., et al. 2020d, The Astrophysical Journal, 905, 98, doi: 10.3847/1538-4357/abc34d

Ho, A. Y. Q., Kulkarni, S. R., Perley, D. A., et al. 2020e, The Astrophysical Journal, 902, 86, doi: 10.3847/1538-4357/aba630

—. 2020f, The Astrophysical Journal, 902, 86, doi: 10.3847/1538-4357/aba630

Ho, A. Y. Q., Perley, D. A., Yao, Y., et al. 2022, The Astrophysical Journal, 938, 85, doi: 10.3847/1538-4357/ac8bd0

Ho, A. Y. Q., Perley, D. A., Gal-Yam, A., et al. 2023, The Astrophysical Journal, 949, 120, doi: 10.3847/1538-4357/acc533

Hook, I. M., Jørgensen, I., Allington-Smith, J. R., et al. 2004, Publications of the Astronomical Society of the Pacific, 116, 425, doi: 10.1086/383624

Hopp, U., Bender, R., Grupp, F., et al. 2014, in Society of Photo-Optical Instrumentation Engineers (SPIE) Conference Series, Vol. 9145, Ground-based and Airborne Telescopes V, ed. L. M. Stepp, R. Gilmozzi, & H. J. Hall, 91452D, doi: 10.1117/12.2054498

Horne, K. 1986, Publications of the Astronomical Society of the Pacific, 98, 609, doi: 10.1086/131801

Howell, D. A., & Global Supernova Project. 2017, in American Astronomical Society Meeting Abstracts, Vol. 230, American Astronomical Society Meeting Abstracts #230, 318.03

Hu, L., Wang, L., Chen, X., & Yang, J. 2019, 936, 157, doi: 10.3847/1538-4357/ac7394

Hu, L., Wang, L., Chen, X., & Yang, J. 2022, The Astrophysical Journal, 936, 157, doi: 10.3847/1538-4357/ac7394

Hu, Y. D., Castro-Tirado, A. J., Kumar, A., et al. 2021, Astronomy and Astrophysics, 646, A50, doi: 10.1051/0004-6361/202039349

Huang, Y.-J., Urata, Y., Huang, K., et al. 2020, The Astrophysical Journal, 897, 69, doi: 10.3847/1538-4357/ab8f9a

Huber, M., Schultz, A., Chambers, K. C., et al. 2022, GRB Coordinates Network, 32758, 1

Hunter, J. D. 2007, Computing in Science & Engineering, 9, 90, doi: 10.1109/MCSE.2007.55

Hussenot-Desenonges, T., Wouters, T., Guessom, N., et al. 2023

Im, M., Paek, G. S. H., Lim, G., et al. 2022, GRB Coordinates Network, 32803, 1

Irwin, C. M., & Hotokezaka, K. 2024, arXiv e-prints, arXiv:2412.06736, doi: 10.48550/arXiv.2412.06736

—. 2025, Monthly Notices of the Royal Astronomical Society, 543, 2917, doi: 10.1093/mnras/staf1618

Issa, D., Gottlieb, O., Metzger, B. D., et al. 2025, The Astrophysical Journal Letters, 985, L26, doi: 10.3847/2041-8213/adc694

Ito, H., Levinson, A., & Nakar, E. 2020, Monthly Notices of the Royal Astronomical Society, 499, 4961, doi: 10.1093/mnras/staa3125

Ivezić, Ž., Kahn, S. M., Tyson, J. A., et al. 2019a, The Astrophysical Journal, 873, 111, doi: 10.3847/1538-4357/ab042c

—. 2019b, The Astrophysical Journal, 873, 111, doi: 10.3847/1538-4357/ab042c

Iwamoto, K., Mazzali, P. A., Nomoto, K., et al. 1998a, Nature, 395, 672, doi: 10.1038/27155

—. 1998b, Nature, 395, 672, doi: 10.1038/27155

Izzo, L. 2025, GRB Coordinates Network, 38912, 1

Izzo, L., Auchettl, K., Hjorth, J., et al. 2020, Astronomy and Astrophysics, 639, L11, doi: 10.1051/0004-6361/202038152

Izzo, L., Saccardi, A., Fynbo, J. P. U., et al. 2022, GRB Coordinates Network, 32765, 1

Izzo, L., Martin-Carrillo, A., Malesani, D. B., et al. 2025, GRB Coordinates Network, 39851, 1

Jakobsson, P., Levan, A., Fynbo, J. P. U., et al. 2006, Astronomy and Astrophysics, 447, 897, doi: 10.1051/0004-6361:20054287

Janka, H.-T. 2017, in Handbook of Supernovae, ed. A. W. Alsabti & P. Murdin, 1095, doi: 10.1007/978-3-319-21846-5_109

Janka, H.-T., Langanke, K., Marek, A., Martínez-Pinedo, G., & Müller, B. 2007, , 442, 38, doi: 10.1016/j.physrep.2007.02.002

Jerkstrand, A., Milisavljevic, D., & Müller, B. 2026, in Encyclopedia of Astrophysics, Volume 2, Vol. 2, 639–668, doi: 10.1016/B978-0-443-21439-4.00090-0

Jester, S., Schneider, D. P., Richards, G. T., et al. 2005, The Astronomical Journal, 130, 873, doi: 10.1086/432466

Jiang, H., Hu, Z., Xu, M., et al. 2018, in Society of Photo-Optical Instrumentation Engineers (SPIE) Conference Series, Vol. 10702, Ground-based and Airborne Instrumentation for Astronomy VII, ed. C. J. Evans, L. Simard, & H. Takami, 107022L, doi: 10.1117/12.2312550

Jiang, S.-Q., Xu, D., van Hoof, A. P. C., et al. 2025, arXiv e-prints, arXiv:2503.04306, doi: 10.48550/arXiv.2503.04306

Johnson, B. D., Leja, J., Conroy, C., & Speagle, J. S. 2021a, The Astrophysical Journal Supplement, 254, 22, doi: 10.3847/1538-4365/abef67

—. 2021b, The Astrophysical Journal Supplement, 254, 22, doi: 10.3847/1538-4365/abef67

Kangas, T., & Fruchter, A. S. 2021, The Astrophysical Journal, 911, 14, doi: 10.3847/1538-4357/abe76b

Kann, D. A., Masetti, N., & Klose, S. 2007, The Astronomical Journal, 133, 1187, doi: 10.1086/511066

Kann, D. A., Schady, P., Olivares E., F., et al. 2019, Astronomy and Astrophysics, 624, A143, doi: 10.1051/0004-6361/201629162

Kann, D. A., Agayeva, S., Aivazyan, V., et al. 2023, The Astrophysical Journal Letters, 948, L12, doi: 10.3847/2041-8213/acc8d0

Kansky, J., Chilingarian, I., Fabricant, D., et al. 2019, Publications of the Astronomical Society of the Pacific, 131, 075005, doi: 10.1088/1538-3873/ab1ceb

Kasen, D., & Bildsten, L. 2010, The Astrophysical Journal, 717, 245, doi: 10.1088/0004-637X/717/1/245

Kasliwal, M. M., Cannella, C., Bagdasaryan, A., et al. 2019a, Publications of the Astronomical Society of the Pacific, 131, 038003, doi: 10.1088/1538-3873/aafbc2

—. 2019b, Publications of the Astronomical Society of the Pacific, 131, 038003, doi: 10.1088/1538-3873/aafbc2

Kasliwal, M. M., Anand, S., Ahumada, T., et al. 2020, The Astrophysical Journal, 905, 145

Kasliwal, M. M., Fremling, C., Yan, L., et al. 2024, Transient Name Server AstroNote, 340, 1

Katz, B., Budnik, R., & Waxman, E. 2010, The Astrophysical Journal, 716, 781, doi: 10.1088/0004-637X/716/1/781

Kelly, B. C. 2007, The Astrophysical Journal, 665, 1489, doi: 10.1086/519947

Kennicutt, Jr., R. C. 1998, Annual Review of Astronomy and Astrophysics, 36, 189, doi: 10.1146/annurev.astro.36.1.189

Kim, V., Krugov, M., Pozanenko, A., et al. 2022a, GRB Coordinates Network, 32670, 1

Kim, Y. L., Rigault, M., Neill, J. D., et al. 2022b, Publications of the Astronomical Society of the Pacific, 134, 024505, doi: 10.1088/1538-3873/ac50a0

Kisaka, S., Ioka, K., & Takami, H. 2015, The Astrophysical Journal, 802, 119, doi: 10.1088/0004-637X/802/2/119

Klose, S., Schmidl, S., Kann, D. A., et al. 2019, Astronomy and Astrophysics, 622, A138, doi: 10.1051/0004-6361/201832728

Kouveliotou, C., Woosley, S. E., Patel, S. K., et al. 2004, The Astrophysical Journal, 608, 872, doi: 10.1086/420878

Kowalski, A. F., Hawley, S. L., Wisniewski, J. P., et al. 2013, The Astrophysical Journal Supplement, 207, 15, doi: 10.1088/0067-0049/207/1/15

Kulkarni, S. R., Frail, D. A., Wieringa, M. H., et al. 1998, Nature, 395, 663, doi: 10.1038/27139

Kulkarni, S. R., Harrison, F. A., Grefenstette, B. W., et al. 2021, arXiv e-prints, arXiv:2111.15608, doi: 10.48550/arXiv.2111.15608

Kumar, A., Maund, J. R., Sun, N. C., et al. 2025, GRB Coordinates Network, 38907, 1

Kumar, A., Pandey, S. B., Gupta, R., et al. 2022a, , 97, 101889, doi: 10.1016/j.newast.2022.101889

Kumar, H., Swain, V., Waratkar, G., et al. 2022b, GRB Coordinates Network, 32662, 1

Kumar, H., Bhalerao, V., Anupama, G. C., et al. 2022c, The Astronomical Journal, 164, 90, doi: 10.3847/1538-3881/ac7bea

—. 2022d, Monthly Notices of the Royal Astronomical Society, 516, 4517, doi: 10.1093/mnras/stac2516

Kumar, P. 1999, The Astrophysical Journal Letters, 523, L113, doi: 10.1086/312265

Kuroda, T., Arcones, A., Takiwaki, T., & Kotake, K. 2020, The Astrophysical Journal, 896, 102, doi: 10.3847/1538-4357/ab9308

Labrie, K., Anderson, K., Cárdenes, R., Simpson, C., & Turner, J. E. H. 2019, in Astronomical Society of the Pacific Conference Series, Vol. 523, Astronomical Data Analysis Software and Systems XXVII, ed. P. J. Teuben, M. W. Pound, B. A. Thomas, & E. M. Warner, 321

Labrie, K., Simpson, C., Cardenes, R., et al. 2023, Research Notes of the American Astronomical Society, 7, 214, doi: 10.3847/2515-5172/ad0044

Lamb, G. P., & Kobayashi, S. 2016, The Astrophysical Journal, 829, 112, doi: 10.3847/0004-637X/829/2/112

—. 2017a, Monthly Notices of the Royal Astronomical Society, 472, 4953, doi: 10.1093/mnras/stx2345

—. 2017b, Monthly Notices of the Royal Astronomical Society, 472, 4953, doi: 10.1093/mnras/stx2345

Lamb, G. P., Tanaka, M., & Kobayashi, S. 2018a, Monthly Notices of the Royal Astronomical Society, 476, 4435, doi: 10.1093/mnras/sty484

—. 2018b, Monthly Notices of the Royal Astronomical Society, 476, 4435, doi: 10.1093/mnras/sty484

Lang, D., Hogg, D. W., Mierle, K., Blanton, M., & Roweis, S. 2010a, The Astronomical Journal, 139, 1782, doi: 10.1088/0004-6256/139/5/1782

—. 2010b, The Astronomical Journal, 139, 1782, doi: 10.1088/0004-6256/139/5/1782

Lang-Bardl, F., Bender, R., Goessl, C., et al. 2016, in Ground-based and Airborne Instrumentation for Astronomy VI, Vol. 9908, SPIE, 1295–1302

Laskar, T., Alexander, K. D., Ayache, E., et al. 2022, GRB Coordinates Network, 32757, 1

Laskar, T., Alexander, K. D., Margutti, R., et al. 2023, arXiv e-prints, arXiv:2302.04388, doi: 10.48550/arXiv.2302.04388

Lazzati, D., Morsony, B. J., Blackwell, C. H., & Begelman, M. C. 2012, The Astrophysical Journal, 750, 68, doi: 10.1088/0004-637X/750/1/68

Lazzati, D., Perna, R., Morsony, B. J., et al. 2018, , 120, 241103, doi: 10.1103/PhysRevLett.120.241103

Lesage, S., Burns, E., Dalessi, S., Roberts, O., & Fermi GBM Team. 2023a, GRB Coordinates Network, 34387, 1

Lesage, S., Veres, P., Roberts, O. J., et al. 2022, GRB Coordinates Network, 32642, 1

Lesage, S., Veres, P., Briggs, M. S., et al. 2023b, The Astrophysical Journal Letters, 952, L42, doi: 10.3847/2041-8213/ace5b4

Leśniewska, A., Michałowski, M. J., Kamphuis, P., et al. 2022, The Astrophysical Journal Supplement, 259, 67, doi: 10.3847/1538-4365/ac5022

Leung, S.-C., Fuller, J., & Nomoto, K. 2021a, The Astrophysical Journal, 915, 80, doi: 10.3847/1538-4357/abfcbe

—. 2021b, The Astrophysical Journal, 915, 80, doi: 10.3847/1538-4357/abfcbe

Levan, A., Nugent, P., Fruchter, A., et al. 2005, The Astrophysical Journal, 624, 880, doi: 10.1086/428657

Levan, A., Gompertz, B. P., Salafia, O. S., et al. 2023a, arXiv e-prints, arXiv:2307.02098, doi: 10.48550/arXiv.2307.02098

Levan, A. J., Cotter, L., Malesani, D. B., Martin-Carrillo, A., & Jonker, P. G. 2025, GRB Coordinates Network, 38909, 1

Levan, A. J., Lamb, G. P., Schneider, B., et al. 2023b, arXiv e-prints, arXiv:2302.07761. https://arxiv.org/abs/2302.07761

Levinson, A., & Nakar, E. 2020, , 866, 1, doi: 10.1016/j.physrep.2020.04.003

LHAASO Collaboration, Cao, Z., Aharonian, F., et al. 2023, Science, 380, 1390, doi: 10.1126/science.adg9328

Li, L., Zhong, S.-Q., & Dai, Z.-G. 2023, The Astrophysical Journal Letters, 952, L39, doi: 10.3847/2041-8213/ace82b

Li, M. L., Ho, A. Y. Q., Ryan, G., et al. 2024, arXiv e-prints, arXiv:2411.07973. https://arxiv.org/abs/2411.07973

Li, R. Z., Chen, X. L., Chatterjee, K., et al. 2025a, GRB Coordinates Network, 38861, 1

—. 2025b, GRB Coordinates Network, 38888, 1

Li, W., Leaman, J., Chornock, R., et al. 2011, Monthly Notices of the Royal Astronomical Society, 412, 1441, doi: 10.1111/j.1365-2966.2011.18160.x

Li, W. X., Zhu, Z. P., Zou, X. Z., et al. 2025c, arXiv e-prints, arXiv:2504.17034, doi: 10.48550/arXiv.2504.17034

Li, X., & Hjorth, J. 2014, arXiv e-prints, arXiv:1407.3506, doi: 10.48550/arXiv.1407.3506

Liang, E., Zhang, B., Virgili, F., & Dai, Z. G. 2007, The Astrophysical Journal, 662, 1111, doi: 10.1086/517959

Lin, D., Irwin, J. A., Berger, E., & Nguyen, R. 2022, The Astrophysical Journal, 927, 211, doi: 10.3847/1538-4357/ac4fc6

Lindegren, L., Klioner, S. A., Hernández, J., et al. 2021, Astronomy and Astrophysics, 649, A2, doi: 10.1051/0004-6361/202039709

Lipunov, V., Kornilov, V., Zhirkov, K., et al. 2022, Monthly Notices of the Royal Astronomical Society, 516, 4980, doi: 10.1093/mnras/stac1906

Lipunov, V., Kornilov, V., Gorbovskoy, E., et al. 2023a, GRB Coordinates Network, 34389, 1

Lipunov, V., Svinkin, D., Kuznetsov, A., et al. 2023b, GRB Coordinates Network, 34396, 1

Liu, Y., Sun, H., Xu, D., et al. 2025, Nature Astronomy, doi: 10.1038/s41550-024-02449-8

Liu, Y.-Q., Modjaz, M., Bianco, F. B., & Graur, O. 2016, The Astrophysical Journal, 827, 90, doi: 10.3847/0004-637X/827/2/90

Lü, H.-J., Lan, L., Zhang, B., et al. 2018, The Astrophysical Journal, 862, 130, doi: 10.3847/1538-4357/aacd03

Lu, W., & Quataert, E. 2023, Monthly Notices of the Royal Astronomical Society, 522, 5848, doi: 10.1093/mnras/stad1336

Lyman, J. D., Bersier, D., & James, P. A. 2014a, Monthly Notices of the Royal Astronomical Society, 437, 3848, doi: 10.1093/mnras/stt2187

—. 2014b, Monthly Notices of the Royal Astronomical Society, 437, 3848, doi: 10.1093/mnras/stt2187

Lyman, J. D., Bersier, D., James, P. A., et al. 2016a, Monthly Notices of the Royal Astronomical Society, 457, 328, doi: 10.1093/mnras/stv2983

—. 2016b, Monthly Notices of the Royal Astronomical Society, 457, 328, doi: 10.1093/mnras/stv2983

MacFadyen, A. I., & Woosley, S. E. 1999, The Astrophysical Journal, 524, 262, doi: 10.1086/307790

Maeda, K., Suzuki, A., & Izzo, L. 2023, Monthly Notices of the Royal Astronomical Society, 522, 2267, doi: 10.1093/mnras/stad1075

Mahabal, A., Rebbapragada, U., Walters, R., et al. 2019, Publications of the Astronomical Society of the Pacific, 131, 038002, doi: 10.1088/1538-3873/aaf3fa

Malesani, D., Tagliaferri, G., Chincarini, G., et al. 2004, The Astrophysical Journal Letters, 609, L5, doi: 10.1086/422684

Malesani, D., Fynbo, J. P. U., Hjorth, J., et al. 2009, The Astrophysical Journal Letters, 692, L84, doi: 10.1088/0004-637X/692/2/L84

Malesani, D. B., Levan, A. J., Izzo, L., et al. 2023a, arXiv e-prints, arXiv:2302.07891, doi: 10.48550/arXiv.2302.07891

—. 2023b, arXiv e-prints, arXiv:2302.07891, doi: 10.48550/arXiv.2302.07891

Mangan, J., Dunwoody, R., Meegan, C., & Fermi GBM Team. 2021, GRB Coordinates Network, 31210, 1

Margalit, B. 2022, The Astrophysical Journal, 933, 238, doi: 10.3847/1538-4357/ac771a

Margutti, R., Milisavljevic, D., Soderberg, A. M., et al. 2014, The Astrophysical Journal, 797, 107, doi: 10.1088/0004-637X/797/2/107

Margutti, R., Guidorzi, C., Lazzati, D., et al. 2015, The Astrophysical Journal, 805, 159, doi: 10.1088/0004-637X/805/2/159

Margutti, R., Alexander, K. D., Xie, X., et al. 2018, The Astrophysical Journal Letters, 856, L18, doi: 10.3847/2041-8213/aab2ad

Margutti, R., Metzger, B. D., Chornock, R., et al. 2019, The Astrophysical Journal, 872, 18, doi: 10.3847/1538-4357/aafa01

Masci, F. J., Laher, R. R., Rusholme, B., et al. 2019, Publications of the Astronomical Society of the Pacific, 131, 018003, doi: 10.1088/1538-3873/aae8ac

Matheson, T., Garnavich, P. M., Stanek, K. Z., et al. 2003, The Astrophysical Journal, 599, 394, doi: 10.1086/379228

Matsumoto, T., Nakar, E., & Piran, T. 2019, Monthly Notices of the Royal Astronomical Society, 486, 1563, doi: 10.1093/mnras/stz923

Matsuoka, M., Kawasaki, K., Ueno, S., et al. 2009, , 61, 999, doi: 10.1093/pasj/61.5.999

Matzner, C. D. 2003, Monthly Notices of the Royal Astronomical Society, 345, 575, doi: 10.1046/j.1365-8711.2003.06969.x

Maund, J. R., Wheeler, J. C., Baade, D., et al. 2009, The Astrophysical Journal, 705, 1139, doi: 10.1088/0004-637X/705/2/1139

Mazzali, P. A. 2000, Astronomy and Astrophysics, 363, 705

Mazzali, P. A., Deng, J., Maeda, K., et al. 2002, The Astrophysical Journal Letters, 572, L61, doi: 10.1086/341504

Mazzali, P. A., Deng, J., Tominaga, N., et al. 2003, The Astrophysical Journal Letters, 599, L95, doi: 10.1086/381259

Mazzali, P. A., Deng, J., Nomoto, K., et al. 2006a, Nature, 442, 1018, doi: 10.1038/nature05081

Mazzali, P. A., Deng, J., Pian, E., et al. 2006b, The Astrophysical Journal, 645, 1323, doi: 10.1086/504415

Mazzali, P. A., Deng, J., Nomoto, K., et al. 2006c, Nature, 442, 1018, doi: 10.1038/nature05081

Mazzali, P. A., Valenti, S., Della Valle, M., et al. 2008, Science, 321, 1185, doi: 10.1126/science.1158088

McCully, C., & Tewes, M. 2019, Astro-SCRAPPY: Speedy Cosmic Ray Annihilation Package in Python, Astrophysics Source Code Library. http://ascl.net/1907.032

McMullin, J. P., Waters, B., Schiebel, D., Young, W., & Golap, K. 2007a, in Astronomical Society of the Pacific Conference Series, Vol. 376, Astronomical Data Analysis Software and Systems XVI, ed. R. A. Shaw, F. Hill, & D. J. Bell, 127

McMullin, J. P., Waters, B., Schiebel, D., Young, W., & Golap, K. 2007b, in Astronomical Society of the Pacific Conference Series, Vol. 376, Astronomical Data Analysis Software and Systems XVI, ed. R. A. Shaw, F. Hill, & D. J. Bell, 127

Meegan, C., Lichti, G., Bhat, P. N., et al. 2009, The Astrophysical Journal, 702, 791, doi: 10.1088/0004-637X/702/1/791

Melandri, A., Pian, E., Ferrero, P., et al. 2012, Astronomy and Astrophysics, 547, A82, doi: 10.1051/0004-6361/201219879

Melandri, A., Malesani, D. B., Izzo, L., et al. 2019a, Monthly Notices of the Royal Astronomical Society, 490, 5366, doi: 10.1093/mnras/stz2900

Melandri, A., Rossi, A., Benetti, S., et al. 2019b, Astronomy and Astrophysics, 621, A81, doi: 10.1051/0004-6361/201833814

Mészáros, P., & Rees, M. J. 1997, The Astrophysical Journal, 476, 232, doi: 10.1086/303625

Mészáros, P., Rees, M. J., & Wijers, R. A. M. J. 1998, The Astrophysical Journal, 499, 301, doi: 10.1086/305635

Metzger, B. D. 2019, Living Reviews in Relativity, 23, 1, doi: 10.1007/s41114-019-0024-0

Metzger, B. D., Margalit, B., Kasen, D., & Quataert, E. 2015, Monthly Notices of the Royal Astronomical Society, 454, 3311, doi: 10.1093/mnras/stv2224

Metzger, B. D., Vurm, I., Hascoët, R., & Beloborodov, A. M. 2014, Monthly Notices of the Royal Astronomical Society, 437, 703, doi: 10.1093/mnras/stt1922

MichałowskI, M. J., Xu, D., Stevens, J., et al. 2018, Astronomy and Astrophysics, 616, A169, doi: 10.1051/0004-6361/201629942

Miller, A. A., Yao, Y., Bulla, M., et al. 2020, The Astrophysical Journal, 902, 47, doi: 10.3847/1538-4357/abb13b

Miller, A. A., Abrams, N. S., Aldering, G., et al. 2025, Publications of the Astronomical Society of the Pacific, 137, 094204, doi: 10.1088/1538-3873/ae02c5

Minaev, P. Y., & Pozanenko, A. S. 2020, Monthly Notices of the Royal Astronomical Society, 492, 1919, doi: 10.1093/mnras/stz3611

Mirabal, N., Halpern, J. P., An, D., Thorstensen, J. R., & Terndrup, D. M. 2006, The Astrophysical Journal Letters, 643, L99, doi: 10.1086/505177

Modjaz, M., Gutiérrez, C. P., & Arcavi, I. 2019, Nature Astronomy, 3, 717, doi: 10.1038/s41550-019-0856-2

Modjaz, M., Liu, Y. Q., Bianco, F. B., & Graur, O. 2016, The Astrophysical Journal, 832, 108, doi: 10.3847/0004-637X/832/2/108

Modjaz, M., Stanek, K. Z., Garnavich, P. M., et al. 2006, The Astrophysical Journal Letters, 645, L21, doi: 10.1086/505906

Modjaz, M., Li, W., Butler, N., et al. 2009, The Astrophysical Journal, 702, 226, doi: 10.1088/0004-637X/702/1/226

Moriya, T. J., Müller, B., Chan, C., Heger, A., & Blinnikov, S. I. 2019, The Astrophysical Journal, 880, 21, doi: 10.3847/1538-4357/ab2643

Moskvitin, A. S., Spiridonova, O. I., & GRB follow-up Team. 2025, GRB Coordinates Network, 38925, 1

Mösta, P., Ott, C. D., Radice, D., et al. 2015, Nature, 528, 376, doi: 10.1038/nature15755

Mösta, P., Roberts, L. F., Halevi, G., et al. 2018, The Astrophysical Journal, 864, 171, doi: 10.3847/1538-4357/aad6ec

Mösta, P., Richers, S., Ott, C. D., et al. 2014, The Astrophysical Journal Letters, 785, L29, doi: 10.1088/2041-8205/785/2/L29

Murase, K., Kashiyama, K., & Mészáros, P. 2016, Monthly Notices of the Royal Astronomical Society, 461, 1498, doi: 10.1093/mnras/stw1328

Mészáros, P. 2006, Reports on Progress in Physics, 69, 2259–2321, doi: 10.1088/0034-4885/69/8/r01

Nagy, A. P. 2018, The Astrophysical Journal, 862, 143, doi: 10.3847/1538-4357/aace56

Nakar, E. 2015, The Astrophysical Journal, 807, 172, doi: 10.1088/0004-637X/807/2/172

Nakar, E., & Piran, T. 2003, , 8, 141, doi: 10.1016/S1384-1076(02)00202-6

—. 2017, The Astrophysical Journal, 834, 28, doi: 10.3847/1538-4357/834/1/28

Nakar, E., Piran, T., & Granot, J. 2002, The Astrophysical Journal, 579, 699, doi: 10.1086/342791

Nakar, E., & Piro, A. L. 2014, The Astrophysical Journal, 788, 193, doi: 10.1088/0004-637X/788/2/193

Nakar, E., & Sari, R. 2010, The Astrophysical Journal, 725, 904, doi: 10.1088/0004-637X/725/1/904

—. 2012, The Astrophysical Journal, 747, 88, doi: 10.1088/0004-637X/747/2/88

Nasa High Energy Astrophysics Science Archive Research Center (Heasarc). 2014, HEAsoft: Unified Release of FTOOLS and XANADU, Astrophysics Source Code Library, record ascl:1408.004. http://ascl.net/1408.004

Navaneeth, P. K., Waratkar, G., Vibhute, A., et al. 2023, GRB Coordinates Network, 34725

Nayana, A. J., Chandra, P., Roy, S., et al. 2017, Monthly Notices of the Royal Astronomical Society, 467, 155, doi: 10.1093/mnras/stx044

Negoro, H., Kohama, M., Serino, M., et al. 2016, , 68, S1, doi: 10.1093/pasj/psw016

Niblett, A. E., Fryer, D. A., & Fryer, C. L. 2025, arXiv e-prints, arXiv:2501.15702, doi: 10.48550/arXiv.2501.15702

Nicholl, M., Guillochon, J., & Berger, E. 2017, The Astrophysical Journal, 850, 55, doi: 10.3847/1538-4357/aa9334

Nordin, J., Brinnel, V., Giomi, M., et al. 2019, Transient Name Server Discovery Report, 2019-1202, 1

—. 2020, Transient Name Server Discovery Report, 2020-1112, 1

Nugent, P., Phillips, M., Baron, E., Branch, D., & Hauschildt, P. 1995, The Astrophysical Journal Letters, 455, L147, doi: 10.1086/309846

Nugis, T., & Lamers, H. J. G. L. M. 2000, Astronomy and Astrophysics, 360, 227

Nysewander, M., Fruchter, A. S., & Pe'er, A. 2009, The Astrophysical Journal, 701, 824, doi: 10.1088/0004-637X/701/1/824

Oates, S. R., Page, M. J., Schady, P., et al. 2009, Monthly Notices of the Royal Astronomical Society, 395, 490, doi: 10.1111/j.1365-2966.2009.14544.x

Obergaulinger, M., & Aloy, M. Á. 2022, Monthly Notices of the Royal Astronomical Society, 512, 2489, doi: 10.1093/mnras/stac613

O'Connor, B., Beniamini, P., & Gill, R. 2024, Monthly Notices of the Royal Astronomical Society, 533, 1629, doi: 10.1093/mnras/stae1941

O'Connor, B., Cenko, S. B., Troja, E., et al. 2022a, GRB Coordinates Network, 32739, 1

—. 2022b, GRB Coordinates Network, 32799, 1

O'Connor, B., Troja, E., Ryan, G., et al. 2023, Science Advances, 9, eadi1405, doi: 10.1126/sciadv.adi1405

O'Connor, B., Pasham, D., Andreoni, I., et al. 2025a, The Astrophysical Journal Letters, 979, L30, doi: 10.3847/2041-8213/ada7f5

O'Connor, B., Beniamini, P., Troja, E., et al. 2025b, The Astrophysical Journal Letters, 993, L37, doi: 10.3847/2041-8213/ae146b

Ohyama, N. 1963, Progress of Theoretical Physics, 30, 170, doi: 10.1143/PTP.30.170

Oke, J. B., & Gunn, J. E. 1982, Publications of the Astronomical Society of the Pacific, 94, 586, doi: 10.1086/131027

Oke, J. B., Cohen, J. G., Carr, M., et al. 1995a, Publications of the Astronomical Society of the Pacific, 107, 375, doi: 10.1086/133562

—. 1995b, Publications of the Astronomical Society of the Pacific, 107, 375, doi: 10.1086/133562

Oke, J. B., Cohen, J. G., Carr, M., et al. 1995, Publications of the Astronomical Society of the Pacific, 107, 375, doi: 10.1086/133562

Omand, C. M. B., Kashiyama, K., & Murase, K. 2018, Monthly Notices of the Royal Astronomical Society, 474, 573, doi: 10.1093/mnras/stx2743

Omand, C. M. B., & Sarin, N. 2024a, Monthly Notices of the Royal Astronomical Society, 527, 6455, doi: 10.1093/mnras/stad3645

—. 2024b, Monthly Notices of the Royal Astronomical Society, 527, 6455, doi: 10.1093/mnras/stad3645

Osterbrock, D. E. 1989, Astrophysics of gaseous nebulae and active galactic nuclei

Ostriker, J. P., & Gunn, J. E. 1971, The Astrophysical Journal Letters, 164, L95, doi: 10.1086/180699

Paczyński, B. 1998, The Astrophysical Journal Letters, 494, L45, doi: 10.1086/311148

Page, K. L., & Swift-XRT Team. 2023, GRB Coordinates Network, 34394, 1

Panaitescu, A., & Kumar, P. 2000, The Astrophysical Journal, 543, 66, doi: 10.1086/317090

—. 2001, The Astrophysical Journal Letters, 560, L49, doi: 10.1086/324061

—. 2002a, The Astrophysical Journal, 571, 779, doi: 10.1086/340094

—. 2002b, The Astrophysical Journal, 571, 779, doi: 10.1086/340094

pandas development team, T. 2020, pandas-dev/pandas: Pandas, latest, Zenodo, doi: 10.5281/zenodo.3509134

Pastorello, A., Smartt, S. J., Mattila, S., et al. 2007, Nature, 447, 829, doi: 10.1038/nature05825

Pastorello, A., Quimby, R. M., Smartt, S. J., et al. 2008, Monthly Notices of the Royal Astronomical Society, 389, 131, doi: 10.1111/j.1365-2966.2008.13603.x

Pastorello, A., Smartt, S. J., Botticella, M. T., et al. 2010, The Astrophysical Journal Letters, 724, L16, doi: 10.1088/2041-8205/724/1/L16

Patat, F., Cappellaro, E., Danziger, J., et al. 2001, The Astrophysical Journal, 555, 900, doi: 10.1086/321526

Patterson, M. T., Bellm, E. C., Rusholme, B., et al. 2019a, Publications of the Astronomical Society of the Pacific, 131, 018001, doi: 10.1088/1538-3873/aae904

—. 2019b, Publications of the Astronomical Society of the Pacific, 131, 018001, doi: 10.1088/1538-3873/aae904

Pélangeon, A., Atteia, J. L., Nakagawa, Y. E., et al. 2008, Astronomy and Astrophysics, 491, 157, doi: 10.1051/0004-6361:200809709

Pellegrin, K., Rumstay, K., & Hartmann, D. 2022, GRB Coordinates Network, 32852, 1

Pellegrino, C., Modjaz, M., Takei, Y., et al. 2024, The Astrophysical Journal, 977, 2, doi: 10.3847/1538-4357/ad8bc5

Perley, D. A. 2019a, Publications of the Astronomical Society of the Pacific, 131, 084503, doi: 10.1088/1538-3873/ab215d

—. 2019b, Publications of the Astronomical Society of the Pacific, 131, 084503, doi: 10.1088/1538-3873/ab215d

Perley, D. A., Cenko, S. B., Corsi, A., et al. 2014, The Astrophysical Journal, 781, 37, doi: 10.1088/0004-637X/781/1/37

Perley, D. A., Mazzali, P. A., Yan, L., et al. 2019, Monthly Notices of the Royal Astronomical Society, 484, 1031, doi: 10.1093/mnras/sty3420

Perley, D. A., Fremling, C., Sollerman, J., et al. 2020, arXiv e-prints, arXiv:2009.01242. https://arxiv.org/abs/2009.01242

Perley, D. A., Ho, A. Y. Q., Fausnaugh, M., et al. 2024, arXiv e-prints, arXiv:2401.16470, doi: 10.48550/arXiv.2401.16470

Perley, R. A., Chandler, C. J., Butler, B. J., & Wrobel, J. M. 2011, The Astrophysical Journal Letters, 739, L1, doi: 10.1088/2041-8205/739/1/L1

Perrott, Y. C., Scaife, A. M. M., Green, D. A., et al. 2013, Monthly Notices of the Royal Astronomical Society, 429, 3330, doi: 10.1093/mnras/sts589

Phillips, M. M. 1993, The Astrophysical Journal Letters, 413, L105, doi: 10.1086/186970

Pian, E., Mazzali, P. A., Masetti, N., et al. 2006, Nature, 442, 1011, doi: 10.1038/nature05082

Piascik, A. S., Steele, I. A., Bates, S. D., et al. 2014, in Society of Photo-Optical Instrumentation Engineers (SPIE) Conference Series, Vol. 9147, Ground-based and Airborne Instrumentation for Astronomy V, ed. S. K. Ramsay, I. S. McLean, & H. Takami, 91478H, doi: 10.1117/12.2055117

Pihlström, Y. M., Taylor, G. B., Granot, J., & Doeleman, S. 2007, The Astrophysical Journal, 664, 411, doi: 10.1086/518955

Piran, T. 2004, Reviews of Modern Physics, 76, 1143, doi: 10.1103/RevModPhys.76.1143

Piro, A. L., Chang, P., & Weinberg, N. N. 2010, The Astrophysical Journal, 708, 598, doi: 10.1088/0004-637X/708/1/598

Piro, A. L., Haynie, A., & Yao, Y. 2021, The Astrophysical Journal, 909, 209, doi: 10.3847/1538-4357/abe2b1

Piro, A. L., & Kollmeier, J. A. 2018, The Astrophysical Journal, 855, 103, doi: 10.3847/1538-4357/aaaab3

Planck Collaboration, Aghanim, N., Akrami, Y., et al. 2020, Astronomy and Astrophysics, 641, A6, doi: 10.1051/0004-6361/201833910

Postigo, A. D. U., Izzo, L., Thoene, C. C., et al. 2022, Transient Name Server Classification Report, 2022-3047, 1

Poznanski, D., Ganeshalingam, M., Silverman, J. M., & Filippenko, A. V. 2011, Monthly Notices of the Royal Astronomical Society, 415, L81, doi: 10.1111/j.1745-3933.2011.01084.x

Prentice, S. J., Mazzali, P. A., Pian, E., et al. 2016, Monthly Notices of the Royal Astronomical Society, 458, 2973, doi: 10.1093/mnras/stw299

Prentice, S. J., Maguire, K., Smartt, S. J., et al. 2018, The Astrophysical Journal Letters, 865, L3, doi: 10.3847/2041-8213/aadd90

Pritchard, T. A., Bensch, K., Modjaz, M., et al. 2021, The Astrophysical Journal, 915, 121, doi: 10.3847/1538-4357/ac00bc

Prochaska, J., Hennawi, J., Westfall, K., et al. 2020a, The Journal of Open Source Software, 5, 2308, doi: 10.21105/joss.02308

Prochaska, J. X., Hennawi, J. F., Westfall, K. B., et al. 2020b, arXiv e-prints, arXiv:2005.06505. https://arxiv.org/abs/2005.06505

Prochaska, J. X., Hennawi, J., Cooke, R., et al. 2019, pypeit/PypeIt: Releasing for DOI, 0.11.0.1, Zenodo, doi: 10.5281/zenodo.3506873

—. 2020c, pypeit/PypeIt: Release 1.0.0, v1.0.0, Zenodo, doi: 10.5281/zenodo.3743493

Prochaska, J. X., Hennawi, J. F., Westfall, K. B., et al. 2020, Journal of Open Source Software, 5, 2308, doi: 10.21105/joss.02308

Pursiainen, M., Childress, M., Smith, M., et al. 2018, Monthly Notices of the Royal Astronomical Society, 481, 894, doi: 10.1093/mnras/sty2309

Quataert, E., & Shiode, J. 2012, Monthly Notices of the Royal Astronomical Society, 423, L92, doi: 10.1111/j.1745-3933.2012.01264.x

Quimby, R. M., Kulkarni, S. R., Kasliwal, M. M., et al. 2011, Nature, 474, 487, doi: 10.1038/nature10095

Quirola-Vásquez, J., Bauer, F. E., Jonker, P. G., et al. 2022, Astronomy and Astrophysics, 663, A168, doi: 10.1051/0004-6361/202243047

—. 2024, Astronomy and Astrophysics, 683, A243, doi: 10.1051/0004-6361/202347629

Quirola-Vásquez, J., Jonker, P. G., Levan, A. J., et al. 2025, arXiv e-prints, arXiv:2511.13314. https://arxiv.org/abs/2511.13314

Rabinak, I., & Waxman, E. 2011, The Astrophysical Journal, 728, 63, doi: 10.1088/0004-637X/728/1/63

Rajabov, Y., Sadibekova, T., Tillayev, Y., et al. 2022, GRB Coordinates Network, 32795, 1

Rastinejad, J., & Fong, W. 2022, GRB Coordinates Network, 32749, 1

Rastinejad, J. C., Gompertz, B. P., Levan, A. J., et al. 2022, Nature, 612, 223, doi: 10.1038/s41586-022-05390-w

Rastinejad, J. C., Levan, A. J., Jonker, P. G., et al. 2025, arXiv e-prints, arXiv:2504.08889. https://arxiv.org/abs/2504.08889

Ravasio, M. E., Burns, E., Jonker, P. G., & Fermi-GBM Team. 2025a, GRB Coordinates Network, 39600, 1

Ravasio, M. E., Burns, E., Wilson-Hodge, C., Jonker, P. G., & Fermi-GBM Team. 2025b, GRB Coordinates Network, 39146, 1

Rho, J., Evans, A., Geballe, T. R., et al. 2021, The Astrophysical Journal, 908, 232, doi: 10.3847/1538-4357/abd850

Rhoads, J. E. 1997, The Astrophysical Journal Letters, 487, L1, doi: 10.1086/310876

Rhodes, L., van der Horst, A. J., Fender, R., et al. 2022, Monthly Notices of the Royal Astronomical Society, 513, 1895, doi: 10.1093/mnras/stac1057

Rhodes, L., van der Horst, A. J., Bright, J. S., et al. 2024, Monthly Notices of the Royal Astronomical Society, 533, 4435, doi: 10.1093/mnras/stae2050

Ricci, R., Troja, E., Yang, Y.-H., et al. 2025, The Astrophysical Journal Letters, 979, L28, doi: 10.3847/2041-8213/ad8b3f

Richardson, D., Jenkins, Robert L., I., Wright, J., & Maddox, L. 2014, The Astronomical Journal, 147, 118, doi: 10.1088/0004-6256/147/5/118

Rigault, M. 2018, ztfquery, a python tool to access ZTF data, doi, Zenodo, doi: 10.5281/zenodo.1345222

Rigault, M., Neill, J. D., Blagorodnova, N., et al. 2019a, Astronomy and Astrophysics, 627, A115, doi: 10.1051/0004-6361/201935344

—. 2019b, Astronomy and Astrophysics, 627, A115, doi: 10.1051/0004-6361/201935344

Rivera Sandoval, L. E., Maccarone, T. J., Corsi, A., et al. 2018, Monthly Notices of the Royal Astronomical Society, 480, L146, doi: 10.1093/mnrasl/sly145

Roberson, M. S., Fremling, C., & Kasliwal, M. M. 2021, DBSP_DRP: DBSP Data Reduction Pipeline, Astrophysics Source Code Library, record ascl:2108.020

Roberts, O. J., Bala, S., Meegan, C., & Fermi GBM Team. 2023, GRB Coordinates Network, 34748

Rodríguez, Ó., Maoz, D., & Nakar, E. 2023a, The Astrophysical Journal, 955, 71, doi: 10.3847/1538-4357/ace2bd

—. 2023b, The Astrophysical Journal, 955, 71, doi: 10.3847/1538-4357/ace2bd

Rodríguez, Ó., Nakar, E., & Maoz, D. 2024a, Nature, 628, 733, doi: 10.1038/s41586-024-07262-x

—. 2024b, Nature, 628, 733, doi: 10.1038/s41586-024-07262-x

Roman Aguilar, L. M., & Bersten, M. C. 2025, Astronomy and Astrophysics, 702, L18, doi: 10.1051/0004-6361/202556610

Roming, P. W. A., Kennedy, T. E., Mason, K. O., et al. 2005a, Space Science Reviews, 120, 95, doi: 10.1007/s11214-005-5095-4

—. 2005b, Space Science Reviews, 120, 95, doi: 10.1007/s11214-005-5095-4

Rossi, A., Maiorano, E., Malesani, D. B., et al. 2022a, GRB Coordinates Network, 32809, 1

Rossi, A., Piranomonte, S., Savaglio, S., et al. 2014, Astronomy and Astrophysics, 572, A47, doi: 10.1051/0004-6361/201423865

Rossi, A., Rothberg, B., Palazzi, E., et al. 2022b, The Astrophysical Journal, 932, 1, doi: 10.3847/1538-4357/ac60a2

Rossi, E. M., Perna, R., & Daigne, F. 2008, Monthly Notices of the Royal Astronomical Society, 390, 675, doi: 10.1111/j.1365-2966.2008.13736.x

Rowlinson, A., O'Brien, P. T., Metzger, B. D., Tanvir, N. R., & Levan, A. J. 2013, Monthly Notices of the Royal Astronomical Society, 430, 1061, doi: 10.1093/mnras/sts683

Ryan, G., van Eerten, H., MacFadyen, A., & Zhang, B.-B. 2015, The Astrophysical Journal, 799, 3, doi: 10.1088/0004-637X/799/1/3

Ryan, G., van Eerten, H., Piro, L., & Troja, E. 2020a, The Astrophysical Journal, 896, 166, doi: 10.3847/1538-4357/ab93cf10.48550/arXiv.1909.11691

—. 2020b, The Astrophysical Journal, 896, 166, doi: 10.3847/1538-4357/ab93cf

Ryan, G., van Eerten, H., Troja, E., et al. 2023, arXiv e-prints, arXiv:2310.02328, doi: 10.48550/arXiv.2310.02328

Sakamoto, T., Lamb, D. Q., Kawai, N., et al. 2005, The Astrophysical Journal, 629, 311, doi: 10.1086/431235

Salafia, O. S., Ghisellini, G., Pescalli, A., Ghirlanda, G., & Nappo, F. 2015, Monthly Notices of the Royal Astronomical Society, 450, 3549, doi: 10.1093/mnras/stv766

Salgundi, A., Swain, V., Kumar, H., et al. 2023, GRB Coordinates Network, 34397, 1

Sanders, N. E., Soderberg, A. M., Levesque, E. M., et al. 2012, The Astrophysical Journal, 758, 132, doi: 10.1088/0004-637X/758/2/132

Sapir, N., & Waxman, E. 2017, The Astrophysical Journal, 838, 130, doi: 10.3847/1538-4357/aa64df

Saraogi, D., Aditya, J. V., Bhalerao, V., et al. 2024, Monthly Notices of the Royal Astronomical Society, 530, 1386, doi: 10.1093/mnras/stae435

Sari, R., Piran, T., & Halpern, J. P. 1999, The Astrophysical Journal Letters, 519, L17, doi: 10.1086/312109

Sari, R., Piran, T., & Narayan, R. 1998, The Astrophysical Journal Letters, 497, L17, doi: 10.1086/311269

Sarin, N., Ashton, G., Lasky, P. D., et al. 2021, arXiv e-prints, arXiv:2105.10108, doi: 10.48550/arXiv.2105.10108

Sarin, N., Hamburg, R., Burns, E., et al. 2022, Monthly Notices of the Royal Astronomical Society, 512, 1391, doi: 10.1093/mnras/stac601

Sarin, N., Hübner, M., Omand, C. M. B., et al. 2023, arXiv e-prints, arXiv:2308.12806, doi: 10.48550/arXiv.2308.12806

—. 2024, Monthly Notices of the Royal Astronomical Society, 531, 1203, doi: 10.1093/mnras/stae1238

Sato, Y., Murase, K., Ohira, Y., & Yamazaki, R. 2023, Monthly Notices of the Royal Astronomical Society, 522, L56, doi: 10.1093/mnrasl/slad038

Sato, Y., Obayashi, K., Yamazaki, R., Murase, K., & Ohira, Y. 2021, Monthly Notices of the Royal Astronomical Society, 504, 5647, doi: 10.1093/mnras/stab1273

Sauer, D. N., Mazzali, P. A., Deng, J., et al. 2006, Monthly Notices of the Royal Astronomical Society, 369, 1939, doi: 10.1111/j.1365-2966.2006.10438.x

Schady, P., Dwelly, T., Page, M. J., et al. 2012, Astronomy and Astrophysics, 537, A15, doi: 10.1051/0004-6361/201117414

Schlafly, E. F., & Finkbeiner, D. P. 2011a, The Astrophysical Journal, 737, 103, doi: 10.1088/0004-637X/737/2/103

—. 2011b, The Astrophysical Journal, 737, 103, doi: 10.1088/0004-637X/737/2/103

Schmidt, M. 2001, The Astrophysical Journal, 552, 36, doi: 10.1086/320450

Schneider, B., Adami, C., Le Floc'h, E., et al. 2022, GRB Coordinates Network, 32753, 1

Schroeder, G., Ho, A., & Perley, D. 2025a, GRB Coordinates Network, 38970, 1

Schroeder, G., Ho, A. Y. Q., Dastidar, R. G., et al. 2025b, arXiv e-prints, arXiv:2507.15928, doi: 10.48550/arXiv.2507.15928

Schroeder, G., Laskar, T., Fong, W.-f., et al. 2022, The Astrophysical Journal, 940, 53, doi: 10.3847/1538-4357/ac8feb

Schroeder, G., Ahumada, T., Ho, A. Y. Q., et al. 2025c, GRB Coordinates Network, 41635, 1

Schulze, S., Klose, S., Björnsson, G., et al. 2011, Astronomy and Astrophysics, 526, A23, doi: 10.1051/0004-6361/201015581

Schulze, S., Malesani, D., Cucchiara, A., et al. 2014, Astronomy and Astrophysics, 566, A102, doi: 10.1051/0004-6361/201423387

Schulze, S., Yaron, O., Sollerman, J., et al. 2021, The Astrophysical Journal Supplement, 255, 29, doi: 10.3847/1538-4365/abff5e

Scotton, L., Kocevski, D., Racusin, J., Omodei, N., & Fermi-LAT Collaboration. 2023, GRB Coordinates Network, 34392, 1

Shankar, S., Mösta, P., Barnes, J., Duffell, P. C., & Kasen, D. 2021, Monthly Notices of the Royal Astronomical Society, 508, 5390, doi: 10.1093/mnras/stab2964

Sharma, Y., Marathe, A., Bhalerao, V., et al. 2021, Journal of Astrophysics and Astronomy, 42, 73, doi: 10.1007/s12036-021-09714-6

Shiode, J. H., & Quataert, E. 2014, The Astrophysical Journal, 780, 96, doi: 10.1088/0004-637X/780/1/96

Shivvers, I., Modjaz, M., Zheng, W., et al. 2017, Publications of the Astronomical Society of the Pacific, 129, 054201, doi: 10.1088/1538-3873/aa54a6

Shrestha, M., Bostroem, K., Sand, D., et al. 2022, GRB Coordinates Network, 32771, 1

Shrestha, M., Sand, D. J., Alexander, K. D., et al. 2023, arXiv e-prints, arXiv:2302.03829, doi: 10.48550/arXiv.2302.03829

Shu, X., Yang, L., Yang, H., et al. 2025, The Astrophysical Journal Letters, 990, L29, doi: 10.3847/2041-8213/adf4cd

Shvartzvald, Y., Waxman, E., Gal-Yam, A., et al. 2024, The Astrophysical Journal, 964, 74, doi: 10.3847/1538-4357/ad2704

Skrutskie, M. F., Cutri, R. M., Stiening, R., et al. 2006, The Astronomical Journal, 131, 1163, doi: 10.1086/498708

Smartt, S. J., Valenti, S., Fraser, M., et al. 2015, Astronomy and Astrophysics, 579, A40, doi: 10.1051/0004-6361/201425237

Smith, R. J., Piascik, A. S., Steele, I. A., & Barnsley, R. M. 2016, in Society of Photo-Optical Instrumentation Engineers (SPIE) Conference Series, Vol. 9913, Software and Cyberinfrastructure for Astronomy IV, ed. G. Chiozzi & J. C. Guzman, 991317, doi: 10.1117/12.2232771

Soderberg, A. M., Nakar, E., Berger, E., & Kulkarni, S. R. 2006a, The Astrophysical Journal, 638, 930, doi: 10.1086/499121

Soderberg, A. M., Kulkarni, S. R., Berger, E., et al. 2004, The Astrophysical Journal, 606, 994, doi: 10.1086/383082

Soderberg, A. M., Kulkarni, S. R., Fox, D. B., et al. 2005, The Astrophysical Journal, 627, 877, doi: 10.1086/430405

Soderberg, A. M., Kulkarni, S. R., Nakar, E., et al. 2006b, Nature, 442, 1014, doi: 10.1038/nature05087

Soderberg, A. M., Berger, E., Page, K. L., et al. 2008, Nature, 453, 469, doi: 10.1038/nature06997

Sollerman, J., Kozma, C., Fransson, C., et al. 2000, The Astrophysical Journal Letters, 537, L127, doi: 10.1086/312763

Sollerman, J., Yang, S., Perley, D., et al. 2022, Astronomy and Astrophysics, 657, A64, doi: 10.1051/0004-6361/202142049

Sollerman, J., Jaunsen, A. O., Fynbo, J. P. U., et al. 2006, Astronomy and Astrophysics, 454, 503, doi: 10.1051/0004-6361:20065226

Speagle, J. S. 2020, Monthly Notices of the Royal Astronomical Society, 493, 3132, doi: 10.1093/mnras/staa278

Srinivasaragavan, G. P., O'Connor, B., Cenko, S. B., et al. 2023, The Astrophysical Journal Letters, 949, L39, doi: 10.3847/2041-8213/accf97

Srinivasaragavan, G. P., Swain, V., O'Connor, B., et al. 2024a, The Astrophysical Journal Letters, 960, L18, doi: 10.3847/2041-8213/ad16e7

Srinivasaragavan, G. P., Yang, S., Anand, S., et al. 2024b, The Astrophysical Journal, 976, 71, doi: 10.3847/1538-4357/ad7fde

Srinivasaragavan, G. P., Hamidani, H., Schroeder, G., et al. 2025a, The Astrophysical Journal Letters, 988, L60, doi: 10.3847/2041-8213/ade870

Srinivasaragavan, G. P., Perley, D. A., Ho, A. Y. Q., et al. 2025b, Monthly Notices of the Royal Astronomical Society, 538, 351, doi: 10.1093/mnras/staf290

Srinivasaragavan, G. P., Li, D., Hall, X. J., et al. 2025c, arXiv e-prints, arXiv:2512.10239, doi: 10.48550/arXiv.2512.10239

Srivastav, S., Chen, T. W., Gillanders, J. H., et al. 2024, arXiv e-prints, arXiv:2409.19070, doi: 10.48550/arXiv.2409.19070

—. 2025, The Astrophysical Journal Letters, 978, L21, doi: 10.3847/2041-8213/ad9c75

Stalder, B., Tonry, J., Smartt, S. J., et al. 2017, The Astrophysical Journal, 850, 149, doi: 10.3847/1538-4357/aa95c1

Stanek, K. Z., & Kochanek, C. S. 2020, Transient Name Server Discovery Report, 2020-3922, 1

Starling, R. L. C., Wiersema, K., Levan, A. J., et al. 2011, Monthly Notices of the Royal Astronomical Society, 411, 2792, doi: 10.1111/j.1365-2966.2010.17879.x

Steele, I. A., Smith, R. J., Rees, P. C., et al. 2004, in Society of Photo-Optical Instrumentation Engineers (SPIE) Conference Series, Vol. 5489, Ground-based Telescopes, ed. J. Oschmann, Jacobus M., 679–692, doi: 10.1117/12.551456

Stern, D., Assef, R. J., Benford, D. J., et al. 2012, The Astrophysical Journal, 753, 30, doi: 10.1088/0004-637X/753/1/30

Stritzinger, M. D., Hamuy, M., Suntzeff, N. B., et al. 2002, in American Astronomical Society Meeting Abstracts, Vol. 200, American Astronomical Society Meeting Abstracts #200, 95.03

Stritzinger, M. D., Taddia, F., Burns, C. R., et al. 2018, Astronomy and Astrophysics, 609, A135, doi: 10.1051/0004-6361/201730843

Sun, H., Zhang, B., & Gao, H. 2017, The Astrophysical Journal, 835, 7, doi: 10.3847/1538-4357/835/1/7

Sun, H., Zhang, B., & Li, Z. 2015, The Astrophysical Journal, 812, 33, doi: 10.1088/0004-637X/812/1/33

Sun, H., Li, W. X., Liu, L. D., et al. 2024, arXiv e-prints, arXiv:2410.02315, doi: 10.48550/arXiv.2410.02315

Sun, H., Wang, C.-W., Yang, J., et al. 2025, National Science Review, 12, nwae401, doi: 10.1093/nsr/nwae401

Suzuki, A., Irwin, C. M., & Maeda, K. 2024, , 76, 863, doi: 10.1093/pasj/psae055

Suzuki, A., & Maeda, K. 2017, Monthly Notices of the Royal Astronomical Society, 466, 2633, doi: 10.1093/mnras/stw3259

—. 2022, The Astrophysical Journal, 925, 148, doi: 10.3847/1538-4357/ac3d8d

Tachibana, Y., & Miller, A. A. 2018a, Publications of the Astronomical Society of the Pacific, 130, 128001, doi: 10.1088/1538-3873/aae3d9

—. 2018b, Publications of the Astronomical Society of the Pacific, 130, 128001, doi: 10.1088/1538-3873/aae3d9

Taddia, F., Sollerman, J., Leloudas, G., et al. 2015, Astronomy and Astrophysics, 574, A60, doi: 10.1051/0004-6361/201423915

Taddia, F., Stritzinger, M. D., Bersten, M., et al. 2018, Astronomy and Astrophysics, 609, A136, doi: 10.1051/0004-6361/201730844

Taddia, F., Sollerman, J., Fremling, C., et al. 2019a, Astronomy and Astrophysics, 621, A71, doi: 10.1051/0004-6361/201834429

—. 2019b, Astronomy and Astrophysics, 621, A71, doi: 10.1051/0004-6361/201834429

Taghizadeh-Popp, M., Kim, J. W., Lemson, G., et al. 2020, Astronomy and Computing, 33, 100412, doi: 10.1016/j.ascom.2020.100412

Tan, J. C., Matzner, C. D., & McKee, C. F. 2001, The Astrophysical Journal, 551, 946, doi: 10.1086/320245

Tanga, M., Krühler, T., Schady, P., et al. 2018, Astronomy and Astrophysics, 615, A136, doi: 10.1051/0004-6361/201731799

Tanvir, N. R., Rol, E., Levan, A. J., et al. 2010, The Astrophysical Journal, 725, 625, doi: 10.1088/0004-637X/725/1/625

Tartaglia, L., Sollerman, J., Barbarino, C., et al. 2021, Astronomy and Astrophysics, 650, A174, doi: 10.1051/0004-6361/202039068

Taylor, G. B., Frail, D. A., Berger, E., & Kulkarni, S. R. 2004, The Astrophysical Journal Letters, 609, L1, doi: 10.1086/422554

Taylor, G. B., Momjian, E., Pihlström, Y., Ghosh, T., & Salter, C. 2005, The Astrophysical Journal, 622, 986, doi: 10.1086/428346

Thompson, C., & Duncan, R. C. 1993, The Astrophysical Journal, 408, 194, doi: 10.1086/172580

Thomsen, B., Hjorth, J., Watson, D., et al. 2004, Astronomy and Astrophysics, 419, L21, doi: 10.1051/0004-6361:20040133

Tiengo, A., Pintore, F., Vaia, B., et al. 2023, arXiv e-prints, arXiv:2302.11518, doi: 10.48550/arXiv.2302.11518

Tody, D. 1986, in Society of Photo-Optical Instrumentation Engineers (SPIE) Conference Series, Vol. 627, Instrumentation in astronomy VI, ed. D. L. Crawford, 733, doi: 10.1117/12.968154

Toma, K., Ioka, K., Sakamoto, T., & Nakamura, T. 2007, The Astrophysical Journal, 659, 1420, doi: 10.1086/512481

Tominaga, N., Deng, J., Mazzali, P. A., et al. 2004, The Astrophysical Journal Letters, 612, L105, doi: 10.1086/424841

Tonry, J., Denneau, L., Heinze, A., et al. 2019, Transient Name Server Discovery Report, 2019-1623, 1

—. 2020, Transient Name Server Discovery Report, 2020-3692, 1

—. 2021a, Transient Name Server Discovery Report, 2021-771, 1

—. 2021b, Transient Name Server Discovery Report, 2021-1406, 1

Tonry, J. L., Denneau, L., Heinze, A. N., et al. 2018, Publications of the Astronomical Society of the Pacific, 130, 064505, doi: 10.1088/1538-3873/aabadf

Toy, V. L., Cenko, S. B., Silverman, J. M., et al. 2016, The Astrophysical Journal, 818, 79, doi: 10.3847/0004-637X/818/1/79

Troja, E., Piro, L., Ryan, G., et al. 2018, Monthly Notices of the Royal Astronomical Society, 478, L18, doi: 10.1093/mnrasl/sly061

Troja, E., van Eerten, H., Ryan, G., et al. 2019, Monthly Notices of the Royal Astronomical Society, 489, 1919, doi: 10.1093/mnras/stz2248

Troja, E., Fryer, C. L., O'Connor, B., et al. 2022, Nature, 612, 228, doi: 10.1038/s41586-022-05327-3

Trotta, R. 2008, Contemporary Physics, 49, 71, doi: 10.1080/00107510802066753

Tsvetkova, A., Frederiks, D., Svinkin, D., et al. 2021, The Astrophysical Journal, 908, 83, doi: 10.3847/1538-4357/abd569

Tucker, M. A. 2021a, Transient Name Server Classification Report, 2021-865, 1

—. 2021b, Transient Name Server Classification Report, 2021-1718, 1

Urata, Y., Huang, K., Yamazaki, R., & Sakamoto, T. 2015, The Astrophysical Journal, 806, 222, doi: 10.1088/0004-637X/806/2/222

Usov, V. V. 1992, Nature, 357, 472, doi: 10.1038/357472a0

Vail, J. L., Li, M. L., Wise, J., et al. 2023, GRB Coordinates Network, 34730

Valenti, S., Benetti, S., Cappellaro, E., et al. 2008, Monthly Notices of the Royal Astronomical Society, 383, 1485, doi: 10.1111/j.1365-2966.2007.12647.x

van Dalen, J. N. D., Levan, A. J., Jonker, P. G., et al. 2024, arXiv e-prints, arXiv:2409.19056, doi: 10.48550/arXiv.2409.19056

—. 2025, The Astrophysical Journal Letters, 982, L47, doi: 10.3847/2041-8213/adbc7e

van der Horst, A. J., Paragi, Z., de Bruyn, A. G., et al. 2014, Monthly Notices of the Royal Astronomical Society, 444, 3151, doi: 10.1093/mnras/stu1664

van der Walt, S. J., Crellin-Quick, A., & Bloom, J. S. 2019a, Journal of Open Source Software, 4, doi: 10.21105/joss.01247

—. 2019b, Journal of Open Source Software, 4, doi: 10.21105/joss.01247

van Dokkum, P. G. 2001, Publications of the Astronomical Society of the Pacific, 113, 1420, doi: 10.1086/323894

van Eerten, H., Zhang, W., & MacFadyen, A. 2010, The Astrophysical Journal, 722, 235, doi: 10.1088/0004-637X/722/1/235

van Paradijs, J., Kouveliotou, C., & Wijers, R. A. M. J. 2000, Annual Review of Astronomy and Astrophysics, 38, 379, doi: 10.1146/annurev.astro.38.1.379

Vinko, J., Bodi, A., Pal, A., et al. 2022, GRB Coordinates Network, 32709, 1

Virgili, F. J., Liang, E.-W., & Zhang, B. 2009a, Monthly Notices of the Royal Astronomical Society, 392, 91, doi: 10.1111/j.1365-2966.2008.14063.x

—. 2009b, Monthly Notices of the Royal Astronomical Society, 392, 91, doi: 10.1111/j.1365-2966.2008.14063.x

Virtanen, P., Gommers, R., Oliphant, T. E., et al. 2020, Nature Methods, 17, 261, doi: 10.1038/s41592-019-0686-2

Walker, M. A. 1998, Monthly Notices of the Royal Astronomical Society, 294, 307, doi: 10.1046/j.1365-8711.1998.01238.x10.1111/j.1365-8711.1998.01238.x

—. 2001, Monthly Notices of the Royal Astronomical Society, 321, 176, doi: 10.1046/j.1365-8711.2001.04104.x

Wang, J., Zhu, Z. P., Xu, D., et al. 2018, The Astrophysical Journal, 867, 147, doi: 10.3847/1538-4357/aae6c3

Wang, X.-G., Zhang, B., Liang, E.-W., et al. 2015, The Astrophysical Journal Supplement, 219, 9, doi: 10.1088/0067-0049/219/1/9

Waxman, E., & Katz, B. 2017, in Handbook of Supernovae, ed. A. W. Alsabti & P. Murdin, 967, doi: 10.1007/978-3-319-21846-5_33

Waxman, E., Kulkarni, S. R., & Frail, D. A. 1998, The Astrophysical Journal, 497, 288, doi: 10.1086/305467

Weaver, T. A. 1976, The Astrophysical Journal Supplement, 32, 233, doi: 10.1086/190398

Wei, J., Cordier, B., Antier, S., et al. 2016a, arXiv e-prints, arXiv:1610.06892, doi: 10.48550/arXiv.1610.06892

—. 2016b, arXiv e-prints, arXiv:1610.06892, doi: 10.48550/arXiv.1610.06892

Weiler, K. W., Panagia, N., & Montes, M. J. 2001, The Astrophysical Journal, 562, 670, doi: 10.1086/322359

Whitesides, L., Lunnan, R., Kasliwal, M. M., et al. 2017, The Astrophysical Journal, 851, 107, doi: 10.3847/1538-4357/aa99de

Williams, M. A., Kennea, J. A., Dichiara, S., et al. 2023, arXiv e-prints, arXiv:2302.03642, doi: 10.48550/arXiv.2302.03642

Williams, P. K. G., Clavel, M., Newton, E., & Ryzhkov, D. 2017, pwkit: Astronomical utilities in Python, Astrophysics Source Code Library, record ascl:1704.001

Williamson, M., Modjaz, M., & Bianco, F. 2019

Willingale, R., Starling, R. L. C., Beardmore, A. P., Tanvir, N. R., & O'Brien, P. T. 2013, Monthly Notices of the Royal Astronomical Society, 431, 394, doi: 10.1093/mnras/stt175

Wilms, J., Allen, A., & McCray, R. 2000a, The Astrophysical Journal, 542, 914, doi: 10.1086/317016

—. 2000b, The Astrophysical Journal, 542, 914, doi: 10.1086/317016

Woosley, S. E. 1993, The Astrophysical Journal, 405, 273, doi: 10.1086/172359

—. 2010, The Astrophysical Journal Letters, 719, L204, doi: 10.1088/2041-8205/719/2/L204

Woosley, S. E., & Bloom, J. S. 2006, Annual Review of Astronomy and Astrophysics, 44, 507, doi: 10.1146/annurev.astro.43.072103.150558

Woosley, S. E., Heger, A., & Weaver, T. A. 2002, Reviews of Modern Physics, 74, 1015, doi: 10.1103/RevModPhys.74.1015

Woosley, S. E., Langer, N., & Weaver, T. A. 1995, The Astrophysical Journal, 448, 315, doi: 10.1086/175963

Woosley, S. E., & Weaver, T. A. 1986, in NATO Advanced Study Institute (ASI) Series C, Vol. 163, Nucleosynthesis and its Implications on Nuclear and Particle Physics, ed. J. Audouze & N. Mathieu, 145–166

Woosley, S. E., Zhang, W., & Heger, A. 2003, in From Twilight to Highlight: The Physics of Supernovae, ed. W. Hillebrandt & B. Leibundgut, 87, doi: 10.1007/10828549_13

Wu, G.-L., Yu, Y.-W., Liu, L.-D., et al. 2025, arXiv e-prints, arXiv:2505.12491, doi: 10.48550/arXiv.2505.12491

Wu, S., & Fuller, J. 2021, The Astrophysical Journal, 906, 3, doi: 10.3847/1538-4357/abc87c

Xie, X., & MacFadyen, A. 2019, The Astrophysical Journal, 880, 135, doi: 10.3847/1538-4357/ab2912

Xu, F., Huang, Y.-F., & Geng, J.-J. 2023, Astronomy and Astrophysics, 679, A103, doi: 10.1051/0004-6361/202346674

Xue, Y. Q., Zheng, X. C., Li, Y., et al. 2019, Nature, 568, 198, doi: 10.1038/s41586-019-1079-5

Yadav, M., Troja, E., Ricci, R., et al. 2025, arXiv e-prints, arXiv:2505.08781, doi: 10.48550/arXiv.2505.08781

Yamazaki, R., Yonetoku, D., & Nakamura, T. 2003, The Astrophysical Journal Letters, 594, L79, doi: 10.1086/378736

Yang, J., Ai, S., Zhang, B.-B., et al. 2022, Nature, 612, 232, doi: 10.1038/s41586-022-05403-8

Yang, S., & Sollerman, J. 2023, arXiv e-prints, arXiv:2302.02082, doi: 10.48550/arXiv.2302.02082

Yang, Y.-H., Troja, E., O'Connor, B., et al. 2023, arXiv e-prints, arXiv:2308.00638, doi: 10.48550/arXiv.2308.00638

Yao, Y., Lu, W., Harrison, F., et al. 2024, The Astrophysical Journal, 965, 39, doi: 10.3847/1538-4357/ad2b6b

Yaron, O., & Gal-Yam, A. 2012, Publications of the Astronomical Society of the Pacific, 124, 668, doi: 10.1086/666656

Ye, X.-M., Wei, D.-M., Zhu, Y.-M., & Jin, Z.-P. 2024, Research in Astronomy and Astrophysics, 24, 045011, doi: 10.1088/1674-4527/ad2b39

Yin, Y.-H. I., Zhang, B.-B., Yang, J., et al. 2024, The Astrophysical Journal Letters, 975, L27, doi: 10.3847/2041-8213/ad8652

Yoon, S. C., Woosley, S. E., & Langer, N. 2010a, The Astrophysical Journal, 725, 940, doi: 10.1088/0004-637X/725/1/940

Yoon, S.-C., Woosley, S. E., & Langer, N. 2010b, The Astrophysical Journal, 725, 940, doi: 10.1088/0004-637X/725/1/940

Yost, S. A., Harrison, F. A., Sari, R., & Frail, D. A. 2003, The Astrophysical Journal, 597, 459, doi: 10.1086/378288

Yu, Y.-W., Zhang, B., & Gao, H. 2013, The Astrophysical Journal Letters, 776, L40, doi: 10.1088/2041-8205/776/2/L40

Yuan, W., Zhang, C., Chen, Y., & Ling, Z. 2022a, in Handbook of X-ray and Gamma-ray Astrophysics, 86, doi: 10.1007/978-981-16-4544-0_151-1

—. 2022b, in Handbook of X-ray and Gamma-ray Astrophysics, ed. C. Bambi & A. Sangangelo, 86, doi: 10.1007/978-981-16-4544-0_151-1

Yuan, W., Zhang, C., Feng, H., et al. 2015, arXiv e-prints, arXiv:1506.07735, doi: 10.48550/arXiv.1506.07735

Yuan, W., Zhang, C., Ling, Z., et al. 2018, in Society of Photo-Optical Instrumentation Engineers (SPIE) Conference Series, Vol. 10699, Space Telescopes and Instrumentation 2018: Ultraviolet to Gamma Ray, ed. J.-W. A. den Herder, S. Nikzad, & K. Nakazawa, 1069925, doi: 10.1117/12.2313358

Yuan, W., Dai, L., Feng, H., et al. 2025, arXiv e-prints, arXiv:2501.07362, doi: 10.48550/arXiv.2501.07362

Zackay, B., Ofek, E. O., & Gal-Yam, A. 2016, The Astrophysical Journal, 830, 27, doi: 10.3847/0004-637X/830/1/27

Zackay, B., Ofek, E. O., & Gal-Yam, A. 2016, ApJ, 830, 27, doi: 10.3847/0004-637x/830/1/27

Zhang, B. 2013, The Astrophysical Journal Letters, 763, L22, doi: 10.1088/2041-8205/763/1/L22

Zhang, B., & Mészáros, P. 2001, The Astrophysical Journal, 559, 110, doi: 10.1086/322400

Zhang, T., Li, W., Tan, H., et al. 2019, Transient Name Server Discovery Report, 2019-1699, 1

Zhang, W., Yuan, W., Ling, Z., et al. 2025, Science China Physics, Mechanics, and Astronomy, 68, 219511, doi: 10.1007/s11433-024-2524-4

Zhang, Z.-D., Yu, Y.-W., & Liu, L.-D. 2022, The Astrophysical Journal, 936, 54, doi: 10.3847/1538-4357/ac8548

Zheltoukhov, S., Dodin, A., Tatarnikov, A., et al. 2020, Transient Name Server Classification Report, 2020-3946, 1

Zheng, J.-H., Zhu, J.-P., Lu, W., & Zhang, B. 2025, arXiv e-prints, arXiv:2503.24266, doi: 10.48550/arXiv.2503.24266

Zheng, W., Filippenko, A. V., & KAIT GRB team. 2023a, GRB Coordinates Network, 34395, 1

—. 2023b, GRB Coordinates Network, 34395, 1

Zhu, J.-P., Zheng, J.-H., & Zhang, B. 2025a, arXiv e-prints, arXiv:2507.18544, doi: 10.48550/arXiv.2507.18544

Zhu, Z. P., Liu, X., Fu, S. Y., et al. 2025b, GRB Coordinates Network, 38885, 1

Zhu, Z. P., Corcoran, G., Levan, A. J., et al. 2025c, GRB Coordinates Network, 38908, 1

—. 2025d, GRB Coordinates Network, 38908, 1

Zou, X., Liu, C., Kumar, B., et al. 2025, GRB Coordinates Network, 38914, 1

Zwart, J. T. L., Barker, R. W., Biddulph, P., et al. 2008, Monthly Notices of the Royal Astronomical Society, 391, 1545, doi: 10.1111/j.1365-2966.2008.13953.x